ACOUSTICALLY MAPPING THE OCEAN

EDITED BY: Kathy Gunn, Katy Sheen and Qunshu Tang
PUBLISHED IN: Frontiers in Marine Science

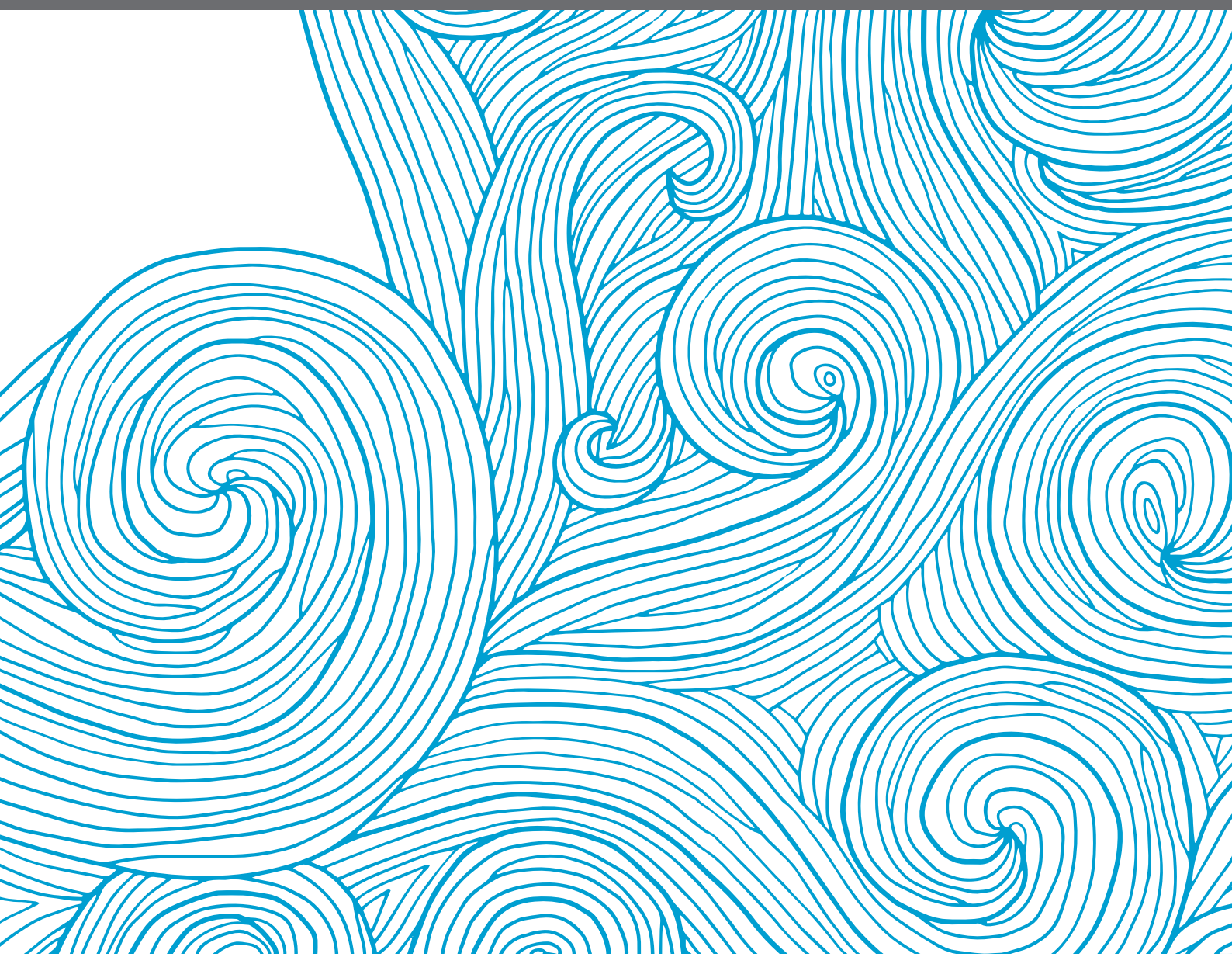

frontiers Research Topics

ISSN 1664-8714
ISBN 978-2-88976-724-3
DOI 10.3389/978-2-88976-724-3

About Frontiers

Frontiers is more than just an open-access publisher of scholarly articles: it is a pioneering approach to the world of academia, radically improving the way scholarly research is managed. The grand vision of Frontiers is a world where all people have an equal opportunity to seek, share and generate knowledge. Frontiers provides immediate and permanent online open access to all its publications, but this alone is not enough to realize our grand goals.

Frontiers Journal Series

The Frontiers Journal Series is a multi-tier and interdisciplinary set of open-access, online journals, promising a paradigm shift from the current review, selection and dissemination processes in academic publishing. All Frontiers journals are driven by researchers for researchers; therefore, they constitute a service to the scholarly community. At the same time, the Frontiers Journal Series operates on a revolutionary invention, the tiered publishing system, initially addressing specific communities of scholars, and gradually climbing up to broader public understanding, thus serving the interests of the lay society, too.

Dedication to Quality

Each Frontiers article is a landmark of the highest quality, thanks to genuinely collaborative interactions between authors and review editors, who include some of the world's best academicians. Research must be certified by peers before entering a stream of knowledge that may eventually reach the public - and shape society; therefore, Frontiers only applies the most rigorous and unbiased reviews.
Frontiers revolutionizes research publishing by freely delivering the most outstanding research, evaluated with no bias from both the academic and social point of view. By applying the most advanced information technologies, Frontiers is catapulting scholarly publishing into a new generation.

What are Frontiers Research Topics?

Frontiers Research Topics are very popular trademarks of the Frontiers Journals Series: they are collections of at least ten articles, all centered on a particular subject. With their unique mix of varied contributions from Original Research to Review Articles, Frontiers Research Topics unify the most influential researchers, the latest key findings and historical advances in a hot research area! Find out more on how to host your own Frontiers Research Topic or contribute to one as an author by contacting the Frontiers Editorial Office: frontiersin.org/about/contact

ACOUSTICALLY MAPPING THE OCEAN

Topic Editors:
Kathy Gunn, Oceans and Atmosphere (CSIRO), Australia
Katy Sheen, University of Exeter, United Kingdom
Qunshu Tang, Zhejiang University, China

Citation: Gunn, K., Sheen, K., Tang, Q., eds. (2022). Acoustically Mapping the Ocean. Lausanne: Frontiers Media SA. doi: 10.3389/978-2-88976-724-3

Table of Contents

frontiers | Frontiers in Marine Science

EDITORIAL
published: 11 July 2022
doi: 10.3389/fmars.2022.961282

Editorial: Acoustically Mapping the Ocean

Kathryn L. Gunn[1*], *Katy L. Sheen*[2] *and Qunshu Tang*[3]

[1] The Commonwealth Scientific and Industrial Research Organisation (CSIRO) Oceans and Atmosphere, Hobart, TAS, Australia , [2] University of Exeter, Penryn, United Kingdom, [3] Ocean College of Zhejiang University, Zhoushan, China

Keywords: seismic oceanography (SO), diapycnal diffusivity, inversion (seismic), ocean front dynamics, internal wave (IWs)

Editorial on the Research Topic

Acoustically Mapping the Ocean

Acoustic oceanography can address ocean observing needs, but it is not yet a standard observational tool. Sound remotely senses the ocean, as it travels further and faster than any other signal underwater.

Since this potential was first recognized in the late 20th century, acoustic oceanography has primarily been used to map the ocean floor using frequencies of 10-100 kHz. These high frequencies have also been turned toward investigating physical and biological oceanographic questions. For example, the strong relationship between demersal fish species – those that live close to the seafloor – and seabed depth has been used to map fish distributions, which is not possible with direct observations. In this Research Topic, Landero Figueroa et al. examine the effectiveness of demersal fish species models; they confirm that depth is the primary variable explaining their distribution, whilst the inclusion of depth derivatives has varying effectiveness depending on the species.

More recently, marine seismic reflection data, at lower frequencies of 10-100 Hz, have seen an explosion in their use. This smaller field of acoustic oceanography, so-called seismic oceanography, is a tool that can be used to map the distribution, properties, and dynamics of water masses and it has the potential to overcome significant observational challenges (see review by Dickinson and Gunn). In this Research Topic, the capability of seismic oceanography is demonstrated via a collection of the latest methodological developments and seismic-based advances in our understanding of oceanic processes.

Inversion of marine seismic reflection data yields oceanic temperature, salinity, and density fields in two-, three, and even four-dimensions. Here, two methodological advances expand the capacity for inversion. Azevedo et al. develop a geostatistical inversion that can be used when contemporaneous and collocated hydrographic measurements are not available, instead leveraging common models of large-scale ocean dynamics and existing vertical profiles of the ocean properties measured by ARGO floats. Without any contemporaneous data, this inversion scheme can produce temperature and salinity fields with accuracies of order 1°C and 0.5 psu. In cases where contemporaneous and collocated hydrographic data are available, Xiao et al. develop an established Markov Chain Monte Carlo approach to show that this method can

OPEN ACCESS

Edited and reviewed by:
Hervé Claustre,
Centre National de la Recherche Scientifique (CNRS), France

****Correspondence:***
Kathryn L. Gunn
kgunn.sc@gmail.com

Specialty section:
This article was submitted to Ocean Observation, a section of the journal Frontiers in Marine Science

Received: *04 June 2022*
Accepted: *08 June 2022*
Published: *11 July 2022*

Citation:
Gunn KL, Sheen KL and Tang Q (2022) Editorial: Acoustically Mapping the Ocean. Front. Mar. Sci. 9:961282. doi: 10.3389/fmars.2022.961282

quantify temperature and salinity fields to within 0.16°C and 0.06 psu.

Uniquely, the causes and consequences of short-term water mass variability can be studied using seismic-derived time series of diapycnal mixing alongside its high-resolution imagery. In the South Atlantic, such time series of diapycnal mixing suggest that at 1,000 km and decadal scales the background diffusivity of the thermocline has changed little, whilst temporally intermittent processes, such as storms (Wei et al.) and frontal advection (Gunn et al.), can temporarily alter diapycnal mixing by an order of magnitude. Similarly, in the South Pacific Ocean, observations of daily frontal meandering cause significant changes in water mass thicknesses and temperatures (Cooper et al.).

Internal waves – which drive intense ocean mixing, contribute to ocean-atmosphere interactions, and impact offshore engineering – are particularly difficult to observe with traditional hydrographic methods. Here, their structure as well as their evolution with time is observed and quantified in detail using seismic oceanography. In depths of 300 m, seismic observations of internal wave evolution confirm results from numerical simulations (Song et al.); during shoaling, the degree of waveform change is related to the waves size, and its amplitude and phase velocity increase onshore. In depths shallower than 50 m, which are invisible to seismic oceanography, higher-frequency acoustic methods show internal waves that have amplitudes extending as much at 20% of the water depth (Feng et al.). These observations from the northeastern South China Sea can be generalized to other regions where strong currents impinge on topographic slopes.

The potential of seismic oceanography to solve oceanographic questions, in conjunction with other acoustic and hydrographic measurements, lies with the abundance and resolution of existing measurements plus the continually growing data sets collected by education and industry initiatives. Existing marine seismic reflection data covers every continental shelf and slope in the world's ocean (Figure 4 of Dickinson and Gunn). Using these data, bulk inversion processing can be applied to access physical properties of water masses at unprecedented spatial resolution on a global scale; just as oceanic models with different resolutions are required to investigate the climate, inversion techniques with different limitations and accuracies are necessary. For example, the inversion of Azevedo et al. could be applied in a bulk sense to measure the volume of water masses, whilst the inversion of Xiao et al. (2021) could be applied in a region of significant data coverage to develop high quality time series of small-scale mixing and stirring processes. Oceanic mixing rates are globally limited, yet seismic oceanography can readily be used to expand this valuable data set, an important link connecting mixing to larger scale climate-mediating processes. For example, Wei et al. use seismic data to extend the record of mixing in the South Atlantic Ocean into the late 2010s, whilst Gunn et al. provide rare time series of mixing rates across a front. Meanwhile, seismic imagery alone provides insight into ocean dynamics yielding daily information about water mass position and thickness variability (Cooper et al.). Acoustic data also yield high-resolution information about the evolution of internal waves on the continental shelf (Song et al., Feng et al.).

In this Research Topic, the role of short-lived and rapidly changing processes are highlighted. Acoustic data sets provide a guide for future observational programs as well as an avenue for defining parameterizations that can be included in models, which often do not realistically resolve temporally intermittent oceanic processes. Overall, these studies show how acoustic methods can be used to augment and overcome observational challenges. Through collaborative development, acoustic techniques can become a staple of the new generation of observational tools.

AUTHOR CONTRIBUTIONS

KLG conceived the Research Topic and wrote the editorial with input and advice from KLS and QT. All authors approved this editorial for publication.

Conflict of Interest: The authors declare that the research was conducted in the absence of any commercial or financial relationships that could be construed as a potential conflict of interest.

frontiers in Marine Science

ORIGINAL RESEARCH
published: 12 August 2021
doi: 10.3389/fmars.2021.685007

Geostatistical Seismic Inversion for Temperature and Salinity in the Madeira Abyssal Plain

Leonardo Azevedo[1], Luís Matias[2], Francesco Turco[3], Renan Tromm[2] and Álvaro Peliz[2]*

[1] CERENA/DECivil, Instituto Superior Técnico, Universidade de Lisboa, Lisbon, Portugal, [2] Instituto Dom Luiz, Faculdade de Ciências da Universidade de Lisboa, Lisbon, Portugal, [3] Department of Geology, University of Otago, Dunedin, New Zealand

A two-dimensional multichannel seismic reflection profile acquired in the Madeira Abyssal Plain during June 2016 was used in a modeling workflow comprising seismic oceanography processing, geostatistical inversion and Bayesian classification to predict the probability of occurrence of distinct water masses. The seismic section was processed to image in detail the fine scale structure of the water column using seismic oceanography. The processing sequence was developed to preserve, as much as possible, the relative seismic amplitudes of the data and enhance the shallow structure of the water column by effectively suppressing the direct arrival. The migrated seismic oceanography section shows an eddy at the expected Mediterranean Outflow Water depths, steeply dipping reflectors, which indicate the possible presence of frontal activity or secondary dipping eddy structures, and strong horizontal reflections between intermediate water masses suggestive of double diffuse processes. We then developed and applied an iterative geostatistical seismic oceanography inversion methodology to predict the spatial distribution of temperature and salinity. Due to the lack of contemporaneous direct measurements of temperature and salinity we used a global ocean model as spatial constraint during the inversion and nearby contemporaneous ARGO data to infer the expected statistical properties of both model parameters. After the inversion, Bayesian classification was applied to all temperature and salinity models inverted during the last iteration to predict the spatial distribution of three distinct water masses. A preliminary interpretation of these probabilistic models agrees with the expected ocean dynamics of the region.

Keywords: seismic oceanography, geostatistical inversion, temperature prediction, salinity prediction, ocean modeling, Madeira Abyssal Plain

OPEN ACCESS

Edited by:
Kathy Gunn,
University of Miami, United States

Reviewed by:
Alex Dickinson,
Newcastle University, United Kingdom
Richard Hobbs,
Durham University, United Kingdom

****Correspondence:***
Leonardo Azevedo
Leonardo.azevedo@tecnico.ulisboa.pt

Specialty section:
This article was submitted to Ocean Observation, a section of the journal Frontiers in Marine Science

Received: *24 March 2021*
Accepted: *19 July 2021*
Published: *12 August 2021*

Citation:
Azevedo L, Matias L, Turco F, Tromm R and Peliz Á (2021) Geostatistical Seismic Inversion for Temperature and Salinity in the Madeira Abyssal Plain. Front. Mar. Sci. 8:685007. doi: 10.3389/fmars.2021.685007

INTRODUCTION

Fine-scale ocean processes happening on ranges from a few meters to a few kilometers have a profound impact on turbulent dynamics, on the ocean energy budget, on primary production and ecosystems, on gas and tracer exchange, and ultimately on the global ocean circulation and climate (e.g., Wunsch and Ferrari, 2004; Mahadevan, 2016). Yet, ocean measurements at high resolutions are limited to fixed point probes or profiling devices. Therefore, quasi-synoptic measurements of simultaneously vertical and lateral high resolutions require detailed planning and

the combination of several probing devices, which are not globally available to sample the ocean (Pascual et al., 2017).

Seismic oceanography (SO) is an interdisciplinary research field that uses common marine multichannel seismic reflection (MCS) data to capture high-resolution images of the ocean's thermohaline structure. This geophysical technique has proven its value in imaging the oceanic structures with an unprecedent detail both in the horizontal and vertical directions in different basins worldwide (Holbrook et al., 2003; Hobbs et al., 2007; Ruddick et al., 2009; Pinheiro et al., 2010). SO data are indirect information of relevant oceanographic features and complement the information provided by conventional oceanographic casts, which are direct measurements of the ocean properties but sparsely distributed. More recently, these data have been used to estimate the oceanic turbulent dissipation (Holbrook et al., 2013; Sallarès et al., 2016; Dickinson et al., 2017; Fortin et al., 2017) and to estimate the spatial distribution of the ocean's temperature and salinity using amplitude-vs.-offset analysis (Páramo and Holbrook, 2005), deterministic seismic oceanography inversion methods (Wood et al., 2008; Sallarès et al., 2009; Papenberg et al., 2010; Kormann et al., 2011; Song et al., 2012; Bornstein et al., 2013; Biescas et al., 2014; Padhi et al., 2015; Blacic et al., 2016; Dagnino et al., 2016, 2018; Minakov et al., 2017; Gunn et al., 2018; Tang et al., 2018, 2019; Gunn et al., 2020), stochastic seismic oceanography inversion (Tang et al., 2016; Azevedo et al., 2018; Jun et al., 2019) and automatic velocity analysis (Chhun and Tsuji, 2020).

In SO, multichannel seismic reflection data is processed to boost the amplitudes corresponding to seismic reflections occurring at interfaces between water layers of different temperature and salinity, where water temperature is the most important property and contributes on average 80% to the reflection coefficient (Ruddick et al., 2009; Sallarès et al., 2009). A challenge for SO data processing is the ability to image reflections near the sea surface, as traditional seismic processing sequences fail to successfully mitigate the effect of the direct wave traveling from source to receivers on the very weak reflections in the near-surface water layer (e.g., Ruddick et al., 2009; Pinheiro et al., 2010). Several processing workflows have been proposed to tackle this limitation. Huang et al. (2012) used an adaptive subtraction scheme. Hardy et al. (2007) and Jones et al. (2008) combined linear moveout with dip filtering. Ristow et al. (2017) used a combination of a linear Radon transformation with adaptive subtraction. Often, another source of coherent noise originates from the echo of the previous shot, but this noise is not addressed herein. The objective of the seismic oceanography processing shown herein is twofold: (1) to effectively attenuate the direct arrival effect using a combination of linear moveout, horizontal median filtering and adaptive subtraction; and (2) to preserve the relative seismic amplitudes of the seismic data. The attenuation of the direct wave arrival ensures a good image of the water structure in the first few hundred of meters, whereas preservation of original amplitudes is required to invert the seismic data for the ocean's physical properties.

Seismic oceanography data represent an indirect measurement of the physical properties of the water column such as temperature and salinity. In fact, seismic reflections present in SO data originate from the interfaces between water masses with distinct properties. From an oceanographic perspective, having the ability to predict the spatial distribution of such properties from SO data would provide insights about oceanographic processes not detected by conventional oceanographic sampling techniques. The spatial prediction of such properties from seismic oceanography data is an inverse problem. Mathematically, seismic oceanography inversion can be expressed as:

$$\mathbf{m} = \mathrm{F}^{-1}(\mathbf{d_{obs}}) + \mathbf{e} \quad (1)$$

where F is the forward operator through which the recorded seismic amplitudes ($\mathbf{d_{obs}}$), with $\mathbf{d}_{\mathrm{obs}} \epsilon \mathbf{R}^{\mathrm{d}}$, are obtained from an ocean's model, $\mathbf{m} \epsilon \mathbf{R}^{\mathrm{m}}$, and $\mathbf{e}$ represents the error term associated with the observations and modeling uncertainties errors present in the seismic oceanography data. In the seismic oceanography case, the ocean's acoustic properties (P-wave propagation velocity and density), $\mathbf{m}$, can be computed from temperature and salinity using the thermodynamic equation of seawater (IOC, SCOR, and IAPSO, 2010).

Seismic inversion methods can be broadly divided in two different classes: deterministic or statistical (Bosch et al., 2010). Deterministic approaches are based on regression models of optimization algorithms providing a single best-fit solution. In deterministic seismic inversion the uncertainty assessment is limited and defined as a linearization around the best-fit inverse solution, which is normally retrieved by least squares, and in this sense, the uncertainty is strictly represented by a local multivariate Gaussian (Tarantola, 2005). In statistical seismic inversion, the solution is expressed as a probability density function in the model parameters space. Therefore, these inversion methods provide a set of alternative models as solution and allow the assessment of the uncertainty associated with the inverted models (Tarantola, 2005). Assessing the uncertainty about the predictions in seismic inversion is critical in any modeling procedure. The uncertainty represents the lack of knowledge about the system under investigation, measurement errors and physical approximation during the data processing (Tarantola, 2005). Also, accounting for uncertainty, and therefore risk, leads to better-informed decisions.

There are different statistical-based seismic inversion methods. These seismic inversion methodologies are iterative procedures based on different stochastic optimization algorithms such as simulated annealing, genetic algorithms, probability perturbation method, gradual deformation, geostatistical simulation and neighborhood algorithm (e.g., Sen and Stoffa, 1991; Bortoli et al., 1993; Sambridge, 1999; Le Ravalec-Dupin and Noetinger, 2002; Soares et al., 2007; González et al., 2008; Grana et al., 2012; Azevedo et al., 2015; Azevedo and Soares, 2017).

Iterative geostatistical seismic inversion methods allow predicting models at higher resolution than the observed data due to their ability to incorporate high-resolution information provided by existing direct observations (e.g., Azevedo and Soares, 2017). This is particularly of interest in oceanographic studies as it might open a window to a reality not yet known. Conventional ocean models built exclusively from the interpolation of sparse direct measurements of ocean properties,

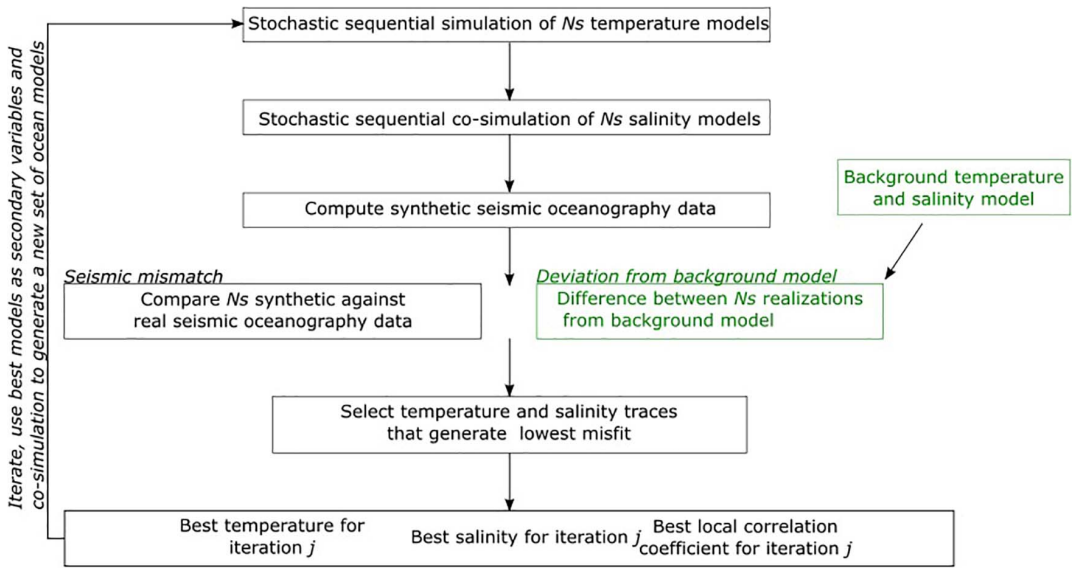

FIGURE 1 | Schematic representation of the proposed geostatistical SO inversion including temperature and salinity background models. Green boxes represent the steps related to the integration of background ocean models.

such as CTD and/or XBT, are always a smooth representation of the true ocean variability and are unable to describe complex features in detail due to the large distances between observations. The inverted models of the ocean properties retrieved from SO data are much richer from a spatial perspective as the SO data constrains the model predictions far from the location of the direct observations (e.g., Dagnino et al., 2016).

In a preliminary work, geostatistical inversion has been successfully applied to predict the spatial distribution of ocean temperature and salinity from seismic oceanography data (Azevedo et al., 2018). These authors showed how geostatistical SO inversion could retrieve a set of high-resolution temperature and salinity models that generate synthetic SO data consistent with observations. Each model represents an alternative scenario that fits equally well the observed data SO data. However, in this approach the model perturbation technique (i.e., geostatistical simulation) (Deutsch and Journel, 1992) requires the existence of contemporaneous and collocated direct measurements of temperature and salinity (e.g., CTD/XBT casts) along the SO section to be inverted. The simultaneous acquisition of CTD/XBT data is difficult due to both operational challenges and costs, and represents a major drawback in the practical use of this technique.

The main objective of this work is to propose an alternative geostatistical SO inversion method to overcome the need for contemporaneous and collocated direct observations of temperature and salinity, which might open the door to the generalization of this type of inversion method in SO studies. Low-resolution models of temperature and salinity are extracted from large-scale ocean simulations and integrated as part of the objective function within the geostatistical SO inversion method. The low-resolution models represent a background model with the expected spatial trend of temperature and salinity (Pereira et al., 2019). In practice the background models act as spatial constraints in the inversion procedure. These models are not included as part of the model parameter space to avoid limiting the exploration of the model parameter space and therefore in a limited uncertainty assessment. The marginal and joint distributions of temperature and salinity, necessary to perform the geostatistical simulations, are borrowed from quasi-contemporaneous and quasi-collocated ARGO floats profiles (Argo, 2000) which were acquired approximately simultaneous during the acquisition of the MCS profile.

As part of the proposed workflow, and to interpret the inverted models obtained in the last iteration of the inversion procedure, we classified the set of inverted models generated during the last iteration of the geostatistical SO inversion into distinct water masses using Bayesian classification (Avseth et al., 2005). From the classified models we computed the probability of occurrence of each water mass. The most likely depths of the different water masses agree with the expected values for the area of interest as proposed by other authors (Comas-Rodríguez et al., 2011).

The following section presents a detailed description of the proposed geostatistical SO inversion methodology and the Bayesian classifier used to predict the spatial distribution of the expected water masses. The proposed inversion method is then applied to a MCS profile acquired over the Madeira abyssal plain (MAP) that was specifically reprocessed for this purpose. The tailored seismic processing workflow is described in the subsequent section. We then show a preliminary and global interpretation of the oceanographic insights provided by the inverted models. The workflow proposed in this work can be applied to other locations worldwide where no contemporaneous direct measurements of salinity and temperatures and global ocean models exist in the vicinity of the seismic profiles.

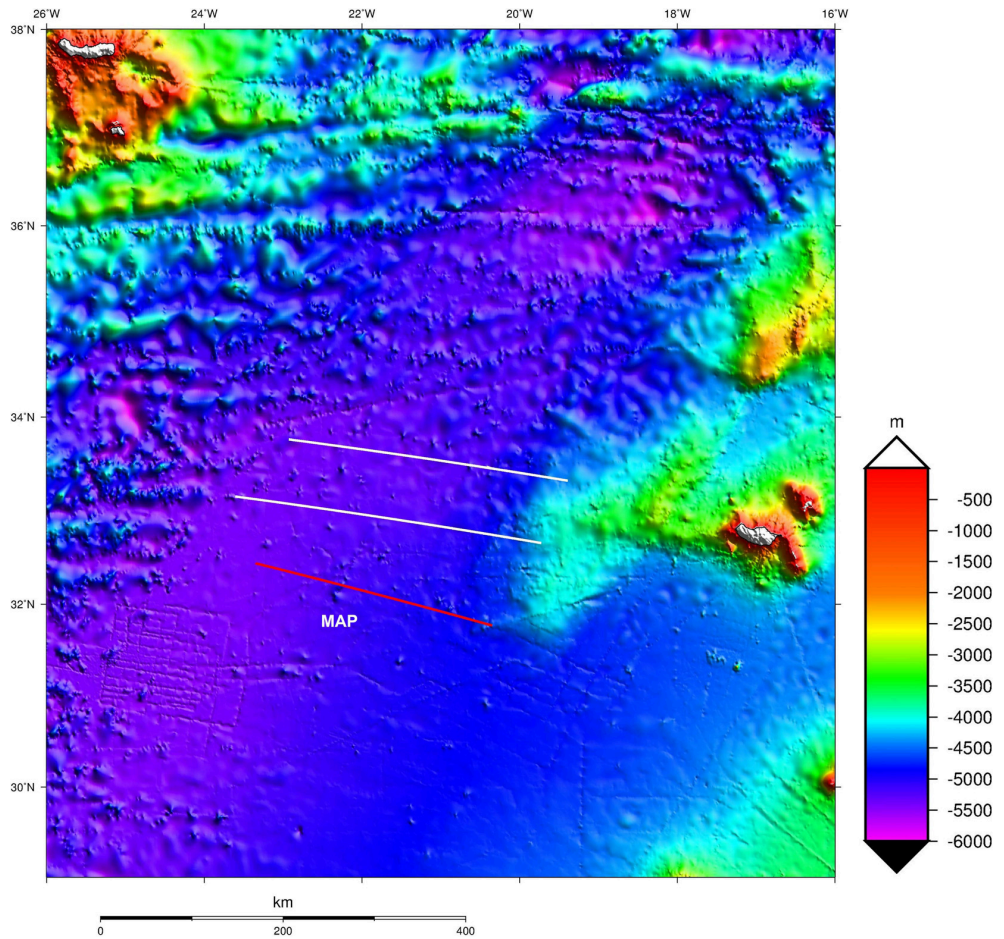

FIGURE 2 | Location of the MAP. The red line shows the location of the SO profile inverted with the proposed method. White lines correspond to other MCS profiles acquired under the same seismic acquisition survey.

GEOSTATISTICAL SEISMIC OCEANOGRAPHY INVERSION

The proposed iterative geostatistical SO inversion method inverts SO data directly for temperature and salinity when no contemporaneous direct observations of the ocean are available. It can be considered an extension of the method introduced by Azevedo et al. (2018). It allows the simultaneous integration of high-resolution direct measurements of temperature and salinity, such as CTD and XBT data, and background models from climatology, data products or numerical ocean simulations. A relevant aspect of the proposed method is that the background models do not constrain the model generation (e.g., used for example as a local mean during the geostatistical simulation), but are included as part of a two-term objective function where they act as a spatial regularizer (Pereira et al., 2019).

The proposed iterative geostatistical SO inversion method can be divided into four main steps: (i) generation of temperature and salinity background models; (ii) generation of high-resolution temperature and salinity models using stochastic sequential simulation and co-simulations; (iii) multi-objective mismatch evaluation; (iv) stochastic update and generation of a new set of models.

TABLE 1 | Summary of the acquisition parameters of the MCS profiles acquired in the MAP.

Recording length (s)	18
Sampling rate (ms)	2
Low-cut filter (Hz)	4.3 at 6 dB/oct
High-cut filter (Hz)	4.3 at 6 dB/oct
Streamer length (m)	7,950
Streamer depth (m)	9 (±1.5 m)
Near-offset distance (m)	190
Number of channels	636
Channel interval (m)	12.5
Source depth (m)	7 (±1.0 m)

In the application example shown herein, two-dimensional large-scale temperature and salinity sections, describing the expected background spatial distribution, were retrieved from global numerical simulations of ocean dynamics provided by the Copernicus Marine Environment Monitoring Service

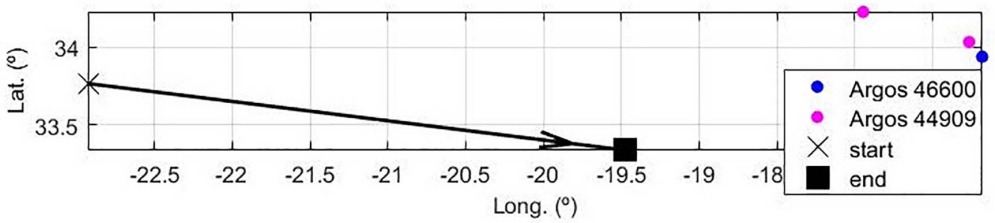

FIGURE 3 | Relative location of the SO seismic profile and the two ARGO floats used for the seismic oceanography inversion.

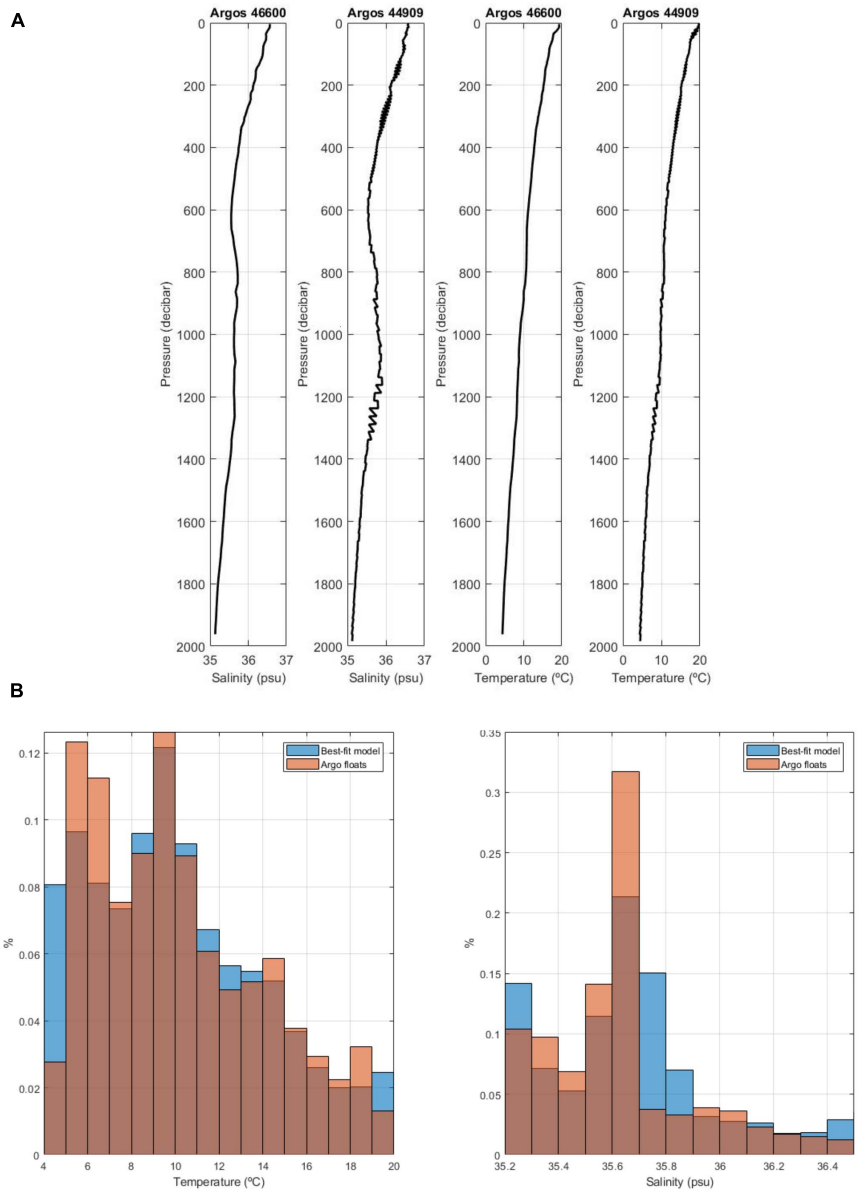

FIGURE 4 | (A) ARGO profiles showing the measured temperature and salinity vs. pressure. **(B)** Comparison between histograms inferred from the temperature and salinity measured by the ARGO floats and the best-fit inverse models.

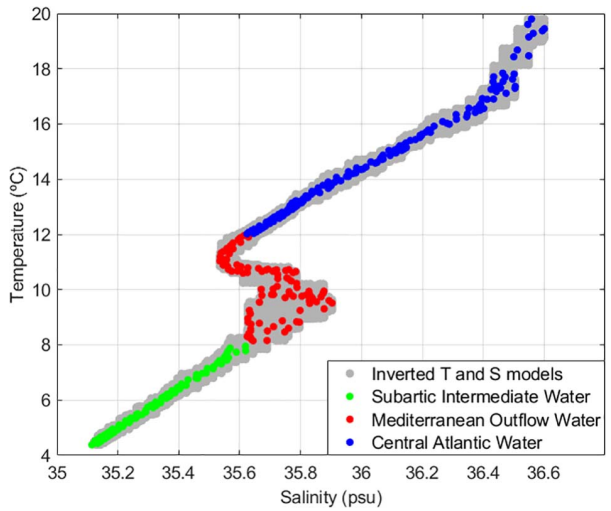

FIGURE 5 | Joint distribution of temperature vs. salinity. Colored markers represent direct measurements from two ARGO floats and were used as training dataset for the Bayesian classification; pair of best-fit inverse models retrieved at the end of the inversion procedure are colored in gray.

(CMEMS, 2016). These sections were extracted for the same geographical location, acquisition date and time of the available SO section. From a geophysical inversion point of view, these simulated profiles can be thought as low-frequency models in conventional seismic inversion methodologies (e.g., Sams and Carter, 2017; Pereira et al., 2019).

Contemporaneous observed high-resolution temperature and salinity vertical profiles acquired close to the seismic oceanography profile were used to infer the marginal and joint distributions of both ocean properties. This information was used during the model generation and perturbation and not as spatial constraining data. These data were used as target marginal and joint distributions to be reproduced by the geostatistical simulation algorithms. In this inversion method, water temperature models are generated with direct sequential simulation (DSS; Soares, 2001) and salinity models were co-simulated with co-DSS with joint probability distributions (Horta and Soares, 2010). The sequential generation of models ensures that the observed relationship between temperature and salinity is reproduced in any given pair of models generated during the iterative procedure. This is essential to guarantee the plausibility of the predicted location and extent of water masses and for classification of distinct water masses as shown below.

The pairs of temperature and salinity models are used to compute water density and P-wave propagation velocity using the international thermodynamic equation of seawater (IOC, SCOR, and IAPSO, 2010). Then, normal incidence reflection coefficients are computed and convolved with a representative wavelet. In cases where contemporaneous and collocated vertical profiles of salinity and temperature are available, the wavelet can be

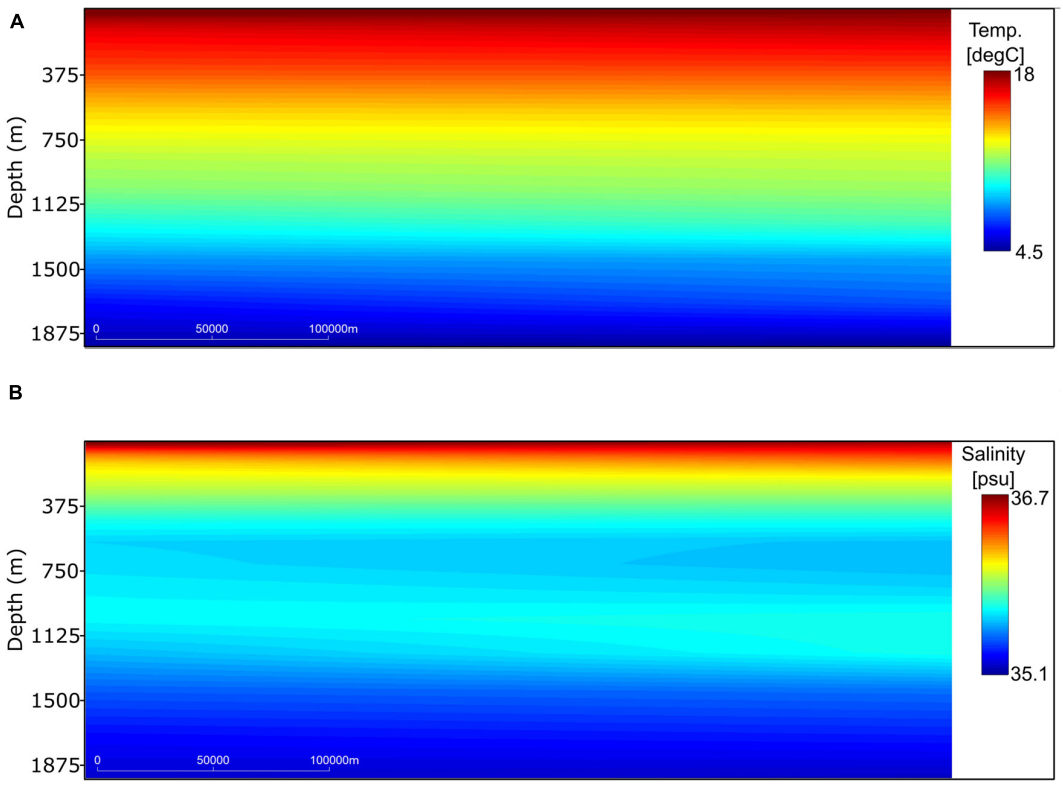

FIGURE 6 | Background models of **(A)** temperature and **(B)** salinity extracted from the large-scale dynamics ocean model.

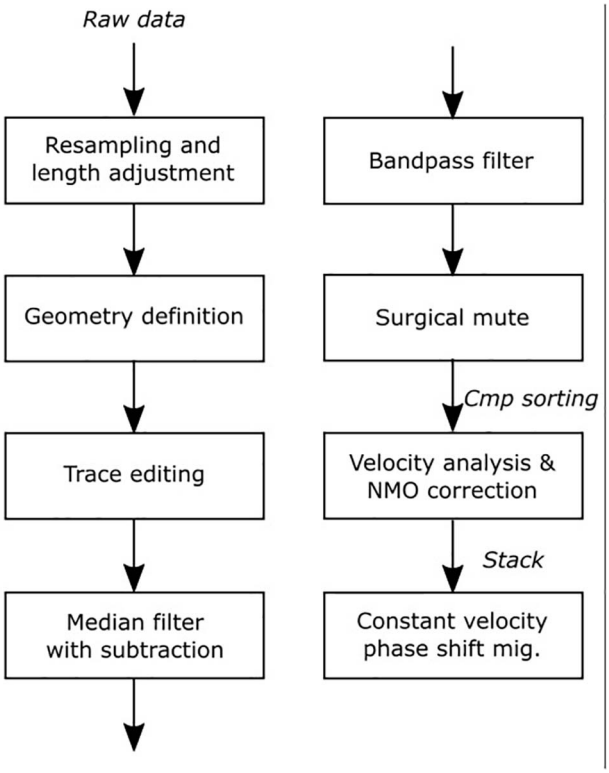

FIGURE 7 | Seismic processing flow applied to the SO profile to enhance the reflections within the water column and in particular the shallow part of the section.

estimated by comparing synthetic seismic traces with the real data (i.e., as in conventional seismic-to-well tie). For this work, however, the wavelet was extracted from the processed SO data by averaging the primary seafloor reflection of several traces selected from a region of relatively flat bathymetry, following the approach used by Warner (1990). The resulting synthetic traces are then compared against the corresponding real traces following:

$$\mathbf{S} = \frac{2 * \sum_{s=1}^{N} (\mathbf{x_s} * \mathbf{y_s})}{\sum_{s=1}^{N} (\mathbf{x_s})^2 * \sum_{s=1}^{N} (\mathbf{y_s})^2}, \quad (2)$$

where $\mathbf{x_s}$ and $\mathbf{y_s}$ are the real and synthetic seismic traces, respectively, with N seismic samples. The similarity, **S**, like the Pearson's correlation coefficient is bounded between −1 and 1, but ensures a simultaneous match of the synthetic seismic on both waveform and amplitude values of the recorded SO data. The plausibility of the inverted models depends on the reproduction of both properties of the observed data.

The deviations (**dev**) of each single realization of temperature and salinity from the background ocean models are computed following:

$$\mathbf{dev} = \left(1 - \left(\frac{|\mathbf{m}_{sim} - \mathbf{m}_{background}|}{\mathbf{m}_{sim} + \mathbf{m}_{background}}\right)\right), \quad (3)$$

where $\mathbf{m}_{sim}$ is a realization of temperature or salinity and $\mathbf{m}_{background}$ is the corresponding background model. Finally, a two-term objective function (OF) is computed combining Eqs. (2) and (3):

$$\mathrm{OF} = w_1 \mathbf{S} + w_2 \left(\frac{\mathbf{dev_T} + \mathbf{dev_S}}{2}\right), \quad (4)$$

where w_1 and w_2 are user defined weights that sum to 1 and control the influence of each term depending on the quality of the existing SO data and the reliability of the background model; $\mathbf{dev_T}$ and $\mathbf{dev_S}$ are the deviations of the simulated parameter from the background model for temperature and salinity, respectively. If the quality of the SO data is low, then w_1 should decrease. Similarly, if the reliability of the background temperature and salinity is poor, w_2 should be reduced. In the application example shown herein w_1 and w_2 were set by trial-and-error. However, these can be optimized under an optimization framework (e.g., Gennert and Yuille, 1988; Mead, 2008; Marler and Arora, 2010). Notice that OF is also bounded between −1 and 1 so it can be used as a proxy of a collocated correlation coefficient in the geostatistical co-simulation of a new set of temperature and salinity models in the subsequent iteration of the inversion (e.g., Soares, 2001).

For a given iteration (*j*), the pairs of temperature and salinity traces (i.e., vertical columns of grid samples) that ensure the maximum OF values are stored in auxiliary temperature and salinity models along with the corresponding OF values. These models are used as secondary variables in the co-simulation of a new set of models in the subsequent iteration. In practice, regions of the seismic profile with low OF will exhibit a large variability of simulated values within the ensemble of simulated models, while region of high *OF* will produce similar models in the next iteration.

The proposed iterative geostatistical SO inversion method is summarized in the following sequence of steps (**Figure 1**):

(i) Create temperature and salinity background models for the entire inversion grid. The background models might be vertical sections extracted from numerical ocean simulations collocated with the existing SO data for the same acquisition time;

(ii) Stochastic sequential simulation (direct sequential simulation; Soares, 2001) of *Ns* temperature models for the entire inversion grid. Direct temperature measurements located nearby the location of the SO profile are used to infer the conditioning distribution;

(iii) Stochastic sequential co-simulation (direct sequential co-simulation with joint probability distributions; Horta and Soares, 2010) of *Ns* salinity models for the entire inversion grid. Direct salinity measurements located nearby the region of interest are used to infer the conditioning distribution. Each temperature model simulated in ii is used as an auxiliary variable to ensure the relationship between both ocean properties are reproduced in each *Ns* pairs of simulated models;

(iv) For each pair of simulated ocean models, calculation of *Ns* reflection coefficient models using the International

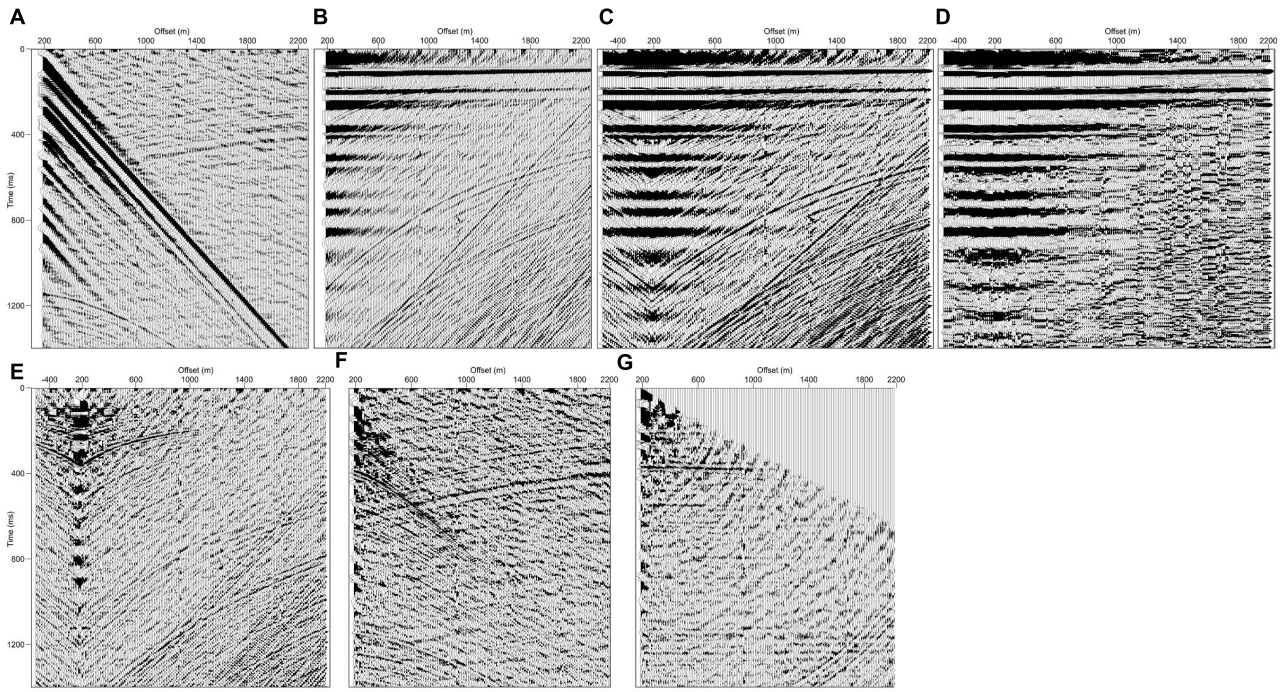

FIGURE 8 | (A) An illustrative field seismic record. Echo from the previous shot is very clear. Shallow reflections from the water layer are obscured by the very strong direct arrival; **(B)** field record after linear moveout; **(C)** doubling the short offsets and merging to build a shot gather that will mitigate the border effects of the median filter; **(D)** after applying the median filter with 11 traces; **(E)** same as **(C)** after subtraction of the median filter shown in **(D)**; **(F)** field record [as shown in **(A)**], after the full processing sequence of horizontal median filter with subtraction to attenuate the energy from the direct wave in the water; **(G)** processed record after NMO correction at 1,500 m/s (50% stretch mute allowed).

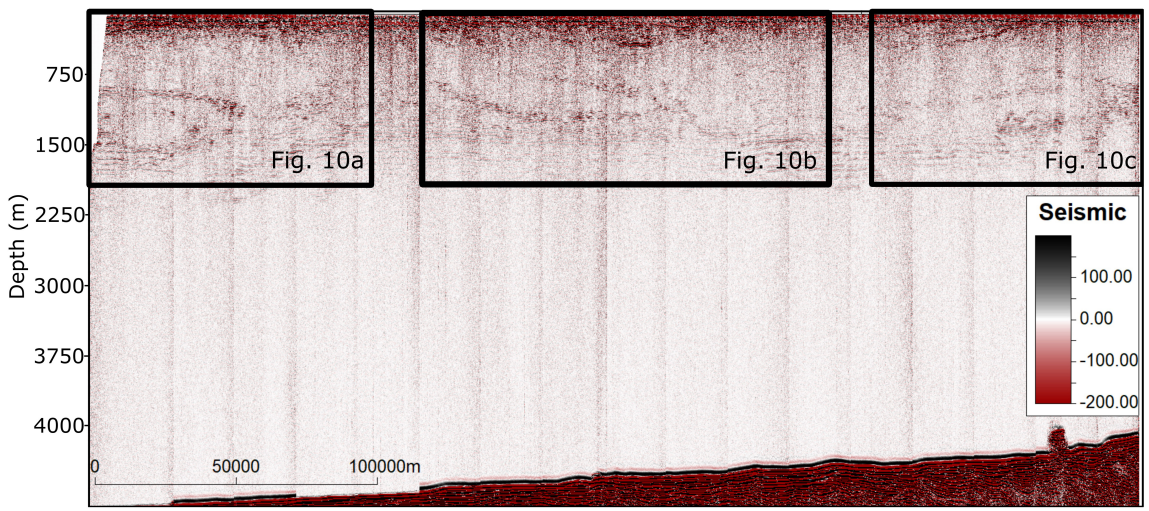

FIGURE 9 | Migrated seismic profile. Black boxes represent the locations of the zoom-ins shown in **Figure 10**.

thermodynamic equation of seawater (IOC, SCOR, and IAPSO, 2010). The resulting *Ns* reflection coefficients volumes are then convolved on a trace-by-trace basis with a wavelet extracted from the recorded seismic reflection data, producing *Ns* synthetic SO sections;

(v) Calculate the objective function (Eq. 4) on a trace-by-trace basis;

(vi) Select and store the temperature and salinity traces that generated the highest OF value in best local salinity and temperature models along with the corresponding OF;

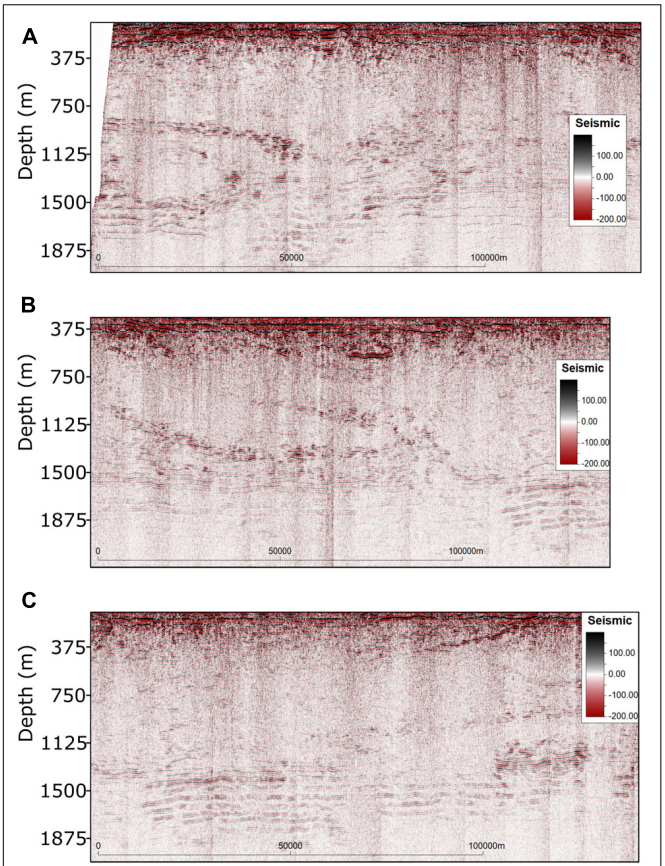

FIGURE 10 | Close-up of: **(A)** the eddy interpreted in the Western part of the profile; **(B)** elliptical shallow feature and oblique reflection within the MOW; and **(C)** bright continuous seismic reflections interpreted as possible double diffusion.

(vii) Use these local best OF, temperature and salinity models as secondary variables in the co-simulation of a new set of temperature and salinity models;

(viii) Return to ii and iterate until the global correlation coefficient between real and synthetic SO data is above a certain threshold or a pre-defined number of iterations is reached.

Temperature and salinity models simulated and co-simulated during the last iteration generate highly correlated synthetic SO data with the observed data. These models were classified into distinct water masses. Bayesian classification (e.g., Avseth et al., 2005; Grana et al., 2017) was trained based on the existing direct measurements of temperature and salinity profiles of spatially located nearby Argo floats taken during the acquisition of the seismic oceanography data. N_w different types of water were identified including the Central Atlantic Water, the Mediterranean Outflow and the Subarctic Intermediate Waters, as described in Comas-Rodríguez et al. (2011). The statistical properties (i.e., mean, covariance and proportions) were inferred from the training data and used to compute the prior and likelihood function for the Bayesian classification according to Bayes' rule:

$$P\left(k|\mathbf{d}\right) = \frac{P\left(\mathbf{d}|k\right)P(k)}{P(\mathbf{d})} = \frac{P\left(\mathbf{d}|k\right)P(k)}{\sum_{k=1}^{N_w} P\left(\mathbf{d}|k\right)P(k)},\ k = 1, \ldots, N_w \tag{5}$$

where, **d** is the vector of the ocean properties used for the classification, the simulated pairs of models, and k is the number of water masses. In Eq. (5), $P\left(\mathbf{d}|k\right)$ is the likelihood function, $P(k)$ is the prior model and $P(\mathbf{d})$ is a normalization constant. The set of Ns models classified in k water masses was then used to compute the probability of occurrence of each water mass.

Finally, the pointwise average models of temperature and salinity inverted during the last iteration of the inversion and the water probability sections were used to perform a simple and preliminary interpretation of the oceanographic features observed in the data. Nevertheless, this is not the main focus of this work.

REAL CASE APPLICATION

Dataset Description

The proposed iterative geostatistical SO inversion method was applied to a seismic profile (WM-MAD01-003) acquired over the MAP with conventional MCS reflection methods (**Figure 2**). A summary of the main acquisition parameters is shown in **Table 1**. This seismic profile was acquired by the Portuguese Task Force for the Extension of the Continental Shelf (EMEPC in its Portuguese acronym) between June 6 and June 8, 2006 and is part of a larger seismic dataset located within the MAP. The typical thermohaline structure of the water column in this area is characterized by surface waters of subtropical type (warmer and saltier) over central waters of subpolar origins (Central Atlantic Waters) with lower temperature and salinity. Below the Central Atlantic Waters between about 500–1,500 m the water becomes saltier and warmer due to the presence of Mediterranean Outflow Water (MOW). Deeper in the water column, at the lower intermediate levels, temperature and salinity decrease with the presence of subpolar type intermediate waters (e.g., Segade et al., 2015). This vertical structure of water masses is unique as far as a considerable thermohaline structure is enclosed in the upper 2,000 m of the water column and a clear structure in the SO data was expected. Besides, this area is characterized by recurrent eddy activity associated with the energetic and unstable Azores Current jet on the upper ocean (Barbosa Aguiar et al., 2011), and with the main path of propagation of the Mediterranean Water Eddies (Richardson et al., 2000; Barbosa Aguiar et al., 2013), which carry very distinct salty and warm water anomalies within its core at intermediate levels.

The MCS profile was processed to image the fine-structure in the water column. Particular attention was given to mitigate the effect of the direct arrival and enhance shallow reflections while preserving true amplitudes by applying processing parameters that minimize amplitude and phase distortion.

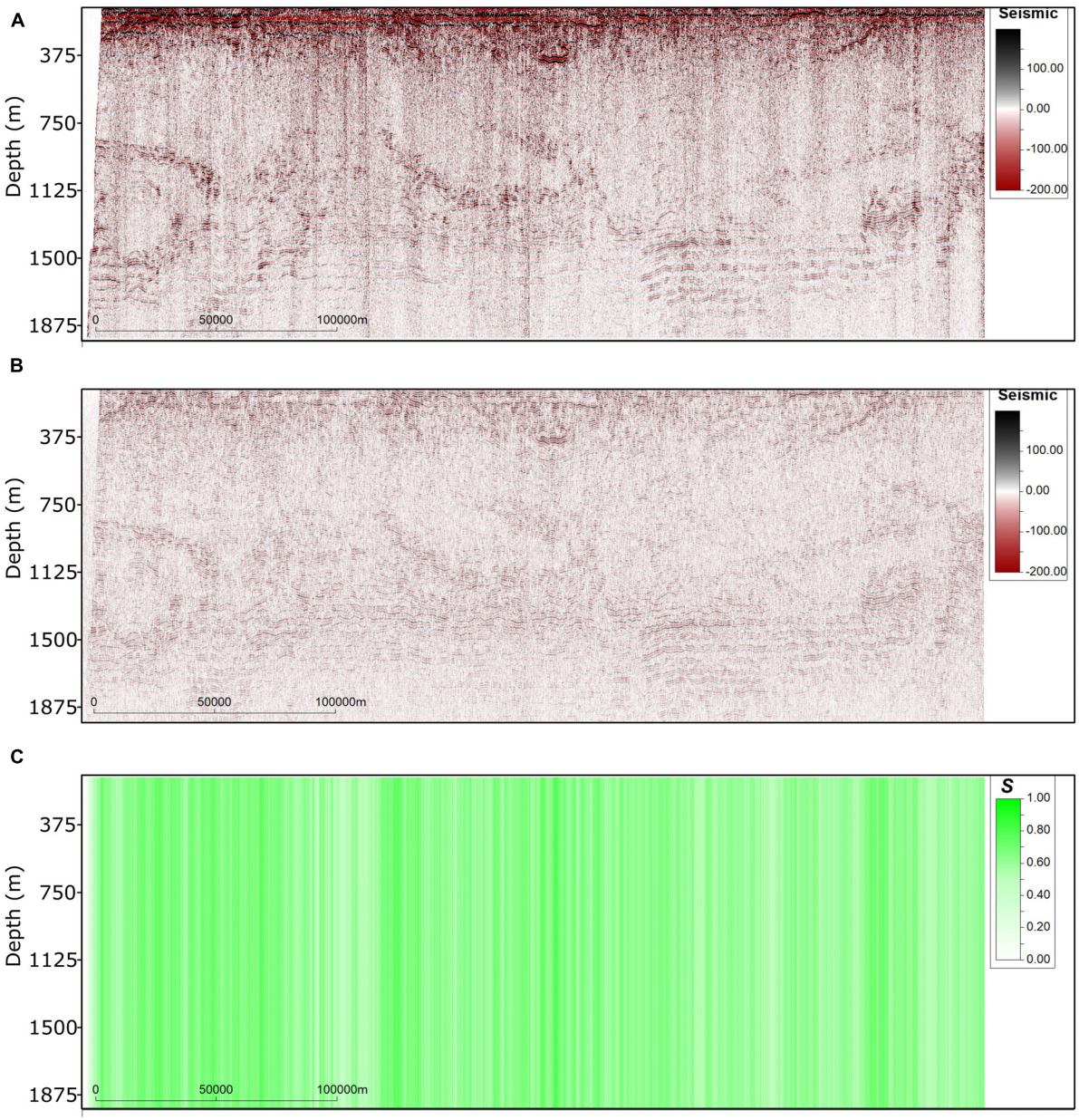

FIGURE 11 | (A) Observed SO data used in the inversion; **(B)** synthetic SO data computed from the pointwise mean temperature and salinity models generated during the last iteration; **(C)** trace-by-trace ***S*** between **(A,B)**.

Different processing sequences would produce different results and impact the models predicted with the SO inversion. The detailed description of the processing sequence is presented in the following sub-section.

As collocated and contemporaneous direct measurements of temperature and salinity were not available, we used three vertical profiles of temperature and salinity (from two ARGO floats—ARGO, 4,660 and 44,909), profiling close to the acquisition period (in May 21 and May 31, 2006) and located in the surroundings of the SO section during the data acquisition (**Figure 3**). The ARGO profiles were used to infer the marginal (**Figure 4**) and joint distributions (**Figure 5**) of both ocean properties and were used as conditioning distributions for the stochastic sequential simulation and co-simulation of temperature and salinity models. We assume that the statistical properties of temperature and salinity measured by these floats hold for the location of the SO profile. According to the temperature and salinity measurements, three distinct water masses could be inferred: central Atlantic water; MOW; and Subarctic Intermediate Water, as described in Comas-Rodríguez et al. (2011). Low-frequency temperature and salinity background models were built using a global ocean dynamics

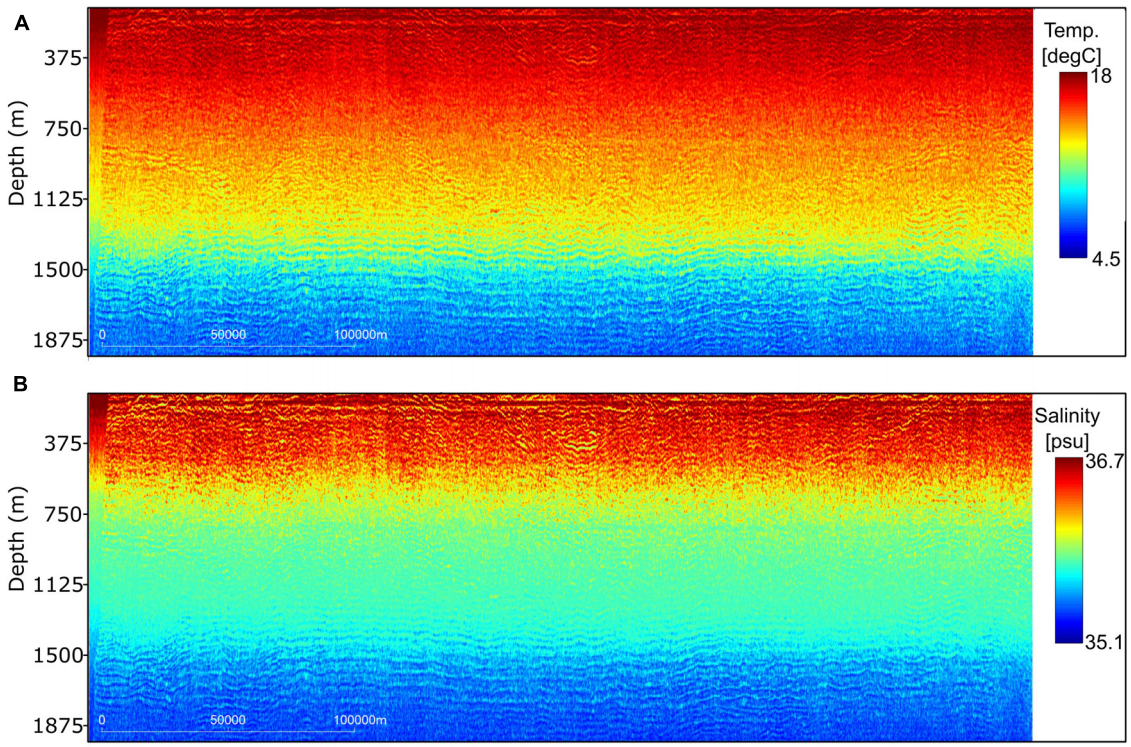

FIGURE 12 | Pointwise mean model of the set of inverted **(A)** temperature and **(B)** salinity models generated during the last iteration of the geostatistical inversion.

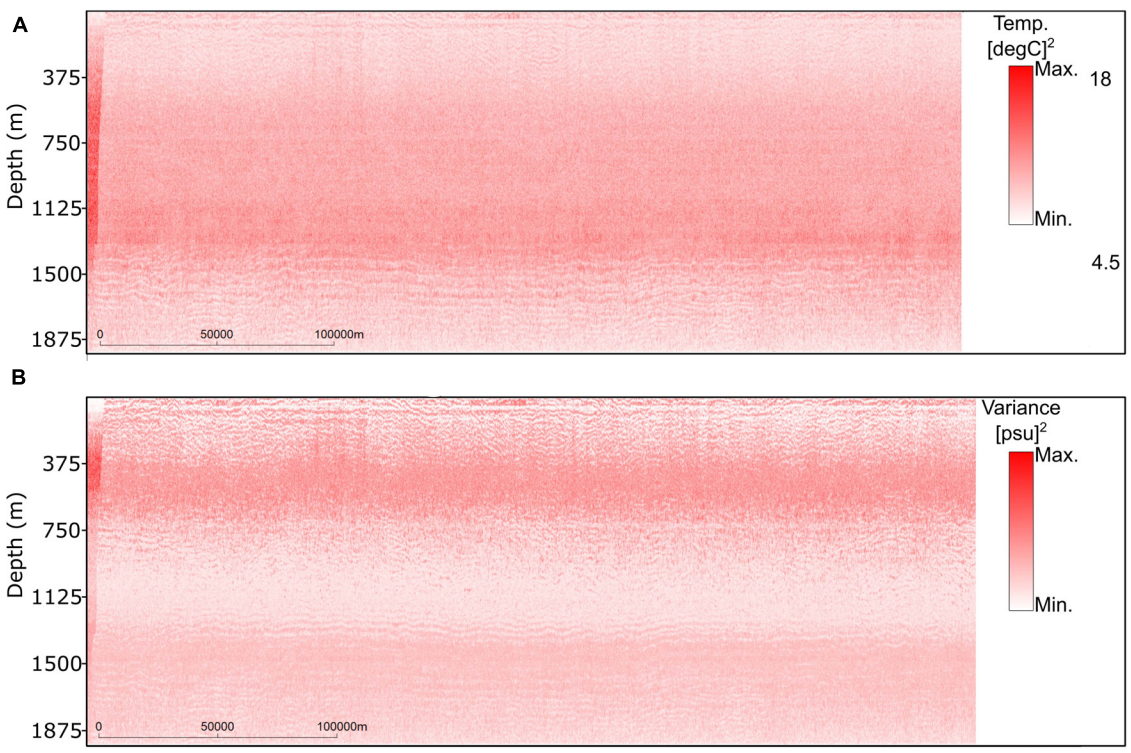

FIGURE 13 | Pointwise variance model of the set of inverted **(A)** temperature and **(B)** salinity models generated during the last iteration of the geostatistical inversion.

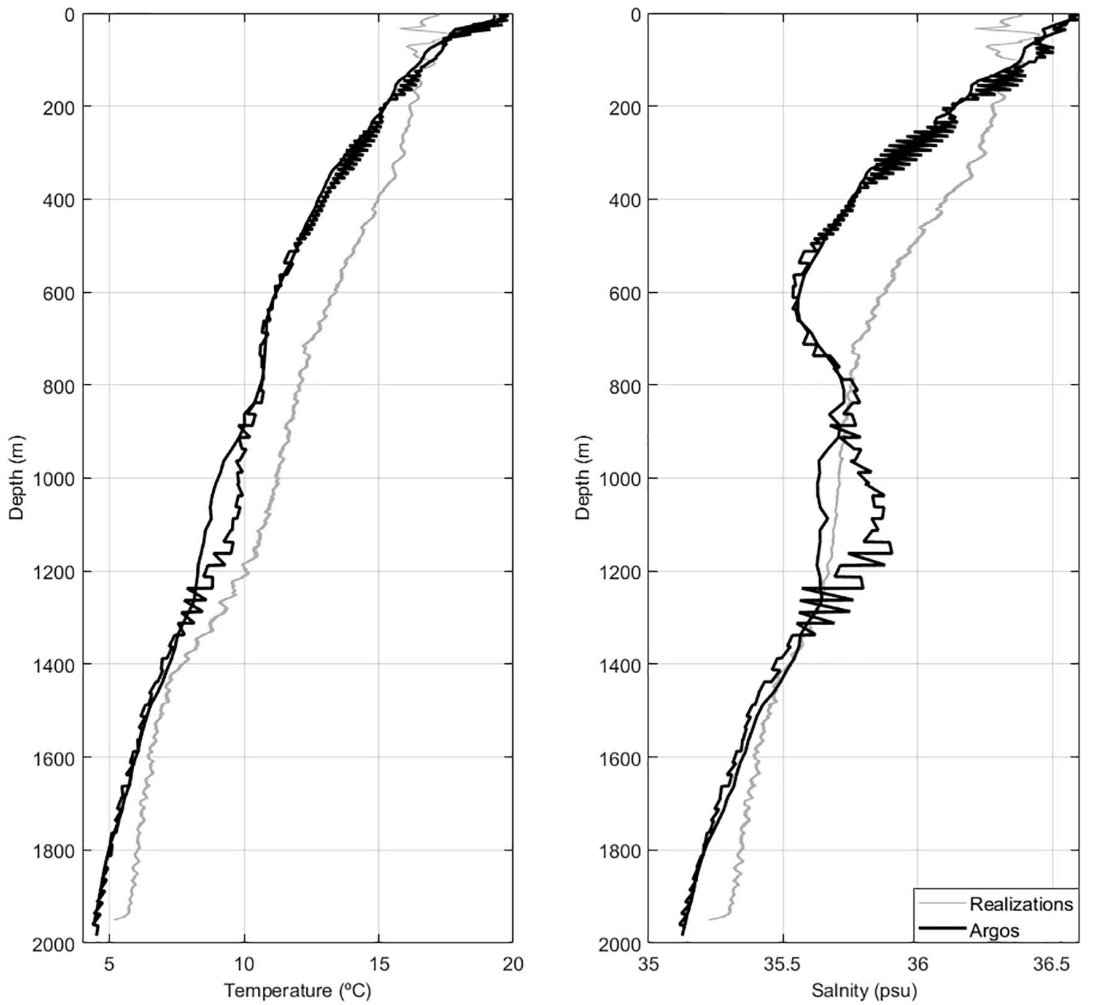

FIGURE 14 | Comparison between the temperature and salinity vertical profiles measured at the ARGO floats locations (**Figure 3**) and the average vertical profile of temperature and salinity for all the thirty-two realizations generated during the last iteration of the geostatistical inversion.

model (CMEMS, 2016) for the dates of seismic acquisition (**Figure 6**). These two-dimensional sections are collocated with the MCS data but are smooth and low resolution. While the background temperature model shows a vertical trend of high temperature at shallower water depths and low temperature at deeper depths, the background salinity model follows the description above and considers the effect of the MOW (i.e., a saltier water layer) around 1,125 m of water depth.

Seismic Processing of Line WM-MAD01-003

The processing sequence (**Figure 7**) included data resampling and recording length reduction to comprise data exclusively above the seafloor. Bad traces, both due to poor signal-to-noise ratio or bad readings, were edited and those unrecoverable were removed from the dataset. The direct arrival was tackled by applying a horizontal median filter with adaptive amplitude subtraction, similar to ocean bottom seismometers data processing (Duncan and Beresford, 1995). This kind of amplitude subtraction aims at minimizing the effects on the resulting amplitudes. This process was performed sequentially in a four-step approach (**Figure 8**): first, field records were flattened using a linear moveout correction with a constant velocity of 1,500 m/s (**Figure 8A**); the flattened records were doubled to avoid edge effects when applying a median filter (**Figure 8B**); a horizontal median filter was applied to those records to preserve horizontal coherent reflection (**Figure 8C**). Finally, the resulting record was subtracted to the doubled flatten record (**Figure 8E**) to eliminate the effect of the direct arrivals and keep reflections in the records (**Figure 8F**). The filtered gather, after applying a normal moveout (NMO) correction with a constant velocity of 1,500 m/s, is shown in **Figure 8G** where the reflections within the water column around 500 ms are enhanced.

The second part of the processing sequence comprises band-pass filtering between 10 and 80 Hz, and surgical mutes to remove

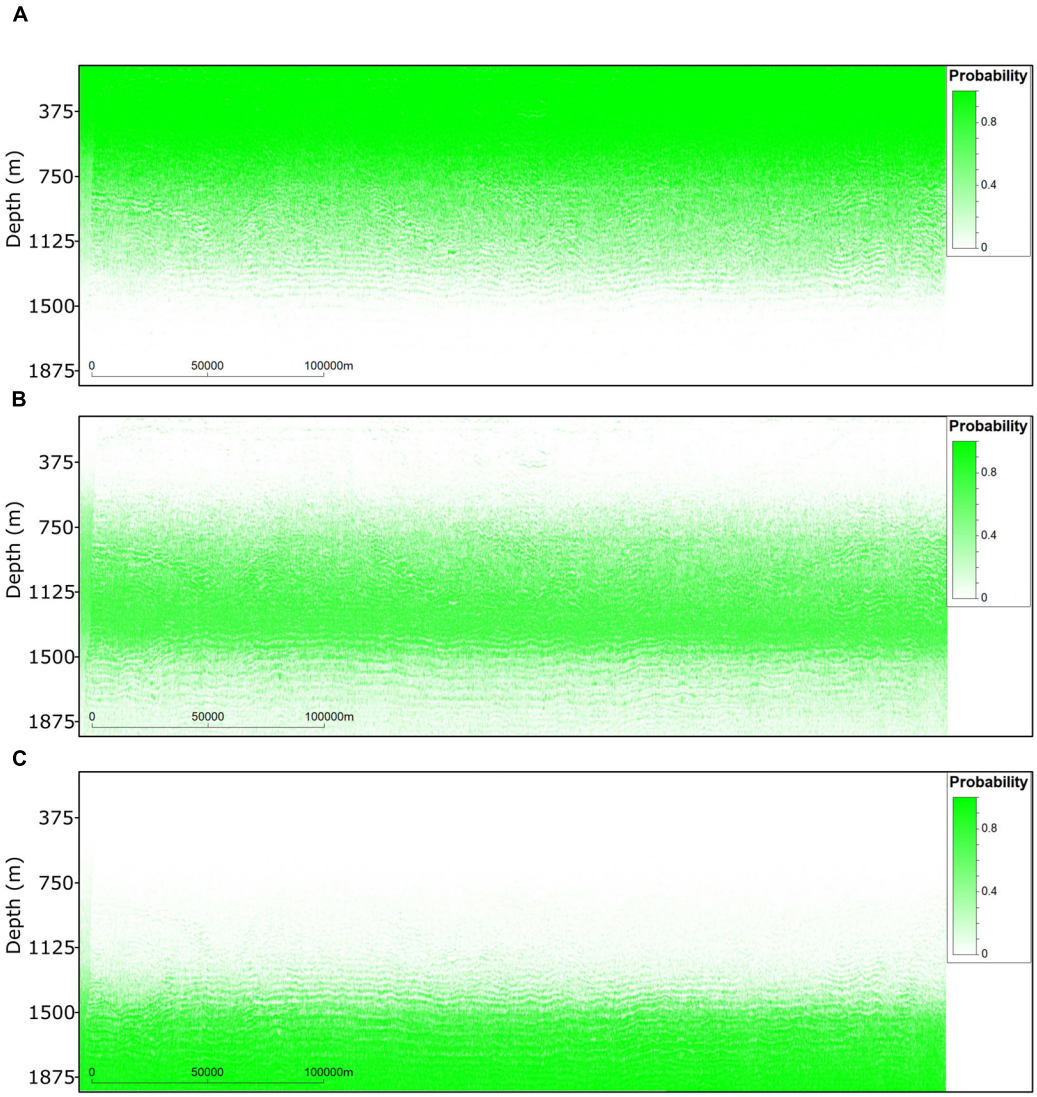

FIGURE 15 | Probability of occurrence of: **(A)** Central Atlantic Water; **(B)** Mediterranean Outflow Water; **(C)** Subarctic Intermediate Water. Probability models calculated from the classification of the thirty-two temperature and salinity models generated during the last iteration of the inversion using the training data shown in **Figure 5**.

bursts of energy at the smallest offsets (Pinheiro et al., 2010). True amplitude recovery was applied to compensate spherical divergence. A detailed velocity analysis was performed along the MCS profile. The resulting velocity field was used in the normal moveout correction of the records. After CMP sorting, the CMP gathers were stacked considering all offsets. Finally, a constant velocity (1,500 m/s) phase-shift migration (Stolt, 1978) and time-to-depth conversion were carried out using the same constant velocity model.

Due to computational constraints, the MCS profile was processed in swaths of 400 field records, with an overlap of 50 records. This computational limitation results in the vertical stripping observed in the final time migrated section, which also affect the inverted temperature and salinity models (**Figure 9**). All sections are plotted in the depth domain to ease interpretation by assuming an average P-wave velocity of 1,500 m/s. However, the inversion of the SO section was performed in the time domain (i.e., prior to depth conversion).

Preliminary Interpretation of Line WM-MAD01-003

A preliminary interpretation of the SO profile allows its vertical division in two layers: the top one, down to approximately 1,875 m, comprises bright and coherent reflections with different seismic signatures and dips; the bottom one, below this depth, which is relatively reflection-free maybe due to the relatively homogeneous North Atlantic Deep Water. For this reason, only

the top layer of the SO profile was considered for the geostatistical inversion (i.e., from 0 to 2.5 s in TWT).

The top layer shows the presence of an eddy at depths where Meddies are typically expected 600–1,500 m (**Figure 10A**). A smaller lenticular feature is also observed at shallow depths (around 750 m) that could be associated with the transition to Mediterranean waters or a secondary feature associated with that eddy (**Figure 10B**). Oblique reflections between 750 and 2,250 m might be related to oceanic fronts within the MOW or an inclined eddy of smaller dimensions as imaged in Tang et al. (2020). A possible double diffusion phenomenon can be detected by the continuous, parallel and bright reflections at approximately 1,500 ms for almost all the profile (**Figure 10C**). Double diffusion generates staircase thermohaline structure. The seismic signature of this oceanic structure has already been observed and investigated in the area near the Lesser Antilles in the Caribbean Sea (e.g., Fer et al., 2010) and in the Gulf of Cadiz associated to Mediterranean Outflow Water eddies (e.g., Biescas et al., 2008).

INVERSION RESULTS

The geostatistical SO inversion ran with six iterations, where at each iteration thirty-two pairs of temperature and salinity models were generated using direct sequential simulation (Soares, 2001) and direct sequential co-simulation with joint probability distributions (Horta and Soares, 2010). The stochastic sequential simulation and co-simulation were conditioned to the histograms and bi-histograms from **Figures 4**, **5**, respectively. Since the ARGO floats were not located along the seismic profile, no spatial conditioning was considered. Vertical variograms for each property were modeled from both ARGO floats while the horizontal variogram was modeled directly on the seismic amplitudes. This is a conventional approach in seismic reservoir characterization and often results in overestimation of the horizontal ranges of the variogram model (Azevedo and Soares, 2017). The objective function (Eq. 4) used to drive the inversion is based on the mismatch between synthetic and real seismic traces used for the inversion and the deviation of each realization of temperature and salinity from the background models shown in **Figure 6**.

The synthetic SO data computed from the pointwise average temperature and salinity models generated during the last iteration is shown in **Figure 11**. These data reproduce the location of the main oceanographic features as interpreted from the observed data as well as their amplitude content. As expected, the synthetic SO data calculated from these models is less noisy than the observed seismic (e.g., Avseth et al., 2005) and, consequently, increases the spatial continuity of the seismic reflections at the bottom part of the section (∼1,500 m). Iterative geostatistical seismic inversion methods are known for the ability to remain unmatched in noisy areas of the observed data (Azevedo and Soares, 2017). This effect is illustrated by the lack of vertical artifacts in the synthetic data. To illustrate the local convergence of the synthetic data, **Figure 11C** shows the trace-by-trace **S** between true and inverted SO data.

The inverted temperature and salinity models (**Figure 12**) capture the oceanic features of interest at finer scale when compared with the observed SO data. This effect is related to the use of geostatistical simulation as model perturbation technique, the geostatistical simulation fills-in the frequency band related to high-frequencies (Azevedo and Soares, 2017). Modeling oceanographic features at these scales is not possible with either deterministic seismic inversion methods or conventional interpolation techniques of direct observations of the ocean properties as represented by CTDs or XBTs. This is one of the main benefits of using geostatistical seismic inversion methods. These models show the filamentation structures around the eddie's core and in particular the warm intrusions around the homogenous nucleus. The use of background temperature and salinity models (**Figure 6**) allows reproducing the expected large-scale vertical distribution of both properties as interpreted from the global ocean models.

Additionally, the benefit of using geostatistical inversion methods is related to the ability to assess the uncertainty associated with the model predictions. **Figure 13** shows the pointwise variance of temperature and salinity computed from the ensemble of models generated for each property during the last iteration of the inversion procedure. It is interesting to discuss the spatial distribution pattern of these models. As temperature is the main contributor for the existence of reflection coefficients (Ruddick et al., 2009; Sallarès et al., 2009) the spatial uncertainty (i.e., the variance) is smaller in regions where the observed SO data exhibits coherent seismic reflections (i.e., above approximately 375 m and below 1,500 m). On the other hand, the region of lower variance for salinity, between the 750 and 1,125 m, matches the depths associated with the saltier layer as observed in the background model (**Figure 6**). The reason for this phenomenon still needs to be further investigated but might be related to: (i) the differences in signal-to-noise ratio in different parts of the seismic section; (ii) the local influence of the background models.

When contemporaneous direct measurements of temperature or salinity along the SO profile are available, one could assess the local performance of the inversion by retaining one observation out of the conditioning data and comparing the inverted traces with the observed data (i.e., a blind-well test in subsurface modeling). In this application example we compare the depth trend of the inverted two-dimensional sections of temperature and salinity of all the realizations generated during the last iteration of the inversion with the vertical one-dimensional profiles acquired by the ARGO floats (**Figure 14**). Note that the ARGO floats are not used to spatially constrain the inversion. In this simple exercise we aim at evaluating if the vertical trend of both properties is reproduced. As expected the direct measurements are not exactly reproduced but we consider the reproduction of the main trends to be a positive result.To illustrate the potential of geostatistical seismic inversion methods we used the ensemble of pairs of temperature and salinity models generated during the last iteration to generate two-dimensional sections of probability of occurrence of different water masses. First each pair of models was classified into three distinct water masses using Bayesian classification.

The *a priori* probabilities were inferred from the ARGO floats profiles, which were used as a training dataset (**Figure 5**). After classification of each pair, the ensemble of 32 models was used to compute the probability of occurrence of each water type (**Figure 15**). The resulting probability sections agree with the overall knowledge of this oceanic basin and with previous results obtained using exclusively large-scale oceanographic observations (Comas-Rodríguez et al., 2011). It is relevant to highlight that the order relationship of the different water masses (i.e., the Central Atlantic Water above the MOW above of the Subarctic Intermediate Water) is reproduced in the probability models, but it is not imposed by any other information rather than the SO data and the background models. As expected the regions of higher uncertainty are located at the boundaries of each water mass.

CONCLUSION

This paper presents the first seismic oceanography images of the Madeira abyssal plain region. The work focuses on two main aspects: (i) the introduction of a simple but efficient way to mitigate the effect of the direct arrival in the data; and (ii) the development of a geostatistical SO inversion that can be used when contemporaneous and collocated direct measurements are not available. The interpretation of the inverted models from an oceanographic perspective is limited, as it would benefit from the processing and inversion of the other two adjacent SO sections.

The processing sequence applied to these data was able to effectively attenuate the effect of the direct wave, revealing reflections in the first few hundred meters below the sea surface (**Figure 10**). The time-migrated section clearly shows fine-scale structure down to 2,000 m, below this depth the SO data shows no reflection. The upper part of the section exhibits a series of interesting oceanographic features that might be interpreted as eddies associated with the MOW and as double diffusive phenomena. However, these features need to be further explored to provide insights about the complex dynamics of the study area (**Figure 10**). The detailed interpretation of these oceanographic features will be performed after inverting the neighbor SO profiles existing in the region.

The processed time-migrated section was inverted using the proposed geostatistical SO inversion. We show how this inversion technique can be applied when no direct and contemporaneous observations of the ocean are available. We leverage common models of large-scale ocean dynamics and existing vertical profiles of the ocean properties measured by ARGO floats. This method was proved to be a useful tool to characterize sub-mesoscale oceanic features and has demonstrated a potential to invert for temperature and salinity. From the inverted models we also propose Bayesian classification of water masses. The probability of occurrence of the different water masses along the profile clearly agrees with the known vertical distribution (**Figure 15**).

As a final remark, it is worthwhile to highlight that the ensemble of inverted temperature and salinity fields generated at the last iteration still exhibits large variability (**Figure 14**). While this uncertainty is related to the lack of knowledge about the system under investigation (i.e., the ocean properties), it may be reduced and better predictions can be obtained by including additional constraints from other oceanographic variables (e.g., density, water column stability) during the inversion procedure. This approach would increase the reliability of the inverted models.

DATA AVAILABILITY STATEMENT

The original contributions presented in the study are included in the article/supplementary material, further inquiries can be directed to the corresponding author/s.

AUTHOR CONTRIBUTIONS

LA conceptualized and implemented 50% of the geostatistical SO inversion and wrote of the manuscript. LM conceptualized and supervised the SO processing data and wrote part of the manuscript. FT implemented 50% of the geostatistical SO inversion, ran the inversion on the application example, and wrote the manuscript. RT applied the SO processing flow. ÁP contributed for the preliminary interpretation of the results from an oceanographic point of view and wrote the manuscript. All authors contributed to the article and approved the submitted version.

ACKNOWLEDGMENTS

We gratefully acknowledge the support of the CERENA (strategic project FCT-UIDB/04028/2020). We would also like to thank EMEPC for acquiring and making this seismic profile available, CGG for the donation of Hampson-Russell used to extract the wavelet from the seismic oceanography data, Schlumberger for the donation of academic licenses of Petrel®, and Parallel Geoscience Corporation for SPW 4.0 used for the processing of the seismic data. These direct measurements of temperature and salinity were collected and made freely available by the International ARGO Program and the national programs that contribute to it (http://www.argo.ucsd.edu and http://argo.jcommops.org). The ARGO Program is part of the Global Ocean Observing System. This study has been conducted using E.U. Copernicus Marine Service Information. We are also grateful to the two reviewers for the detailed and extensive review of the original manuscript.

REFERENCES

Argo (2000). Argo float data and metadata from global data assembly centre (Argo GDAC). *SEANOE*. doi: 10.17882/42182

Avseth, P., Mukerji, T., and Mavko, G. (2005). *Quantitative Seismic Interpretation*. Cambridge: Cambridge University Press.

Azevedo, L., Huang, X., Pinheiro, L. M., Nunes, R., Caeiro, M. H., Song, H., et al. (2018). Geostatistical inversion of seismic oceanography data for ocean salinity

and temperature models. *Math. Geosci.* 50, 477–489. doi: 10.1007/s11004-017-9722-x

Azevedo, L., Nunes, R., Correia, P., Soares, A., Guerreiro, L., and Neto, G. S. (2015). Integration of well data into geostatistical seismic amplitude variation with angle inversion for facies estimation. *Geophysics* 80, M113–M128.

Azevedo, L., and Soares, A. (2017). *Geostatistical Methods for Reservoir Geophysics*, 1st Edn. Salmon Tower Building, NY: Springer International Publishing.

Barbosa Aguiar, A., Peliz, A., and Carton, X. (2013). A census of Meddies in a long-term high-resolution simulation. *Progr. Oceanogr.* 116, 80–94. doi: 10.1016/j.pocean.2013.06.016

Barbosa Aguiar, A. C., Peliz, A. J., Cordeiro Pires, A., and Le Cann, B. (2011). Zonal structure of the mean flow and eddies in the Azores Current system. *J. Geophys. Res.* 116.

Biescas, B., Ruddick, B. R., Nedimovic, M. R., Sallarès, V., Bornstein, G., and Mojica, J. F. (2014). Recovery of temperature, salinity, and potential density from ocean reflectivity. *J. Geophys. Res. Oceans* 119, 3171–3184. doi: 10.1002/2013JC009662

Biescas, B., Sallarès, V., Pelegrí, J. L., Machín, F., Carbonell, R., Buffett, G., et al. (2008). Imaging meddy finestructure using multichannel seismic reflection data. *Geophys. Res. Lett.* 35:11.

Blacic, T. M., Jun, H., Rosado, H., and Shin, C. (2016). Smooth 2-D ocean sound speed from Laplace and Laplace-Fourier domain inversion of seismic oceanography data. *Geophys. Res. Lett.* 43, 1211–1218. doi: 10.1002/2015GL067421

Bornstein, G., Biescas, B., Sallarès, V., and Mojica, J. F. (2013). Direct temperature and salinity acoustic full waveform inversion. *Geophys. Res. Lett.* 40, 4344–4348. doi: 10.1002/grl.50844

Bortoli, L. J., Alabert, F., Haas, A., and Journel, A. G. (1993). "Constraining stochastic images to seismic data," in *Geostatistics Troia'92*, ed. A. Soares (Dordrecht: Kluwer), 325–337.

Bosch, M., Mukerji, T., and González, E. F. (2010). Seismic inversion for reservoir properties combining statistical rock physics and geostatistics: A review. *Geophysics* 75:75A165. doi: 10.1190/1.3478209

Chhun, C., and Tsuji, T. (2020). Sound speed of thermohaline fine structure in the Kuroshio Current inferred from automatic sound speed analysis. *Expl. Geophys.* 51, 581–590. doi: 10.1080/08123985.2020.1736548

CMEMS (2016). Global Ocean 1/12° Physics Analysis and Forecast Updated Daily. Available online at: https://sextant.ifremer.fr/record/eec7a997-c57e-4dfa-9194-4c72154f5cc5/

Comas-Rodríguez, I., Hernández-Guerra, A., Fraile-Nuez, E., Martínez-Marrero, A., Benítez-Barrios, V. M., Pérez-Hernández, M. D., et al. (2011). The Azores Current System from a meridional section at 24.5°W. *J. Geophys. Res.* 116:C09021. doi: 10.1029/2011JC007129

Dagnino, D., Sallarès, V., Biescas, B., and Ranero, C. R. (2016). Fine-scale thermohaline ocean structure retrieved with 2-D prestack full-waveform inversion of multichannel seismic data: Application to the Gulf of Cadiz (SW Iberia). *J. Geophys. Res. Oceans* 121, 5452–5469. doi: 10.1002/2016JC011844

Dagnino, D., Sallarès, V., and Ranero, C. R. (2018). Waveform-preserving processing flow of multichannel seismic reflection data for Adjoint-State Full-waveform inversion of ocean Thermohaline Structure. *IEEE Trans. Geosci. Remote Sen.* 56, 1615–1625. doi: 10.1109/TGRS.2017.2765747

Deutsch, C. V., and Journel, A. G. (1992). *GSLIB: Geostatistical Software Library and User's Guide*. New York, NY: Oxford University Press.

Dickinson, A., White, N. J., and Caulfield, C. P. (2017). Spatial variation of diapycnal diffusivity estimated from seismic imaging of internal wave field, Gulf of Mexico. *J. Geophys. Res. Oceans* 122, 9827–9854. doi: 10.1002/2017jc013352

Duncan, G., and Beresford, G. (1995). Median filter behaviour with seismic data. *Geophys. Prospect.* 43, 329–345. doi: 10.1111/j.1365-2478.1995.tb00256.x

Fer, I., Nandi, P., Holbrook, W. S., Schmitt, R. W., and Páramo, P. (2010). Seismic imaging of a thermohaline staircase in the western tropical North Atlantic. *Ocean Sci.* 6, 621–631. doi: 10.5194/os-6-621-2010

Fortin, W. F. J., Holbrook, W. S., and Schmitt, R. W. (2017). Seismic estimates of turbulent diffusivity and evidence of nonlinear internal wave forcing by geometric resonance in the South China Sea. *J. Geophys. Res. Oceans* 122, 8063–8078. doi: 10.1002/2017jc012690

Gennert, M. A., and Yuille, A. L. (1988). "Determining the optimal weights in multiple objective function optimization," in *Proceedings of the Second International Conference on Computer Vision*, (Tampa, FL), 87–89.

González, E. F., Mukerji, T., and Mavko, G. (2008). Seismic inversion combining rock physics and multiple-point geostatistics. *Geophysics* 73, R11–R21. doi: 10.1190/1.2803748

Grana, D., Lang, X., and Wu, W. (2017). Statistical facies classification from multiple seismic attributes: comparison between Bayesian classification and expectation-maximization method and application in petrophysical inversion. *Geophys. Prospect.* 65, 544–562. doi: 10.1111/1365-2478.12428

Grana, D., Mukerji, T., Dvorkin, J., and Mavko, G. (2012). Stochastic inversion of facies from seismic data based on sequential simulations and probability perturbation method. *Geophysics* 77, M53–M72. doi: 10.1190/geo2011-0417.1

Gunn, K. L., White, N., and Caulfield, C.-c. P (2020). Time-Lapse seismic imaging of oceanic fronts and transient lenses within South Atlantic Ocean. *J. Geophys. Res. Oceans* 125:e2020JC016293. doi: 10.1029/2020JC016293

Gunn, K. L., White, N. J., Larter, R. D., and Caulfield, C. P. (2018). Calibrated seismic imaging of eddy-dominated warm-water transport across the Bellingshausen Sea, Southern Ocean. *J. Geophys. Res. Oceans* 123, 3072–3099. doi: 10.1029/2018JC013833

Hardy, R., Jones, S., Hardy, D., and Hobbs, R. (2007). *Seismic Oceanography: Processing Data From the Rockall Trough, West of Ireland. SEG Technical Program Expanded Abstracts*. Tulsa, OK: Society of Exploration Geophysicists, 894–898.

Hobbs, R., Carbonell, R., Artale, V., Geli, L., Gutscher, M., Huthnance, J., et al. (2007). *GO—Geophysical Oceanography: A New Tool to Understand the Thermal Structure and Dynamics of Oceans*. Durham: Durham University.

Holbrook, W. S., Fer, I., Schmitt, R. W., Lizarralde, D., Klymak, J. M., Helfrich, L. C., et al. (2013). Estimating oceanic turbulence dissipation from seismic images. *J. Atmospheric Oceanic Technol.* 30, 1767–1788. doi: 10.1175/jtech-d-12-00140.1

Holbrook, W. S., Paramo, P., Pearse, S., and Schmitt, R. W. (2003). Thermohaline fine structure in an oceanographic front from seismic reflection profiling. *Science* 301, 821–824. doi: 10.1126/science.1085116

Horta, A., and Soares, A. (2010). Direct sequential co-simulation with joint probability distributions. *Math. Geosci.* 42, 269–292. doi: 10.1007/s11004-010-9265-x

Huang, X., Song, H., Bai, Y., Chen, J., and Liu, B. (2012). Estimation of seawater movement based on reflectors from a seismic profile. *Acta Oceanol. Sin* 31, 46–53. doi: 10.1007/s13131-012-0235-7

IOC, SCOR, and IAPSO (2010). *The International Thermodynamic Equation of Seawater - 2010: Calculation and Use of THERMODYNAMIC PROPERTIES. INTERGOVERNMENTAL Oceanographic Commission, Manuals and Guides No. 56*. Paris: UNESCO, 196.

Jones, S. M., Hardy, R. J. J., Hobbs, R. W., and Hardy, D. (2008). The new synergy between seismic reflection imaging and oceanography. *First Break* 26: 8010.

Jun, H., Cho, Y., and Noh, J. (2019). Trans-dimensional Markov chain Monte Carlo inversion of sound speed and temperature: application to yellow sea multichannel seismic data J. *Mar. Syst.* 197:103180. doi: 10.1016/j.jmarsys.2019.05.006

Kormann, J., Biescas, B., Korta, N., de la Puente, J., and Sallarès, V. (2011). Application of acoustic full waveform inversion to retrieve high-resolution temperature and salinity profiles from synthetic seismic data. *J. Geophys. Res* 116:C11039. doi: 10.1029/2011JC007216

Le Ravalec-Dupin, M., and Noetinger, B. (2002). Optimization with the gradual deformation method. *Math. Geol.* 34, 125–142.

Mahadevan, A. (2016). the impact of submesoscale physics on primary productivity of plankton. *Ann. Rev. Mar. Sci.* 8, 161–184. doi: 10.1146/annurev-marine-010814-015912

Marler, R. T., and Arora, J. S. (2010). The weighted sum method for multi-objective optimization: new insights Struct. *Multidiscip. Optim.* 41, 853–862. doi: 10.1007/s00158-009-0460-7

Mead, J. L. (2008). Parameter estimation: a new approach to weighting a priori information. *J. Inverse Ill-posed Probl.* 16, 175–193. doi: 10.1515/JIIP.2008.011

Minakov, A., Keers, H., Kolyukhin, D., and Tengesdal, H. C. (2017). Acoustic waveform inversion for ocean turbulence. *J. Phys. Oceanogr.* 47, 1473–1491. doi: 10.1175/jpo-d-16-0236.1

Padhi, A., Mallick, S., Fortin, W., Holbrook, W. S., and Blacic, T. M. (2015). 2-D ocean temperature and salinity images from pre-stack seismic waveform

inversion methods: an example from the South China Sea. *Geophys. J. Int.* 202, 800–810. doi: 10.1093/gji/ggv188

Papenberg, C., Klaeschen, D., Krahmann, G., and Hobbs, R. W. (2010). Ocean temperature and salinity inverted from combined hydrographic and seismic data. *Geophys. Res. Lett.* 37:L04601.

Páramo, P., and Holbrook, W. S. (2005). Temperature contrasts in the water column inferred from amplitude-versus-offset analysis of acoustic reflections. *Geophys. Res. Lett.* 32:L24611. doi: 10.1029/2005GL024533

Pascual, A., Ruiz, S., Olita, A., Troupin, C., Claret, M., Casas, B., et al. (2017). Multiplatform experiment to unravel meso- and submesoscale processes in an intense front (AlborEx). *Front. Mar. Sci.* 4:39. doi: 10.3389/fmars.2017.00039

Pereira, P., Azevedo, L., Nunes, R., and Soares, A. (2019). The impact of a priori elastic models into iterative geostatistical seismic inversion. *J. Appl. Geophys.* 170:103850. doi: 10.1016/j.jappgeo.2019.103850

Pinheiro, L. M., Song, H., Ruddick, B., Dubert, J., Ambar, I., Mustafa, K., et al. (2010). Detailed 2-D imaging of the mediterranean outflow and meddies off W Iberia from multichannel seismic data. *J. Mar. Syst.* 79, 89–100. doi: 10.1016/j.jmarsys.2009.07.004

Richardson, P. L., Bower, A., and Zenk, W. (2000). A census of meddies tracked by floats. *Prog. Oceanogr.* 45, 209–250. doi: 10.1016/s0079-6611(99)00053-1

Ristow, J. P., Cordioli, J. A., Barão, M. V. C., Klein, A. H. F., and Barrault, G. F. G. (2017). "Development of methodological proceeding for seismic oceanography using legacy multi-channel seismic data of the oil and gas industry," in *Proceedings of the 2017 IEEE/OES Acoustics in Underwater Geosciences Symposium (RIO Acoustics)*, (Rio de Janeiro), 1–8. doi: 10.1109/RIOAcoustics.2017.8349710

Ruddick, B., Song, H. B., Dong, C. Z., and Pinheiro, L. (2009). Water column seismic images as maps of temperature gradient. *Oceanography* 22, 192–205. doi: 10.5670/oceanog.2009.19

Sallarès, V., Biescas, B., Buffett, G., Carbonell, R., Dañobeitia, J. J., and Pelegrí, J. L. (2009). Relative contribution of temperature and salinity to ocean acoustic reflectivity. *Geophys. Res. Lett.* 36:L00D06.

Sallarès, V., Mojica, J. F., Biescas, B., Klaeschen, D., and Gràcia, E. (2016). Characterization of the submesoscale energy cascade in the Alboran Sea thermocline from spectral analysis of high-resolution MCS data. *Geophys. Res. Lett.* 43, 6461–6468. doi: 10.1002/2016gl069782

Sambridge, M. (1999). Geophysical inversion with a neighbourhood algorithm-I. Searching a parameter space. *Geophys. J. Int.* 138, 479–494. doi: 10.1046/j.1365-246x.1999.00876.x

Sams, M., and Carter, D. (2017). Stuck between a rock and a reflection: a tutorial on low-frequency models for seismic inversion. *Interpretation* 5, B17–B27.

Segade, L. I. C., Gilcoto, M., Mercier, H., and Pérez, F. F. (2015). Quasi-synoptic transport, budgets and water mass transformation in the Azores–Gibraltar Strait region during summer 2009. *Progress Oceanogr.* 130, 47–64. doi: 10.1016/j.pocean.2014.09.006

Sen, M. K., and Stoffa, P. L. (1991). Nonlinear one dimensional seismic waveform inversion using simulated annealing. *Geophysics* 56, 1624–1638. doi: 10.1190/1.1442973

Soares, A. (2001). Direct sequential simulation and cosimulation. *Math. Geol.* 33, 911–926.

Soares, A., Diet, J. D., and Guerreiro, L. (2007). "Stochastic inversion with a global perturbation method," in *Proceedings of the Petroleum Geostatistics EAGE*, (Houten: European Association of Geoscientists and Engineers), 10–14.

Song, H. B., Huang, X. H., Pinheiro, L. M., Song, Y., Dong, C. Z., and Bai, Y. (2012). "Inversion studies in seismic oceanography," in *Computational Methods for Applied Inverse Problems*, Chap. 16, eds Y. Wang, A. G. Yagola, and C. Yang (Berlin, Boston: De Gruyter), 395–410. doi: 10.1515/9783110259056.395

Stolt, R. H. (1978). Migration by Fourier transform. *Geophysics* 43, 23–48.

Tang, Q., Gulick, S. P. S., Sun, J., Sun, L., and Jing, Z. (2020). Submesoscale features and turbulent mixing of an oblique anticyclonic eddy in the Gulf of Alaska investigated by marine seismic survey data. *J. Geophys. Res. Oceans* 125:e2019JC015393. doi: 10.1029/2019JC015393

Tang, Q., Hobbs, R., Zheng, C., Biescas, B., and Caiado, C. (2016). Markov Chain Monte Carlo inversion of temperature and salinity structure of an internal solitary wave packet from marine seismic data. *J. Geophys. Res. Oceans* 121, 3692–3709. doi: 10.1002/2016JC011810

Tang, Q., Tong, V. C. H., Hobbs, R. W., and Morales Maqueda, M. Á (2019). Detecting changes at the leading edge of an interface between oceanic water layers. *Nat. Commun.* 10:4674. doi: 10.1038/s41467-019-12621-8

Tang, Q., Xu, M., Zheng, C., Xu, X., and Xu, J. (2018). A locally generated high-mode nonlinear internal wave detected on the shelf of the northern South China Sea from marine seismic observations. *J. Geophys. Res. Oceans* 123, 1142–1155. doi: 10.1002/2017JC013347

Tarantola, A. (2005). *Inverse Problem Theory and Methods for Model Parameter Estimation*. Philadelphia: Society for Industrial and Applied Mathematics, 1–54.

Warner, M. (1990). Absolute reflection coefficients from deep Seismic reflections. *Tectonophysics* 173, 15–23. doi: 10.1016/0040-1951(90)90199-I

Wood, W. T., Holbrook, W. S., Sen, M. K., and Stoffa, P. L. (2008). Full waveform inversion of reflection seismic data for ocean temperature profiles. *Geophys. Res. Lett.* 35:L04608. doi: 10.1029/2007GL032359

Wunsch, C., and Ferrari, R. (2004). Vertical mixing, energy, and the general circulation of the oceans. *Annu. Rev. Fluid Mech.* 36, 281–314. doi: 10.1146/annurev.fluid.36.050802.122121

Conflict of Interest: The authors declare that the research was conducted in the absence of any commercial or financial relationships that could be construed as a potential conflict of interest.

Publisher's Note: All claims expressed in this article are solely those of the authors and do not necessarily represent those of their affiliated organizations, or those of the publisher, the editors and the reviewers. Any product that may be evaluated in this article, or claim that may be made by its manufacturer, is not guaranteed or endorsed by the publisher.

frontiers in Marine Science

ORIGINAL RESEARCH
published: 05 October 2021
doi: 10.3389/fmars.2021.697179

Vertical Mixing and Heat Fluxes Conditioned by a Seismically Imaged Oceanic Front

Kathryn L. Gunn[1*†], *Alex Dickinson*[1†], *Nicky J. White*[1] *and Colm-cille P. Caulfield*[2,3]

[1] Bullard Laboratories, Department of Earth Sciences, University of Cambridge, Cambridge, United Kingdom, [2] BP Institute, University of Cambridge, Cambridge, United Kingdom, [3] Department of Applied Mathematics and Theoretical Physics, University of Cambridge, Cambridge, United Kingdom

OPEN ACCESS

Edited by:
Fabien Roquet,
University of Gothenburg, Sweden

Reviewed by:
Jen-Ping Peng,
Leibniz Institute for Baltic Sea Research (LG), Germany
Gerd Krahmann,
GEOMAR Helmholtz Center for Ocean Research Kiel, Germany

***Correspondence:**
Kathryn L. Gunn
klg48@esc.cam.ac.uk;
kgunn.sc@gmail.com

†Present address:
Kathryn L. Gunn,
Centre for Southern Hemisphere Oceans Research (CSHOR), CSIRO Oceans and Atmosphere, Hobart, TAS, Australia
Alex Dickinson,
School of Natural and Environmental Sciences, Drummond Building, Newcastle University, Newcastle-upon-Tyne, United Kingdom

Specialty section:
This article was submitted to Ocean Observation, a section of the journal Frontiers in Marine Science

Received: 19 April 2021
Accepted: 02 September 2021
Published: 05 October 2021

Citation:
Gunn KL, Dickinson A, White NJ and Caulfield CP (2021) Vertical Mixing and Heat Fluxes Conditioned by a Seismically Imaged Oceanic Front. Front. Mar. Sci. 8:697179. doi: 10.3389/fmars.2021.697179

The southwest Atlantic gyre connects several distinct water masses, which means that this oceanic region is characterized by a complex frontal system and enhanced water mass modification. Despite its significance, the distribution and variability of vertical mixing rates have yet to be determined for this system. Specifically, potential conditioning of mixing rates by frontal structures, in this location and elsewhere, is poorly understood. Here, we analyze vertical seismic (i.e., acoustic) sections from a three-dimensional survey that straddles a major front along the northern portion of the Brazil-Falkland Confluence. Hydrographic analyses constrain the structure and properties of water masses. By spectrally analyzing seismic reflectivity, we calculate spatial and temporal distributions of the dissipation rate of turbulent kinetic energy, ε, of diapycnal mixing rate, K, and of vertical diffusive heat flux, F_H. We show that estimates of ε, K, and F_H are elevated compared to regional and global mean values. Notably, cross-sectional mean estimates vary little over a 6 week period whilst smaller scale thermohaline structures appear to have a spatially localized effect upon ε, K, and F_H. In contrast, a mesoscale front modifies ε and K to a depth of 1 km, across a region of $O(100)$ km. This front clearly enhances mixing rates, both adjacent to its surface outcrop and beneath the mixed layer, whilst also locally suppressing ε and K to a depth of 1 km. As a result, estimates of F_H increase by a factor of two in the vicinity of the surface outcrop of the front. Our results yield estimates of ε, K and F_H that can be attributed to identifiable thermohaline structures and they show that fronts can play a significant role in water mass modification to depths of 1 km.

Keywords: seismic oceanography, diapycnal diffusivity, diffusive heat flux, fronts, Brazil-Falkland Confluence

1. INTRODUCTION

Gyres are a key component of the large-scale meridional overturning circulation since they provide exchange sites between warm and cold water masses. In the southwest Atlantic Ocean, the Brazil-Falkland Confluence connects subtropical with subantarctic water masses. This confluence is a region of significant water mass modification. Nevertheless, a paucity of sufficiently well-resolved observations has hampered efforts to understand the extent of water mass variability associated with vertical exchanges. Here, we address this knowledge gap by exploiting a seismic (i.e., acoustic) technology that enables full-depth vertical sections of thermohaline structure and vertical mixing

rates to be recovered. These seismic sections are hundreds of kilometers long and complement hydrographic sections acquired by the Global Ocean Ship-based Hydrographic Investigations Program (GO-SHIP), albeit with a dramatically improved horizontal resolution of ∼10 m.

The southward-flowing western boundary current of the South Atlantic subtropical gyre, known as the Brazil Current (BC), connects warm subtropical waters with cold subantarctic water masses of the northward flowing Falkland Current (FC; **Figure 1A**). Hydrographic transects, ship-based observations, and satellite measurements demonstrate that this region is a site of strong water mass modification (e.g., Bianchi et al., 2001; Saraceno et al., 2004). Jullion et al. (2010) showed that horizontal heat and salt exchanges account for up to one half of the total poleward heat flux across the Antarctic Circumpolar Current. These insights are necessarily based upon intermittently obtained hydrographic measurements that cannot easily constrain water mass modification which occurs as a result of vertical mixing. Thus, the distribution and variability of vertical mixing rates have yet to be diagnosed.

Concentration of large-scale temperature gradients creates complex frontal systems, that tend to be important sites for water mass modification. Shallow (i.e., 0–500 m) observations obtained by towed instruments and floats demonstrate that the upper portions of fronts are often regions of enhanced vertical mixing (e.g., Nagai et al., 2009, 2015; D'Asaro et al., 2011; Johnston et al., 2011; Peng et al., 2020). These locations can contribute significantly to the vertical re-distribution of heat and salt, thus impacting thermohaline circulation (Liang et al., 2015; Frazão and Waniek, 2021). A paucity of observations in the southwest Atlantic Ocean has left a gap in our understanding of the magnitude and variability of vertical heat fluxes in the Brazil-Falkland Confluence. Even less is known about the role that fronts play in moderating dissipation rates at depths greater than ∼500 m.

Here, we address these knowledge gaps with the aid of seismic reflection profiling. This technology exploits low (i.e., 5–100 Hz) frequency sources and multiple towed cables with dense arrays of hydrophone receivers (Holbrook et al., 2003; Ruddick et al., 2009). Acoustic waves are transmitted through, and reflected from, temperature fluctuations on length scales that vary from tens of meters to tens of kilometers. The resultant seismic sections can be used to delineate and map oceanic structure and water masses with contrasting thermohaline properties over a hitherto unsurpassed range of scales (e.g., Sallarès et al., 2009; Sheen et al., 2012; Gunn et al., 2018). Resultant images can be inverted and spectrally analyzed to obtain simultaneous distributions of temperature and vertical mixing rates, respectively, that span the full depth of the water column (e.g., Dickinson et al., 2017; Gunn et al., 2020). This emerging field of research is generally referred to as Seismic Oceanography.

We analyze thermohaline structures and mixing properties across a portion of the northern Brazil-Falkland Confluence. First, we describe three seismic sections that straddle this confluence, spanning a period of 6 weeks between 1st February 2013 and 15th March 2013. Each of these sections is ∼140 km in length. They were acquired sequentially and any one section is laterally offset by several kilometers. Our study builds upon a previously published contribution which describes the structure and hydrographic properties of a deeply penetrating front and of a transient mesoscale eddy that both advect across the seismic survey (Gunn et al., 2020). Secondly, we spectrally analyze these seismic sections in order to calculate spatial distributions of diapycnal mixing rates, which can then be combined with seismically determined temperature profiles to estimate vertical diffusive heat fluxes. Finally, we compare recovered distributions of mixing and heat flux with observed oceanographic processes and we discuss how these distributions may evolve as a function of time.

2. OBSERVATIONAL CONSTRAINTS

2.1. Seismic Reflection Survey

We present time-lapse imagery extracted from a three-dimensional (3D) seismic reflection survey that straddles a small northern portion of the Brazil-Falkland confluence of the southwest Atlantic Ocean (**Figure 1A**). This seismic survey was acquired between November 2012 and April 2013 by Polarcus Limited OSE. During acquisition, a pair of alternately firing airgun arrays, each of which has 36 guns with a combined volume of 70 L (4240 in^3), were deployed off the stern of the vessel at a depth of ∼5 m. Ten streamers (i.e., acoustically sensitive cables), each of which is 6 km in length, were towed behind the vessel (for further details see Gunn et al., 2020). The vessel steamed with an average azimuth of 41° in what is known as the racetrack mode of acquisition at an average speed of 2.5 m s^{-1} (Yilmaz, 2001). Each individual pass of the vessel acquired a single 3D swath of seismic data that is ∼120–150 km long and ∼600 m wide. The seismic sections presented here are extracted from the center of each swath which were acquired between 1st February 2013 and 15th March 2013 (**Figures 1B–D** and **Table 1**).

2.2. Hydrographic and Satellite Observations

Independent hydrographic and satellite observations are used to calibrate this seismic reflection survey. Coincident and dense hydrographic measurements are unavailable. Instead, we exploit conductivity-temperature-depth (CTD) profiles from three nearby GO-SHIP transects (A10, A11, and A17). These transects approximately bound the Brazil-Falkland Confluence at its northern, southern and eastern boundaries, respectively (Jullion et al., 2010). Given the planform of the Brazil and Falkland Currents, these transects are representative of BC (i.e., subtropical), FC (i.e., subantarctic), and mixed water masses, respectively (**Figure 1**). A subset of CTD casts from each GO-SHIP transect are used to generate average profiles of temperature and salinity (**Figure 2**). Along transects A10 and A11, these CTD casts are positioned away from the continental shelf and extend offshore by the approximate width of the Brazil and Falkland Currents, respectively (**Figure 1A**). For transect A17, a monthly composite of sea surface currents and float trajectories are used to gauge the latitudinal range of enhanced eddy kinetic energy associated with the confluence between 34 and 42° S (Iglesias, 2019). We conclude that these average

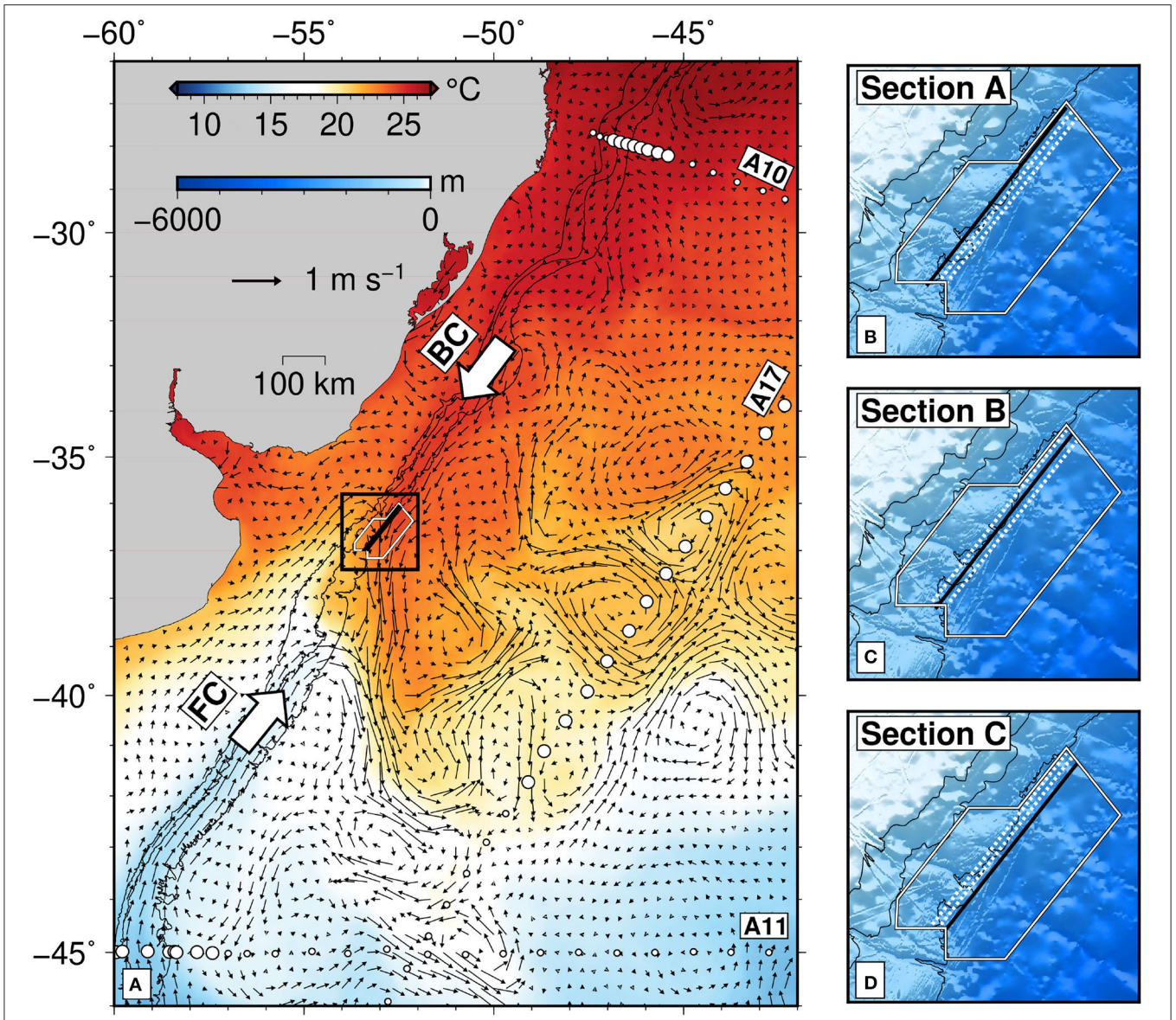

FIGURE 1 | (A) Map of southwest Atlantic Ocean where red/blue colors represent warm/cold mean sea-surface temperatures for monthly composite centered on 16th February 2013 (taken from Multi-scale Ultra-high resolution (MUR) satellite sea-surface temperature measurements which have monthly and 1 km resolution). Thin black lines = 300/1,000/2,000 m bathymetric contours; field of black arrows = average sea surface geostrophic current velocities calculated for 5-day composite centered on 15 February 2013 from OSCAR satellite measurements (scale at top left-hand side); labeled arrows 0= 0Brazil Current (BC) and Falkland (i.e., Malvinas) Current (FC); black box = zoom region shown in panels **(B–D)**; white polygon 0= 0location of 3D seismic reflection survey; thick black line within polygon 0= 0locus of three transects displayed in **Figures 4**–**9**; small white circles = loci of conductivity temperature depth (CTD) probes acquired as part of GO-SHIP transects A10 (December 1992), A17 (April 2019) and A11 (December 1992); large white circles = loci of CTDs used to compute average hydrographic profiles (**Figure 2**). **(B–D)** Zoomed portion shown in **(A)**. Blue shading = water depth according to scale bar at top left-hand of **(A)**; thin black lines = 300/1,000/2,000 m bathymetric contours; white polygon 0= 0location of 3D seismic reflection survey; solid black line inside polygon = seismic transect acquired on given date; dotted white lines 0= 0other transects.

profiles are representative of water masses entering and exiting the confluence at the location of the seismic survey.

Maps of sea surface temperature for the southwest Atlantic Ocean highlight the confluence of warm and cold water masses (**Figure 3**). Confluent flow of warm BC and cold FC concentrates large-scale temperature gradients that are clearly visible in satellite imagery, generating a frontal system that is marked by several discrete fronts which occur between 36 and 39° S (Gordon, 1989; Peterson and Stramma, 1991). Temperature maps also show the variability in the location and properties of this confluence as a function of time. They are consistent with other satellite observations, which confirm the presence of

TABLE 1 | Seismic acquisition information (**Figure 1**).

Section	Length, km	dd/mm/yy	Azimuth
A	123	01/02/13	SW–NE
B	142	13/02/13	SW–NE
C	135	15/03/13	SW–NE

Note that Section B is equivalent to Section 6 of Gunn et al. (2020).

this oscillation of the Brazil–Falkland Confluence at this time of year (Garzoli and Garraffo, 1989; Saraceno et al., 2004; Combes and Matano, 2014). After converging, sea surface current and float trajectory measurements show that these subtropical and subantarctic water masses turn eastward, spreading out into the center of the Atlantic Ocean (**Figure 1**; Iglesias, 2019).

3. METHODS

3.1. Signal Processing of Seismic Imagery

In the context of Seismic Oceanography, an important goal is to combine individual seismic records to order to generate an image which represents a full-depth vertical section through the water column (**Figure 4A**). To construct these sections, we adopt standard signal processing techniques that have previously been applied to this survey and that are described in more detail by Gunn et al. (2020). Significant processing steps include application of a 20–90 Hz band-pass filter with a roll-off of 24 dB per octave, muting of the bright and irregular sea-bed reflection, removal of high amplitude acoustic energy that travels horizontally along the length of each streamer (i.e., the direct arrival), velocity picking, and stacking (i.e., combining multiple seismic records). The data used to construct a single stacked section take several hours to acquire since the vessel steams at $\sim$2.5 m s^{-1}. It is important to emphasize that during the stacking process, many repeated shot-receiver pairs that image an identical portion of the sub-surface are summed together. The vertical resolution of a seismic section is given by $v/(4f)$ where v and f are the speed of sound through water and the dominant frequency of the acoustic source, respectively. In this region, $v =$ 1,510 $\pm$ 30 m s^{-1} and the peak value of $f =$ 35$\pm$ 5 Hz, which yields a nominal vertical resolution of 10–20 m (Gunn et al., 2020). In contrast to GO-SHIP transects, vertical and horizontal resolution are equal.

The observed reflectivity is generated by changes in acoustic impedance (i.e., the product of sound speed and density). Within the water column, acoustic impedance is predominantly controlled by sound speed variation, which depends upon temperature gradient and, to a much lesser extent, upon salinity gradient (Sallarès et al., 2009). When confluent flow of warm subtropical and cold subantarctic water masses concentrates large-scale temperature gradients across a large region, this confluence is characterized by strong impedance contrasts which gives rise to bright reflectivity (**Figure 4A**). In summary, each seismic section represents a near-instantaneous, full-depth vertical slice through the oceanic volume that is essentially a well-resolved map of vertical temperature gradient.

3.2. Seismically Determined Properties

The temperature distribution along each seismic section is calculated using an adapted iterative method (Papenberg et al., 2010; Gunn et al., 2018, 2020). Acoustic inverse schemes that rely upon densely sampled hydrographic measurements are less easy to exploit since coincident observations of temperature and salinity are unavailable (Azevedo et al., 2021). Instead, we use a pragmatic approach that side-steps this limitation and takes advantage of the dominant dependency of acoustic sound speed upon temperature. First, we construct the long-wavelength sound speed field for each section by analyzing pre-stack seismic records (**Figures 6**, **7** of Gunn et al., 2020). Secondly, each sound speed field is iteratively converted into an equivalent distribution of temperature using the equation of state for seawater.

Due to a paucity of coeval hydrographic measurements, we reasonably assume that density varies as a function of depth and that salinity is a function of both temperature and depth, which can be estimated at 10 m depth intervals. The temperature-salinity relationship is calculated from the regional CTD casts shown in **Figures 1A**, **2** and it is in accordance with regional hydrographic measurements (Gunn et al., 2020). Given these assumptions, seismic sections can be converted into temperature (**Figure 4B**). Seismically derived temperature and salinity estimates enable contemporaneous fields of vertical temperature gradient and of density to be estimated which can then be used to calculated vertical diffusive heat fluxes (Equation 3). Note that recovery of temperature fields from seismic images is contingent upon the distribution of horizontally continuous reflections. As a consequence, there is greater uncertainty in the details of any recovered field beneath 1,000 m and above $\sim$150 m where reflections can be difficult to trace see **Figure 6** of (Gunn et al., 2020). Nevertheless, this method is a useful way to calculate contemporaneous temperature fields, especially because it enables the vertical temperature gradient to be recovered. A conservative depth-averaged uncertainty of seismically determined temperature estimates is $\leq \pm 1^{\circ}$ C (Gunn et al., 2020).

3.3. Dissipation and Diapycnal Mixing Rates

Oceanic circulation is maintained by the cascade of energy from large-scale flows down to the smallest length scales of turbulent mechanical mixing (Munk, 1966). On horizontal length scales of 0.1–10 km, this cascade can be interrogated by tracking and spectrally analyzing reflections from stacked seismic sections (e.g., Sheen et al., 2009; Holbrook et al., 2013; Dickinson et al., 2017). Small vertical displacements along quasi-horizontal reflections record perturbations of the background stratification caused by a combination of internal waves and turbulence. Variations in the size of these vertical displacements as a function of horizontal wavelength are obtained by calculating the power spectrum of vertical displacements as a function of horizontal wavenumber k_x. This approach enables the internal wave and turbulent subranges to be identified and modeled to obtain the dissipation rate of turbulent kinetic energy, ε, and thence diapycnal diffusivity, K. Sheen et al. (2009) and

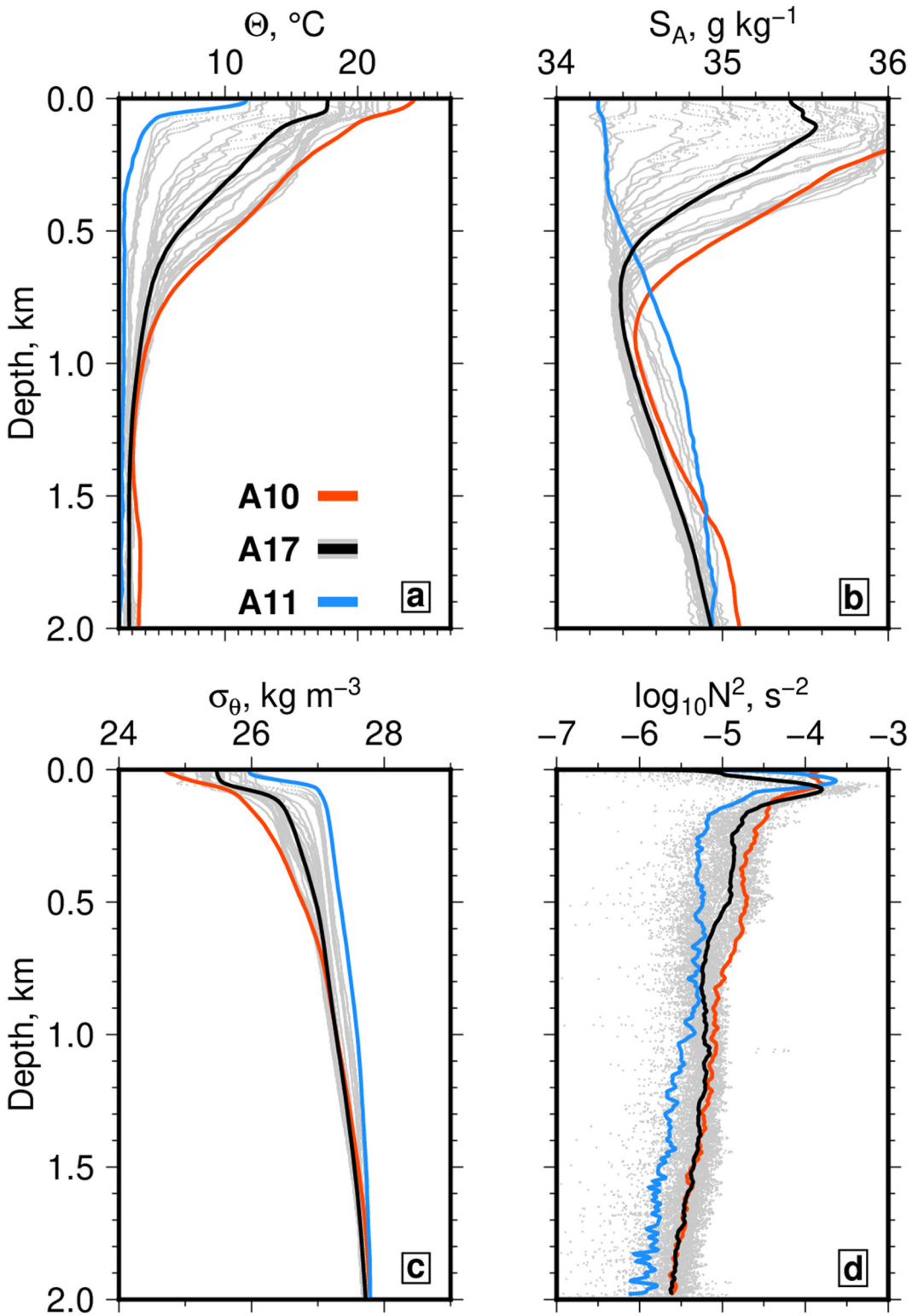

FIGURE 2 | Hydrographic profiles calculated from CTD casts acquired along GO-SHIP sections A10, A11, and A17 that are representative of subtropical, subantarctic and intermediate water masses, respectively (see **Figure 1A** for location). **(A)** Conservative temperature, Θ, plotted as function of depth. **(B)** Absolute salinity, S_A, plotted as function of depth. **(C)** Potential density anomaly, σ_θ, plotted as function of depth. **(D)** Buoyancy (Brunt-Väisälä) frequency squared, N^2, plotted on logarithmic scale as function of depth. In each panel, gray lines = individual profiles of A17 casts; red line = average profile calculated from 8 CTD casts along A10; blue line = average profile calculated from 8 CTD casts along A11; black line = average profile calculated from 14 CTD casts acquired along A17 (see enlarged white circles in **Figure 1A**). All profiles smoothed using 100 m low-pass Butterworth filter.

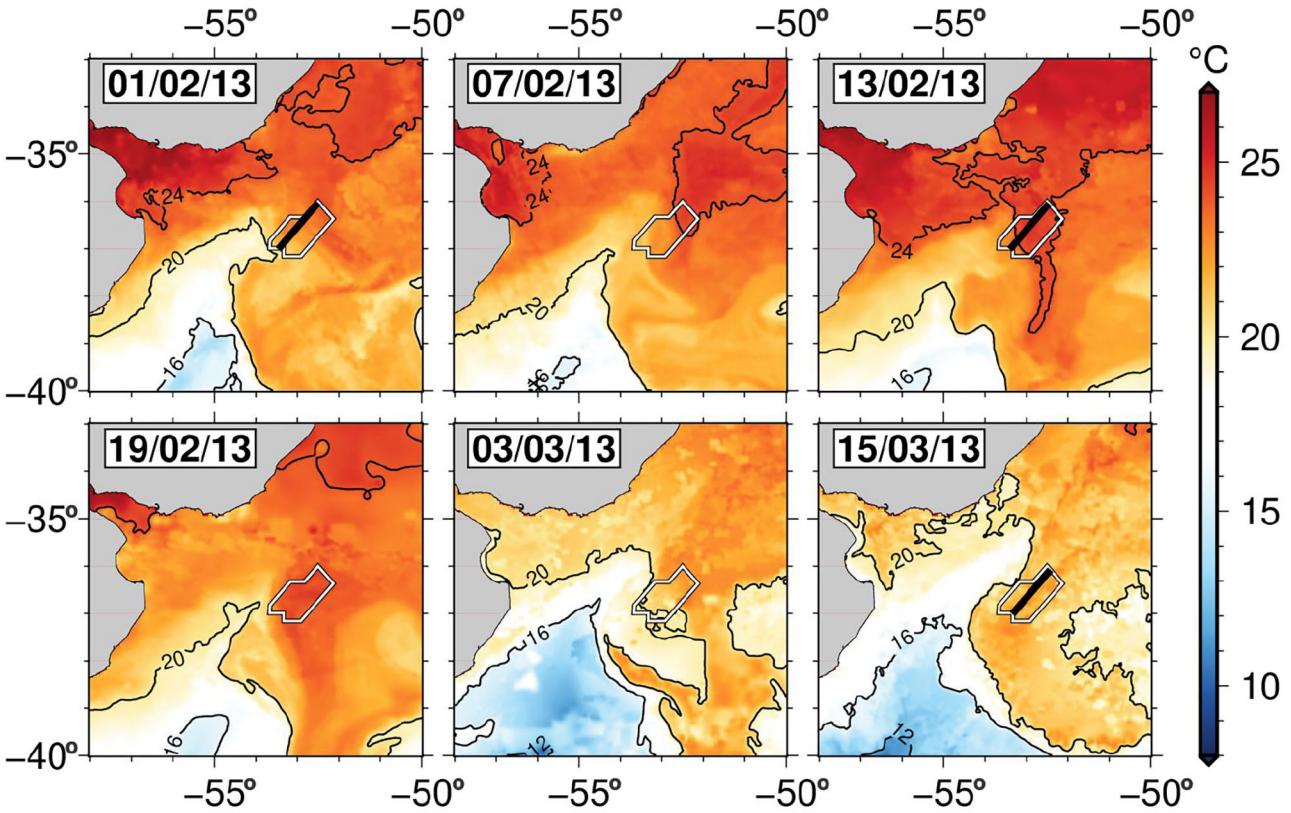

FIGURE 3 | Selected maps of sea-surface temperature for southwest Atlantic Ocean showing temporal variability of Brazil-Falkland Confluence. Red/blue colors = warm/cold sea surface temperatures from 1st February 2013 to 15th April 2013 (date shown at top left-hand side). Satellite sea-surface temperature observations from L4 gridded products of GHRSST database that have daily and 1 km resolutions. White polygon = location of 3D seismic survey; thick black line = loci of seismic sections for 01/02/13, 13/02/13, and 15/03/13; thin black lines = sea surface temperature contoured at 4° C intervals.

Holbrook et al. (2013) demonstrated that seismic reflections generally track isopycnal surfaces and they showed that the turbulent subrange can be reliably isolated with careful signal processing. The methodology is divided into three stages (**Figure 5**).

3.3.1. Tracking Reflective Events

Each trace of seismic amplitude is converted into the cosine of the instantaneous phase angle. Application of this seismic attribute helps to emphasize the continuity of reflections in a way that does not influence resolution of the seismic image (Holbrook et al., 2013). Reflective events are tracked by contouring with a constant value of the instantaneous phase (**Figure 5A**). The choice of contour value does not affect the geometry of tracked reflections but it can influence the number of tracked reflections (Dickinson et al., 2017). Reflections with lengths that are greater than 1 km are chosen since they yield the best-resolved spectra. At this stage, the midpoints along each contoured event are calculated and taken to represent isopycnal surfaces, thus providing information about horizontal wavenumber, k_x. These midpoints are used to estimate vertical displacements of the isopycnal surfaces (**Figure 5B**).

3.3.2. Spectral Analysis of Tracked Reflections

Power of vertical displacement, Φ_ξ, as a function of k_x is calculated from each linearly detrended tracked reflection using a multi-taper Fourier Transform, $F(k_x)$, where $\Phi_\xi = |F(k_x)|^2$ (Thomson, 1982). Φ_ξ is a measure of the power distribution of the decomposed signal as a function of k_x (**Figure 5C**). Horizontal wavenumber power spectra are converted into power spectra of the horizontal gradient of vertical displacement, Φ_{ξ_x}, by multiplying Φ_ξ by $(2\pi k_x)^2$ (Klymak and Moum, 2007a,b). $\Phi_{\xi_x}(k_x)$ is usually referred to as the slope spectrum.

In the oceanic realm, slope spectra calculated from seismic images, as well as from autonomous gliders, reveal two distinctive regimes with the characteristic spectral slopes of the internal wave and turbulent components of the oceanic energy spectrum (Klymak and Moum, 2007a,b; Sheen et al., 2009). The internal wave regime is visible at low wavenumbers of $10^{-3} < k_x < 10^{-2}$ m^{-1}, corresponding to horizontal length scales of >100–1,000 m (**Figure 5D**). At high wavenumbers of $k_x > 10^{-2}$ m^{-1}, internal waves break and there is a clear transition to a regime with a characteristic turbulent spectral slope. The spectral slope of this regime matches the Kolmogorov exponent of $-5/3$ which, when multiplied by $(2\pi k_x)^2$ to create horizontal gradient (i.e., slope) spectra, becomes $+1/3$

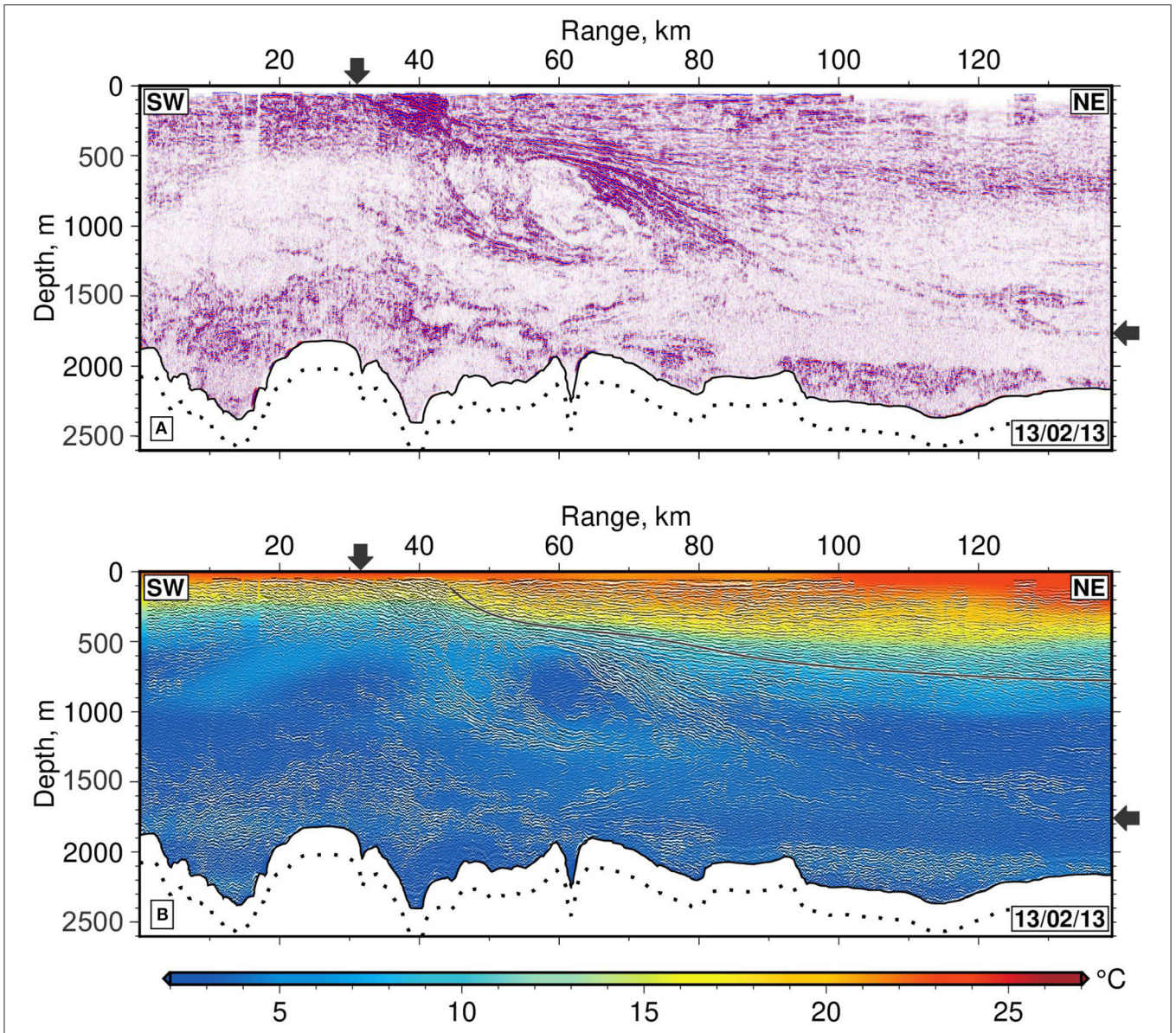

FIGURE 4 | (A) Seismic reflection section B that crosses oceanic front (see also **Figure 1C** and panel dated 13/02/13 of **Figure 3**). Red/blue stripes represent positive/negative polarity reflections generated by temperature changes as small as ∼ 0.01°C within water column; irregular solid/dotted lines = seabed; black arrows = maximal extent of front at sea surface and at depth. **(B)** Corresponding conservative temperature field calculated using iterative inversion procedure (Gunn et al., 2018, 2020). Warm/cool colors = temperatures according to scale bar; solid black line = smoothed potential density anomaly contour of 26.8 kg m^{-3} which highlights shallowest sub-surface expression of front (see **Figures 3**, **8E,F** of Gunn et al., 2020 for more detailed treatment).

(Spalding, 1991). Significantly, this slope is still observed at horizontal scales that exceed the Ozmidov length scale, which means that a slope of $-5/3$ should not be thought of as purely isotropic turbulence. At these longer scales, this slope probably represents layered anisotropic stratified turbulence (LAST; Riley and Lindborg, 2008; Falder et al., 2016). White noise has a gradient of $+2$ and is clearly visible at the highest wavenumbers (e.g., $k_x > 10^{-1.7}$ m^{-1}). Given this ability to seismically identify spectral slopes, it is possible to model the observed turbulent subrange and to estimate both the dissipation rate of turbulent kinetic energy, ε, and the diapycnal diffusivity, K.

3.3.3. Dissipation and Diffusivity Calculations

It is straightforward to identify internal wave, turbulent, and white (i.e., ambient) noise subranges by examining $\Phi_{\zeta_x}(k_x)$ spectra (**Figures 5E–I**). Here, we focus on analyzing observed turbulent subranges following the approach described by Sheen et al. (2009) and later refined by Dickinson et al. (2017). For a given spectrum, the gradient of the turbulent subrange,

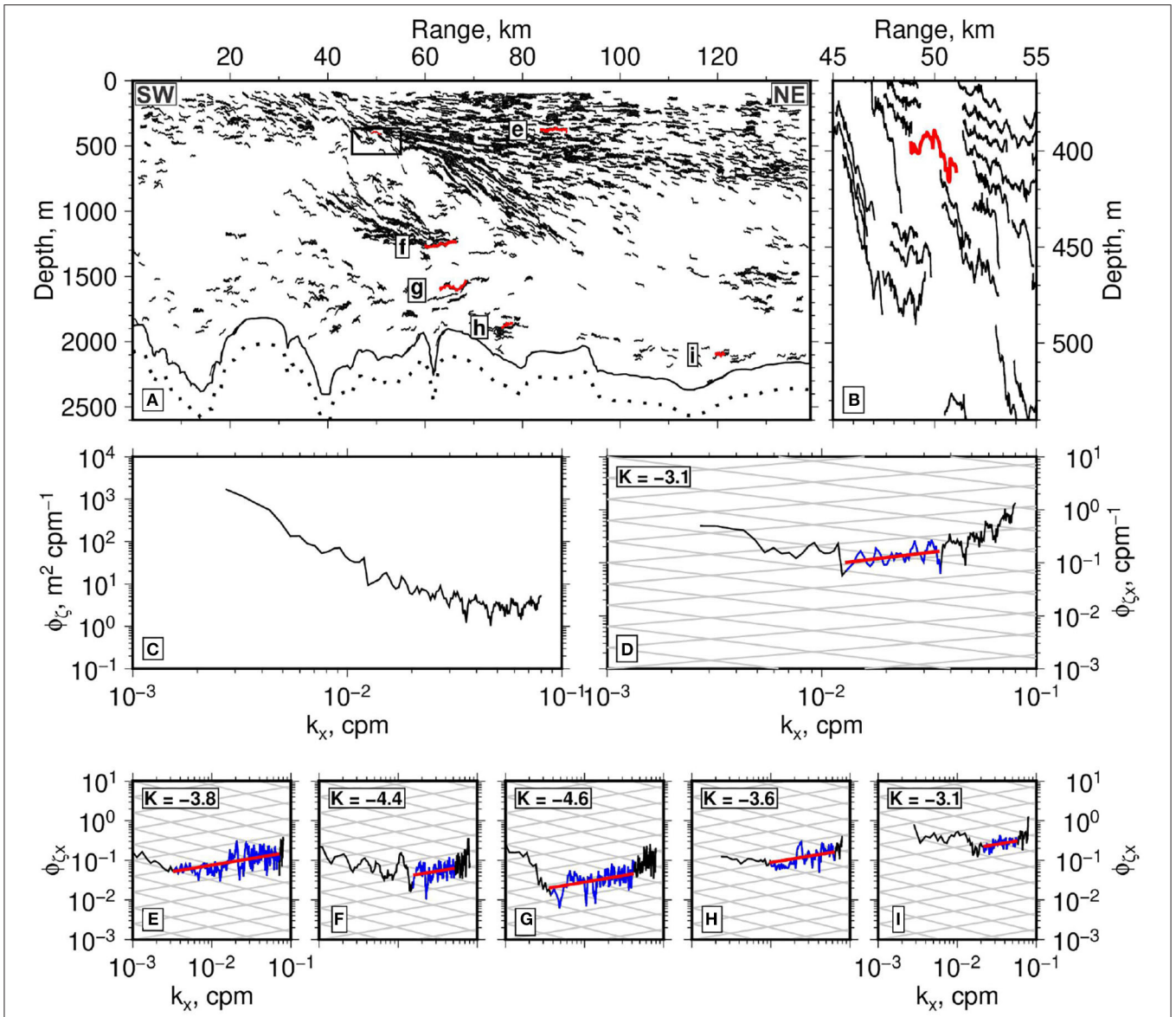

FIGURE 5 | (A) Auto-tracked version of section B. Black box = zoomed portion shown in **(B,C)** where red line = auto-tracked reflection analyzed in **(C,D)**; labeled red lines = auto-tracked reflections that are spectrally analyzed in **(E–I)**. **(B)** Zoomed portion of **(A)** with auto-tracked reflection that is spectrally analyzed in **(C,D)**. **(C)** Power of vertical displacement, Φ_ξ, plotted as function of horizontal wavenumber, k_x, which has units of cycles per meter (cpm). Spectrum calculated using multi-taper Fourier transform of linearly detrended tracked reflection highlighted in **(B)**. Internal wave, turbulent, and noise subranges characterized by spectral slopes of −2, −5/3 and 0, respectively. **(D)** $\Phi_{\xi x}$ (i.e., $\Phi_\xi \times (2\pi k_x)^2$) plotted as function of k_x. On this slope spectrum, black/blue/black lines = internal wave/turbulent/noise subranges characterized by spectral slopes of −1/2, +1/3 and +2, respectively; red line = best-fitting model of turbulent subrange; label in top right = calculated value of $\log_{10} K$; gray reticule = slopes of internal wave and turbulent subranges with spectral gradients of −1/2 and +1/3, respectively. **(E–I)** Slope spectra for other auto-tracked reflections shown in **(A)**. Symbols and labels as for **(D)**.

the co-ordinates of the intersection between the internal wave and turbulent subranges, and width of the turbulent subrange determine the value of $\Phi_{\zeta_x}(k_x)$. A misfit function that measures the difference between observed and calculated values of $\Phi_{\zeta_x}(k_x)$ is minimized by adjusting the values of gradient, co-ordinates of intersection, and width for each spectrum (see Appendix D3 of Dickinson et al., 2020). In this way, $\Phi_{\zeta_x}(k_x)$ is calculated for each spectrum and used to estimate the turbulent dissipation rate, ε, using a simplified version of the Batchelor et al. (1959) model where

$$\Phi_{\zeta_x} = \frac{4\pi\Gamma}{N^2} C_T \varepsilon^{2/3} (2\pi k_x)^{1/3}. \quad (1)$$

$C_T = 0.4$ is the Obukhov-Corrsin constant, $\Gamma = 0.2$ is the turbulent flux coefficient, and N is the Brunt-Väisälä (i.e., buoyancy) frequency which is obtained from regional

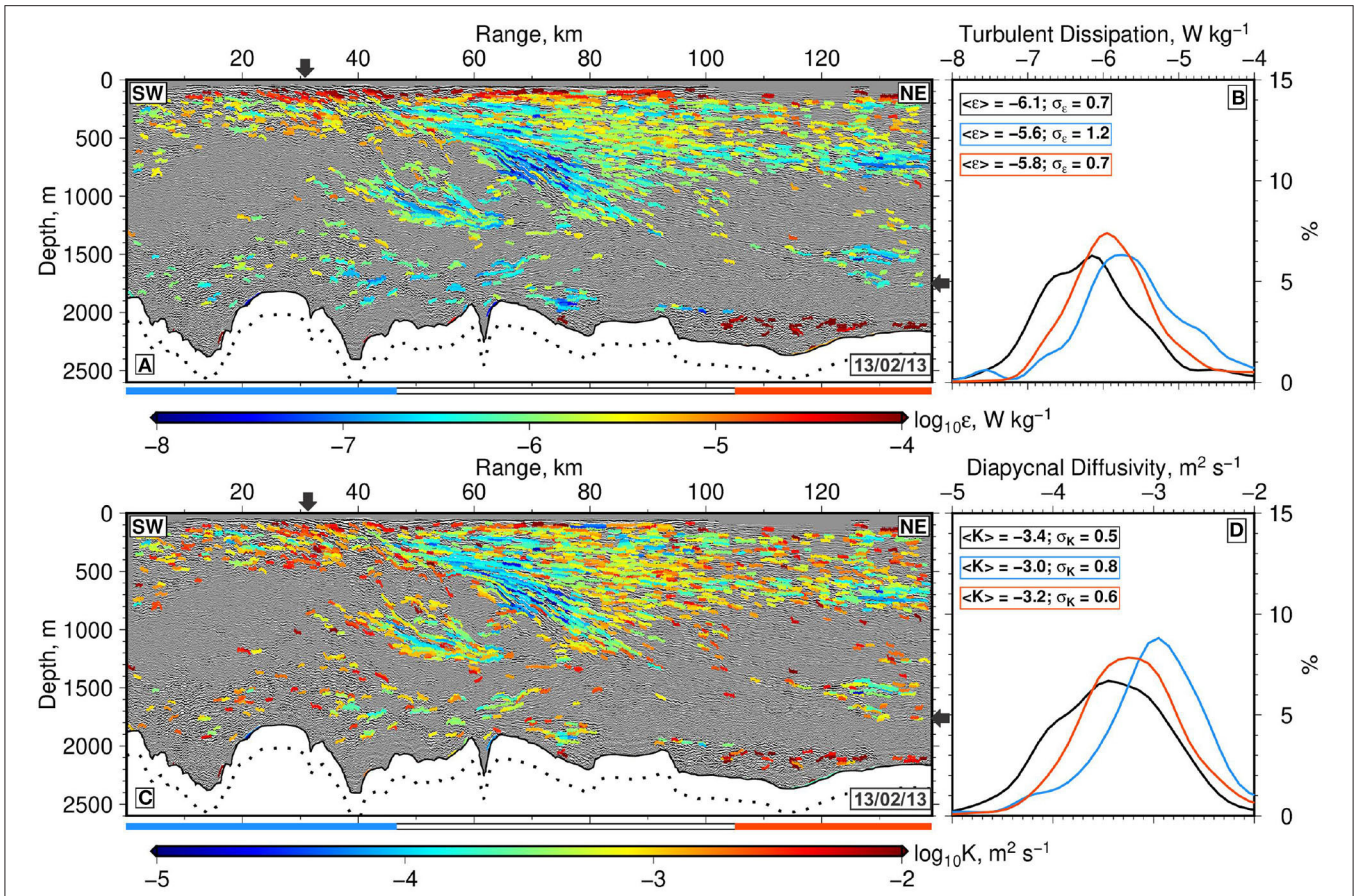

FIGURE 6 | (A) Spatial variation of turbulent dissipation rate, $\log_{10}\varepsilon$, for section B where warm/cool colors indicate higher/lower values according to scale bar along base of panel; black arrows = maximal extent of front at sea surface and at depth. **(B)** Histogram showing spatially averaged distribution of dissipation, $<\varepsilon>$. Envelopes calculated using bin widths of 0.1 and Gaussian filter lengths of 1 for spatial ranges of 0–40 (blue), 40–90 (black line and white bar), and 90–140 km (red). **(C,D)** Same for spatial variation of diapycnal mixing, $\log_{10} K$ and its average value, <K>.

hydrographic measurements [i.e., **Figure 2** D black line; (Osborn, 1980; Mashayek et al., 2017)]. Since the observed turbulent subrange extends to wavenumbers that are smaller than the Ozmidov scale, our use of this inertial-convective parametrization implicitly assumes that there is continuity between the LAST and inertial-convective regimes (Riley and Lindborg, 2008). Finally, diapycnal diffusivity, K, is obtained using the Osborn (1980) relationship where

$$K = \frac{\Gamma \varepsilon}{N^2}. \tag{2}$$

Spatial variations of ε and K for Section B are presented in **Figure 6**.

3.4. Diffusive Heat Flux

The diapycnal diffusive heat flux, F_H, is calculated in accordance with standard molecular (Fickian) diffusion where

$$F_H = -\rho_\circ C_p K(\mathrm{d}\Theta/\mathrm{d}z). \tag{3}$$

$\rho_\circ$ is potential density, C_p is the isobaric heat capacity of seawater, and $\mathrm{d}\Theta/\mathrm{d}z$ is the vertical gradient of conservative temperature. Here, we calculate the spatial and temporal variability of F_H using temperature and density fields obtained from calibrated seismic reflection sections together with the spatial and temporal variation of K (e.g., **Figures 4B**, **6C**). So, the four parameters on the right-hand side of this equation vary as a function of time and space. Since the nominal vertical resolution is $O(10)$ m, values of $\mathrm{d}T/\mathrm{d}z$, $\rho_\circ$, and C_p are measured at intervals of 10 m. The units of F_H are W m^{-2} where positive heat flux is downward. Note that our estimates of F_H do not take advective contributions into account since well-resolved velocity measurements are unavailable.

3.5. Uncertainty Estimates

Following Dickinson et al. (2020), the maximum likely uncertainty for $\log_{10} K$ is ±0.4 logarithmic units. This value is gauged in the following way. First, uncertainty in N is given by its standard deviation which is ±0.3 cph. This uncertainty is combined in quadrature with the uncertainty of the fitted intercept (i.e., 0.02–0.1) to yield an estimated mean uncertainty for $\log_{10} K$ of ±0.15 logarithmic units. Secondly, we acknowledge that assuming constant values of C_T and Γ is a significant

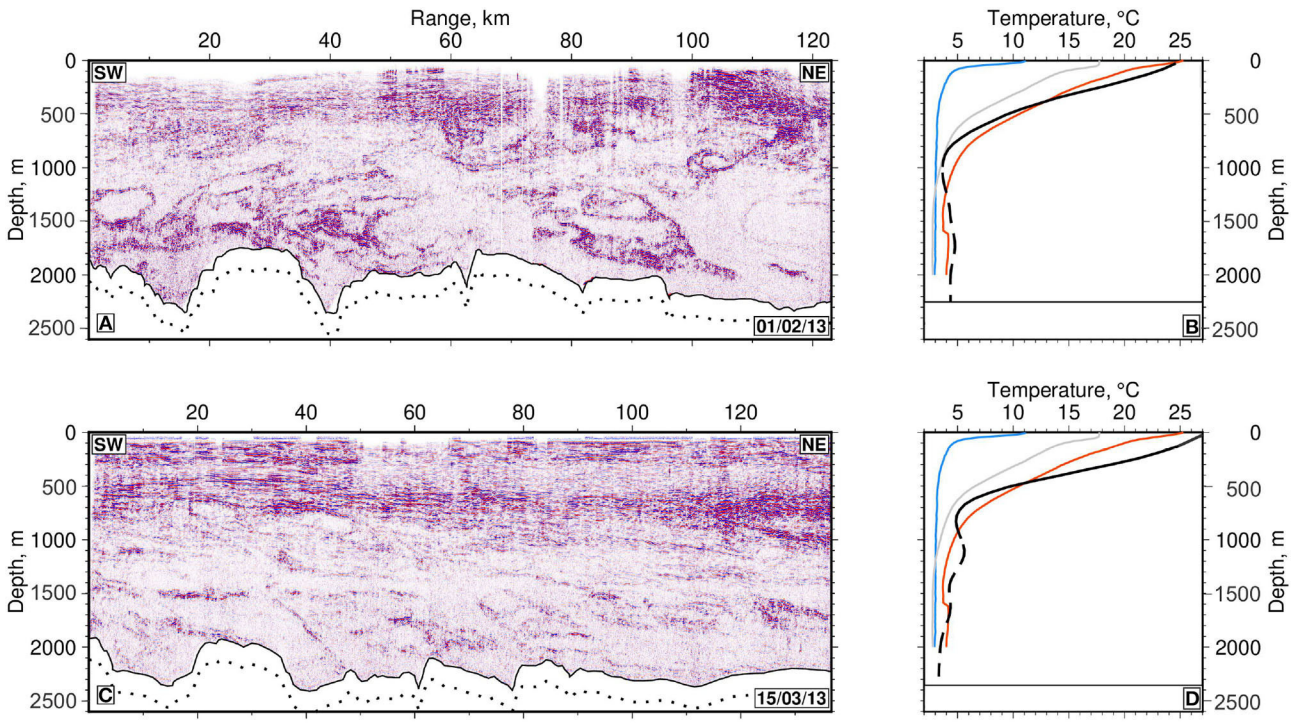

FIGURE 7 | (A) Section A of seismic reflection survey. **(B)** Conservative temperature as function of depth. Black line = horizontally averaged temperature profile calculated for Section A using iterative inversion procedure; dashed line = portions of same profile where calculation is uncertain due to lack of continuous reflections at depths $\gtrsim$1,000 m; red/blue/gray lines = average temperature profile obtained from GO-SHIP hydrographic sections A10/A11/A17, which represent subantarctic/subtropical/mixed water masses, respectively (see **Figure 1A**). **(C)** Section C of seismic reflection survey. **(D)** Same as **(B)** for Section C.

simplification (Mashayek et al., 2017). This assumption can be tested by considering their upper and lower bounds, which yields a maximum uncertainty of ±0.25 logarithmic units (Dickinson et al., 2020). Notwithstanding uncertainties associated with absolute values of mixing rate, we are confident that these relative variations are robust.

Given that the conservative upper bound of uncertainty for $\log_{10} K$ is ±0.4 logarithmic units, the propagated uncertainty for F_H can be estimated by combining uncertainties for $\log_{10} K$ and $\mathrm{d}\Theta/\mathrm{d}z$. The uncertainty for Θ is conservatively estimated as ±1° C (Gunn et al., 2020). After taking the vertical gradient over 10 m, we obtain an uncertainty of ±0.1 K m^{-1} for $\mathrm{d}T/\mathrm{d}z$. Uncertainties for $\rho_\circ$ and C_p are ±0.1 kg m^{-3} and ±0.8 J kg^{-1} K^{-1}, respectively. Thus, the propagated uncertainty for our estimates of F_H is ±3 W m^{-2}.

4. RESULTS

4.1. Water Mass Structure

On Section B, which was acquired on 13th February 2013, the most obvious feature is a band of gently dipping reflectivity that crops out at the sea surface over a range of 30–40 km (**Figure 4A**). This band represents a deeply penetrating front. Over much of its length, a bright and continuous reflection that dips northward is visible that can be traced down to a depth of 1.8 km. This front separates a wedge of smooth and horizontally continuous reflections to the north from more discontinuous, and even swirling, reflectivity to the south. A prominent tilted lens with a complex pattern of internal reflectivity centered at a range of 60 km sits against the front. Within 400 m of the sea surface, the front splits into a several strands that encase lens-shaped and acoustically transparent features that are interpreted as intra-thermoclinic eddies (Gunn et al., 2020). On both sides of the front, the thermocline is generally visible as a band of reflectivity that extends to a depth of 1,000 m which is consistent with hydrographic measurements (**Figure 2**). The calculated temperature field shows that the northern end of Section B is characterized by a wedge of warm subtropical water, the Brazil Current, that abuts the front (**Figure 4B**). South of the front, cooler temperatures are consistent with the presence of an intermediate water mass generated by mixing of subtropical and subantarctic waters.

On Section A, which was acquired on 1st February 2013, a thick band of approximately flat reflectivity that extents to a depth of 1,000 m defines the thermocline (**Figure 7A**). The vertical extent of the thermocline is corroborated by the horizontally averaged temperature distribution extracted from the seismic image (**Figure 7B**). From the sea surface down to a depth of 1,000 m, temperature values decreases from 25 to 5°C, which is comparable to the observed temperature distribution of subtropical water masses along GO-SHIP transect A10 (**Figure 2A**). Temperatures of ∼5°C are diagnostic of AAIW,

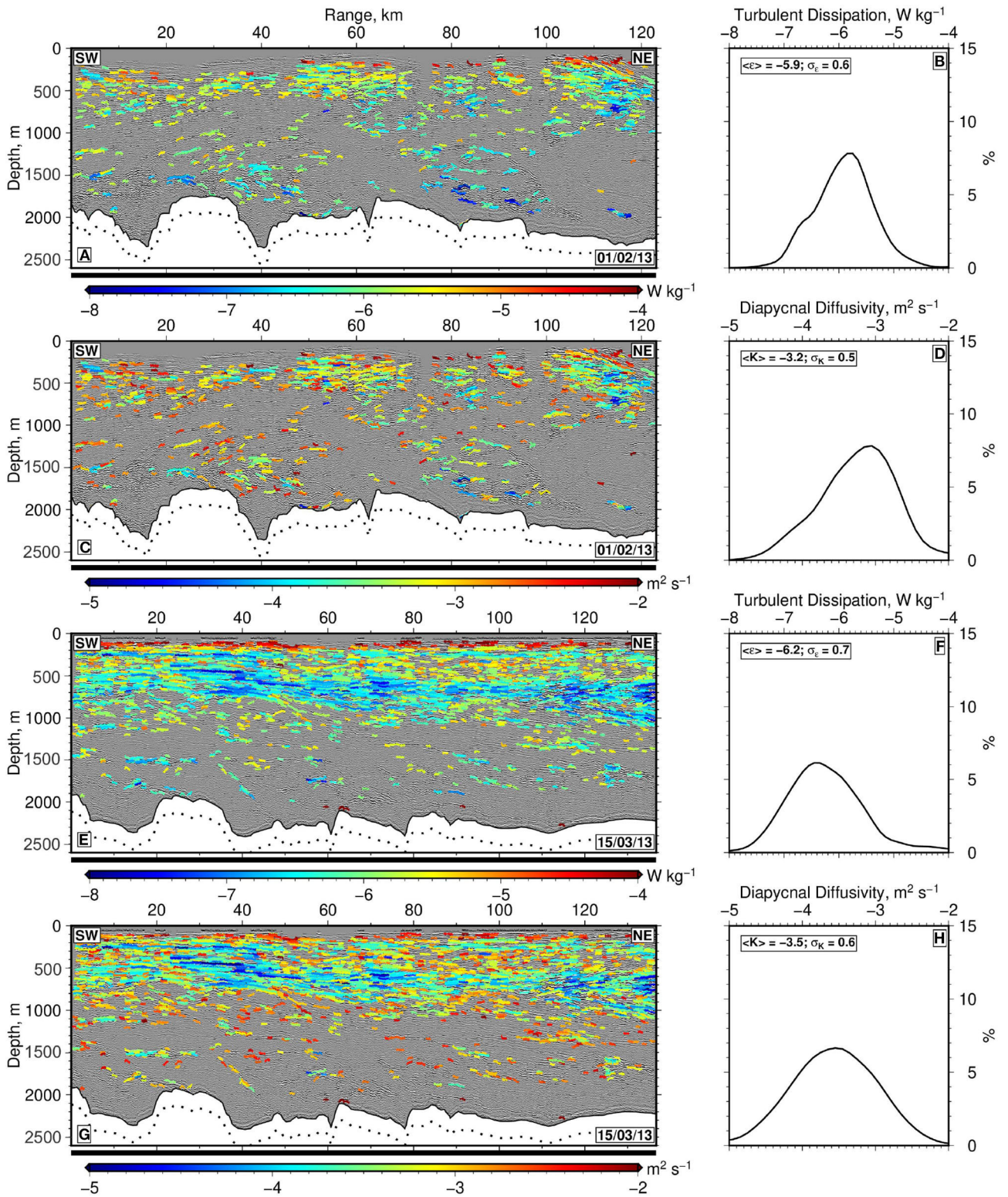

FIGURE 8 | (A) Section A of seismic reflection survey overlain with spatial distribution of turbulent dissipation rate, $\log_{10}\varepsilon$, calculated using spectral analysis of tracked reflectivity. Colored wiggly lines = 1,841 auto-tracked reflections where color indicates value of $\log_{10}\varepsilon$ according to scale bar at base of **(E)**. **(B)** Histogram showing spatially averaged distribution of $\log_{10}\varepsilon$ for **(A)** calculated using bin width of 0.1 and Gaussian filter length of 1. Numbers = weighted mean, $<\varepsilon>$, and standard deviation, σ_ε, of values from Section A. **(C)** Same overlain with spatial distribution of diapycnal diffusivity, $\log_{10}K$. Colored wiggly lines = individual auto-tracked reflections where color indicates value of $\log_{10}K$ according to scale bar at base of **(E)**. Note that global mean $\log_{10}K$ is –5 (e.g., Waterhouse et al., 2014) and that uncertainty of calculated $\log_{10}K$ is 0.4. **(D)** Histogram showing spatially averaged distribution of K. **(E–H)** Same for Section C with 2,310 tracked reflections.

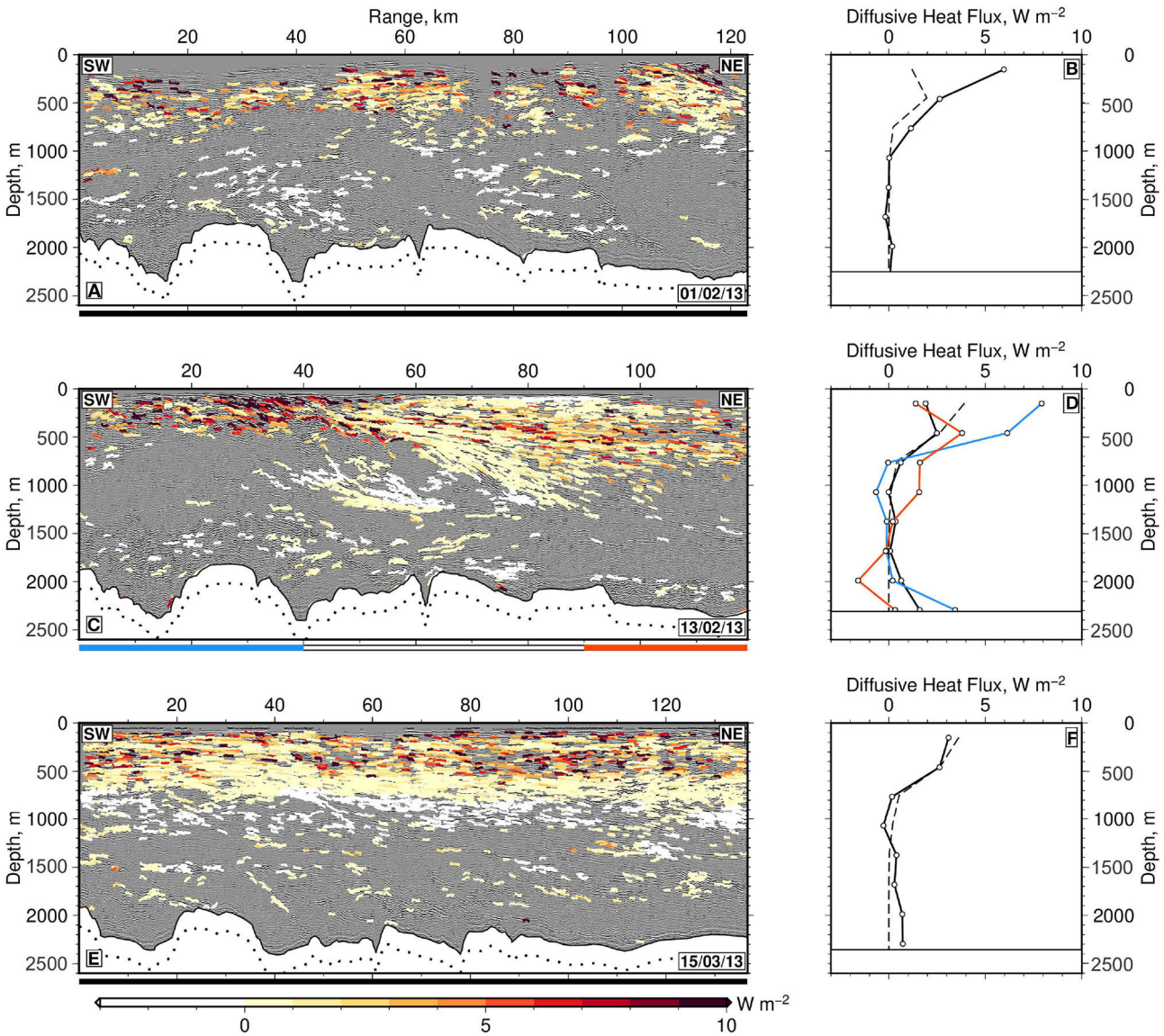

FIGURE 9 | (A) Section A of seismic reflection survey overlain with spatial distribution of vertical diffusive heat flux, F_H, calculated using seismically determined mixing estimates and temperature distribution. Colored wiggly lines = 1,017 auto-tracked reflections where color indicates value of F_H according to scale bar at base of **(E)**. Positive values indicate downward-directed heat flux and uncertainty in F_H is 3 W m^{-2}. Black bar along base of image = range used to calculate horizontal mean of F_H reported in **(B)**. **(B)** Horizontal mean of F_H in 300 m depth bins. White circles and solid black line = binned mean values of F_H calculated using seismically, determined values of $\Theta(z)$; dashed black line = binned mean values of F_H calculated using CTD-measured values of $\Theta(z)$ (see **Figure 2A**). **(C,D)** Same for Section B with 1,841 tracked reflections. Blue/white/red bar along base of image = three ranges used to calculate horizontally averaged profiles of F_H. **(E,F)** Same for Section C with 2,310 tracked reflections.

CDW, and NADW at these depths (Piola and Matano, 2017). At the northeastern end of Section A, the thermocline terminates in a set of bright reflections which are abruptly cut off at a range of 100 km by weaker dipping reflections. We interpret this pattern of localized reflectivity as the upper portion of a partially imaged front. This intepretation is consistent with coeval surface temperature measurements (**Figure 3**). Beneath a depth of 1,000 m, water masses are characterized by complex swirling patterns of reflectivity that form a mixture of lenses and filaments that deform as a function of time (Gunn et al., 2020). A vortex-like structure, reminiscent of that observed between subtropical and subantarctic water masses at the Subantarctic Front by Sheen et al. (2011), occurs at a depth of 1,000 m centered at a range of 105 km. These complex reflection patterns imply that imaged water masses are deforming and/or undergoing lateral displacement. Considerable mixing is probably also occurring.

On Section C, which was acquired on 15th March 2013, the front is no longer visible (**Figure 7C**). Instead, layered and

continuous reflections form a 1,000 m thick band that extends across the entire section. Beneath 1,000 m, sparser reflectivity delineates elongated filaments of $O(10)$ km lengthscales. As in the case of Sections A and B, the average temperature distribution indicates that this section is representative of subtropical water masses (see **Figure 7D**). Apart from methodological uncertainties, seismically-derived property distributions are limited by the observed density of continuous horizontal reflections. Due to the limitations of seismic acquisition, reflections are often not clearly imaged at depths shallower than ∼150 m. On the seismic sections presented here, there is also limited reflectivity at depths that exceed 1,000 m (**Figures 7B,D**). At these depths, horizontally averaged temperature profiles are inevitably less well constrained and tend to be discrepant with respect to hydrographic observations. Nonetheless, it is important to note that the vertical temperature gradient is faithfully recovered.

Given the depth and temperature of the thermocline together with the location of the seismic survey with respect to the confluence during February 2013, these seismic sections evidently cross the northern portion of the confluence since it is characterized by subtropical water masses of the Brazil Current (**Figure 1A**). The thermocline has a vertical extent of 1,000 m, which is consistent with steep temperature gradients observed within these subtropical water masses (**Figures 7B,D**; Piola and Matano, 2017). These observations are consistent with sea surface temperatures, which demonstrate that the seismic survey straddles the warmer portion of the confluence during February and March 2013 (**Figure 3**). Over a 6 week period, the depth of the thermocline remains consistent and its continuity is only disrupted adjacent to the dipping front, most likely the Brazil Current Front whose appearance and disappearance is caused by the observed oscillation of the confluence at this time of year (Olson et al., 1988; Saraceno et al., 2004; Severov et al., 2012; Gunn et al., 2020). The patterns of reflectivity also reveal other transient oceanic processes, including deformation of filaments and lenses, which have previously been interpreted as manifestations of stirring and cross-frontal mixing (Jullion et al., 2010; Gunn et al., 2020). This complex vertical and horizontal thermohaline structure has previously been observed on lengthscales of tens of kilometers using CTD probes (Reid et al., 1977; Gordon, 1989; Bianchi et al., 2001).

4.2. Vertical Mixing Rates

Section B demonstrates that dissipation and mixing rates are conditioned by the presence of a front (**Figure 6**). On the southern, denser side of the front, mixing rates are highest (e.g., 10^{-3}–10^{-2} m^2 s^{-1}), especially at ranges of 20–40 km where the front crops out at the sea surface. North of a range of 40 km, the front deepens and its different reflective strands are characterized by suppressed mixing rates of $\sim 10^{-4}$ m^2 s^{-1} (**Figure 6C**). Similarly low mixing rates are found at the base of the prominent tilted lens. Beyond a range of 90 km, mixing rates increase up to values of $\sim 10^{-3}$–10^{-2} m^2 s^{-1}. These qualitative observations are supported by full-depth weighted mean values of $\log_{10}\varepsilon$ (i.e., –6.1, –5.6, –5.8) and $\log_{10} K$ (–3.0, –3.4, –3.2) for ranges of 0–40, 40–90, and 90–140 km, respectively (**Figure 6D**). These section-averaged values reveal the overall effect that the front has upon vertical mixing rates— mixing is enhanced at its surface outcrop but it is locally suppressed along its dipping interface down to a depth of about 1 km.

Two weeks earlier (i.e., 1st February 2013), dissipation and mixing estimates for Section A range over three orders of magnitude (**Figures 8A,C**). Recovered estimates are much more spatially patchy which is consistent with the observed patterns of reflectivity. The highest mixing rates occur beneath the mixed layer (e.g., ∼200 m) and in association with small-scale structures at ranges of 30–40 km and depths of 1,000–1,400 m. Lowest mixing estimates occur adjacent to the front at the northeastern portion of Section A between 100 and 120 km. A weighted histogram of recovered mixing estimates indicates that the mean, $<$K$>$, and standard deviation, σ_K, of $\log_{10} K$ are −3.2 and 0.5, respectively (**Figure 8D**). One month later, the thermocline is much more continuous and the deeply penetrating front is no longer visible (**Figures 8E,G**). Mixing rates are lowest in the thermocline and greatest at the base of the mixed layer with sporadically higher mixing throughout the deeper portions of the water column. $<$K$>$ is $10^{-3.5}$ m^2 s^{-1} (i.e., $\sim 3\times10^{-4}$ m^2 s^{-1}), which is consistent with mean values calculated for the two other sections.

Mixing rates calculated for other seismic sections that also image the deeply penetrating front have similar spatial patterns of diapycnal diffusivity. Given our conservative estimate of uncertainty of ± 0.4 for $\log_{10} K$, these observed patterns of diapycnal diffusivity— enhanced K the surface outcrop of the front and suppressed values of K along its dipping interface— are robust. We conclude that this front conditions mixing rates on lengthscales of O(10–100) km.

4.3. Diffusive Heat Flux

Seismically-derived heat fluxes, F_H, range from –3 to 10 W m^{-2} (**Figure 9**). For all three seismic sections, the highest values of F_H occur along the base of the mixed layer. F_H decreases with depth along each seismic section (**Figures 9A,C,E**). Horizontally averaged profiles show that there is a marked decrease in the value of F_H from 1–8 W m^{-2} at the sea surface to 0 W m^{-2} at 1,000 m depth (**Figures 9B,D,E**). Profiles of F_H calculated using the mean $\Theta(z)$ distribution taken from transect A17 show the same trend within uncertainty (**Figures 9B,D,F** dashed lines). This behavior is expected since F_H describes Fickian diffusion, by which mixing rate acts upon vertical temperature gradient. Since $\mathrm{d}\Theta/\mathrm{d}z$ decreases with depth, the effect of mixing becomes increasingly limited. The vertical variation of F_H for sections A and C is broadly similar. Therefore, at mesoscale length scales in the absence of a front, F_H does not appear to significantly change over the 6 week period.

On the other hand, we also observe conditioning of F_H by the front itself (**Figures 9C,D**). Close to the surface outcrop of the front, heat fluxes reach their greatest values (**Figure 9D**). Enhancement of these heat fluxes exceeds the uncertainty of ± 3 W m^{-2} and it is directly associated with the vigorous mixing observed here (**Figure 6C**). Along the dipping boundary of the front, F_H is also elevated. Here, elevated values are a result of the significant vertical temperature gradient caused by the presence

of a wedge of warm water that is banked up against the front where it overlies cooler water (**Figure 4B**). We conclude that this major front conditions vertical diffusive heat flux on length scales of O(10–100) km.

5. DISCUSSION

A suite of seismic reflectivity sections is employed to shed light on the internal structure of a small portion of the northern Brazil-Falkland Confluence— a complex and dynamic frontal system with intense mesoscale eddy activity. Thermohaline structures that are seismically imaged, including evolving vortices and filaments, are consistent with both hydrographic observations and with satellite imagery that show frontal structure and a vigorous eddy field (Bianchi et al., 2001; Saraceno et al., 2004; Jullion et al., 2010). Here, we build upon these physical oceanographic observations in two significant ways. First, seismic imagery helps to overcome observational limitations since it yields full-depth vertical sections that have a horizontal extent of ∼140 km length, that have a vertical resolution of O(10) m, and that span a period of 6 weeks. Secondly, these sections can be converted into simultaneous distributions of temperature and mixing rate. For these reasons, seismic reflection technology provides an unprecedented view of oceanic structure which help to unlock an improved understanding of ocean mixing.

This portion of the Brazil-Falkland Confluence is a region of vigorous mixing where <K> is approximately 50×10^{-5} m^2 s^{-1} (**Figures 6**, **8**). Spatial and temporal averaging on length scales of 100 km and time scales of 6 weeks suggests that this mean value does not vary significantly (**Figure 8**). Similarly, vertical diffusive heat flux, F_H, does not vary significantly either (**Figure 9**). Sparser hydrographic observations indicate that this region is a significant hotspot for mixing. For example, Bianchi et al. (2001) use CTD profiles to estimate the thermal diffusivity across fronts in the vicinity of 39°S in the southwest Atlantic Ocean. Within the upper 1,000 m, their estimates range between 1.3 and 3.4×10^{-5} m^2 s^{-1}. More direct estimates of ε and K obtained by microstructure profilers reveal elevated mixing rates across the continental slope east of Uruguay (Waterhouse et al., 2014; Iglesias, 2019). As part of the GEOTRACES experiment, a suite of full-depth microstructure profilers were deployed across the Argentine Basin between 36 and 41°S during January 2012 (www.geotraces.org). The average mixing rate across this oceanic basin is 1.2×10^{-5} m^2 s^{-1}, which is consistent with the global mean value (1×10^{-5} m^2 s^{-1}; Waterhouse et al., 2014). However, at the western edge of the basin close to the continental slope and within 100 km of the seismic survey discussed here, mixing rates are O(100–1,000$\times10^{-5}$) m^2 s^{-1} (Iglesias, 2019). Enhanced mixing rates were also obtained above rough topography close to the shelf break. These remarkably elevated direct observations, which were acquired in the same location, bathymetric range, and season as the seismic survey, corroborate the values of mixing rate presented here. Notwithstanding the uncertainties associated with each methodology, these different studies suggest that mixing rates within this small northern portion of the Brazil-Falkland Confluence are at least one order of magnitude greater than the global mean value.

It is generally accepted that enhanced mixing rates prevail in regions where there is a combination of rougher bathymetry, higher shear, and enhanced kinetic energy (e.g., Ledwell et al., 2000; Garabato, 2004; Smyth and Moum, 2012; Whalen et al., 2012). In the South Atlantic Ocean, confluent flow of warm and cold water focusses large-scale temperature gradients at the continental slope (**Figure 1A**; Gordon, 1989; Peterson and Stramma, 1991). As a result of this convergent flow, vertical shear is enhanced which results in shear-driven mixing (e.g., Gordon and Greengrove, 1986; Bianchi et al., 2001; Sheen et al., 2012). This confluence also lies above the continental slope where it is exposed to the open ocean. In this setting, it has been shown that a complex field of locally and remotely generated tidal energy can develop which can elevate mixing rates by several orders of magnitude (Moum et al., 2003; Nash et al., 2012). Here, we hypothesize that elevated mean mixing rates are generated by a combination of the continental slope setting and exposure to the open ocean.

Apart from large-scale oceanographic and bathymetric drivers of mixing, the combination of high-resolution seismic imagery and the calculated spatial variability of K shows that the distribution of mixing is moderated by local water mass structure and/or dynamic processes. In particular, we observe conditioning of mixing rates by a major front, by smaller scale lenses, and by filaments. On seismic sections where the front is clearly observed, it is evident that the front itself, rather than distal processes, can simultaneously trigger elevated and suppressed mixing rates. Elevated values of K imply that the surface outcrop of the front is a region of enhanced water mass modification. This observation is consistent with microstructural and SeaSoar observations adjacent to fronts which indicate elevated mixing rates (Dewey and Moum, 1990; Nagai et al., 2009; D'Asaro et al., 2011; Johnston et al., 2011; Peng et al., 2020). However, these surveys are typically limited to a depth range of ≤500 m. We also observe enhanced mixing rates extending down to depths of 500 m. Additionally, we find that mixing rates along the frontal interface itself are suppressed to depths of about 1,000 m. These direct observations show that the modification of diapycnal mixing by a front is not isolated to the upper water column but can affect water masses across the entire thermocline.

Here, we demonstrate that vigorous vertical mixing can play a significant role in water mass modification by calculating coeval vertical sections of diffusive heat flux. From a global perspective, vertical heat flux is difficult to quantify due to the lack of sufficient diapycnal diffusivity and vertical velocity measurements. Consequently, global estimates are often obtained by numerical simulations. Based upon an ocean state estimate with a resolution of ≥30 km, the global average value of F_H is positive (i.e., downward) at all depths, decreasing from 1 W m^{-2} at the sea surface to 0.1 W m^{-2} at a depth of 1,000 m (Liang et al., 2015). Vertical advective heat fluxes have a similar magnitude although its mean value is negative (Liang et al., 2015). Here, we obtain diffusive heat fluxes that decrease from ≤8 W m^{-2} at the sea surface to ∼0 W m^{-2} at a depth of 1,000 m (**Figures 9B,D,F**). Compared with the global mean, we infer that this northern

portion of the Brazil-Falkland Confluence is a key site for vertical diffusive heat exchange. This inference contrasts with the predictions of non-eddy-resolving global simulations, which generally imply that the majority of diffusive heat flux occurs at high latitudes as a consequence of the vertical projection of isopycnal surfaces (Liang et al., 2015).

Instead, our observations are consistent with eddy-resolving models which have spatial resolutions of ∼10 km. This consistency implies that subtropical zones are key sites for diffusive heat flux as a consequence of elevated eddy kinetic energy (Wolfe et al., 2008). Despite low mean values, the temporal standard deviation of F_H in global simulations of diffusive heat fluxes are large in the Brazil-Falkland Confluence, which suggests that the role of F_H varies significantly with time (Liang et al., 2015). Here, we provide observational evidence that diffusive heat fluxes play a more significant role in the vertical redistribution of heat than previously thought and that enhanced fluxes are associated with an advecting front. Our results indicate that high resolution measurements of diapycnal diffusivity and of vertical velocity are required to comprehensively constrain spatial and temporal patterns of vertical heat flux.

On longer timescales than those considered in this contribution, seasonal variations of mixing and of diffusive heat flux are probably due to the oscillation of the confluence. Argo float measurements have been used to infer seasonal variation of K at depths of 500, 750, and 1,000 m (Huang and Xu, 2019). At 36.5°S in the Atlantic Ocean, Huang and Xu (2019) find that rates of diapycnal transport, which approximates to mixing, are lowest between January and March at depths of 500 and 750 m but greater at 1,000 m depth. At depths of 500 and 750 m, mixing rates peak between July and September. This shallow seasonal variation is attributed to seasonal changes in wind power. Huang and Xu (2019) also find that mixing rates at 500 m are less than those at 1,000 m within the confluence region, which is consistent with the distribution of K values calculated from seismic sections— compare what is observed between depths of 500 and 1,000 m on **Figures 5C**, **8G**. These results suggest that seismically observed mixing rates are part of a seasonal cycle but further investigation is required both to confirm and to quantify this signal.

We conclude by considering the implications for parameterization of mixing in numerical simulations. The eddy dynamics assumed in these simulations typically exploit the KPP vertical mixing scheme of Large et al. (1994). This scheme combines the parametization of significant processes—including turbulent boundary mixing, shear instability, and convection—as potential modifiers of diapycnal diffusivity. We find that elevated values of F_H occur in the vicinity of the surface outcrop of the front and along its dipping interface as a consequence of elevated mixing rate and large values of $d\Theta/dz$, respectively. Oceanic fronts are usually omitted from numerical simulations because of computational constraints (Ferrari, 2011). Hence, these seismic-based observations have significant implications for the parameterization of mixing in these simulations since our results demonstrate that fronts can play a critical role in modifying dissipation rates and diffusive heat fluxes within the upper 1,000 m of the water column.

6. SUMMARY

The scale and complexity of major oceanic fronts present formidable logistical challenges for observing ocean processes at appropriate spatial and temporal scales. Existing seismic reflection technology has a hitherto unsurpassed ability to resolve thermohaline structures on spatial scales of tens of meters to hundreds of kilometers and on temporal scales of minutes to days. In combination with simultaneous hydrographic observations, this ability has the potential to transform our understanding of frontal systems. Here, we show how appropriately calibrated seismic sections can be used to extract estimates of both diapycnal diffusivity and diffusive heat flux. Analysis of three seismic sections demonstrate that enhanced values of mixing and heat flux are associated with the surface expression of a major front and with deforming eddies and filaments at depths of more than 1,000 m. Mixing is suppressed along the frontal interface between 500 and 1,000 m. Elevated values of diffusive heat flux underline the global importance of these regions of confluence.

DATA AVAILABILITY STATEMENT

The datasets presented in this article are not readily available because Repeat hydrographic data were acquired and made publicly available by Global Ocean Ship-based Hydrographic Investigations Program and contributing national programs (GO-SHIP; http://www.go-ship.org/). The seismic reflection survey is owned by the Administración Nacional de Combustibles, Alcoholes y Portland of Uruguay to whom requests for access are referred. Requests to access the datasets should be directed to njw10@cam.ac.uk.

AUTHOR CONTRIBUTIONS

This research project was conceived by KG and NW. Data analysis was carried out by KG with guidance from AD, NW and CPC. The manuscript was written by KG and NW with contributions from AD and CPC. Figures were created by KG with advice from NW.

FUNDING

This research project was funded by the University of Cambridge. AD was funded by Natural Environment Research Council and by North East Local Enterprise Partnership.

ACKNOWLEDGMENTS

We are grateful to Administración Nacional de Combustibles, Alcoholes y Portland and to Shell Global for generously providing seismic field tapes. Requests for access to these tapes and near-coeval hydrographic measurements should be directed to these organizations. Seismic processing was carried out using the Omega2 software package provided by Schlumberger Research Services. GO-SHIP observations were downloaded from Clivar

and Carbon Hydrographic Data Office (http://cchdo.ucsd.edu/) for lines/expocodes A10 06MT22_5, A11 74DI199_1, and A17 29HE20190405). Hydrographic measurements were analyzed using a Python implementation of GSW TEOS-10 equation of state for seawater (github.com/TEOS-10/GSW-Python). Ocean Surface Current Analysis Real-time (OSCAR), Group for High Resolution Sea Surface Temperature (GHRSST), and Multi-scale Ultra-high Resolution (MUR) Sea Surface Temperature datasets were extracted from ERDDAP (https://coastwatch.pfeg.noaa.gov/erddap). Figures were prepared using Generic Mapping Tools (gmt.soest.hawaii.edu). We are grateful to D. Bright, I. Frame, C. Jones, D. Lyness, J. Selvage, K. Sheen and A. Woods for their help. Cambridge Earth Sciences contribution number esc.6032.

REFERENCES

Azevedo, L., Matias, L., Turco, F., Tromm, R., and Peliz, Á. (2021). Geostatistical seismic inversion for temperature and salinity in the Madeira abyssal plain. *Front Mar Sci*. 8:685007. doi: 10.3389/fmars.2021.685007

Batchelor, G. K., Howells, I. D., and Townsend, A. A. (1959). Small-scale variation of convected quantities like temperature in turbulent fluid: Part 2. The case of large conductivity. *J. Fluid Mech*. 5, 134–139. doi: 10.1017/S0022112059000106

Bianchi, A. A., Piola, A. R., and Collino, G. J. (2001). Evidence of double diffusion in the Brazil-Malvinas Confluence. *Deep Sea Res. I Oceanogr. Res. Pap*. 49, 41–52. doi: 10.1016/S0967-0637(01)00039-5

Combes, V., and Matano, R. P. (2014). Trends in the Brazil/Malvinas Confluence region. *Geophys. Res. Lett*. 41, 8971–8977. doi: 10.1002/2014GL062523

D'Asaro, E., Lee, C., Rainville, L., Harcourt, R., and Thomas, L. (2011). Enhanced turbulence and energy dissipation at ocean fronts. *Science* 6027, 318–322. doi: 10.1126/science.1201515

Dewey, R. K., and Moum, J. N. (1990). Enhancement of fronts by vertical mixing. *J. Geophys. Res*. 95, 9433–9445. doi: 10.1029/JC095iC06p09433

Dickinson, A., White, N. J., and Caulfield, C. P. (2017). Spatial variation of diapycnal diffusivity estimated from seismic imaging of internal wave field, Gulf of Mexico. *J. Geophys. Res. Oceans* 122, 1–28. doi: 10.1002/2017JC013352

Dickinson, A., White, N. J., and Caulfield, C. P. (2020). Time-lapse acoustic imaging of mesoscale and fine-scale variability within the faroe-shetland channel. *J. Geophys. Res. Oceans* 125:e2019JC015861. doi: 10.1029/2019JC015861

Falder, M., White, N. J., and Caulfield, C. P. (2016). Seismic imaging of rapid onset of stratified turbulence in the South Atlantic Ocean. *J. Phys. Oceanogr*. 46, 1023–1044. doi: 10.1175/JPO-D-15-0140.1

Ferrari, R. (2011). A frontal challenge for climate models. *Science* 332, 316–317. doi: 10.1126/science.1203632

Fraz ao, H. C., and Waniek, J. J. (2021). Mediterranean water properties at the eastern limit of the north atlantic subtropical Gyre since 1981. *Oceans* 2, 266–280. doi: 10.3390/oceans2010016

Garabato, A. C. N. (2004). Widespread intense turbulent mixing in the southern ocean. *Science* 303, 210–213. doi: 10.1126/science.1090929

Garzoli, S. L., and Garraffo, Z. (1989). Transports, frontal motions and eddies at the Brazil-Malvinas currents confluence. *Deep Sea Res. A Oceanogr. Res. Pap*. 36, 681–703. doi: 10.1016/0198-0149(89)90145-3

Gordon, A. L. (1989). Brazil-Malvinas Confluence-1984. *Deep Sea Res*. 36, 359–384. doi: 10.1016/0198-0149(89)90042-3

Gordon, A. L., and Greengrove, C. L. (1986). Abyssal eddy in the southwest Atlantic. *Deep Sea Res*. 33, 839–847. doi: 10.1016/0198-0149(86)90091-9

Gunn, K. L., White, N., and Caulfield, C. C. P. (2020). Time-lapse seismic imaging of oceanic fronts and transient lenses within South Atlantic Ocean. *J. Geophys. Res. Oceans* 125:e2020JC016293. doi: 10.1029/2020JC016293

Gunn, K. L., White, N. J., Larter, R. D., and Caulfield, C. P. (2018). Calibrated seismic imaging of eddy-dominated warm-water transport across the bellingshausen sea, southern ocean. *J. Geophys. Res. Oceans* 123, 3072–3099. doi: 10.1029/2018JC013833

Holbrook, W. S., Fer, I., Schmitt, R. W., Lizarralde, D., Klymak, J. M., Helfrich, L. C., et al. (2013). Estimating oceanic turbulence dissipation from seismic images. *J. Atmosphere. Oceanic Technol*. 30, 1767–1788. doi: 10.1175/JTECH-D-12-00140.1

Holbrook, W. S., Páramo, P., Pearse, S., and Schmitt, R. W. (2003). Thermohaline fine structure in an oceanographic front from seismic reflection profiling. *Science* 301, 821–824. doi: 10.1126/science.1085116

Huang, C., and Xu, Y. (2019). Spatial and seasonal variability of global ocean diapycnal transport inferred from Argo profiles. *J. Oceanol. Limnol*. 37, 498–512. doi: 10.1007/s00343-019-7290-2

Iglesias, D. O.-E. (2019). *The Brazil-Malvinas Confluence: From Local to Global Scales*. Ph.D. thesis.

Johnston, T. M., Rudnick, D. L., and Pallàs-Sanz, E. (2011). Elevated mixing at a front. *J. Geophys. Res. Oceans* 116, 1–14. doi: 10.1029/2011JC007192

Jullion, L., Heywood, K. J., Naveira Garabato, A. C., and Stevens, D. P. (2010). Circulation and water mass modification in the Brazil–Malvinas Confluence. *J. Phys. Oceanogr*. 40, 845–864. doi: 10.1175/2009JPO4174.1

Klymak, J. M., and Moum, J. M. (2007a). Oceanic isopycnal slope spectra. Part I: internal waves. *J. Phys. Oceanogr*. 37, 1232–1245. doi: 10.1175/JPO3073.1

Klymak, J. M., and Moum, J. N. (2007b). Oceanic isopycnal slope spectra. Part II: turbulence. *J. Phys. Oceanogr*. 37, 1232–1245. doi: 10.1175/JPO3074.1

Large, W. G., McWilliams, J. C., and Doney, S. C. (1994). Oceanic vertical mixing: a review and a model with a nonlocal boundary layer parameterization. *Rev. Geophys*. 32, 363–403. doi: 10.1029/94RG01872

Ledwell, J. R., Montgomery, E. T., Polzin, K. L., Laurent, L. C. S., Schmitt, R. W., and Toole, J. M. (2000). Evidence for enhanced mixing over rough topography in the abyssal ocean. *Nature* 403, 179–182. doi: 10.1038/35003164

Liang, X., Wunsch, C., Heimbach, P., and Forget, G. (2015). Vertical redistribution of oceanic heat content. *J. Clim*. 28, 3821–3833. doi: 10.1175/JCLI-D-14-00550.1

Mashayek, A., Salehipour, H., Bouffard, D., Caulfield, C. P., Ferrari, R., Nikurashin, M., et al. (2017). Efficiency of turbulent mixing in the abyssal ocean circulation. *Geophys. Res. Lett*. 44, 6296–6306. doi: 10.1002/2016GL072452

Moum, J. N., Farmer, D. M., Smyth, W. D., Armi, L., and Vagle, S. (2003). Structure and generation of turbulence at interfaces strained by internal solitary waves propagating shoreward over the continental shelf. *J. Phys. Oceanogr*. 33, 2093–2112. doi: 10.1175/1520-0485(2003)033<2093:SAGOTA>2.0.CO;2

Munk, W. H. (1966). Abyssal recipes. *Deep Sea Res*. 13, 707–730. doi: 10.1016/0011-7471(66)90602-4

Nagai, T., Tandon, A., Kunze, E., and Mahadevan, A. (2015). Spontaneous generation of near-inertial waves by the kuroshio front. *J. Phys. Oceanogr*. 45, 2381–2406. doi: 10.1175/JPO-D-14-0086.1

Nagai, T., Tandon, A., Yamazaki, H., and Doubell, M. J. (2009). Evidence of enhanced turbulent dissipation in the frontogenetic Kuroshio Front thermocline. *Geophys. Res. Lett*. 36, 1–6. doi: 10.1029/2009GL038832

Nash, J. D., Kelly, S. M., Shroyer, E. L., Moum, J. N., and Duda, T. F. (2012). The unpredictable nature of internal tides on continental shelves. *J. Phys. Oceanogr*. 42, 1981–2000. doi: 10.1175/JPO-D-12-028.1

Olson, D. B., Podestá, G. P., Evans, R. H., and Brown, O. B. (1988). Temporal variations in the separation of Brazil and Malvinas Currents. *Deep Sea Res. A Oceanogr. Res. Pap*. 35, 1971–1990. doi: 10.1016/0198-0149(88)90120-3

Osborn, T. R. (1980). Estimates of the local rate of vertical diffusion from dissipation measurements. *J. Phys. Oceanogr*. 10, 83–89. doi: 10.1175/1520-0485(1980)010<0083:EOTLRO>2.0.CO;2

Papenberg, C., Klaeschen, D., Krahmann, G., and Hobbs, R. W. (2010). Ocean temperature and salinity inverted from combined hydrographic and seismic data. *Geophys. Res. Lett*. 37, 6–11. doi: 10.1029/2009GL042115

Peng, J.-P., Holtermann, P., and Umlauf, L. (2020). Frontal instability and energy dissipation in a submesoscale upwelling filament. *J. Phys. Oceanogr*. 50, 2017–2035. doi: 10.1175/JPO-D-19-0270.1

Peterson, R. G., and Stramma, L. (1991). Upper-level circulation in the South Atlantic Ocean. *Prog. Oceanogr*. 26, 1–73. doi: 10.1016/0079-6611(91)90006-8

Piola, A. R., and Matano, R. P. (2017). "Reference module in earth systems and environmental sciences," in *Ocean Currents: Atlantic Western Boundary–Brazil Current/Falkland* (Malvinas), 340–349.

Reid, J. L., Nowlin, W. D., and Patzert, W. C. (1977). On the Characteristics and circulation of the southwestern atlantic ocean. *J. Phys. Oceanogr*. 7, 62–91. doi: 10.1175/1520-0485(1977)007<0062:OTCACO>2.0.CO;2

Riley, J. J., and Lindborg, E. (2008). Stratified turbulence: a possible interpretation of some geophysical turbulence measurements. *J. Atmosphere. Sci*. 65, 2416–2424. doi: 10.1175/2007JAS2455.1

Ruddick, B., Song, H., Dong, C., and Pinheiro, L. (2009). Water column seismic images as maps of temperature gradient. *Oceanography* 22, 192–205. doi: 10.5670/oceanog.2009.19

Sallarès, V., Biescas, B., Buffett, G., Carbonell, R., Da nobeitia, J. J., and Pelegrí, J. L. (2009). Relative contribution of temperature and salinity to ocean acoustic reflectivity. *Geophys. Res. Lett*. 36, 1–6. doi: 10.1029/2009GL040187

Saraceno, M., Provost, C., Piola, A. R., Bava, J., and Gagliardini, A. (2004). Brazil Malvinas Frontal System as seen from 9 years of advanced very high resolution radiometer data. *J. Geophys. Res. Oceans* 109, 1–14. doi: 10.1029/2003JC002127

Severov, D. N., Pshennikov, V., and Remeslo, A. V. (2012). Fronts and thermohaline structure of the Brazil-Malvinas Confluence System. *Adv. Space Res*. 49, 1373–1387. doi: 10.1016/j.asr.2012.01.024

Sheen, K. L., White, N., Caulfield, C. P., and Hobbs, R. W. (2011). Estimating geostrophic shear from seismic images of oceanic structure. *J. Atmosphere. Oceanic Technol*. 24, 1–5. doi: 10.1175/JTECH-D-10-05012.1

Sheen, K. L., White, N. J., Caulfield, C. P., and Hobbs, R. W. (2012). Seismic imaging of a large horizontal vortex at abyssal depths beneath the Sub-Antarctic Front. *Nat. Geosci*. 5, 542–546. doi: 10.1038/ngeo1502

Sheen, K. L., White, N. J., and Hobbs, R. W. (2009). Estimating mixing rates from seismic images of oceanic structure. *Geophys. Res. Lett*. 36, 1–5. doi: 10.1029/2009GL040106

Smyth, W. D., and Moum, J. N. (2012). Ocean mixing by Kelvin-Helmholtz instability. *Oceanography* 25, 140–149. doi: 10.5670/oceanog.2012.49

Spalding, B. D. (1991). Kolmogorov's two-equation model of turbulence. *Proc. Math. Phys. Sci*. 434, 211–216. doi: 10.1098/rspa.1991.0089

Thomson, D. J. (1982). Spectrum estimation and harmonic analysis. *Proc. IEEE* 70, 1055–1096. doi: 10.1109/PROC.1982.12433

Waterhouse, A. F., Mackinnon, J. A., Nash, J. D., Alford, M. H., Kunze, E., Simmons, H. L., et al. (2014). Global patterns of diapycnal mixing from measurements of the turbulent dissipation rate. *J. Phys. Oceanogr*. 44, 1854–1872. doi: 10.1175/JPO-D-13-0104.1

Whalen, C. B., Talley, L. D., and MacKinnon, J. A. (2012). Spatial and temporal variability of global ocean mixing inferred from Argo profiles. *Geophys. Res. Lett*. 39, 1–6. doi: 10.1029/2012GL053196

Wolfe, C. L., Cessi, P., McClean, J. L., and Maltrud, M. E. (2008). Vertical heat transport in eddying ocean models. *Geophys. Res. Lett*. 35, L23605. doi: 10.1029/2008GL036138

Yilmaz, Ö. (2001). Seismic data analysis: processing, inversion, and interpretation of seismic data. *Soc. Explorat. Geophys*. 1–2027. doi: 10.1190/1.9781560801580

Conflict of Interest: The authors declare that the research was conducted in the absence of any commercial or financial relationships that could be construed as a potential conflict of interest.

Publisher's Note: All claims expressed in this article are solely those of the authors and do not necessarily represent those of their affiliated organizations, or those of the publisher, the editors and the reviewers. Any product that may be evaluated in this article, or claim that may be made by its manufacturer, is not guaranteed or endorsed by the publisher.

frontiers in Marine Science

ORIGINAL RESEARCH
published: 11 October 2021
doi: 10.3389/fmars.2021.688815

Testing the Improvement of Coral Reef Associated Fish Distribution Models Based on Multibeam Bathymetry by Adding Seafloor Backscatter Data

Marcela Montserrat Landero Figueroa[1], Miles J. G. Parsons[2], Benjamin J. Saunders[3], Ben Radford[2] and Iain M. Parnum[1]*

[1] Centre for Marine Science and Technology (CMST), Curtin University, Perth, WA, Australia, [2] Australian Institute of Marine Science, Nedlands, WA, Australia, [3] School of Molecular and Life Sciences, Curtin University, Perth, WA, Australia

OPEN ACCESS

Edited by:
Katy Sheen,
University of Exeter, United Kingdom

Reviewed by:
Camilo Roa,
Florida International University, United States
Chris Taylor,
National Centers for Coastal Ocean Science (NOAA), United States

***Correspondence:**
Marcela Montserrat Landero Figueroa
monserrat.landero@curtin.edu.au
orcid.org/0000-0001-6529-0676

Specialty section:
This article was submitted to Ocean Observation, a section of the journal Frontiers in Marine Science

Received: *31 March 2021*
Accepted: *20 September 2021*
Published: *11 October 2021*

Citation:
Landero Figueroa MM, Parsons MJG, Saunders BJ, Radford B and Parnum IM (2021) Testing the Improvement of Coral Reef Associated Fish Distribution Models Based on Multibeam Bathymetry by Adding Seafloor Backscatter Data. Front. Mar. Sci. 8:688815. doi: 10.3389/fmars.2021.688815

Demersal fishes constitute an essential component of the continental shelf ecosystem, and a significant element of fisheries catch around the world. However, collecting distribution and abundance data of demersal fish, necessary for their conservation and management, is usually expensive and logistically complex. The increasing availability of seafloor mapping technologies has led to the opportunity to exploit the strong relationship demersal fish exhibit with seafloor morphology to model their distribution. Multibeam echo-sounder (MBES) systems are a standard method to map seafloor morphology. The amount of acoustic energy reflected by the seafloor (backscatter) is used to estimate specific characteristics of the seafloor, including acoustic hardness and roughness. MBES data including bathymetry and depth derivatives were used to model the distribution of *Abalistes stellatus, Gymnocranius grandoculis, Lagocephalus sceleratus, Lethrinus miniatus, Loxodon macrorhinus, Lutjanus sebae*, and *Scomberomorus queenslandicus*. The possible improvement of model accuracy by adding the seafloor backscatter was tested in three different areas of the Ningaloo Marine Park off the west coast of Australia. For the majority of species, depth was a primary variable explaining their distribution in the three study sites. Backscatter was identified to be an important variable in the models, but did not necessarily lead to a significant improvement in the demersal fish distribution models' accuracy. Possible reasons for this include: the depth and derivatives were capturing the significant changes in the habitat, or the acoustic data collected with a high-frequency MBES were not capturing accurately relevant seafloor characteristics associated with the species distribution. The improvement in the accuracy of the models for certain species using data already available is an encouraging result, which can have a direct impact in our ability to monitor these species.

Keywords: demersal fish, habitat models, multibeam, seafloor backscatter, bathymetry, depth derivatives

INTRODUCTION

Coral reef fish constitute an essential component of the continental shelf ecosystem, and a significant element of fisheries catch around the world (Anderson et al., 2009). Successful management and conservation of these demersal fishes rely on our ability to monitor their abundance and distribution. However, collecting distribution and abundance data is often expensive and logistically complex (Anderson et al., 2009). Increasing availability of seafloor mapping technologies, such as Multibeam echo-sounders (MBES), has led to the opportunity to exploit the strong relationship demersal fish species exhibit with seafloor morphology to model their distribution in a cost-effective manner (Brown et al., 2012).

Multibeam echo-sounders (MBES) are used to map the seafloor by transmitting acoustic energy toward the seafloor. The two-way travel time of this energy, to and from the transducer, combined with the angle of its travel, is used to determine the depth (bathymetry). The amount of acoustic energy reflected by the seafloor (backscatter) is used to estimate specific characteristics of the seafloor, including acoustic hardness and roughness (Fonseca and Mayer, 2007). The importance of depth to the assemblage of demersal fish has been well established (Fitzpatrick et al., 2012; Garcia-Alegre et al., 2014). As well as the direct influence depth has on demersal fish, it is also seen as a proxy for a broader set of variables involved in processes that occur at different levels of the water column which are usually harder to sample, e.g., temperature and light (Sih et al., 2017). Depth derivatives (e.g., ruggedness) are used to describe the complexity of the seafloor which can also influence the distribution of demersal fish at a variety of scales (Monk et al., 2011; Costa et al., 2014). Differences in the seafloor backscatter are used to help discriminate between benthic habitats, which can be closely related to the distribution of demersal species (e.g., sand vs. rock bottom; Monk et al., 2010; Monk et al., 2011). Therefore, the inclusion of seafloor backscatter data in demersal fish distribution models is slowly becoming more common. Multiple descriptors can be derived from the original backscatter data adding several lines of potentially useful information for species distribution modeling (Hasan et al., 2012a).

One of the most common products derived from the raw backscatter data is a mosaic, where the backscattered energy (measured as the backscatter strength on the dB scale, and backscatter intensity on the linear scale) received from different grazing angles is normalized for a certain angle or a range of angles. This method produces a regular grid usually with a resolution equal to the bathymetry layer (Fonseca et al., 2009). However, the relationship between the backscatter strength/intensity and grazing angle is related, for certain frequencies, to particular properties of the seafloor (Fonseca and Mayer, 2007). Normalizing the data to a specific angle dismisses valuable information contained in the angular response curve (ARC) (Hamilton and Parnum, 2011). Another approach is to characterize the seafloor using the Angle vs. Range Analysis (ARA) (Fonseca et al., 2009). During the ARA analysis, the backscatter response observed is compared to expected acoustic response curves based on a mathematical model, the Jackson Model (Jackson et al., 1986). In particular, the ARA analysis can be used to estimate the sediment grain size, which has been shown in some demersal species to be a driver of distribution, or at least a correlate. Previous studies have focused on testing the relevance of including the backscatter and its derivatives to model the distribution of benthic habitat classes (Ierodiaconou et al., 2007; Brown et al., 2012; Hasan et al., 2012a). Less attention has been placed in testing the benefit of adding the angular response data in modeling the distribution of demersal fishes which traditionally included the mosaic image and derivatives e.g., texture features (Hasan et al., 2014).

In the present study, terrain variables were used to model the distribution of fish data derived from Baited Remote Underwater Stereo-Video (stereo-BRUVS). The overarching aim was to test the possible improvement of a model's accuracy if the backscatter data is included. This was tested in three areas of the Ningaloo Marine Park (NMP) with different bathymetry and levels of terrain complexity. Seven species where chosen as an indicative evaluation of the accuracy of species distribution models: starry triggerfish (*Abalistes stellatus),* Robinson's seabream (*Gymnocranius grandoculis),* silver toadfish *(Lagocephalus sceleratus),* red throat emperor *(Lethrinus miniatus),* sliteye shark *(Loxodon macrorhinus),* red emperor *(Lutjanus sebae),* and school mackerel (*Scomberomorus queenslandicus).* The probability of presence of each of these species was modeled using depth, depth derivatives and backscatter (mosaic and ARC) data as explanatory variables.

MATERIALS AND METHODS

Study Area

Ningaloo Reef (NR) is the longest fringing coral reef in Australia, and is considered a biodiversity hotspot and to be in a good state of conservation compared with other coral reefs (Gazzani and Marinova, 2007; Schonberg and Fromont, 2012). The NMP was designed to protect 90% of these iconic waters (CALM and MPRA, 2005). A biodiversity analysis of different phyla including demersal fish, sponges, and soft corals showed the NMP is a biogeographical overlap zone, where more tropical species occur in the northern section and both tropical and temperate species are present in the southern area (Simpson and Waples, 2012). In the present study, three areas of the NMP were used to model the distribution of demersal species of fish using depth derivatives and backscatter information. Mandu in the northern area, Point Cloates in the central area and Gnaraloo in the southern zone (**Figure 1**).

Baited Remote Underwater Stereo-Video

A multidisciplinary project was conducted in NMP between 2006 and 2009 by the Western Australia Marine Science Institution (WAMSI) and associates (Waples and Hollander, 2008). As part of this project, many aspects of the NMP were studied, including the demersal fish composition using Baited Remote Underwater Stereo-Video (stereo-BRUVS). A total of 656 stereo-BRUVS were deployed across the areas in **Figure 1** in March-May 2009, between depths of 15 and 350 m. The stereo-BRUVS data

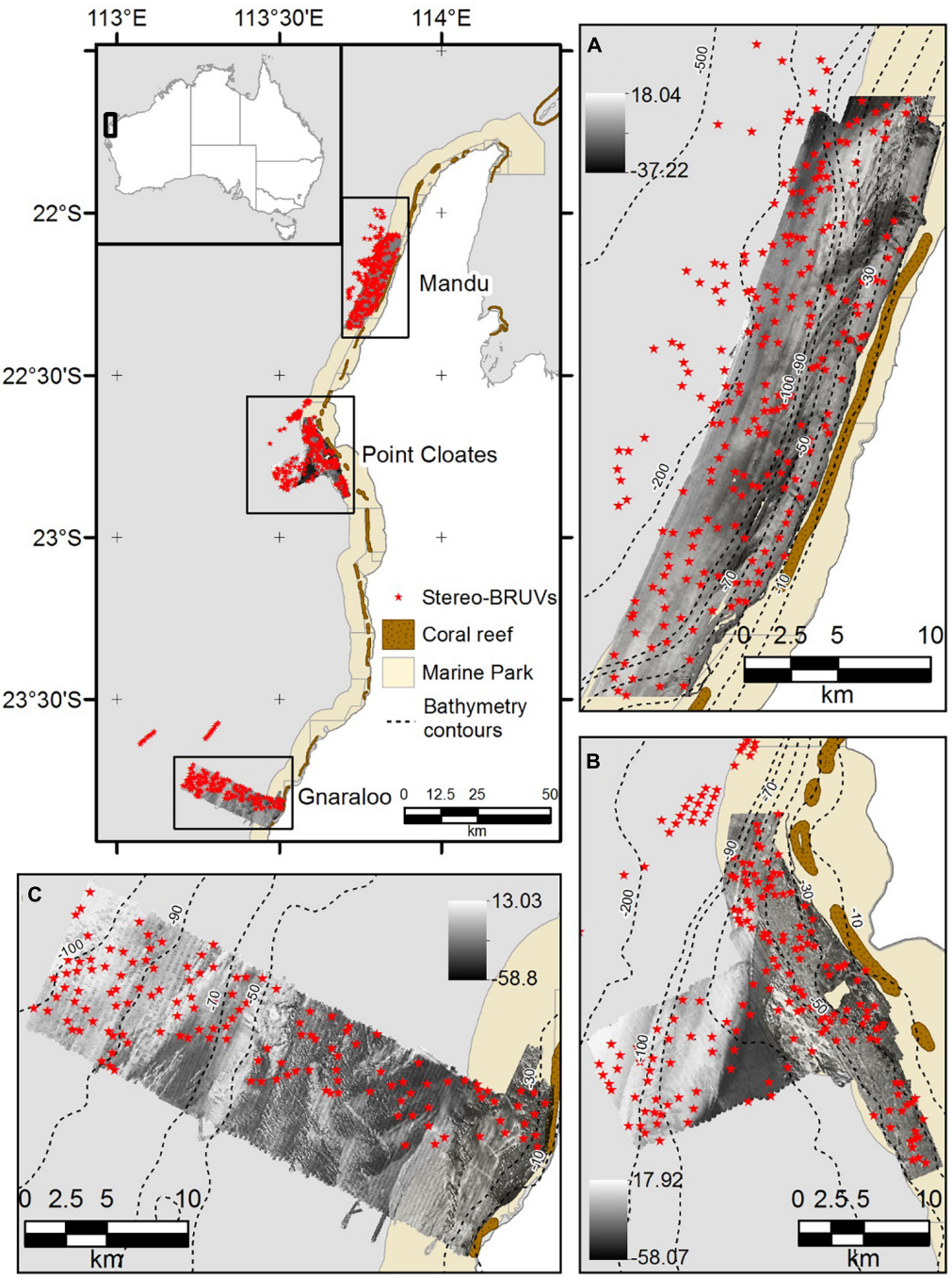

FIGURE 1 | Study site. **(A)** Mandu in the northern area of the NMP, **(B)** Point Cloates in the central area, and **(C)** Gnaraloo in the southern area of the NMP. The deployment location of the stereo-BRUVS is shown as red stars, and the backscatter mosaics are shown as black and white images.

included 239 deployments in Mandu, 185 in Pt Cloates and 155 in Gnaraloo (Waples and Hollander, 2008; Simpson and Waples, 2012). A database that included relative abundance, produced by the Australian Institute of Marine Science (AIMS), was used in the present study. The commonly used metric, MaxN, corresponds to the maximum number of individuals of the same species observed together in one frame at any one time, during the analyzed period of the video, and has been shown to provide a conservative estimate of relative abundance (Willis et al., 2000; Cappo et al., 2003). Only the first hour of recording was used for the MaxN estimation analysis, which commences the moment the cameras touch the bottom. More details on the collection and analysis of the stereo-BRUVS can be found in Harvey et al. (2007).

Depth and Depth Derivatives

Depth and depth derivatives MBES surveys of the study areas were conducted in 2008 by Geoscience Australia and AIMS, using a Kongsberg EM3002, operating at 300 kHz. The MBES bathymetry was downloaded from the Geoscience Australia (GA) website as a raster with 3 m resolution. Ten depth derivatives were calculated from the bathymetry as shown in **Table 1** (Moore et al., 2010, 2011). Some of the derivatives were produced using the raster package (Hijmans, 2016) of the free software R (R Development Core Team, 2017) and the rest were produced using Landserf v2.3 as specify in **Table 1**. Ecological processes occurring at different scales can affect the distribution and abundance of demersal fishes. Therefore, four different windows sizes were used in the production of the derivatives. The finest scale of analysis was fixed by the resolution of the MBES data (3 m) and a 3×3 window of analysis, while the other three were chosen based on the spatial dependence of the species. A variogram analysis was used to identify the maximum distance at which the species display spatial dependency (the range) (Holmes et al., 2008). For the species with spatial dependency, the range was above 4 km. Therefore, the scales were chosen to cover the span between the finest resolution and below the maximum range of any of the species using four windows sizes of analysis (number of cells) 3 by 3 (81 m^2), 9 by 9 (729 m^2), 15 by 15 (2,025 m^2), and 21 by 21 (3,969 m^2). The largest windows size was selected to be within the maximum range of the species, but also based on the pixel size of the ARA-phi layer (60 m). For the fractal dimension calculation, the smallest windows size allowed in Landserf is 9 by 9. Therefore, the 3 by 3 window analysis was not used for this variable.

Backscatter Derivatives

The backscatter information was included in the models as two different layers. The first one was the full-coverage, 3-m resolution mosaic, downloaded from the GA website. The second one is an approximation of the sediment phi size estimated using the ARA (Fonseca et al., 2009), applied to the raw files.

Angle vs. Range Analysis

The relationship between the backscatter strength and the grazing angle is commonly known as the ARC. ARC is related, for certain frequencies, to particular properties of the seafloor (Hasan et al., 2014). Therefore, the ARC can be used to infer characteristics of the seafloor using the Angle vs. Range Analysis (ARA; Fonseca et al., 2009). In this study, we used the FMGT software (version 7.8) to conduct an ARA analysis using the raw MBES backscatter data. A full description of the method followed during the ARA analysis in FMGT can be found in Fonseca and Mayer (2007), a brief description of the method is given here.

The backscatter angular response is first corrected for radiometric and geometric distortions to locate each ping to its correct angular position. In the next step, a group of consecutive pings is stacked in the along-track direction, 30 pings were stacked. The stack of the pings produces two seafloor patches, one for the port side and another for the starboard side. The size of the patch being analyzed is approximately half of the swath of the MBES system coverage. The stacking of the pings in a patch has the effect of reducing the resolution of the final layer, but it is a necessary step to reduce the speckle noise, typical to any acoustic method. An average ARC calculated for each patch is then compared to a formal mathematical model which relates the observed backscatter with seafloor properties in a process called the ARA-inversion. During the inversion, the model is used to produce an approximation of the acoustic impedance, roughness and consequently the mean grain size of the patch under analysis. An ARA-inversion analysis was conducted for all the patches in the three studied sites to obtain maps of the distribution of grain size, with a resolution of 60 m. During the analysis, only incidence angles between 20 and 60° were included, as the angles in the near nadir and outer angle regions tend to be noisy with less power of discrimination between different types of substrate (Hasan et al., 2012b).

As part of the WAMSI project, 290 sediment samples were collected using a Van-Veen grab sampler for surface and subsurface material between 2007 and 2006 (Colquhoun et al., 2007). The grain size estimated for this ground-truth data was compared with sediment phi size estimated using the ARA analysis, correlation and regression was used to test the relationship between them.

Species Distribution Models

The environmental variables including depth, depth derivatives, and the backscatter data were used as explanatory variables to explain the probability of presence of *A. stellatus, G. grandoculis, L. sceleratus, L. miniatus, L. macrorhinus, L. sebae,* and *S. queenslandicus*. The species were selected based on a minimum 25 presence in each of the sampled areas. All the species included in the present study are carnivores with different degrees of generalist feeding behavior using a variety of benthic habitats (**Table 2**). Lutjanids and lethirinids including *G. grandoculis, L. miniatus,* and *L. sebae* have a strong association to hard bottom or substrate with a certain degree of vertical relief (Parrish, 1987). *L. sceleratus* and *A. stellatus,* on the other hand, have a preference for sandy bottoms (Randall, 1967; Rousou et al., 2014). Seafloor backscatter can help to differentiate hard from sandy bottoms; therefore, this study has the hypothesis that the inclusion of seafloor backscatter will improve the accuracy of the models for the lutjanids and lethirinids species. For *S. queenslandicus* and *L. macrorhinus*, water column variables may be more important in explaining their distribution (Collette and Nauen, 1983; Gutteridge et al., 2011), and it is expected that the inclusion of seafloor backscatter data to have a marginal effect on their models.

Random Forest (RF) is a robust statistical method with many advantages to solving ecological problems, including high classification accuracy and particularly high capacity to model complex interactions without statistical pre-assumptions like normality (Breiman, 2001). The algorithm begins by selecting a bootstrap sample from the data, approximately 63% of the original observations are used at least once in the bootstrap sample. The rest of the observations not selected for the bootstrap sample are called out-of-bag (OOB) observations. RF fits a tree to each bootstrap sample, but in each node, only a subsample of the variables is available for the binary partitioning (one-third of the total number of variables in the case of regression and the square

TABLE 1 | Depth derivatives produced from bathymetry. Aspect (orientation of the slope) was divided in two variables using trigonometric transformations.

Variable		Abbreviation	Description	Software	References
Slope		Slope	Rate of change in elevation over the analysis windows express in degrees	Landserf v2.3	Wood, 1996
Aspect	Northness	NS	Cosine of aspect (e.g., slopes facing north (NS = 1), facing south (NS = –1)	Landserf v2.3	Wood, 1996
	Eastness	WE	Sine of aspect (e.g., slopes facing east (WE = 1), or west (WE = –1)	Landserf v2.3	Wood, 1996
Curvature	Profile	Profc	Curvature of a line formed by intersecting the vertical plane oriented in the direction of the steepest slope with the terrain surface	Landserf v2.3	Wood, 1996
	Plan	Planc	Curvature of a line formed by intersecting the horizontal plane oriented in the direction of the steepest slope with the terrain surface	Landserf v2.3	Wood, 1996
	Mean	Meanc	Mean curvature in any plane	Landserf v2.3	Wood, 1996
Fractal dimension		Fractal	Indicates how surface roughness changes over space with a minimum value of 2.0 indicating smooth, scale invariant behavior and a theoretical maximum of 3.0 indicating a space filling rough surface	Landserf v2.3	Wood, 1996
Standard deviation of depth		SD	Standard deviation of depth	R raster package	Holmes et al., 2008
Benthic position index		BTI	Measure of the position of a particular pixel concerning the average depth of its surrounding neighbors. Positive values showing depth above the average (ridges), and negative values for pixels below the average (though).	R raster package	Wilson et al., 2007
Terrain ruggedness index		TRI	Men of the absolute difference between the value of a cell and its neighboring cells	R raster package	Wilson et al., 2007
Roughness		Rough	Difference between the maximum and the minimum depth of a cell and its neighboring cells	R raster package	Wilson et al., 2007

TABLE 2 | Habitat and feeding preference of the species included in the study.

Species	Habitat	Feeding preferences	References
Gymnocranius grandoculis	Hard substrata or substrata having some vertical relief	Benthic invertebrates and small fishes	Parrish, 1987
Lethrinus miniatus			
Lutjanus sebae			
Scomberomorus queenslandicus	Pelagic in bays and around islands and coastal reefs	Neritic species	Collette and Nauen, 1983
Lagocephalus sceleratus	Sandy, rocky substrates and seagrass meadows	Benthic invertebrates and small fishes	Rousou et al., 2014
Loxodon macrorhinus	Inshore habitats with clear waters	Benthic invertebrates and small fishes	Gutteridge et al., 2011
Abalistes stellatus	Sand, sponge, and weed areas on deep slopes.	Feeds on benthic animals	Randall, 1967

root in the case of classification). All the trees are fully grown and used to predict the OOB observations. The predicted value for each observation is based on the average value predicted by the trees (Breiman, 2001). In this study, we used RF classification to model the presence/absence of the nine selected species and RF regression for the richness of species.

For the RF classification, the sensitivity and specificity were evaluated using the Area Under the Curve (AUC) of the Receiver Operator Curve. The AUC varies between 0 and 1. Values higher than 0.9 are considered outstanding whereas values between 0.9 and 0.7 indicate good performance. Values lower than 0.7 indicate poor prediction and values lower than 0.5 indicate that the model is not better than a random classification (Hosmer et al., 2013). The performance of the models was also tested using the F1, and Kappa statistics. The F1 is the harmonic mean of precision and sensitivity while the Kappa statistic (K) measures the level of chance-corrected agreement between the observed and predicted classes. According to Landis and Koch (1977) the level of agreement measured with K can be classified as $K < 0.0$ poor, $0 \leq K < 0.2$ slight, $0.21 \leq K < 0.4$ fair, $0.41 \leq K < 0.6$ moderate, $0.61 \leq K < 0.8$ substantial, $K > 0.8$ almost perfect. The effect of including the backscatter data as explanatory variables in the accuracy of the models was examined using two scenarios, the first one including depth and depth derivatives (DV) and in the second one the two backscatter variables were added (DVBS). A fivefold cross-validation procedure was used, for each fold 65 percent of the data was used to train the model and the rest to test it, an AUC, F1, and K was obtained for each fold and the mean and standard error of the statistics is reported. The difference in the mean AUC, F1, and K for the DV and DVBS scenarios was tested using a *t*-test in R. The mean importance of the co-variables was also calculated. For the RF regression the accuracy was measured by the mean square error (MSE), and also the percentage of variance explained by the model is reported.

RESULTS

Angle vs. Range Analysis

A significant correlation was found in the Mandu area between the phi sediment size estimated using the backscatter data in the ARA analysis and the ground-truth sediment samples grain size ($r = 0.59, p < 0.001, r^2 = 0.25, p < 0.001$). A significant correlation was also found in the Pt Cloates area between the phi sediment size estimated using the backscatter data in the ARA analysis and the ground-truth sediment samples grain size ($r = 0.47, p = 0.003, r^2 = 0.22, p < 0.001$). The relationship between the grab grain size and the ARA-phi for the full data combined was also significant ($p < 0.001$, **Figure 2**). No significant correlation was found for the Gnaraloo site.

Species Distribution Models

The performance of the models was species- and area-dependent with some species being better modeled in some areas than others and all species models having acceptable levels of accuracy (mean AUC > 0.7) in at least one of the studied sites (**Figure 3A**). The effect of adding the backscatter data (DVBS) also varied by species and study site with no consistent improvement in the accuracy of the models. The Mandu area had fewer models of species with acceptable levels of accuracy (mean AUC > 0.7) while Pt Cloates had only one species with model mean AUC consistently < 0.7. A similar pattern was observed in terms of K with lower values $K < 0.2$ in the Mandu area and higher mean K-values in the Pt Cloates area $K > 0.4$ considered as moderate performance (**Figure 3B**). The majority of the species had relatively high F1 mean > 0.7 (**Figure 3C**).

For *G. grandoculis*, the inclusion of the seafloor backscatter had a positive effect on the performance of the models increasing the mean AUC, K and F1 in all the three study sites. The increase on the mean value was significant for the K statistic in the Mandu and Pt Cloates area, and for the F1 in the Pt Cloates area. The significant increase of the F1 in the Pt Cloates area meant the accuracy of the resulting model was F1 > 0.7. The significant increase of the mean K also meant the model including the seafloor backscatter had an accuracy considered moderate ($K > 0.4$). Although the increase of the mean AUC in the *G. grandoculis* models was not significant, the mean AUC (± se) for Pt Cloates area was > 0.7 after the inclusion of the seafloor backscatter data (**Figure 3A**).

The DVBS scenario had a better performance in the models of *L. miniatus,* and *S. queensladicus* in at least two of the study sites, with different levels of improvement. The inclusion of DVBS resulted in a significant increase of the mean AUC for *L. miniatus* in the Pt Cloates area (**Figure 3A**) and a significant increase in the mean K in the *S. queensladicus* model in the Gnaraloo area (**Figure 3B**). A significant increase in the mean AUC was observed for the *L. sceleratus* model (**Figure 3A**) in the Mandu area, and a significant increase of the mean K in the Gnaraloo area (**Figure 3B**), when the seafloor backscatter was included; however, the mean AUC of the model in the Mandu area remained < 0.7.

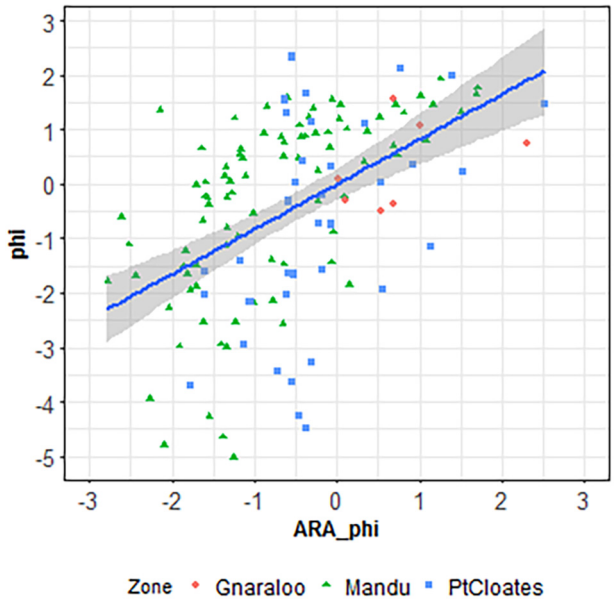

FIGURE 2 | Linear regression between the grain size calculated with the ARA analysis and the phi size calculated from the ground-truth samples.

Richness

The RF for the richness of demersal species explained different level of variance in the three study sites (**Table 3**). The model with the lowest level of mean explained variance was at Gnaraloo, although, the DVBS scenario produced a significant increase of explained variance by 5% ($P < 0.05$). In the Mandu area, a significant portion of variance was explained by the models, with more than 25% of mean explained variance. However, no change in explained variance was observed in the DVBS scenario. The richness of demersal fish species was particularly well modeled in the Pt Cloates area with variance explained of greater than 40%. The importance of the backscatter data was evident with an increase of the explained variance in the DVBS scenario, although the increase was not significant (**Table 3**).

Variables Importance in the Distribution Models

A summary of the most important variables explaining the distribution of the species is shown in **Table 4**. Depth and seafloor backscatter were the most important variables in the construction of the models for the majority of the species in the three study sites (**Table 4**). Depth was key for the majority of the species in the three study areas, with some exceptions. Variables related to terrain variability (including roughness, TRI, and standard deviation of depth) were important for many of the species, in particular at a broad-scale (15–21 neighbors). For the models of *L. sceleratus, L. macrorhinus*, and *S. queenlandicus,* for example, the terrain variability variables had higher importance than depth in the Pt Cloates area.

The seafloor backscatter, and the ARA-phi layer, were among the three most important variables in the models of six of the seven studied species in at least one of the study areas. For *G. grandoculis*, the ARA-phi was the second most important

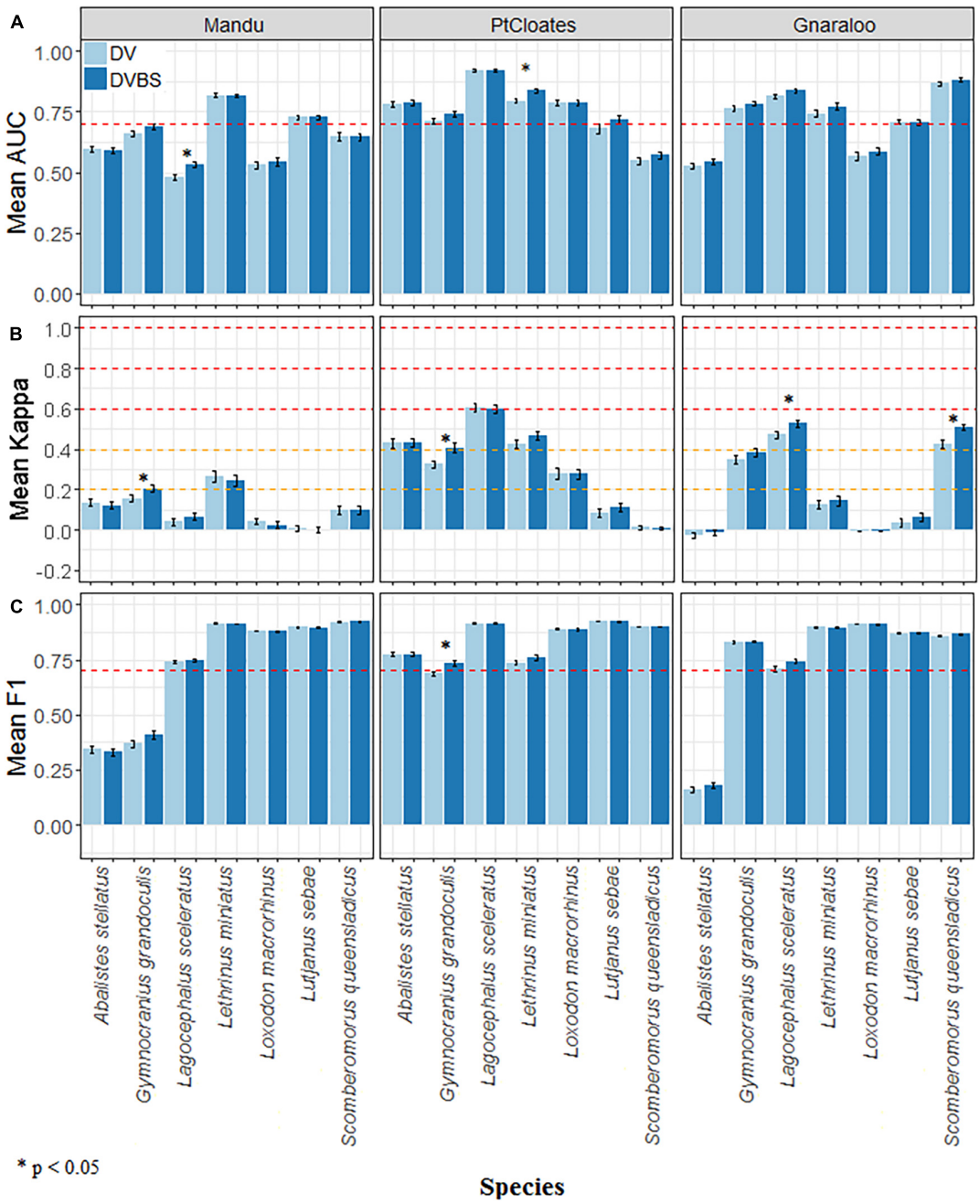

FIGURE 3 | (A) Mean AUC, **(B)** Kappa, and **(C)** F1, and standard error of the Random Forest distribution models for *A. stellatus*, *G. grandoculis*, *L. sceleratus*, *L. miniatus*, *L. macrorhinus*, *L. sebae,* and *S. queenslandicus* in the three study sites of the Ningaloo Marine Park. The depth and depth derivative scenario (DV), and the depth, depth derivatives plus the backscatter data (DVBS) scenario are shown. Red dotted horizontal lines in (A,C) show AUC = 0.7 and F1 = 0.7 respectively, and for **(B)** the orange dotted lines indicate $K = 0.2$ and $K = 0.4$, while the red ones indicate $K = 0.6$ and $K = 0.8$. * denotes significance at the 0.05 level.

variable in the models of the three study sites, confirming its importance for this species as shown by higher mean AUC, F1 and K of the DVBS models compared to the DV scenario. For *L. sceleratus* DVBS models in both the Mandu and Gnaraloo areas the ARA-phi and the backscatter mosaic ranked among the three most important variables in the models. The ARA-phi variable was identified as one of the three most important variables in the models of *L. miniatus, S. queenslandicus*, in both Pt Cloates and Gnaraloo areas. For the *L. macrorhinus* and *L. sebae* model, the ARA-Phi was important in the Gnaraloo and Pt Cloates areas, respectively.

Depth was the most important variable in the construction of the model for the richness of species in the Mandu area, in both DV and DVBS scenarios. For the Pt Cloates area, TRI, followed

TABLE 3 | Mean percentage of variance explained by the Random Forest for the total richness of species in the three study sites for both the depth and depth derivatives (DV, BT + DV) and depth, depth derivatives and seafloor backscatter data (DVBS, BT + DV + BS) scenarios.

Variable	Scenario	Variance explained		
		Mandu	Pt Cloates	Gnaraloo
Richness	DV	26%	42%	2%
	DVBS	26%	46%	7%**

*** denotes significance at the 0.01 level.*

by the profile curvature were the most important variables explaining the richness of species. The ARA-phi layer was also considered important when included in the model for Pt Cloates, although with a lower ranking. For the Gnaraloo area, slope, profile curvature and depth were the most important variables in the DV model, while for the DVBS model, both the ARA-phi layer and backscatter mosaic were second and third in importance.

DISCUSSION

The accuracy of the species distribution models based on depth and depth derivatives varied among species and study sites. Higher accuracies were observed, in general, for the species in the Pt Cloates area, which is considered to have a complex seafloor. The terrain variables were less successful in modeling the presence of the species in the Mandu area. The addition of the seafloor backscatter in the species distribution models did not necessarily increase the model's accuracy in a significant manner, although, in the majority of the cases the ARA-phi layer was ranked as an important variable when included in the models. The ARA-phi layer was particularly important in the model of *G. grandoculis* in the three study sites, and *L. miniatus* in two areas, increasing the accuracy of the models. A significant portion of the species richness variation was explained using the terrain variables, and the addition of the seafloor backscatter improved the accuracy of the model in the Gnaraloo area.

Backscatter Derivatives

A significant relationship was found between the phi size estimated with the ARA analysis and the grain sediment size measured from the grab samples. However, the ARA-phi analysis did not identify coarse gravel sediments (cobbles) with phi values below −3. Previous studies have suggested the inclusion of backscatter, and in particular, the use of the angular response of the backscatter can add to the discrimination between benthic habitats (Hasan et al., 2014). However, the seafloor backscatter intensity can be affected in different ways by the frequency of the echo-sounder, sediment grain size, nature, and magnitude of seabed roughness, and volume scattering by subsurface scatters (Ferrini and Flood, 2006). For example, previous studies have shown that the use of high-frequency MBES (e.g., 300 kHz) can lead to misclassification of coarse sediments when the grain size is larger than the acoustic wavelength of the sonar. In such cases, there is a decrease in the backscatter values for sediments of increasing grain size (i.e., $\lambda = -2.3\ \phi$, equal to 5 mm; Eleftherakis et al., 2014). In this study, something similar was observed with a significant correlation between grain size and the acoustic backscatter (ARA-phi), but low agreement between the two for large grain sizes. Also, scattering register by a high-frequency echo-sounder would be related to seabed surface roughness while scattering by particles under the sediment-water interface will be relatively more important at lower frequencies (Jackson et al., 1986). A previous study compared a high (200 kHz) and low (50 kHz) frequency echo-sounders and its ability to discriminate sediment grain size and found the higher frequency system failed to differentiate between sediment grain sizes even between mud and sand (Freitas et al., 2008). The importance of the different variables influencing the backscatter of the seafloor can also vary between sampling sites (Ferrini and Flood, 2006). Therefore the seafloor backscatter on its own has limitations to predict seabed characteristics (Ferrini and Flood, 2006).

A drawback in the approach adopted in this study was using a constant number of stack pings during the ARA analysis, as the area sampled would then depend on the water depth. As a result, the sampling areas in the shallowest depths were around three times smaller than in the deepest zones. This can produce a misinterpretation of the sediment class in deeper areas, in particular, in areas of transition between two different classes. However, the vast majority of stereo-BRUVs deployments were not located in areas of transition between different ARA-phi classes reducing the risk of mixing sediment classes. Hence, it is unlikely that the different resolutions of the ARA-phi size layer had a significant effect on the species distribution models. The high ranking of the ARA-phi in the models of species distribution, reinforce the idea that the resolution of the variable was appropriate.

Species Distribution Models

For the majority of species, depth was a primary variable in explaining their distribution across the three study sites and for both DV and DVBS scenarios. Depth is a common variable influencing the distribution of species in coral reef areas, as it is related to the effects of light availability on community composition and function (Hill et al., 2014).

The importance of the depth derivatives at different window sizes varied among species and study sites. For the most abundant species, such as *A. stellatus*, *L. sceleratus,* and *G. grandoculis*, broader-scale variables (15 × 15 and 21 × 21 windows size) of TRI, roughness, slope and fractal dimension were considered key variables in explaining their distribution. These results agree with previous studies, showing that broad-scale variables are more relevant for species with higher mobility and larger home ranges that use a variety of benthic habitats (Franklin et al., 2009; Tamburello et al., 2015). For other species, like *L. macrorhinus*, which had the lowest prevalence in the study, the fine-scale variables were more important in two of the study areas, indicating a higher level of specialization. For the remaining species, a mix of fine and broad-scale variables was important in the construction of the distribution models.

The ARA-phi layer which was calculated with a broad resolution of 60 m, was found to be one of the three most

TABLE 4 | Summary of variable importance in the construction of the distribution models for the species included in the study.

Species	Importance	Area/scenario					
		Mandu		Pt Cloates		Gnaraloo	
		DV	DVBS	DV	DVBS	DV	DVBS
A. stellatus	*1*	Depth	Depth	Depth	Depth	NS9	NS9
	2	Rough21	Rough21	TRI21	TRI21	Depth	Depth
	3	Slope15	Slope15	Slope21	Slope21	BPI9	Profc15
G. grandoculis	*1*	Depth	Depth	Depth	Depth	Depth	Depth
	2	Rough9	**ARA_Phi**	Slope15	**ARA_Phi**	Meanc21	**ARA_Phi**
	3	BPI3	TRI15	SD15	**BS**	Fractal21	Profc15
L. sceleratus	*1*	Depth	**ARA_Phi**	TRI21	TRI21	Depth	Depth
	2	NS3	Depth	SD21	SD21	WE21	**ARA_Phi**
	3	Planc9	**BS**	TRI15	TRI15	NS21	WE21
L. miniatus	*1*	Rough15	Rough15	Depth	**ARA_Phi**	Depth	Depth
	2	Profc15	Profc15	SD9	SD9	TRI9	**BS**
	3	Depth	Rough21	Rough9	Depth	Profc3	TRI9
L. macrorhinus	*1*	Depth	Depth	TRI9	TRI9	TRI15	TRI15
	2	Rough3	Rough3	TRI15	TRI15	TRI21	TRI21
	3	TRI21	TRI3	SD9	SD9	SD3	**ARA_Phi**
L. sebae	*1*	Depth	Depth	Depth	Depth	Slope9	Slope9
	2	Profc21	Profc21	Rough21	Rough21	Rough21	Rough21
	3	SD3	Rough3	SD21	**ARA_Phi**	Depth	Depth
S. queenslandicus	*1*	Fractal9	Fractal9	Planc15	**ARA_Phi**	Depth	Depth
	2	Fractal21	Fractal21	Profc15	Profc15	WE21	**ARA_Phi**
	3	Fractal15	Depth	Profc21	Planc15	NS21	WE21
Richness	*1*	Depth	Depth	TRI15	TRI15	Slope9	Depth
	2	Slope15	Slope15	Profc21	Profc21	Profc9	**BS**
	3	SD9	Slope9	SD15	**ARA_Phi**	Depth	**ARA_Phi**

Only the three variables with highest ranking of importance are included for each species and each scenario. The scenario of depth and derivatives (DV) and depth, depth derivatives and backscatter data (DVBS) scenarios are shown.

important variables in the species models. This reaffirms the importance of broad-scale variables for roaming species with a wide niche (Monk et al., 2011; Moore et al., 2011). The backscatter mosaic at 3 m resolution was often included as a key variable, though to a lesser extent. This study investigated the hypothesis that the addition of the seafloor backscatter would increase the accuracy of the models, in particular, for *G. grandoculis*, *L. miniatus, L. sebae, L. sceleratus,* and A. *stellatus* models. Seafloor backscatter data were consistently important in the models of *G. grandoculis*, increasing the model's accuracy for the three study sites. *G. grandoculis* is a species that inhabits rocky bottoms (Dorenbosch et al., 2005), which can explain the importance of backscatter in the construction of the models as this variable can be used to differentiate between soft/hard bottoms (Kloser et al., 2010). *L. miniatus* is associated with sand around coral reefs areas where it feeds on benthic invertebrates, which could explain the importance of the seafloor backscatter in the models of two of the study sites (Carpenter and Niem, 1998). However, results showed only an increase of 2–5% in the model mean AUC for *G. grandoculis, L. miniatus* and L. *sceleratus*, in at least two of the study sites, and similar incremental increases in F1 and K. Also, the increase of the mean AUC was only significant for *L. sceleratus* and *L. miniatus*, therefore the improvement can only be seen as indicative. *L. miniatus* is often more prevalent in shallow waters, such as on the Great Barrier Reef where it was found in 12–18 m of water (Newman and Williams, 2001), which may explain the lack of importance in the model accuracy for this species in the Mandu area. Depth might play a more important role at Mandu, where rapid changes in bathymetry are observed (Brooke et al., 2009). *L. sceleratus*, inhabits offshore sandy bottoms in their early life stages with a habitat shift to deeper or rocky grounds for the largest individuals (Fitzpatrick et al., 2012). The inclusion of the ARA layer may, therefore, add useful information to differentiate between sandy and rocky habitats. For *L. sebae*, the inclusion of the seafloor backscatter had a positive effect on the accuracy of the models for the Pt Cloates while variables measuring the rugosity of the seafloor were particularly important for this species in the three study sites. This species is associated with exposed reef slope (Fitzpatrick et al., 2012) which could explain the importance of variables related to the complexity of the seafloor as coral reef areas have, in general, higher levels of terrain complexity and rugosity.

Depth and backscatter were not considered as important in explaining the distribution of some species. For example, *L. macrohinus* is a small species of shark whose distribution was more related to variables measuring the rugosity of the

seafloor. Another species, *S. queenslandicus*, is an epipelagic neritic schooling species (Collette and Nauen, 1983; Kailola et al., 1993), which might explain the poor performance of the models for this species in two of the study sites, as variables of the terrain might not be related to its distribution.

Previous studies have found the addition of backscatter metrics can be important in the construction of models of demersal fish distribution (Monk et al., 2011) or suggested further studies were needed to assess the relationship between seafloor backscatter and the assemblage of demersal fish (Schultz et al., 2014). The results of this study showed that the seafloor backscatter was an important variable in the models of demersal fish distribution. However, the inclusion of this variable did not necessarily lead to an improvement in the accuracy of the models. Possible reasons for that may be that the depth and derivatives were capturing the significant changes in the habitat, or that the substrate was not a significant driver for the species distribution.

Another factor is the uncertainty associated with the use of seafloor backscatter to approximate specific characteristics of the seafloor, including roughness and hardness, but also sediment grain size. The amount of energy reflected by the seafloor is affected by the frequency of the MBES, and although higher frequencies are more affected by seabed roughness, they have less penetration in the sediment. For example, a 100 kHz frequency in fine sediment is expected to penetrate between 0.1–1 m (Fonseca et al., 2002), while a 12 kHz can penetrate up to 12 m in muddy deposits (Schneider von Deimling et al., 2013). The level of penetration in the sediments of high frequencies is also highly sensitive to small changes in sediment properties, in particular, between fine sediments (Gaida et al., 2018). Higher frequencies are also less effective to map coarse sediment larger than the wavelength of the MBES, which will have a lower level of acoustic reflectance. Therefore, the high frequency of the MBES (300 kHz) could limit the power of discrimination between benthic habitats (Boscoianu et al., 2008; Schneider von Deimling et al., 2013), that might be relevant for habitat selection of demersal fish. The use of multi-frequencies could increase our ability to discriminate between seabed environments (Feldens et al., 2018; Gaida et al., 2020). Previous studies have shown the use of multiple frequencies, in particular lower frequencies (e.g., 100 kHz) can help differentiate between soft sediments (Costa, 2019). However, the possible improvement of benthic habitat discrimination will also be related to the characteristics of the study site, as shown by Gaida et al. (2018).

The analysis of the 656 stereo-BRUVS showed that only around 3% of the species were moderately prevalent, occurring in $\geq$ 20% of the sampling point (Simpson and Waples, 2012). In the present study, we included some of these species, those with a minimum of 25 occurrences on each of the three sites in an effort to compare the model performance in different areas of the NMP. Therefore, they all presented a certain degree of generalist behavior which is related to less specialized habitat requirements, and as a result it is more difficult to produce well performing models of the species distributions (Wilson et al., 2008). Finally, the combination of stereo-BRUVS with acoustic data in itself includes a certain degree of uncertainty, for example, by the use of bait which can attract fish from the areas around the deployment. The possible impact of the incorrect location of presence records in the models of species distribution will be less likely for species for which depth and ARA-phi variables were important, considering that both variables have a high local spatial autocorrelation (in an area of 500 m around the stereo-BRUVs deployment) (Naimi et al., 2014). Future studies using more than one frequency are needed to better test the benefit of using the seafloor backscatter in habitat distribution models of species of demersal fish, in particular, for non-generalist species.

CONCLUSION

Demersal species were well modeled with the depth and depth derivatives in the majority of the species analyzed, in at least one of the study sites. The addition of the backscatter data increased the accuracy of the models for some species, in particular, a consistent positive effect was observed for *G. grandoculis*. Depth derivatives can integrate some of the seafloor roughness information which may explain the limited benefit of adding the backscatter data in some of the species distribution models. Additional information related to the hardness/roughness not included in the depth derivatives were important for some species for which the inclusion of the backscatter data had a positive effect.

For some species the mosaic backscatter layer appeared as an important variable in explaining their distribution. In general, however, the ARA-layer was more important for the variables in the construction of the models. This is an encouraging result that demonstrates that the use of novel derivatives which take advantage of the angular response can produce models with higher accuracies. Although the increase in the accuracy of the models was not significant for the majority of the species, it can be considered an indicative result, and more efforts are needed to confirm this pattern.

DATA AVAILABILITY STATEMENT

The raw data supporting the conclusions of this article will be made available by the authors, without undue reservation.

ETHICS STATEMENT

The animal study was reviewed and approved by the Curtin University Ethics Committee, AEC approval number: AEC_2014_09.

AUTHOR CONTRIBUTIONS

ML: conceptualization, methodology, formal analysis, writing-original draft, writing-review, and editing. MP: conceptualization, supervision, writing-original draft, writing-review, and editing. BS: conceptualization, methodology, writing-review, and editing. BR: conceptualization, formal analysis, writing-review, and editing. IP: conceptualization,

investigation, supervision, writing-review, and editing. All authors contributed to the article and approved the submitted version.

FUNDING

Consejo Nacional de Ciencia y Tecnologia (CONACYT), provided a Ph.D. scholarship CVU 230139 for ML.

ACKNOWLEDGMENTS

We would like to thank Geoscience Australia for making the bathymetry and backscatter data available and particularly Justy Siwabessy for helping provide the raw MBES data. We would also like to thank WAMSI for funding research and making data available from NMP. Stereo-BRUVS data were collected through the Western Australian Marine Science Institute (WAMSI) Node 3 Project 1 Subproject 3.1.1: Deepwater communities at Ningaloo Marine Park.

REFERENCES

Anderson, T. J., Syms, C., Roberts, D. A., and Howard, D. F. (2009). Multi-scale fish-habitat associations and the use of habitat surrogates to predict the organisation and abundance of deep-water fish assemblages. *J. Exp. Mar. Biol. Ecol.* 379, 34–42. doi: 10.1016/j.jembe.2009.07.033

Boscoianu, M., Molder, C., Arhip, J., Stanciu, M. I, and Vizitiu, I. C. (2008). "Feature sets based on fuzzy reasoning for automatic sea floor characterization," in *Proceedings of the 10th WSEAS international conference on Mathematical Methods, Computational Techniques, Non-Linear Systems, Intelligent Systems*, eds N. E. Mastorakis, M. Poulos, V. Mladenov, Z. Bojkovic, D. Simian, and S. Kartalopoulos (Athens: World Scientific and Engineering Academy and Society), 234–239.

Breiman, L. (2001). Random forests. *Mach. Learn.* 45, 5–32. doi: 10.1023/a:1010933404324

Brooke, B., Nichol, S., Hughes, M., McArthur, M., Anderson, T., Przeslawski, R., et al. (2009). *Carnarvon Shelf Survey Post-Survey Report*. Canberra, ACT: Geoscience Australia Record.

Brown, C. J., Sameoto, J. A., and Smith, S. J. (2012). Multiple methods, maps, and management applications: purpose made seafloor maps in support of ocean management. *J. Sea Res.* 72, 1–13. doi: 10.1016/j.seares.2012.04.009

CALM and MPRA (eds) (2005). *Management Plan for the Ningaloo Marine Park and Muiron Islands Marine Management Area 2005–2015*. Perth, WA: Government of Western Australia.

Cappo, M., Harvey, E., Malcolm, H., and Speare, P. (2003). "Potential of video techniques to monitor diversity, abundance and size of fish in studies of marine protected areas," in *Potential of Video Techniques to Monitor Diversity, Abundance and Size of Fish in Studies of Marine Protected Areas*, eds J. P. Beumer, A. Grant, and D. C. Smith (Queensland, QLD: University of Queensland).

Carpenter, K. E., and Niem, V. H. (1998). *The Living Marine Resources of the Western Central Pacific: Bony fishes part 4 (Labridae to Latimeriidae), Estuarine Crocodiles, Sea Turtles, Sea Snakes and Marine Mammals*. Rome: Food and Agriculture Organization of the United Nations.

Collette, B. B., and Nauen, C. E. (1983). *Scombrids of the World: An Annotated and Illustrated Catalogue of Tunas, Mackerels, Bonitos, and Related Species Known to Date*. United Nations Development Programme. Rome: Food and Agriculture Organization of the United Nations.

Colquhoun, J., Heyward, A., Rees, M., Twiggs, E., Fitzpatrick, B., McAllister, F., et al. (2007). *Ningaloo Reef Marine Park Deepwater Benthic Biodiversity Survey*. Metadata Report -Number 2. Crawley WA: : Australian Institute of Marine Science.

Costa, B. (2019). Multispectral acoustic backscatter: how useful is it for marine habitat mapping and management? *J. Coast. Res.* 35:1062. doi: 10.2112/jcoastres-d-18-00103.1

Costa, B., Taylor, J. C., Kracker, L., Battista, T., and Pittman, S. (2014). Mapping reef fish and the seascape: using acoustics and spatial modeling to guide coastal management. *PLoS One* 9:e85555. doi: 10.1371/journal.pone.0085555

Dorenbosch, M., Grol, M. G. G., Christianen, M. J. A., Nagelkerken, I., and van der Velde, G. (2005). Indo-Pacific seagrass beds and mangroves contribute to fish density coral and diversity on adjacent reefs. *Mar. Ecol. Prog. Ser.* 302, 63–76. doi: 10.3354/meps302063

Eleftherakis, D., Snellen, M., Amiri-Simkooei, A., Simons, D. G., and Siemes, K. (2014). Observations regarding coarse sediment classification based on multi-beam echo-sounder's backscatter strength and depth residuals in Dutch rivers. *J. Acoust. Soc. Am.* 135, 3305–3315. doi: 10.1121/1.4875236

Feldens, P., Schulze, I., Papenmeier, S., Schoenke, M., and von Deimling, J. S. (2018). Improved interpretation of marine sedimentary environments using multi-frequency multibeam backscatter data. *Geosciences* 8:214. doi: 10.3390/geosciences8060214

Ferrini, V. L., and Flood, R. D. (2006). The effects of fine-scale surface roughness and grain size on 300 kHz multibeam backscatter intensity in sandy marine sedimentary environments. *Mar. Geol.* 228, 153–172. doi: 10.1016/j.margeo.2005.11.010

Fitzpatrick, B. M., Harvey, E. S., Heyward, A. J., Twiggs, E. J., and Colquhoun, J. (2012). Habitat specialization in tropical continental shelf demersal fish assemblages. *PLoS One* 7:e39634. doi: 10.1371/journal.pone.0039634

Fonseca, L., Brown, C., Calder, B., Mayer, L., and Rzhanov, Y. (2009). Angular range analysis of acoustic themes from Stanton Banks Ireland: a link between visual interpretation and multibeam echosounder angular signatures. *Appl. Acoust.* 70, 1298–1304. doi: 10.1016/j.apacoust.2008.09.008

Fonseca, L., and Mayer, L. (2007). Remote estimation of surficial seafloor properties through the application angular range analysis to multibeam sonar data. *Mar. Geophys. Res.* 28, 119–126. doi: 10.1007/s11001-007-9019-4

Fonseca, L., Mayer, L., Orange, D., and Driscoll, N. (2002). The high-frequency backscattering angular response of gassy sediments: model/data comparison from the Eel River Margin, California. *J. Acoust. Soc. Am.* 111, 2621–2631. doi: 10.1121/1.1471911

Franklin, J., Wejnert, K. E., Hathaway, S. A., Rochester, C. J., and Fisher, R. N. (2009). Effect of species rarity on the accuracy of species distribution models for reptiles and amphibians in southern California. *Divers. Distrib.* 15, 167–177. doi: 10.1111/j.1472-4642.2008.00536.x

Freitas, R., Rodrigues, A. M., Morris, E., Lucas Perez-Llorens, J., and Quintino, V. (2008). Single-beam acoustic ground discrimination of shallow water habitats: 50 kHz or 200 kHz frequency, survey? *Estuar. Coast. Shelf Sci.* 78, 613–622. doi: 10.1016/j.ecss.2008.02.007

Gaida, T. C., Ali, T. A. T., Snellen, M., Amiri-Simkooei, A., van Dijk, T. A. G. P., and Simons, D. G. (2018). A multispectral bayesian classification method for increased acoustic discrimination of seabed sediments using multi-frequency multibeam backscatter data. *Geosciences* 8:455. doi: 10.3390/geosciences8120455

Gaida, T. C., Mohammadloo, T. H., Snellen, M., and Simons, D. G. (2020). Mapping the seabed and shallow subsurface with multi-frequency multibeam echosounders. *Remote Sens.* 12:52. doi: 10.3390/rs12010052

Garcia-Alegre, A., Sanchez, F., Gomez-Ballesteros, M., Hinz, H., Serrano, A., and Parra, S. (2014). Modelling and mapping the local distribution of representative species on the Le Danois Bank, El Cachucho Marine Protected Area (Cantabrian Sea). *Deep Sea Res. Part II Top. Stud. Oceanogr.* 106, 151–164. doi: 10.1016/j.dsr2.2013.12.012

Gazzani, F., and Marinova, D. (2007). "Using choice modelling to account for biodiversity conservation: non-use value for ningaloo reef," in *MODSIM07 - Land, Water and Environmental Management: Integrated Systems for Sustainability*, eds L. Oxley and D. Kulasiri (Christchurch: Modelling and Simulation Society of Australia and New Zealand).

Gutteridge, A., Bennett, M., Huveneers, C., and Tibbetts, I. (2011). Assessing the overlap between the diet of a coastal shark and the surrounding prey communities in a sub−tropical embayment. *J. Fish Biol.* 78, 1405–1422. doi: 10.1111/j.1095-8649.2011.02945.x

Hamilton, L. J., and Parnum, I. (2011). Acoustic seabed segmentation from direct statistical clustering of entire multibeam sonar backscatter curves. *Cont. Shelf Res.* 31, 138–148. doi: 10.1016/j.csr.2010.12.002

Harvey, E. S., Cappo, M., Butler, J. J., Hall, N., and Kendrick, G. A. (2007). Bait attraction affects the performance of remote underwater video stations in assessment of demersal fish community structure. *Mar. Ecol. Prog. Ser.* 350, 245–254. doi: 10.3354/meps07192

Hasan, R. C., Ierodiaconou, D., and Laurenson, L. (2012a). Combining angular response classification and backscatter imagery segmentation for benthic biological habitat mapping. *Estuar. Coast. Shelf Sci.* 97, 1–9. doi: 10.1016/j.ecss.2011.10.004

Hasan, R. C., Ierodiaconou, D., and Monk, J. (2012b). Evaluation of four supervised learning methods for benthic habitat mapping using backscatter from multibeam sonar. *Remote Sens.* 4, 3427–3443. doi: 10.3390/rs4113427

Hasan, R. C., Ierodiaconou, D., Laurenson, L., and Schimel, A. (2014). Integrating multibeam backscatter angular response, mosaic and bathymetry data for benthic habitat mapping. *PLoS One* 9:e97339. doi: 10.1371/journal.pone.0097339

Hijmans, R. J. (2016). *raster: Geographic Data Analysis and Modeling.*

Hill, N. A., Lucieer, V., Barrett, N. S., Anderson, T. J., and Williams, S. B. (2014). Filling the gaps: predicting the distribution of temperate reef biota using high resolution biological and acoustic data. *Estuar. Coast. Shelf Sci.* 147, 137–147. doi: 10.1016/j.ecss.2014.05.019

Holmes, K. W., Van Niel, K. P., Radford, B., Kendrick, G. A., and Grove, S. L. (2008). Modelling distribution of marine benthos from hydroacoustics and underwater video. *Cont. Shelf Res.* 28, 1800–1810. doi: 10.1016/j.csr.2008.04.016

Hosmer, D. W., Lemeshow, S., and Sturdivant, R. X. (2013). *Applied Logistic Regression*. New York, NY: Wiley.

Ierodiaconou, D., Laurenson, L., Burq, S., and Reston, M. (2007). Marine benthic habitat mapping using Multibeam data, georeferencedvideo and image classification techniques in Victoria, Australia. *J. Spat. Sci.* 52, 93–104. doi: 10.1080/14498596.2007.9635105

Jackson, D. R., Winebrenner, D. P., and Ishimaru, A. (1986). Application of the composite roughness model to high-frequency bottom backscattering. *J. Acoust. Soc. Am.* 79, 1410–1422. doi: 10.1121/1.393669

Kailola, P., Williams, M., Stewart, P., Reichelt, R., McNee, A., and Grieve, C. (1993). *Australian Fisheries Resources*. Canberra, ACT: Bureau of Resource Sciences.

Kloser, R. J., Penrose, J. D., and Butler, A. J. (2010). Multi-beam backscatter measurements used to infer seabed habitats. *Cont. Shelf Res.* 30, 1772–1782. doi: 10.1016/j.csr.2010.08.004

Landis, J. R., and Koch, G. G. (1977). The Measurement of observer agreement for categorical data. *Biometrics* 33:159. doi: 10.2307/2529310

Monk, J., Ierodiaconou, D., Bellgrove, A., Harvey, E., and Laurenson, L. (2011). Remotely sensed hydroacoustics and observation data for predicting fish habitat suitability. *Cont. Shelf Res.* 31, S17–S27. doi: 10.1016/j.csr.2010.02.012

Monk, J., Ierodiaconou, D., Versace, V. L., Bellgrove, A., Harvey, E., Rattray, A., et al. (2010). Habitat suitability for marine fishes using presence-only modelling and multibeam sonar. *Mar. Ecol. Prog. Ser.* 420, 157–174. doi: 10.3354/meps08858

Moore, C. H., Harvey, E. S., and Van Niel, K. (2010). The application of predicted habitat models to investigate the spatial ecology of demersal fish assemblages. *Mar. Biol.* 157, 2717–2729. doi: 10.1007/s00227-010-1531-4

Moore, C. H., Van Niel, K., and Harvey, E. S. (2011). The effect of landscape composition and configuration on the spatial distribution of temperate demersal fish. *Ecography* 34, 425–435. doi: 10.1111/j.1600-0587.2010.06436.x

Naimi, B., Hamm, N. A. S., Groen, T. A., Skidmore, A. K., and Toxopeus, A. G. (2014). Where is positional uncertainty a problem for species distribution modelling? *Ecography* 37, 191–203. doi: 10.1111/j.1600-0587.2013.00205.x

Newman, S. J., and Williams, D. M. (2001). Spatial and temporal variation in assemblages of Lutjanidae, Lethrinidae and associated fish species among mid-continental shelf reefs in the central Great Barrier Reef. *Mar. Freshw. Res.* 52, 843–851. doi: 10.1071/MF99131

Parrish, J. D. (1987). "The trophic biology of snappers and groupers," in *Tropical Snappers and Groupers: Biology and Fisheries Management*, eds J. J. Polovina and S. Ralston (Boulder, CO: Westview Press), 405–463.

R Development Core Team (2017). *R: A Language and Environment for Statistical Computing*. Vienna: R Foundation for Statistical Computing.

Randall, J. E. (1967). *Food Habits of Reef Fishes of the West Indies*. Honolulu, HI: Hawaii Institute of Marine Biology University of Hawaii.

Rousou, M., Ganias, K., Kletou, D., Loucaides, A., and Tsinganis, M. (2014). Maturity of the pufferfish *Lagocephalus sceleratus* in the southeastern Mediterranean Sea. *Sex. Early Dev. Aquat. Organ.* 1, 35–44. doi: 10.3354/sedao00005

Schneider von Deimling, J., Weinrebe, W., Tóth, Z., Fossing, H., Endler, R., Rehder, G., et al. (2013). A low frequency multibeam assessment: spatial mapping of shallow gas by enhanced penetration and angular response anomaly. *Mar. Pet. Geol.* 44, 217–222. doi: 10.1016/j.marpetgeo.2013.02.013

Schonberg, C. H. L., and Fromont, J. (2012). Sponge gardens of Ningaloo reef (Carnarvon Shelf, Western Australia) are biodiversity hotspots. *Hydrobiologia* 687, 143–161. doi: 10.1007/s10750-011-0863-5

Schultz, A. L., Malcolm, H. A., Bucher, D. J., Linklater, M., and Smith, S. D. A. (2014). Depth and medium-scale spatial processes influence fish assemblage structure of unconsolidated habitats in a subtropical marine park. *PLoS One* 9:e96798. doi: 10.1371/journal.pone.0096798

Sih, T. L., Cappo, M., and Kingsford, M. (2017). Deep-reef fish assemblages of the Great Barrier Reef shelf-break (Australia). *Sci. Rep.* 7, 1–18. doi: 10.1038/s41598-017-11452-1

Simpson, C., and Waples, K. (2012). *Node 3: Managing and Conserving the Marine State*. Perth, WA: Western Australian Marine Science Institution.

Tamburello, N., Côté, I. M., and Dulvy, N. K. (2015). Energy and the scaling of animal space use. *Am. Natural.* 186, 196–211. doi: 10.1086/682070

Waples, K., and Hollander, E. (2008). *Ningaloo Research Progress Report: Discovering Ningaloo–Latest Findings and Their Implications for Management in Ningaloo Research Coordinating Committee, Ningaloo Research Program*. Perth, WA: Department of Environment and Conservation.

Willis, T. J., Millar, R. B., and Babcock, R. C. (2000). Detection of spatial variability in relative density of fishes: comparison of visual census, angling, and baited underwater video. *Mar. Ecol. Prog. Ser.* 198, 249–260. doi: 10.3354/meps198249

Wilson, M. F. J., O'Connell, B., Brown, C., Guinan, J. C., and Grehan, A. J. (2007). Multiscale terrain analysis of multibeam bathymetry data for habitat mapping on the continental slope. *Mar. Geod.* 30, 3–35. doi: 10.1080/01490410701295962

Wilson, S. K., Burgess, S. C., Cheal, A. J., Emslie, M., Fisher, R., Miller, I., et al. (2008). Habitat utilization by coral reef fish: implications for specialists vs. generalists in a changing environment. *J. Anim. Ecol.* 77, 220–228. doi: 10.1111/j.1365-2656.2007.01341.x

Wood, J. (1996). *The Geomorphological Characterisation of Digital Elevation Models*. Ph.D. Thesis. Leicester: University of Leicester.

Conflict of Interest: The authors declare that the research was conducted in the absence of any commercial or financial relationships that could be construed as a potential conflict of interest.

Publisher's Note: All claims expressed in this article are solely those of the authors and do not necessarily represent those of their affiliated organizations, or those of the publisher, the editors and the reviewers. Any product that may be evaluated in this article, or claim that may be made by its manufacturer, is not guaranteed or endorsed by the publisher.

frontiers in Marine Science

ORIGINAL RESEARCH
published: 21 October 2021
doi: 10.3389/fmars.2021.751385

Temporal Variability of Thermohaline Fine-Structure Associated With the Subtropical Front Off the Southeast Coast of New Zealand in High-Frequency Short-Streamer Multi-Channel Seismic Data

Joanna K. Cooper[1,2], Andrew R. Gorman[1], M. Hamish Bowman[1] and Robert O. Smith[3]*

[1] Department of Geology, University of Otago, Dunedin, New Zealand, [2] Department of Geoscience, University of Calgary, Calgary, AB, Canada, [3] Department of Marine Science, University of Otago, Dunedin, New Zealand

OPEN ACCESS

Edited by:
Qunshu Tang, South China Sea Institute of Oceanology, Chinese Academy of Sciences (CAS), China

Reviewed by:
Francisco Lajús Junior, Federal University of Santa Catarina, Brazil
Grant George Buffett, Independent Researcher, Barcelona, Spain

***Correspondence:**
Andrew R. Gorman
andrew.gorman@otago.ac.nz

Specialty section:
This article was submitted to Ocean Observation, a section of the journal Frontiers in Marine Science

Received: *01 August 2021*
Accepted: *29 September 2021*
Published: *21 October 2021*

Citation:
Cooper JK, Gorman AR, Bowman MH and Smith RO (2021) Temporal Variability of Thermohaline Fine-Structure Associated With the Subtropical Front Off the Southeast Coast of New Zealand in High-Frequency Short-Streamer Multi-Channel Seismic Data. Front. Mar. Sci. 8:751385. doi: 10.3389/fmars.2021.751385

Seismic oceanography generally makes use of multi-channel seismic reflection data sourced by air gun arrays and long hydrophone streamers to image oceanographic water masses and processes—often piggybacking on surveys that target deeper geological features below the seafloor. However, due to the acquisition methods employed, shallow (upper 200 m or so) regions of the ocean can be poorly imaged with this technique, and resolution is often lower than desirable for imaging fine-structure within the water column. In 2012, we collected a set of higher-resolution seismic lines off the southeast coast of New Zealand, with a generator-injector airgun source and hydrophone streamer configuration designed to improve images of shallower water masses and their boundaries. The seismic lines were acquired with coincident expendable bathythermograph deployments which provides direct ties between physical oceanographic data and seismic data, allowing for definitive identification of the Subtropical Front and associated water masses in the subsurface. Repeat acquisition along the same transect shows significant temporal variability on the scale of hours, illustrating the highly dynamic nature of this important ocean boundary. Comparisons to conventional low-frequency seismic data in the same location show the value of high-resolution acquisition methods in imaging the near-surface of the ocean and allowing subsurface features to be linked to their expressions at the surface.

Keywords: seismic oceanography, generator-injector airgun source, time-lapse imaging, water column imaging, Subtropical water, Subantarctic water, Subtropical Front

INTRODUCTION

The Subtropical Front (STF) is a global ocean boundary separating warm, salty Subtropical Water (STW) from relatively cool, fresh Subantarctic Water (SAW) (e.g., Orsi et al., 1995). This global front primarily lies between 30 and 45°S, but in the vicinity of New Zealand (**Figure 1**) it is deflected further south by the continental landmass (e.g., Heath, 1981; Smith et al., 2013). Along the southeast coast of the South Island, the front approximately follows the continental shelf break,

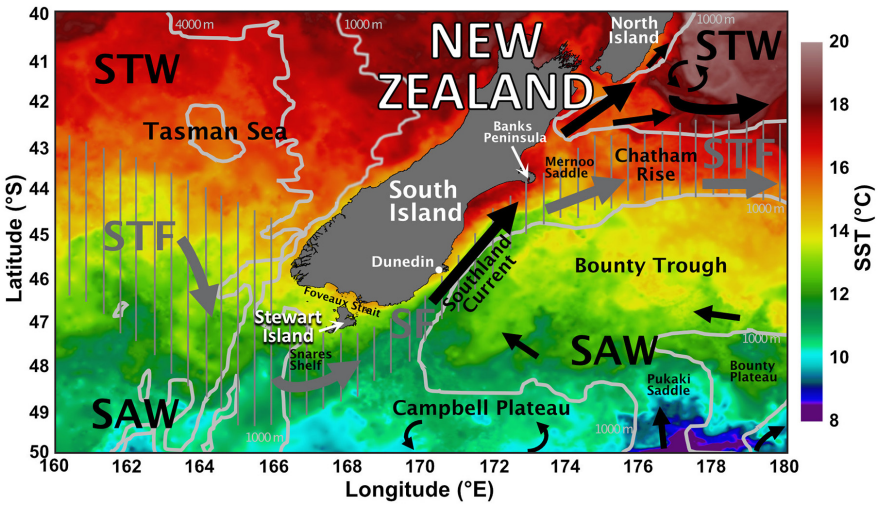

FIGURE 1 | Regional oceanographic setting of the South Island of New Zealand. 1,000 and 4,000 m bathymetric contours are shown and major bathymetric features are labeled. Sea surface temperature (SST) dataset is a composite reanalysis of a number of SST products for 2012/01/21 NASA's JPL's GHRSST MUR Level 4 SST Analysis (JPL MUR Measures Project, 2015) accessed in July 2021. Major water masses and oceanic fronts after Neil et al. (2004). STW, Subtropical Water, SAW, Subantarctic Water, STF, Subtropical Front, SF, Southland Front.

just 20–40 km offshore, where it is locally known as the Southland Front (Burling, 1961), and is associated with the northward-flowing Southland Current (Heath, 1972; Sutton, 2003). Burling (1961) described the Southland Front as being characterized by steeply sloping isotherms and isohalines at 8–9°C and 34.5–34.6 at depths > 70 m. At this boundary, mixing processes are important for the transfer of heat, salt, and nutrients between the two water masses (e.g., Chiswell, 2001). The Subantarctic Water of the Southern Ocean south of the Subtropical Front represents a significant potential carbon sink (e.g., Currie and Hunter, 1998); this involvement in the global carbon cycle highlights the importance of studying temporal changes in oceanographic properties including circulation and ocean-atmosphere interaction in this region (e.g., Chiswell et al., 2015).

Previous studies have examined the variability of the Subtropical Front in the study area both in terms of structure and location; these have included CTD studies such as Jillett (1969) and Jones et al. (2013), which found strong seasonal variations in sea-surface temperature, with the highest values inshore in late summer (February) and the lowest values offshore in late winter (August). An important finding of Jillett (1969) was that warming and/or dilution of nearshore Neritic Water can lower its density such that it extends seaward over STW that occupies the shelf; similarly, warming of the offshore SAW, particularly in summer, can cause it to move shoreward resulting in the STW becoming hidden beneath the surface. This has also been observed in subsequent CTD studies in this region (e.g., Currie and Hunter, 1999); Currie et al. (2011) suggest that this phenomenon causes blurring of the STF at the surface. Studies of the front using satellite sea-surface temperature data suggest that the mean surface position of the STF is strongly controlled by bathymetry; it is located consistently just beyond the shelf break near the 500 m isobath (Shaw and Vennell, 2001; Hopkins et al., 2010), and seasonally appears overall to move shoreward in summer and seaward in winter.

Since the pioneering study of Holbrook et al. (2003), seismic oceanography has developed into a significant tool for investigating oceanographic features. The technique represents an adaptation of conventional marine reflection seismology; acoustic waves are generated by a source towed just below the sea surface, travel through the water column, reflect off contrasts in acoustic impedance (controlled by thermohaline fine-structure), and are then recorded by a near-surface array of hydrophone sensors towed behind the ship. Processing of the recorded data produces cross-sectional images of the water-column. Seismic oceanography allows for the mapping of features over large areas at a horizontal resolution rarely achieved with conventional oceanographic methods (meters to tens of meters). It can also provide information about the three-dimensionality of structures as well as temporal changes, on a scale ranging from hours to seasons and potentially to years. The method has been applied to the examination of fronts, water masses, currents, eddies, thermohaline intrusions and staircases, internal waves, and mixing processes (e.g., Biescas et al., 2008; Sheen et al., 2009; Blacic and Holbrook, 2010; Pinheiro et al., 2010; Tang et al., 2013; Tang et al., 2014; Buffett et al., 2017; Gorman et al., 2018; Ruddick, 2018).

In this study, high-frequency multi-channel seismic data were acquired along with coincident oceanographic measurements in the form of expendable bathythermographs (XBTs). The goals of the acquisition were (1) to produce higher-frequency seismic images for comparison with existing legacy seismic data (industrial seismic data acquired for other purposes and lacking coincident oceanographic data), particularly in the shallow part of the water column, (2) to use coincident oceanographic data to "ground-truth" reflections seen in this seismic data set as well

as in legacy seismic data where similar features are seen, (3) to characterize the structure of the STF at the surface and in the subsurface at high horizontal resolution, (4) to examine short to medium term time-lapse changes, determining if reflective features observed are stable or changing over the time-scale of the survey (cf. Buffett et al., 2012; Gunn et al., 2020), and (5) to test an affordable research-scale set-up that could be used for dedicated seismic oceanography cruises. These goals address some of the issues raised by Ruddick (2018) that may lead to better acceptance and uptake of the seismic oceanography technique.

DATA AND METHODS

Seismic and oceanographic data were acquired along two crossing transects referred to here as transect CB and the Munida Transect (**Figure 2**). Transect CB follows the course of public-domain seismic line CB82-94, acquired during a 1982 petroleum exploration survey in the Canterbury Basin (Western Geophysical Company/Shell BP Todd Canterbury Services Ltd, 1982). The Munida Time-Series Transect, established in 1998, has a history of repeated oceanographic records, including temperature and salinity profiling (e.g., Currie et al., 2011). In January 2012 aboard *RV Kaharoa*, two full passes (KAH1201-1 on 20 Jan. and KAH1201-3 on 21 Jan.) and one partial pass (KAH1201-2 on 20 Jan.) of the Munida Transect were undertaken to collect coincident seismic and oceanographic data. One near-complete pass along transect CB was acquired (KAH1201-5 on Jan. 21); the line was aborted slightly early and further planned data acquisition was canceled due to adverse weather conditions. **Supplementary Tables 1**, **2** contain summary information for the data acquisition. **Figure 2** also shows the same SST data seen in **Figure 1**, that is a composite reanalysis of a number of SST products for 2012/01/21 (JPL MUR Measures Project, 2015).

Seismic Data

Seismic line CB82-94 (Western Geophysical Company/Shell BP Todd Canterbury Services Ltd, 1982) was acquired in December 1982 aboard *MV Western Odyssey* using an array of 18 airguns with a total volume of 1220 in^3 (20 L) at a depth of 6 m and a 120-channel 3,000 m long hydrophone array (25 m group spacing) towed at a depth of 11 m, with a near source-receiver offset of 168 m. The shot spacing was also 25 m resulting in a nominal fold of 60. A sample rate of 4 ms was used, with a record length of 6 s. Locational positioning was undertaken using microwave ranging to land-based stations.

The KAH1201 seismic data were acquired in January 2012 using a Sodera 45/105 in^3 (0.74/1.72 L) GI (Generator-Injector) airgun operating at a depth of 5 m. A Geometrics GeoEel Digital Streamer was used, consisting of three active segments each 100 m long, with a total of 24 groups spaced at 12.5 m. Each group included 16 equally spaced hydrophone elements. The streamer was flown at a depth of 2.5 m, except on line KAH1201-2, where it was set to 4 m during bad weather. The depth of the streamer was controlled by a 5011 Digicourse bird at the head of each the three active segments. The near source-receiver offset was 30 m and the crossline offset between source and streamer was 8.2 m. The source was fired every 10.8 s with the vessel traveling at 4.5 kts, giving an average shot spacing of 25 m. Nominal fold is therefore 6. A sample rate of 1 ms was used, with a record length of 5 s. Satellite navigation was used for locational positioning.

The seismic data were processed using the GLOBE Claritas software package (Ravens, 2001). Details of the processing are described by Cooper (2021). For the KAH1201 data, the flow included 10/20 Hz high-pass filtering of the shot records and the application of a direct arrival filter by way of 5-trace median subtraction filtering after linear moveout at 1,498 m/s. The data were sorted into common-midpoint gathers, binned using the receiver group spacing (twice the natural midpoint spacing) to increase the nominal fold of the data from 6 to 12. Gain correction was applied using an automatic gain control (AGC) operator of 50 ms. Normal moveout correction was performed using velocities derived from the XBT data. Although "hand-picked" stacking velocities are often preferred in seismic processing (e.g., Fortin and Holbrook, 2009), the small source-receiver offsets of KAH1201 make the data unsuitable for semblance analysis, and relatively insensitive to small changes in NMO velocity, as discussed in more detail by Cooper (2021). Before stacking, a 15/30/150/180 Hz bandpass filter was applied, and channels 1, 9, and 17 were removed due to excess noise, possibly caused by the depth-control devices at the start of each of the three streamer segments. After stacking, a 25/40/150/180 Hz bandpass filter was applied and the data were muted below the seafloor. A poststack deconvolution was then applied, in the form of a zero-phase spectral whitening with a 5 Hz smoothing operator in the frequency domain. The data were migrated using a finite-difference time-domain algorithm with interval velocities calculated from the XBTs. A post-migration coherency filter was applied to remove random noise, consisting of a 5-trace weighted summation in the f-x domain. The 25/40/150/180 Hz bandpass filter and the seafloor mute were reapplied to remove noise created by the migration. A 45 ms taper was applied at the top of the section to remove migration artifacts created in the shallowest portion of the section where there is no signal due to the near offset. Finally, a static shift of 6 ms for line KAH1201-2 and 5 ms for the other lines was applied to account for the source and receiver depths.

Profile CB82-94 was processed using a similar flow. However, for these lower frequency data an AGC operator length of 100 ms was used and the bandpass filter was 2/15/100/120 Hz. The greater number of channels meant that a longer 11-trace filter was optimal for the direct arrival and coherency filtering. CDP binning was assigned using the same geometrical constraints and 12.5 m spacing as the KAH1201-5 profile to facilitate direct comparisons of the two datasets. Velocities used in the CB82-94 processing were determined using interactive semblance-based NMO velocity analysis every 50 CDPs.

Oceanographic Data

Oceanographic data were collected in the form of expendable bathythermographs (XBTs), providing measurements of temperature with depth at select locations along the seismic lines. Two types of XBTs were used: 40 Sippican Deep Blue XBTs for

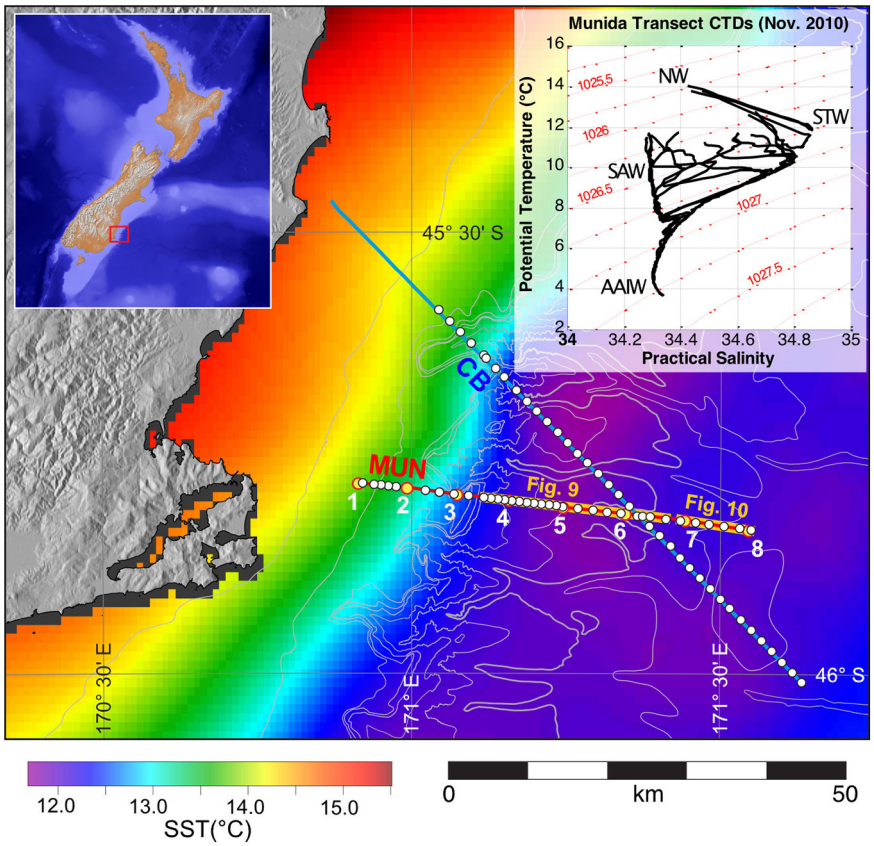

FIGURE 2 | Location of the Munida (MUN) and Canterbury Basin (CB) transects. Seismic lines KAH1201-1, -2, and -3 were acquired along transect MUN, and line KAH1201-5 was acquired along transect CB. SST dataset (same as in **Figure 1**) is enlarged to highlight focus area of this manuscript in the vicinity of the Subtropical Front. XBT positions are indicated by white dots. Subsets of transects shown in **Figures 9**, **10** are highlighted. Inset in upper left shows a map including bathymetry in the region surrounding New Zealand. The area of the main figure is indicated by a red box. Land topography shading is derived from NASA's SRTM data. Projection is UTM 59 South. Inset in upper right shows a temperature-salinity diagram based on eight conductivity-temperature-depth (CTD) profiles collected along the Munida transect in November 2010 (CTD cast locations are indicated by yellow dots in the main figure and are labeled 1–8). Red contours are potential density (in kg/m^3). Water mass interpretations are labeled: NW, Neritic Water; STW, Subtropical Water; SAW, Subantarctic Water; AAIW, Antarctic Intermediate Water.

shallower seafloor depths and 40 Sippican T5 XBTs for deeper water. The XBTs were deployed at an average spacing of 1 nautical mile (∼1.85 km) along lines KAH1201-1 and KAH1201-5, with repeat measurements at select locations along KAH1201-2 and -3 (see **Supplementary Tables 1**, **2**). Sound speed values were calculated using the Mackenzie (1981) equation; both RMS and interval velocities were calculated for use in seismic processing. Since the XBTs do not provide salinity data, a constant salinity of 34.4 was used in the Mackenzie equation, which is the average salinity from previous CTD profiles along the Munida transect (e.g., **Figure 2**). The sensitivity of seismic velocity to salinity is known to be relatively small (e.g., Sallarès et al., 2009) and tests on the CTD data show that the difference between velocities calculated using measured salinities compared to the constant salinity is no more than 0.04% (0.6 m/s).

Synthetic seismograms were calculated from the XBTs for use in comparing to the processed seismic data. Synthetic seismograms are a simulation of the seismic response of a given vertical distribution of density and seismic velocity (which are both functions of water temperature, salinity, and depth) to a particular source wavelet (e.g., Yilmaz, 2001). The synthetic seismograms were computed in MATLAB using functions in the CREWES toolbox (see Margrave and Lamoureux, 2019). The source wavelet used was modeled on a wavelet extracted from the processed seismic data; the extraction was performed in a window around a strong, isolated water-column reflection in the final image from line KAH1201-5.

RESULTS

Seismic Images

Figure 3 shows the seismic images from lines KAH1201-1 and KAH1201-3 along the Munida Transect, and **Figure 4** shows line KAH1201-5 along transect CB. The seismic images display strong reflectivity between 0.05 and 0.5 s; above 0.05 s (∼40 m) muting of the direct arrival has removed any data, and below 0.5 s (375 m) reflections are not visible over the noise level. Annotations show several reflective regions. In particular, strong reflections are visible at around 0.1 s (75 m) in the offshore region, sometimes

in vertical stacks going down to 0.25 s (∼190 m) in isolated areas. Blank zones are present on the shelf and near the shelf break, and below the strong offshore reflections. Dipping reflections are visible near the shelf break, with dips of up to 3°. Above these shoreward-dipping reflections is a seaward-dipping reflection near the surface, especially in lines KAH1201-1 (**Figure 3A**) and KAH1201-5 (**Figure 4**), with a dip around 0.3°. Undulations are visible in most of the reflections, with the largest amplitudes in the shallow reflections in line KAH1201-3 (**Figure 3B**); these are interpreted to be internal waves, following similar interpretations

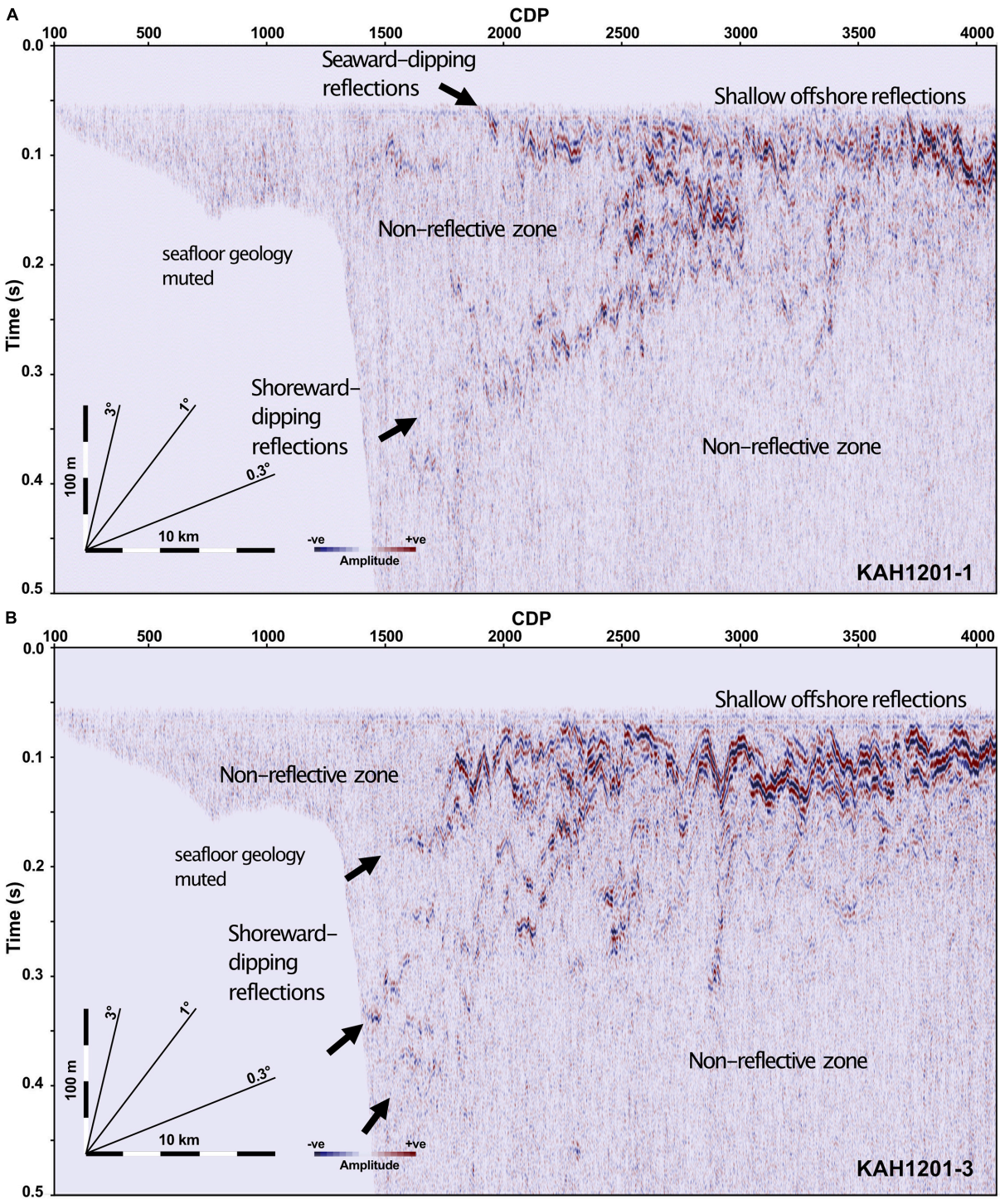

FIGURE 3 | Processed seismic images for lines **(A)** KAH1201-1 and **(B)** KAH1201-3 from the MUN transect.

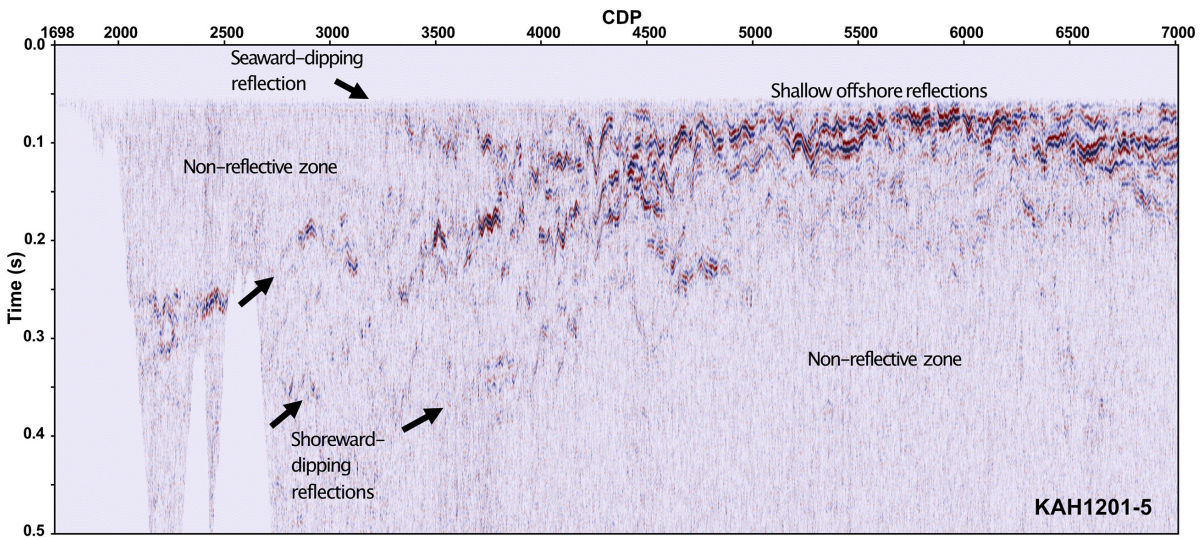

FIGURE 4 | Processed seismic image for line KAH1201-5 from the CB transect.

in other seismic oceanography studies (e.g., Holbrook et al., 2003; Holbrook and Fer, 2005; Krahmann et al., 2008; Piété et al., 2013).

Oceanographic Data and Synthetic Seismograms

The XBT section from KAH1201-1 is shown in **Figure 5**, with both temperature (A) and vertical temperature gradient (B) plotted. These data allow for the identification of the main water masses present, with warm (>∼11°C) STW on the shelf and near the shelf break, and cooler (<∼8°C) SAW further offshore. At depth, the two water masses are separated by a shoreward-dipping region of strong temperature gradients, indicated by the closely spaced isotherms approximately centered around the 9–9.5°C contours. This region is highlighted by the inclined dashed lines and represents the subsurface expression of the STF. The position of the STF can also be seen at the surface; the surface trace at the top of the section shows a ∼2°C temperature drop, with the approximate midpoint of this gradient region shown by an arrow. The surface trace was created by extracting the shallowest measured temperature from each XBT along the line. The satellite SST image in **Figure 2** provides confirmation that this position corresponds to the location of the STF at the surface. In the offshore region, the SAW is overlain by a surface mixed layer with a sharp thermocline at its base. Small areas of temperature inversions can be seen in the middle of the section, particularly on the 9 and 10°C contours.

Figure 5 also shows the synthetic seismograms for line KAH1201-1 overlain on both the XBT and seismic data. The synthetic traces help identify which oceanographic features are expected to be imaged in the seismic data, specifically what the different water masses will look like and what boundaries should be visible. One strong, continuous seismic response is associated with large temperature gradients at the base of the mixed layer (at depths of ∼50–100 m), present in offshore regions (over kms 30–50). Another region of high reflectivity is present in the shoreward-dipping zone of high temperature gradients separating STW and SAW that intersects the shelf break at depths between ∼200 and 400 m; this extends out to approximately the 30 km mark and represents the subsurface STF. Line KAH1201-1 also shows a seaward-dipping reflective region at shallow depths (0–50 m) in the middle of the section (kms 15–30), approaching the surface near the surface location of the STF; this region is highlighted by a dashed oval. The seaward- and shoreward-dipping reflective zones trace the outline of a warm-water "wedge" extending seaward from the shelf break. The synthetic seismograms show that the warm STW "wedge" region is largely non-reflective. However, an additional shoreward-dipping reflection is present on the shelf (kms 2–7), particularly visible in the gradient section, which could be a neritic front separating warm, salty STW from inshore warm, fresher neritic water. On the seaward side of the STF, the region beneath the mixed layer occupied by cool SAW is also a zone of low reflectivity.

The XBT section from line KAH1201-5 (**Figure 6**) shows a similar pattern to line KAH1201-1. Temperatures are slightly higher in the warm-water wedge, with the 11.5–12°C contour region occupying a greater area, whereas the 10.5–11°C contour region was larger in KAH1201-1. The surface temperature drop occurs over a longer distance than in line KAH1201-1 (over kms 66–50 compared to kms 7–14), but this is partly expected due to the more oblique angle of the line as seen in **Figure 2**). The midpoint of this gradient region is taken to represent the surface position of the STF, and is indicated in **Figure 6** by an arrow. One feature that is present in line KAH1201-5 is a minimum in surface temperatures in the middle of the section (kms 50–30), with warmer surface temperatures both inshore and offshore; this feature is seen to a lesser degree in line KAH1201-1. Temperature inversions are again visible, in the 8–12°C contours.

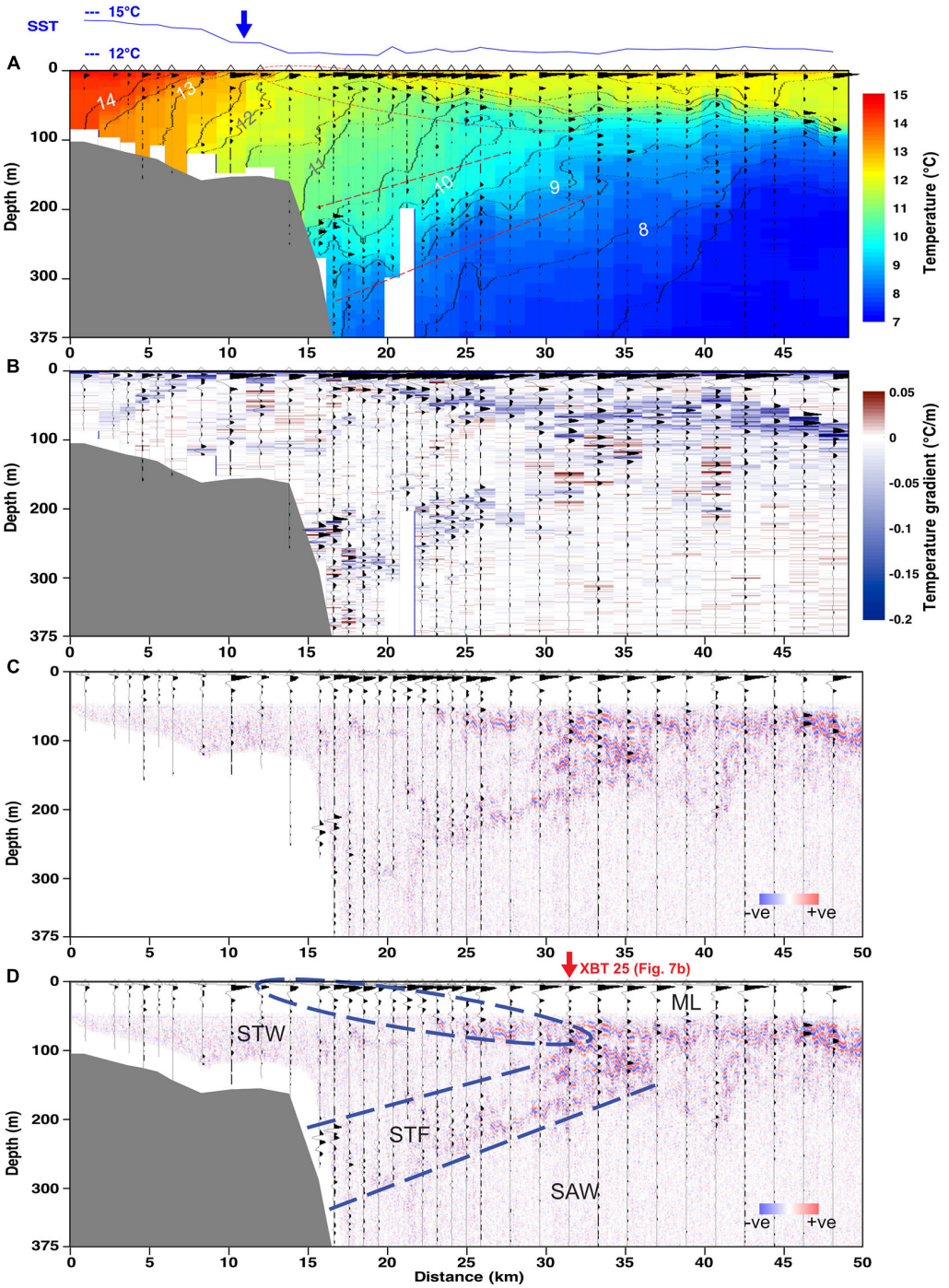

FIGURE 5 | (A) Temperature, **(B)** vertical temperature gradient, **(C)** uninterpreted seismic image, and **(D)** interpreted seismic image for line KAH1201-1, with synthetic seismograms overlain on each image. Shoreward- and seaward-dipping reflective zones separating interpreted water masses are highlighted by dashed lines. STW, Subtropical Water; STF, Subtropical Front; SAW, Subantarctic Water; ML, mixed layer. The surface temperature trace, with approximate surface STF location indicated with an arrow, is shown at the top of **(A)**. Arrow in **(D)** indicates the location of XBT shown in **Figure 7**.

Synthetic seismograms overlain on the XBT and seismic data in **Figure 6** again show three main zones of high reflectivity. These are associated with the high temperature gradients at the base of the mixed layer (depths of ∼50–100 m between kms 30–0), the enhanced gradients of the STF in a shoreward-dipping zone intersecting the continental slope (outlined by dashed lines), and a smaller shallow seaward-dipping zone associated with temperature inversions (dashed oval outline). Two zones of low

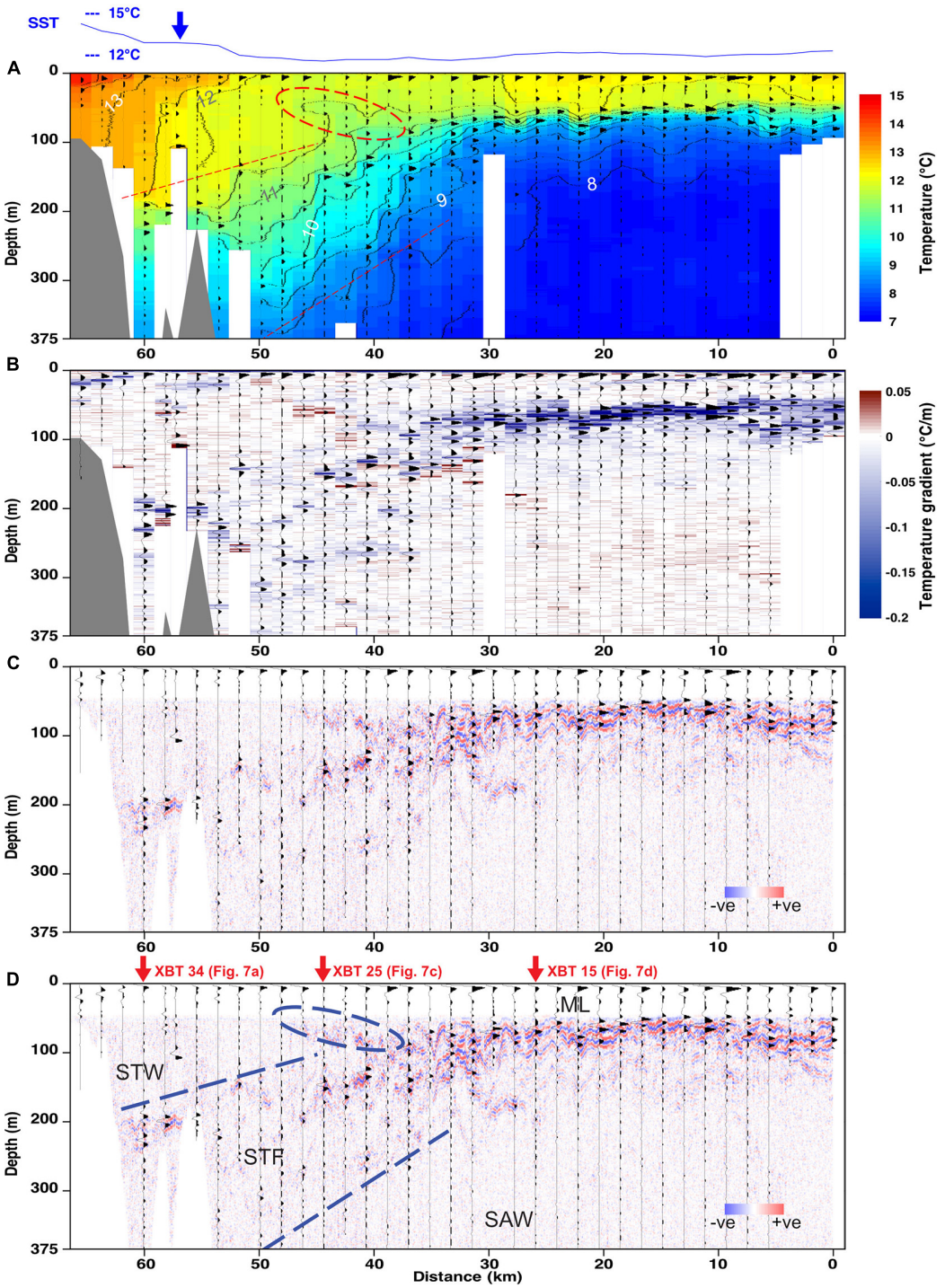

FIGURE 6 | (A) Temperature, **(B)** vertical temperature gradient, **(C)** uninterpreted seismic image, and **(D)** interpreted seismic image for line KAH1201-5, with synthetic seismograms overlain on each image. Shoreward- and seaward-dipping reflective zones separating interpreted water masses are highlighted by dashed lines. STW, Subtropical Water; STF, Subtropical Front; SAW, Subantarctic Water; ML, mixed layer. The surface temperature trace, with approximate surface STF location indicated with an arrow, is shown at the top of **(A)**. Arrows in **(D)** indicate the location of XBTs shown in **Figure 7**.

reflectivity are also present, corresponding to warm STW inshore of the STF and cool SAW seaward of the STF and beneath the mixed layer.

The temperature cross-sections in **Figures 5**, **6** show a significant difference between the surface and subsurface expressions of the STF. In both lines the subsurface expression

of the STF, seen as the dipping region of enhanced temperature gradients separating the warmer STW from cooler SAW, extends much further offshore (by up to ∼25 km) than the surface location of the STF as seen in the surface traces. The XBT data show the surface expression on the shelf or near the shelf break, while the subsurface expression (seen in both the XBT and seismic data) is a broader region extending much further offshore. The strong mixed layer overprints the subsurface expression of the front in the offshore region, which means that it is not visible in the surface temperature data, including satellite SST.

Seismic Interpretations

General comparisons between the synthetic seismograms and seismic images in **Figures 5**, **6** allow for the matching of oceanographic features identified in the XBT sections, including Subtropical and Subantarctic water masses, the Subtropical Front, and the base of the offshore mixed layer, to their corresponding expressions in the KAH1201 seismic images. These oceanographic features have been observed with similar distributions in many previous CTD transects in the region (e.g., Jillett, 1969; Sutton, 2003; Jones et al., 2013), as well as in nearby legacy seismic data (e.g., Gorman et al., 2018; Cooper, 2021), but the coincident acquisition of oceanographic and seismic data in this study allow for specific reflections to be examined in more detail, giving more insight into their oceanographic origins; this is accomplished by way of individual synthetic ties such as those shown in **Figure 7**.

Figures 5, **6** previously showed a large non-reflective zone associated with warm temperatures in the shallow, inshore portion of the seismic images, corresponding to STW. Reflections are visible at the base of this zone near the shelf break, and in particular on line KAH1201-5 where canyons cut through the shelf. **Figure 7A** shows a synthetic tie for this region, confirming the non-reflective nature of the shallow STW above the STF.

In **Figures 5**, **6** the STF manifests as dipping reflections associated with high temperature gradients in the subsurface, with warm non-reflective STW above, cool weakly reflective SAW below, and temperatures suggesting a mixture of the two water masses in between. **Figure 7** shows several synthetic ties in this region, with distinct negative-polarity reflections where the temperature gradient contains sharp steps over a

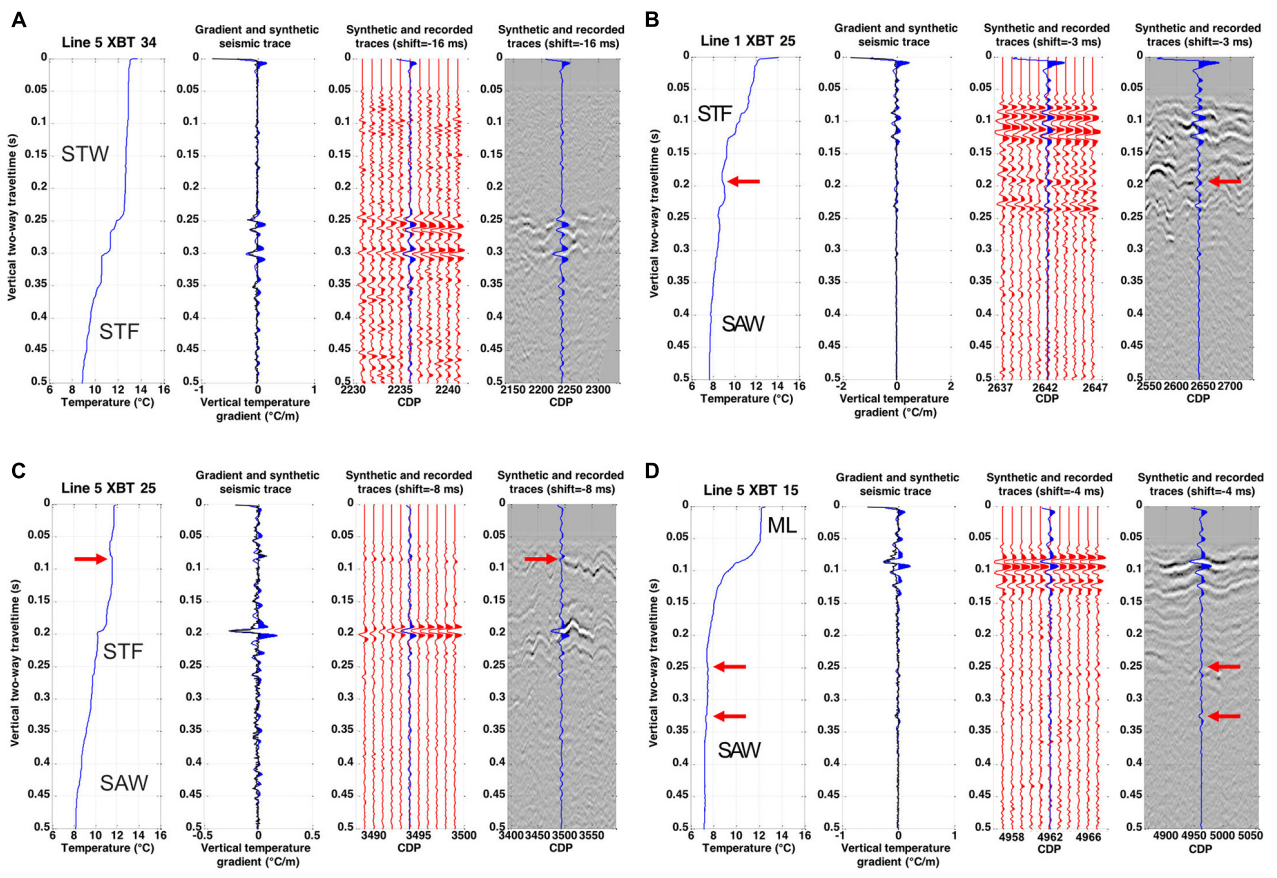

FIGURE 7 | Synthetic seismic ties for XBTs showing STW **(A)**, the STF **(A–C)**, SAW **(B–D)**, and the mixed layer (ML) **(D)**. Each of **(A–D)** consists of four panels, from left to right: temperature as a function of seismic travel time, vertical temperature gradient (black) and the synthetic seismic trace (blue), the synthetic seismic trace (blue) overlain on 11 adjacent traces from the recorded seismic data (red wiggle traces), and the synthetic seismic trace (blue) overlain on 201 adjacent traces from the recorded seismic data (greyscale image). Red arrows in **(B,C)** indicate temperature inversions associated with positive-polarity reflections. Arrows in d indicate weak reflections within SAW.

range of depths (in A and C), creating a stack of interfering reflections where the isotherms come together at the tip of the warm-water wedge (B). The STF region also shows examples of temperature inversions and associated positive-polarity reflections; an example is highlighted in **Figure 7B**. The seismic peaks associated with temperature inversions in the STF region are not particularly continuous laterally in the full seismic images, suggesting perhaps that these features are not stable.

One positive-polarity reflection that is laterally continuous is the seaward-dipping reflection identified earlier in the shallow region overlying the warm-water wedge. **Figure 7C** shows a synthetic tie for this feature. At 0.08 s (∼60 m) there is a temperature inversion, with temperatures near 12°C above and below, and a small region of cooler 11.5°C water in between, and a positive-polarity reflection is present. This feature is interpreted to represent the boundary between warm, shallow SAW present in the mixed layer offshore and warm STW or STW/SAW mix present on the shelf and in the subsurface warm-water wedge. While the temperature difference between the warm SAW mixed layer and the warm subsurface STW is small, the salinity difference between these two water types is large, as seen in previous CTD data in this region (e.g., **Figure 2**), meaning that subsurface salinity data would show this boundary more clearly than the XBT sections.

Further offshore, **Figures 5**, **6** show a shallow high-reflectivity zone associated with the mixed layer, separated by a strong thermocline from underlying SAW. **Figure 7D** shows a synthetic tie for this region. The mixing history of the near-surface layer is preserved in the character of the mixed layer reflections; multiple, stacked reflections represent different mixing events causing discontinuities in the overall temperature gradient. Beneath the mixed-layer reflections, the SAW is non- or weakly reflective; reflections in this zone are associated with small temperature fluctuations indicating slight heterogeneity in the SAW. The weakly reflective nature of the SAW is consistent with observations in previous legacy seismic investigations in the study area (Smillie, 2012; Gorman et al., 2018; Cooper, 2021). Particularly non-reflective zones may be associated with very homogeneous near 7°C Subantarctic Mode Water, which is known to be present in the region (e.g., McCartney, 1977; Morris et al., 2001; Chiswell et al., 2015).

DISCUSSION

Comparison to Legacy Seismic Data

Because KAH1201-5 and the legacy industry seismic line CB82-94 are co-located, the main features identified in KAH1201-5 can be traced to CB82-94. **Figure 8** shows both lines on the same scale. The major differences in water-column imaging between the lines are a result of the vastly different acquisition parameters, with CB82-94 acquired using a large low-frequency airgun array compared to the small single G/I gun of KAH1201-5, and a longer streamer containing many more receivers (3 km and 120 channels vs. 300 m and 24 channels). The resulting differences include the higher frequency content of line KAH1201-5; a comparison of the amplitude spectra of the data gives a dominant frequency of 70 Hz in KAH1201-5 and 20 Hz in CB82-94, indicating that the KAH1201 data can image layers that are less than a third of the thickness of those observed by the legacy seismic set-up. The smaller near offset in the source-streamer geometry of KAH1201 results in more detail at shallow depths, especially with the seaward-dipping reflection connecting the surface and subsurface expressions of the front, but the lower energy of the source and lower fold result in greatly reduced reflectivity observed in the deeper portion of the water column. The CB82-94 line has a larger gap in the shallow part of the image (∼60 m vs. 40 m) due to direct-arrival interference and muting, but shows significant reflectivity at greater depths; the synthetic seismograms suggest that this is the transition between SAW and underlying Antarctic Intermediate Water (AAIW), expected at depths between 500 and 1,000 m, and therefore not imaged in the KAH1201 data. The deep, non-reflective AAIW and a possible lens or eddy-like feature at the end of the line between CDPs 6400 and 6800 are also present in the CB82-94 image. Since the eddy feature is centered near 0.5 s (375 m) in the legacy data and the KAH1201 data show no reflectivity below 0.5 s it is possible that similar features may be present in the KAH1201 data but are not (or only partially) imaged.

At shallow depths, the two seismic lines show many similarities in their reflectivity pattern, but also some strong differences. Similarities include the reflections in the canyons just off the shelf break, the strong shallow reflections offshore, and the shoreward-dipping reflections. These are consistent with the base of the STW, the base of the mixed layer, and the subsurface expression of the STF. The features are not identical, however, as expected due to the 29-year time gap between the acquisition of the images. Seasonally, the two lines are similar, with CB82-94 acquired in late December, compared to the late January KAH1201 cruise. Observable differences include the canyon reflection (at CDPs 2000–2500) that is deeper by about 0.2 s (∼150 m) in CB82-94 and dipping reflections (CDPs 2700–3250 and 3600–4200) that are deeper by a similar amount and approximately twice as steep (∼2°) in CB82-94, perhaps indicating a stronger front and current at that time. The non-reflective STW does not appear to extend as far offshore in CB82-94 (ending near CDP 3200 vs. 3800 in KAH1201-5, a difference of ∼5 km), and the reflective region outlining the warm-water wedge extends further offshore (CDP 4800 vs. 4600, ∼2.5 km). The mixed layer region at CDPs > 5250 in the CB82-94 image is composed of two strong continuous reflections extending to ∼0.24 s (∼180 m), as opposed to the mostly solitary, shallower (∼0.05–0.16 s or 40–120 m) mixed layer reflection in the KAH1201-5 image.

Time-Lapse Comparisons

Time-lapse changes can be observed by comparing lines KAH1201-1, 2, and -3, all acquired along the Munida Transect, with lines 1 and 2 acquired continuously, followed by a gap of 11 h and 20 min before the start of line 3. Line KAH1201-2 was aborted early so only the offshore portion of the Munida Transect was imaged, while both KAH1201-1 and -3 imaged the entire transect. Initial comparisons of the lines made previously (**Figure 3**) showed overall similarities, but also significant

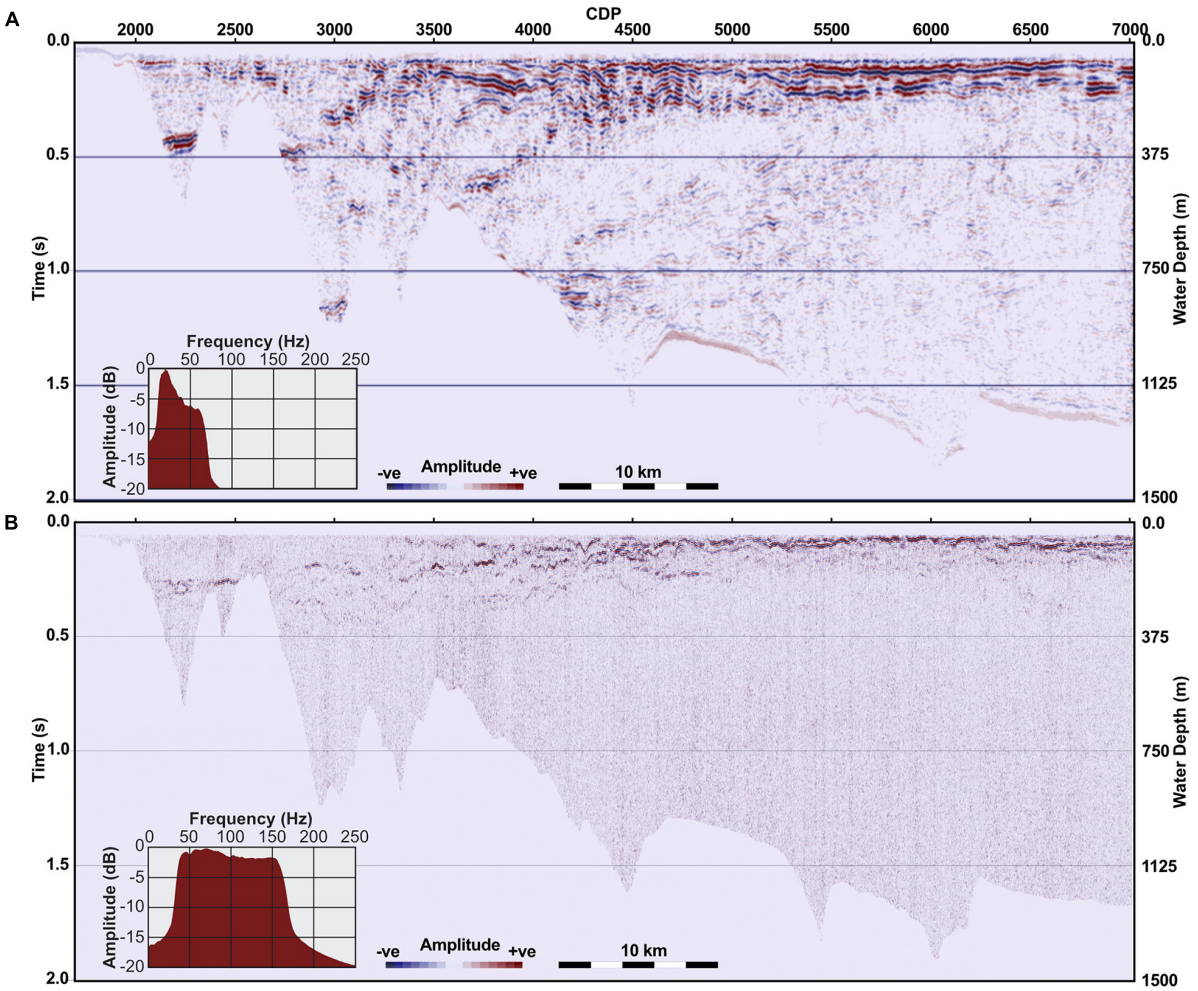

FIGURE 8 | Seismic data from the CB transect, showing comparison between **(A)** industry line CB82-94 collected in 1982 and **(B)** line KAH1201-5. Amplitude spectra calculated from water column reflectivity show the difference in frequency content of the two datasets.

changes in the mixed-layer reflection and associated internal waves, as well as in the reflections associated with the STF. In particular, the difference between lines 1 and 3 is striking, given their identical location and short time between acquisition. **Figure 9** shows in more detail the difference in the STF reflections in lines KAH1201- and -3, with XBT temperatures overlain. The bulk of the shoreward-dipping reflective zone moved shoreward from line 1 to line 3 (approximately from CDP 3000 to 2400, or 7.5 km), but the XBTs show that warm STW (indicated by the blank zone with red temperatures and the reflection at its base) moved further seaward (∼from CDP 1500 to 1700, or 2.5 km). This is similar to the change observed between lines KAH1201-5 and CB82-94: in line CB82-94 the STW did not extend as far offshore, but the zone of dipping STF reflections extended further offshore than in line 5. If the motion of the STF (as represented by the dipping reflections) was confined to the plane of the section, movement of ∼7.5 km in the ∼19 h elapsed between lines KAH1201-1 and -3 would suggest a minimum velocity of ∼0.1 m/s. However, some of the apparent variability in the STF reflections is likely spatial in origin. Satellite sea-surface temperature images of this region indicate a high degree of meandering in the front toward and away from shore (e.g., **Figure 2**; Shaw and Vennell, 2001). These meanders would be carried within the overall flow of the northeastward-flowing Southland Current and pass through the position of the seismic line, causing apparent along-section movement of the water mass boundaries and associated reflections.

Time-lapse changes can also be observed in the seismic images from the seaward end of the Munida Transect. **Figure 10** shows the equivalent portions of lines KAH1201-1, -2, and -3. Lines 1 and 2 were acquired consecutively, so the extreme right-hand side of both images is nearly identical with only a 10-min delay as the ship turned, but the differences in the rest of the image are large, with individual reflections not able to be correlated between the two images. Despite that, the character of the two images is similar, especially when compared to line KAH1201-3. Line 3 contains strong, continuous stacks of reflections, with long-wavelength perturbations, whereas lines 1 and 2 contain

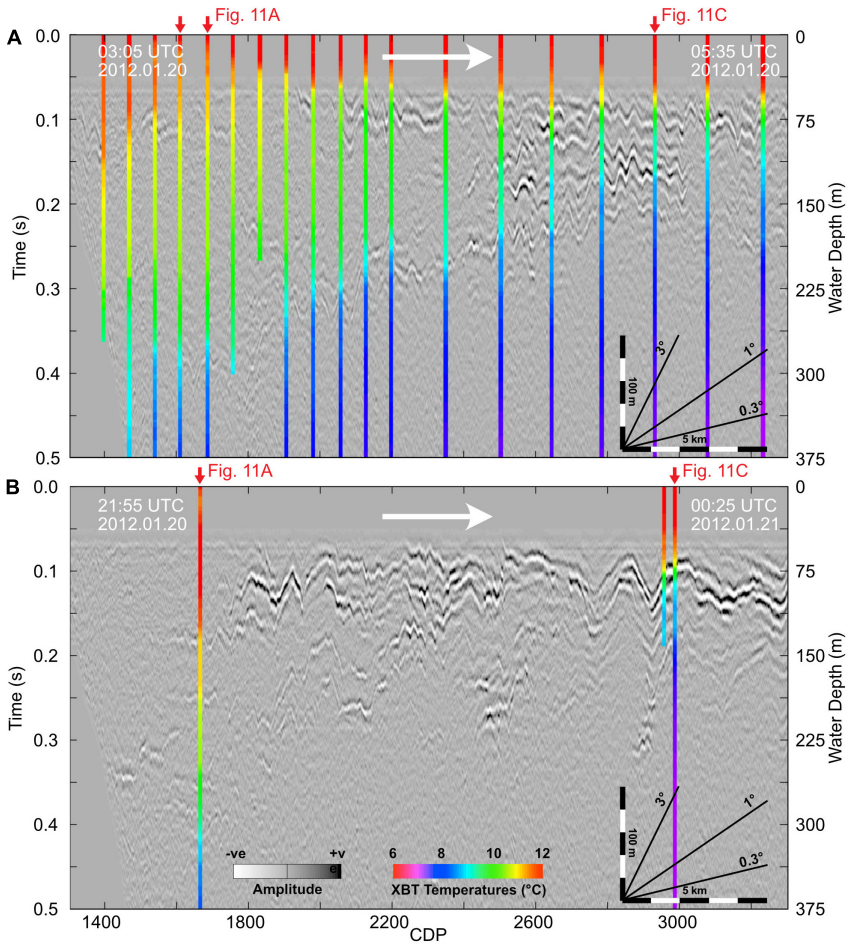

FIGURE 9 | Portions of lines KAH1201-1 **(A)** and KAH1201-3 **(B)** acquired in the same location (as indicated in **Figure 2**), with acquisition times and directions indicated by white arrows. Differences in STF reflections (cf. **Figure 5D**) can be observed. XBT temperatures are overlain in color. Red arrows indicate the location of XBTs shown in **Figure 11**.

reflections that are weaker and less laterally continuous, with shorter wavelength internal waves. The difference could be due to the surface weather conditions, with strong winds causing the termination of line 2 and the nearly 12-h time delay before the start of acquisition of line 3, potentially resulting in mixing of the surface layer and the development of a new, sharper and more continuous thermocline. Some of the difference could also be because of weather-induced data quality deterioration causing reflections to appear weaker and less continuous in lines 1 and 2.

During the seismic acquisition, XBTs were repeated at different locations, which provide more insight into the differences observed in the seismic data from repeat passes. **Figure 11A** shows three XBTs taken along the Munida Transect at approximately the same location within the STF region (indicated by the arrows in **Figure 9**), occupied during lines KAH1201-1 and -3. The two XBTs on line 1 were acquired 6 min apart, and show great similarity in the temperature profile, as well as similarity in the seismic character laterally between the two locations. The XBT on line 3, 19 h later, shows much warmer temperatures over most of the depth range displayed, and more steps in the temperature profile compared to the smoother gradient on line 1. As a result, the seismic section displays a greater number of reflections in the middle of the image. As noted previously, this change is very striking as it occurred over such a short time period and demonstrates the highly dynamic nature of the STF in this region. A change of 1°C in temperature at the same location in less than 24 h suggests significant meandering of the front spatially, at least at depth; unfortunately, a surface temperature trace was not available for line 3 to compare the surface position of the STF between the two lines.

The XBTs from the seaward ends of the lines in **Figure 10** are displayed in **Figure 11B**. The two XBTs from line 1 and 2 were acquired 25 min apart, and the XBT from line 3 was acquired 18.5 h later. The three temperature profiles are nearly identical in the mixed layer and below the thermocline. The XBTs from lines 2 and 3 are most similar, despite the larger time delay, suggesting that spatial differences are the greater factor when considering changes in the base of the mixed layer, rather than time lapse changes over these time scales. This is also evident by

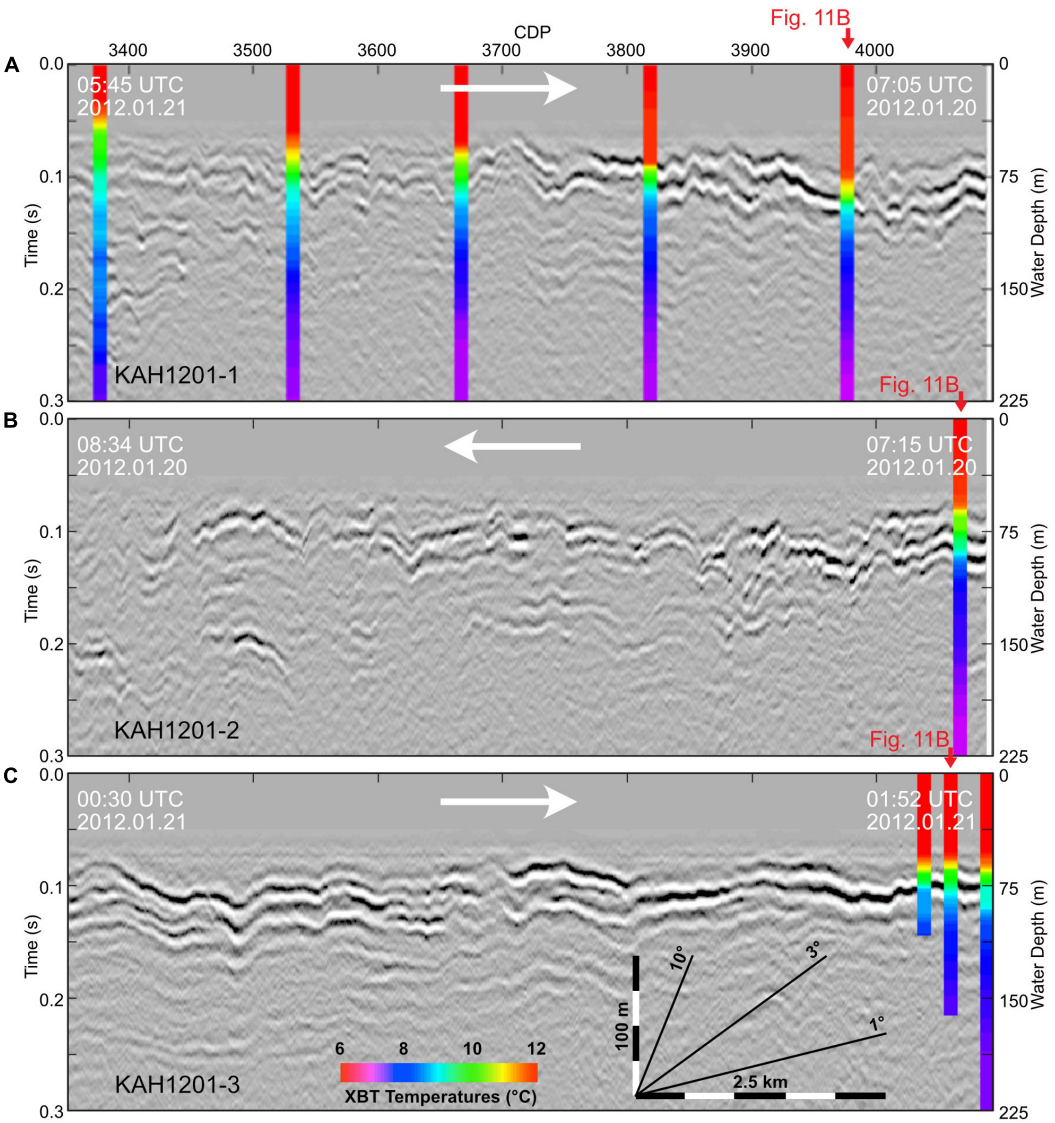

FIGURE 10 | Portions of lines KAH1201-1 **(A)**, KAH1201-2 **(B)**, and KAH1201-3 **(C)** acquired in the same location (as indicated in **Figure 2**), with acquisition times and directions indicated by white arrows. XBT temperatures are overlain in color. Red arrows indicate the location of XBTs shown in **Figure 11**.

the significant lateral changes in the mixed-layer reflections seen in the seismic sections. Internal waves displacing the mixed-layer reflections are also likely to contribute to the time-lapse changes.

The last location sampled with XBTs repeatedly was the intersection point between transects MUN and CB. The location was visited three times, during the recording of lines KAH1201-1, -3, and -5 (**Figure 11C**). Its position is indicated on **Figure 9** for the MUN lines; it corresponds to km 31 on line KAH1201-5 (**Figure 6**). The three temperature profiles again show differences in the thermocline at the base of mixed layer, with line 1 showing a deep strong reflection with weaker shallow reflections, line 3 showing a shallow strong reflection, and line 5 showing several moderate reflections. The XBT from line 3 differs from the other two profiles at depth, with cooler temperatures measured below 0.18 s (∼135 m). The previous comparison of lines 1 and 3 noted that the dipping STF reflections and associated high temperature-gradient region moved shoreward between the two lines; the process appears to have been reversed by the time of the acquisition of line 5. Another possibility is that the temperature difference at depth in line 3 is related to a possible eddy suggested by the "V"-shaped feature seen in the mixed-layer reflection to the left of the XBT location. Though this XBT just misses the stack of reflections extending downwards from the "V" to 0.31 s, it may be showing the effect of the feature. Either way, the changes in the seismic images and temperature profiles are evidence for a highly variable front over short timescales (on the order of hours).

Methodological Impact

The results of cruise KAH1201 demonstrate that cost-effective research-scale experiments can be used for dedicated seismic

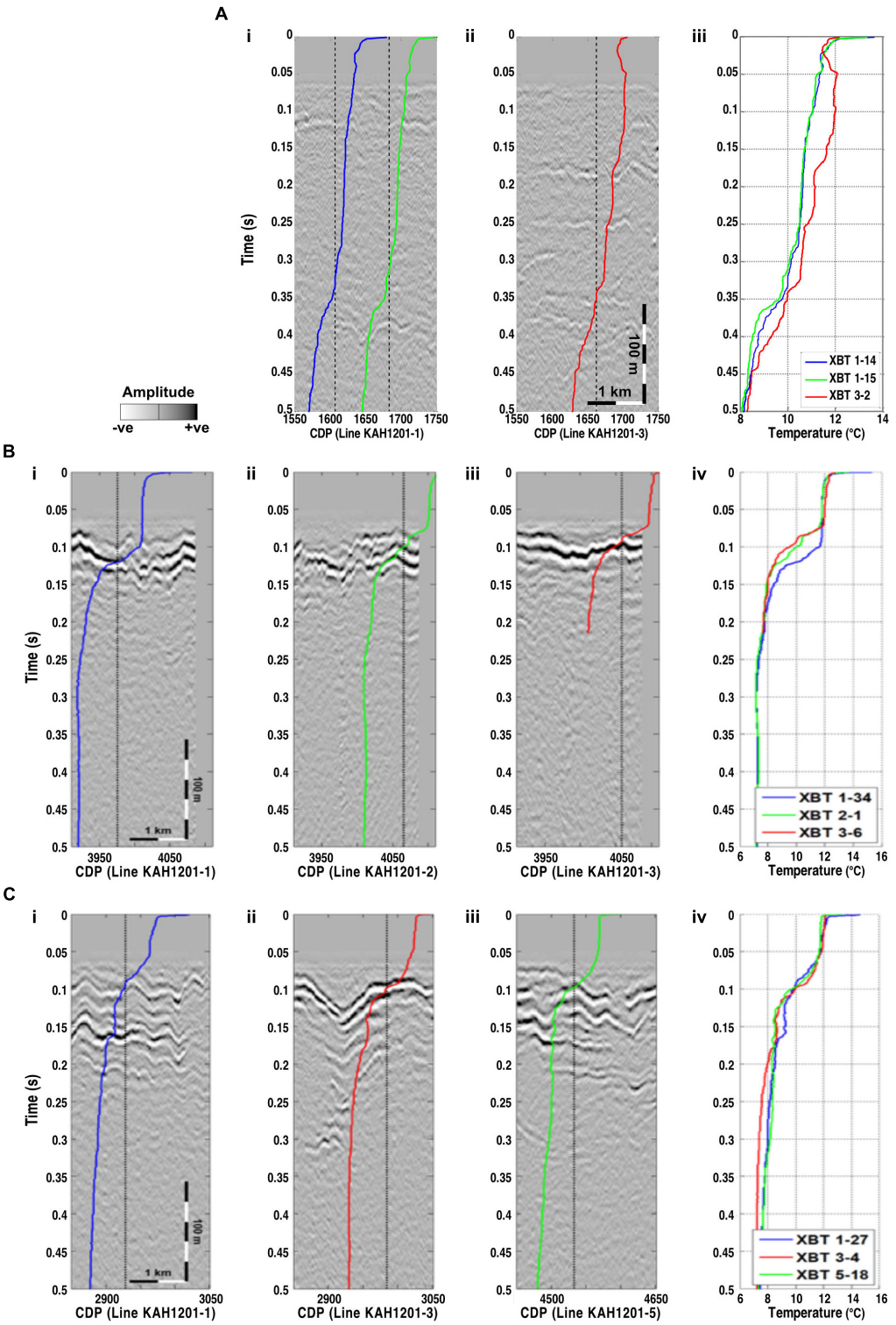

FIGURE 11 | Time-lapse XBT comparisons. Temperature traces are overlain on the seismic data, with the XBT locations shown by vertical dotted lines. **(A)** Portions of lines KAH1201-1 (i) and KAH1201-3 (ii) acquired in the same location within the STF zone. The three XBTs are plotted together in (iii). The time delay between XBTs 1-14 and 1-15 was 6 min, and between 1-15 and 3-2 was 19 h. **(B)** Portions of lines KAH1201-1 (i), KAH1201-2 (ii), and KAH1201-3 (iii) acquired in the same location at the seaward end of the Munida Transect. The three XBTs are plotted together in (iv). The time delay between XBTs 1-34 and 2-1 was 25 min, and between 2-1 and 3-6 was 18.5 h. **(C)** Portions of lines KAH1201-1 (i), KAH1201-3 (ii), and KAH1201-5 (iii) acquired at the intersection point of transects MUN and CB. The three XBTs are plotted together in (iv). The time delay between XBTs 1-27 and 3-4 was 19 h, and between XBTs 3-4 and 5-18 was 8 h.

oceanography research examining shallow (e.g., < 400 m water depth) oceanographic features. The cruise yielded reasonable quality, high-frequency seismic data, with coincident oceanographic data. This cruise was the first time that unambiguous water-column reflections were visible in a dedicated seismic oceanography voyage in this area. The seismic images have much greater horizontal resolution than the coincident XBT sections alone and even higher resolution than previous CTD sections along the 8-station Munida Transect. Although poor weather adversely affected the amount of seismic data collected during this cruise, one seismic profile was able to be repeated during the cruise to examine time-lapse changes in the reflectivity—importantly with repeat oceanographic data as well.

The KAH1201 survey resulted in good-quality high-frequency seismic images with significantly more detail in the shallow portion of the water column (<150 m) compared to legacy seismic data (**Figure 8**). Although the legacy data have a higher signal-to-noise ratio and contain reflections in the deeper portion of the water column which are not seen in the KAH1201 images, smaller and shallower layers are able to be resolved in the new data, including the seaward-dipping portion of the STF connecting its surface and subsurface expressions. One disadvantage of the shorter hydrophone streamer in the KAH1201 survey is that it did not produce long enough source-receiver offsets for stacking velocity analysis to help with identifying water masses, which would be useful in situations where coincident oceanographic data are not available. On the other hand, the small source-receiver offsets mean that detailed (and potentially time-consuming) interactive velocity analysis is not needed for these types of surveys, in contrast to long-offset data (e.g., Fortin and Holbrook, 2009); for the KAH1201 data, even using a constant velocity for stacking produced virtually identical stacks to using XBT-derived velocities (Cooper, 2021).

As mentioned previously, when creating the final seismic images for the KAH1201 data, an AGC operator was applied. Compared to other gain correction methods such as spherical divergence, AGC can cause distortion of the relative amplitudes of seismic reflections. A more rigorous amplitude-preserving flow would be required for further analysis of this dataset (e.g., for the application of seismic inversion). However, for these shallow seismic data with high levels of background noise, a simpler processing flow was sufficient for producing images of the main water masses and boundaries, and comparisons with synthetic seismograms show that relative amplitudes were adequately preserved (e.g., **Figure 7**).

This survey adds to a growing body of work using similar methods to study a range of oceanographic problems. The frequency content of the new seismic data compares favorably to other high-frequency seismic oceanography studies (e.g., Hobbs et al., 2009; Carniel et al., 2012; Piété et al., 2013). The acquisition of repeat seismic lines along the same transect to examine time lapse changes has similarities to the investigations of Tsuji et al. (2005), Nakamura et al. (2006), Géli et al. (2009), and Gunn et al. (2020). Expendable bathythermographs were used to acquire oceanographic data, in a manner similar to other single-vessel seismic oceanography cruises (e.g., Nandi et al., 2004; Nakamura et al., 2006).

The XBTs provide corroboration of the oceanographic features observed in the seismic images. In particular, the data illustrate the presence of STW, SAW, and a mixing zone between the two, and a well-developed mixed layer offshore. Surface traces constructed from the XBTs were also tied to satellite sea-surface temperatures, which was important in comparing the surface and subsurface expressions of the Subtropical Front.

Synthetic seismograms confirmed that prominent reflections originate from the base of the mixed layer and from the Subtropical Front in the subsurface, seen as high temperature gradient regions. Overall, similar reflective features are observed in both the KAH1201 and CB82-94 data, which provides confidence in the interpretation of significant oceanographic features in legacy seismic data that typically lack coincident oceanographic data. This provides support for previous interpretations of water column features (e.g., Gorman et al., 2018), and also for interpretation of further legacy seismic data in the same framework. The reflections associated with the Subtropical Front show, in particular, that the subsurface expression of the front is much more complex than suggested by its surface expression, consisting of a highly variable zone of mixing including temperature inversions. This illustrates the value of seismic oceanography in this region, as the seismic data have a horizontal resolution that cannot practically be achieved using CTDs or XBTs; even with the dense XBT deployment used in this survey, the seismic images still represent over 100 times greater spatial sampling than the XBT sections, with a 12.5 m trace spacing compared to the ∼1.85 km XBT spacing.

Another first for this survey was the acquisition of time-lapse seismic data over the Subtropical Front. Although earlier work (Smillie, 2012; Gorman et al., 2018) examined nearby legacy seismic surveys that were acquired 2 years apart, this survey involved the acquisition of short-turnaround time-lapse images of the identical transect. Time-lapse changes in reflections were significant over small timescales. There were large changes in the mixed-layer reflections and the internal waves affecting the base of the mixed layer, even on the scale of minutes as seen in changes between lines KAH1201-1 and -2. There were also significant changes in the reflections associated with the STF over the scale of hours, as seen in changes between lines KAH1201-1 and -3. In general, the seismic data show that features and patterns are consistent between datasets, which allows for confidence in interpreting future data without acquiring large amounts of coincident oceanographic data. However, the time-lapse passes show that for detailed analysis, as opposed to general interpretations, the acquisition of significant oceanographic data on each repeat pass is needed at this stage to deepen our understanding of the reflective changes in the seismic data.

Importantly, this survey helps to constrain the minimum requirements for a successful seismic oceanography cruise studying features like the STF in New Zealand waters. This cruise tested a relatively affordable research-scale operation, using a vessel and acquisition system (45/105 in^3 (0.74/1.72 L) GI gun and 300 m streamer) much smaller in scale than those of an industry seismic survey, that resulted in satisfactory seismic data and adequate accompanying oceanographic data, even in poor

weather conditions. In fact, this cruise was smaller-scale in terms of seismic acquisition parameters (source size, streamer length, or both) than other "high-frequency" or "high-resolution" surveys of Géli et al. (2009) and Hobbs et al. (2009), and the GI gun surveys of Nakamura et al. (2006); Carniel et al. (2012), Piété et al. (2013), and Sarkar et al. (2015). This means that, apart from the Piété et al. (2013) sparker data where only the mixed layer is imaged, this cruise represents new minimum requirements for successful seismic oceanography acquisition.

Frontal Structure and Dynamics

The reflective region representing the STF in the KAH1201 seismic data is similar to other seismic oceanography studies of frontal zones which show enhanced seismic reflectivity and dipping reflections associated with thermohaline intrusions and interleaving, such as the work of Holbrook et al. (2003); Mirshak et al. (2010), Sheen et al. (2012), and Rice et al. (2014). Synthetic ties between the XBTs and recorded seismic data show individual reflections resulting from step-like changes in temperature as well as inversions within the overall zone of high temperature gradients. Inversions such as these are a known feature of the STF, both in temperature and salinity (e.g., Garner, 1967; Heath, 1975; Gilmour and Cole, 1979; Harris et al., 1993).

In addition to the zone of shoreward-dipping reflections, the high-frequency seismic images also show the presence of an overlying shallow seaward-dipping reflection connecting the tip of the reflective warm-water wedge to the surface at a position further inshore. This inshore position appears to correspond to the surface position of the STF as seen in surface temperature traces and satellite sea-surface temperature images. In this study the surface STF position is found near the shelf break, consistent with previous satellite SST studies. The surface temperatures also show a consistent pattern with the lowest surface temperatures immediately seaward of the surface STF position, overlying the subsurface STF reflective region, and slightly warmer waters offshore. These low surface temperatures have been previously identified as a cold "tongue" created by upwelling associated with the flow of the Southland Current (e.g., Burling, 1961; Hawke, 1989; Shaw, 1998; Hopkins et al., 2010). The association of the low-temperature zone with the Southland Current supports the interpretation of the high-reflectivity zone in the subsurface as representing the mixed STW and SAW in the core of the Southland Current.

In this study the subsurface zone of high reflectivity in the seismic images consistently extends further seaward than the surface position of the STF, by a distance of ∼25 km. The difference between the surface and subsurface expressions of the STF has been observed in previous studies using SST and CTDs. While the surface and subsurface positions of the STF are strongly linked (e.g., Smith et al., 2013), the surface expression of the STF, particularly with respect to temperature, can be disrupted, decoupled, or even erased (e.g., Burling, 1961; Ridgway, 1975; Jeffrey, 1986; Butler et al., 1992; Szymanska and Tomczak, 1994; Chiswell, 1996; James et al., 2002; Tomczak et al., 2004). The effect changes seasonally, with the front more plainly visible at the surface in winter (e.g., Hopkins et al., 2010). In summer, surface SAW moves shoreward to overlie the subsurface STW, and coastal Neritic Water can also move seaward to completely obscure the STW at the surface (e.g., Jillett, 1969; Currie and Hunter, 1999; Jones et al., 2013). The subsurface seaward extension of STW in summer has been observed in the study area by Jillett (1969) and (Kirchlechner, 1999); the subsurface reflective zone in the seismic data extending further offshore than the surface expression of the STF is probably related to this phenomenon.

In addition to seasonal warming causing density changes that result in movement of surface water masses laterally, wind forcing may have a role in movement of the mixed layer above the subsurface front at shorter timescales. In the Indian Ocean, Tomczak et al. (2004) observed wind-driven decoupling of the surface temperature front in the mixed layer from the subsurface STF, with either poleward or (more commonly) equatorward shifting of the summer surface layer. At other continental shelf-break fronts, Siedlecki et al. (2011) and Carranza et al. (2017) also describe the effect of oscillation in along-front winds (both up-front and down-front) causing tilting of frontal isopycnals and movement of the front both at the surface and at depth, with implications for upwelling of nutrients. In the New Zealand region, variations in wind are thought to affect the STF on intra- and inter-annual timescales (e.g., Shaw and Vennell, 2001; Hopkins et al., 2010; Smith, 2017), and local-scale wind variability has been correlated to changes in the flow of the Southland Current (Chiswell, 1996; Fernandez et al., 2018). Further examination of the mechanisms causing the short-term variability and differing surface and subsurface expressions of the STF in this region, as observed in the seismic images in this study, is warranted.

CONCLUSION

The survey presented here was the first-ever successful seismic oceanography cruise in Australasia. The cruise involved the acquisition of 12-fold seismic data using a 300 m long streamer and a single GI gun source. During the seismic acquisition, oceanographic data were also acquired in the form of 79 XBTs. The data were acquired along two transects, coincident with previously analyzed seismic data and CTDs.

The seismic data exhibit significant reflectivity in the upper 500 ms (375 m) of the water column, coincident with dense temperature measurements along the two transects. A reflective zone corresponding to mixed Subtropical and Subantarctic Waters was consistently observed to extend further seaward than the surface position of the STF as identified in seismic images and sea-surface temperature data.

Repeat seismic images acquired along the Munida Transect show significant changes in STF reflections on the time-scale of hours. For example, the seaward extent of the reflective warm-water wedge moves ∼7.5 km in images produced about 19 h apart, and other individual reflections within the wedge cannot be correlated between images. Repeat XBTs at the same location within the frontal zone show differences of up to 1°C at depths between 50 and 300 m, indicating the highly variable nature of the STF in this region.

Seismic oceanography represents a significant tool for investigating oceanographic features in the dynamic waters surrounding New Zealand. This study clearly shows the ability of seismic oceanography to image the Subtropical Front in the subsurface at much higher horizontal resolution than conventional oceanographic methods. The results emphasize the importance of subsurface data, including seismic reflection data, in studying the frontal region, as there is a disparity between the surface and subsurface expression of oceanographic features. The work provides a foundation for future seismic oceanography studies to further understand mixing processes at this important boundary.

DATA AVAILABILITY STATEMENT

The datasets presented in this study can be found in online repositories. The URLs of the repositories are: https://www.nzpam.govt.nz/maps-geoscience/exploration-database/ (for seismic line CB82-94) and https://ourarchive.otago.ac.nz (search for the Ph.D. thesis of Cooper (2021), and its associated associated seismic and oceanographic data).

AUTHOR CONTRIBUTIONS

Data acquisition, processing and interpretation was undertaken as part of JC's Ph.D. thesis research, and she led writing and figure development. AG proposed the initial research and collaborated at all stages of manuscript development. MB participated in field data collection and lab analyses. RS collaborated with discussion of results. All authors were involved with manuscript revision and advice.

FUNDING

New Zealand government funding for seismic data acquisition and analysis was provided through the Royal Society of New Zealand Marsden Grant UOO0920 to AG. JC was supported by a University of Otago Ph.D. Scholarship and a Society of Exploration Geophysicists Foundation Scholarship.

ACKNOWLEDGMENTS

The crew of *RV Kaharoa* during cruise KAH1201 and staff at NIWA Vessels are thanked for their assistance in this short research voyage. Sam Bain assisted with field data collection. Public domain seismic data for line CB82-94 were obtained from New Zealand Petroleum and Minerals, a division of the Ministry of Business, Innovation and Employment. Seismic processing has been undertaken with academic licenses for GLOBE Claritas from Petrosys and MATLAB. Bathymetric data were provided by NIWA. The two reviewers are thanked for their constructive reviews that improved the final manuscript.

SUPPLEMENTARY MATERIAL

The Supplementary Material for this article can be found online at: https://www.frontiersin.org/articles/10.3389/fmars.2021.751385/full#supplementary-material

REFERENCES

Biescas, B., Sallarès, V., Pelegrí, J. L., Machín, F., Carbonnell, R., Buffett, G., et al. (2008). Imaging meddy finestructure using multichannel seismic reflection data. *Geophys. Res. Lett.* 35:L11609. doi: 10.1029/2008GL033971

Blacic, T. M., and Holbrook, W. S. (2010). First images and orientation of fine structure from a 3-D seismic oceanography data set. *Ocean Sci.* 6, 431–439. doi: 10.5194/os-6-431-2010

Buffett, G. G., Krahmann, G., Klaeschen, D., Schroeder, K., Sallares, V., Papenberg, C., et al. (2017). Seismic oceanography in the Tyrrhenian Sea: thermohaline staircases, eddies, and internal waves. *J. Geophys. Res. Oceans* 122, 8503–8523. doi: 10.1002/2017JC012726

Buffett, G. G., Pelegrí, J. L., De La Puente, J., and Carbonell, R. (2012). Real time visualization of thermohaline finestructure using Seismic Offset Groups. *Methods Oceanogr.* 3–4, 1–13. doi: 10.1016/j.mio.2012.07.003

Burling, R. W. (1961). *Hydrology of Circumpolar Waters South of New Zealand*. Owen: Government printer.

Butler, E., Butt, J., Lindstrom, E., Teldesley, P., Pickmere, S., and Vincent, W. (1992). Oceanography of the subtropical convergence Zone around southern New Zealand. *N. Zeal. J. Mar. Freshw. Res.* 26, 131–154. doi: 10.1080/00288330.1992.9516509

Carniel, S., Bergamasco, A., Book, J. W., Hobbs, R. W., Sclavo, M., and Wood, W. T. (2012). Tracking bottom waters in the Southern Adriatic Sea applying seismic oceanography techniques. *Continental Shelf Res.* 44, 30–38. doi: 10.1016/j.csr.2011.09.004

Carranza, M., Gille, S., Piola, A. R., Charo, M., and Romero, S. (2017). Wind modulation of upwelling at the shelf-break front off P atagonia: observational evidence. *J. Geophys. Res. Oceans* 122, 2401–2421. doi: 10.1002/2016JC012059

Chiswell, S. M. (1996). Variability in the southland current, New Zealand. *N. Zeal. J. Mar. Freshw. Res.* 30, 1–17. doi: 10.1080/00288330.1996.9516693

Chiswell, S. M. (2001). Eddy energetics in the subtropical front over the Chatham Rise, New Zealand. *N. Zeal. J. Mar. Freshw. Res.* 35, 1–15. doi: 10.1080/00288330.2001.9516975

Chiswell, S. M., Bostock, H. C., Sutton, P. J., and Williams, M. J. (2015). Physical oceanography of the deep seas around New Zealand: a review. *N. Zeal. J. Mar. Freshw. Res.* 49, 286–317. doi: 10.1080/00288330.2014.992918

Cooper, J. K. (2021). *Characterising the Subtropical Front and Associated Water Masses Offshore Otago Using Seismic Oceanography*. Ph.D. Thesis. Dunedin: University of Otago.

Currie, K. I., and Hunter, K. A. (1998). Surface water carbon dioxide in the waters associated with the subtropical convergence, east of New Zealand. *Deep Sea Res. I Oceanogr. Res. Pap.* 45, 1765–1777. doi: 10.1016/S0967-0637(98)00041-7

Currie, K. I., and Hunter, K. A. (1999). Seasonal variation of surface water CO2 partial pressure in the Southland Current, east of New Zealand. *Mar. Freshw. Res.* 50, 375–382. doi: 10.1071/MF98115

Currie, K. I., Reid, M. R., and Hunter, K. A. (2011). Interannual variability of carbon dioxide drawdown by subantarctic surface water near New Zealand. *Biogeochemistry* 104, 23–34. doi: 10.1007/s10533-009-9355-3

Fernandez, D., Bowen, M., and Sutton, P. (2018). Variability, coherence and forcing mechanisms in the New Zealand ocean boundary currents. *Prog. Oceanogr.* 165, 168–188. doi: 10.1016/j.pocean.2018.06.002

Fortin, W. F. J., and Holbrook, W. S. (2009). Sound speed requirements for optimal imaging of seismic oceanography data. *Geophys. Res. Lett.* 36:L00D01. doi: 10.1029/2009GL038991

Garner, D. M. (1967). *Hydrology of the Southern Hikurangi Trench Region*. New Zealand: Department of Scientific and Industrial Research.

Géli, L., Cosquer, E., Hobbs, R. W., Klaeschen, D., Papenberg, C., Thomas, Y., et al. (2009). High resolution seismic imaging of the ocean structure using a small volume airgun source array in the Gulf of Cadiz. *Geophys. Res. Lett.* 36:L00D09. doi: 10.1029/2009GL040820

Gilmour, A., and Cole, A. (1979). The subtropical convergence east of New Zealand. *N. Zeal. J. Mar. Freshw. Res.* 13, 553–557. doi: 10.1080/00288330.1979.9515833

Gorman, A. R., Smillie, M. W., Cooper, J. K., Bowman, M. H., Vennell, R., Holbrook, W. S., et al. (2018). Seismic characterization of water masses and mesoscale eddies associated with the Subtropical and Subantarctic fronts SE of New Zealand. *J. Geophys. Res. Oceans* 123, 1519–1532. doi: 10.1002/2017JC013459

Gunn, K. L., White, N., and Caulfield, C. C. P. (2020). Time-lapse seismic imaging of oceanic fronts and transient lenses within South Atlantic Ocean. *J. Geophys. Res. Oceans* 125:e2020JC016293. doi: 10.1029/2020JC016293

Harris, G., Feldman, G., and Griffiths, F. (1993). "Global oceanic production and climate change," in *Ocean Colour: Theory and Applications in a Decade of CZCS Experience*, eds V. Barale and P. M. Schlittenhardt (Berlin: Springer), 237–270. doi: 10.1007/978-94-011-1791-3_10

Hawke, D. J. (1989). Hydrology and near-surface nutrient distribution along the South Otago continental shelf, New Zealand, in summer and winter 1986. *N. Zeal. J. Mar. Freshw. Res.* 23, 411–420. doi: 10.1080/00288330.1989.9516377

Heath, R. A. (1972). The Southland current. *N. Zeal. J. Mar. Freshw. Res.* 6, 497–533. doi: 10.1080/00288330.1972.9515444

Heath, R. A. (1975). *Oceanic Circulation and Hydrology Off the Southern Half of South Island, New Zealand*. Wellington: New Zealand Oceanographic Institute Wellington.

Heath, R. A. (1981). Oceanic fronts around southern New Zealand. *Deep Sea Res. A Oceanogr. Res. Pap.* 28, 547–560. doi: 10.1016/0198-0149(81)90116-3

Hobbs, R. W., Klaeschen, D., Sallarès, V., Vsemirnova, E., and Papenberg, C. (2009). Effect of seismic source bandwidth on reflection sections to image water structure. *Geophys. Res. Lett.* 36:L00D08. doi: 10.1029/2009GL040215

Holbrook, W. S., and Fer, I. (2005). Ocean internal wave spectra inferred from seismic reflection transects. *Geophys. Res. Lett.* 32:L15604. doi: 10.1029/2005GL023733

Holbrook, W. S., Páramo, P., Pearse, S., and Schmitt, R. W. (2003). Fine-scale thermohaline structure in an oceanographic front revealed by seismic reflection profiling. *Science* 301, 821–824. doi: 10.1126/science.1085116

Hopkins, J., Shaw, A. G. P., and Challenor, P. (2010). The Southland front, New Zealand: variability and ENSO correlations. *Continental Shelf Res.* 30, 1535–1548. doi: 10.1016/j.csr.2010.05.016

James, C., Tomczak, M., Helmond, I., and Pender, L. (2002). Summer and winter surveys of the Subtropical front of the southeastern Indian Ocean 1997–1998. *J. Mar. Syst.* 37, 129–149. doi: 10.1016/S0924-7963(02)00199-9

Jeffrey, M. (1986). *Climatological Features of The Subtropical Convergence in Australian and New Zealand Waters*. Camperdown: Ocean Sciences Institute, University of Sydney.

Jillett, J. (1969). Seasonal hydrology of waters off the Otago peninsula, South-Eastern New Zealand. *N. Zeal. J. Mar. Freshw. Res.* 3, 349–375. doi: 10.1080/00288330.1969.9515303

Jones, K. N., Currie, K. I., Mcgraw, C. M., and Hunter, K. A. (2013). The effect of coastal processes on phytoplankton biomass and primary production within the near-shore subtropical frontal zone. *Estuar. Coast. Shelf Sci.* 124, 44–55. doi: 10.1016/j.ecss.2013.03.003

JPL MUR Measures Project (2015). *GHRSST Level 4 MUR Global Foundation Sea Surface Temperature Analysis. Ver. 4.1*. Pasadena, CA: PO.DAAC.

Kirchlechner, T. M. (1999). *Biogeochemical Aspects of the New Zealand Sector of the Southern Ocean*. Ph.D. thesis. Dunedin: University of Otago.

Krahmann, G., Brandt, P., Lklaeschen, D., and Reston, T. J. (2008). Mid-depth internal wave energy off the Iberian Peninsula estimated from seismic reflection data. *J. Geophys. Res.* 113:C12016. doi: 10.1029/2007JC004678

Mackenzie, K. V. (1981). Nine-term equation for sound speed in the oceans. *J. Acoust. Soc. Am.* 70, 807–812. doi: 10.1121/1.386920

Margrave, G. F., and Lamoureux, M. P. (2019). *Numerical Methods of Exploration Seismology: With Algorithms in MATLAB®* . Cambridge, MA: Cambridge University Press. doi: 10.1017/9781316756041

McCartney, M. S. (1977). "Subantarctic mode water," in *A Voyage of Discovery: George Deacon 70th Anniversary Volume, Supplement to Deep-Sea Research*, ed. M. Angel (Oxford: Pergamon Press), 103–119.

Mirshak, R., Nedimovic, M. R., Greenan, B. J. W., Ruddick, B. R., and Louden, K. (2010). Coincident reflection images of the Gulf Stream from seismic and hydrographic data. *Geophys. Res. Lett.* 37:L05602. doi: 10.1029/2009GL042359

Morris, M., Stanton, B., and Neil, H. (2001). Subantarctic oceanography around New Zealand: preliminary results from an ongoing survey. *N. Zeal. J. Mar. Freshw. Res.* 35, 499–519. doi: 10.1080/00288330.2001.9517018

Nakamura, Y., Noguchi, T., Tsuji, T., Itoh, S., Niiono, H., and Matsuoka, T. (2006). Simultaneous seismic reflection and physical oceanographic observations of oceanic fine structure in the Kurioshio extension front. *Geophys. Res. Lett.* 33:L23605. doi: 10.1029/2006GL027437

Nandi, P., Holbrook, W. S., Pearse, S., Páramo, P., and Schmitt, R. W. (2004). Seismic reflection imaging of water mass boundaries in the Norwegian Sea. *Geophys. Res. Lett.* 31:L23311. doi: 10.1029/2004GL021325

Neil, H. L., Carter, L., and Morris, M. Y. (2004). Thermal isolation of campbell plateau, New Zealand, by the antarctic circumpolar current over the past 130 kyr. *Paleoceanography* 19:A4008. doi: 10.1029/2003PA000975

Orsi, A. H., Whitworth, T. III, and Nowlin, W. D. Jr. (1995). On the meridional extent and fronts of the antarctic circumpolar current. *Deep Sea Res. I Oceanogr. Res. Pap.* 42, 641–673. doi: 10.1016/0967-0637(95)00021-W

Piété, H., Marié, L., Marsset, B., Thomas, Y., and Gutscher, M. A. (2013). Seismic reflection imaging of shallow oceanographic structures. *J. Geophys. Res. Oceans* 118, 2329–2344. doi: 10.1002/jgrc.20156

Pinheiro, L. M., Song, H., Ruddick, B., Dubert, J., Ambar, I., Mustafa, K., et al. (2010). Detailed 2-D imaging of the Mediterranean outflow and meddies off W Iberia from multichannel seismic data. *J. Mar. Syst.* 79, 89–100. doi: 10.1016/j.jmarsys.2009.07.004

Ravens, J. (2001). *GLOBE Claritas, Seismic Processing Software Manual*, 3rd Edn. Lower Hutt: GNS Science.

Rice, A. E., Book, J. W., and Wood, W. T. (2014). *Understanding Thermohaline Mixing in the Agulhas Return Current from Seismic and Finestructure Observations*. Hancock County: Naval Research Laboratory Oceanography Division Stennis Space Center.

Ridgway, N. (1975). *Hydrology of the Bounty Islands Region*. Auckland: New Zealand Oceanographic Institute.

Ruddick, B. R. (2018). Seismic oceanography's failure to flourish: a possible solution. *J. Geophys. Res. Oceans* 123, 4–7. doi: 10.1002/2017JC013736

Sallarès, V., Biescas, B., Buffett, G., Carbonell, R., Dañobeitia, J. J., and Pelegrí, J. L. (2009). Relative contribution of temperature and salinity to ocean acoustic reflectivity. *Geophys. Res. Lett.* 36:6. doi: 10.1029/2009GL040187

Sarkar, S., Sheen, K. L., Klaeschen, D., Brearley, J. A., Minshull, T. A., Berndt, C., et al. (2015). Seismic reflection imaging of mixing processes in Fram Strait. *J. Geophys. Res. Oceans* 120, 6884–6896. doi: 10.1002/2015JC011009

Shaw, A. G. P. (1998). *The Temporal and Spatial Variability of the Southland Front, New Zealand Using AVHRR SST Imagery*. Ph.D. thesis. Dunedin: University of Otago.

Shaw, A. G. P., and Vennell, R. (2001). Measurements of an oceanic front using a front-following algorithm for AVHRR SST imagery. *Remote Sens. Environ.* 75, 47–62. doi: 10.1016/S0034-4257(00)00155-3

Sheen, K., White, N., Caulfield, C., and Hobbs, R. (2012). Seismic imaging of a large horizontal vortex at abyssal depths beneath the Sub-Antarctic front. *Nat. Geosci.* 5:542. doi: 10.1038/ngeo1502

Sheen, K. L., White, N. J., and Hobbs, R. W. (2009). Estimating mixing rates from seismic images of oceanic structure. *Geophys. Res. Lett.* 36:L00D04. doi: 10.1029/2009GL040106

Siedlecki, S., Archer, D., and Mahadevan, A. (2011). Nutrient exchange and ventilation of benthic gases across the continental shelf break. *J. Geophys. Res. Oceans* 116:e006365. doi: 10.1029/2010JC006365

Smillie, M. W. (2012). *Seismic Oceanographical Imaging of the Ocean S.E. of New Zealand*. Dunedin: University of Otago.

Smith, R. O. (2017). *Variability of the Subtropical Front in the Tasman Sea*. Dunedin: University of Otago.

Smith, R. O., Vennell, R., Bostock, H. C., and Williams, M. J. (2013). Interaction of the subtropical front with topography around southern New Zealand. *Deep Sea Res. I Oceanogr. Res. Pap.* 76, 13–26. doi: 10.1016/j.dsr.2013.02.007

Sutton, P. J. (2003). The Southland current: a subantarctic current. *N. Zeal. J. Mar. Freshw. Res.* 37, 645–652. doi: 10.1080/00288330.2003.9517195

Szymanska, K., and Tomczak, M. (1994). Subduction of central water near the subtropical front in the southern Tasman Sea. *Deep Sea Res. I Oceanogr. Res. Pap.* 41, 1373–1386. doi: 10.1016/0967-0637(94)90103-1

Tang, Q., Gulick, S., and Sun, L. (2014). Seismic observations from a Yakutat eddy in the northern Gulf of Alaska. *J. Geophys. Res. Oceans* 119, 3535–3547. doi: 10.1002/2014JC009938

Tang, Q., Wang, D., Li, J., Yan, P., and Li, J. (2013). Image of a subsurface current core in the southern South China Sea. *Ocean Sci.* 9, 631–638. doi: 10.5194/os-9-631-2013

Tomczak, M., Pender, L., and Liefrink, S. (2004). Variability of the subtropical front in the Indian Ocean south of Australia. *Ocean Dyn.* 54, 506–519. doi: 10.1007/s10236-004-0095-6

Tsuji, T., Noguchi, T., Niiono, H., Matsuoka, T., Nakamura, Y., Tokuyama, H., et al. (2005). Two-dimensional mapping of fine structures in the Kurosiho Current using seismic reflection data. *Geophys. Res. Lett.* 32:L14609. doi: 10.1029/2005GL023095

Western Geophysical Company/Shell BP Todd Canterbury Services Ltd (1982). *Final Operation Report. Canterbury Bight. PPL's 38202 and 38203*. Wellington: Ministry of Economic Development - Crown Minerals.

Yilmaz, Ö (2001). *Seismic Data Analysis: Processing, Inversion, and Interpretation of Seismic Data*. Chicago: SEG Books. doi: 10.1190/1.9781560801580

Conflict of Interest: The authors declare that the research was conducted in the absence of any commercial or financial relationships that could be construed as a potential conflict of interest.

Publisher's Note: All claims expressed in this article are solely those of the authors and do not necessarily represent those of their affiliated organizations, or those of the publisher, the editors and the reviewers. Any product that may be evaluated in this article, or claim that may be made by its manufacturer, is not guaranteed or endorsed by the publisher.

frontiers in Marine Science

ORIGINAL RESEARCH
published: 11 November 2021
doi: 10.3389/fmars.2021.733959

Observations of Internal Structure Changes in Shoaling Internal Solitary Waves Based on Seismic Oceanography Method

Haibin Song[1], Yi Gong[1]*, Shengxiong Yang[2,3] and Yongxian Guan[2,3]*

[1] State Key Laboratory of Marine Geology, School of Ocean and Earth Science, Tongji University, Shanghai, China, [2] Southern Marine Science and Engineering Guangdong Laboratory, Guangzhou, China, [3] Guangzhou Marine Geological Survey, China Geological Survey, Guangzhou, China

OPEN ACCESS

Edited by:
Kathy Gunn,
University of Miami, United States

Reviewed by:
Andrey Serebryany,
P. P. Shirshov Institute of Oceanology, Russian Academy of Sciences (RAS), Russia
Shuqun Cai,
South China Sea Institute of Oceanology, Chinese Academy of Sciences (CAS), China

***Correspondence:**
Haibin Song
hbsong@tongji.edu.cn
Yi Gong
cqdbc024@126.com

Specialty section:
This article was submitted to Ocean Observation, a section of the journal Frontiers in Marine Science

Received: *30 June 2021*
Accepted: *13 October 2021*
Published: *11 November 2021*

Citation:
Song H, Gong Y, Yang S and Guan Y (2021) Observations of Internal Structure Changes in Shoaling Internal Solitary Waves Based on Seismic Oceanography Method. Front. Mar. Sci. 8:733959. doi: 10.3389/fmars.2021.733959

High spatial resolution and deep detection depths of seismic reflection surveying are conducive to studying the fine structure of the internal solitary wave. However, seismic images are instantaneous, which are not conducive to observing kinematic processes of the internal solitary waves. We improved the scheme of seismic data processing and used common-offset gathers to continuously image the same location. In this way, we can observe internal fine structure changes during the movement of the internal solitary waves, especially the part in contact with the seafloor. We observed a first-mode depression internal solitary wave on the continental slope near the Dongsha Atoll of the South China Sea and short-term shoaling processes of the internal solitary wave by using our improved method. We found that the change in shape of waveform varies at different depths. We separately analyzed the evolution of the six waveforms at different depths. The results showed that the waveform in deep water deforms before that in shallow water and the waveform in shallow water deforms to a greater degree. We measured four parameters of the six waveforms during the shoaling including phase velocity, amplitude, wavelength, and slopes of leading and trailing edge. The phase velocity and amplitudes of waveforms in shallow water increase, the wavelengths decrease, and the slopes of trailing edge gradually become larger than that of the leading edge, while the amplitudes of the deep water waveforms do not change significantly and the phase velocities decrease. Our results are consistent with previous studies made by numerical simulations, which suggest the effectiveness of the new processing scheme. This improved scheme cannot only study the internal solitary waves shoaling, but also has great potential in the study of other ocean dynamics.

Keywords: internal fine structure, internal solitary wave, shoaling, northern South China Sea, seismic oceanography

INTRODUCTION

Internal solitary waves are an important oceanographic phenomenon, which affect not only the marine environment, but also affect human activities in the ocean. Internal solitary waves play an important role in energy transfer (Wunsch and Ferrari, 2004) and vertical mixing (Klymak and Moum, 2003; Moum et al., 2003, 2007). Internal solitary waves have proved to be an important mechanism for transport, which often induce sediment resuspension (Bogucki and Redekopp, 1999; Masunaga et al., 2015; Boegman and Stastna, 2019) or change distribution of nutrients and biomass (Haury et al., 1983; Lamb, 1997, 2003; Scotti and Pineda, 2004). In addition, the internal solitary waves can generate strong shear forces, which pose a potential threat to offshore engineering and submarines (Apel et al., 1997; Vlasenko et al., 2000). At present, researchers have made progress in the study of the internal solitary waves both theoretically and observationally, but observations of fine vertical structure and the study of interaction with topography are still insufficient. The South China Sea is a region where the internal solitary waves are well developed (Zhao et al., 2004; Zheng et al., 2007; Cai et al., 2012; Guo and Chen, 2014) and the shoaling internal solitary waves are often observed on the continental shelf-slope. For this reason, the region is an excellent site to study the interaction between the internal solitary waves and submarine topography. Therefore, we decided to use this region to develop a seismic data processing scheme that can study the evolution of the internal solitary waves.

Propagation of the internal solitary waves onto the continental slope is a complex dynamic process. When the internal solitary waves propagate into shallow water, the waveform will deform due to the imbalances between non-linear and dispersion effects. During the shoaling process, the internal solitary waves possibly transform from a depression wave to an elevation wave (Liu et al., 1998) and may be breaking due to mixing (Aghsaee et al., 2010) or form vortices in the core (Lamb, 2002). These processes have been verified in numerical (Holloway et al., 1997; Liu et al., 1998; Zhao et al., 2003; Grimshaw et al., 2010) and physical laboratory simulations (Boegman et al., 2005; Cheng and Hsu, 2010) and observed by means of mooring, high-frequency acoustics, and remote sensing (Orr and Mignerey, 2003; Zhao et al., 2003; Lynch et al., 2004; Bourgault et al., 2007; Shroyer et al., 2008; Fu et al., 2012). However, these observations of the shoaling processes are inadequate, since the observational techniques are unable to visualize the evolution and internal fine structure of the internal solitary waves. High-frequency acoustics can only observe a few scattering interfaces. More importantly, these methods cannot be used to observe the interactions between the topography and internal solitary waves. These observational constraints have limited our understanding of shoaling process of the internal solitary waves.

With the development of seismic oceanography (Holbrook et al., 2003), seismic reflection surveying has been applied to study various oceanographic phenomena including fronts (Holbrook et al., 2003; Tsuji et al., 2005), water mass boundaries (Nandi et al., 2004), mesoscale eddies (Pinheiro et al., 2010), internal waves (Holbrook and Fer, 2005; Bai et al., 2017), the Mediterranean undercurrent (Buffett et al., 2009; Biescas et al., 2010), and submesoscale processes (Sallarès et al., 2016; Tang et al., 2020). More recently, seismic reflection studies have now been used to look at the evolution of oceanic processes over time (Dickinson et al., 2020; Gunn et al., 2020; Zou et al., 2021). This method has high spatial resolution. The vertical resolution can be less than 10 m and the lateral resolution is approximately 6.25 or 12.5 m. Such vertical resolution is close to the scale of the "step-like" vertical profile of temperature and salinity induced by double diffusion in some areas (Magnell, 1976), so seismic oceanography can observe the internal fine structure of water column (Geli et al., 2009). This high resolution ensures that fine structure of the shoaling internal solitary waves is observable by using the seismic reflection method. However, conventional processing schemes of seismic data are not conducive to imaging the motion and evolution of the internal solitary waves, since they yield a single, static image of the water column.

In this observational contribution, we use an adapted acoustic method to report the parameters of the internal solitary waves at different stages of their shoaling. This methodology provides dynamic and high-resolution observations of internal solitary waves (ISWs) that are difficult to otherwise obtain. We hope that such observations can be used to improve theoretical understanding of these phenomena in the future. We improve the processing scheme of seismic data and obtain a series of images (i.e., a time-lapse) of the shoaling internal solitary wave in the northern South China Sea. These images clearly record the evolution of internal structure, according to which we analyze the process of waveform deformation and the influence of topography on the internal solitary wave. In section "Data and Methods," we introduce the seismic data used in this study and the improved processing scheme. The description of wave properties is given in section "Results." The shoaling process is analyzed in detail in section "Discussion." Finally, the concluding remarks are presented in section "Conclusion."

DATA AND METHODS

Seismic Data Acquisition and Buoyancy Frequency

The Guangzhou Marine Geological Survey acquired a set of two-dimensional (2D) multi-channel reflection seismic data in the South China Sea near the Dongsha Atoll in the summer of 2009. The streamer has a total length of 6 km and contains 480 channels. The trace interval is 12.5 m and the sampling interval is 2 ms. The energy generated by airgun sources has a total volume of 5,080 in^3 (1 in = 2.54 cm) and the dominant frequency of the wavelet is 35 Hz. The shot interval is 25 m and the shot time interval is about 10 s. The minimum offset is 250 m. We found the shoaling internal solitary wave on the seismic line Ls, whose location is shown by the red line in **Figure 1**. The seismic line is located on the continental slope and the slope of the topography is gentle. The observation direction is from southeast to northwest, which is almost the same as the propagation direction of most internal solitary waves near the Dongsha Atoll

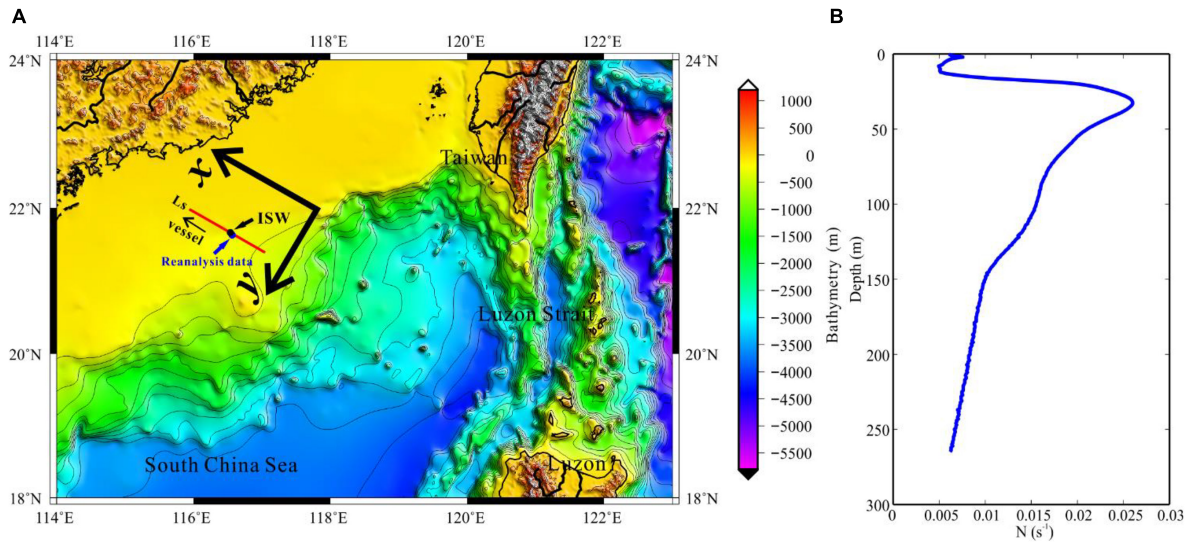

FIGURE 1 | (A) The observation location and bathymetry. The red line is location of seismic section (Ls). The black dot is the location of the internal solitary wave in seismic section. The blue dot is the location of reanalysis data. The arrow indicates the direction of vessel. **(B)** The buoyancy frequency estimated from reanalysis data.

(Alford et al., 2015). Temperature and salinity measurements from reanalysis data are used to calculate a local buoyancy frequency profile (**Figure 1B**). The reanalysis data are provided by the Copernicus Marine Environment Monitoring Service (CMEMS) in daily averages. We extract data from the summer of 2009 that are close to the location of the internal solitary wave.

Typical Seismic Section Processing

The processing scheme of stacked seismic section includes the definition of geometry, direct wave attenuation and noise removal, common midpoint (CMP) gathers sorting, velocity analysis, stacking, and migration (Ruddick et al., 2009). Firstly, we define the survey geometry to create a coordinate system for seismic data. Secondly, we apply a high-pass filter to remove low-frequency background noise and attenuate the direct waves by using a median filter. Thirdly, we sort the shot gathers into CMPs and perform a velocity analysis. We use the results of the velocity analysis to apply a normal moveout (NMO) correction to the CMP gathers, so that the reflection events become flat and can be stacked. Stacking means that adding all the tracks in each CMP gather to form one trace. Finally, we implement poststack migration to improve the imaging accuracy of the stacked seismic section. Yilmaz (2001) describes a more detailed description of seismic reflection processing.

Improved Seismic Section Processing

Multi-channel reflection seismic data will cover a section multiple times during the acquisition, so that we can image the water column multiple times to study the motion of it (Sheen et al., 2012). However, poststack sections generated by the traditional processing schemes require multiple receiver channels to be stacked in order to improve signal-to-noise ratio (SNR). This operation can neither visualize the motion of water column nor fine structure changes during the motion. In order to utilize the multiple coverage information in the seismic data, we resort the CMPs into a number of common offset gathers (COGs), where the offset is the distance between source and receiver. Each COG can be considered as a snapshot of water column. In this way, the motion of water column can be visualized as an animation.

Processing schemes for COG migrated sections are the same as those for conventional stacked seismic section, except that the NMO correction is not applied and CMPs are not stacked. After the third step in section "Typical Seismic Section Processing," the COGs are resorted from the CMPs according to the offset and a prestack time migration is applied to the COGs. After completing the above steps, a series of COG migrated sections can be obtained.

Two key points are worth noting here. Firstly, as offset increases, the high frequency components in the seismic data will attenuate, which affect imaging quality. To reduce this attenuation, we use a low-pass filter to limit the frequency of all the COGs to less than 80 Hz, so that seismic data of all the COGs are normalized to the same frequency band. Secondly, the imaging range of each COG migrated section is not always the same. Thus, it is necessary to select COG migrated sections with the same CMP range. To ensure these conditions are met, we selected COGs every four channels from the 3rd to the 95th channel and obtain a total of 23 groups of COG migrated sections. Then, by arranging these COG migrated sections according to offset, a series of images, which map the motion of water column over time, can be obtained.

Waveform Characteristics Estimate From Seismic Section

Some waveform characteristics can be directly obtained from the seismic section such as amplitude, wavelength, and the slopes of

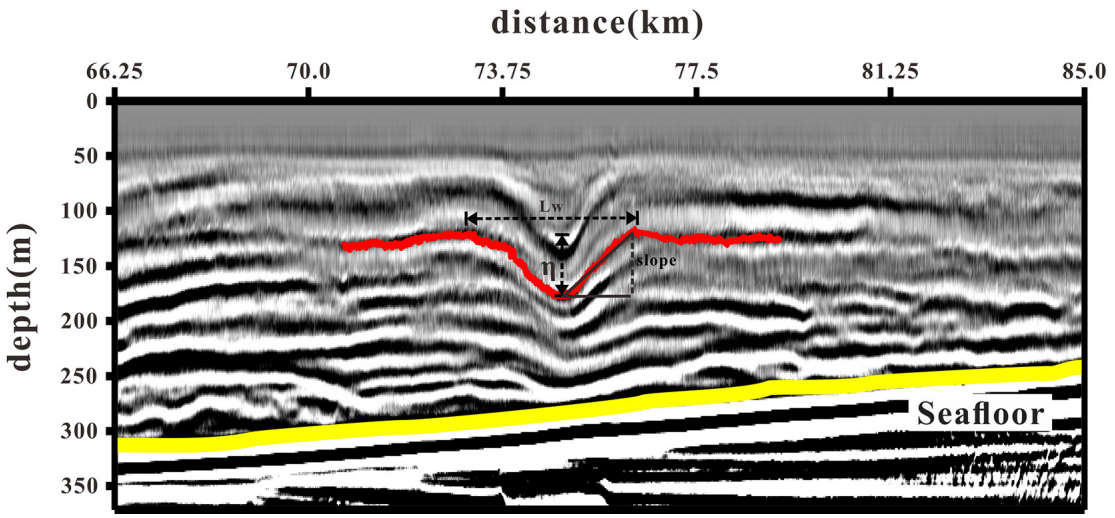

FIGURE 2 | Schematic diagram of amplitude (η), wavelength (Lw), and the slope of the leading and trailing edges (slope) calculation. The red line is one of the seismic events. The yellow line indicates the seafloor.

the front and rear edges of the internal solitary wave. Seismic sections reflect the vertical gradient structure of temperature and salinity (Ruddick et al., 2009) and we refer to this structure as reflective interfaces. Usually, reflective interfaces are parallel to isopycnal surfaces (Holbrook et al., 2003; Sallarès et al., 2009); therefore, they can be traced to extract information about the internal solitary waves. In **Figure 2**, the black and white stripes indicate the position of an example of reflective interface at a depth of 130 m. The adjacent black and white stripes are caused by the signature of the source rather than changes in ocean properties and we call them seismic events. So, to track the seismic events, we only trace one color stripe. Now, with the isopycnal surface of the internal solitary wave, we can estimate its amplitude, wavelength, and the slope of its leading and trailing edges. Note how these parameters change with depth. In this way, we can use seismic data to study the vertical structure of the internal solitary waves (Gong et al., 2021).

Wave Phase Velocity Estimate From Prestack Seismic Data

The method to estimate the section velocity of the reflection events is based on prestack seismic data and has been successfully applied to the phase velocity estimation of first mode and the second mode internal solitary waves (Tang et al., 2015; Fan et al., 2021). We first trace the same reflection event of an internal solitary wave from a series of COG sections (the black line in **Figure 3**). Then, we record the shot number and CMP number of a fixed reflection point on these events, which can be easily read from prestack seismic data. It should be noted that the selected reflection point must be a feature that is not affected by seismic imaging such as the trough or crest of the internal solitary wave (the black dot in **Figure 3**). The change in the shot number of the reflection point represents the change in time and the change in the CMP number represents the change in distance. Then, the

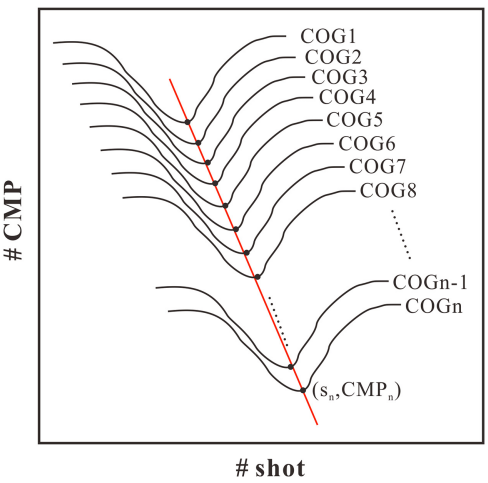

FIGURE 3 | Schematic diagram of calculating the internal solitary wave phase velocity by using pre-stack seismic data.

phase velocity of the internal solitary wave can be expressed as:

$$v = \frac{dCMP}{ds \cdot dt} \tag{1}$$

where, the *dCMP* is the change in CMP number, *ds* represents the change in shot number, and *dt* is the shot time interval.

RESULTS

Internal Solitary Wave in the Stacked Seismic Section

We found a first-mode depression internal solitary wave in seismic line Ls. As shown in **Figure 4**, the internal solitary wave

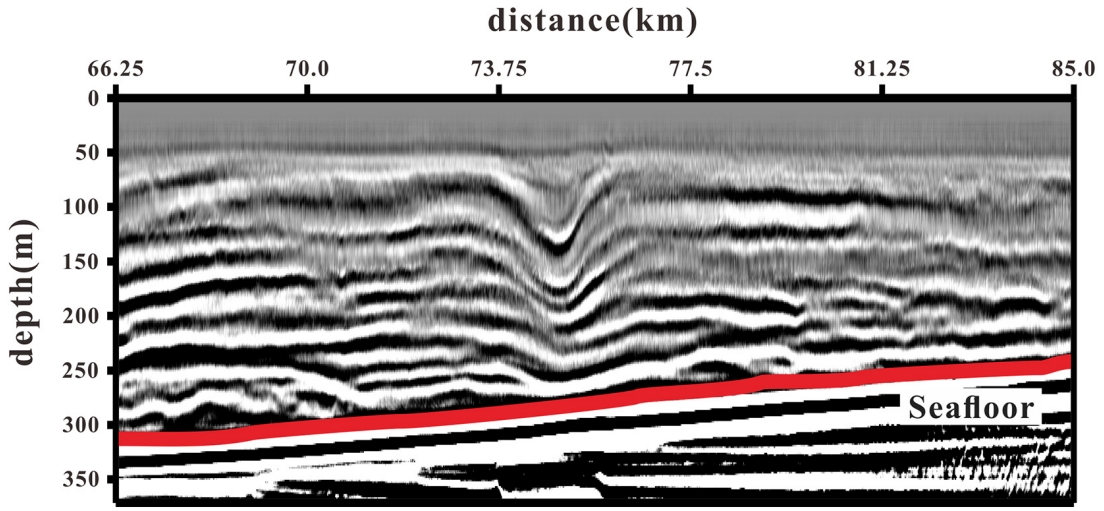

FIGURE 4 | Stacked section of the internal solitary wave. The red line represents seafloor.

only has one concave downward waveform. The observation direction is from southeast to northwest, which is consistent with the movement direction of the internal solitary wave. The stacked section is plotted as if the internal solitary wave was propagating from left to right. In **Figure 4**, the internal solitary wave was shoaling onto the continental slope.

A demarcation of the shoaling process is the "transition point." Before the transition point, the structure of the internal solitary wave will not change much, while after the transition point, the internal solitary wave reverse polarity or break due to mixing. In the two-layer ocean model, the transition point is defined as the position where the pycnocline is close to the mid-depth of water (Grimshaw et al., 2010). The pycnocline depth can be determined by the depth of the extrema of the buoyancy frequency (Liao et al., 2014). According to **Figure 1B**, the maximum buoyancy frequency is about 37 m deep, which is not within the observation range of the seismic section. According to the two-layer model theory, the depth of the "transition point" should be 74 m, so that the internal solitary wave observed has not yet reached the "transition point."

The seismic events show continuity over 20 km, which indicate that the stratification is stable. However, the seismic events near the seafloor have bifurcated and broken due to the interaction between the internal solitary wave and topography. According to the study of the vertical structure of the internal solitary wave (Geng et al., 2019), the maximum amplitude of the internal solitary wave is 70 m, which is located at a water depth of 100 m. As the water depth increases, the amplitude gradually decreases. According to Chen et al. (2019), the maximum amplitude of the mode-one internal solitary wave found near the Dongsha Atoll is 87 m, which is similar to the amplitude of the internal solitary wave. In addition, Ramp et al. (2004) observed many internal solitary waves in the east of Dongsha islands and they showed that the amplitude of the internal solitary waves ranged from 29 to 140 m. We conclude that seismic reflection data are a useful and accurate tool to observe the internal solitary wave amplitudes.

Waveform Evolution of the Internal Solitary Wave

Eight time-lapse images of the internal solitary wave are shown in **Figure 5**. Each image is of the same location, but separated by about 47 s (total observing time of 23 COGs is 18 min). It can be seen from the figure that the shape of waveform in shallow water changed more dramatically than that in deep water. As the offset increases, the reflections in shallow water gradually weaken at the leading edge. In the large offset COG migrated section, the shallow parts of reflection were cutoff due to the large stretching effect of NMO at these offsets, so that the events gradually became indistinct. Due to the fact that the increasing offset resulted in increasing frequency attenuation of seismic data (the raypath increasing), the events in the large offset COG migrated sections had become thicker.

To investigate the waveform evolution in more detail, we pick six seismic events from the eight COG migrated sections (**Figure 5**), which are shown in **Figure 6**. Those seismic events represent the waveforms at six different depths. As shown in **Figure 6A**, as the internal solitary wave moved rightward on the slope, its rear edge shallowed and its slope increased, while the leading edge gradually became flat and the slope decreased. The shape change of waveforms at the different depths is clearly different. In **Figures 6B–G**, the shape change of each waveform can be viewed, respectively. The first waveform (**Figure 6B**) was somewhat symmetrical in the first four frames of the image and changed significantly from the fifth frame. In frame 5, the depth of leading edge increased and the shape became flat. An abnormal reflection like "knotting" appeared in the trough. The trailing edge became shallower and the slope increased. Subsequently, in frame 6, the trailing edge continued to become shallower and there was a break in the trough, which resulted in

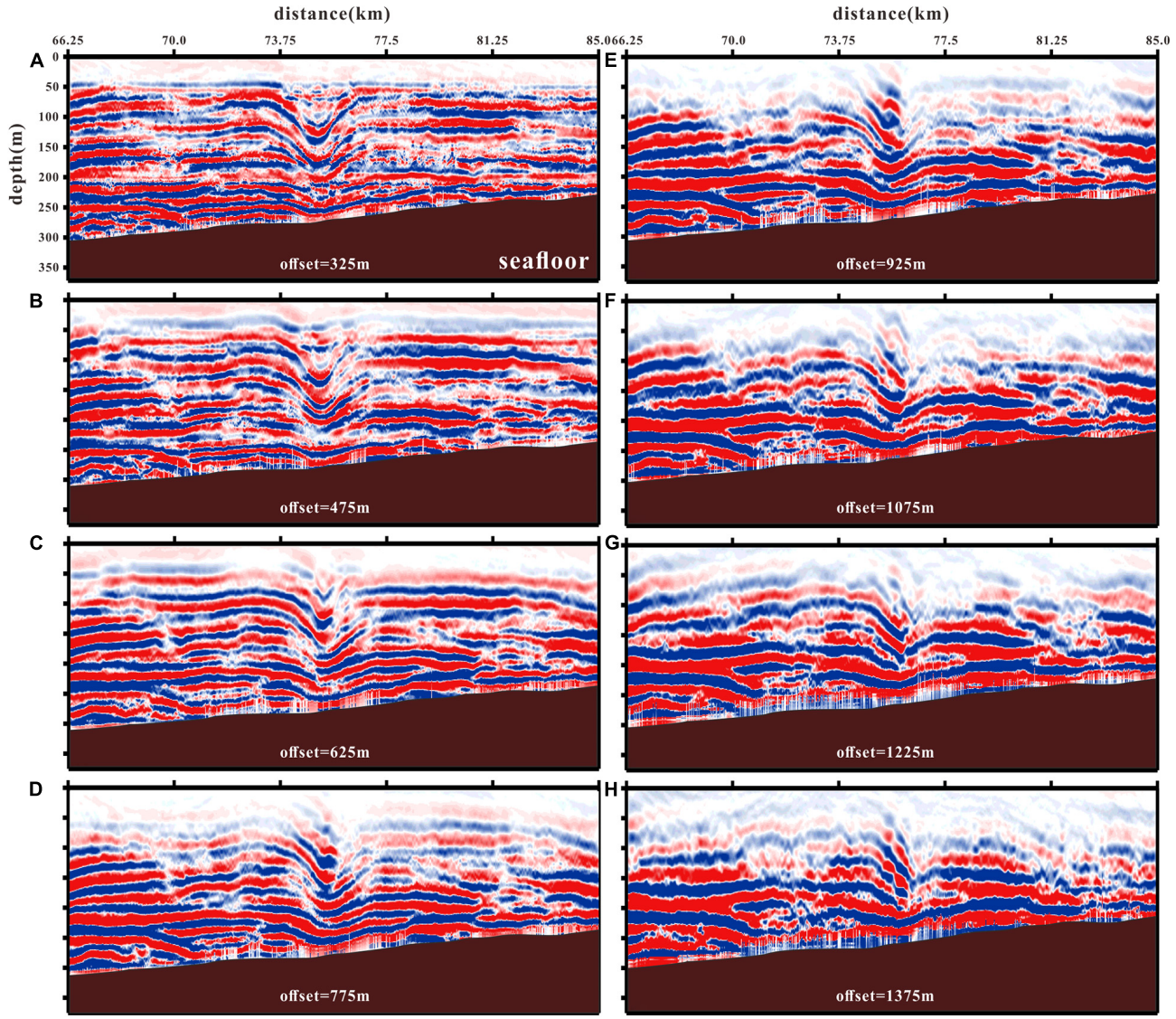

FIGURE 5 | (A–H) Common offset gather (COG) migrated sections with different offsets. For conciseness, only eight sections are shown out of 23 collected. The brown areas represent topography. Seismic section displayed in color and red events are traced to study the internal solitary wave waveforms.

leading edge reflection missing. The broken waveform in frame 7 was connected to the leading edge of the third waveform below and formed a complete new waveform again. There is no first waveform in the frame 8 image because it cannot be accurately identified in the corresponding COG migrated section. The second waveform (**Figure 6C**) is similar to the first one. The shape of waveform changed from a somewhat symmetrical shape to one with increasing trailing edge slope and decreasing leading edge slope. Eventually, the leading edge broke and the trailing edge connected to the third waveform. The third waveform (**Figure 6D**) maintained a good symmetry in frame 1 to frame 6 and the change started in frame 7. In frame 7, the waveform was broken and connected to the fourth waveform in frame 8. Except for breaking in frame 8, the fourth waveform (**Figure 6E**) remained intact in the rest of frames. This waveform is close to the seafloor and the phenomenon that trailing edge slope is larger than leading edge slope already appeared in the first frame. The fifth waveform (**Figure 6F**) and the sixth waveform (**Figure 6G**) did not change significantly and there was almost no change in the shape, except for the wave moving up-slope in all the eight frames.

Phase Velocities of Waveforms

We measured four parameters of the picked six waveforms in 23 COG migrated sections, which are phase velocity, amplitude, wavelength, and slopes of the leading and trailing edge. The data of the four parameters are shown in **Table 1**. The phase velocity is calculated by tracing the trough of seismic events in CMP-shot coordinates, which have been converted into distance-time coordinates (**Figure 7**). In this study, we traced the trough to

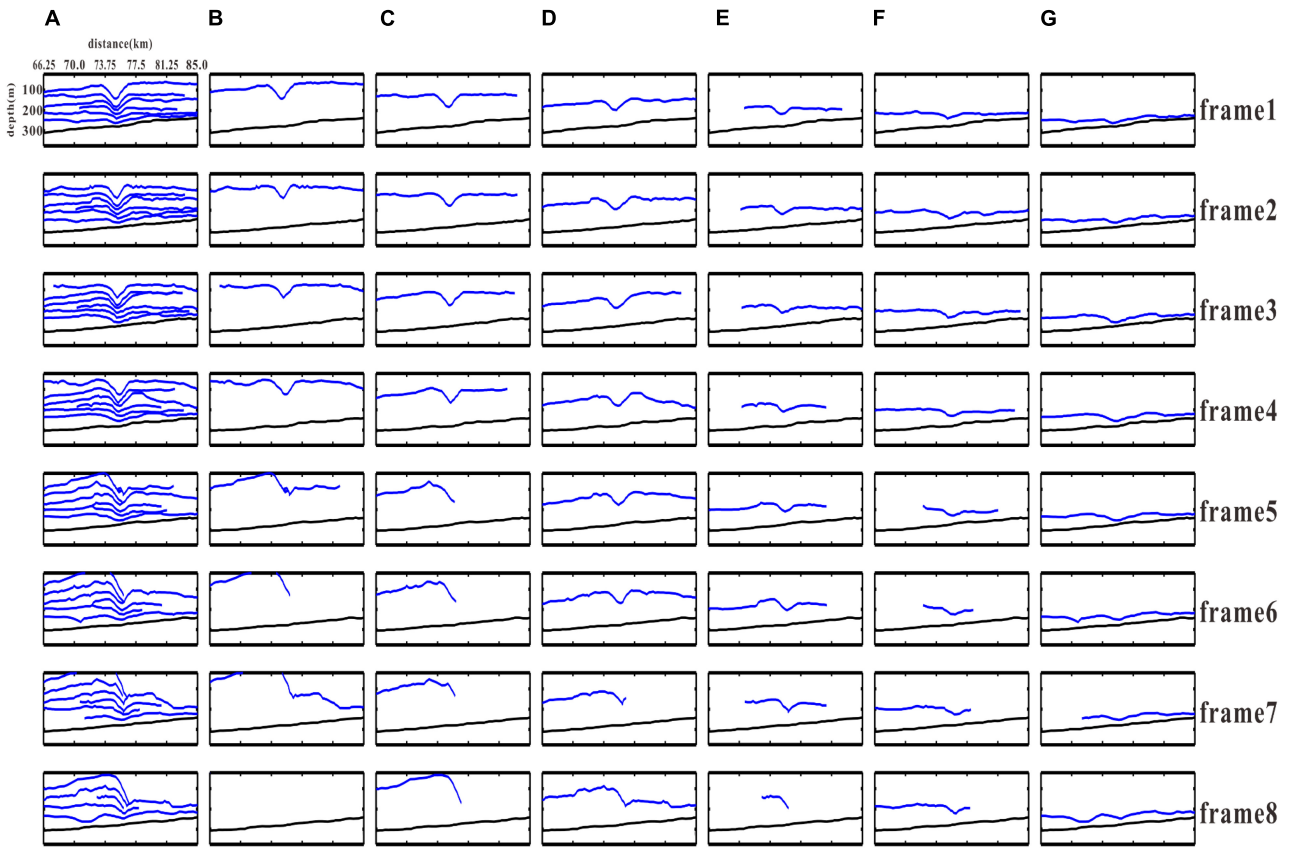

FIGURE 6 | Events (blue lines) picked from COG migrated sections showing the shape change of waveform. **(A)** Full six waveforms at different depths. **(B–G)** Separate display of the first to sixth waveform.

calculate the phase velocities of the six waveforms. It can be seen from the figure that the phase velocities of the six waveforms are different. The first waveform (**Figure 7A**) had two different motion regimes, i.e., there was an obvious acceleration in the range of 9–10 km and the phase velocity accelerated from 1.23 (± 0.05) to 2.38 m/s (± 0.55). This acceleration was caused by a large deformation after the waveform was broken. The second (**Figure 7B**) and the third waveform (**Figure 7C**) had the same situation, but their phase velocities were different. The phase velocity of the second waveform changed from 1.13 (± 0.05) to 2.44 m/s (± 0.57), while the phase velocity of the third waveform changed from 1.39 (± 0.06) to 2.07 m/s (± 0.55). The fourth (**Figure 7D**) and the fifth waveform (**Figure 7E**) did not show any obvious acceleration and their phase velocities were 1.66 m/s (±0.24) and 1.46 m/s (±0.13), respectively. The sixth waveform (**Figure 7F**) is unique and its phase velocity was reduced from 1.23 (±0.08) to 0.89 m/s (±0.03). Since the sixth waveform was closest to the seafloor, this deceleration might be caused by the friction between the seafloor and internal solitary wave. Comparing the phase velocities of each waveform, we show that the shallower the waveform depth, the more the phase velocity increases. The increase in phase velocity is related to the enhancement of non-linearity, so that the shallow waveform is more susceptible to non-linear effects. The phase velocity of the waveform near the seafloor decreases due to the interaction between the internal solitary waves and seafloor.

Amplitudes and Wavelength of Waveforms

Figure 8 shows a distribution diagram of amplitudes of the six waveforms. Since the leading edge gradually flattened when the internal solitary wave was shoaling, we defined the vertical distance between the trough and trailing edge as amplitude. It can be seen from the figure that the amplitudes decreased with the water depth increasing and this rule had been maintained during shoaling process of the internal solitary wave. As it is shown by the fitted straight line of amplitudes in **Figure 8**, the amplitude of each waveform gradually increased when the soliton was shoaling. Numerical simulation results show that the shoaling effect will cause the amplitude of the internal solitary waves to increase in the uphill topography (Cai et al., 2002; Cai and Xie, 2010), which is consistent with our observations. However, the growth rates of the six waveforms were different. As the water depth increased, the growth rate of amplitude gradually decreased.

We counted the wavelengths (apparent wavelengths) of the six waveforms, which are shown in **Figure 9**. It should be

TABLE 1 | The four parameters of the internal solitary wave calculated from seismic data.

	Amplitude (m)						Wavelength (km)						Leading edge slope						Trailing edge slope						Wave speed (m/s)					
	WF1	WF2	WF3	WF4	WF5	WF6	WF1	WF2	WF3	WF4	WF5	WF6	WF1	WF2	WF3	WF4	WF5	WF6	WF1	WF2	WF3	WF4	WF5	WF6	WF1	WF2	WF3	WF4	WF5	WF6
Frame1	64.46	61.32	46.38	35.38	23.58	14.94	3.41	3.41	3.69	2.66	2.99	3.11	−0.05	−0.04	−0.03	−0.02	−0.01	−0.01	0.04	0.03	0.02	0.03	0.02	0.01	1.23 ± 0.05	1.13 ± 0.05	1.39 ± 0.06	1.66 ± 0.24	1.46 ± 0.13	1.23 ± 0.08
Frame2	66.03	58.17	40.88	36.16	27.51	14.94	3.11	3.41	4.66	2.47	4.12	3.15	−0.06	−0.05	−0.02	−0.02	−0.01	−0.01	0.04	0.03	0.03	0.03	0.01	0.01	1.23 ± 0.05	1.13 ± 0.05	1.39 ± 0.06	1.66 ± 0.24	1.46 ± 0.13	1.23 ± 0.08
Frame3	58.96	58.96	51.10	35.38	34.59	18.08	3.25	3.72	4.42	2.94	4.00	3.86	−0.06	−0.04	−0.03	−0.03	−0.01	−0.01	0.05	0.03	0.03	0.02	0.02	0.01	1.23 ± 0.05	1.13 ± 0.05	1.39 ± 0.06	1.66 ± 0.24	1.46 ± 0.13	1.23 ± 0.08
Frame4	55.03	61.32	54.24	37.73	26.73	16.51	2.75	3.74	3.62	2.85	2.85	3.11	−0.05	−0.03	−0.03	−0.02	−0.02	−0.01	0.04	0.03	0.03	0.03	0.04	0.01	1.23 ± 0.05	1.13 ± 0.05	1.39 ± 0.06	1.66 ± 0.24	1.46 ± 0.13	1.23 ± 0.08
Frame5	55.03	62.10	41.66	37.73	26.73	14.94	2.33	3.69	3.58	2.82	3.20	3.36	−0.06	−0.04	−0.03	−0.02	−0.01	−0.01	0.05	0.04	0.99	0.03	0.02	0.01	1.23 ± 0.05	1.13 ± 0.05	1.39 ± 0.06	1.66 ± 0.24	1.46 ± 0.13	1.23 ± 0.08
Frame6	55.03	65.25	44.81	35.38	30.66	18.87	3.41	3.67	3.62	2.59	3.32	3.62	−2.53	−1.00	−0.03	−0.02	−0.02	−0.01	0.04	0.04	0.03	0.03	0.02	0.02	1.23 ± 0.05	1.13 ± 0.05	1.39 ± 0.06	1.66 ± 0.24	1.46 ± 0.13	1.23 ± 0.08
Frame7	57.39	65.25	44.81	38.52	33.80	23.58	3.74	3.67	3.60	3.60	3.55	3.13	−0.05	−0.04	−0.03	−0.01	−0.01	−0.01	0.04	0.28	0.03	0.03	0.03	0.02	1.23 ± 0.05	1.13 ± 0.05	1.39 ± 0.06	1.66 ± 0.24	1.46 ± 0.13	1.23 ± 0.08
Frame8	60.53	66.82	43.24	37.73	29.87	22.80	4.00	3.60	3.58	3.01	3.67	3.22	−0.03	−0.05	−0.04	−0.01	−0.47	−0.01	0.03	0.90	0.03	0.03	0.02	0.02	1.23 ± 0.05	1.13 ± 0.05	1.39 ± 0.06	1.66 ± 0.24	1.46 ± 0.13	1.23 ± 0.08
Frame9	56.60	69.18	45.60	37.73	29.09	23.58	3.46	3.60	3.48	3.25	3.13	3.06	−0.04	−0.03	−0.04	−0.01	−0.01	−0.01	0.04	0.04	0.03	0.03	0.02	0.02	1.23 ± 0.05	1.13 ± 0.05	1.39 ± 0.06	1.66 ± 0.24	1.46 ± 0.13	1.23 ± 0.08
Frame10	70.75	69.97	44.81	38.52	29.09	23.58	3.25	3.72	3.29	3.27	3.06	3.18	−0.05	−0.05	−0.03	−0.01	−0.01	−0.01	0.04	0.04	0.04	0.03	0.02	0.01	1.23 ± 0.05	1.13 ± 0.05	1.39 ± 0.06	1.66 ± 0.24	1.46 ± 0.13	1.23 ± 0.08
Frame11	81.76	72.32	46.38	38.52	27.51	23.58	3.93	3.53	3.34	2.49	2.99	3.20			−0.04	−0.01	−0.01	−0.01			0.03	0.04	0.02	0.02	1.23 ± 0.05	1.13 ± 0.05	1.39 ± 0.06	1.66 ± 0.24	1.46 ± 0.13	1.23 ± 0.08
Frame12	83.33	68.39	47.17	41.66	30.66	22.01	3.76	4.07	3.46	2.85	2.89	3.32			−0.04	−0.02	−0.01	−0.01			0.04	0.04	0.02	0.01	1.23 ± 0.05	1.13 ± 0.05	1.39 ± 0.06	1.66 ± 0.24	1.46 ± 0.13	1.23 ± 0.08
Frame13	100.62	79.40	49.53	39.31	27.51	20.44	3.79	3.74	3.32	2.92	2.85	3.15			−0.04	−0.02	−0.01	−0.01			0.04	0.03	0.02	0.01	2.38 ± 0.55	2.44 ± 0.57	1.39 ± 0.06	1.66 ± 0.24	1.46 ± 0.13	1.23 ± 0.08
Frame14		82.54	53.46	40.88	29.87	18.87		3.46	3.55	3.03	2.99	3.01			−0.04	−0.02	−0.01	−0.01			0.04	0.03	0.02	0.01	2.38 ± 0.55	2.44 ± 0.57	1.39 ± 0.06	1.66 ± 0.24	1.46 ± 0.13	1.23 ± 0.08
Frame15		89.62	53.46	37.73	32.23	18.87		3.22	3.27	3.27	2.99	3.11			−0.04	−0.02	−0.01	−0.01			0.03	0.04	0.02	0.01	2.38 ± 0.55	2.44 ± 0.57	1.39 ± 0.06	1.66 ± 0.24	1.46 ± 0.13	1.23 ± 0.08
Frame16		97.48	53.46	52.67	32.23	18.87		3.22	2.78	3.11	2.78	2.94			−0.04	−0.02	−0.01	−0.01			0.03	0.03	0.02	0.01	2.38 ± 0.55	2.44 ± 0.57	1.39 ± 0.06	1.66 ± 0.24	1.46 ± 0.13	1.23 ± 0.08
Frame17		98.27	47.95	55.03	29.87	16.51		3.65	3.11	2.89	2.63	3.06			−0.06	−0.02	−0.01	−0.01			0.03	0.04	0.02	0.01	2.38 ± 0.55	2.44 ± 0.57	1.39 ± 0.06	1.66 ± 0.24	1.46 ± 0.13	1.23 ± 0.08
Frame18		80.18	47.95	52.67	31.45	20.44		2.00	2.45	3.06	2.54	3.41			−0.03	−0.02	−0.01	−0.01			0.03	0.04	0.02	0.01	2.38 ± 0.55	2.44 ± 0.57	1.39 ± 0.06	1.66 ± 0.24	1.46 ± 0.13	0.89 ± 0.03
Frame19		81.76	51.88	55.03	29.09	18.08		1.65	2.87	2.87	2.61	3.36			−0.06	0.01	−0.01	−0.01			0.04	0.06	0.03	0.01	2.38 ± 0.55	2.44 ± 0.57	1.39 ± 0.06	1.66 ± 0.24	1.46 ± 0.13	0.89 ± 0.03
Frame20		84.90	84.90	57.39	32.23	18.87		2.21	2.75	2.85	2.38	3.13				−0.02	−0.01	−0.01				0.04	0.03	0.01	2.38 ± 0.55	2.44 ± 0.57	2.07 ± 0.55	1.66 ± 0.24	1.46 ± 0.13	0.89 ± 0.03
Frame21		91.98	77.04	55.81	34.59	19.65			2.49	2.71	3.20	3.51					−0.04	−0.01					0.02	0.01	2.38 ± 0.55	2.44 ± 0.57	2.07 ± 0.55	1.66 ± 0.24	1.46 ± 0.13	0.89 ± 0.03
Frame22			84.12	58.17	37.73	21.23			2.85	2.47	2.49	3.25					−0.02	−0.01					0.03	0.01	2.38 ± 0.55	2.44 ± 0.57	2.07 ± 0.55	1.66 ± 0.24	1.46 ± 0.13	0.89 ± 0.03
Frame23			85.69	70.75	36.16	22.01				2.28	2.16	3.53					−0.02	−0.01					0.02	0.01	2.38 ± 0.55	2.44 ± 0.57	2.07 ± 0.55	1.66 ± 0.24	1.46 ± 0.13	0.89 ± 0.03

WF represents waveform.

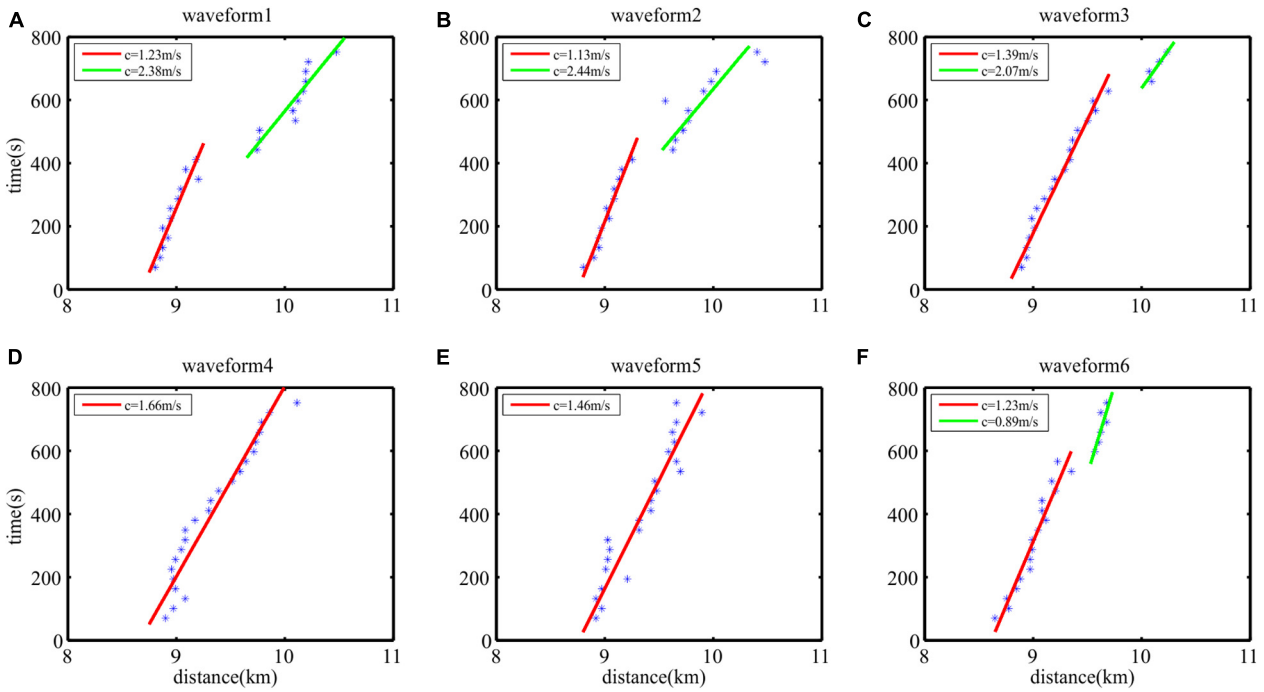

FIGURE 7 | Linear fitting in phase velocity calculation process of the six waveforms. **(A–F)** The blue asterisks indicate the trough of waveform. The red and green lines are fitting lines of blue asterisks. The common midpoint (CMP)-shot coordinates have been converted into the distance-time coordinates, so that the slope of fitting line is the phase velocity. The red and green lines are different fitting of asterisks, which indicate that the internal solitary waves travel in different phase velocity.

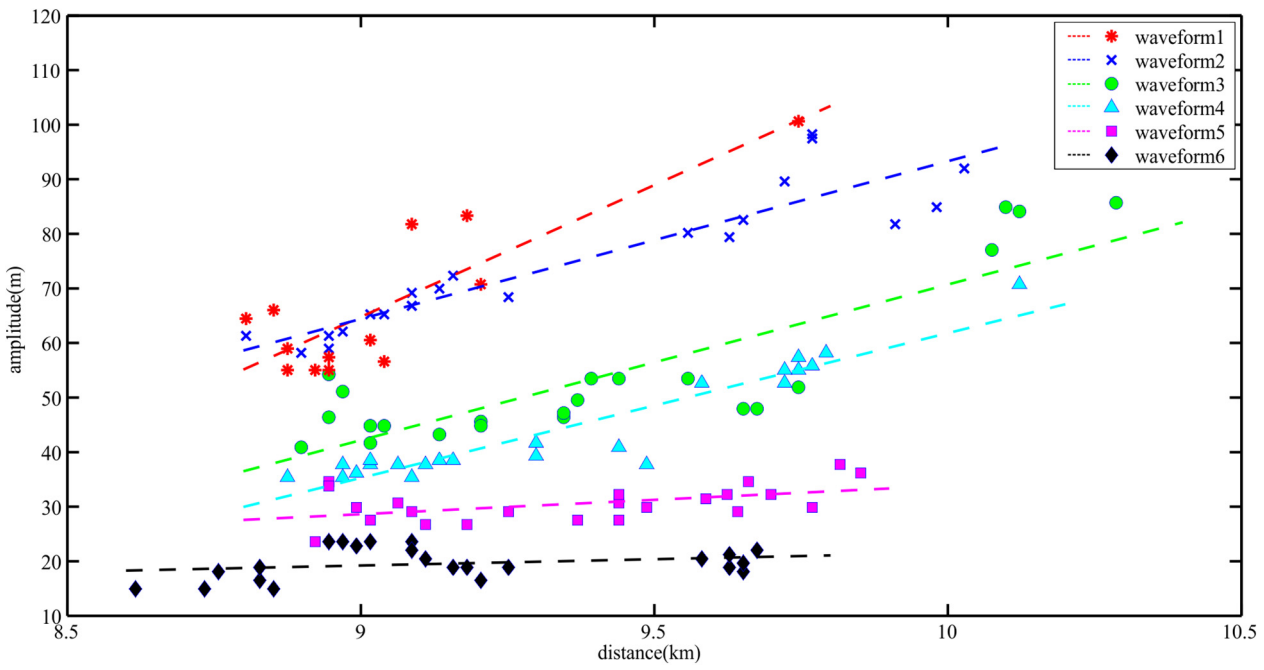

FIGURE 8 | The change in amplitudes of the six waveforms. The amplitudes picked from different waveform are shown by colored scatters. The lines are linear fitting of the marks with same color. The meaning of each colored mark is shown in the upper right legend. The internal solitary wave is moving forward along the X coordinate.

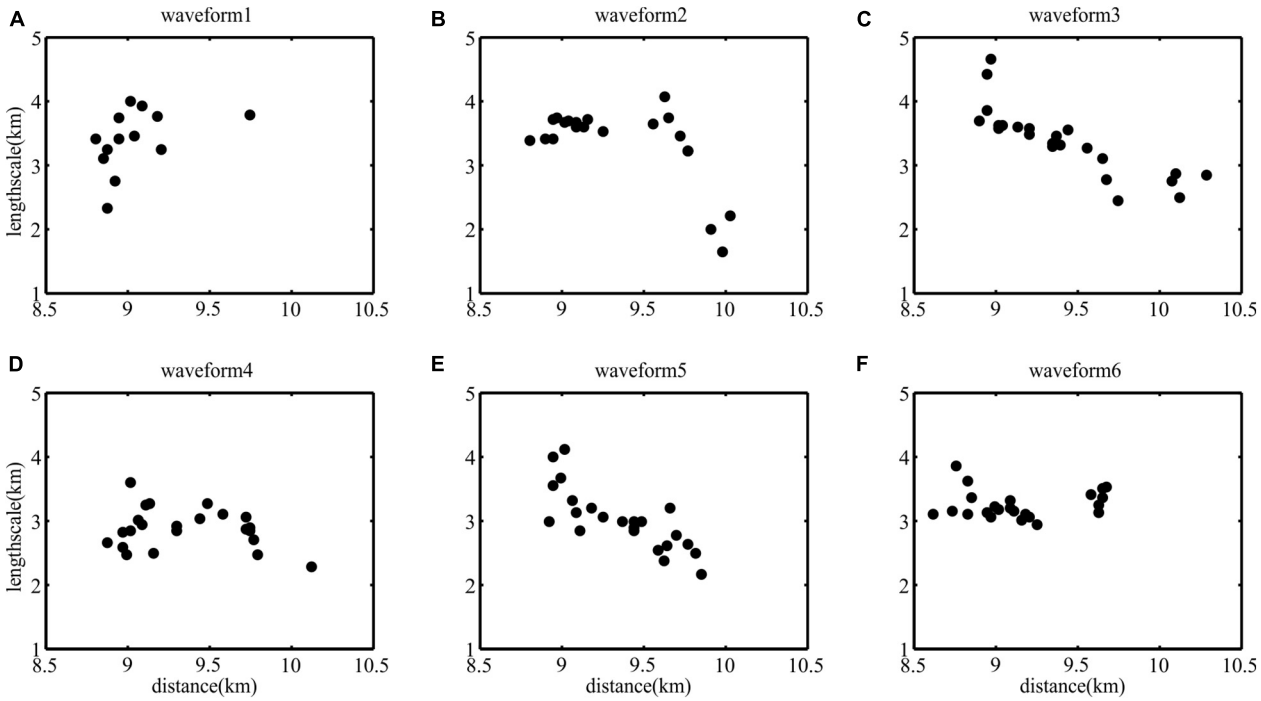

FIGURE 9 | The change in wavelength of the six waveforms. **(A–F)** The black dots are observed wavelength.

noted that the seismic data will be affected by the Doppler-like effect (Bai et al., 2017), so that there is an error between the wavelength picked from seismic section and the true wavelength. In this study, we only discuss the change of wavelength. Since the leading edge of the first and second waveforms in part of COG migrated sections are so flat that we cannot accurately calculate the wavelength, the sample points of the first and second waveforms are less than 23. In **Figure 9**, the changing trend of wavelength of the first waveform (**Figure 9A**) was not clear and the wavelength of the sixth waveform (**Figure 9F**) did not change much during shoaling process. The wavelengths of the remaining waveforms (**Figures 9B–E**) gradually decrease with the shoaling process, but their decreasing rates are different.

Leading and Trailing Edge Slopes of Waveforms

Figure 10 shows the slopes of the leading and trailing edge of the six waveforms. In the first waveform (**Figure 10A**), the slope of the leading edge gradually decreased and the slope of the trailing edge had no obvious changing trend. In the second waveform (**Figure 10**), the slope of the leading edge decreased and the slope of the trailing edge increased. In the third waveform (**Figure 10C**), the slopes of the leading and trailing edge increased simultaneously. In the fourth waveform (**Figure 10D**) and the fifth waveform (**Figure 10E**), the leading edge slope was almost unchanged and the trailing edge slope increased. In the sixth waveform (**Figure 10F**), the leading edge slope was almost unchanged and the trailing edge slope was slightly decreased. Comparing the slopes of the six waveforms, we show that the slopes of the leading and trailing edge gradually decreased as the water depth increased.

DISCUSSION

In this study, we have observed a first-mode depression internal solitary wave shoaling onto the continental slope by utilizing prestack seismic data. The shoaling process took place in the northern South China Sea near the Dongsha Atoll. From the shape of the waveform, it can be found that the internal solitary wave was still in the early stage of shoaling and had not reversed polarity. During shoaling, the slope of the leading edge decreased and the slope of the trailing edge increased. Each waveform in **Figure 6** has shown this behavior. This result is consistent with previous observations (Orr and Mignerey, 2003; Zhao et al., 2003; Bourgault et al., 2007; Shroyer et al., 2008; Fu et al., 2012) and the results of numerical simulation (Liu et al., 1998; Vlasenko and Stashchuk, 2007). In this study, we use seismic data to observe the internal solitary wave motion and use these observations to improve our understanding of their evolution.

Uniquely, seismic data allow us to visualize the evolution of thermohaline fine structure. Seismic data record an image of water column thermohaline differences (Ruddick et al., 2009) and the reflection events represent the interface of thermohaline differences. By analyzing the change of reflection events, we can understand how thermohaline structure evolves. In the seismic section, we picked six events at the different depths (**Figure 6A**), which represent the six waveforms of the internal solitary wave. Excluding the two near-seafloor internal solitary

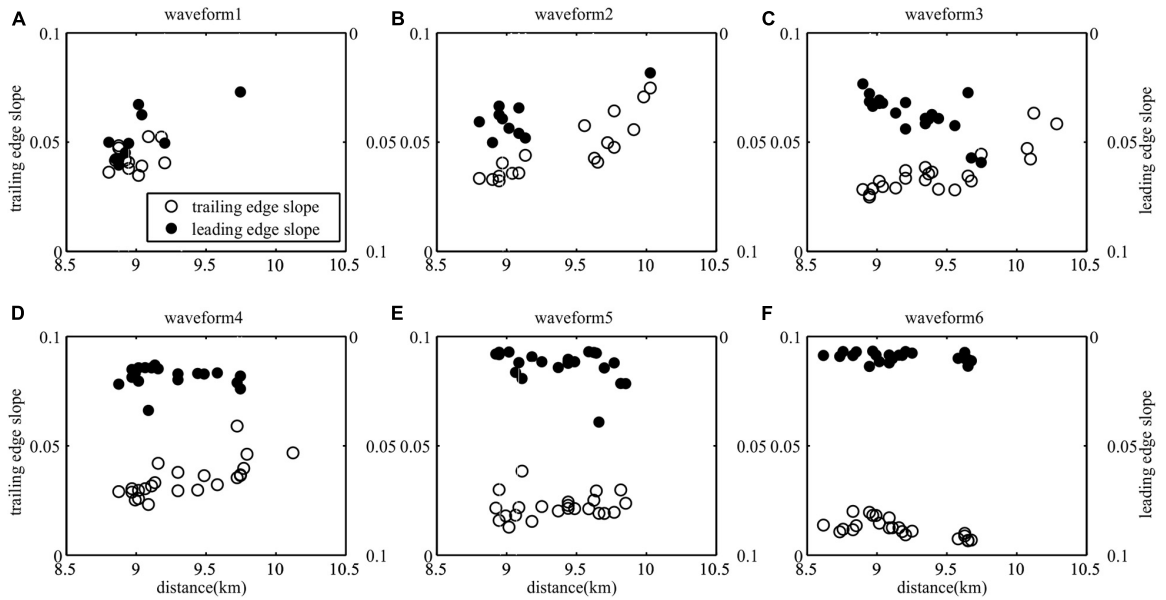

FIGURE 10 | The changes in the slope of the leading and trailing edge of the six waveforms. **(A–F)** The solid black dots represent the slope of the leading edge and the slope magnitude is shown in the right-hand side. The open dots represent the slope of the trailing edge and the slope magnitude is shown in the left-hand side.

waves, all the waveforms leading to edges broke, as they shoaled and we hypothesize that this change is related to instability, whereby mixing reduces the local temperature and salinity gradient causing the reflection event too weaken. This is shown as seismic events breaking in the seismic section. During shoaling process, the internal solitary waves could form vortices due to the instability (Aghsaee et al., 2010) or with trapped cores (Lamb, 2002), which promote mixing in the water column and changes to the thermohaline structure. In **Figure 6**, the first three waveforms broke and were connected to other waveforms below. This shows that the thermohaline differences of water column weakened or disappeared under the influence of instability, so that the interface of thermohaline difference no longer existed and was eventually replaced by other reflective interfaces. All the breaks appeared in the leading edge of the internal solitary wave, which indicate that the leading edge of the internal solitary wave is more unstable during shoaling. It can be seen from **Figure 6A** that the depth of the internal solitary wave leading edge gradually became deeper. This is similar to the phenomenon that the depth of bottom boundary of the mixed layer at the leading edge became deeper when the internal solitary waves was shoaling, which was observed by Orr and Mignerey (2003).

Our results show that the change of waveforms is different at different depths. During shoaling, the leading edge of the waveform becomes slower and the trailing edge becomes steeper. But, the waveforms at different depths do not change simultaneously. The waveform at deeper water changes earlier than that at shallower water. These observations develop out the understanding of the causes of the shape changes of waveform. The waveform changes are believed to be driven by topography, water depth, and background flow shear (Serebryanyi, 1990; Serebryany, 1996; Vlasenko and Hutter, 2002; Orr and Mignerey, 2003). Near-seafloor waveforms are mostly affected by topography. Shroyer et al. (2008) found that the shape change of waveform was due to a greater phase velocity at the leading edge than that of the trough and trailing edge. This shear causes the leading edge to broaden, while the trailing edge remains steep. This behavior explains near-seafloor waveform changes, since the trough of waveform will first contact the seafloor and decelerate, causing the leading edge to be faster than the trough. However, the waveforms in shallow water had the same shape change without contacting the topography. We speculate that the troughs of waveforms in shallow water were decelerated by viscous forces. Due to the greater amplitude of waveforms in shallow water, the trough is more susceptible to the resistance from deep stratification. Therefore, the phase velocity of trough will gradually become smaller than that of leading edge. In addition, the amplitude is related to the degree of change in the waveform. The amplitudes of shallow waveforms are greater than those in deeper water, while deep waveforms that are constrained by topography change less with time. In summary, topography is the main inducing factor of waveform evolution, while larger amplitudes cause the waveform changes more during shoaling.

Similarly, the changes in phase velocity, amplitude, wavelength, and the leading- and trailing-edge slope are different for each waveform. During shoaling, phase velocity and amplitude increase, wavelength decreases, and the slopes of the trailing edges become larger than the leading edges. Although the phase velocities of the fourth and fifth waveforms were approximately constant, it can be seen from their trajectories in the distance-time coordinates that the non-linearity is significant. These observations indicate that non-linear effects increase as the internal solitary waves shoal and are consistent with numerical simulations results that use the

Korteweg-de Vries (KdV) equations with higher-order non-linear terms (Liu et al., 1985; Liu, 1988; Grimshaw et al., 2004; Zhang and Fan, 2013). The high-order non-linear effect of the internal solitary wave observed is significant because of the large amplitudes of the waveforms. At the same time, changes in topography can also enhanced the non-linearity (Liu, 1988). The increasing non-linearity affects the internal solitary waves by increasing their amplitude and phase velocity, while decreasing their wavelengths. Shroyer et al. (2008) find a phase velocity change similar to ours. However, the initial amplitude of the wave is only 20 m, which is much smaller than the amplitude of the internal solitary wave observed and amplitude change is related to non-linearity. The amplitude of the weakly non-linear internal solitary wave increases after shoaling, but the amplitude of strongly non-linear internal wave decreases as shown by the numerical simulations (Small, 2001; Vlasenko et al., 2005) and observations (Rybak and Serebryanyi, 2011). However, the amplitude of strongly non-linear internal waves increases first at the initial stage of shoaling and then decreases rapidly. Our observations capture this process, which generally occurs in water depths of about 300 m (Small, 2001). On the other hand, Serebryany and Pao (2008) simulate a small-amplitude (14 m) internal solitary wave and show that its amplitude decreases during shoaling. Although the nonlinearity of small-amplitude internal solitary wave is weak, the shallow water depth (about 33 m) used in Serebryany and Pao's simulation makes the nonlinearity increase, the waveform cannot adjust gradually and changes rapidly. To summarize, our observations build upon the results of numerical simulations by showing that the interplay between non-linearity and topography plays a critical role in waveform evolution during shoaling.

CONCLUSION

We used seismic reflection surveying to observe a first-mode depression internal solitary wave in the South China Sea near the Dongsha Atoll. The internal solitary wave was located on the continental slope and propagated from east to west toward the shelf. The maximum amplitude of the internal solitary waves is about 70 m. In order to study the evolution process of the shoaling internal solitary wave, we improved the processing scheme of seismic data. We used COGs instead of CMP gathers to image the internal solitary wave, so as to obtain 23 COG migrated sections. We are able to use these time-lapse images of internal fine structure to map the evolution of the internal solitary waves.

Seismic sections show that internal reflection structure changes during shoaling. In shallow water, the waveforms break and were connected to other waveforms. We believe that this phenomenon results from instabilities that cause the thermohaline structure of the water column to change and leads to disappearance or weakening of seismic events.

Common offset gather sections show that waveform evolution varies with depth during shoaling. Six reflection events, with different depths, reveal that topography affects deeper waveforms earlier than shallower waveforms. The degree of waveform change is related to its amplitude. Furthermore, phase velocity, amplitude, wavelength, and the leading- and trailing-edge slope also vary as a function of depth. When the internal solitary wave shoals, its amplitude and phase velocity increase, wavelength decreases, and the slope of the leading edge decreases, while the slope of the trailing edge increases. Our observations are consistent with the numerical simulations and other observations, and our adapted seismic method has furthered our understanding of the internal solitary waves. This method also has potential for studying the evolution of other physical ocean phenomena.

DATA AVAILABILITY STATEMENT

The original contributions presented in the study are included in the article/supplementary material, further inquiries can be directed to the corresponding author/s.

AUTHOR CONTRIBUTIONS

HS contributed to the conceptualization, methodology, writing, reviewing, editing, and investigation of the manuscript. YGo contributed to the investigation and writing of the manuscript. SY and YGu contributed to the investigation, data curation, and validation of the manuscript. All authors contributed to the article and approved the submitted version.

FUNDING

This study was supported by the National Natural Science Foundation of China (Grant Numbers 41976048 and 91128205) and the National Key R&D Program of China (2018YFC0310000).

ACKNOWLEDGMENTS

We would like to thank the Guangzhou Marine Geological Survey for providing 2D seismic data. The bathymetry data were provided by the General Bathymetric Chart of the Oceans (GEBCOs) (http://www.gebco.net/). The reanalysis data were provided by the CMEMS (https://resources.marine.copernicus.eu/). We would like to thank the GEBCO and the CMEMS for supporting the data in this study. We would like to thank Seismic Unix (SU) and Generic Mapping Tool (GMT) for the software support for this study. We would also like to thank the Guest Editor and reviewers for their constructive reviews and comments on the manuscript.

REFERENCES

Aghsaee, P., Boegman, L., and Lamb, K. G. (2010). Breaking of shoaling internal solitary waves. *J. Fluid Mech.* 659, 289–317. doi: 10.1017/s002211201000248x

Alford, M. H., Peacock, T., MacKinnon, J. A., Nash, J. D., Buijsman, M. C., Centurioni, L. R., et al. (2015). The formation and fate of internal waves in the South China Sea. *Nature* 521, 65–69. doi: 10.1038/nature14399

Apel, J., Badiey, R. M., Chiu, C., Finette, S. S., Headrick, R., Kemp, J., et al. (1997). An overview of the 1995 SWARM shallow-water internal wave acoustic scattering experiment. *IEEE J. Oceanic Engin.* 22, 465–500. doi: 10.1109/48.611138

Bai, Y., Song, H., Guan, Y., and Yang, S. (2017). Estimating depth of polarity conversion of shoaling internal solitary waves in the northeastern South China Sea. *Continent. Shelf Res.* 143, 9–17. doi: 10.1016/j.csr.2017.05.014

Biescas, B., Armi, L., Sallarès, V., and Gràcia, E. (2010). Seismic imaging of staircase layers below the Mediterranean Undercurrent. *Deep Sea Res. Part I: Oceanogr. Res. Papers* 57, 1345–1353. doi: 10.1016/j.dsr.2010.07.001

Boegman, L., Ivey, G., and Imberger, J. (2005). The degeneration of internal waves in lakes with sloping topography. *Limnol. Oceanogr.* 50, 1620–1637. doi: 10.4319/lo.2005.50.5.1620

Boegman, L., and Stastna, M. (2019). Sediment resuspension and transport by internal solitary waves. *Annu. Rev. Fluid Mech.* 51, 129–154. doi: 10.1146/annurev-fluid-122316-045049

Bogucki, D. J., and Redekopp, L. G. (1999). A mechanism for sediment resuspension by internal solitary waves. *Geophys. Res. Lett.* 26, 1317–1320. doi: 10.1029/1999gl900234

Bourgault, D., Blokhina, M. D., Mirshak, R., and Kelley, D. E. (2007). Evolution of a shoaling internal solitary wavetrain. *Geophys. Res. Lett.* 34:L03601. doi: 10.1029/2006gl028462

Buffett, G. G., Biescas, B., Pelegrí, J. L., Machín, F., Sallarès, V., Carbonell, R., et al. (2009). Seismic reflection along the path of the Mediterranean Undercurrent. *Continent. Shelf Res.* 29, 1848–1860. doi: 10.1016/j.csr.2009.05.017

Cai, S., Gan, Z., and Long, X. (2002). Some characteristics and evolution of the internal soliton in the northern South China Sea. *Chinese Sci. Bull.* 47, 21–26. doi: 10.1360/02tb9004

Cai, S., and Xie, J. (2010). A propagation model for the internal solitary wavesin the northern South China Sea. *J. Geophys. Res. Oceans* 115:C12074. doi: 10.1029/2010JC006341

Cai, S., Xie, J., and He, J. (2012). An overview of internal solitary waves in the South China Sea. *Surveys Geophys.* 33, 927–943. doi: 10.1007/s10712-012-9176-0

Chen, L., Zheng, Q., Xiong, X., Yuan, Y., Xie, H., Guo, Y., et al. (2019). Dynamic and statistical features of internal solitarywaves on the continental slope in the Northern SouthChina Sea derived from mooring observations. *J. Geophys. Res. Oceans* 124, 4078–4097. doi: 10.1029/2018JC014843

Cheng, M.-H., and Hsu, J. R. C. (2010). Laboratory experiments on depression interfacial solitary waves over a trapezoidal obstacle with horizontal plateau. *Ocean Engin.* 37, 800–818. doi: 10.1016/j.oceaneng.2010.02.016

Dickinson, A., White, N. J., and Caulfield, C. P. (2020). Time-lapse acoustic imaging of mesoscale and fine-scale variability within the Faroe-Shetland Channel. *J. Geophys. Res. Oceans* 125:e2019JC015861. doi: 10.1029/2019JC015861

Fan, W., Song, H., Gong, Y., Sun, S., Zhang, K., Wu, D., et al. (2021). The shoaling mode-2 internal solitary waves in the Pacific coast of Central America investigated by marine seismic survey data. *Continent. Shelf Res.* 212:104318.

Fu, K.-H., Wang, Y.-H., St. Laurent, L., Simmons, H., and Wang, D.-P. (2012). Shoaling of large-amplitude nonlinear internal waves at The Dongsha Atoll in the northern South China Sea. *Continent. Shelf Res.* 37, 1–7. doi: 10.1016/j.csr.2012.01.010

Geli, L., Cosquer, E., Hobbs, R. W., Klaeschen, D., Papenberg, C., Thomas, Y., et al. (2009). High resolution seismic imaging of the ocean structure using a small volume airgun source array in the Gulf of Cadiz. *Geophys. Res. Lett.* 36:L00D09. doi: 10.1029/2009gl040820

Geng, M., Song, H., Guan, Y., and Bai, Y. (2019). Analyzing amplitudes of internal solitary waves in the northern South China Sea by use of seismic oceanography data. *Deep Sea Research Part I: Oceanogr. Res. Papers* 146, 1–10. doi: 10.1016/j.dsr.2019.02.005

Gong, Y., Song, H., Zhao, Z., Guan, Y., and Kuang, Y. (2021). On the vertical structure of internal solitary waves in the northeastern SouthChina Sea. *Deep Sea Research Part I: Oceanogr. Res. Papers* 173:103550. doi: 10.1016/j.dsr.2021.103550

Grimshaw, R., Pelinovsky, E., Talipova, T., and Kurkin, A. (2004). Simulation of the transformation of internal solitary waves on oceanic shelves. *J. Phys. Oceanogr.* 34, 2774–2791. doi: 10.1175/jpo2652.1

Grimshaw, R., Pelinovsky, E., Talipova, T., and Kurkina, O. (2010). Internal solitary waves: propagation, deformation and disintegration. *Nonlinear Process. Geophys.* 17, 633–649. doi: 10.5194/npg-17-633-2010

Gunn, K. L., White, N., and Caulfield, C. P. (2020). Time-lapse seismic imaging of oceanic fronts and transient lenses within South Atlantic Ocean. *J. Geophys. Res. Oceans* 125:e2020JC016293. doi: 10.1029/2020JC016293

Guo, C., and Chen, X. (2014). A review of internal solitary wave dynamics in the northern South China Sea. *Progress Oceanogr.* 121, 7–23. doi: 10.1016/j.pocean.2013.04.002

Haury, L. R., Wiebe, P. H., Orr, M. H., and Briscoe, M. G. (1983). Tidally generated high-frequency internal wave packets and their effects on plankton in Massachusetts Bay. *J. Mar. Res.* 41, 65–112. doi: 10.1357/002224083788223036

Holbrook, W. S., and Fer, I. (2005). Ocean internal wave spectra inferred from seismic reflection transects. *Geophys. Res. Lett.* 32:L15604. doi: 10.1029/2005GL023733

Holbrook, W. S., Páramo, P., Pearse, S., and Schmitt, R. W. (2003). Thermohaline fine structure in an oceanographic front from seismic reflection profiling. *Science* 301, 821–824. doi: 10.1126/science.1085116

Holloway, P., Pelinovsky, E. E., Talipova, T., and Barnes, B. (1997). A nonlinear model of internal tide transformation on the Australian North West Shelf. *J. Phys. Oceanogr.* 27, 871–896. doi: 10.1175/1520-048519970272.0.CO;2

Klymak, J. M., and Moum, J. N. (2003). Internal solitary waves of elevation advancing on a shoaling shelf. *Geophys. Res. Lett.* 30, OCE 3-1–OCE 1-4. doi: 10.1029/2003gl017706

Lamb, K. G. (1997). Particle transport by nonbreaking, solitary internal waves. *J. Geophys. Res. Oceans* 102, 18641–18660. doi: 10.1029/97jc00441

Lamb, K. G. (2002). A numerical investigation of solitary internal waves with trapped cores formed via shoaling. *J. Fluid Mech.* 451, 109–144. doi: 10.1017/s002211200100636x

Lamb, K. G. (2003). Shoaling solitary internal waves: on a criterion for the formation of waves with trapped cores. *J. Fluid Mech.* 478, 81–100. doi: 10.1017/s0022112002003269

Liao, G., Xu, X., Liang, C., Dong, C., Zhou, B., Ding, T., et al. (2014). Analysis of kinematic parameters of Internal Solitary Waves in the Northern South China Sea. *Deep Sea Res. Part I: Oceanogr. Res. Papers* 94, 159–172. doi: 10.1016/j.dsr.2014.10.002

Liu, A., Holbrook, K., and Apel, J. (1985). Nonliner internal wave evolution in the Sulu Sea. *J. Phys. Oceanogr.* 15, 1613–1624. doi: 10.1175/1520-048519850152.0.CO;2

Liu, A. K. (1988). Analysis of nonlinear internal waves in the New York Bight. *J. Geophys. Res.* 93:12317. doi: 10.1029/JC093iC10p12317

Liu, A. K., Chang, Y. S., Hsu, M.-K., and Liang, N. K. (1998). Evolution of nonlinear internal waves in the East and South China Seas. *J. Geophys. Res. Oceans* 103, 7995–8008. doi: 10.1029/97jc01918

Lynch, J. F., Ramp, S. R., Chiu, C. S., Tang, T. Y., Yang, Y. J., and Simmen, J. A. (2004). Research highlights from the Asian seas international acoustics experiment in the South China Sea. *IEEE J. Oceanic Engin.* 29, 1067–1074.

Magnell, B. (1976). Salt fingers observed in the Mediterranean Outflow region (34°N, 11°W) using a towed sensor. *J. Phys. Oceanogr.* 6, 511–523. doi: 10.1175/1520-04851976006<0511:sfoitm<2.0.co;2

Masunaga, E., Homma, H., Yamazaki, H., Fringer, O. B., Nagai, T., Kitade, Y., et al. (2015). Mixing and sediment resuspension associated with internal bores in a shallow bay. *Continent. Shelf Res.* 110, 85–99. doi: 10.1016/j.csr.2015.09.022

Moum, J. N., Farmer, D. M., Shroyer, E. L., Smyth, W. D., and Armi, L. (2007). Dissipative losses in nonlinear internal waves propagating across the continental shelf. *J. Phys. Oceanogr.* 37, 1989–1995. doi: 10.1175/jpo3091.1

Moum, J. N., Farmer, D. M., Smyth, W. D., Armi, L., and Vagle, S. (2003). Structure and generation of turbulence at interfaces strained by internal solitary waves propagating shoreward over the continental shelf. *J. Phys. Oceanogr.* 33, 2093–2112. doi: 10.1175/1520-04852003033<2093:SAGOTA<2.0.CO;2

Nandi, P., Holbrook, W. S., Pearse, S., Páramo, P., and Schmitt, R. W. (2004). Seismic reflection imaging of water mass boundaries in the Norwegian Sea. *Geophys. Res. Lett.* 31, 345–357. doi: 10.1029/2004GL021325

Orr, M. H., and Mignerey, P. C. (2003). Nonlinear internal waves in the South China Sea: Observation of the conversion of depression internal waves to elevation internal waves. *J. Geophys. Res.* 108:3064. doi: 10.1029/2001jc001163

Pinheiro, L. M., Song, H., Ruddick, B., Dubert, J., Ambar, I., Mustafa, K., et al. (2010). Detailed 2-D imaging of the Mediterranean outflow and meddies off W Iberia from multichannel seismic data. *J. Mar. Syst.* 79, 89–100. doi: 10.1016/j.jmarsys.2009.07.004

Ramp, S. R., Tang, T. Y., Duda, T. F., Lynch, J. F., Liu, A. K., Chiu, C.-S., et al. (2004). Internal solitons in the Northeastern South China SeaPart I: Sources and deep waterpropagation. *IEEE J. Oceanic Engin.* 29, 1157–1181. doi: 10.1109/JOE.2004.840839

Ruddick, B., Song, H., Dong, C., and Pinheiro, L. (2009). Water column seismic images as maps of temperature gradient. *Oceanography* 21, 192–205. doi: 10.5670/oceanog.2009.19

Rybak, S. A., and Serebryanyi, A. N. (2011). Nonlinear internal waves over the inclined bottom: observations with the use of an acoustic profiler. *Acoustical Phys.* 57, 77–82. doi: 10.1134/S1063771011010155

Sallarès, V., Biescas, B., Buffett, G., Carbonell, R., Dañobeitia, J. J., and Pelegrí, J. L. (2009). Relative contribution of temperature and salinity to ocean acoustic reflectivity. *Geophys. Res. Lett.* 36:L00D06. doi: 10.1029/2009gl040187

Sallarès, V., Mojica, J. F., Biescas, B., Klaeschen, D., and Gràcia, E. (2016). Characterization of the submesoscale energy cascade in the Alboran Sea thermocline from spectral analysis of high-resolution MCS data. *Geophys. Res. Lett.* 43, 6461–6468. doi: 10.1002/2016GL069782

Scotti, A., and Pineda, J. (2004). Observation of very large and steep internal waves of elevation near the Massachusetts coast. *Geophys. Res. Lett.* 31:L22307. doi: 10.1029/2004gl021052

Serebryany, A. N. (1996). Steepening of the leading and back faces of solitary internal waves depressions and its connections with tidal currents. *Dynamics Atmos. Oceans* 23, 2075–2091. doi: 10.1016/0377-0265(95)00427-0

Serebryany, A. N., and Pao, H. P. (2008). Transition of a nonlinear internal wave through an overturning point on a shelf. *Doklady Earth Sci.* 420, 714–718. doi: 10.1134/S1028334X08040430

Serebryanyi, A. N. (1990). Internal wave effects of nonlinearity at the shelf. Izvestia Akademii nauk SSSR. *Fizika Atmosfery i Okeana* 26, 285–293.

Sheen, K. L., White, N. J., Caulfield, C. P., and Hobbs, R. W. (2012). Seismic imaging of a large horizontal vortex at abyssal depths beneath the Sub-Antarctic Front. *Nature Geosci.* 5, 542–546. doi: 10.1038/ngeo1502

Shroyer, E. L., Moum, J. N., and Nash, J. D. (2008). Observations of polarity reversal in shoaling nonlinear internal waves. *J. Phys. Oceanogr.* 39, 691–701. doi: 10.1175/2008JPO3953.1

Small, J. (2001). A nonlinear model of the shoaling and refraction of internal solitary waves in the ocean. Part I: development of the model and investigations of the shoaling effect. *J. Phys. Oceanogr.* 31, 3163–3183. doi: 10.1175/1520-04852001031<3163:ANMOTS<2.0.CO;2

Tang, Q., Gulick, S. P. S., Sun, J., Sun, L., and Jing, Z. (2020). Submesoscale features and turbulent mixing of an oblique anticyclonic eddy in the Gulf of Alaska investigated by marine seismic survey data. *J. Geophys. Res. Oceans* 125:e2019JC015393. doi: 10.1029/2019jc015393

Tang, Q., Hobbs, R., Wang, D., Sun, L., Zheng, C., Li, J., et al. (2015). Marine seismic observation of internal solitary wave packets in the northeast South China Sea. *J. Geophys. Res. Oceans* 120, 8487–8503. doi: 10.1002/2015jc011362

Tsuji, T., Noguchi, T., Niino, H., Matsuoka, T., Nakamura, Y., Tokuyama, H., et al. (2005). Two-dimensional mapping of fine structures in the Kuroshio Current using seismic reflection data. *Geophys. Res. Lett.* 32:L14609. doi: 10.1029/2005gl023095

Vlasenko, V., Brandt, P., and Rubino, A. (2000). Structure of large-amplitude internal solitary waves. *J. Phys. Oceanogr.* 30, 2172–2185. doi: 10.1175/1520-04852000030<2172:SOLAIS<2.0.CO;2

Vlasenko, V., and Hutter, K. (2002). Numerical experiments on the breaking of solitary internal waves over a slope–shelf topography. *J. Phys. Oceanogr.* 32, 1779–1793. doi: 10.1175/1520-04852002032<1779:NEOTBO<2.0.CO;2

Vlasenko, V., Ostrovsky, L., and Hutter, K. (2005). Adiabatic behavior of strongly nonlinear internal solitary waves in slope shelf areas. *J. Geophys. Res.* 110:C04006. doi: 10.1029/2004JC002705

Vlasenko, V., and Stashchuk, N. (2007). Three-dimensional shoaling of large-amplitude internal waves. *J. Geophys. Res.* 112:C11018. doi: 10.1029/2007jc004107

Wunsch, C., and Ferrari, R. (2004). Vertical mixing, energy, and the general circulation of the oceans. *Annu. Rev. Fluid Mech.* 36, 281–314. doi: 10.1146/annurev.fluid.36.050802.122121

Yilmaz, Ö (2001). Seismic data analysis: Processing, inversion, and interpretation of seismic data. *Soc. Explorat. Geophys.* 10:2092. doi: 10.1190/1.9781560801580

Zhang, S.-W., and Fan, Z.-S. (2013). Effects of high-order nonlinearity and rotation on the fission of internal solitary waves in the South China Sea. *J. Hydrodyn.* 25, 226–235. doi: 10.1016/s1001-6058(13)60357-1

Zhao, Z., Klemas,V., Zheng, Q., Li, X. and Yan, X. H. (2003). Satellite observation of internal solitary waves converting polarity. *Geophys. Res. Lett.* 30:1988. doi: 10.1029/2003gl018286

Zhao, Z., Klemas, V., Zheng, Q., and Yan, X.-H. (2004). Remote sensing evidence for baroclinic tide origin of internal solitary waves in the northeastern South China Sea. *Geophys. Res. Lett.* 31:L06302. doi: 10.1029/2003gl019077

Zheng, Q., Susanto, R. D., Ho, C.-R., Song, Y. T., and Xu, Q. (2007). Statistical and dynamical analyses of generation mechanisms of solitary internal waves in the northern South China Sea. *J. Geophys. Res.* 112:C03021. doi: 10.1029/2006jc003551

Zou, Z., Rad, P. B., Macelloni, L., and Zhang, L. (2021). Temporal and spatial variations in three-dimensional seismic oceanography. *Ocean Sci.* 17, 1053–1066. doi: 10.5194/os-17-1053-2021

Conflict of Interest: The authors declare that the research was conducted in the absence of any commercial or financial relationships that could be construed as a potential conflict of interest.

Publisher's Note: All claims expressed in this article are solely those of the authors and do not necessarily represent those of their affiliated organizations, or those of the publisher, the editors and the reviewers. Any product that may be evaluated in this article, or claim that may be made by its manufacturer, is not guaranteed or endorsed by the publisher.

frontiers in Marine Science

ORIGINAL RESEARCH
published: 25 November 2021
doi: 10.3389/fmars.2021.734075

Internal Solitary Waves Observed on the Continental Shelf in the Northern South China Sea From Acoustic Backscatter Data

Yingci Feng[1,2], Qunshu Tang[1,2], Jian Li[1,2]*, Jie Sun[1,2] and Wenhuan Zhan[1,2]*

[1] Key Laboratory of Ocean and Marginal Sea Geology, South China Sea Institute of Oceanology, Innovation Academy of South China Sea Ecology and Environmental Engineering, Chinese Academy of Sciences, Guangzhou, China, [2] Southern Marine Science and Engineering Guangdong Laboratory (Guangzhou), Guangzhou, China

Internal solitary waves (ISWs) are investigated offshore of Guangdong in the northern South China Sea (SCS) using high-frequency acoustic backscatter data of 100 kHz acquired in July 2020. Simultaneous XBT profiles and satellite images are incorporated to understand their propagation, evolution, and dissipation processes in shallow water at depths less than 50 m. The water column structures revealed by acoustic backscatter data and XBT profiles are consistent with a small difference of less than 3 m. A soliton train with apparent vertical and horizontal scales of ∼7 and 100 m, respectively, is captured three times in 20 h in the repeated acoustic sections, which provides spatiotemporal constraints to the solitons. The characteristics of ISW phase speeds are estimated from acoustic backscatter data and satellite data and using theoretical two-layer Korteweg-de Vries (KdV) and extended KdV (eKdV) models. The acoustically observed phase speed of ISWs is approximately 0.4–0.5 m/s, in agreement with the estimates from both satellite data and model results. The shallow solar-heated water in summer (∼10–20 m) lying on the bottom cold water is responsible for the extensive occurrence of ISWs in the study region. ISWs are dissipated at the transition zone between the heated surface water and the upwelled water, forming a wide ISW dissipation zone in the coastal area, as observed from satellites. The acoustic backscatter method could be an effective way to observe ISWs with high resolution in shallow water and thus a potential compensatory technique for imaging the shallow blind zone of so-called seismic oceanography.

Keywords: internal solitary waves, propagation, acoustic backscatter data, shallow water, northern South China Sea

OPEN ACCESS

Edited by:
Joanna Staneva,
Institute of Coastal Systems
Helmholtz Centre Hereon, Germany

Reviewed by:
SungHyun Nam,
Seoul National University,
South Korea
Yonggang Jia,
Ocean University of China, China
DX Wang,
Sun Yat-sen University, China

***Correspondence:**
Qunshu Tang
tqsh@scsio.ac.cn
Jian Li
jianli@scsio.ac.cn

Specialty section:
This article was submitted to Ocean Observation, a section of the journal Frontiers in Marine Science

Received: *30 June 2021*
Accepted: *05 November 2021*
Published: *25 November 2021*

Citation:
Feng Y, Tang Q, Li J, Sun J and Zhan W (2021) Internal Solitary Waves Observed on the Continental Shelf in the Northern South China Sea From Acoustic Backscatter Data. Front. Mar. Sci. 8:734075. doi: 10.3389/fmars.2021.734075

INTRODUCTION

The northeastern South China Sea (SCS) is reportedly one of the strongest occurrence sites of internal solitary waves (ISWs) with vertical amplitudes over 200 m (e.g., Ramp et al., 2004; Helfrich and Melville, 2006; Buijsman et al., 2010; Guo and Chen, 2014; Alford et al., 2015). ISWs are generated by the interaction between the strong tidal currents and abrupt topography in the Luzon Strait. Their propagation and evolution processes, including transmission in the deep basin,

waveform steepening and disintegration across the continental slope, polarity conversion, and ultimately dissipation over the broad continental shelf, are spatiotemporally complex due to the variable ISW governing factors of stratification, currents, fronts, eddies, and topography (e.g., Cai et al., 2002; Yuan et al., 2006; Farmer et al., 2009; Buijsman et al., 2010). Satellite images show that these non-linear internal waves can propagate from the deep sea basin into coastal regions with water depths less than 50 m in the northern SCS (Zhao et al., 2004; Li et al., 2011). Most previous studies of ISWs have focused on internal wave propagation across the SCS and their interactions with the continental shelf at water depths greater than 100 m (Cai et al., 2012; Guo and Chen, 2014; Alford et al., 2015), while ISWs in the northern coastal region, where ISWs undergo polarity conversion, wave breaking, and dissipation, are seldom reported primarily because internal solitons with limited wave amplitudes are not easy to observe hydrographically.

Echosounder recording acoustic backscatter signals with frequencies higher than 10 kHz can be used to remotely map internal waves (Farmer and Armi, 1999; Orr and Mignerey, 2003; Reeder et al., 2011). This equipment transmits and receives high-frequency signals through its transducers and thus detects scattered signals responding to gradients in oxygen, light, temperature, salinity, and physical oceanographic conditions from the water below the transducers (Boswell et al., 2020). Its spatial resolution is approximately 10 cm. This sort of equipment has been used to observe a variety of ocean phenomena, including internal waves, turbulence, sediment resuspension, biomass spatial distribution, and biomigration, in various ocean environments (e.g., Trevorrow, 1998; Orr and Mignerey, 2003; Reeder et al., 2011; Masunaga et al., 2015; Klevjer et al., 2016, 2020; Cascão et al., 2017).

The ISWs in the shallow coastal region generally propagate perpendicular to the isobaths (Fu et al., 2012; Alford et al., 2015). Polarity reversal of ISWs occurs when the ratio of the upper mixed and lower layers of the water column reaches the turning point along the wave propagation pathway (Shroyer et al., 2009; Reeder et al., 2011). As the depth of mixed layers varies seasonally, both elevation waves and depression waves could occur in the same shoaling regions (Cai et al., 2012). The evolution of an ISW with an asymmetric waveform on a continental shelf mainly goes through four stages (Vlasenko and Hutter, 2002; Chang et al., 2021): (1) the frontal edge becomes more gently sloping while the rear edge becomes steeper; (2) overturning of the rear edge leads to heavy bottom fluid over light fluid; (3) the heavier fluid from the rear edge plunges into the wave core; and (4) heavier fluid in the wave core forms an enclosed isopycnal region. Strong water motion by ISWs can enhance bottom-boundary turbulence, water exchange in coastal areas, and surface phytoplankton primary productivity (van Haren et al., 2012; Shishkina et al., 2013; Alford et al., 2015; Masunaga et al., 2017; Jia et al., 2019). However, the spatiotemporal propagation and dissipation of a specific ISW in coastal areas are seldom reported.

In this study, we analyze ISWs in the shallow water offshore Guangdong Province using acoustic backscatter data collected in July 2020, combined with satellite images and *in situ* hydrographic observations (**Figure 1**). The main topics in this paper are organized as follows: first, the acoustic backscatter data are processed, and the images with ISWs are shown; second, the characteristics of the ISWs are derived from the acoustic backscatter data, simultaneous satellite images, and theoretical two-layer Korteweg-de Vries (KdV) and extended KdV (eKdV) models; and third, the possible generation and propagation processes of the ISWs are investigated from the joint interpretation of the acoustic backscatter data, satellite images, and hydrographic observations. This study improves our understanding of internal wave generation, propagation, evolution, dissipation, and its contributions to ocean mixing, sediment resuspension, and biological processes.

MATERIALS AND METHODS

Acoustic Backscatter Data Acquisition and Processing

In the shallow water offshore Guangdong Province (**Figure 1**), approximately 3100 km acoustic backscatter data were collected in July 2020 using an Innomar SES2000 Light parametric sub-bottom profiler, with primary frequency (approximately 100 kHz) and ping rate (up to 50 pings/s). The draft (source depth) of the transducer was 2 m. In this study, we focused on the four easternmost lines with a NW-SE direction (L1–L4; **Figures 1**, **2**) to study the spatiotemporal evolution of the ISWs on the continental shelf. These lines captured a soliton train three times in 20 h repeatedly (**Figure 2**).

Innomar ISE software (Innomar Technologies GmbH) was used to process the acoustic backscatter data. The acoustic image processing flow was (1) envelope algorithm imaging; (2) noise attenuation by median filter; and (3) time-depth conversion assuming an averaged sound speed of 1500 m/s.

Satellite Imagery

Optical satellite images, such as Moderate Resolution Imaging Spectroradiometer (MODIS) and Visible Infrared Imaging Radiometer Suite (VIIRS) images, are widely used in ISW studies (Li et al., 2013; Tang et al., 2014, 2015, 2018). True color satellite images with a spatial resolution of 250 m are available from the website.[1] In this study, the data from MODIS and VIIRS sensors on NASA spacecraft (Terra, Aqua, NOAA-20, and Suomi) were used to image the sea surface signature induced by ISWs (**Figures 3**, **4**). Benefitting from the good weather conditions on July 18 and 19, 2020, the ISWs in the shallow water region were clearly imaged by three satellite datasets. The mean wave propagation speeds and directions can be measured from the spatiotemporal variations in the satellite images and acoustic backscatter data (**Figures 3**, **4**).

Hydrographic Data

During the cruise, two XBTs were deployed simultaneously along the survey lines on July 9th at 13:24 and July 10th at 20:25 UTC (**Figures 1**, **5**). The *in situ* XBT data, less than 50 km away from

[1] worldview.earthdata.nasa.gov

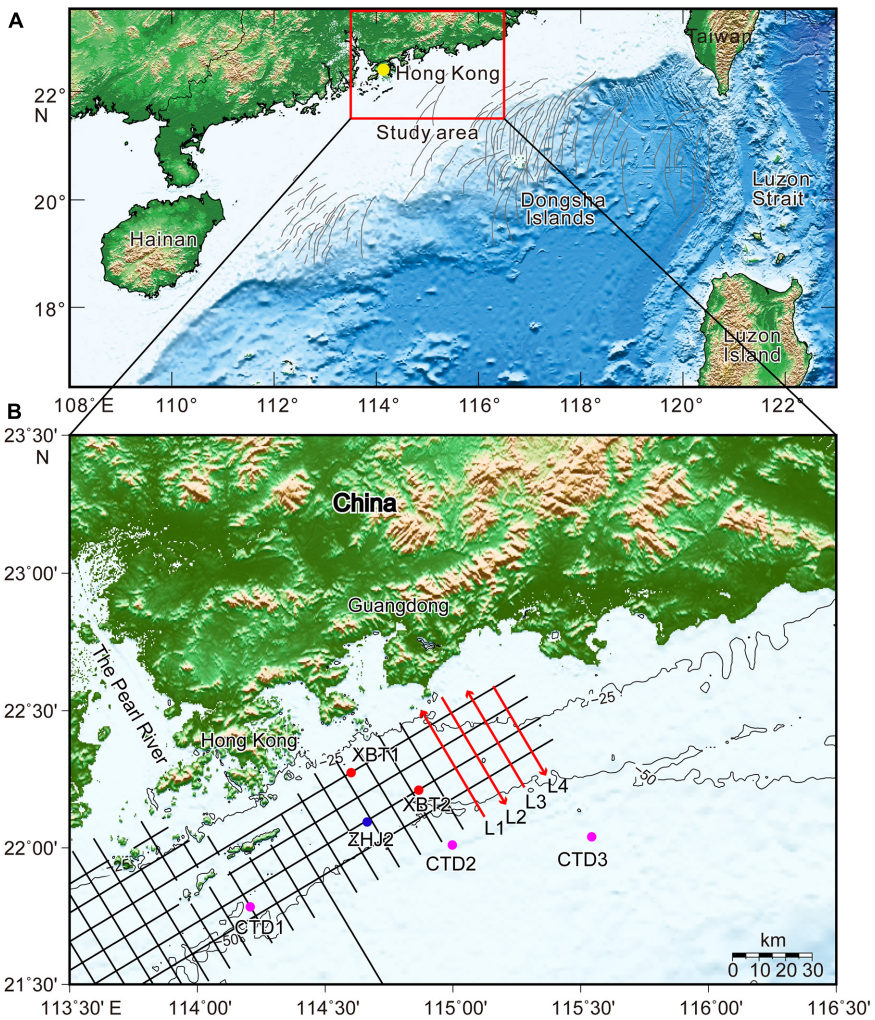

FIGURE 1 | Bathymetry of the northern South China Sea **(A)** and shallow water offshore of Guangdong **(B)**. Gray curves are the satellite-imaged ISWs modified from Zhao et al. (2004) and Li et al. (2011). The black and red lines denote the acoustic backscatter survey lines acquired in July 2020. The red arrows indicate the directions of the survey lines. The solid circles show the locations of two XBT sites (red), CTD stations (magenta, Chen et al., 2017), and taut-line mooring station ZHJ2 (blue, Lee et al., 2021).

the four acoustic backscatter survey lines (L1, L2, L3, and L4), could be used as the background temperature structure in the study area in early summer (**Figure 5**).

Depth profiles of temperature and salinity from three CTD stations were collected from July 27th to August 16th, 2009 (**Figures 6A,B**; Chen et al., 2017). These historical temperature and salinity data reveal that the water structure can be simplified as a two-layer structure according to the depth of the mixed layer in the study region (**Figure 6**). Therefore, two-layer structures are finally composited for theoretical KdV and eKdV model calculations and result validation for corresponding ISWs.

Sea surface temperature (SST) images used in this study were derived from the Group for High Resolution Sea Surface Temperature (GHRSST) data, which are available from the NOAA website.[2] The daily GHRSST data are satellite-composite products by the Jet Propulsion Laboratory (JPL) with a spatial resolution of 1 km derived from the Advanced Microwave Scanning Radiometer (AMSRE), MODIS, WindSat, Advanced Very High Resolution Radiometer (AVHRR), and *in situ* observation data.

Theoretical Two-Layer Model of Korteweg-de Vries and Extended KdV Equations

In the continental shelf of this study region (shallower than 300 m), the water column stratification can often be simplified as a two-layer structure according to the density structure (**Figure 6**). Therefore, we can use a two-layer model to calculate the non-linear phase velocity and the characteristic half-width of ISWs in the study area (Ostrovsky and Stepanyants, 1989). An internal soliton propagation process in continuous

[2]www.ncei.noaa.gov

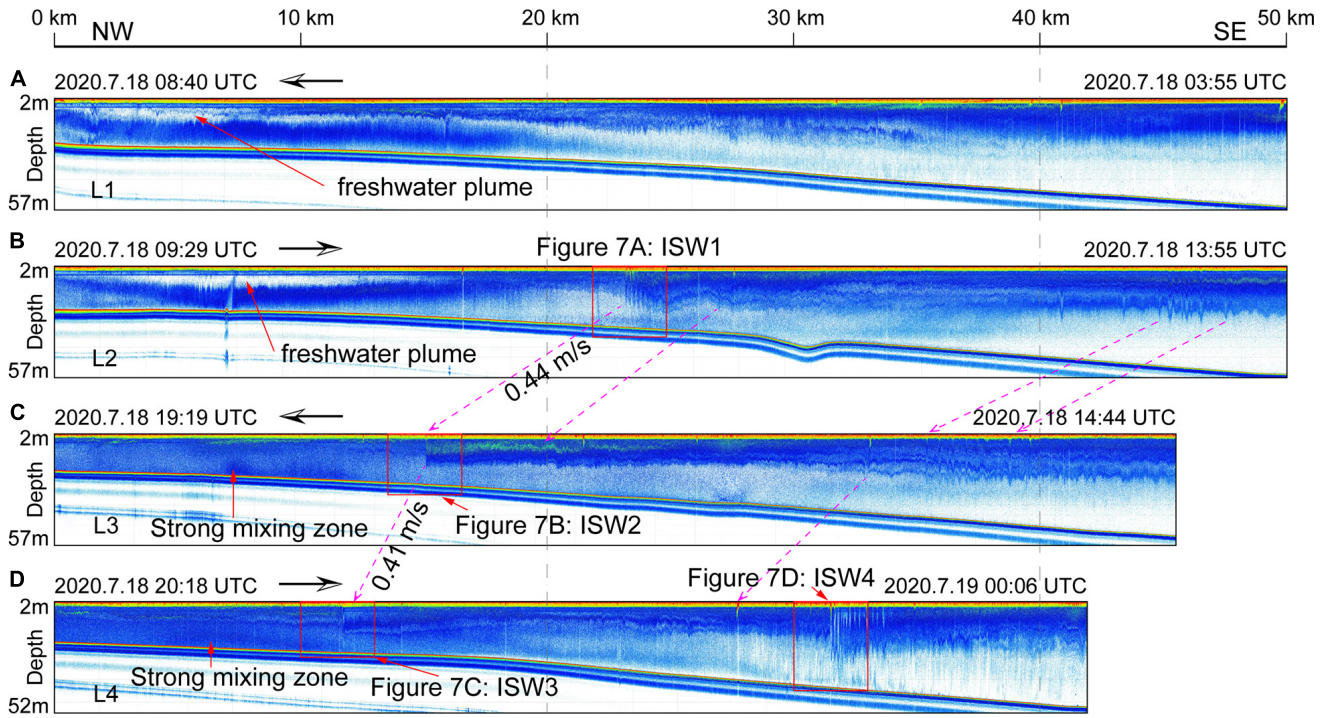

FIGURE 2 | Acoustic backscatter images of ISWs show the fine structure of the water column along the survey lines of L1 **(A)**, L2 **(B)**, L3 **(C)**, and L4 **(D)** in **Figure 1**. The survey times and directions are marked by notes and black lines with arrows. Magenta dashed lines with arrows indicate that the same wave crests acquired more than once in different backscatter images, and the mean phase velocities between ISW1, ISW2, and ISW3 are marked. Note that a soliton train (ISW1, ISW2, and ISW3), with apparent vertical and horizontal scales of ∼7 and 100 m, respectively, was captured up to three times within 20 h.

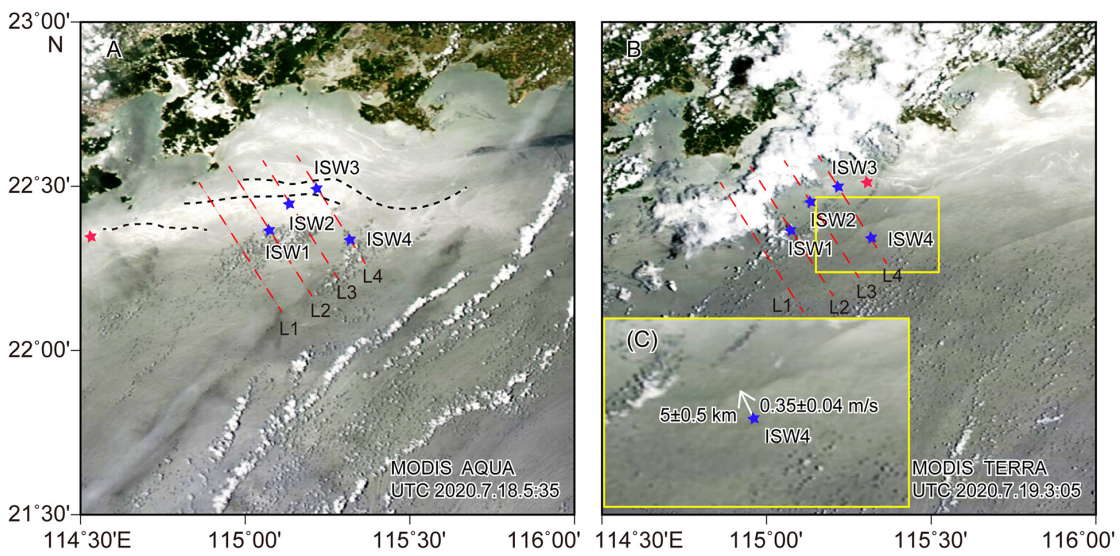

FIGURE 3 | Moderate Resolution Imaging Spectroradiometer images of the ISWs acquired by NASA Aqua **(A)** and Terra satellites **(B)** at 05:35 UTC on July 18, 2020 and 03:05 UTC on July 19, 2020. The yellow border illustration **(C)** is a partial enlargement of panel **(B)**. Red dashed lines are the acoustic backscatter survey lines of L1, L2, L3, and L4, and solid blue pentagrams show ISW positions identified from the backscatter images. The black dashed curves in panel **(A)** indicate the wave crest of ISWs with large displacement in the study area. Red solid pentagrams indicate the western boundary of the strong ISW dissipation zone, and the distance between the positions of these two pentagrams is approximately 82 km (eastward-moving velocity 1 m/s).

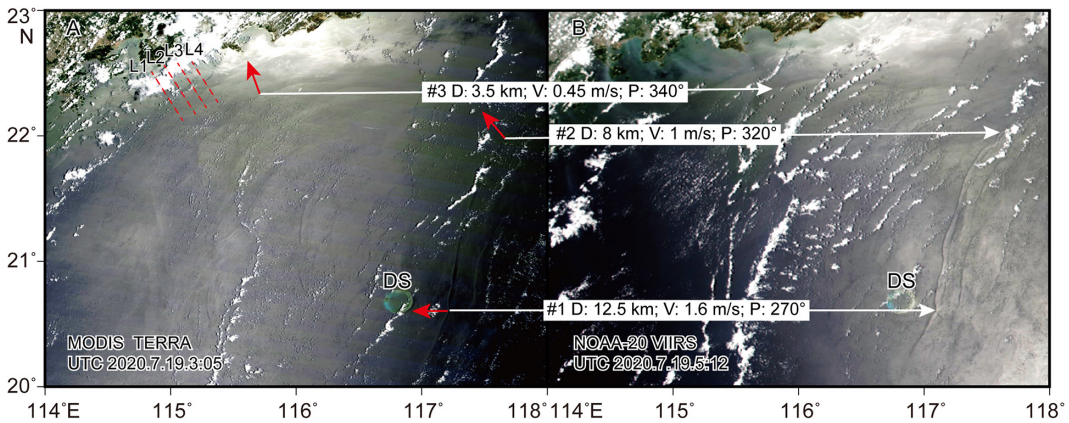

FIGURE 4 | Two satellite images of the ISWs acquired by NASA MODIS Terra **(A)** and 20 VIIRS satellites **(B)** with an approximately 2-h lag. Propagation distances, mean velocities, and directions (solid red lines with arrows) were measured between the two images with similar wave crests (white solid lines with arrows). Red dashed lines are the acoustic backscatter survey lines of L1, L2, L3, and L4. D, distance; V, mean speed; P, direction of propagation (clockwise from north); DS, Dongsha Plateau.

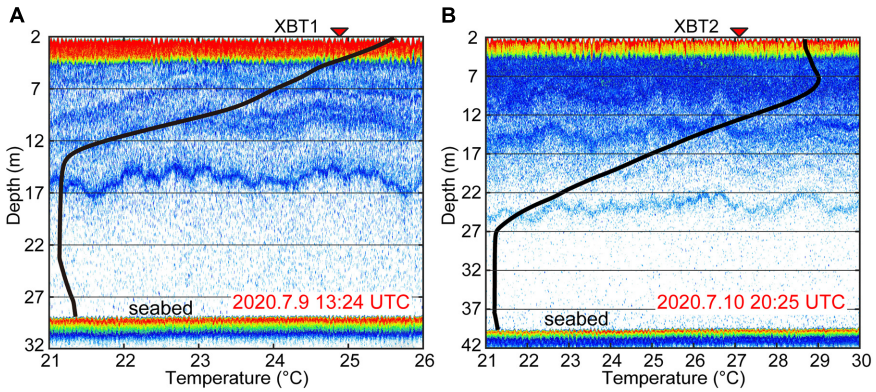

FIGURE 5 | Comparisons of acoustic backscatter images and *in situ* XBT1 **(A)** and XBT2 **(B)** data (black curves) with each other with a small difference of fewer than 3 m, and the red characters indicate the time of acquiring XBT data. Locations of the stations are shown in **Figure 1**.

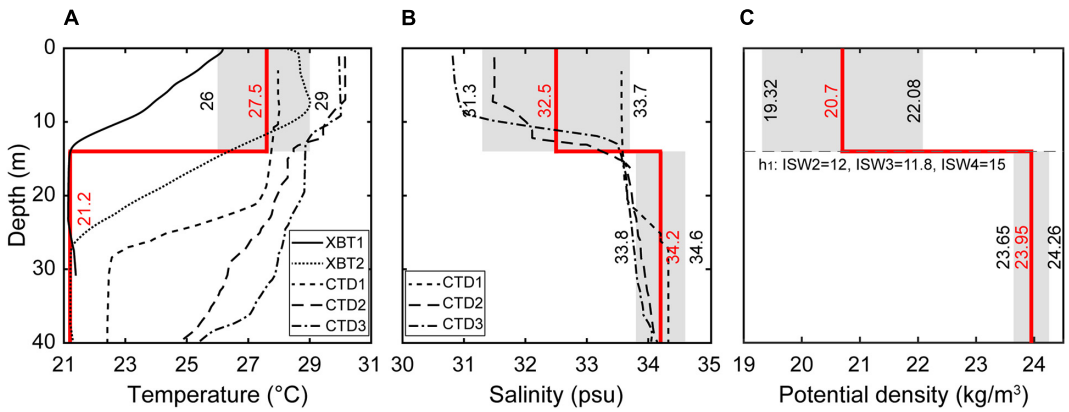

FIGURE 6 | Temperature profiles of the XBT and CTD stations **(A)** and salinity profiles of the CTD stations **(B)**. The CTD data were collected from July 27 to August 16, 2009 (modified by Chen et al., 2017). The gray filled shades indicate the possible ranges of the temperature **(A)**, salinity **(B)**, and potential density **(C)** of the upper layer and the lower layer in the study area according to the XBT2, CTD1–3, and ZHJ2 data, and the solid red lines represent the median values of the possible range. The locations of the XBT, CTD, and ZHJ2 stations are shown in **Figure 1**.

water stratification can be described by the KdV equation (Djordjevic and Redekopp, 1978):

$$\frac{\partial \eta}{\partial t} + (c + \alpha\eta)\frac{\partial \eta}{\partial x} + \beta\frac{\partial^3 \eta}{\partial x^3} = 0 \quad (1)$$

and eKdV equation:

$$\frac{\partial \eta}{\partial t} + (c + \alpha\eta + \alpha_1\eta^2)\frac{\partial \eta}{\partial x} + \beta\frac{\partial^3 \eta}{\partial x^3} = 0 \quad (2)$$

where c, β, α, and α_1 are the linear phase velocity, dispersive coefficient, quadratic, and cubic non-linear parameters, respectively. For the simplified two-layer water stratification model, these parameters can be calculated from the following relationships (Ostrovsky and Stepanyants, 1989):

$$c = [\frac{g(\rho_2 - \rho_1)h_2h_1}{\rho_2h_1 + \rho_1h_2}]^{1/2}, \quad (3)$$

$$\beta = \frac{ch_1h_2}{6}\frac{\rho_1h_1 + \rho_2h_2}{\rho_2h_1 + \rho_1h_2}, \quad (4)$$

$$\alpha = \frac{3}{2}\frac{c}{h_1h_2}\frac{\rho_2h_1^2 - \rho_1h_2^2}{\rho_2h_1 + \rho_1h_2}, \quad (5)$$

$$\alpha_1 = \frac{3c}{(h_1h_2)^2}[\frac{7}{8}(\frac{\rho_2h_1^2 - \rho_1h_2^2}{\rho_2h_1 + \rho_1h_2})^2 - \frac{\rho_2h_1^3 + \rho_1h_2^3}{\rho_2h_1 + \rho_1h_2}], \quad (6)$$

where h_1, h_2, ρ_1, and ρ_2 are the thicknesses and the densities for the upper and lower layers, respectively.

For finite-amplitude waves, the theoretical ISW solutions of Equations 1, 2 have the following form (Ostrovsky and Stepanyants, 1989):

$$\begin{cases} \eta = \eta_0 \mathrm{sech}^2[\frac{x - Vt}{\Delta}] \\ V_{KdV} = \mathrm{c} + \frac{\alpha\eta_0}{3} \\ \Delta^2 = \frac{12\beta}{\alpha\eta_0} \end{cases} \quad (7)$$

$$\begin{cases} \eta = \frac{A}{1 + B\cosh(\frac{x - vt}{D})} \\ B = 1 + \frac{\alpha_1}{\alpha}\eta_0 \\ A = \eta_0(1 + B) \\ V_{\mathrm{eKdV}} = \mathrm{c} + \frac{\alpha A}{6} = V_{KdV} + \frac{\alpha_1\eta_0^2}{6} \\ D^2 = \frac{6\beta}{\alpha A} \end{cases} \quad (8)$$

where Δ, D, V_{KdV}, and V_{eKdV} are the characteristic widths and the phase velocities from the KdV and eKdV models, respectively.

Therefore, the vertical velocities of particle motions can be computed from the analytical solutions (7) and (8) *via* partial derivative $W(x) = \partial\eta(x, t)/\partial t|_{t=0}$ (Trevorrow, 1998; Teague et al., 2011):

$$W(x) = -\frac{2V_{KdV}\eta_0}{\Delta}\mathrm{sech}^2(x)\tanh(x) \quad (9)$$

and

$$W(x) = \frac{BV_{\mathrm{eKdV}}}{AD}\eta^2(\frac{x}{D})\sinh(\frac{x}{D}) \quad (10)$$

for the KdV and eKdV models, respectively.

RESULTS

Characteristics of Internal Solitary Wave Packets

Many ISW packets were captured during the survey cruise using 100-kHz acoustic backscatter data in early summer 2020 (**Figure 2**). Due to continuous and repeated observations of the ISWs, some soliton trains were captured more than once, as shown with similar features and reasonable locations on different lines. In this study, four representative wave packets (ISW1, ISW2, ISW3, and ISW4) at water depths from 24.5 to 40 m were selected for further analysis (**Figure 2**). **Figure 7** shows the detailed backscatter feature and the strategy of deriving the waveform parameters for ISW1, ISW2, ISW3, and ISW4. The captured locations for each leading soliton are plotted in **Figure 3**, while the observed parameters of positions, times, upper layer thicknesses, water depths, amplitudes, and full widths of these ISWs are listed in **Table 1**.

ISW1, ISW2, and ISW3 are from the same soliton train captured three times within 20 h from west to east on the repeating acoustic sections of L2–L4 (**Figures 2**, **7**). ISWs propagated from deeper water (32 m) to the shoaling water (24.5 m) from approximately south to north (**Figures 2**, **7A–F** and **Table 1**). The wave packet ISW1 was first captured on the L2 section, as it had no appearance on the preceding section L1 (**Figure 2**). The packet consists of at least four solitons with positive polarity and representative waveforms within the first 0.5 km from the leading soliton (**Figure 7A**). The solitons' amplitudes are not ordered from the leading soliton to the trailing ones. The third soliton has the largest amplitude of 9 m, while the leading wave amplitude is approximately 7 m. Approximately 0.5 km behind the leading soliton, wave fields become chaos, and solitons are not easy to identify. The passing packet deepens the mixed layer, forming a bore-like structure of ∼2 km. At the trough of the bore, the thickened mixed layer induced by the passing ISWs reverses the non-linear parameter α, and thus, elevated waves are formed (**Figure 2B**).

In contrast, packets ISW2 and ISW3 only have one leading soliton individually (**Figures 2C,D**, **7C–F**). Similar to ISW1, the amplitudes of the leading waves of ISW2 and ISW3 are ∼7 m, but their following wave amplitudes are only 1–2 m and cannot be recognized as solitons. The mixed layer is suppressed to specific depths after passing the solitons, forming hydraulic jumps. Therefore, the solitons only have leading edges, and rear edges are not well developed, indicating a significant energy loss, and the stratifications are failed to be restored to the starting depths within ∼10 km (**Figures 2C,D**).

On line L4 in the deeper water region, the large soliton train (ISW4) with more than 10 following well-developed solitons was captured 2 h beyond ISW3 and ∼20 km away from ISW3 (**Figures 2D**, **7G**). The soliton amplitudes of ISW4 are sequentially ordered from the leading wave (∼13.3 m) to the trailing waves (∼5 m). In addition to the deepened mixed layer, the sediments were suspended several meters above the seafloor

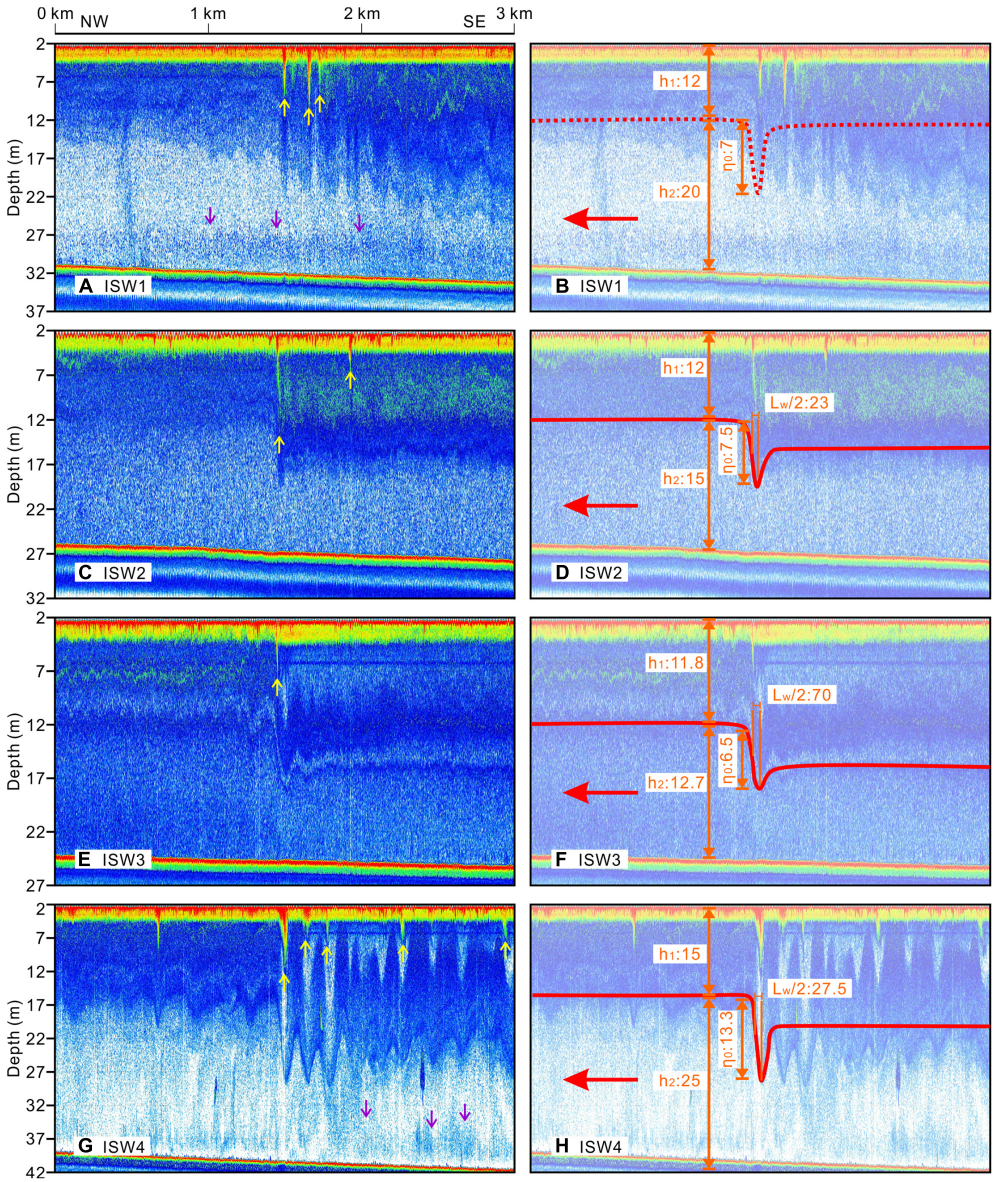

FIGURE 7 | Acoustic backscatter images show the waveforms (left) of ISW1 **(A)**, ISW2 **(C)**, ISW3 **(E)**, and ISW4 **(G)**. The red lines and orange notes (right) are used to derive the waveform parameters of ISW1 **(B)**, ISW2 **(D)**, ISW3 **(F)**, and ISW4 **(H)**. The red, yellow, and purple arrows represent the propagation directions of these ISWs, the ISW-induced bubble plumes, and sediment resuspension, respectively.

TABLE 1 | Observed parameters of the ISWs*.

ISW#	Long (E)	Lat (N)	Time (UTC)	h_1 (m)	WD (m)	η_0 (m)	L_w (m)
1	115°4′24.82″	22°22′1.03″	2020.7.18 11:33		32	7	
2	115°8′2.02″	22°26′58.49″	2020.7.18 17:48	12 ± 1.5	27	7.5 ± 1.5	42
3	115°13′0.43″	22°29′48.82″	2020.7.18 21:22	11.8 ± 1	24.5	6.5 ± 1	140
4	115°19′2.46″	22°20′17.82″	2020.7.18 23:10	15 ± 1.5	40	13.3 ± 1.5	55

**Long/Lat and time, position, and time of ISWs' wave trough captured by acoustic backscatter survey; h_1, observed upper layer parameter for two layers KdV (eKdV) theoretical calculation; WD, water depth; η_0, amplitude; L_w, full width of the trough at half amplitude from acoustic backscatter images.*

after passing the solitons (**Figure 7G**). Meanwhile, because of its larger spatial scale, ISW4 can be observed from the satellite image (**Figures 3B,C**).

From two satellite images acquired by NASA MODIS Terra and NOAA-20 VIIRS satellites on July 19th, 2020 (1 day after acoustic backscatter survey), many alternating dark and light

curving signatures were caused by ISWs from the Dongsha Plateau to the Guangdong coastal water (**Figure 4**). The propagation speeds and directions vary significantly from the deep-water region to the shallow water region according to the position differences of the ISW crests with a 2-h lag (**Figure 4**). The propagation speeds at locations #1–#3 gradually decrease from ∼1.6 to 0.45 m/s, and the propagation directions turn from ∼270° to 340°, corresponding to the shoaling water depth from the continental shelf to the coastal area. Therefore, it is expected that the ISWs observed from the acoustic images in the study region should have propagation parameters similar to those of the satellite-observed results at location #3 (**Figure 4**).

By identifying the time and space differences of the wave crests using the backscatter data, the estimated mean propagation velocities were ∼0.44 m/s (between ISW1 and ISW2) to ∼0.41 m/s (between ISW2 and ISW3), assuming that the ISWs were propagating northward (**Figure 2**). However, the propagation velocities of ISW1, ISW2, and ISW3 cannot be determined by satellites because of their small spatial scales. Therefore, we resort to the theoretical calculation to verify the propagation in the next section. In contrast, ISW4 on L4 was captured by the MODIS image ∼4 h after capture by acoustic backscatter observation (**Figure 3C**). The estimated mean propagation velocity of ISW4 from the acoustic backscatter to the satellite is ∼0.35 ± 0.04 m/s, which is less than the results from two satellite images in the coastal region (**Figure 4**).

Characteristics of the Internal Solitary Wave Packet From Theoretical Calculations

Water Properties and the Simplified Two-Layer Model

In situ XBT data show that the temperature of the upper mixed layer gradually decreases from the near-surface to the lower layers (XBT1: 26.2–21.2°C; XBT2: 29–21.2°C; **Figure 5**). In contrast, the lower layer temperature is nearly homogeneous with a small temperature variation (21.14–21.38°C). The acoustic backscatter images show multiple strong scattering layers in the upper mixed layer, corresponding well to the strong temperature stratification. The scattering feature in the lower layer is substantially weak without a continuous scattering interface. The overall water column stratification revealed by acoustic backscatter data (XBT1: 15 m; XBT2: 24 m) and XBT profiles (XBT1: 14 m; XBT2: 27 m) is consistent with a small vertical difference of less than 3 m, indicating that the acoustic backscatter technique is suitable for imaging the water structure. Therefore, the thicknesses of the upper and lower layers were derived from acoustic backscatter data (**Figure 7** and **Table 1**).

For the simplified two-layer model, which is used to estimate the theoretical parameters for the ISWs, proper temperature and salinity values must be calculated for each layer. The model temperature is straightforwardly derived from *in situ* XBT2 because XBT2 is closer to the study region and fits well to the historical CTD data (**Figure 6A**). Therefore, the upper layer is assigned 27.5°C, and the lower layer is assigned 21.2°C (**Figure 6A**). Meanwhile, according to the salinity data of the CTD stations, as well as the ZHJ2 station (**Figure 6B**), the salinity values of the upper and lower layers are assigned to be 32.5 and 34.2 psu, respectively (**Figure 6B**). Thus, the density models can be estimated using the equation of state of seawater (**Figure 6C**; Millero et al., 1980; Fofonoff and Millard, 1983).

Propagation Velocities From the Model Prediction

A proper ISW propagation model can be used to predict the ISW speed, which should be comparable to the values from satellite and acoustic methods (e.g., Tang et al., 2015). Here, phase velocities are derived from two-layer KdV and eKdV models with varying salinity (**Figure 6**) for ISW packets: 0.48/0.41 (ISW2), 0.44/0.38 (ISW3), and 0.63/0.5 m/s (ISW4) (**Figure 8**). The results show that the salinity variation in the range of 31 to 34 psu in the upper layer can significantly affect the phase speed. We can see that the KdV model predicted values of ISW2 and ISW3 are slightly larger than the propagation velocities estimated from the acoustic backscatter data, while the eKdV model predicted values

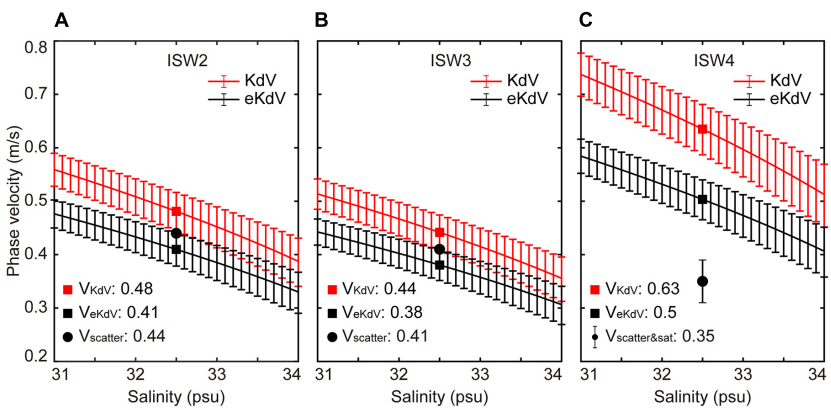

FIGURE 8 | Phase velocities of ISW2 **(A)**, ISW3 **(B)**, and ISW4 **(C)** derived from the two-layer KdV (red) and eKdV (black) models with different salinity parameters of the upper layers (curves with error bars). The solid squares represent phase velocities calculated using the median densities of two layers shown in **Figure 6C**. The solid black circles and solid black circle with error bar indicate the phase velocities of the ISW packets derived from acoustic backscatter data and satellite and acoustic backscatter data, respectively.

are slightly smaller than the estimated propagation velocities. The analytical result of ISW4 (0.63/0.5 m/s) is larger than the acoustic satellite measured velocity (0.35 m/s). The two-layer eKdV model result of ISW4 returns much better agreement with the observations than the KdV model result. A lower salinity value in the two-layer model, the uncertainty of layer thickness, and the spatial resolution of the satellite images may be error sources for both predicted and measured propagation speeds.

Waveforms

Using Equations 7, 8, the analytical waveforms and the characteristic widths for the ISWs are calculated (**Figure 9**). The analytical waveforms overall patterns of the KdV and eKdV models are similar. However, the detailed features of the observed and theoretical waveforms are quite different. For example, analytical waveforms are in perfect symmetry, while the observed waveforms are in typical asymmetry with distinct differences between the leading edge and the rear edge.

Since the wavelengths L_w are derived from the analytical ratio of 1.76 between the wavelength parameter L_w and the characteristic width Δ of the KdV model (Tang et al., 2014, 2015). The waveform parameters of wavelengths of ISW2, ISW3, and ISW4 are compared from the analytical and acoustical results (**Table 1** and **Figure 9**), as wavelength of ISW1 cannot be obtained from the backscatter data (**Figure 7A**). The L_w values of ISW2 and ISW3 measured directly from the acoustic backscatter data are ∼42 and ∼140 m, respectively. The angle theta between the near-northward wave propagation and the backscatter observation line may make the imaged apparent wavelength wider by a factor of $\cos^{-1}$ (30°). In addition, the Doppler effect for the same/opposite moving directions of the ship and wave stretches/shortens the observed wavelength by a factor of $V_1/(V_1 - V_2)$ or $V_1/(V_1+V_2)$, where V_1 and V_2 are the ship and the ISW velocity, respectively. Therefore, the actual wavelengths are ∼32 and ∼136 m by considering the overall contribution between these two effects. The ISW2 wavelength measured from the observed result is half of the analytical result, while the ISW3 observed result matches the analytical result of 127.2 m. For ISW2, the low ratio of 0.8 is probably underestimated since we used the leading edge to estimate the length.

As the survey line is nearly perpendicular to the wave crest (**Figure 3B**), the leading soliton L_w of ISW4 is 67.6 or 62 m after removing the Doppler effect. The KdV prediction wavelength of 66.2 m is very close to the observed result.

Vertical Particle Motion

Studies have shown that vertical velocities can be measured from acoustically imaged waveforms and predicted from the KdV and eKdV models (e.g., Tang et al., 2015). Vertical particle motion along the waveforms of ISW2, ISW3, and ISW4 can be expressed by Equations 9, 10 (**Figure 9**). In particular, the maximum velocities and mean velocities (W_{av}, averaged from the half-width point to the trough of the leading edges, shaded zones) of these three ISWs are also derived (**Figure 9**). The W_{max} values from the KdV and eKdV models for ISW2, ISW3, and ISW4 are 6.3/5.2, 3/2.2, and 15.1/13.6 cm/s, respectively, while the mean vertical velocities are 4.7/3.8, 2.2/1.6, and 11.1/10 cm/s, respectively. The vertical velocity ISW2 is nearly twice that of ISW3 from the same packet. The W_{max} and W_{av} of ISW4 at a depth of 40 m are nearly twice those of foregoing packet ISW2 at a depth of 27 m.

Other Phenomena Related to Internal Solitary Waves

Internal Solitary Wave-Induced Sediment Resuspension

Strong ISW-induced currents scour the seafloor periodically and successively by shaping the seafloor morphology, suspending the

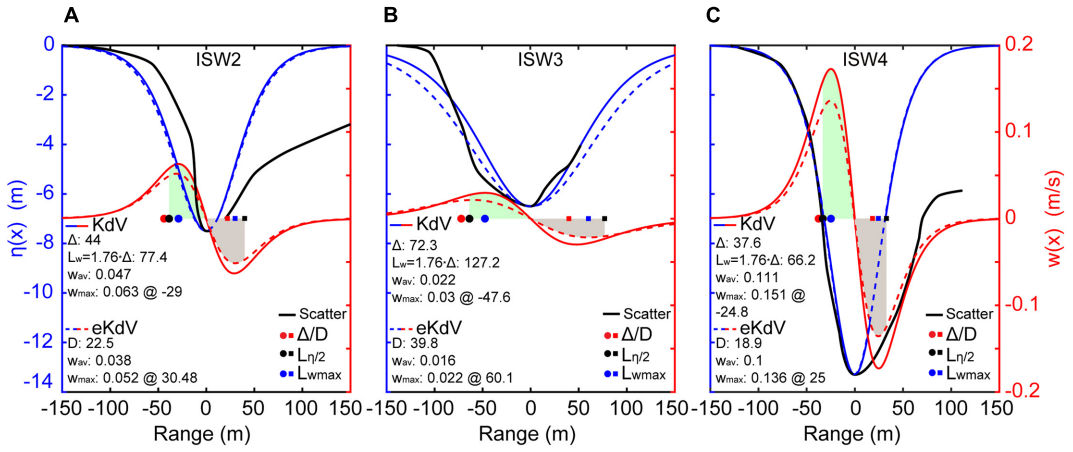

FIGURE 9 | Double-axis plots of the predicted waveforms (blue) and vertical velocities (red) using the two-layer KdV (solid curves) and eKdV (dashed curves) model for ISW2 **(A)**, ISW3 **(B)**, and ISW4 **(C)**. Three solid dots and squares are the characteristic width Δ/D (red), half-width $L_{\eta/2}$ = L/2 (black), and maximum vertical velocity point L_{wmax} (blue). The filled shades are for integrating the mean vertical velocity of the two-layer KdV (green) and eKdV (gray) model between the half-width point and the trough. Black lines are the waveforms derived from backscatter data. Δ/D, characteristic width; L_w, half-wave width; W_{av}, mean vertical velocity; W_{max}, maximum vertical velocity.

seabed sediments, and controlling the grain size of the regional sediments (Ma et al., 2016; Tian et al., 2019a,b, 2021). The phenomena of sediment resuspension can be easily observed from high-resolution acoustic backscatter data (Cacchione et al., 2002; Reeder et al., 2011; Masunaga et al., 2015; Tian et al., 2019a). In this study, patches of weak scattering intensity (purple arrows) are often observed in the near-bottom layers after passing the ISWs (**Figures 7A,G**), showing the sediment resuspension process induced by the ISWs. Sediment resuspension is larger than 5 m height above the seafloor, and affects over tens of kilometers. This phenomena, which called bottom nepheloid layer (BNL), is widely recognized in the global ocean (Masunaga et al., 2017; Tian et al., 2019a).

Internal Solitary Wave-Induced Bubble Plumes

Near the sea surface, there is always an extremely strong acoustic scattering layer of a few meters on the acoustic backscatter data (yellow layer; **Figures 2**, **7**). They are caused by bubbles in the near-surface water (e.g., Trevorrow, 2003). The occurrence of a soliton enhances the bubbles and carries the near-surface bubbles into the soliton core, forming a downwelling bubble plume (yellow arrows; **Figure 7**). Previous studies have shown that these ISW-induced bubble plumes have a bubble size distribution and concentration similar to those of bubble plumes caused by breaking surface waves, which generally begin to appear with wind speeds over 2.5 m/s (e.g., Trevorrow, 1998).

In this study, the plume penetration depths and width induced by ISW1–4 ranged from 8 to 12 and 30 to 70 m, respectively (**Figure 7**). The penetration depths are controlled by the amplitude of the solitons or the isopycnal of the surface layer. Taking ISW4 as an example, the largest bubble plume with penetration depth (12 m) and width (70 m) is above the core of the leading soliton, and the relatively small bubble plumes with penetration depth (∼7 m) and width (∼20–70 m) correspond to the following small solitons. Such downwelling process forces influence near-surface physical and biogeochemical cycles.

DISCUSSION

Origins of Internal Solitary Waves on the Continental Shelf

There are generally two generation sources of ISWs observed on the continental shelf of the northern SCS. One is remotely from the Luzon Strait, and the other is locally from the northern SCS continental shelf (Lien et al., 2005; Cai et al., 2012). According to satellite images, most ISWs in the northern SCS propagate westward from the Luzon Strait and are refracted near the Dongsha Plateau and then torn by the island into two new trains (northern and southern arms) continuing to propagate northwestward to coastal areas (Li et al., 2013; Wang et al., 2013; Ma et al., 2016).

In this study, we suggest that large-scale ISWs were also generated in the Luzon Strait based on the following considerations. Two satellite images within the acoustic backscatter observation period directly show that large-amplitude ISWs are successively distributed from the Dongsha Plateau to the coastal areas (**Figure 4**). Meanwhile, ISWs at the Dongsha Plateau must be generated in the Luzon Strait, and ISWs are still traceable tens of kilometers south of the study region evolved from the northern arm of the ISW train (**Figure 4**). Moreover, the surface signature of ISW4 was clear enough and was captured by both satellite and acoustic backscatter data. Therefore, it can be safely inferred that the periodically active ISWs in the coastal region are generated at the Luzon Strait and then propagate into the study region after long-range evolution.

The acoustic backscatter data may have captured some locally generated internal waves with internal tides on the continental shelf. For example, there is an isolated ISW approximately 1 km ahead of ISW4 in **Figure 7G**. This ISW does not belong to either the trailing soliton of ISW3 or the leading soliton of ISW4, which are successive ISW packets from the Luzon Strait. Therefore, the isolated ISW might be generated locally with steep topography, most likely at the continental shelf break by the internal tide. More integrated observations are necessary to identify the origins of these ISWs.

Evolution of Internal Solitary Waves on the Continental Shelf

In this study, all ISWs have large amplitude frontal edges and small amplitude rear edges (**Figure 7**). The frontal edges are steep and well-developed. In contrast, the rear edges are much weaker and fail to resort to the normal depth. It is suggested that these divergent zones of the rear edges were under collapse by losing potential energy and finally forming asymmetric waveforms. The breaking event of ISWs is mostly caused by Kelvin–Helmholtz instability and convective overturn in the steep rear edge, forming the breaking tail of the ISWs. These features are similar to previous simulated and observed results in shelf-coastal regions (Ostrovsky and Stepanyants, 1989; Novotryasov et al., 2015).

Dissipation of Internal Waves in the Coastal Area

Numerical simulations suggest that large internal waves always dissipate energy by developing a dispersive wave tail on gentle slopes (e.g., Vlasenko and Hutter, 2002). The coastal topography in the study region is gentle (slope angle $\gamma < 0.17°$) with small variation, and seawater stratification might be a key factor affecting the propagation and dissipation of ISWs. Following the ISW breaking criterion $h_b = h_1 + \eta_0/(0.8°/\gamma + 0.4)$, where h_b is the critical water depth for solitary wave breaking (Vlasenko and Hutter, 2002), and according to the stratification parameters of ISW1–4 (**Table 1**), the critical water depth h_b is approximately 17.5 m. Such a water depth is typically smaller than the water depth (∼30 m) of the study. Therefore, the prediction suggests that stratification favors passing ISWs through the study area with a large leading wave and dispersive trailing waves, consistent with acoustic observations (**Figure 7**). The trailing waves weaken as the ISWs propagate toward coastal water.

Strong dissipation zones could be identified as a series of bright (white) bands in the northern part of the study region (**Figures 3**, **4**). However, these dissipation zones should differ from the ISW-induced dissipation zones, although they

highly overlap with the ISW field spatially. First, there are no clear frontal lines relating to the leading waves of the ISWs. Second, the dissipation zones move eastward with a very high speed, contradicting the northwestward propagating ISWs with quite low speeds.

The water masses in the coastal region are complex. They include solar-heated SCS water in the south, eastward drifting river water, along coastal wind-driven currents, and coastal upwelling cold water. On L1 and L2 in the shallow water region, the acoustic backscatter images show the upper layers with substantially weak without a continuous scattering interface are above the lower thick strong scattering layers (**Figure 2**). We suggest that these phenomena were the river plumes sitting on top of the seawater close to the river mouth side. Moreover, the SST acquired on July 18 and 19, 2020 in the northern SCS reveals high-temperature SCS water in the south, low temperature close to the shore region, and a transition zone between (**Figure 10**).

The dissipation zones are highly correlated with the temperature transition zone or the frontal zone between the northern ventilated water and southern heated water (**Figures 3**, **10**, **11**). On the L3 and L4 acoustic backscatter sections, the scattering feature has been intensified even before the arrival of ISWs (**Figure 2**). This region is within the dissipation zone on the satellite images and the temperature transition zone on the SST image (**Figures 3**, **10**, **11**). Therefore, a schematic model is proposed for internal wave propagation and dissipation in this study region (**Figure 12**). Far field ISWs generated at the Luzon Strait can penetrate into the wide shelf region because of the strong stratification caused by solar-headed surface water. Distinct dissipation processes at the trailing waves of the ISW packets make the ISWs weaken toward the

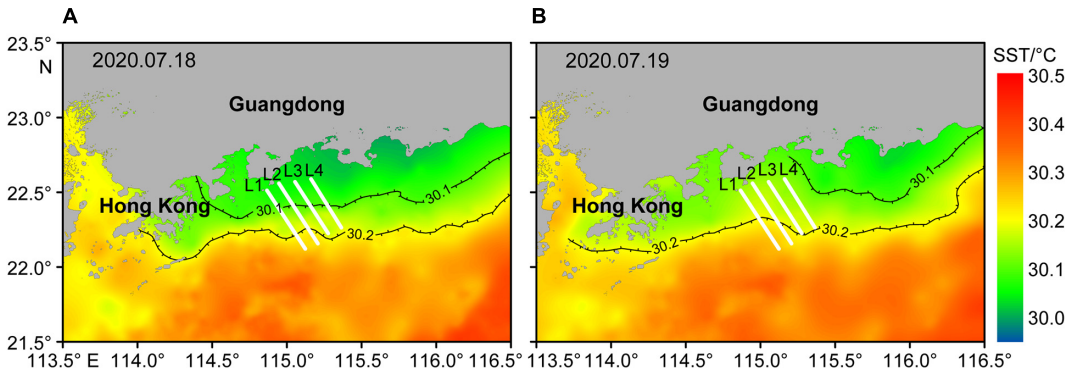

FIGURE 10 | The satellite-composite sea surface temperature (SST) on July 18, 2020 **(A)** and July 19, 2020 **(B)** indicates that the study area was influenced by coastal cold water upwelling. The black lines with half ticks represent the transition zone (30.1°C < SST < 30.2°C) and upwelling zone (SST < 30.1°C). The white lines denote the acoustic backscatter survey lines.

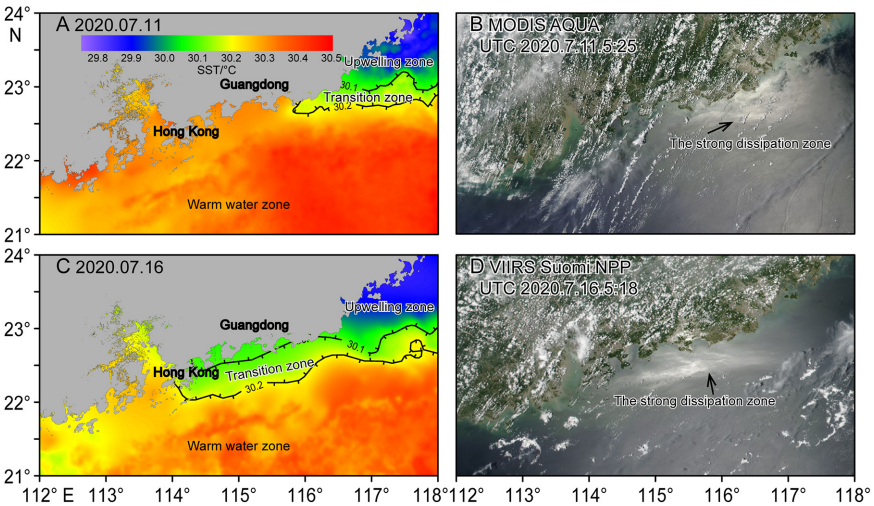

FIGURE 11 | The satellite-composite sea surface temperature (SST) in the study area on July 11, 2020 **(A)** and July 16, 2020 **(C)**. Satellite images of the surface roughness acquired by MODIS Aqua and VIIRS Suomi NPP at 05:25 UTC on July 11, 2020 **(B)** and 05:18 UTC on July 16, 2020 **(D)**. Comparisons of SST images and satellite images on the same day show that the strong ISW dissipation zones (white wave crests) coincided with the transition zone of the upwelling region (30.1°C < SST < 30.2°C).

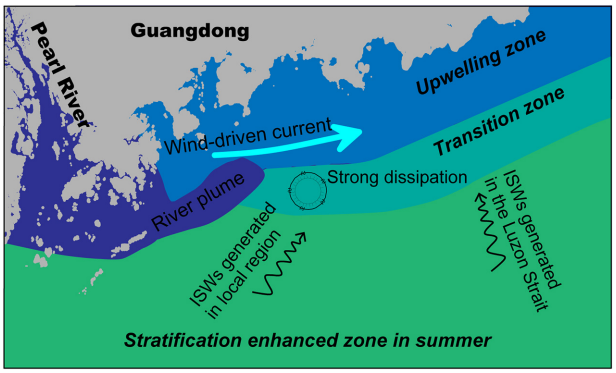

FIGURE 12 | Schematic diagram describing the propagation and dissipation processes of the ISWs. The ISWs on the continental shelf of the northern SCS are generated in the Luzon Strait and northern SCS shelf. The dissipation and evolution of ISWs couple multiple mechanisms among river plume dispersal, upwelling mixing, and wind-driven currents.

shoreward region. These ISWs finally disappear before entering the upwelling cold water, as their stratification does not support ISW transmission. The surface dissipation patches are near-surface internal wave breaks induced by the wind force. Their occurrences show a quick response to the wind force along the frontal instability zone.

Offshore Engineering Implications

Our study area is offshore of the Guangdong–Hong Kong–Macao Greater Bay Area. It is one of the most developed areas in China. There are numerous near-shore artificial facilities in the study area, such as wind power facilities, cross-sea bridges, oil platforms, and submarine cables. Large amplitude ISWs can lead to strong horizontal and vertical currents in the ocean. A few studies have been carried out to evaluate the impact induced by strong waves on offshore structures (e.g., Cai et al., 2006). This study shows that the duration of ISWs is a few minutes, and the vertical displacements and vertical velocities are on the order of ∼10 m and 10 cm/s, respectively. For example, ISWs recorded that the vertical displacement was up to 20 m at a period of ∼6–8 h at station ZHJ2 (**Figure 1**; Lee et al., 2021).

During the cruise, a high-resolution multichannel streamer, which is geophysical equipment used in near-surface engineering surveys, was deployed simultaneously with acoustic backscatter. Due to the lack of depth controlling units, the streamer went through strong vertical movements induced by ISWs, resulting in apparent undulating topography waves of ∼500 m wavelength and ∼2–4 m amplitude. Tang et al. (2015) have also reported that the streamer with depth controlling units was uplifted to the surface by the ISWs for ∼20 min (∼3 km) in NE SCS. In addition, offshore engineering vessel operations, such as dynamic positioning and drilling, are often influenced by ISWs.

Artificial facility safety is sensitive to sediment siltation or erosion on the seafloor. ISWs can give rise to remarkable interactions between the seafloor and ocean currents in a relatively short time (Apel et al., 2007; Huang et al., 2016). The total amount of sediments resuspended by the ISWs is 2.7 times that of the sediments supplied by the river in the northern SCS (Jia et al., 2019). The suspended sediments diffuse along the isopycnals and redeposit in a different area depending on sediment grain sizes and ocean currents (Tian et al., 2019a,b). Acoustic backscatter data have shown that ISWs induce large-scale sediment resuspension offshore of Guangdong. Therefore, ISWs combining coastal currents may have potential harm to offshore engineering structures by inducing large-scale sediment siltation or erosion.

CONCLUSION

We analyzed the ISWs in shallow water offshore Guangdong Province using acoustic backscatter data in combination with satellite and hydrographic data that were simultaneously collected in July 2020. The satellite images show that the ISWs in coastal areas originate from the Luzon Strait. Four large-scale ISW packets were encountered during the survey cruise at a water depth of 20–50 m. A soliton train with apparent vertical and horizontal scales of ∼7 and 100 m, respectively, was captured three times in 20 h on the repeating acoustic sections (ISW1, ISW2, and ISW3). Another soliton train (ISW4) with a more complex and stronger amplitude (∼13.3 m) was captured on both satellite and acoustic backscatter data. The phase speeds (0.4–0.5 m/s) and waveshapes (e.g., half-wave width 60–140 m) of ISWs measured from acoustic data agree with the results derived using a theoretical two-layer model of the KdV and eKdV equations.

The water column structures revealed by acoustic backscatter data and XBT profiles are consistent with each other, with a small difference of fewer than 3 m. The shallow mixed layer depth (∼10–20 m) in summer is responsible for the extensive occurrence of ISWs in the study region. The temperature transition zone between the solar-heated SCS water in the south and the upwelling cold water near the coast might be a hydrographic front zone, where strong dissipation is prone to occur for both ISWs and wind-induced near-surface waves.

DATA AVAILABILITY STATEMENT

The original contributions presented in the study are included in the article/supplementary material, further inquiries can be directed to the corresponding authors.

AUTHOR CONTRIBUTIONS

YF: conceptualization, methodology, software, validation, formal analysis, investigation, writing – original draft, writing – review and editing, and visualization. QT: conceptualization, software, resources, writing – review and editing, and funding acquisition. JL: investigation and writing – review and editing. JS and WZ: resources, supervision, project administration, and funding acquisition. All authors contributed to the article and approved the submitted version.

FUNDING

This work was financially supported by the Key Special Project for Introduced Talents Team of Southern Marine Science and Engineering Guangdong Laboratory (Guangzhou) (GML2019ZD0204), the Special Foundation for National Science and Technology Basic Research Program of China (2017FY201406), the National Key Research and Development Program of China (2017YFC1500401), the National Natural Science Foundation of China (92058201 and 41876067), the Youth Innovation Promotion Association, Chinese Academy of Sciences (Y202076), the Rising Star Foundation of the South China Sea Institute of Oceanology (NHXX2019DZ0101), and the Key Laboratory of Ocean and Marginal Sea Geology, Chinese Academy of Sciences (OMG18-11).

ACKNOWLEDGMENTS

We thank the crew and science party of R/V YUEXIAYUZHI20026 for acquiring the acoustic backscatter data and XBT data. We also thank the reviewers for the constructive comments and detailed suggestions that improved the manuscript.

REFERENCES

Alford, M. H., Peacock, T., Mackinnon, J. A., Nash, J. D., Buijsman, M. C., Centurioni, L. R., et al. (2015). The formation and fate of internal waves in the South China Sea. *Nature* 521, 65–69. doi: 10.1038/nature14399

Apel, J. R., Ostrovsky, L. A., Stepanyants, Y. A., and Lynch, J. F. (2007). Internal solitons in the ocean and their effect on underwater sound. *J. Acoust. Soc. Am.* 121, 695–722. doi: 10.1121/1.2395914

Boswell, K. M., D'elia, M., Johnston, M. W., Mohan, J. A., Warren, J. D., Wells, R. J. D., et al. (2020). Oceanographic structure and light levels drive patterns of sound scattering layers in a low-latitude oceanic system. *Front. Mar. Sci.* 7:51. doi: 10.3389/fmars.2020.00051

Buijsman, M. C., Kanarska, Y., and Mcwilliams, J. C. (2010). On the generation and evolution of nonlinear internal waves in the South China Sea. *J. Geophys. Res.* 115:C02012. doi: 10.1029/2009JC005275

Cacchione, D. A., Pratson, L. F., and Ogston, A. S. (2002). The Shaping of continental slopes by internal tides. *Science* 296, 724–727. doi: 10.1126/science.1069803

Cai, S., Long, X., and Gan, Z. (2002). A numerical study of the generation and propagation of internal solitary waves in the Luzon Strait. *Oceanol. Acta* 25, 51–60. doi: 10.1016/S0399-1784(02)01181-7

Cai, S., Wang, S., and Long, X. (2006). A simple estimation of the force exerted by internal solitons on cylindrical piles. *Ocean Eng.* 33, 974–980. doi: 10.1016/j.oceaneng.2005.05.012

Cai, S., Xie, J., and He, J. (2012). An overview of internal solitary waves in the South China Sea. *Surv. Geophys.* 33, 927–943. doi: 10.1007/s10712-012-9176-0

Cascão, I., Domokos, R., Lammers, M. O., Marques, V., Domínguez, R., Santos, R. S., et al. (2017). Persistent enhancement of micronekton backscatter at the summits of seamounts in the azores. *Front. Mar. Sci.* 4:25. doi: 10.3389/fmars.2017.00025

Chang, M.-H., Cheng, Y.-H., Yang, Y. J., Jan, S., Ramp, S. R., Reeder, D. B., et al. (2021). Direct measurements reveal instabilities and turbulence within large amplitude internal solitary waves beneath the ocean. *Commun. Earth Environ.* 2:15. doi: 10.1038/s43247-020-00083-6

Chen, Z., Pan, J., Jiang, Y., and Lin, H. (2017). Far-reaching transport of Pearl River plume water by upwelling jet in the northeastern South China Sea. *J. Mar. Syst.* 173, 60–69. doi: 10.1016/j.jmarsys.2017.04.008

Djordjevic, V. D., and Redekopp, L. G. (1978). The fission and disintegration of internal solitary waves moving over two-dimensional topography. *J. Phys. Oceanogr.* 8, 1016–1024.

Farmer, D., and Armi, L. (1999). The generation and trapping of solitary waves over topography. *Science* 283, 188–190. doi: 10.1126/science.283.5399.188

Farmer, D., Li, Q., and Park, J. H. (2009). Internal wave observations in the South China Sea: The role of rotation and non-linearity. *Atmos. Ocean* 47, 267–280. doi: 10.3137/oc313.2009

Fofonoff, N. P., and Millard, R. Jr. (1983). *Algorithms for the Computation of Fundamental Properties of Seawater. UNESCO Technical Papers in Marine Science 44*. Paris: UNESCO, 53.

Fu, K.-H., Wang, Y.-H., St. Laurent, L., Simmons, H., and Wang, D.-P. (2012). Shoaling of large-amplitude nonlinear internal waves at Dongsha Atoll in the northern South China Sea. *Cont. Shelf Res.* 37, 1–7. doi: 10.1016/j.csr.2012.01.010

Guo, C., and Chen, X. (2014). A review of internal solitary wave dynamics in the northern South China Sea. *Prog. Oceanogr.* 121, 7–23. doi: 10.1016/j.pocean.2013.04.002

Helfrich, K. R., and Melville, W. K. (2006). Long nonlinear internal waves. *Annu. Rev. Fluid Mech.* 38, 395–425. doi: 10.1146/annurev.fluid.38.050304.092129

Huang, X., Chen, Z., Zhao, W., Zhang, Z., Zhou, C., Yang, Q., et al. (2016). An extreme internal solitary wave event observed in the northern South China Sea. *Sci. Rep.* 6:30041. doi: 10.1038/srep30041

Jia, Y., Tian, Z., Shi, X., Liu, J. P., Chen, J., Liu, X., et al. (2019). Deep-sea sediment resuspension by internal solitary waves in the northern South China Sea. *Sci. Rep.* 9:12137. doi: 10.1038/s41598-019-47886-y

Klevjer, T. A., Irigoien, X., Rostad, A., Fraile-Nuez, E., Benitez-Barrios, V. M., and Kaartvedt, S. (2016). Large scale patterns in vertical distribution and behaviour of mesopelagic scattering layers. *Sci. Rep.* 6:19873. doi: 10.1038/srep19873

Klevjer, T. A., Melle, W., Knutsen, T., and Aksnes, D. L. (2020). Vertical distribution and migration of mesopelagic scatterers in four north Atlantic basins. *Deep Sea Res. Part II Top. Stud. Oceanogr.* 180:104811. doi: 10.1016/j.dsr2.2020.104811

Lee, J., Liu, J. T., Lee, I. H., Fu, K. H., Yang, R. J., Gong, W., et al. (2021). Encountering shoaling internal waves on the dispersal pathway of the pearl river plume in summer. *Sci. Rep.* 11:999. doi: 10.1038/s41598-020-80215-2

Li, D., Chen, X., and Liu, A. (2011). On the generation and evolution of internal solitary waves in the northwestern South China Sea. *Ocean Modell.* 40, 105–119. doi: 10.1016/j.ocemod.2011.08.005

Li, X., Jackson, C. R., and Pichel, W. G. (2013). Internal solitary wave refraction at Dongsha Atoll, South China Sea. *Geophys. Res. Lett.* 40, 3128–3132. doi: 10.1002/grl.50614

Lien, R. C., Tang, T. Y., Chang, M. H., and D'asaro, E. A. (2005). Energy of nonlinear internal waves in the South China Sea. *Geophys. Res. Lett.* 32:L05615. doi: 10.1029/2004GL022012

Ma, X., Yan, J., Hou, Y., Lin, F., and Zheng, X. (2016). Footprints of obliquely incident internal solitary waves and internal tides near the shelf break in the northern South China Sea. *J. Geophys. Res. Oceans* 121, 8706–8719. doi: 10.1002/2016JC012009

Masunaga, E., Arthur, R. S., Fringer, O. B., and Yamazaki, H. (2017). Sediment resuspension and the generation of intermediate nepheloid layers by shoaling internal bores. *J. Mar. Syst.* 170, 31–41. doi: 10.1016/j.jmarsys.2017.01.017

Masunaga, E., Homma, H., Yamazaki, H., Fringer, O. B., Nagai, T., Kitade, Y., et al. (2015). Mixing and sediment resuspension associated with internal bores in a shallow bay. *Cont. Shelf Res.* 110, 85–99. doi: 10.1016/j.csr.2015.09.022

Millero, F. J., Chen, C.-T., Bradshaw, A., and Schleicher, K. (1980). A new high pressure equation of state for seawater. *Deep Sea Res. Part A Oceanogr. Res. Pap.* 27, 255–264. doi: 10.1016/0198-0149(80)90016-3

Novotryasov, V. V., Stepanov, D. V., and Yaroshchuk, I. O. (2015). Observations of internal undular bores on the Japan/East Sea shelf-coastal region. *Ocean Dyn.* 66, 19–25. doi: 10.1007/s10236-015-0905-z

Orr, M. H., and Mignerey, P. C. (2003). Nonlinear internal waves in the South China Sea: Observation of the conversion of depression internal waves to elevation internal waves. *J. Geophys. Res.* 108:3064. doi: 10.1029/2001JC001163

Ostrovsky, L., and Stepanyants, Y. A. (1989). Do internal solitions exist in the ocean? *Rev. Geophys.* 27, 293–310. doi: 10.1029/RG027i003p00293

Ramp, S. R., Tang, T. Y., Duda, T. F., Lynch, J. F., Liu, A. K., Chiu, C. S., et al. (2004). Internal solitons in the northeastern South China Sea part I: sources and deep water propagation. *IEEE J. Oceanic Eng.* 29, 1157–1181. doi: 10.1109/joe.2004.840839

Reeder, D. B., Ma, B. B., and Yang, Y. J. (2011). Very large subaqueous sand dunes on the upper continental slope in the South China Sea generated by episodic, shoaling deep-water internal solitary waves. *Mar. Geol.* 279, 12–18. doi: 10.1016/j.margeo.2010.10.009

Shishkina, O. D., Sveen, J. K., and Grue, J. (2013). Transformation of internal solitary waves at the "deep" and "shallow" shelf: satellite observations and laboratory experiment. *Nonlinear Process. Geophys.* 20, 743–757. doi: 10.5194/npg-20-743-2013

Shroyer, E., Moum, J., and Nash, J. (2009). Observations of polarity reversal in shoaling nonlinear internal waves. *J. Phys. Oceanogr.* 39, 691–701. doi: 10.1175/2008JPO3953.1

Tang, Q., Hobbs, R., Wang, D., Sun, L., Zheng, C., Li, J., et al. (2015). Marine seismic observation of internal solitary wave packets in the northeast South China Sea. *J. Geophys. Res. Oceans* 120, 8487–8503. doi: 10.1002/2015JC011362

Tang, Q., Wang, C., Wang, D., and Pawlowicz, R. (2014). Seismic, satellite and site observations of internal solitary waves in the NE South China Sea. *Sci. Rep.* 4:5374. doi: 10.1038/srep05374

Tang, Q., Xu, M., Zheng, C., Xu, X., and Xu, J. (2018). A locally generated high-mode nonlinear internal wave detected on the shelf of the northern south China Sea from marine seismic observations. *J. Geophys. Res. Oceans* 123, 1142–1155. doi: 10.1002/2017JC013347

Teague, W. J., Wijesekera, H. W., Avera, W. E., and Hallock, Z. R. (2011). Current and density observations of packets of nonlinear internal waves on the outer New Jersey Shelf. *J. Phys. Oceanogr.* 41, 994–1008. doi: 10.1175/2010jpo4556.1

Tian, Z., Jia, Y., Chen, J., Liu, J., Zhang, S., Ji, C., et al. (2021). Internal solitary waves induced deep-water nepheloid layers and seafloor geomorphic changes on the continental slope of the northern South China Sea. *Phys. Fluids* 33:053312. doi: 10.1063/5.0045124

Tian, Z., Jia, Y., Zhang, S., Zhang, X., Li, Y., and Guo, X. (2019a). Bottom and intermediate nepheloid layer induced by shoaling internal solitary waves: impacts of the angle of the wave group velocity vector and slope gradients. *J. Geophys. Res. Oceans* 124, 5686–5699. doi: 10.1029/2018JC014721

Tian, Z., Zhang, S., Guo, X., Yu, L., and Jia, Y. (2019b). Experimental investigation of sediment dynamics in response to breaking high-frequency internal solitary wave packets over a steep slope. *J. Mar. Syst.* 199:103191. doi: 10.1016/j.jmarsys.2019.103191

Trevorrow, M. V. (1998). Observations of internal solitary waves near the Oregon coast with an inverted echo sounder. *J. Geophys. Res. Oceans* 103, 7671–7680. doi: 10.1029/98JC00101

Trevorrow, M. V. (2003). Measurements of near-surface bubble plumes in the open ocean with implications for high-frequency sonar performance. *J. Atmos. Oceanic Technol.* 114, 2672–2684. doi: 10.1121/1.1621008

van Haren, H., Gostiaux, L., Laan, M., Van Haren, M., Van Haren, E., and Gerringa, L. J. (2012). Internal wave turbulence near a Texel beach. *PLoS One* 7:e32535. doi: 10.1371/journal.pone.0032535

Vlasenko, V., and Hutter, K. (2002). Numerical experiments on the breaking of solitary internal wavesover a slope–shelf topography. *J. Phys. Oceanogr.* 32, 1779–1793.

Wang, J., Huang, W., Yang, J., Zhang, H., and Zheng, G. (2013). Study of the propagation direction of the internal waves in the South China Sea using satellite images. *Acta Oceanol. Sin.* 32, 42–50. doi: 10.1007/s13131-013-0312-6

Yuan, Y., Zheng, Q., Dai, D., Hu, X., Qiao, F., and Meng, J. (2006). Mechanism of internal waves in the Luzon Strait. *J. Geophys. Res.* 111:C11S17. doi: 10.1029/2005JC003198

Zhao, Z., Klemas, V., Zheng, Q., and Yan, X.-H. (2004). Remote sensing evidence for baroclinic tide origin of internal solitary waves in the northeastern South China Sea. *Geophys. Res. Lett.* 31:L06302. doi: 10.1029/2003GL019077

Conflict of Interest: The authors declare that the research was conducted in the absence of any commercial or financial relationships that could be construed as a potential conflict of interest.

Publisher's Note: All claims expressed in this article are solely those of the authors and do not necessarily represent those of their affiliated organizations, or those of the publisher, the editors and the reviewers. Any product that may be evaluated in this article, or claim that may be made by its manufacturer, is not guaranteed or endorsed by the publisher.

frontiers in Marine Science

ORIGINAL RESEARCH
published: 20 December 2021
doi: 10.3389/fmars.2021.734125

Temperature and Salinity Inverted for a Mediterranean Eddy Captured With Seismic Data, Using a Spatially Iterative Markov Chain Monte Carlo Approach

Wuxin Xiao[1], Katy Louise Sheen[1], Qunshu Tang[2], Jamie Shutler[1], Richard Hobbs[3] and Tobias Ehmen[1]*

[1] College of Life and Environmental Sciences, University of Exeter, Penryn Campus, Penryn, United Kingdom, [2] Key Laboratory of Ocean and Marginal Sea Geology, South China Sea Institute of Oceanology, Innovation Academy of South China Sea Ecology and Environmental Engineering, Chinese Academy of Sciences (CAS), Guangzhou, China, [3] Department of Earth Sciences, Durham University, Durham, United Kingdom

OPEN ACCESS

Edited by:
Ananda Pascual, Mediterranean Institute for Advanced Studies, Spanish National Research Council (CSIC), Spain

Reviewed by:
Frédéric Cyr, Fisheries and Oceans Canada, Canada
Valenti Sallares, Institute of Marine Sciences, Spanish National Research Council (CSIC), Spain

***Correspondence:**
Wuxin Xiao
wx231@exeter.ac.uk

Specialty section:
This article was submitted to Ocean Observation, a section of the journal Frontiers in Marine Science

Received: *30 June 2021*
Accepted: *26 November 2021*
Published: *20 December 2021*

Citation:
Xiao W, Sheen KL, Tang Q, Shutler J, Hobbs R and Ehmen T (2021) Temperature and Salinity Inverted for a Mediterranean Eddy Captured With Seismic Data, Using a Spatially Iterative Markov Chain Monte Carlo Approach. Front. Mar. Sci. 8:734125. doi: 10.3389/fmars.2021.734125

Ocean submesoscale dynamics are thought to play a key role in both the climate system and ocean productivity, however, subsurface observations at these scales remain rare. Seismic oceanography, an established acoustic imaging method, provides a unique tool for capturing oceanic structure throughout the water column with spatial resolutions of tens of meters. A drawback to the seismic method is that temperature and salinity are not measured directly, limiting the quantitative interpretation of imaged features. The Markov Chain Monte Carlo (MCMC) inversion approach has been used to invert for temperature and salinity from seismic data, with spatially quantified uncertainties. However, the requisite prior model used in previous studies relied upon highly continuous acoustic reflection horizons rarely present in real oceanic environments due to instabilities and turbulence. Here we adapt the MCMC inversion approach with an iteratively updated prior model based on hydrographic data, sidestepping the necessity of continuous reflection horizons. Furthermore, uncertainties introduced by the starting model thermohaline fields as well as those from the MCMC inversion itself are accounted for. The impact on uncertainties of varying the resolution of hydrographic data used to produce the inversion starting model is also investigated. The inversion is applied to a mid-depth Mediterranean water eddy (or meddy) captured with seismic imaging in the Gulf of Cadiz in 2007. The meddy boundary exhibits regions of disrupted seismic reflectivity and rapid horizontal changes of temperature and salinity. Inverted temperature and salinity values typically have uncertainties of 0.16°C and 0.055 psu, respectively, and agree well with direct measurements. Uncertainties of inverted results are found to be highly dependent on the resolution of the hydrographic data used to produce the prior model, particularly in regions where background temperature and salinity vary rapidly, such as at the edge of the meddy. This further advancement of inversion techniques to extract temperature and salinity from seismic data will help expand the use of ocean acoustics for understanding the mesoscale to finescale structure of the interior ocean.

Keywords: oceanography, seismic, eddy, inversion, Mediterranean, acoustic, Bayesian, thermohaline

INTRODUCTION

Mediterranean water eddies, or "meddies," are anti-cyclonically rotating, sub-surface lenses of warm, salty water formed where the Mediterranean Sea outflows into the Atlantic Ocean (e.g., Richardson et al., 2000). They are thought to separate from the Mediterranean Undercurrent as it interacts with topographic features such as canyons along the Iberian continental margin (Serra et al., 2005). Meddies are typically 20–100 km in diameter, have rotation periods of a few days, and have cores that are 500–1,000 m thick centered near 1,200 m depth (Armi and Zenk, 1984; Prater and Sanford, 1994; Richardson et al., 2000). Meddies carry waters with temperatures of 11.5–13.5°C and salinities 36.2–36.8 within their cores (Armi and Zenk, 1984; Schultz-Tokos and Rossby, 1991; Pingree and Le Cann, 1993; Prater and Sanford, 1994; Richardson et al., 2000; Paillet et al., 2002; Carton et al., 2010). With 15–20 Meddies produced annually, meddies transport most of the Mediterranean outflow into the wider Atlantic Ocean (Bower et al., 1997; Richardson et al., 2000).

While the cores of meddies are largely homogeneous, high gradients of temperature and salinity, with interleaving, thermohaline intrusions and "layering" are commonly found at the meddy periphery (Armi and Zenk, 1984; Ruddick, 1992; Ménesguen et al., 2009; Pinheiro et al., 2010; Biescas et al., 2014). These layering structures typically have vertical scales of 20–75 m and are thought to be generated by both stirring and double diffusive processes (Ruddick and Hebert, 1988; Pinheiro et al., 2010; Song et al., 2011; Meunier et al., 2015). Such finescale layering formations likely play a key role in the eventual disintegration of the meddy through the shedding and mixing of their Mediterranean-water core to the surrounding cooler, fresher Atlantic waters (Armi et al., 1989; Hebert et al., 1990; Song et al., 2011; Hua et al., 2013; Meunier et al., 2015). Meddies are also known to decay through collision with seamounts (Schultz Tokos et al., 1994; Richardson et al., 2000). Accounting for these various mixing and decay processes, meddies typically last 1–5 years. With translation speeds of a few cm/s, typically south-westward, they can transport Mediterranean water more than a thousand kilometers from its source (Richardson et al., 2000).

Seismic oceanography has been used to image the finescale to submesoscale structures associated with meddies, aiding understanding of the important role that they play in the redistribution of heat and salt across the North Atlantic (Wang and Dewar, 2003; Biescas et al., 2008; Ménesguen et al., 2009; Papenberg et al., 2010; McWilliams, 2016). Seismic oceanography is a widely used technique that utilizes acoustic energy (of typically 20–200 Hz) reflected at temperature and salinity changes within the water column (Holbrook et al., 2003; Ruddick et al., 2009; Sallarès et al., 2009). Resultant acoustic images display oceanic structure with vertical and horizontal resolutions of order ten meters, over regions tens of km long and to full depth (e.g., Sheen et al., 2012; Gunn et al., 2020). Physical phenomena such as internal waves, heat fluxes and turbulent mixing can be quantitatively estimated by interpreting the spatial structure of reflectors, which are often assumed to follow isopycnals (Sheen et al., 2009; Papenberg et al., 2010; Fortin et al., 2016, 2017; Sallarès et al., 2016; Dickinson et al., 2017; Gunn et al., 2018, 2020). Seismic ocean data essentially captures the relative strength of the thermohaline stratification but does not explicitly measure absolute values of temperature, salinity or density. As such the ability to interpret and quantitatively assess many of the fascinating structures imaged is limited. Seismic inversion techniques which produce high resolution temperature and salinity fields with quantified uncertainties are required and could represent a step-change in our ability to observe the sub-surface ocean on sufficient spatial scales.

Various different strategies have been applied to solve the ocean seismic inversion problem including both full waveform inversion and the inversion of temperature and salinity from acoustic impedance calculated from reflection amplitudes and hydrographic data (Wood et al., 2008; Papenberg et al., 2010; Kormann et al., 2011; Bornstein et al., 2013; Biescas et al., 2014; Padhi et al., 2015; Dagnino et al., 2016). The accuracy of inverted temperature and salinity values are typically estimated by comparison to "co-located" hydrographic data such as conductivity-temperature-depth (CTD) casts or expendable bathymetry (XBT) data. This approach to estimating the inversion uncertainty, however, does not account for a time or depth shift between CTD/XBT and seismic data. As such Tang et al. (2016) developed a Bayesian Markov Chain Monte Carlo (MCMC) inversion technique. In this Bayesian approach, the uncertainty of inverted temperature and salinity values are assessed by how well a distribution of possible solutions fit the observed seismic acoustic reflectivity. However, due to the band-limited nature of seismic data, which fails to capture the background thermohaline structure (i.e., scales greater than ∼100 m), the MCMC approach only encompasses the uncertainty of the high frequency temperature and salinity variability. The MCMC approach therefore requires an accurate background temperature-salinity starting model to provide information about the larger scale background variability. Tang et al. (2016) found that a starting model produced from available hydrographic (i.e., XBT cast) data did not capture enough of the horizontal variability to successfully recover thermohaline fields using the MCMC approach. However, by applying the MCMC method to the specific case of an internal solitary wave, Tang et al. (2016) were instead able to exploit the highly continuous nature of the internal wave reflection horizons to produce an initial model with sufficient horizontal resolution: the undulating seismic reflection horizons associated with the solitary internal wave were treated as isothermals/isohalines and used to characterize the finer scale horizontal temperature and salinity variability in between XBT casts. However, the internal solitary wave is a rather unique situation: firstly, it is not always possible to assume that reflection horizons follow isothermals or isopycnals (Biescas et al., 2014); secondly, reflection horizons are typically highly discontinuous due to complex water structures, instabilities, or unstable seismic acquisition conditions and noise. To

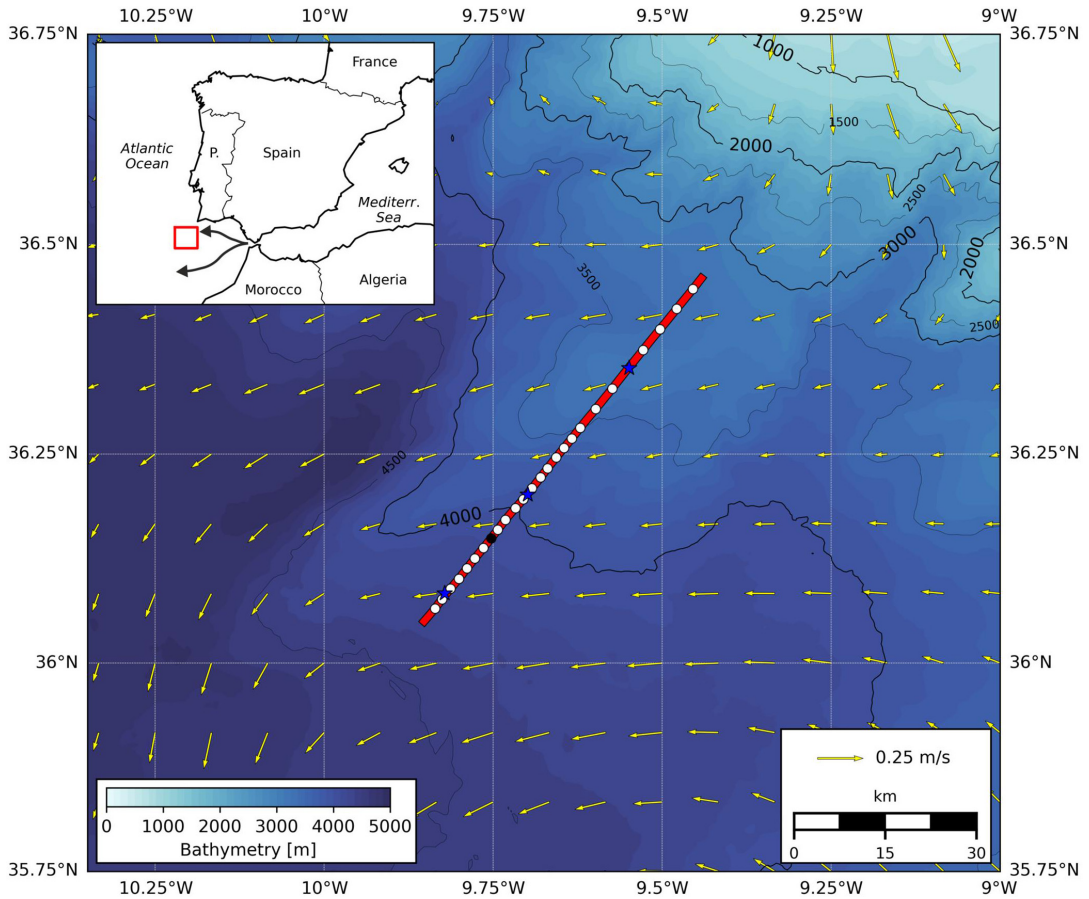

FIGURE 1 | Bathymetry of data collection region. Red line = seismic transect GOLR12; white dots = 24 XBT casts deployed coincident with seismic acquisition; black dot = 1 XCTD cast; blue stars = 3 CTD casts deployed before and after the seismic survey; yellow arrows = surface geostrophic velocity vectors for 7th May 2007. Inset shows location of the research area, and schematic of Mediterranean outflow pathway. Bathymetry was produced from the GEBCO 2020 dataset (GEBCO Bathymetric Compilation Group, 2020). Altimeter products were generated using the Iberia Biscay Ireland Regional Seas Ocean Physics Reanalysis Product with a resolution of 1/12° × 1/12° (https://resources.marine.copernicus.eu/?option=com_csw&view=details&product_id=IBI_MULTIYEAR_PHY_005_002).

enable the MCMC inversion technique to be applied more ubiquitously across seismic datasets, here a spatially iterative MCMC inversion approach is developed which allows the accurate inversion of temperature and salinity from a prior model built from XBT data alone. The uncertainty associated with the low frequency starting model is assessed and incorporated into final inverted confidence limits, alongside the dependence on the sampling resolution of the input hydrographic data.

This study focuses on seismic oceanographic data collected by the Geophysical Oceanography (GO) research survey in 2007 (Hobbs, 2007). The seismic data are unique as XBT casts were deployed at unusually high spatial resolutions during seismic acquisition (e.g., typically every 2 km). These data are therefore ideal for investigating the influence of prior model resolution on inversion results and providing a comprehensive dataset with which to compare inverted values. Furthermore, the GO survey focused on imaging sub-surface meddies, which typically display rapidly changing temperatures and salinities and disrupted reflectivity at their boundaries (Biescas et al., 2008; Ménesguen et al., 2009). These data thus provide a challenging environment with which to test the inversion.

MATERIALS AND METHODS

Data Acquisition and Processing

The seismic transect analyzed here, GOLR12, was acquired between 09:37 and 17:45 on the 7th May 2007, in the Gulf of Cadiz (**Figure 1**). Data were acquired as part of the Geophysical Oceanography (GO) cruise number D318b on the *RRS Discovery*. The seismic source consisted of six Bolt 1500LL airguns with a usable bandwidth of 5–70 Hz. The source array was shot every 20 s and the acoustic reflection energy was recorded using a 2,400 m long SERCEL streamer with 192 channels and 12.5 m group spacing. Standard signal processing was carried out with particular attention to retaining true reflection amplitudes, paramount for later inversion. Seismic data processing included: (1) Geometry setting; (2) Removal of direct waves using an eigenvector filter applied to the raw shot

gathers (Jones and Levy, 1987); (3) Incident angle, directivity and spherical divergence corrections; (4) Noise attenuation by applying a Butterworth band pass filter of 10–80 Hz to shot gathers and compressing traces of anomalous amplitudes; (5) Common midpoint (CMP) sorting; (6) Velocity picking performed every 100 CMPs; (7) Source deconvolution: a reweight deconvolution strategy (Sacchi, 1997) was applied to extract the reflectivity from stacked seismic sections basing on the source wavelet, which was modeled from the source array geometry and airgun volumes using the Nucleus+ software; (8) Amplitude calibration using the seafloor reflection and its first multiple (Warner, 1990); (9) Conversion from two-way travel time to depth using sound velocity derived from XBT data. The final stacked section is shown in **Figure 2A**. The same seismic line (GOLR12) is used to invert the temperature and salinity by Papenberg et al. (2010).

Hydrographic data was collected by two ships: the *RSS Discovery* and the *FS Poseidon*. In total, twenty-four expendable bathythermographs (XBTs) and one expendable conductivity/temperature profiler (XCTD) were deployed from the *RSS Discovery* coincident with seismic data acquisition (**Figure 1**). XBTs were deployed approximately every 2.3 km reaching a depth of 1,830 m. Three CTDs were deployed by the *FS Poseidon*, along the seismic transect a few hours before or after seismic acquisition. Using the neural network approach of Ballabrera-Poy et al. (2009), the CTD data allowed for the estimation of salinity from XBT data. 70% of the CTD data were used as training data, 15% as validation data and 15% as testing data. Using only CTD data coincident with the seismic line (as opposed to all 43 CTD casts collected on the GO cruise) produced lower errors in the derived salinity values, likely because the local depth-temperature-salinity relationship associated with the meddy was better represented. Low frequency interpolated temperature and salinity sections are shown in **Figure 2**: these were used to form the prior model for the MCMC inversion.

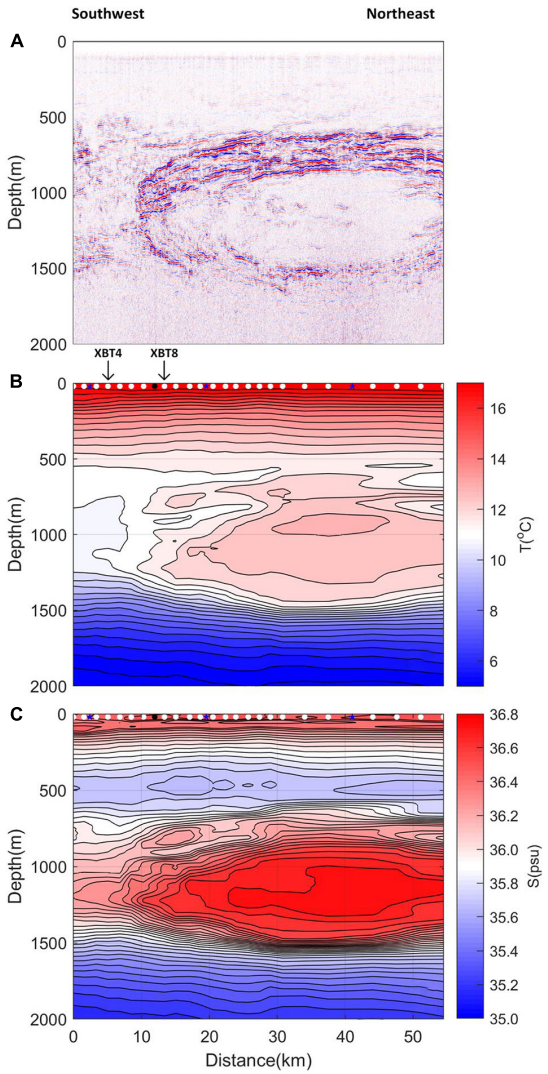

FIGURE 2 | (A) Seismic section of the GOLR12 dataset. Red and blue lines represent reflection horizons caused by temperature and salinity changes in the water column. White (black) dots = 24 XBT (1 XCTD) casts deployed coincident with seismic acquisition; blue stars = 3 CTD casts deployed before and after the seismic survey. **(B)** Low frequency temperature section built from interpolation of XBT data. A linear interpolation was used with a vertical smoothing (moving average) of 35 m. **(C)** Low frequency salinity section built from interpolation of salinity estimated from XBT and CTD data following Ballabrera-Poy et al. (2009). Panels **(B,C)** form the prior model for the MCMC inversion. Note positions of XBT 4 and XBT 8 are indicated on panel **(B)** (see section "Comparing Inverted Results to Observations").

Markov Chain Monte Carlo Inversion

Following Tang et al. (2016), a Bayesian Markov Chain Monte Carlo (MCMC) approach is used to recover temperature and salinity fields from the seismic data, alongside their probability distributions (i.e., the posterior distribution), at the resolution of the seismic image [i.e., $O(10\ \mathrm{m})$]. In this approach, a probability distribution associated with a prior model is used to iteratively randomly draw N solutions at each inversion point. A likelihood function determines how well each random sample fits the observed data (i.e., seismic reflectivity), and whether to accept or reject the solution. After a sufficient number of iterations (i.e., the "burn-in" period) the posterior distribution converges and fluctuates within a given range. The mean and standard deviation of the posterior distribution, with burn-in-period removed, are used to estimate the final temperature and salinity, and their associated uncertainties (Gamerman and Lopes, 2006). Here, the inversion was conducted on reflectivity values and performed at every seismic reflectivity profile or common midpoint (CMP) and depth coordinate across the seismic section. The Markov chain length, N, was set to 2,000 and the first $\frac{1}{3}N$ iterations discarded as burn-in iterations. The likelihood function of reflectivity, R given the model, m was computed as

$$L\left(m \mid R(CMP, d)\right) \propto$$

$$\exp\left[-\sum \frac{\{R_{obs}\left(CMP, d\right) - R_{pred}\left(CMP, d\right)\}^2}{2{\sigma_e}^2}\right]$$

where $R_{obs}(CMP, d)$ and $R_{pred}(CMP, d)$ represent the measured and predicted reflectivity data at each CMP and depth, and σ_e is the measured data uncertainty. R_{obs} was computed by summing the high frequency component of the reflectivity, $R_{high\_freq\_seismic}$, obtained from the seismic data (band-pass filtered to 10–80 Hz), with the low frequency component (<10 Hz, $R_{low\_freq\_XBT}$) deduced using XBT interpolated temperature and salinity fields (**Figure 2**) following Biescas et al. (2014). As such $R_{obs} = R_{high\_freq\_seismic} + R_{low\_freq\_XBT}$. $R_{pred}(CMP, d)$ was computed from the vertical profile of the starting model ($R_{low\_freq\_XBT}$), but with the temperature or salinity value at depth, d, sampled from a prior distribution. This prior distribution was obtained using the standard deviation of starting model temperature and salinity values within a vertical 40 m window of d (i.e., the vertical spatial resolution, $L_0 \sim 40$ m, corresponds to a frequency, f_o, of 10 Hz following $L_o = c/4f_o$, where $c = 1,500\ ms^{-1}$ is the sound speed (Sheriff and Geldart, 1995). σ_e was estimated as 7.06×10^{-6}, the ambient seismic noise calculated as the standard deviation of seismic reflectivity within an area beneath the meddy where there are no strong seismic reflections. The ambient noise was found to follow a normal distribution. See Tang et al. (2016) for further details of inversion procedures.

Iteratively Improving the Prior Model

As shown later, the success of the MCMC inversion is highly reliant on the accuracy of the low frequency component of the prior model, $R_{low\_freq\_XBT}$. A similar conclusion was noted by Tang et al. (2016). To improve the start temperature-salinity model for the inversion, we investigated iteratively updating the prior model at each inverted common mid-point (CMP), using previous inverted results. The seismic survey was broken up into "inversion units," defined by XBT locations such that each unit was bordered by an XBT profile (XBT_i and XBT_{ii}) with N_s CMPs, or seismic reflectivity profiles, in between. For each inversion unit, the MCMC inversion process was started at the CMP closest to XBT_i (i.e., CMP 1), with the prior model computed by linearly interpolating data from XBT_i and XBT_{ii}. Inverted temperatures and salinities at CMP 1

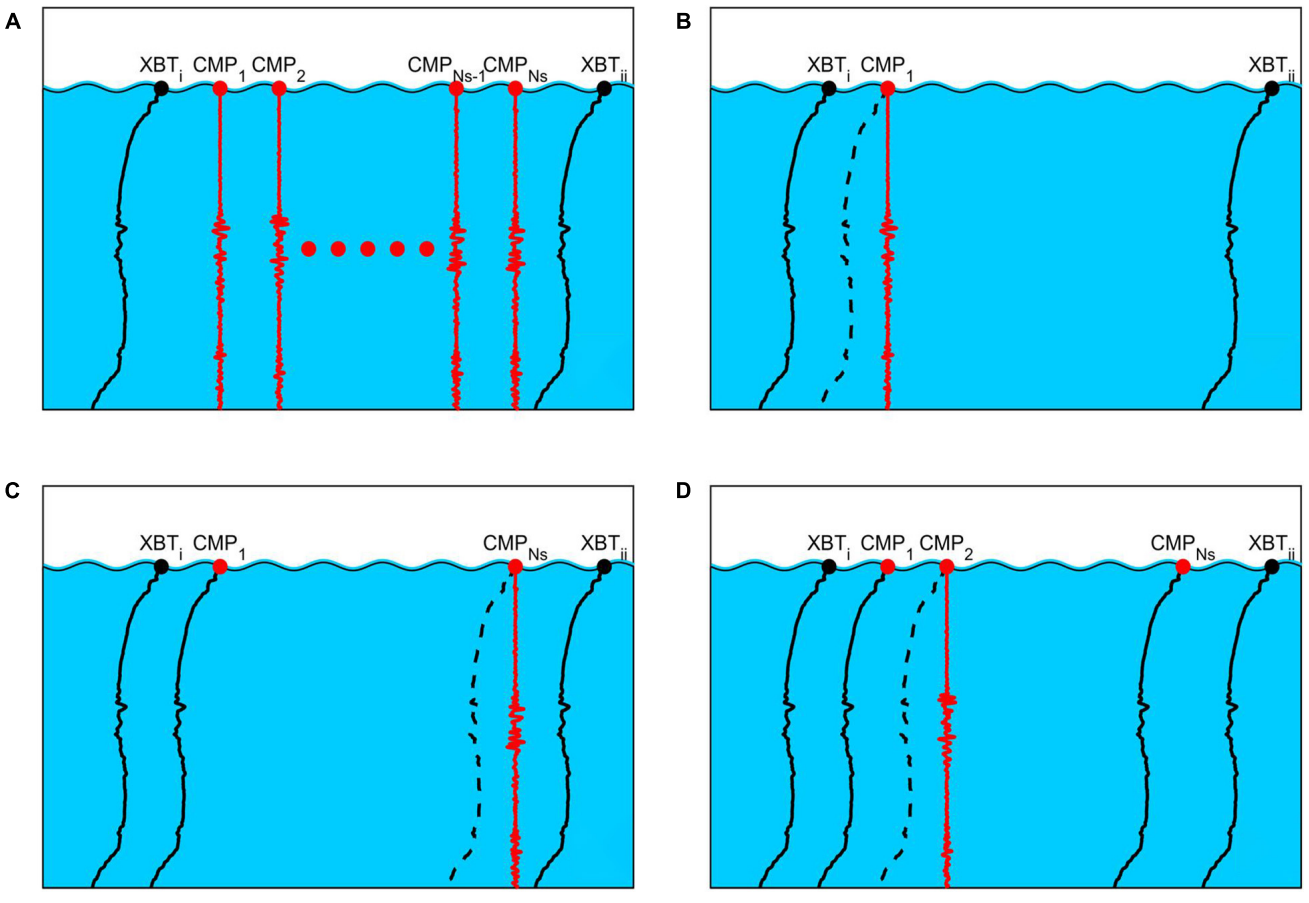

FIGURE 3 | Schematic of inversion unit and iterative MCMC approach. Black dots indicate XBT positions that bound the inversion unit (XBT_i and XBT_{ii}). Solid black lines represent the prior temperature-depth model as a function of depth. Red dots represent positions of Ns seismic CMPs, and red wiggles show associated seismic reflectivity depth profiles used in inversion. Dashed lines represent newly inverted temperature-depth profiles. **(A)** Starting data within inversion unit. **(B)** CMP 1 is inverted using prior model from XBT data. **(C)** Inverted data from CMP 1 is used to update the prior model. CMP Ns is inverted. **(D)** Inversion from CMP Ns is used to update prior model, and CMP 2 is inverted. The process is repeated for CMP Ns-2. . .CMP 3. . . until the whole inversion section has been processed.

were then combined with XBT_i and XBT_{ii}, to produce a new prior model. The updated prior model was used for the next CMP inversion, which was conducted at the CMP closest to XBT_{ii} (i.e., CMP N_s). The process was repeated at CMP 2, CMP N_s -1, CMP 3, CMP N_s-2. . ., until the whole unit had been inverted: see **Figure 3** for a schematic. Inverted results were not incorporated into the prior model if an associated posterior uncertainty anomaly (i.e., compared to a depth moving average of 100 m) was above a chosen threshold of 0.04°C. At each inversion step therefore, the prior model was iteratively updated to incorporate both the hydrographic data and previous inversion results. Recovered temperatures and salinities using the iteratively updated prior model were compared to those using a stationary prior model.

Uncertainty Estimation

Uncertainties introduced to the high-frequency component of the recovered temperature and salinity fields by noise in the seismic data and any mis-alignment of XBT data is accounted for in calculating the standard deviation of the posterior MCMC distribution (Tang et al., 2016). Contamination to the reflectivity field associated with the ringyness of the seismic source and other receiver responses has been minimized by performing a deconvolution on the seismic data using the source wavelet. In this study we also quantify the uncertainty introduced by inaccuracies in the low frequency starting temperature and salinity models. Firstly, the error associated with the estimation of the salinity from XBT temperature data using the non-linear approach of Ballabrera-Poy et al. (2009) was evaluated by applying the technique to CTD-based temperatures. The RMS error between estimated and measured salinities was computed for the 15% of CTD data not used in the model training (with CTD data recorded every 1 m this equates to a total of 6,090 data points, with 914 used for validation). The RMS salinity error was found to obey a normal distribution from which the standard deviation was used to compute the uncertainty. Secondly, errors introduced as a result of the interpolation of XBT data were considered. Starting models were recomputed using 12, 7, 5, and 4 XBTs, corresponding to typical XBT spacings of 4.6 km, 9.1 km, 13.6 km and 18.2 km, respectively. The distribution of RMS errors between the starting model temperature and salinities, and those measured from the removed XBTs were used to estimate the interpolation uncertainty for different XBT spacings (i.e., the standard deviation of the error distribution which was found to follow a normal distribution). For the case of all 24 XBTs (spacing of ∼2.3 km), the error distribution was computed using half the difference of XBT neighboring pairs. We note that the position of reflectors can get distorted and reflection amplitudes weakened by moving water effects (Klaeschen et al., 2009; Vsemirnova et al., 2009; Papenberg et al., 2010). Maximum current velocities in the survey region were ∼0.4 ms^{-1} and hence uncertainties associated with moving water to the inverted fields are likely small compared to other uncertainty sources (Papenberg et al., 2010). A summary of the inversion process, along with sources of uncertainties, is shown schematically in **Figure 4**.

RESULTS

Markov Chain Monte Carlo Inversion of the Seismic Section

The final recovered temperature and salinity fields, alongside computed potential densities, for the meddy are shown in **Figure 5**. The meddy shows a distinctive lens-shaped core of warm (∼12.5°C), salty (∼36.7 psu) water between 650 and 1,500 m depth. The meddy core temperature drops smoothly with depth, while salinities appear slightly greater at the core center. Overall the core is stably stratified. Layering filament features with vertical scales of typically 30 m surround the meddy core, where the velocity shear is likely greatest (e.g., Armi et al., 1989). These thermohaline intrusions are more continuous and distinct at the top of the meddy, where they encompass a region of roughly 300 m depth. On the western boundary of the meddy the finescale structures become more disrupted and the erosion of the meddy through mixing with cooler, fresher north Atlantic water is apparent. Fewer filaments are present on the lower surface of the meddy. The dynamics of these imaged thermohaline intrusions and their variability around the meddy core will be investigated in further studies. On the northeast of the section, along the upper edge of the meddy, there is one reflection horizon with anomalously low temperatures, high salinities and unstable density: this region should be interpreted with caution due to the high posterior MCMC inversion uncertainties here (see section "Markov Chain Monte Carlo Inversion Uncertainties").

Figure 6 shows an example of the MCMC inversion process at 539 m depth for CMP 2300 (i.e., a transect distance of 8.1 km), located at the midpoint of an inversion unit. The temperature and salinity decrease steadily in the first 300 inversion iterations before stabilizing after about iteration 600 (the "burn-in" period). Comparison of prior and posterior distributions show the reduced uncertainty in inverted compared to initial model temperatures and salinities, with the mean temperature and salinity dropping from 11.6 to 11.4°C and from 35.73 to 35.68 psu after the MCMC inversion.

Markov Chain Monte Carlo Inversion Uncertainties

One of the developments to previous inversions of the GO project meddies [e.g., see Papenberg et al. (2010) and Biescas et al. (2014)] presented here is that the Bayesian framework of the MCMC inversion allows for the posterior uncertainty at each inversion point to be computed and thus the spatial distribution of recovered temperature and salinity uncertainties analyzed. While MCMC posterior distribution uncertainties vary spatially, section averaged uncertainties are used for the uncertainty associated with interpolation of the prior model, and the error associated with estimating salinity from XBT data (see **Table 1**). The final section uncertainty is shown in **Figure 7**. Maximum uncertainties of the recovered temperature and salinity are 0.28°C and 0.12 psu, respectively. Regions of higher reflectivity at the meddy boundary tend to correspond to higher uncertainties. Despite the higher signal to noise ratio

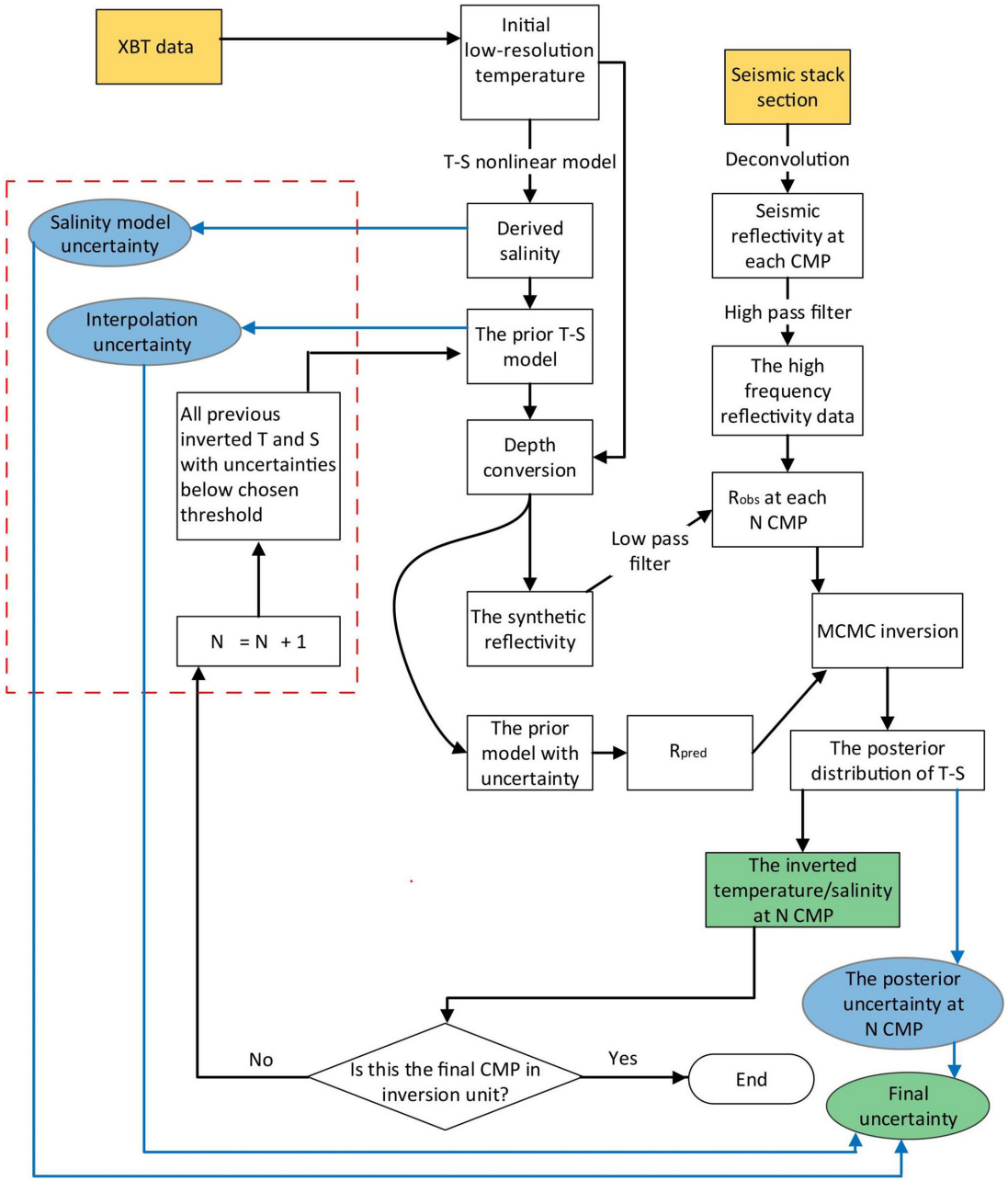

FIGURE 4 | Flow diagram summarizing the iterative MCMC inversion procedure. Rectangular shapes represent processing steps. Yellow rectangles represent the starting points of one inversion loop (input temperature profile and seismic data). Blue circles indicate the uncertainties relating to methods, data or models. Green rectangles represent output of inverted results and their corresponding uncertainties. Stages surrounded by red dashed lines represent updates to Tang et al. (2016). Note that the synthetic reflectivity is calculated from the prior temperature-salinity model following Ruddick et al. (2009).

in these regions, MCMC posterior distribution uncertainties increase due to higher thermohaline variability (Tang et al., 2016). In particular, a short band of high uncertainties most notable in the salinity field is found on the northeastern upper meddy boundary. These high uncertainties are associated with one reflection horizon and indicate the MCMC inversion did not perform as well here, likely due to the high variability in the temperature and salinity at the edge of the meddy and associated disruptions to the reflectivity. Uncertainties in the meddy core are typically 0.15°C and 0.06 psu.

Table 1 summarizes the inversion uncertainties averaged across the seismic section associated with the MCMC posterior distribution, the interpolation used to produce the starting model, and the estimation of salinity from XBT data using the neural network fitting approach. The error associated with the interpolation of the hydrographic data to produce the low

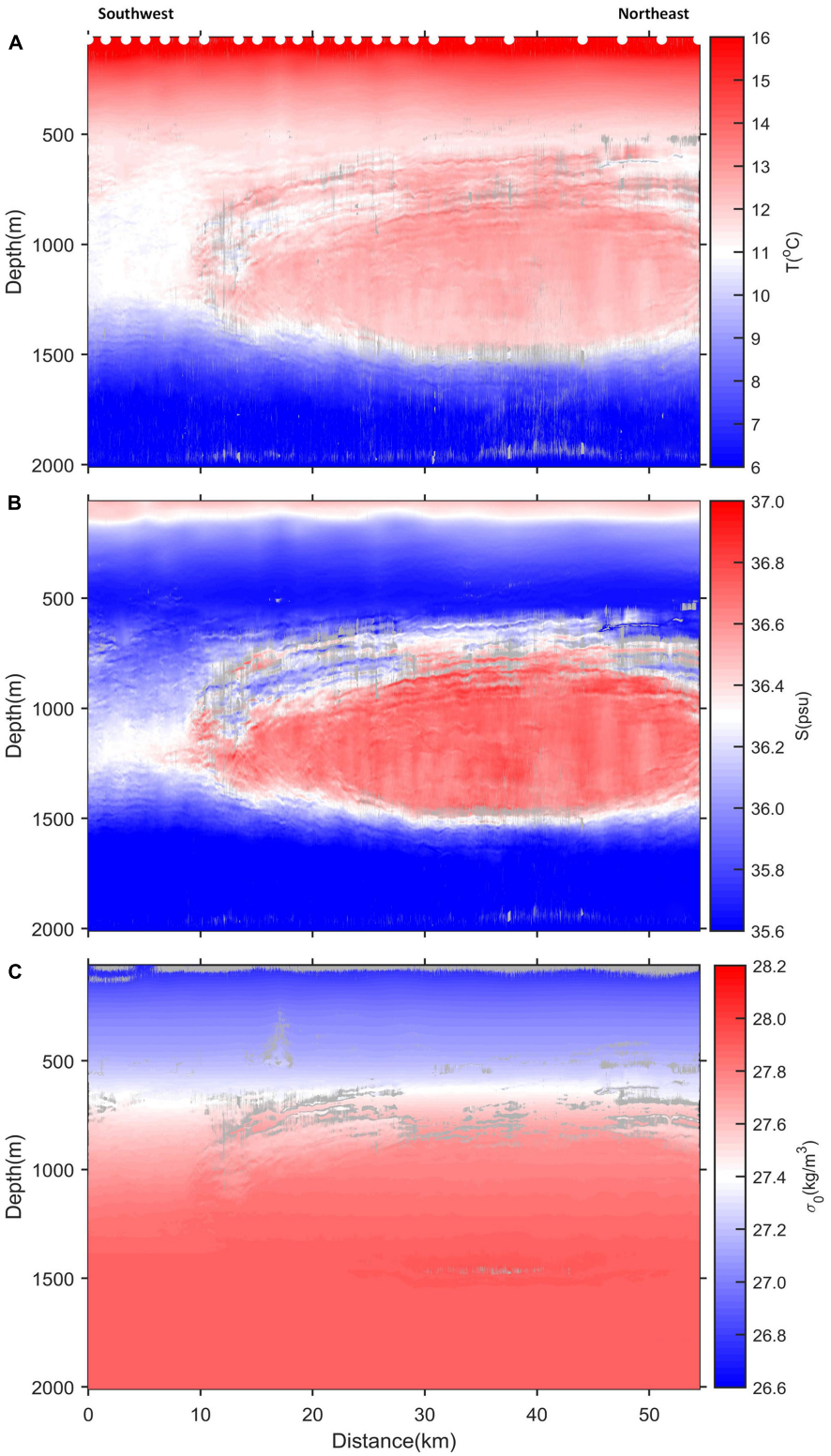

FIGURE 5 | MCMC inversion results of seismic section for **(A)** temperature, **(B)** salinity and **(C)** potential density anomaly. 24 XBTs (white dots) are used to compute the prior model, which is iteratively updated with inversion results. The inversion is performed at every CMP. Seismic data above 60 m depth is discarded due to the contamination from the residual direct wave. No reflectors were present below 2,000 m. Grayed out regions mark areas of high uncertainty (i.e., within the top 5% of uncertainties across the section).

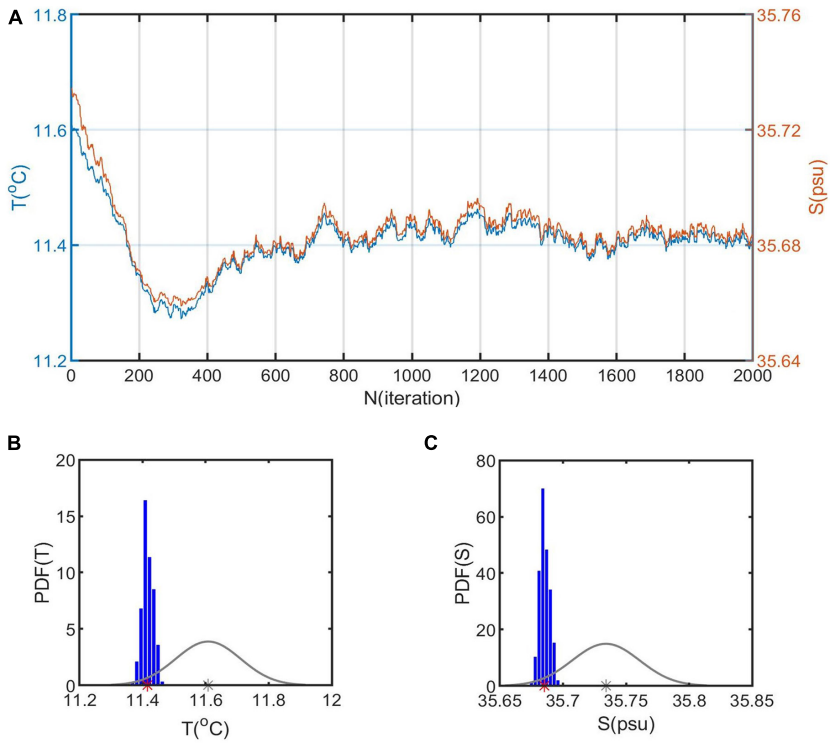

FIGURE 6 | (A) The Markov temperature and salinity chain at depth 539 m, CMP 2300. **(B)** Associated temperature prior and posterior probability density functions (PDFs). Gray curve = prior distribution of temperature. Gray star = mean of temperature prior distribution. Blue bars = posterior distribution. Red star = the mean temperature of the posterior distribution. **(C)** As for panel **(B)** but for salinities.

TABLE 1 | Uncertainties across the seismic section for an MCMC inverted temperatures and salinities with all 24 XBTs used to produce the prior model which is iteratively updated with inversion results.

	Interpolation	MCMC posterior	T-S model salinity	Overall
Temperature, °C	0.14	0.02	–	**0.16**
Salinity, psu	0.040	0.005	0.010	**0.055**

MCMC posterior uncertainty is the average of spatially varying posterior distribution uncertainties. The bold values are the sum of all uncertainties.

frequency prior model dominates the total uncertainty as also found by Biescas et al. (2014). For example, when all 24 XBTs are used to compute the starting model, 88% of the total temperature uncertainty is due to errors associated with the low frequency starting model. The error associated with estimating salinity from XBT data makes up roughly 18% of the total salinity uncertainty. The impact of reduced XBT sampling on recovered temperature and salinity uncertainties is shown in **Figure 8**.

Comparing Inverted Results to Observations

To evaluate results, measured XBT data were compared with inverted values: the inversion was re-run with every other XBT removed, for independent validation of inverted results. Here we show validation examples from two locations on the seismic section: XBT 4, located to the west of the meddy, and XBT 8 which was deployed at the edge of the meddy where horizontally the temperature changes rapidly (see **Figure 2** for XBT locations). Results are shown in **Figure 9**. Outside the meddy (XBT 4) measured and inverted temperatures and salinities are extremely well matched, with RMS error standard deviations for temperature and salinity of 0.14°C and 0.04 psu, respectively. However, the quality of the initial model degrades significantly in regions of rapid temperature or salinity change after removing half of the XBTs. At the meddy edge (XBT 8) inverted temperatures differ from XBT data by more than 1°C at some depths, such as between 1,000 and 1,200 m. The MCMC was found to converge in this region, and the signal-to-noise of the seismic data here is not unusually low. As such it is likely the inaccuracy of the initial model that has resulted in these poor inversion results (**Figures 9E–H**). Considering the reduced uncertainty associated with increased XBT sampling (**Figure 8**), inversion results are likely much better at XBT 8 for the case where all 24 XBTs are utilized. An appropriately sampled low frequency prior model is key for accurate inversion results.

Comparing an Iteratively Updated to a Stationary Prior Model in the Markov Chain Monte Carlo Inversion

Alongside improving the uncertainty estimates of inverted temperature and salinity fields, we have also built on the

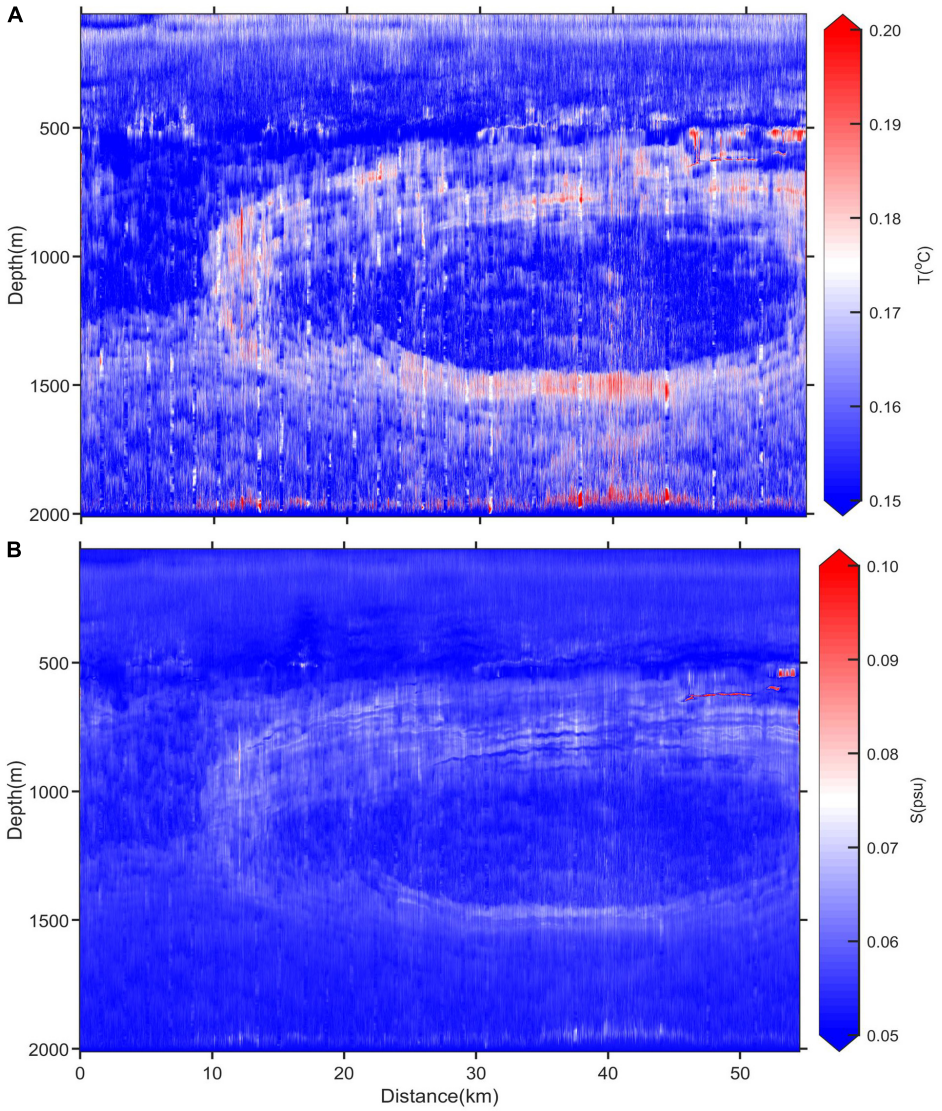

FIGURE 7 | Spatial distribution of final inversion uncertainties for **(A)** temperature and **(B)** salinity using all 24 XBTs. Uncertainties include the standard deviation of the posterior MCMC distribution, errors introduced from interpolation of the prior low frequency model, and the uncertainty in estimating salinity from XBT temperature values.

MCMC inversion methods developed by Tang et al. (2016) by iteratively updating the prior model at each step of the inversion (see section "Materials and Methods"). Comparison of inverted temperature and salinity uncertainties using an iteratively updated prior model to a stationary prior model are shown in **Figure 10**. Although the prior uncertainties of the two methods are similar, posterior distribution uncertainties (i.e., as computed from the MCMC process) are reduced in the iterative approach. In particular, the more extreme MCMC uncertainties are reduced in the iterative approach as shown by the smaller tails in the uncertainty distributions (**Figure 10**). The mean posterior temperature and salinity uncertainties using the stationary prior model method are 0.03°C and 0.008 psu compared to 0.02°C and 0.005 psu for the iteratively updated model, implying that inverted results are closer to the field data if an iterative prior model is used. Differences in inverted fields between a stationary and iteratively updated prior model become most apparent when a lower resolution starting model is used with reduced XBTs (as is the case in many seismic oceanographic datasets), as shown in **Figure 11**. Here MCMC inverted temperatures for a region at the edge of the meddy using a prior model with a reduced XBT spacing of ∼30 km are shown, using both a traditional stationary prior model and an iteratively updated prior model. Note that apart from the uncertainty analysis, the stationary MCMC approach is essentially equivalent to the conventional linearized inversion approach as used by Papenberg et al. (2010) and Biescas et al. (2014). Both

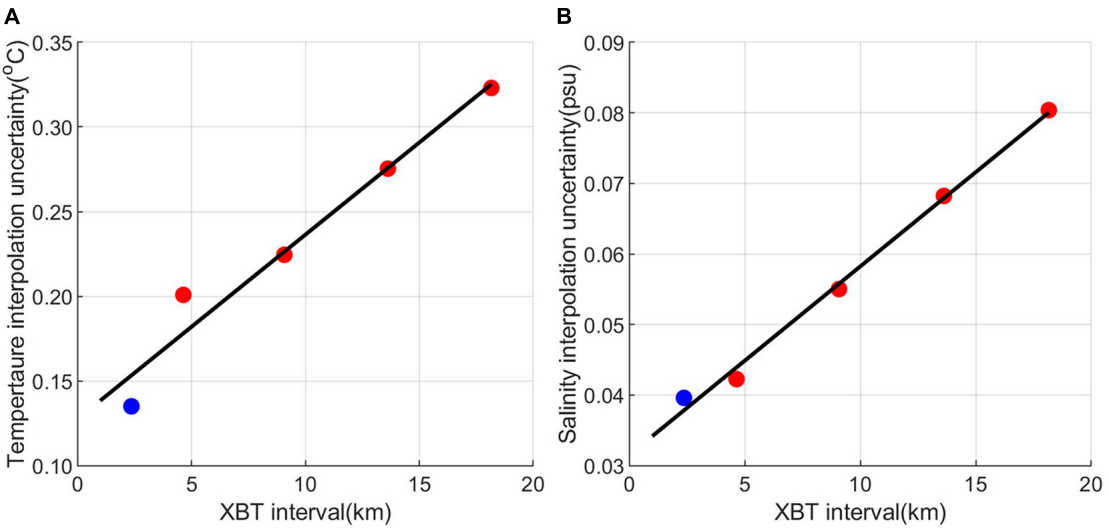

FIGURE 8 | (A) Variation of prior model interpolation temperature uncertainty (for the whole section) with XBT sampling resolution. Blue dot highlights slightly different method used to compute uncertainty when all 24 XBTs are included (see section "Materials and Methods"). **(B)** As for panel **(A)** but for salinity uncertainties.

inversion approaches are compared to the high-resolution temperature field constructed from all XBTs (i.e., with a spacing of approximately 2 km). The temperature field from the stationary method is found to vary little from the prior model, and displays a far more coherent horizontal structure when compared with both the iterative approach and high-resolution XBT section (for example along the top in the region at depths 600–800 m and transect distance 28–37 km). The stationary prior model inversion thus appears to be highly constrained to the interpolated background starting model. Iteratively updating the prior model with previous inversion results overcomes this constraint, and in many places results in a more representative temperature inversion that reflects the horizontal variability and complexity at the edge of the meddy better. However, we note that there are some regions where the non-stationary approach matches the high-resolution XBT data better, such as just outside the meddy core (e.g., depths 1,200–1,350 m; transect distance 13–20 km) and we find that the mean absolute difference between the inverted results and the high-resolution temperature section for both approaches are comparable. In conclusion, an iterative MCMC approach reduces posterior uncertainties and removes contamination from linear interpolation of the start model, but a high-resolution prior model is still key for reconstructing detailed temperature and salinity fields.

DISCUSSION AND CONCLUSION

The Bayesian MCMC approach has been applied to a seismic oceanographic dataset to recover the temperature and salinity of a meddy, with lateral and vertical resolutions of $O(10\ \mathrm{m})$. A typical meddy with a stably stratified core of 12.5°C and 36.7 psu, and complex layering and finestructure at the meddy periphery is imaged. Uncertainties in the inverted temperature and salinity results are estimated as 0.16°C and 0.055 psu, respectively. Whilst on face value these uncertainties appear higher than other inversion studies e.g., Papenberg et al. (2010), Biescas et al. (2014) and Tang et al. (2016), here the inclusion of uncertainties associated with both the high frequency and low frequency data components reflect more realistic confidence intervals in recovered temperature and salinity values. Furthermore, the use of the Bayesian MCMC approach has allowed the spatial variability of uncertainties across the meddy to be quantified.

In addition to improved uncertainty analysis, we also investigated the impact of iteratively updating the prior model used in the inversion with previous inverted results, such that MCMC inversion approaches can be used on seismic datasets that may not have coincident high-resolution XBT data [e.g., as in Papenberg et al. (2010) and Biescas et al. (2014)], or continuous reflections as in Tang et al. (2016). The iterative approach is found to both reduce inversion uncertainties and reduce artifacts introduced into the prior model by the interpolation of XBTs. Overall, the iterative MCMC inversion better represents the complex horizontal structure as found around the meddy. However, it should be emphasized that the improvements associated with the iterative approach are secondary to the impact of using a starting model of appropriate resolution: by quantifying and comparing the contribution of uncertainties from different sources we find that the main contributor to the final uncertainty is the low frequency start model as derived from the XBT interpolation. For example, a starting model based on XBT spaced at $\sim$ 2 km reduces uncertainties in inverted temperature and salinities by 0.16°C and 0.04 psu, respectively, compared to a starting model with XBTs spaced at roughly 18 km. By comparison uncertainties associated with the MCMC inversion

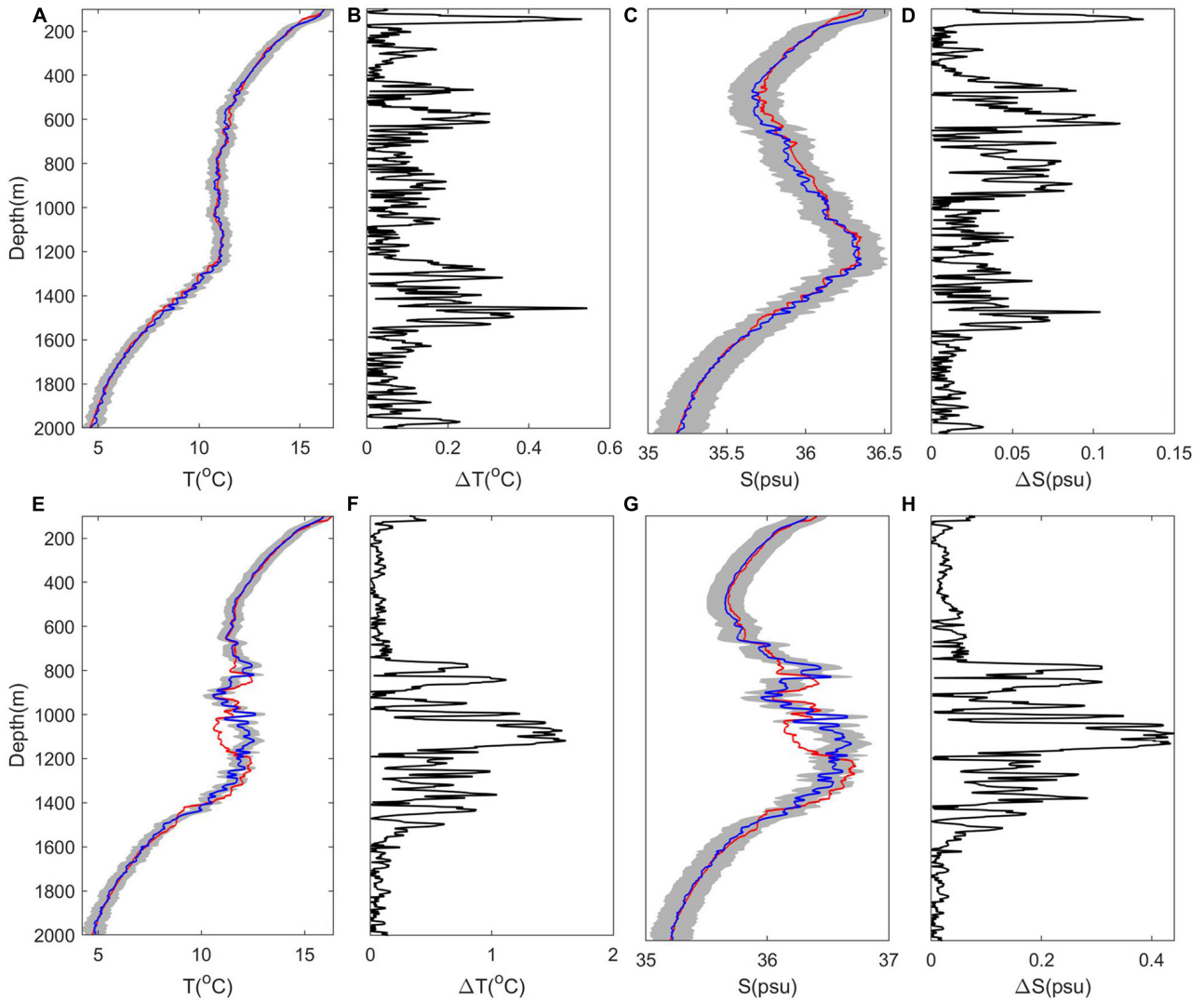

FIGURE 9 | (A) Temperature depth profiles deduced from the MCMC inversion using an iteratively updated prior model computed from half the XBTs (blue) and the observed data computed from the removed XBT 4 (red) to the west of the meddy. Gray shaded regions show 95% uncertainty bands. **(B)** Differences between inverted and measured XBT temperature at XBT 4. **(C,D)** As for panels **(A,B)** but for salinity data. **(E–H)** as for panels **(A–D)** but for the XBT 8, located at the edge of the meddy. Note that the edge of the meddy (depths ∼1,100 m), where interpolation errors are particularly high, is one of the regions where the observations do not fall within our 95% uncertainty estimate.

of the high-frequency information contained within the seismic data are much smaller, being 0.02°C and 0.005 psu. In conclusion, although the iterative MCMC improves inverted results, an accurate starting model is crucial for reducing the final inversion uncertainty particularly in highly heterogeneous regions such as sub-surface eddies. Other inversion studies also note the necessity of accurate reference models (Biescas et al., 2014; Dagnino et al., 2016; Tang et al., 2016). As such we strongly recommend that high-resolution XBT deployments, ideally deployed every few km, are conducted alongside future seismic studies.

For analysis of legacy data sets lacking coincident, high resolution hydrographic data, or seismic horizons that are not continuous enough to extend prior models as achieved by Tang et al. (2016), other approaches must be adopted to produce spatially improved starting models. One option may be to adopt the method used by Gunn et al. (2018), whereby low resolution temperature fields were extracted from seismic data using the RMS sound velocity picked during velocity analysis of prestack seismic data. This approach could enable the inversion of temperature and salinity fields from seismic data without the need for coincident hydrographic data, useful for analyzing legacy seismic datasets as collected by the hydrocarbon industry. Alternatively, the MCMC inversion approach could be combined with full waveform inversion techniques which despite being computationally expensive are applied directly to pre-stack data, avoiding assumptions associated with seismic stacking techniques and deconvolution

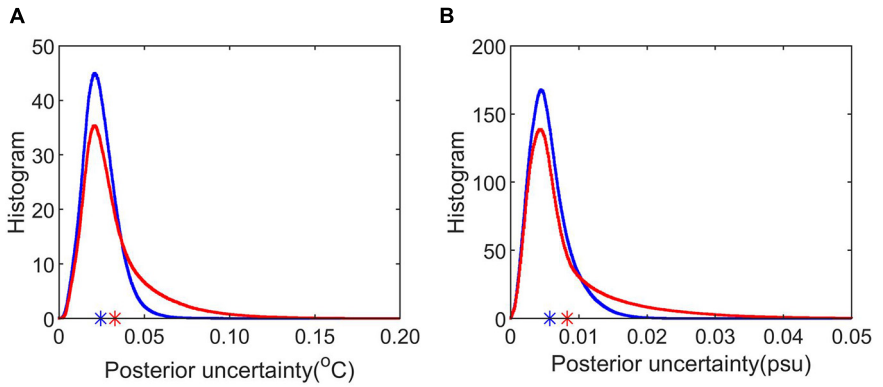

FIGURE 10 | Comparison of stationary and iteratively updated posterior inversion uncertainties. **(A)** Red (blue) lines show the histogram of posterior temperature uncertainty MCMC distribution for stationary (iterative) prior model. Stars indicate the mean of distribution. **(B)** As for panel **(A)** but for salinity uncertainties.

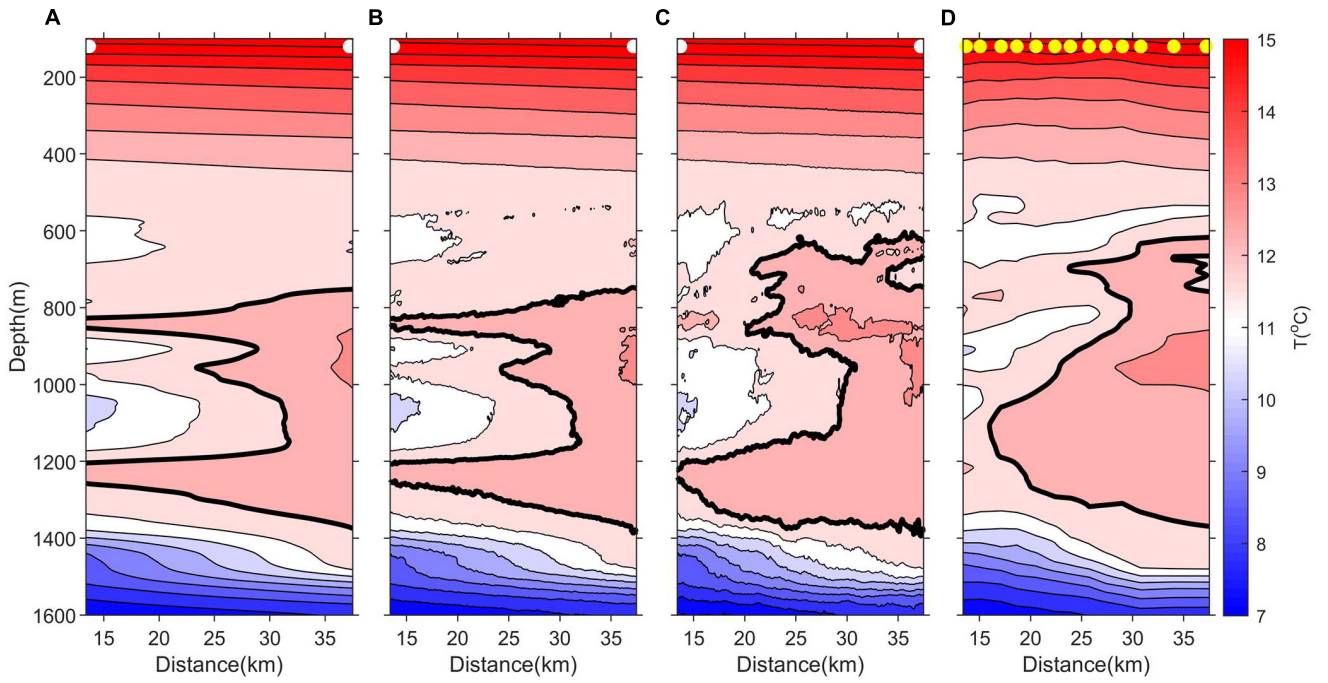

FIGURE 11 | Comparison of MCMC inverted temperature fields using a stationary and iteratively updated starting model. Colored contours show temperature fields, and the thick black line follows the 12.21°C temperature contour, chosen to highlight the meddy structure. **(A)** Initial reduced XBT-based temperature model used for inversion results shown in panels **(B,C)** based on interpolation of two XBTs approximately 30 km apart: white dots mark XBT locations. **(B)** Inverted temperatures using the starting model as shown in panel **(A)** at each inversion location (i.e., a stationary prior model). **(C)** Inverted temperature field in which the starting model is iteratively updated at each horizontal position with previous inversion results (see section "Iteratively Improving the Prior Model"). **(D)** As for panel **(A)** but the high-resolution temperature field constructing using all available XBT data. Yellow dots mark XBT locations.

(Wood et al., 2008; Dagnino et al., 2016). Furthermore, the combination of MCMC inverted seismic oceanographic field studies, as demonstrated here, with coincident data from underwater autonomous vehicles would provide a complete picture of finescale to mesoscale structures. Seismic experimental set up also impacts the final resolution of inversion results (Hobbs et al., 2009).

This work contributes to the growing approaches to extracting temperature and salinity data from marine seismic surveys, key to understanding finescale and submesoscale oceanic structure and how they relate to larger scale (mesoscale) dynamics. The temperature and salinity fields of the meddy presented here are of high enough resolution and accuracy to be used for further dynamical analysis, such estimating isopycnal displacements and dissipation levels (Sheen et al., 2009; Dickinson et al., 2017) and using spice anomalies to diagnose lateral stirring mechanisms (Klymak et al., 2015). Such data will ultimately improve our understanding of the role that sub-surface eddies

play in the distribution of heat, salt, nutrients and other tracers within the ocean.

DATA AVAILABILITY STATEMENT

The raw data supporting the conclusions of this article will be made available by the authors, without undue reservation.

AUTHOR CONTRIBUTIONS

RH and KLS conceived the idea for the work. WX developed the analysis with guidance from all co-authors. WX conducted the data analysis with some input from QT. WX and KLS wrote the initial draft of the manuscript. RH led the collection of the original *in situ* dataset. RH, JS, KLS, and QT provided analytical and conceptual advice throughout the project. TE supported data processing and figure production. All authors contributed to the article and approved the submitted version.

FUNDING

WX was supported by the China Scholarship Council and University of Exeter. This work was supported by the EU project GO (15603) (NEST). QT was supported by the Youth Innovation Promotion Association, CAS (Y202076), and the Rising Star Foundation of the South China Sea Institute of Oceanology (NHXX2019DZ0101).

ACKNOWLEDGMENTS

This study has been conducted using E. U. Copernicus Marine Service Information. Seismic sections were produced using OMEGA/Western-Schlumberger, and Seismic Unix software, visualization used MATLAB. Nucleus+ airgun modeling software was provided to Durham University under an academic license by PGS.

REFERENCES

Armi, L., Hebert, D., Oakey, N., Price, J. F., Richardson, P. L., Rossby, H. T., et al. (1989). Two years in the life of a Mediterranean salt lens. *J. Phys. Oceanogr.* 19, 354–370. doi: 10.1175/1520-04851989019<0354:TYITLO<2.0.CO;2

Armi, L., and Zenk, W. (1984). Large lenses of highly saline Mediterranean water. *J. Phys. Oceanogr.* 14, 1560–1576. doi: 10.1175/1520-04851984014<1560:LLOHSM<2.0.CO;2

Ballabrera-Poy, J., Mourre, B., Garcia-Ladona, E., Turiel, A., and Font, J. (2009). Linear and non-linear T–S models for the eastern North Atlantic from Argo data: role of surface salinity observations. *Deep Sea Res. I Oceanogr. Res. Pap.* 56, 1605–1614. doi: 10.1016/j.dsr.2009.05.017

Biescas, B., Ruddick, B. R., Nedimovic, M. R., Sallarès, V., Bornstein, G., and Mojica, J. F. (2014). Recovery of temperature, salinity, and potential density from ocean reflectivity. *J. Geophys. Res. Oceans* 119, 3171–3184. doi: 10.1002/2013JC009662

Biescas, B., Sallarès, V., Pelegrí, J. L., Machín, F., Carbonell, R., Buffett, G., et al. (2008). Imaging meddy finestructure using multichannel seismic reflection data. *Geophys. Res. Lett.* 35:L11609. doi: 10.1029/2008GL033971

Bornstein, G., Biescas, B., Sallarès, V., and Mojica, J. F. (2013). Direct temperature and salinity acoustic full waveform inversion. *Geophys. Res. Lett.* 40, 4344–4348. doi: 10.1002/grl.50844

Bower, A. S., Armi, L., and Ambar, I. (1997). Lagrangian observations of meddy formation during a Mediterranean undercurrent seeding experiment. *J. Phys. Oceanogr.* 27, 2545–2575. doi: 10.1175/1520-04851997027<2545:LOOMFD<2.0.CO;2

Carton, X., Daniault, N., Alves, J., Cherubin, L., and Ambar, I. (2010). Meddy dynamics and interaction with neighboring eddies southwest of Portugal: observations and modeling. *J. Geophys. Res. Oceans* 115:C06017. doi: 10.1029/2009JC005646

Dagnino, D., Sallarès, V., Biescas, B., and Ranero, C. R. (2016). Fine-scale thermohaline ocean structure retrieved with 2-D prestack full-waveform inversion of multichannel seismic data: application to the Gulf of Cadiz (SW Iberia). *J. Geophys. Res. Oceans* 121, 5452–5469. doi: 10.1002/2016JC011844

Dickinson, A., White, N. J., and Caulfield, C. P. (2017). Spatial variation of diapycnal diffusivity estimated from seismic imaging of internal wave field, Gulf of Mexico. *J. Geophys. Res. Oceans* 122, 9827–9854. doi: 10.1002/2017JC013352

Fortin, W. F. J., Holbrook, W. S., and Schmitt, R. W. (2016). Mapping turbulent diffusivity associated with oceanic internal lee waves offshore Costa Rica. *Ocean Sci.* 12, 601–612. doi: 10.5194/os-12-601-2016

Fortin, W. F. J., Holbrook, W. S., and Schmitt, R. W. (2017). Seismic estimates of turbulent diffusivity and evidence of nonlinear internal wave forcing by geometric resonance in the South China Sea. *J. Geophys. Res. Oceans* 122, 8063–8078. doi: 10.1002/2017JC012690

Gamerman, D., and Lopes, H. F. (2006). *Markov Chain Monte Carlo – Stochastic Simulation for Bayesian Inference*. London: Chapman and Hall/CRC.

GEBCO Bathymetric Compilation Group (2020). *The GEBCO_2020 Grid – A Continuous Terrain Model of the Global Oceans and land*. Liverpool, UK: British Oceanographic Data Centre, National Oceanography Centre, NERC. doi: 10.5285/a29c5465-b138-234d-e053-6c86abc040b9

Gunn, K. L., White, N., and Caulfield, C. P. (2020). Time-lapse seismic imaging of oceanic fronts and transient lenses within South Atlantic Ocean. *J. Geophys. Res. Oceans* 125:e2020JC016293. doi: 10.1029/2020JC016293

Gunn, K. L., White, N. J., Larter, R. D., and Caulfield, C. P. (2018). Calibrated seismic imaging of eddy-dominated warm-water transport across the Bellingshausen Sea, Southern Ocean. *J. Geophys. Res. Oceans* 123, 3072–3099. doi: 10.1029/2018JC013833

Hebert, D., Oakey, N., and Ruddick, B. (1990). Evolution of a Mediterranean salt lens: scalar properties. *J. Phys. Oceanogr.* 20, 1468–1483. doi: 10.1175/1520-04851990020<1468:EOAMSL<2.0.CO;2

Hobbs, R. W. (2007). Geophysical oceanography (GO): a new tool to understand the thermal structure and dynamics of oceans. *AAPG Eur. Reg. Newslett.* 2:7.

Hobbs, R. W., Klaeschen, D., Sallarès, V., Vsemirnova, E., and Papenberg, C. (2009). Effect of seismic source bandwidth on reflection sections to image water structure. *Geophys. Res. Lett.* 36:L00D08. doi: 10.1029/2009GL040215

Holbrook, W. S., Páramo, P., Pearse, S., and Schmitt, R. W. (2003). Thermohaline fine structure in an oceanographic front from seismic reflection profiling. *Science* 301, 821–824. doi: 10.1126/science.1085116

Hua, B. L., Ménesguen, C., Le Gentil, S., Schopp, R., Marsset, B., and Aiki, H. (2013). Layering and turbulence surrounding an anticyclonic oceanic vortex: in situ observations and quasi-geostrophic numerical simulations. *J. Fluid Mech.* 731, 418–442. doi: 10.1017/jfm.2013.369

Jones, I. F., and Levy, S. (1987). Signal-to-noise ratio enhancement in multichannel seismic data via the Karhunen-Loeve transform*. *Geophys. Prospect.* 35, 12–32. doi: 10.1111/j.1365-2478.1987.tb00800.x

Klaeschen, D., Hobbs, R. W., Krahmann, G., Papenberg, C., and Vsemirnova, E. (2009). Estimating movement of reflectors in the water column using seismic oceanography. *Geophys. Res. Lett.* 36:L00D03. doi: 10.1029/2009GL038973

Klymak, J. M., Crawford, W., Alford, M. H., MacKinnon, J. A., and Pinkel, R. (2015). Along-isopycnal variability of spice in the North Pacific. *J. Geophys. Res. Oceans* 120, 2287–2307. doi: 10.1002/2013JC009421

Kormann, J., Biescas, B., Korta, N., De La Puente, J., and Sallars, V. (2011). Application of acoustic full waveform inversion to retrieve high-resolution temperature and salinity profiles from synthetic seismic data. *J. Geophys. Res. Oceans* 116:C11039. doi: 10.1029/2011JC007216

McWilliams, J. C. (2016). Submesoscale currents in the ocean. *Proc. R. Soc. A Math. Phys. Eng. Sci.* 472:20160117. doi: 10.1098/rspa.2016.0117

Ménesguen, C., Hua, B. L., Papenberg, C., Klaeschen, D., Géli, L., and Hobbs, R. (2009). Effect of bandwidth on seismic imaging of rotating stratified turbulence surrounding an anticyclonic eddy from field data and numerical simulations. *Geophys. Res. Lett.* 36:L00D05. doi: 10.1029/2009GL039951

Meunier, T., Ménesguen, C., Schopp, R., and Le Gentil, S. (2015). Tracer stirring around a meddy: the formation of layering. *J. Phys. Oceanogr.* 45, 407–423. doi: 10.1175/JPO-D-14-0061.1

Padhi, A., Mallick, S., Fortin, W., Holbrook, W. S., and Blacic, T. M. (2015). 2-D ocean temperature and salinity images from pre-stack seismic waveform inversion methods: an example from the South China Sea. *Geophys. J. Int.* 202, 800–810. doi: 10.1093/gji/ggv188

Paillet, J., Le Cann, B., Carton, X., Morel, Y., and Serpette, A. (2002). Dynamics and evolution of a Northern Meddy. *J. Phys. Oceanogr.* 32, 55–79. doi: 10.1175/1520-04852002032<0055:DAEOAN<2.0.CO;2

Papenberg, C., Klaeschen, D., Krahmann, G., and Hobbs, R. W. (2010). Ocean temperature and salinity inverted from combined hydrographic and seismic data. *Geophys. Res. Lett.* 37, 6–11. doi: 10.1029/2009GL042115

Pingree, R. D., and Le Cann, B. (1993). Structure of a meddy (Bobby 92) southeast of the Azores. *Deep Sea Res. I Oceanogr. Res. Pap.* 40, 2077–2103. doi: 10.1016/0967-0637(93)90046-6

Pinheiro, L. M., Song, H., Ruddick, B., Dubert, J., Ambar, I., Mustafa, K., et al. (2010). Detailed 2-D imaging of the Mediterranean outflow and meddies off W Iberia from multichannel seismic data. *J. Mar. Syst.* 79, 89–100. doi: 10.1016/j.jmarsys.2009.07.004

Prater, M. D., and Sanford, T. B. (1994). A meddy off cape St. Vincent. Part I: description. *J. Phys. Oceanogr.* 24, 1572–1586. doi: 10.1175/1520-04851994024<1572:AMOCSV<2.0.CO;2

Richardson, P. L., Bower, A. S., and Zenk, W. (2000). A census of meddies tracked by floats. *Prog. Oceanogr.* 45, 209–250. doi: 10.1016/S0079-6611(99)00053-1

Ruddick, B. (1992). Intrusive mixing in a Mediterranean salt lens—intrusion slopes and dynamical mechanisms. *J. Phys. Oceanogr.* 22, 1274–1285. doi: 10.1175/1520-04851992022<1274:IMIAMS<2.0.CO;2

Ruddick, B., and Hebert, D. (1988). The mixing of meddy sharon. *Elsevier Oceanogr. Ser.* 46, 249–261. doi: 10.1016/S0422-9894(08)70551-8

Ruddick, B. B., Song, H., Dong, C., and Pinheiro, L. (2009). Water column seismic images as maps of temperature. *Oceanography* 22, 192–205. doi: 10.5670/oceanog.2009.19

Sacchi, M. D. (1997). Reweighting strategies in seismic deconvolution. *Geophys. J. Int.* 129, 651–656. doi: 10.1111/j.1365-246X.1997.tb04500.x

Sallarès, V., Biescas, B., Buffett, G., Carbonell, R., Dañobeitia, J. J., and Pelegrí, J. L. (2009). Relative contribution of temperature and salinity to ocean acoustic reflectivity. *Geophys. Res. Lett.* 36:L00D06. doi: 10.1029/2009GL040187

Sallarès, V., Mojica, J. F., Biescas, B., Klaeschen, D., and Gràcia, E. (2016). Characterization of the submesoscale energy cascade in the Alboran Sea thermocline from spectral analysis of high-resolution MCS data. *Geophys. Res. Lett.* 43, 6461–6468. doi: 10.1002/2016GL069782

Schultz-Tokos, K., and Rossby, T. (1991). Kinematics and dynamics of a Mediterranean salt lens. *J. Phys. Oceanogr.* 21, 879–892. doi: 10.1175/1520-04851991021<0879:KADOAM<2.0.CO;2

Schultz Tokos, K. L., Hinrichsen, H.-H., and Zenk, W. (1994). Merging and migration of two meddies. *J. Phys. Oceanogr.* 24, 2129–2141. doi: 10.1175/1520-0485(1994)024<2129:MAMOTM>2.0.CO;2

Serra, N., Ambar, I., and Käse, R. H. (2005). Observations and numerical modelling of the Mediterranean outflow splitting and eddy generation. *Deep. Res. II Top. Stud. Oceanogr.* 52, 383–408. doi: 10.1016/j.dsr2.2004.05.025

Sheen, K. L., White, N. J., Caulfield, C. P., and Hobbs, R. W. (2012). Seismic imaging of a large horizontal vortex at abyssal depths beneath the sub-Antarctic. *Front. Nat. Geosci.* 5, 542–546. doi: 10.1038/ngeo1502

Sheen, K. L., White, N. J., and Hobbs, R. W. (2009). Estimating mixing rates from seismic images of oceanic structure. *Geophys. Res. Lett.* 36:L00D04. doi: 10.1029/2009GL040106

Sheriff, R. E., and Geldart, L. P. (1995). *Exploration Seismology*. Cambridge: Cambridge University Press. doi: 10.1017/CBO9781139168359

Song, H., Pinheiro, L. M., Ruddick, B., and Teixeira, F. C. (2011). Meddy, spiral arms, and mixing mechanisms viewed by seismic imaging in the Tagus Abyssal Plain (SW Iberia). *J. Mar. Res.* 2, 827–842. doi: 10.1357/002224011799849309

Tang, Q., Hobbs, R., Zheng, C., Biescas, B., and Caiado, C. (2016). Markov Chain Monte Carlo inversion of temperature and salinity structure of an internal solitary wave packet from marine seismic data. *J. Geophys. Res. Oceans* 121, 3692–3709. doi: 10.1002/2016JC011810

Vsemirnova, E., Hobbs, R., Serra, N., Klaeschen, D., and Quentel, E. (2009). Estimating internal wave spectra using constrained models of the dynamic ocean. *Geophys. Res. Lett.* 36:L00D07. doi: 10.1029/2009GL039598

Wang, G., and Dewar, W. K. (2003). Meddy–seamount interactions: implications for the Mediterranean salt tongue. *J. Phys. Oceanogr.* 33, 2446–2461. doi: 10.1175/1520-04852003033<2446:MIIFTM<2.0.CO;2

Warner, M. (1990). Absolute reflection coefficients from deep seismic reflections. *Tectonophysics* 173, 15–23. doi: 10.1016/0040-1951(90)90199-I

Wood, W. T., Holbrook, W. S., Sen, M. K., and Stoffa, P. L. (2008). Full waveform inversion of reflection seismic data for ocean temperature profiles. *Geophys. Res. Lett.* 35:L04608. doi: 10.1029/2007GL032359

Conflict of Interest: The authors declare that the research was conducted in the absence of any commercial or financial relationships that could be construed as a potential conflict of interest.

Publisher's Note: All claims expressed in this article are solely those of the authors and do not necessarily represent those of their affiliated organizations, or those of the publisher, the editors and the reviewers. Any product that may be evaluated in this article, or claim that may be made by its manufacturer, is not guaranteed or endorsed by the publisher.

frontiers in Marine Science

ORIGINAL RESEARCH
published: 20 January 2022
doi: 10.3389/fmars.2021.771973

Mid-Ocean Ridge and Storm Enhanced Mixing in the Central South Atlantic Thermocline

Jingxuan Wei[1], Kathryn L. Gunn[2] and Robert Reece[1]*

[1] Department of Geology and Geophysics, Texas A&M University, College Station, TX, United States, [2] Centre for Southern Hemisphere Oceans Research (CSHOR), CSIRO Oceans and Atmosphere, Hobart, TAS, Australia

We investigate the spatial distribution of diapycnal mixing and its drivers in the central South Atlantic thermocline between the Rio-Grande Rise to the Mid-Atlantic Ridge. Diapycnal mixing in the ocean interior influences the slowly evolving meridional circulation, yet there are few observations of its variability with space and time or its drivers. To overcome this gap, seismic reflection data are spectrally analyzed to produce a 1,600 km long full-thermocline vertical section of diapycnal diffusivity, that has a vertical and horizontal resolution of $O(10)$ m and spans a period of 4 weeks. We compare seismic-derived diffusivities with CTD-derived diffusivities and direct observations from 1996, 2003, and 2011. In the mean and on decadal scales, we find that thermocline diffusivities have changed little in this region, retaining a background value of 1×10^{-5} m^2 s^{-1}. Imprinted upon the background rates, mixing is heterogeneous at mesoscales. Enhanced mixing, exceeding 10×10^{-5} m^2 s^{-1} and spreading between 200 and 700 m depth, is found above the Mid-Atlantic Ridge suggesting the ridge enhances diffusivity by at least one order of magnitude across the entire water column. Rapid decay of diffusivities within 30 km of the ridge implies local dissipation of tidal energy. Above smooth topography, patches of enhanced mixing are possibly caused by a recent storm that injects near-inertial energy into the water column and elevates mixing from 3×10^{-5} m^2 s^{-1} to 50×10^{-5} m^2 s^{-1} down to depths of more than 600 m. The propagation speed of near-inertial energy varies substantially from 17 to 27 m/day. Faster speed, and therefore greater penetration depths of 800 m, are probably facilitated by an eddy. Together, these data extend the observational record of central South Atlantic thermocline mixing and provide insights into drivers of mesoscale variability.

Keywords: seismic oceanography, diapycnal diffusivity, mid-ocean ridge, storm, South Atlantic

OPEN ACCESS

Edited by:
Qunshu Tang,
South China Sea Institute of Oceanology, Chinese Academy of Sciences (CAS), China

Reviewed by:
Zhao Jing,
Ocean University of China, China
Qingxuan Yang,
Ocean University of China, China

****Correspondence:***
Jingxuan Wei
jingxuan.wei@tamu.edu

Specialty section:
This article was submitted to Ocean Observation, a section of the journal Frontiers in Marine Science

Received: *07 September 2021*
Accepted: *09 December 2021*
Published: *20 January 2022*

Citation:
Wei J, Gunn KL and Reece R (2022) Mid-Ocean Ridge and Storm Enhanced Mixing in the Central South Atlantic Thermocline. Front. Mar. Sci. 8:771973. doi: 10.3389/fmars.2021.771973

INTRODUCTION

Turbulent diapycnal mixing maintains global overturning circulation (Munk and Wunsch, 1998). Diapycnal mixing is primarily caused by breaking of internal waves that transfer energy from large to small scales, ultimately leading to irreversible mixing. Understanding the spatial and temporal distribution of mixing is important in developing ocean circulation and climate models (Harrison and Hallberg, 2008). Analytical modeling suggests that an average diffusivity of $O(10 \times 10^{-5})$ m^2 s^{-1} is required to maintain abyssal stratification (Munk and Wunsch, 1998), while $O(1 \times 10^{-5})$ m^2 s^{-1}

is required in the main thermocline (Lumpkin and Speer, 2007). However, diapycnal mixing is extremely patchy in the real world and presents a unique observational challenge.

Enhanced mixing is mostly concentrated above rough topography such as ridges (Polzin et al., 1997; Klymak et al., 2006) and seamounts (Kunze and Toole, 1997), and is associated with sustained wind input (Price et al., 1986). Barotropic tidal energy converts to internal tide energy when it flows over topography (Munk, 1966; Munk and Wunsch, 1998; St. Laurent et al., 2001) and energy input from wind propagates into the ocean interior by generating near-inertial energy in the upper ocean mixed layer (Gill, 1984; D'Asaro, 1985; D'Asaro et al., 1995; Alford, 2003a). It is clear that external energy supply for the internal wave continuum comes from tides and winds primarily. Less is known about mixing in the ocean interior, away from rough topography and strong coastal winds, in particular in the central South Atlantic thermocline due to a historical lack of observations.

Via a subtropical gyre, the South Atlantic transports surface water equatorward to compensate the southward flow of the North Atlantic Deep Water (Garzoli and Matano, 2011; Cabré et al., 2019) (**Figure 1** inset). Previous research in the South Atlantic has mostly focused on low-frequency variability of its large-scale circulation (Stramma and England, 1999; Dong et al., 2015), or mesoscale variability near boundaries like the Brazil-Falkland confluence (Garzoli, 1993; Valla et al., 2018). The Brazil Basin Tracer Release Experiment (BBTRE) is the only microstructure survey in the mid-ocean of the South Atlantic (Polzin et al., 1997). The BBTRE collected microstructure measurements and discovered heightened mixing throughout much of the water column above the Mid-Atlantic Ridge (MAR). Diffusivities exceeding 100×10^{-5} m^2 s^{-1} were found within 150 m of the sea floor, while rates of 1×10^{-5} m^2 s^{-1} are found above smooth plains (Polzin et al., 1997; Ledwell et al., 2000; St. Laurent et al., 2001). Since this experiment in the late 1990s, there have been no further direct observations of diffusivity above the MAR, so it is unknown if the observed enhanced mixing rates are representative of the mean state. At basin scales, finescale parameterization applied to Argos and Conductivity-Temperature-Depth (CTD) probes has shown that the distribution of mixing in the South Atlantic interior is spatially patchy and temporally intermittent (Sloyan, 2005; Whalen et al., 2012). However, these studies mostly focus on the global pattern of mixing; the origin and evolution of the patchy mixing in the quiescent mid-ocean remain unknown.

More recently, studies have shown that storms are an effective method of wind energy injection (Dohan and Davis, 2011). In the wake of storms, diapycnal diffusivity is enhanced by 9×10^{-5} m^2 s^{-1} (Jing et al., 2015). Quantifying the effect of storms on oceanic mixing is especially difficult as they are moving, short-duration events. Conventional one-dimensional (1D) hydrographic measurements such as CTDs and Vertical Microstructure Profilers (VMPs) are unlikely to capture their effects. In particular, little is known about how storms contribute to mixing in the quiescent ocean interior, especially in basins like the central South Atlantic that are not covered by storm tracking system such as NOAA. In a warming world with increasing storm intensity (Walsh et al., 2019), it is important to develop two-dimensional (2D) tools that can yield a deeper understanding of the effects of storms on ocean mixing.

Seismic oceanography (SO) is a powerful tool that can be used to overcome these observational gaps. SO provides observations of physical processes across a horizontal length scale of $\sim O(10^5)$ m to $\sim O(10^2)$ m (Ruddick, 2018). The method utilizes low frequency (e.g., 5–120 Hz) acoustic sources and towed cable(s) containing a dense array of hydrophones to receive acoustic energy that is transmitted and reflected at boundaries created by temperature and salinity differences. Nandi et al. (2004) demonstrated that SO is able to capture temperature difference as small as 0.03°C. Sallarès et al. (2009) further confirmed that reflectivity has a stronger correlation with temperature than salinity. The frequency bandwidth of the acoustic source is capable of imaging thermohaline fine structure with lateral and vertical resolutions on the order of 10 m, meaning that the method is capable of mapping mesoscale structures such as fronts, internal waves, and eddies that are always missing in conventional hydrographic measurements. This relatively high resolution makes SO an ideal method for turbulence mixing analysis. Studies that calculated turbulent diffusivities from slope spectra of seismic reflections demonstrate the suitability of the method in exploring spatial and temporal changes of mixing (Sheen et al., 2009; Fortin et al., 2016; Mojica et al., 2018; Tang et al., 2019; Dickinson et al., 2020). The instantaneous spatial distribution of mixing derived from seismic data represents a near-full energy cascade from internal waves to turbulence (Ruddick, 2018), implying the potential use of seismic derived parameterization in future ocean models (Tang et al., 2021). When combined with hydrographic data, seismic oceanography studies can be used to overcome significant observational gaps.

Here, we present and analyze a ∼1,600 km-long 2D seismic transect starting from the eastern edge of the Rio Grande Rise (RGR) to the MAR, covering one of the major pathways of the Atlantic meridional overturning circulation (**Figure 1**). We calculate diapycnal diffusivities across the thermocline using the slope spectra method with seismic sections, as well as using finescale parameterization with CTD and Argo data. Our primary objective is to examine the spatial distribution of mixing in the central South Atlantic thermocline and extend its observational record. We also present the most likely hypotheses for drivers of enhanced mixing. Our results extend the observational record of diapycnal mixing in the central South Atlantic thermocline by providing diffusivities in 2003, 2011, and 2016, and provide further insights into the drivers of mesoscale mixing variability.

DATA AND METHODS

Seismic Data and Processing

This research uses seismic reflection data collected during the Crustal Reflectivity Experiment Southern Transect (CREST) experiment aboard the R/V Marcus G. Langseth (Estep et al., 2019). The primary goal of the CREST survey was to investigate the evolution of oceanic crust at 30° S, and it spans the eastern edge of the RGR to the MAR, including a ∼1,600 km-long

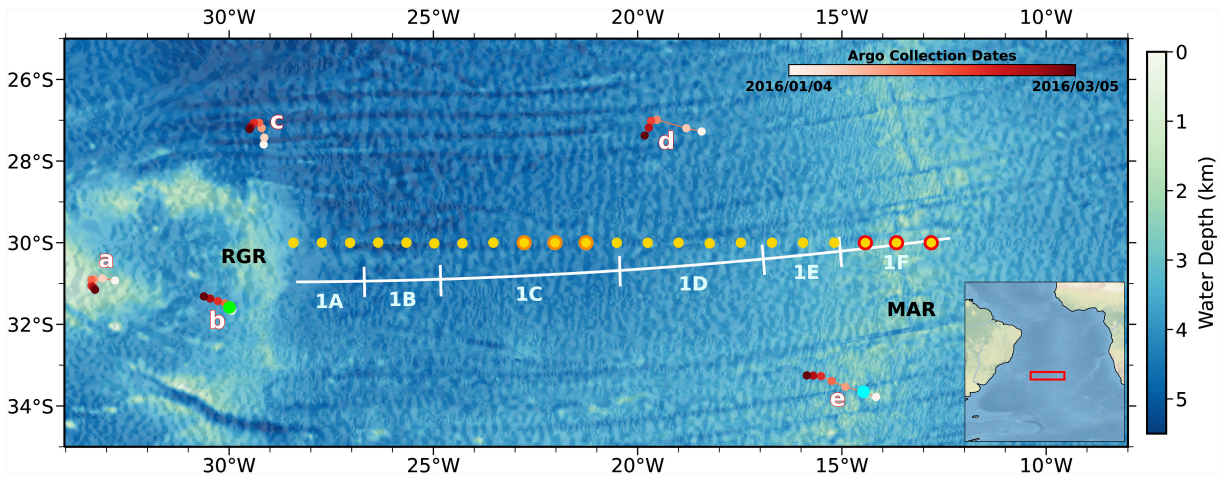

FIGURE 1 | Bathymetric map of seismic survey location. Bathymetry from the Global Multi-Resolution Topography Synthesis (Ryan et al., 2009). White lines = seismic profiles collected between January 29 and February 14, 2016, short meridional lines mark the connection point between zonal lines; yellow dots = CTD casts from GO-SHIP survey acquired in October 2011, yellow dots with orange/red edges correspond to orange/red profiles in **Figure 2** (GO-SHIP 2003 CTDs within 0.5° of 2011 CTDs and are not shown); red dots = Argo float trajectories between January 4 and March 5, 2016, labeled a–e; green and cyan dots = Argo floats used for mixing calculation to compare with seismic results in **Figure 6**. RGR, Rio-Grande Rise; MAR, Mid-Atlantic Ridge. Inset shows regional setting, with red box marking the location of the study area.

continuous east-west data transect (**Figure 1**). The transect sits at the center of the South Atlantic subtropical gyre and provides an opportunity to investigate the change of mesoscale mixing processes along a significant distance in a region that contains the returning limb of the Atlantic meridional overturning circulation (Cabré et al., 2019).

Seismic data were collected between January and February of 2016 (**Figure 4**). The acoustic source was a 36 bolt air-gun array with a total volume of 6,600 in^3 and 37.5 m shot spacing. Acoustic records were collected using a 12.6 km acoustically sensitive cable (i.e., streamer). The streamer contained 1,008 hydrophones with 12.5 m spacing. This survey design collects repeat reflections from the same subsurface point (i.e., common mid-points, CMPs) every 6.25 m. To ensure the maximum depth of imaging to be more than 1,000 m, while maintaining a high signal-to-noise ratio for turbulence analysis, we used the first 400 near-source acoustic records.

Seismic data were processed with a standard, but adapted, processing sequence typically used to image the solid earth (Yilmaz, 2001): geometry definition, noise attenuation, CMP sorting, sound speed analysis, stacking, amplitude correction, and migration (Fortin and Holbrook, 2009; Hobbs et al., 2009). Particular adaptations were made in the noise attenuation step to produce a high-quality image of oceanic fine structures. First, an eigenvector filter is applied to remove the direct waves that overprint the first 1 s of data. Second, the relatively small shot spacing (37.5 m) generates reverberations between the sea surface and seafloor which share the same frequency range with primary signals. We filter out reverberations in the frequency-wavenumber domain based on the curvature differences between these coherent noises and primary signals in shot gathers. Thirdly, to reliably extract turbulent regimes from seismic data, random noise must be attenuated, we follow the recommendations of Holbrook et al. (2013) by applying a 30–80 Hz band-pass filter. Lastly, shot-generated harmonic noise is suppressed by applying a notch filter centered at harmonic spikes (every 0.0267 cpm, cpm = cycles per meter) in the wavenumber domain (Holbrook et al., 2013). In addition, we implement a denoising convolutional neural network (DnCNN) to suppress random noise after stacking. We use the recommended steps and parameters of 17 layers and a mini-batch size of 128 (Zhang et al., 2017; Jun et al., 2020). We train the DnCNN model for 40 epochs and the number of iterations within each epoch is 220. After a series of noise attenuation, the signal-to-noise ratio of the entire seismic data increases by a factor of 6.

Seismic-Derived Diffusivities

Background

Based on the assumption that seismic reflections are a reasonable approximation of isopycnal surfaces (Krahmann et al., 2009; Holbrook et al., 2013), studies have shown that turbulent diffusivity can be accurately measured from vertical displacement spectra of tracked reflections (e.g., **Figure 3A**) from both the internal wave subrange (Sheen et al., 2009; Dickinson et al., 2017) and turbulent subrange (Holbrook et al., 2013; Fortin et al., 2016; Mojica et al., 2018; Tang et al., 2019; Gunn et al., 2021). To clearly recognize the transition from internal wave regimes to turbulent regimes in log-log space, the vertical displacement spectra are multiplied by $(2\pi k_x)^2$ to produce the slope spectra. Here we estimate the turbulent dissipation rate ε through the slope spectra method in the turbulent subrange, φ_ζ^{Turb}, via a model proposed by Klymak and Moum (2007):

$$\varphi_{\zeta_x}^{Turb} = 4\pi \frac{\Gamma \varepsilon}{N^2} [C_T \varepsilon^{-\frac{1}{3}} (2\pi k_x)^{\frac{1}{3}}] \quad (1)$$

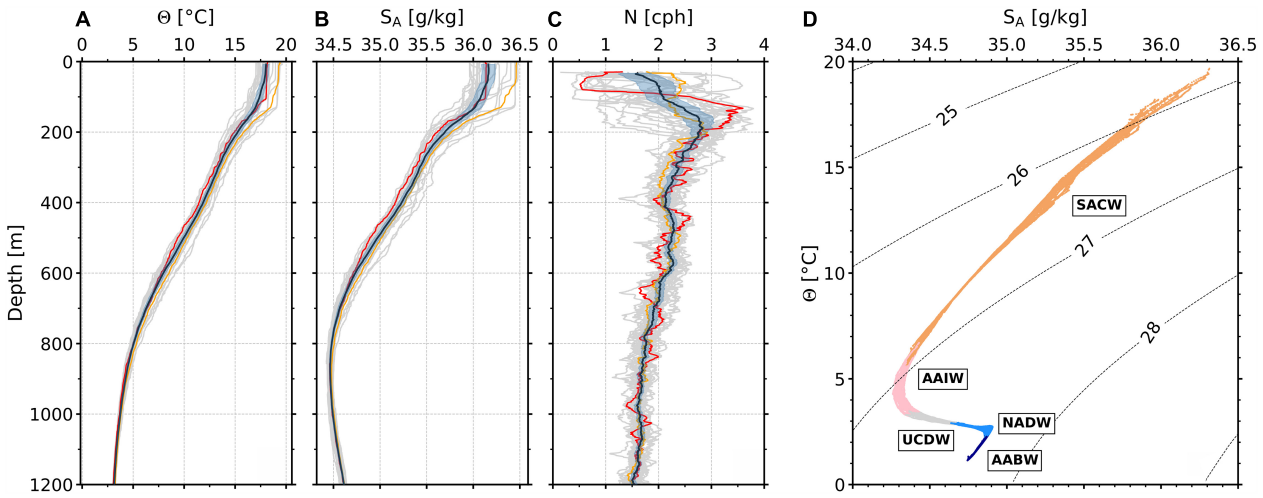

FIGURE 2 | Water properties from 22 GO-SHIP 2011 CTD casts (yellow dots in **Figure 1**). **(A)** Conservative temperature, Θ, as a function of depth. Black line = average profile; gray lines = individual profiles; blue patch = 95% confidence interval; and red/orange lines = average profiles of CTDs with red/orange edges (**Figure 1**). **(B)** Absolute salinity, S_A, as a function of depth. **(C)** Buoyancy frequency, N, as a function of depth. [cph = cycles per hour]. **(D)** Conservative temperature (Θ) – Absolute salinity (S_A) diagram. Points colored according to the water mass definition of Hernández-Guerra et al. (2019). Orange dots = South Atlantic Central Water (SACW); pink dots = Antarctic Intermediate water (AAIW); gray dots = Upper Circumpolar Deep Water (UCDW); blue dots = North Atlantic Deep Water (NADW); dark blue dots = Antarctic Bottom Water (AABW). Labeled dotted lines = potential density anomaly surfaces.

where $\Gamma = 0.2$ is the empirical mixing efficiency (Osborn and Cox, 1972), N is the horizontally averaged buoyancy frequency calculated from 22 historical CTD casts within the survey area (**Figure 2C**, black line), $C_T = 0.4$ is the Kolmogorov constant, and k_x is the horizontal wavenumber. Equation (1) produces a turbulence subrange with a slope of +1/3 in log-log space. Diapycnal diffusivity, K, is then calculated using the Osborn relationship (Osborn, 1980):

$$K = \Gamma \varepsilon / N^2 \quad (2)$$

where ε is spectrally estimated from seismic data and varies as a function of distance along the section and depth.

To generate high-resolution maps of diffusivity across the entire seismic section, two complementary methods are used to calculate K. These methods allow us to extract turbulent information across a range of depths and scales, as they take advantage of both low and high amplitude reflectivity (Fortin et al., 2016).

Relative Turbulent Energy From Amplitude Spectra

First, amplitude spectra are calculated following Holbrook et al. (2013) through direct Fourier data transform. These spectra are calculated directly from seismic amplitudes (i.e., no tracking) along depth slices, and are first used to identify whether the turbulent subrange exists. For the CREST data, the turbulent subrange exists between k_x 0.025–0.045 cpm (22.2–40 m) (**Figure 3B**). The advantage of using amplitude spectra is reflected in its preservation of all horizontal wavenumbers, therefore relative turbulent energy from all reflections can be extracted. In other words, amplitude spectra can provide relative levels of turbulence across the entire seismic section. However, amplitude spectra cannot provide absolute diffusivities because they are affected by the variation of seismic amplitudes, it is necessary to scale them with absolute diffusivities calculated from slope spectra of tracked reflections (hereafter, reflector slope spectra).

Absolute Diffusivities From Reflector Slope Spectra

Reflector slope spectra are calculated based on vertical displacement of undulating reflections that follows isopycnals, they are independent of seismic amplitude and thus can be used to estimate absolute diffusivity. We calculate reflector slope spectra using Fourier transform lengths of 256 points as recommended by Holbrook et al. (2013), equivalent to a reflection length of 1.6 km. Turbulent dissipation is then estimated by fitting reflector slope spectra to model (1) within the previously identified turbulent subrange (0.025–0.045 cpm) using least square inversion. Diffusivity is then calculated using equation (2) (**Figure 3C**).

Using reflector slope spectra also has its limitations. Tracked reflections, that yield slope spectra, must have high amplitude and good continuity, corresponding to the steepest temperature and salinity gradients (Ruddick et al., 2009). This limitation implies that absolute diffusivities cannot be estimated from weaker and discontinuous reflections that still possess turbulent information. Lower reflection amplitudes represent lower temperature and salinity gradients, corresponding to weaker stratification regions that are prone to mixing. Discontinuous reflections could be caused by mixing instabilities such as interleaving, internal wave breaking, turbulence, and double diffusion (Tang et al., 2018). Therefore, a simple spatial smoothing of diffusivities calculated from stronger and continuous reflections over the entire seismic section could result in underestimation of diffusivities in areas of weaker and discontinuous reflections. As discussed above, because amplitude spectra preserve all horizontal wavenumbers

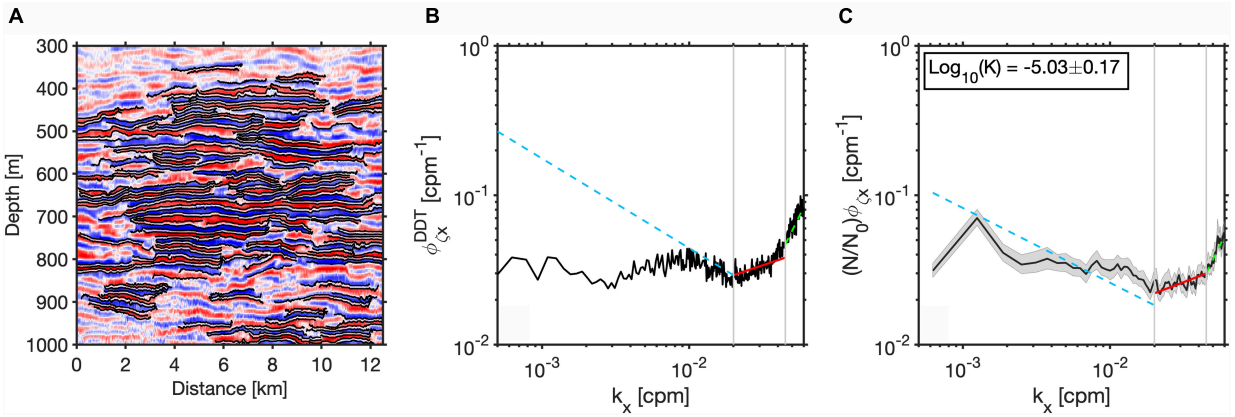

FIGURE 3 | Example of spectral analysis from line 1A (a rolling window used in section "Zonal Variability of Diffusivities"). **(A)** Seismic data overlapped with tracked reflections. Black lines = tracked reflections. **(B)** Direct data transform (DDT) of seismic data in panel **(A)**. **(C)** Average slope spectrum calculated from all the tracked reflections in panel **(A)**. Shaded gray area = 95% bootstrap confidence intervals. Dashed blue lines ($k^{-1/2}$), solid red lines ($k^{1/3}$) and dashed green lines (k^2) = the internal wave subrange, turbulence subrange and white noise, respectively (Garrett and Munk, 1975; Klymak and Moum, 2007; Holbrook et al., 2013). Two vertical gray lines bound the turbulent subrange used to calculate diffusivity. The calculated diffusivity and its uncertainty are shown in the upper left corner.

regardless of the strength of the reflections, we can overcome this limitation by joining and applying these two techniques in different window sizes to honor turbulent information in both types of reflections.

Combining Amplitude and Reflector Slope Spectra

The seismic section is divided into regional windows of size 6.25 km wide and 50 m deep for reflector slope spectra analysis. The size of the window is chosen to include enough reflections to minimize artifacts and provide accurate estimations of absolute diffusivities. An average reflector slope spectrum is calculated from all the tracked reflections within each regional window, and an absolute diffusivity is estimated for that window (**Figure 3C**). To complement the reflector slope spectra method, we calculate amplitude spectra in a much smaller window size of 400 m wide and 10 m deep. The window width is determined to include at least 10 horizontal wavelengths as calculated from the lower bound of the identified turbulent subrange (Fortin et al., 2017). Then, by integrating amplitude spectra energy over the turbulent subrange within each window, a map of relative turbulent energy across the entire seismic section can be obtained. Finally, relative turbulent energy is scaled by the absolute diffusivities within each regional window to produce the final high-resolution diffusivity map which has a horizontal and vertical resolution of 400 and 10 m, respectively (**Figure 5**). Fortin et al. (2016, 2017) have shown that this technique can reliably measure turbulent diffusivities from weaker reflections and seismically transparent zones where mixed water resides. Thus, these complementary techniques are able to produce high-resolution 2D maps of diffusivities. To avoid inaccurate estimation of diffusivity, seismic data shallower than 200 m are discarded because of the contamination caused by residual direct wave energy.

Depth- and Zonally-Averaged Diffusivity

We investigate the distribution of thermocline diffusivities as functions of longitude and depth by taking appropriate means (**Figure 6**). So that seismic-derived diffusivities are comparable with lower resolution hydrographic data, we calculate depth-averaged, zonally varying diffusivities in rolling half overlapping windows. The window starts at the beginning of line 1A to the end of line 1F, covering a total length of 1,625 km and has a width of 12.5 km, with an overlap of 6.25 km. The depth range of each window is 300–1,000 m, for which the starting depth is chosen to match Argos and CTDs depth limitations. Within each window, depth-averaged diffusivity is estimated using the average reflector slope spectrum (e.g., **Figure 3C**), rather than the amplitude spectra. The average diffusivity within each window is assigned to the center longitude of that window. Ultimately, we obtain depth-averaged diffusivities that span longitudes 28.3° W to 12.4° W with a sampling interval of 6.25 km (**Figure 6**).

Zonal-averaged, depth-varying diffusivities are calculated based on their topographic setting. Each seismic section is divided vertically into 256 m half-overlapping windows and into regions above smooth and rough topography. Within each window, an average spectrum is calculated to estimate diffusivity. Diffusivities derived from different seismic sections are normalized by the lengths of the sections then horizontally averaged to produce zonal-averaged, depth-varying diffusivities.

Error Analysis

Following Dickinson et al. (2020), we conservatively estimate an uncertainty for seismically derived diffusivities as ±0.4 logarithmic units. This value combines sampling and methodological errors. The sampling error mostly derives from the uncertainty in N, which we estimate as 0.28 cph using the standard deviation of CTD data. Methodological errors include the assumption of constant C_T and Γ and the process of fitting a straight-line model to reflector slope spectra. These uncertainties have been quantified by Dickinson et al. (2020), and are 0.25 log units. Combined in quadrature, the total uncertainty is ± 0.4 logarithmic units.

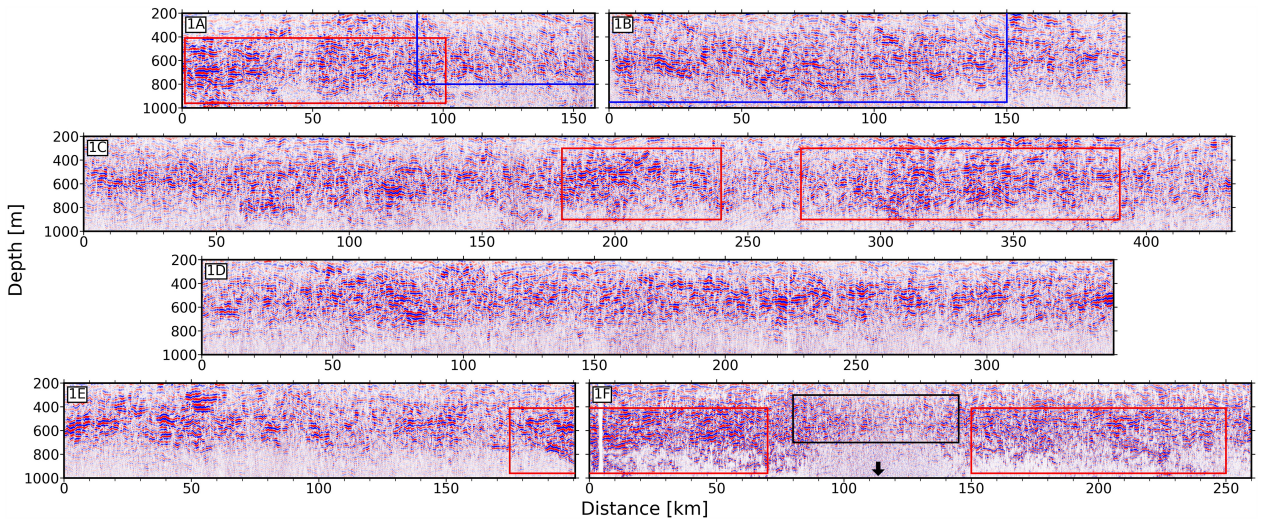

FIGURE 4 | Seismic sections from west (line 1A) to east (line 1F). Red boxes = locations of continuous, high amplitude reflections; blue boxes = an example location of shorter, discontinuous reflections; black box = water mass above the MAR. Black arrow = location of crest of the MAR.

Conductivity-Temperature-Depth- and Argo-Derived Diffusivities

Diffusivities are estimated from CTD and Argo data and can be seen as representative of mean and spot measurements of mixing, respectively. We estimate diffusivities from five nearby Argos and 44 co-located CTDs (**Figure 1**). We use CTD datasets from two repeat surveys occupying GO-SHIP A10 transect in 2003 and 2011 at 30° S (Sloyan et al., 2019). Argos were collected around the same time as the seismic survey (data downloaded from Global Argo Data Repository). All of the Argo profiles used in this study record depths larger than 1,000 m, and have vertical resolution less than 10 m. Argos b and e are ideally placed to provide spot measurements of mixing above smooth and rough topography conditions, respectively. Argo b was collected 176 km from the western end of line 1A, above the RGR, and only 2 days before the start of seismic acquisition (**Figure 1**, green dot). Argo e traveled across the MAR during January 2016 and is used to compare with seismically derived and depth-averaged diffusivities across the MAR (**Figure 1**, cyan dot). Although the Argo data are not co-located with the seismic survey, they provide meaningful measurements of the oceanic field above similar geological settings at two key locations.

From these hydrographic profiles, we computed potential density and buoyancy frequency. The selected profiles were then divided into 256 m half-overlapping segments. Following Kunze et al. (2006), the shallowest segment (0–256 m) is discarded due to the presence of sharp pycnoclines. For the remaining segments, we use a strain-based finescale parameterization to estimate ε (Kunze et al., 2006):

$$\varepsilon = \varepsilon_0 \frac{\overline{N^2}}{N_0^2} \frac{\langle \xi_z^2 \rangle^2}{\langle \xi_z^2 \rangle_{GM}^2} H(R_\omega) L(f, N) \quad (3)$$

$\varepsilon_0 = 6.73 \times 10^{-10}$ m^2 s^{-2}, $N_0 = 5.24 \times 10^{-3}$ rad s^{-1}, $\langle \xi_z^2 \rangle$ is the observed strain variance, $\langle \xi_z^2 \rangle_{GM}^2$ is the strain variance from the Garrett-Munk model spectrum (Garrett and Munk, 1975). $\overline{N^2}$ is the vertically averaged buoyancy frequency for each segment, which is estimated as linear fits to the specific volume anomaly depth profiles using the adiabatic leveling method (Bray and Fofonoff, 1981). $H(R_\omega)$ is a function related to the shear-to-strain ratio R_ω, which is set to 7 in this study (Kunze et al., 2006). $L(f, N)$ is a correction for the effects of latitude (Gregg et al., 2003). Finally, the diffusivity is given by equation (2).

RESULTS

Thermocline Structure

The thermocline is visible as a 1,000 m thick band of reflectivity that extends 1,600 km across all seismic sections and is consistent with the regional temperature structure (**Figures 2A**, **4**). Between 0 and 800–900 m depth, we observe stronger reflections and weaker reflectivity at greater depths. This vertical distribution of reflection amplitude corresponds to highly stratified SACW and weakly stratified AAIW, respectively (**Figure 2**). At 800–900 m depth, weakening reflection amplitude shows zonal variability indicating that the depth of the SACW/AAIW boundary shoals eastward by 100 m (**Figure 4,1A**).

Within the thermocline, reflectivity varies greatly in the lateral direction, changing from longer, higher amplitude to, shorter, lower amplitude and more disrupted reflectivity. Mesoscale patches of high-amplitude and more continuous reflectivity suggest the presence of eddy-scale processes, these patches extend to depths of 900 m and across tens of kilometers zonally (**Figure 4**, red boxes). Between 90 km and 150 km (**Figure 4**, blue boxes), a set of shorter, discontinuous reflections dip to the east which we interpret as a shear event typical of the region.

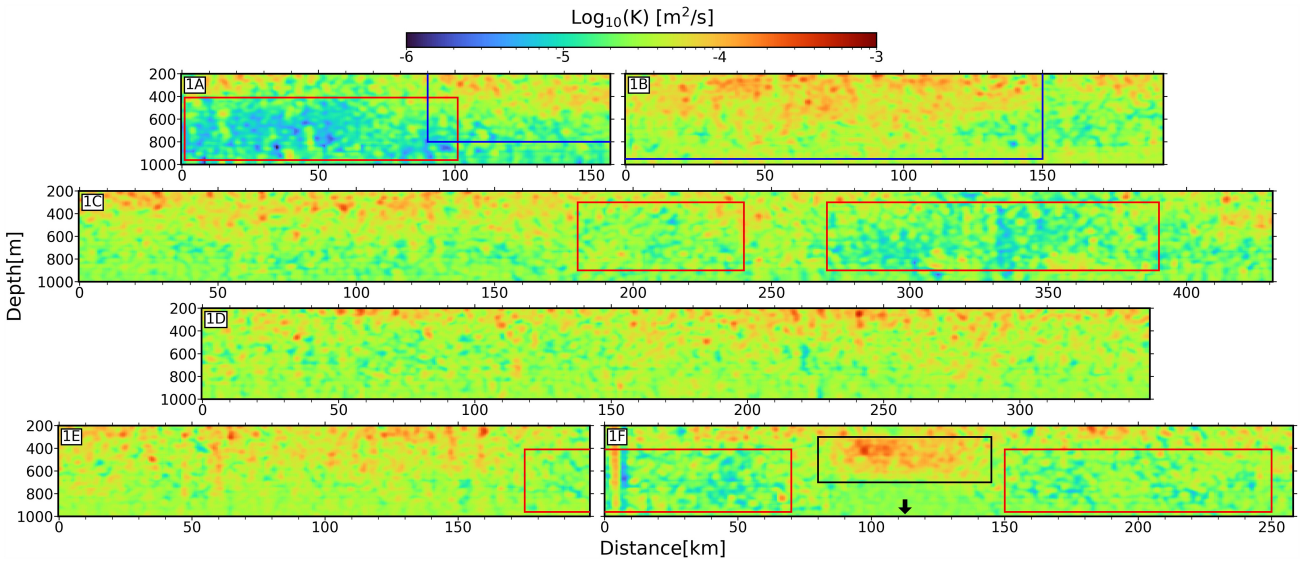

FIGURE 5 | Turbulent diffusivity maps derived from seismic sections in **Figure 4**. Red boxes = locations of lower diffusivities; blue boxes = an example location of enhanced mixing; black box = enhanced mixing above the MAR. Black arrow points at the location of the crest of the MAR. Colored boxes are the same as in **Figure 4**.

We do not observe submesoscale structures here, although these are often found in more energetic ocean environments such as boundary currents.

Above the MAR, reflections are clearly disrupted. In line 1F from 80 to 150 km weaker discontinuous reflections can only be seen from the surface down to 700 m (**Figure 4**, black box and arrow). This anomalous patch of low reflectivity extends approximately 30 km on either side of the ridge. Data below 700 m are severely contaminated by noise that has been diffracted by the hard igneous seafloor of this mid-ocean ridge and is too complicated to be sufficiently removed using noise attenuation.

Diffusivity of the Central South Atlantic Thermocline

Across the 1,600 km section of the central South Atlantic thermocline, the mean seismic-derived diffusivity is 3.96×10^{-5} m^2 s^{-1} (**Figure 5**). The value is similar to the microstructure observations made almost 20 years earlier in the Brazil Basin at longitudes of 28° W to 16° W (Polzin et al., 1997). The authors found a mean diffusivity of 1–5 $\times$ 10^{-5} m^2 s^{-1} in the upper 1,000 m of the water column. These seismic-derived (2016) and microstructure (1996) values are also consistent with CTD-derived diffusivities, which can be seen as representative of means for 2003 and 2011. The mean CTD estimates for 2003 and 2011 are 7.45×10^{-5} m^2 s^{-1} and 4.15×10^{-5} m^2 s^{-1}, respectively. The 2003 estimate is biased high by an anomalously elevated diffusivity around 13.5° W (**Figure 6**, green line). When this point is removed, the mean decreases to 3.57×10^{-5} m^2 s^{-1} which is remarkably consistent with the 2011 measurement and the mean seismic-derived diffusivity.

The spatial standard deviation of the seismic estimates is of a similar magnitude, 2.9×10^{-5} m^2 s^{-1}, to the mean revealing the heterogeneity of the thermocline diffusivities. Variability is clearly related to variations in the thermocline structure, as we observe a strong correlation between seismic reflection amplitudes (i.e., strength of stratification) and corresponding diffusivity maps. Weaker and discontinuous reflections are found to have an average diffusivity of 4.79×10^{-5} m^2 s^{-1}, a factor of four greater than locations dominated by stronger and more continuous reflections that have a mean value of 1.2×10^{-5} m^2 s^{-1}. This spatial correlation is most apparent in lines 1A,B. From the beginning of line 1A to about 90 km [**Figure 4,1A** (red box)], where seismic reflections appear to be stronger and laterally continuous, the corresponding diffusivity map shows low diffusivities close to the canonical value of 1×10^{-5} m^2 s^{-1} [**Figure 5,1A** (red box)]. However, starting at 100 km and moving eastward into line 1B, the strength of seismic reflections diminish as they become discontinuous [**Figures 4,1A,B** (blue boxes)], while diffusivities start to increase to the level of 10×10^{-5} m^2 s^{-1} from shallower water (∼250 m) into deeper water (∼900 m). In line 1B, at about 120 km, diffusivities start to gradually increase from deeper water (∼800 m) to shallower water (∼300 m), and eventually form a bowl-shape region populated by diffusivity hotspots across lines 1A,B [**Figures 5,1A,B** (blue boxes)]. Similar correlation patterns between the seismic images and diffusivity maps can also be observed in all remaining profiles.

Taken as a whole, there are identifiable mesoscale patterns in the diffusivity. In areas that show elevated diffusivities, diffusivity hotspots of 7.5–10 $\times$ 10^{-5} m^2 s^{-1} largely dominate, while scattered higher diffusivities of 20–50 $\times$ 10^{-5} m^2 s^{-1} also exist. These hotspots are mostly located in the upper 600 m, with an exception in line 1B from 50 to 100 km where they spread deeper than 800 m. In lower diffusivity regions, we see the canonical background value of 1×10^{-5} m^2 s^{-1} that mostly resides in

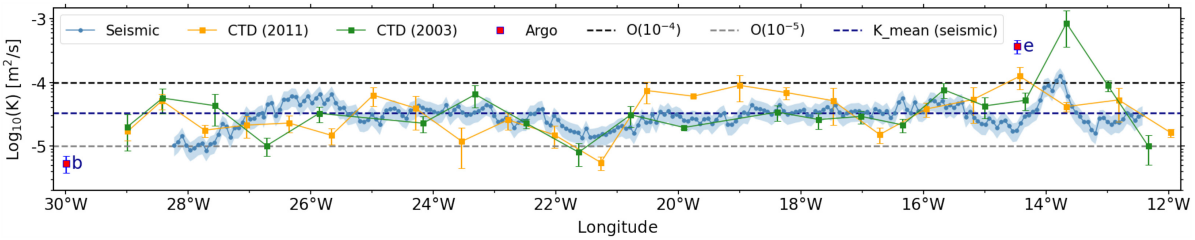

FIGURE 6 | Depth-averaged diffusivities derived from seismic and CTDs in the zonal direction, plotted with depth-averaged diffusivities calculated from two Argo profiles (green and cyan dots in **Figure 1**). Blue shade represents uncertainties of seismic estimates discussed in section "Depth- and Zonally-Averaged Diffusivity." Error bars show the standard error of depth-averaged diffusivity of CTD/Argo profiles.

the mid-depth from 400 to 800 m; diffusivities are slightly higher outside of this depth range.

Above the MAR, we observe the highest diffusivities of 25–50 $\times$ 10^{-5} m^2 s^{-1} that are densely distributed from 80 to 150 km within the 300 to 700 m depth range (**Figure 5,1F**). These estimates show that diffusivities are enhanced by an order of magnitude compared with background values. No reflections were tracked below 700 m because of severe noise contamination, which hinders our ability to reliably calculate diffusivities at deeper depths (**Figures 4**, **5,1F**). Nevertheless, the signal-to-noise ratio for the 300–700 m depth range is high enough for diffusivity estimation. Away from the ridge crest, diffusivities rapidly decay to about 1 $\times$ 10^{-5} m^2 s^{-1} within ∼30 km.

Zonal Variability of Diffusivities

Depth-averaged diffusivities reveal zonal variability in thermocline diffusivity, which is heterogenous of mesoscale length scales. Depth-averaged diffusivities vary from 0.9 $\times$ 10^{-5} to 12.6 $\times$ 10^{-5} m^2 s^{-1}, with the highest diffusivity above the MAR. Around 26° W, there is a second region of elevated diffusivity of 6.5 $\times$ 10^{-5} m^2 s^{-1}. Diffusivities are lowest in the west at approximately 1 $\times$ 10^{-5} m^2 s^{-1}. These depth-averaged diffusivities serve as an instantaneous snapshot of mixing during February 2016. They reveal that there is no zonal trend in diffusivities, rather diffusivities are enhanced in localized patches.

We now compare seismic-derived diffusivities to hydrographic-derived and depth-averaged diffusivities. CTD-derived and depth-averaged (mean taken over 300–1,000 m) diffusivities that vary with longitude range between 0.6 $\times$ 10^{-5} m^2 s^{-1} and 85 $\times$ 10^{-5} m^2 s^{-1} (GO-SHIP 2003, 2011; **Figure 6**, green and yellow line). The CTD estimates increase by one order of magnitude at the MAR. Two Argo profiles above smooth and rough topographic conditions serve as spot measurements of turbulence tuned to differing bathymetric conditions (**Figure 6**, magenta squares). The diffusivity calculated from Argo b (smooth) is 0.5 $\times$ 10^{-5} m^2 s^{-1}, it has a similar magnitude to the western end of line 1A, which has a seismic-derived diffusivity of 0.9 $\times$ 10^{-5} m^2 s^{-1}. Diffusivities above the rough topography of the MAR calculated from Argo e (37 $\times$ 10^{-5} m^2 s^{-1}) and seismic (12 $\times$ 10^{-5} m^2 s^{-1}) are both one order of magnitude higher than over smooth topography and are within error of each other (**Figure 6**).

Depth Variability of Diffusivities Over Different Topographic Settings

Zonally averaged diffusivities reveal the depth response of thermocline diffusivities over smooth (**Figures 7A–C**) and rough (**Figures 7D–F**) topographic settings. Above smooth topography, diffusivities are fairly constant with depth and are typically 1 $\times$ 10^{-5} m^2 s^{-1}. There is little difference between the seismic- and CTD-derived diffusivities here. Above rough topography, diffusivities are enhanced everywhere in the upper 700 m, and are 5.5 $\times$ 10^{-5} m^2 s^{-1} for seismic-derived estimates and 2.7 $\times$ 10^{-5} m^2 s^{-1} to 17 $\times$ 10^{-5} m^2 s^{-1} for CTD-derived estimates (**Figures 7D,E**). Below 700 m, seismic data cannot reliably recover diffusivities because of noise contamination, and the CTD data are used to fill this gap. The deep CTD-derived estimates show a sharp increase from 600 to 1,000 m (**Figure 7D**). We find that, at 30° S in the South Atlantic Ocean, diffusivities across the entire thermocline (up to 1,000 m depth) are modified by the presence, or lack of, rough topography (e.g., compare **Figures 7C,F**).

DISCUSSION

Here, we extend the observational record of ocean interior diapycnal mixing in the central South Atlantic, and, for the first time, we resolve diffusivities at mesoscale lengths for this location. High-resolution seismic diffusivity maps provide an unprecedented view of the variability of diapycnal mixing across 1,600 km of the thermocline. By combining high-resolution seismic-derived diffusivities with low spatial resolution CTD-derived and low temporal resolution Argo-derived diffusivities, we can assess the likely drivers of mixing in this location.

Temporal and Spatial Variability of South Atlantic Thermocline Diffusivities

At synoptic (∼1,000 km) and decadal scales, the background diffusivity of the South Atlantic thermocline has changed little at this location. In 1996, direct turbulent diffusivities measurements across the Brazil Basin revealed that the upper 1,000 m of the South Atlantic typically had diffusivities of around 1–5 $\times$ 10^{-5} $m^2 s^{-1}$ (Polzin et al., 1997). CTD-derived mixing estimates from 2003 and 2011 also show a mean diffusivity of 3–4 $\times$ 10^{-5} m^2 s^{-1}, while seismic data collected in 2016 show

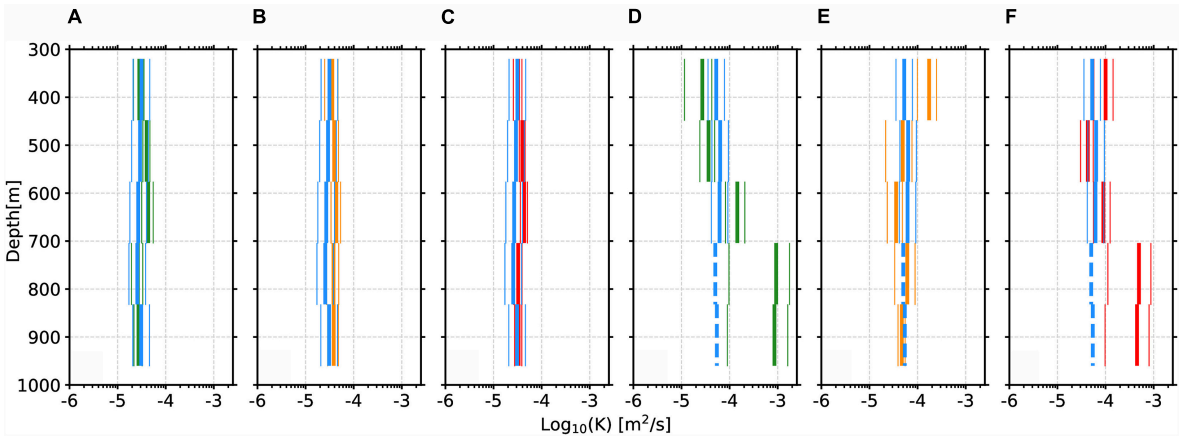

FIGURE 7 | (A–C) Averaged vertical profiles of diffusivity above smooth topography (data from seismic lines 1A–E and CTDs west of 15° W). Thick blue bars, green bars, orange bars = averaged vertical profiles derived from seismic, GO-SHIP CTD 2003, and 2011, respectively. Red bars = averaged vertical profiles derived from both GO-SHIP 2003 and 2011. Thin bars represent standard errors between CTD profiles or seismic sections. **(D–F)** Same to **(A–C)** but above the MAR (data from seismic line 1F and the three eastern most CTDs from GO-SHIP 2003 and 2011). Dashed blue lines represent unreliable diffusivities calculated from regions contaminated by noise.

a similar mean diffusivity in the upper 1,000 m of 4×10^{-5} m^2 s^{-1}. Taken together, these four decadal snapshots (1996, 2003, 2011, and 2016) suggest that there is little variability in the mean diffusivity of the thermocline. Using a global coupled climate model, Hieronymus et al. (2019) found that oceanic background diffusivity has a significant impact on the climate. They found that increased background diffusivity leads to increased meridional heat transport and stronger overturning in the ocean. Our observations suggest that on decadal timescales the mean thermocline diffusivity has changed little in this location, which may imply steady meridional overturning circulation in the South Atlantic thermocline.

Imprinted upon the background diffusivity, we show that diffusivities are heterogeneous and can be enhanced by up to one order of magnitude. Regions of high mixing correspond to seismic transparent zones or disrupted reflections. The correlation between seismic reflectivity and turbulent mixing is typical of seismic oceanography studies (Dickinson et al., 2017; Fortin et al., 2017; Tang et al., 2021) and these observations have shown that higher reflectivity is caused by sharper temperature and salinity gradients, hence stronger stratification, while lower reflectivity represents weaker stratification that facilitates mixing or homogeneous water masses. Weakened reflectivity above the MAR corresponds to enhanced mixing and weaker stratification (**Figure 4**, black box). Seismic-derived, CTD-derived, and Argo-derived diffusivities are all enhanced by an order of magnitude. This result is consistent with lower resolution diffusivity measurements made by Polzin et al. (1997), who showed that diffusivities exceed 1×10^{-5} $m^2 s^{-1}$ in the thermocline above the ridge. Depth-averaged N shows stronger stratification (2.13 cph) above smooth plains compared to weaker stratification (2.01 cph) above the MAR (**Figure 2C**). The high resolution and depth coverage of the seismic data also reveal that mixing across the entire thermocline (200–1,000 m) is enhanced within 30 km of the ridge. Away from the ridge, several other patches of high-diffusivity are observed that also correspond with low amplitude and disrupted reflectivity.

The spatial heterogeneity of mixing suggests that the mid-ocean thermocline is not quiescent. Enhanced mixing in the ocean interior is primarily caused by breaking of internal waves (Gregg et al., 2003) for which the energy input generally comes from tidal flows impinging upon topography (Munk and Wunsch, 1998) and wind forced near-inertial waves below the mixed layer (D'Asaro, 1985; Alford, 2003b). We discuss the possible drivers of observed enhanced mixing below.

Drivers of Enhanced South Atlantic Thermocline Diffusivities

Rough Topography at the Mid-Atlantic Ridge

Enhanced mixing in the thermocline above the MAR is most likely driven by barotropic tides impinging on the rough bathymetry of the ridge. Due to a lack of observations, the effect of the MAR on upper water column (<1,000 m) mixing has been less clear than its effect on abyssal water. Here, both seismic-derived and hydrographic-derived estimates of K show that diffusivities across the entire water column are enhanced by at least one order of magnitude compared with background values. These rates are consistent with shallow microstructure observations above mid-ocean ridges (Polzin et al., 1997; Mauritzen et al., 2002; St Laurent and Thurnherr, 2007) and recent work by Li and Xu (2014) who found the influence of rough topography on turbulent mixing can extend 3,300 m upward into the ocean interior. Seismic estimates (limited to 700 m) show larger diffusivities at shallow depths (**Figure 5,1F**), while microstructure measurements show that diffusivities increase significantly below 700 m depth, as found by Polzin et al. (1997). Therefore, it is also possible that an upward source or mesoscale oceanic process is enhancing the shallow mixing further and is only captured by the high-resolution

siemsic data. Due to the presence of the ridge and consistency of these high diffusivities over time, we conclude that at 30° S, the MAR enhances diffusivities across the entire water column by at least one order of magnitude.

The rapid decay of diffusivities within ∼30 km away from the MAR is shorter than similar decays of ∼60 km at the Hawaiian Ridge and the Mariana Ridge (Klymak et al., 2006; Tang et al., 2021). This discrepancy indicates that at the Hawaiian Ridge and the Mariana Ridge, a large portion of tidal energy radiates away, while at the MAR, a significant portion of tidal energy is dissipated locally, which is consistent with previous interpretations (Waterhouse et al., 2014).

Storm and Eddy

The causes of enhanced mixing over smooth topography are less clear. Irregular patches of enhanced mixing in these seismic lines could be caused by a variety of mechanisms, such as dissipation of high-mode near-inertial energy, breaking of low-mode tidal or near-inertial waves through wave-wave interactions, and energy dissipation through mesoscale eddy fields (MacKinnon et al., 2013). Numerical studies predict enhanced mixing caused by dissipation of semidiurnal tides near latitudes of 29° N/S (MacKinnon and Winters, 2005; Simmons, 2008).

Of these mechanisms, wind-induced mixing is the most pervasive globally (Alford et al., 2016). Winds inject energy into the ocean through wind stress impulses such as traveling midlatitude storms. These storms can excite frequency response in the near-inertial band and generate near-inertial internal waves (Pollard, 1970; Gill, 1984; Alford et al., 2016). Horizontal convergence and divergence of the ocean's mixed layer can provide pathways for wind injected energy to propagate downward and eventually generate near-inertial waves in the stratified water below (D'Asaro, 1985; D'Asaro et al., 1995; Young and Jelloul, 1997). Much of the energy exerted by winds goes into low-mode near-inertial waves that propagate for great distances (D'Asaro et al., 1995; Alford, 2003b), while the remaining portion oscillates as high-mode near-inertial waves that promote mixing because of their potential for higher shear (Alford and Gregg, 2001; Alford, 2010). Thus, in our study, enhanced mixing over smooth topography may reveal the energy cascading process of high-mode near-inertial waves breaking into small-scale turbulence during downward propagation. In addition, using Lagrangian observations, Chaigneau et al. (2008) showed that winds inject near-inertial energy into the mixed layer in the subtropical South Atlantic. Given this knowledge and our observations of mixing hotspots are mostly above 600 m depth, we hypothesize that the observed enhanced mixing above smooth topography is wind-induced and modified by mesoscale currents in the mixed layer. We explore this hypothesis by analyzing wind stress data and sea-surface geostrophic currents.

Spatial and Temporal Variability of Wind Stress

We now assess the likelihood of a storm driving unusually elevated diffusivities in the mid-ocean. Since rays of near-inertial waves propagate horizontally as well as downward, the location of wind energy input may not be the same as enhanced mixing. Theoretical modeling suggests that at 30° S, near-inertial waves travel ∼330 km horizontally before reaching the seafloor (Garrett, 2001). Therefore, we evaluate if strong winds were present prior to and within ±3 degree (in both zonal and meridional directions) of the seismic survey. Six hourly wind speed data from the NCEP reanalysis 2 (Kanamitsu et al., 2002) are converted to wind stress using the method of Large and Pond (1981). Wind stress is then averaged within the geographic boundary of 33° W, 9° W, 27° S, 33° S for 60 days before the survey (**Figure 8**). This time span of 60 days is chosen given a near-inertial wave propagating vertically to 800 m depth with a speed of 13 m day^{-1}. The depth limit of 800 m is determined from the maximum depth of enhanced mixing observed in profile line 1B (**Figure 5,1B**). 13 m day^{-1} is chosen to approximate the mean downward propagation speed for near-inertial waves, and is based on a 2-year record of acoustic Doppler current profilers (Alford et al., 2012). Given these time and space limits, we now investigate the temporal and spatial variability of wind around the seismic survey and its relation to enhanced mixing above smooth topography.

Over the 60-day period before the seismic survey, wind stresses greater than 8 standard deviations from the mean occur about 30 days prior to the survey between January 01 and January 08, 2016 (**Figure 8A**, upper panel). We interpret this high wind stress event as a storm. After linearly interpolating the wind stress on an hourly time grid, we use a Butterworth bandpass filter to extract the wind stress in the near-inertial band of $0.8f$-$1.2f$, where f is the Coriolis frequency. Slight changes of lower and upper bounds of the near-inertial band do not significantly affect the results of this analysis. The storm shows a substantial increase in strength within the near-inertial band compared to the rest of the 60-day period (**Figure 8A**, lower panel), which indicates the important role of this storm in injecting near-inertial energy into the ocean interior.

We spatially track the storm across the seismic survey location by calculating average wind stress along 30° S with a series of rolling windows. Each window has size 4° × 4° and is centered every 2° from 30° W to 12° W (**Figures 8B–K**). The movement of the storm correlates with the zonal trends of diffusivities. First, higher wind stresses with higher strength in the near-inertial band are shown from 32° W to 14° W during the time of the storm (**Figures 8B–I**), consistent with the locations of enhanced mixing in seismic derived diffusivity sections (**Figure 5,1A–E**). Second, the far eastern end of the seismic survey that is above the MAR (15° W to 12° W) did not experience wind forcing as high as regions further west (**Figures 8J,K**). Correspondingly, we observe lower diffusivities at this location (**Figure 5**, from the eastern end of lines 1E,F). We note that weaker wind forcing and lower diffusivities at both sides of the MAR provide additional support to our interpretation above - enhanced mixing directly above the MAR is caused by rough topography. The enhanced mixing on lines 1A–E is likely caused by this storm for three reasons: (i) there were no other wind stress peaks within the relevant time range, (ii) enhanced diffusivities track the movement of the storm, and (iii) this region is away from topographic boundaries.

Argo-derived diffusivities support our hypothesis of storm-induced mixing (**Figures 1**, **9**). Argos a, b, c, d were selected because they are within the region of the storm during the time span of the analysis. All Argos show enhanced mixing over a depth range of 300–600 m after wind forcing (**Figure 9**, red

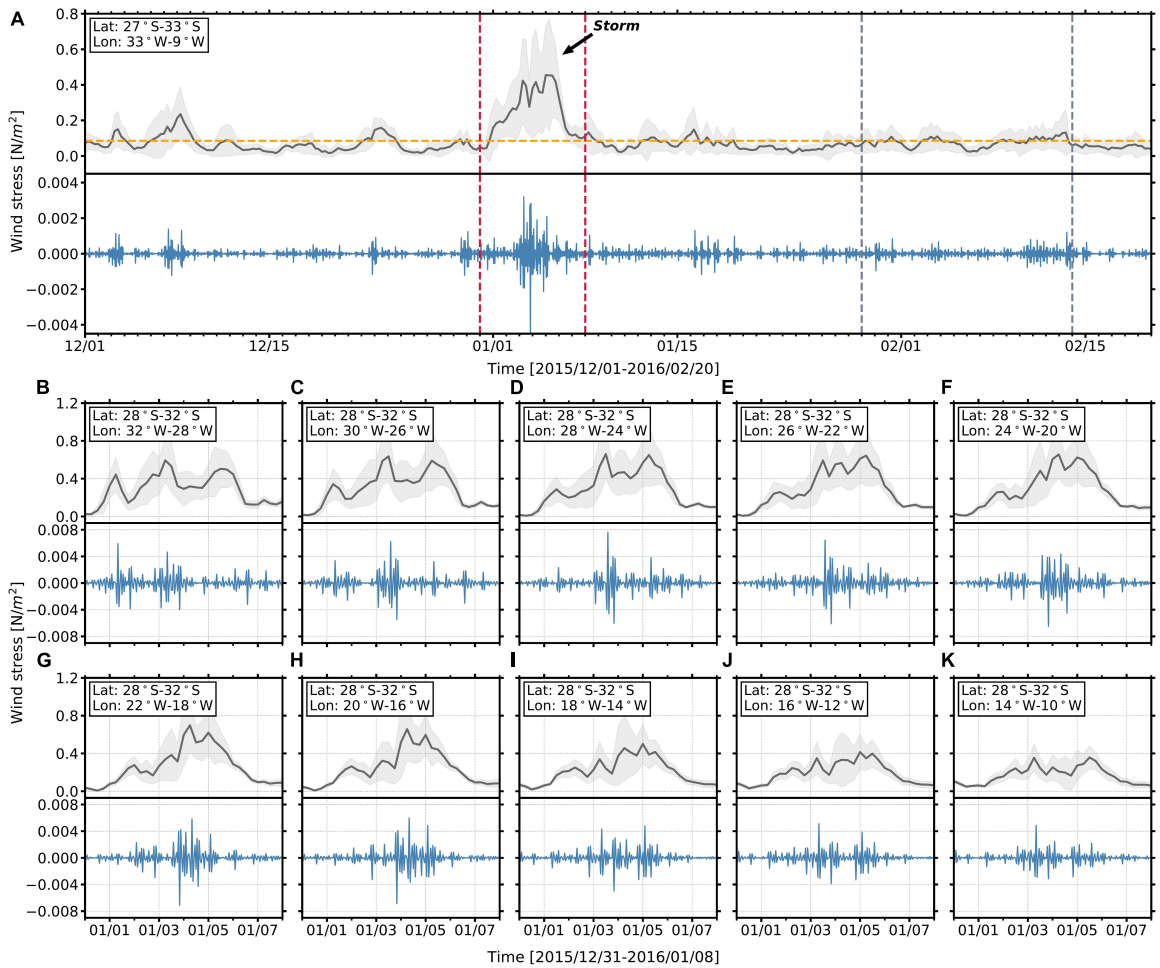

FIGURE 8 | Wind stress variability in time and space. **(A)** Spatially averaged wind stress as a function of time for region 33° W, 9° W, 27° S, 33° S (upper panel) and its corresponding bandpass filtered near-inertial wind stress (lower panel). Black line = averaged wind stress; blue line = near-inertial wind stress; horizontal dash yellow line = average wind stress for the entire time period. Light gray shade represents the standard deviation of measurements. Vertical red dashed lines bound the time of high wind stress that are analyzed individually as a function of space from panels **(B–K)**. Vertical gray dashed lines bound the days of the seismic survey. **(B–K)** Same as **(A)** but for averaged wind stress during the storm analyzed in a series of spatially overlapping windows described in the text. The region of each window is shown in the box at the upper right corner of each figure. The black arrow points to the feature that we interpreted as a storm because its wind stress is greater than eight standard deviations from the mean. Wind stress are calculated from wind speed data from NCEP reanalysis 2 (Kanamitsu et al., 2002).

shading), although the timing and strength of these changes vary substantially. Argo a experienced a relatively high level of mixing throughout the time of our analysis. The reason of higher diffusivity of 8.1×10^{-5} m^2 s^{-1} before the storm is unknown, however, there is a noticeable increase of mixing from 3.9×10^{-5} m^2 s^{-1} to 9.9×10^{-5} m^2 s^{-1} after the storm around January 15, then diffusivities maintained above the level of 5.2×10^{-5} m^2 s^{-1}. Argo b shows enhanced mixing during and after the storm, diffusivities increased significantly from 2.4×10^{-5} m^2 s^{-1} to 23×10^{-5} m^2 s^{-1} in the time of December 26 to January 15. Argo c and d show enhanced mixing during the storm but diffusivities decrease immediately afterward. We also notice a significant increase of diffusivities in Argo a, b, and c about 50, 60, and 30 days after the storm, respectively, while there was no apparent increase in wind stress during these periods of time (**Figure 8A**). There are two possible reasons for the differences. The first is out of plane effects and the second is local mesoscale flows. While we analyze the diffusivities as a function of time, Argo floats change their spatial location. All floats traveled about 100 km during the time span of analysis (**Figure 10**). Their Lagrangian behavior means that the diffusivities in **Figure 9** do not reflect changes in time at a fixed location. Therefore, other oceanic processes may affect the recovered diffusivities. For example, energy from other events such as wave-wave interactions and near-inertial waves propagating in from elsewhere can have effects on the observed mixing pattern (Plueddemann and Farrar, 2006). However, it is beyond the scope of this contribution to account for out-of-plane influences.

On the other hand, local mesoscale processes may cause differences between the distribution of ocean mixing and the presence of wind stress at the sea surface. For example, the presence, or lack thereof, of mesoscale eddies has been shown

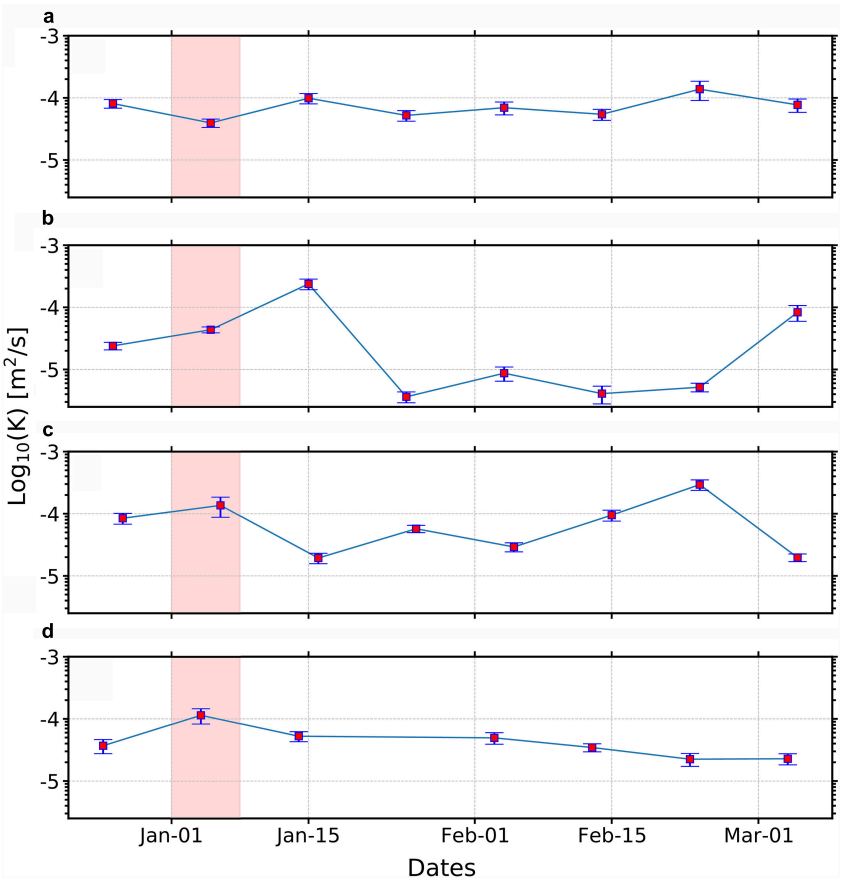

FIGURE 9 | Depth (300–600 m) averaged diffusivity from Argo floats (a–d) as a function of time during and after the storm. Vertical red bands mark the time of the storm. Error bars represent standard errors.

to play an important role in controlling downward propagation of near-inertial energy (Zhai et al., 2005), resulting in different speeds of downward propagation at different times and locations. From the seismic data, we use the different depths of enhanced mixing (**Figure 5**) and a period of 30 days to calculate the downward propagation speeds of near-inertial energy and find a large range of 17–27 m/day. Furthermore, mismatches between the patterns of wind stress and diffusivities suggest that local mesoscale flows are playing a role in distributing near-inertial energy. For example, the western end of the seismic survey (line 1A) shows the lowest diffusivities while the wind stress was high (**Figure 8B**). Similarly, we observe diffusivities slightly higher than the background level between 22° W and 20° W (**Figure 6**), but the wind stress around this region shows sharp spikes in the near-inertial band (**Figures 8G,H**). Since this region hosts an energetic eddy field, we now consider the possible impact of mesoscale eddies in the mixed layer on propagation of wind-induced near-inertial energy.

Possible Contribution of Eddies

We use satellite observations of sea surface geostrophic current velocities to investigate mesoscale eddies in the mixed layer during the time of the storm. **Figure 10** shows the evolution of sea surface geostrophic current velocities from January 03, 2016 to February 14, 2016, covering the time period from the start of the storm to the end of the seismic survey (each plot is separated by 2 weeks). An anticyclonic eddy, centered around 30° W, 31° S and identified by high velocities of ∼0.35 m s^{-1}, is present during the storm. The intensity of the eddy weakens as time goes by **Figures 10A–D**. The eastern and western portions of seismic lines 1A,B, respectively, cross the easterly side of the eddy. Here, we observe enhanced mixing that propagates to depths greater than ∼800 m in line 1B (**Figure 6,1B**). The convergence of high velocity currents at this location suggests more complex structures of mesoscale flows compared to other locations (**Figure 10A**), which could be an explanation for the deeper penetration of enhanced mixing in line 1B. If we consider the eastern edge of the eddy as the input location of deep propagating energy, the location of the deepest penetration is at 50–100 km in line 1B, implying near-inertial energy propagates both vertically and laterally. These findings are consistent with limited previous observations (Jing et al., 2011; Whalen et al., 2018) and numerical studies (Danioux et al., 2008) that reveal the importance of mesoscale eddies in draining energy to great depths. Taken together, these observations suggest that mesoscale eddies enhance the depth-penetration of wind-induced mixing from 600 to 800 m.

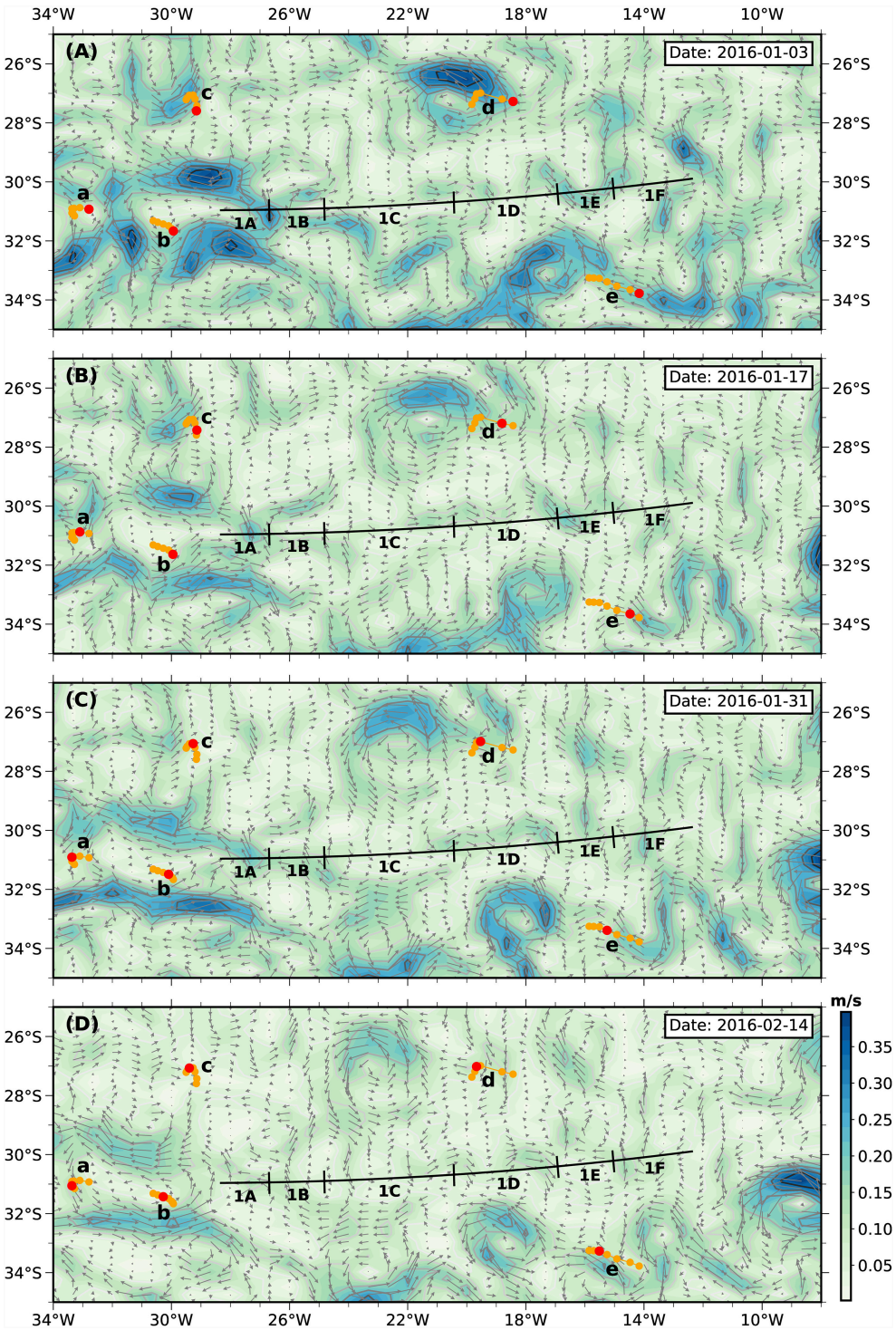

FIGURE 10 | (A) Maps of sea surface geostrophic current velocities calculated for 5 days composite centered on 2016/01/03 from Ocean Surface Current Analyses Real-time (OSCAR) satellite measurements. Black lines = seismic survey lines. Orange dots = the trajectory of the Argo floats a–e shown in **Figure 1**. Red dots = the positions of the Argo floats closest to the date of the satellite measurements. **(B–D)** Same as **(A)** but separated 2 weeks apart following **(A)**.

To summarize, we hypothesize that wind generated near-inertial energy is a likely candidate for the enhanced mixing away from rough topography, with surface mesoscale flows playing an important role. The enhanced diffusivities we observe are higher than the background level by an order of magnitude in some cases. If our hypothesis of wind-induced mixing

holds true, given that the seismic survey was conducted in a non-stormy season, our results demonstrate that wind-induced mixing plays an important role in the central South Atlantic thermocline diffusivities.

CONCLUSION

We map vertical diffusivities across 1,600 km of the central South Atlantic thermocline using six seismic reflectivity sections, CTD, and Argo data. Seismic reflectivity yields continuous high-resolution diapycnal diffusivity maps of the thermocline during February 2016. These data help to overcome observational limitations since they yield full-thermocline vertical sections that have a horizontal extent of 1,600 km length, vertical and horizontal resolution of $O(10)$ m, and that span a period of 4 weeks. Meanwhile, CTD data from 2003 and 2011 provide low spatial resolution diffusivity estimates that can be seen as representative of the time mean. Argo data provide spot measurements and Lagrangian tracers of mixing over different topographic settings and at different times. Together, these data extend the observational record of diapycnal mixing in the ocean interior and provide insights into the variability and drivers of mixing.

The South Atlantic thermocline is seismically imaged as an 800–900 m band of reflectivity with no clear submesoscale patterns within it (**Figure 4**). Seismic-derived and CTD-derived diffusivities show that, in the mean, thermocline diffusivities have remained relatively consistent at close to or less than 1×10^{-5} m^2 s^{-1} since the 1990s (**Figures 5**, **6**). We find low/high diffusivities over smooth/rough topography, and these values are particularly enhanced over the Mid-Atlantic Ridge ($25–50 \times 10^{-5}$ m^2 s^{-1}). Imprinted upon the synoptic scale mean, mixing is heterogeneous, showing enhanced diffusivities that exceed the background level of 1×10^{-5} m^2 s^{-1} in many regions where reflections are weaker and disrupted (**Figures 5–7**).

We examined the most likely drivers of mixing variability (**Figures 8–10**). Above the Mid-Atlantic Ridge, diffusivities are enhanced by barotropic tides impinging on the rough bathymetry of the ridge. The rapid decay of diffusivities within ∼30 km away from the ridge implies local dissipation of tidal energy. Above smooth topography, we hypothesize that with limited hydrographic data, we cannot fully decipher what caused the enhanced mixing above smooth topography, however, our best assessment suggests it is likely caused by localized wind-generated near-inertial energy (i.e., a storm). The dissipation of such energy during downward propagation resulted in elevated diffusivities ranging from 3×10^{-5} m^2 s^{-1} to 50×10^{-5} m^2 s^{-1}. The loci and depth of energy propagation vary substantially, possibly affected by the surface wind forcing and mesoscale flows in the mixed layer. The maximum depth of enhanced mixing is about 800 m, taking place close to the edge of an anticyclonic eddy, suggesting mesoscale eddies encourage deeper propagation of near-inertial energy.

The interaction between surface wind, mesoscale flows in the mixed layer, and high mode near-inertial waves is a complex process that remains poorly understood. It is beyond the scope of this study to fully explain the heterogeneity of mixing along the entire seismic survey with limited hydrographic measurements. However, high-resolution seismic observations along with concurrent hydrographic and wind measurements provide an opportunity to untangle these mechanisms. More simultaneous observations are needed in the vicinity of rough topography and strong storm forcing regions to improve our understanding of the global mixing budget and to contribute to more accurate ocean circulation and climate models.

DATA AVAILABILITY STATEMENT

Publicly available datasets were analyzed in this study. These data can be found here: Seismic field data are available at the NSF-sponsored Academic Seismic Portal hosted by Lamont-Doherty Earth Observatory (https://www.marine-geo.org/tools/search/entry.php?id=MGL1601). GO-SHIP observations were downloaded from CLIVAR and Carbon Hydrographic Data Office (https://cchdo.ucsd.edu/) for expocodes A10 49NZ20031106 and 33RO20110926. Argo data were downloaded from the Global Argo Data Repository (https://www.ncei.noaa.gov/products/global-argo-data-repository). Ocean Surface Current Analysis Real-time (OSCAR) and NCEP 2 wind speed datasets were extracted from the following ERDDAP website, respectively: https://upwell.pfeg.noaa.gov/erddap/index.html and https://apdrc.soest.hawaii.edu/erddap/index.html.

AUTHOR CONTRIBUTIONS

JW and RR conceived the research project. JW carried out data analysis with guidance and wrote the manuscript with contributions from KG and RR. All authors contributed to the article and approved the submitted version.

FUNDING

CREST was supported by the National Science Foundation (NSF) grant OCE-1537108 to Texas A&M University.

ACKNOWLEDGMENTS

We thank the captain, crew, and science party of cruise MGL1601 of the R/V Marcus G. Langseth for their expert assistance during the CREST cruise. We are grateful to W. Fortin for generously providing codes and instructions for calculating high-resolution diffusivity maps. We also thank Q. Tang, K. Sheen, R. Hobbs, J. Estep, H. Potter, R. Hetland, S. Holbrook, and R. Schmitt for their help. Seismic processing was carried out using Seismic Unix (https://github.com/JohnWStockwellJr/SeisUnix) and the Paradigm seismic software applications, Echos, provided by Emerson. Hydrographic measurements were analyzed using the GSW TEOS-10 equation of state for seawater (github.com/TEOS-10/GSW-Python).

REFERENCES

Alford, M. H. (2003a). Improved global maps and 54-year history of wind-work on ocean inertial motions. *Geophys. Res. Lett.* 30, 1424–1427. doi: 10.1029/2002GL016614

Alford, M. H. (2003b). Redistribution of energy available for ocean mixing by long-range propagation of internal waves. *Nature* 423, 159–162. doi: 10.1038/nature01628

Alford, M. H. (2010). Sustained, full-water-column observations of internal waves and mixing near Mendocino Escarpment. *J. Phys. Oceanogr.* 40, 2643–2660. doi: 10.1175/2010JPO4502.1

Alford, M. H., and Gregg, M. C. (2001). Near-inertial mixing: modulation of shear, strain and microstructure at low latitude. *J. Geophys. Res.* 106, 16947–16968. doi: 10.1029/2000JC000370

Alford, M. H., Cronin, M. F., and Klymak, J. M. (2012). Annual cycle and depth penetration of wind-generated near-inertial internal waves at Ocean Station Papa in the northeast Pacific. *J. Phys. Oceanogr.* 42, 889–909. doi: 10.1175/JPO-D-11-092.1

Alford, M. H., MacKinnon, J. A., Simmons, H. L., and Nash, J. D. (2016). Near-inertial internal gravity waves in the ocean. *Annu. Rev. Mar. Sci.* 8, 95–123. doi: 10.1146/annurev-marine-010814-015746

Bray, N. A., and Fofonoff, N. (1981). Available potential energy for MODE eddies. *J. Phys. Oceanogr.* 11, 30–47. doi: 10.1175/1520-0485(1981)011<0030:APEFME>2.0.CO;2

Cabré, A., Pelegrí, J., and Vallès-Casanova, I. (2019). Subtropical-tropical transfer in the South Atlantic Ocean. *J. Geophys. Res.* 124, 4820–4837. doi: 10.1029/2019JC015160

Chaigneau, A., Pizarro, O., and Rojas, W. (2008). Global climatology of near-inertial current characteristics from Lagrangian observations. *Geophys. Res. Lett.* 35:5. doi: 10.1029/2008GL034060

Danioux, E., Klein, P., and Rivière, P. (2008). Propagation of wind energy into the deep ocean through a fully turbulent mesoscale eddy field. *J. Phys. Oceanogr.* 38, 2224–2241. doi: 10.1175/2008JPO3821.1

D'Asaro, E. A. (1985). The energy flux from the wind to near-inertial motions in the surface mixed layer. *J. Phys. Oceanogr.* 15, 1043–1059. doi: 10.1175/1520-0485(1985)015<1043:TEFFTW>2.0.CO;2

D'Asaro, E. A., Eriksen, C. C., Levine, M. D., Niiler, P., and Van Meurs, P. (1995). Upper-ocean inertial currents forced by a strong storm. Part I: data and comparisons with linear theory. *J. Phys. Oceanogr.* 25, 2909–2936. doi: 10.1175/1520-0485(1995)025<2909:UOICFB>2.0.CO;2

Dickinson, A., Jeremiah White, N., and Patrick Caulfield, C.-C. (2017). Spatial variation of diapycnal diffusivity estimated from seismic imaging of internal wave field, gulf of mexico. *JCR Oceans* 122, 9827–9854. doi: 10.1002/2017JC013352

Dickinson, A., White, N., and Caulfield, C. (2020). Time-lapse acoustic imaging of mesoscale and fine-scale variability within the faroe-shetland channel. *J. Geophys. Res.* 125:e2019JC015861. doi: 10.1029/2019JC015861

Dohan, K., and Davis, R. E. (2011). Mixing in the transition layer during two storm events. *J. Phys. Oceanogr.* 41, 42–66. doi: 10.1175/2010JPO4253.1

Dong, S., Goni, G., and Bringas, F. (2015). Temporal variability of the south atlantic meridional overturning circulation between 20 s and 35 S. *Geophys. Res. Lett.* 42, 7655–7662. doi: 10.1002/2015GL065603

Estep, J., Reece, R., Kardell, D. A., Christeson, G. L., and Carlson, R. L. (2019). Seismic layer 2a: evolution and thickness from 0-to 70-ma crust in the slow-intermediate spreading south atlantic. *J. Geophys. Res. Solid Earth* 124, 7633–7651. doi: 10.1029/2019JB017302

Fortin, W. F. J., and Holbrook, W. S. (2009). Sound speed requirements for optimal imaging of seismic oceanography data. *Geophys. Res. Lett.* 36:L00D01. doi: 10.1029/2009GL038991

Fortin, W. F., Holbrook, W. S., and Schmitt, R. W. (2016). Mapping turbulent diffusivity associated with oceanic internal lee waves offshore Costa Rica. *Ocean Sci.* 12, 601–612. doi: 10.5194/os-12-601-2016

Fortin, W. F., Holbrook, W. S., and Schmitt, R. W. (2017). Seismic estimates of turbulent diffusivity and evidence of nonlinear internal wave forcing by geometric resonance in the South China Sea. *J. Geophys. Res.* 122, 8063–8078. doi: 10.1002/2017JC012690

Garrett, C. (2001). What is the "near-inertial" band and why is it different from the rest of the internal wave spectrum? *J. Phys. Oceanogr.* 31, 962–971. doi: 10.1175/1520-0485(2001)031<0962:WITNIB>2.0.CO;2

Garrett, C., and Munk, W. (1975). Space-time scales of internal waves: a progress report. *J. Geophys. Res.* 80, 291–297. doi: 10.1029/JC080i003p00291

Garzoli, S. L. (1993). Geostrophic velocity and transport variability in the Brazil-Malvinas Confluence. *Deep Sea Res. Part I* 40, 1379–1403. doi: 10.1016/0967-0637(93)90118-M

Garzoli, S. L., and Matano, R. (2011). The south atlantic and the atlantic meridional overturning circulation. *Deep Sea Res. Part II* 58, 1837–1847. doi: 10.1016/j.dsr2.2010.10.063

Gill, A. (1984). On the behavior of internal waves in the wakes of storms. *J. Phys. Oceanogr.* 14, 1129–1151. doi: 10.1175/1520-0485(1984)014<1129:OTBOIW>2.0.CO;2

Gregg, M. C., Sanford, T. B., and Winkel, D. P. (2003). Reduced mixing from the breaking of internal waves in equatorial waters. *Nature* 422, 513–515. doi: 10.1038/nature01507

Gunn, K. L., Dickinson, A., White, N., and Caulfield, C.-C. P. (2021). Vertical mixing and heat fluxes conditioned by a seismically imaged oceanic front. *Front. Mar. Sci.* 8:1379. doi: 10.3389/fmars.2021.697179

Harrison, M., and Hallberg, R. (2008). Pacific subtropical cell response to reduced equatorial dissipation. *J. Phys. Oceanogr.* 38, 1894–1912. doi: 10.1175/2008JPO3708.1

Hernández-Guerra, A., Talley, L. D., Pelegrí, J. L., Vélez-Belchí, P., Baringer, M. O., Macdonald, A. M., et al. (2019). The upper, deep, abyssal and overturning circulation in the Atlantic Ocean at 30° S in 2003 and 2011. *Progr. Oceanogr.* 176:102136. doi: 10.1016/j.pocean.2019.102136

Hieronymus, M., Nycander, J., Nilsson, J., Döös, K., and Hallberg, R. (2019). Oceanic overturning and heat transport: the role of background diffusivity. *J. Clim.* 32, 701–716. doi: 10.1175/JCLI-D-18-0438.1

Hobbs, R. W., Klaeschen, D., Sallarès, V., Vsemirnova, E., and Papenberg, C. (2009). Effect of seismic source bandwidth on reflection sections to image water structure. *Geophys. Res. Lett.* 36:L00D08. doi: 10.1029/2009GL040215

Holbrook, W. S., Fer, I., Schmitt, R. W., Lizarralde, D., Klymak, J. M., Helfrich, L. C., et al. (2013). Estimating oceanic turbulence dissipation from seismic images. *J. Atmos. Oceanic Technol.* 30, 1767–1788. doi: 10.1175/JTECH-D-12-00140.1

Jing, Z., Chang, P., DiMarco, S. F., and Wu, L. (2015). Role of near-inertial internal waves in subthermocline diapycnal mixing in the northern Gulf of Mexico. *J. Phys. Oceanogr.* 45, 3137–3154. doi: 10.1175/JPO-D-14-0227.1

Jing, Z., Wu, L., Li, L., Liu, C., Liang, X., Chen, Z., et al. (2011). Turbulent diapycnal mixing in the subtropical northwestern Pacific: spatial-seasonal variations and role of eddies. *J. Geophys. Res.* 116:C10028. doi: 10.1029/2011JC007142

Jun, H., Jou, H.-T., Kim, C.-H., Lee, S. H., and Kim, H.-J. (2020). Random noise attenuation of sparker seismic oceanography data with machine learning. *Ocean Sci.* 16, 1367–1383. doi: 10.5194/os-16-1367-2020

Kanamitsu, M., Ebisuzaki, W., Woollen, J., Yang, S.-K., Hnilo, J., Fiorino, M., et al. (2002). Ncep–doe amip-ii reanalysis (r-2). *Bull. Am. Meteorol. Soc.* 83, 1631–1644. doi: 10.1175/BAMS-83-11-1631

Klymak, J. M., and Moum, J. N. (2007). Oceanic isopycnal slope spectra. Part II: turbulence. *J. Phys. Oceanogr.* 37, 1232–1245. doi: 10.1175/JPO3074.1

Klymak, J. M., Moum, J. N., Nash, J. D., Kunze, E., Girton, J. B., Carter, G. S., et al. (2006). An estimate of tidal energy lost to turbulence at the Hawaiian Ridge. *J. Phys. Oceanogr.* 36, 1148–1164. doi: 10.1175/JPO2885.1

Krahmann, G., Papenberg, C., Brandt, P., and Vogt, M. (2009). Evaluation of seismic reflector slopes with a Yoyo-CTD. *Geophys. Res. Lett.* 36:L00D02. doi: 10.1029/2009GL038964

Kunze, E., and Toole, J. M. (1997). Tidally driven vorticity, diurnal shear, and turbulence atop Fieberling Seamount. *J. Phys. Oceanogr.* 27, 2663–2693. doi: 10.1175/1520-0485(1997)027<2663:TDVDSA>2.0.CO;2

Kunze, E., Firing, E., Hummon, J. M., Chereskin, T. K., and Thurnherr, A. M. (2006). Global abyssal mixing inferred from lowered ADCP shear and CTD strain profiles. *J. Phys. Oceanogr.* 36, 1553–1576. doi: 10.1175/JPO2926.1

Large, W., and Pond, S. (1981). Open ocean momentum flux measurements in moderate to strong winds. *J. Phys. Oceanogr.* 11, 324–336. doi: 10.1175/1520-0485(1981)011<0324:OOMFMI>2.0.CO;2

Ledwell, J., Montgomery, E., Polzin, K., Laurent, L. S., Schmitt, R., and Toole, J. (2000). Evidence for enhanced mixing over rough topography in the abyssal ocean. *Nature* 403:179. doi: 10.1038/35003164

Li, Y., and Xu, Y. (2014). Penetration depth of diapycnal mixing generated by wind stress and flow over topography in the northwestern Pacific. *J. Geophys. Res.* 119, 5501–5514. doi: 10.1002/2013JC009681

Lumpkin, R., and Speer, K. (2007). Global ocean meridional overturning. *J. Phys. Oceanogr.* 37, 2550–2562. doi: 10.1175/JPO3130.1

MacKinnon, J., and Winters, K. (2005). Subtropical catastrophe: significant loss of low-mode tidal energy at 28.9°. *Geophys. Res. Lett.* 32:L15605. doi: 10.1029/2005GL023376

MacKinnon, J., St Laurent, L., and Garabato, A. C. N. (2013). Diapycnal mixing processes in the ocean interior. *Int. Geophys.* 103, 159–183. doi: 10.1016/B978-0-12-391851-2.00007-6

Mauritzen, C., Polzin, K., McCartney, M., Millard, R., and West-Mack, D. (2002). Evidence in hydrography and density fine structure for enhanced vertical mixing over the Mid-Atlantic Ridge in the western Atlantic. *J. Geophys. Res.* 107, 11-11–11-19. doi: 10.1029/2001JC001114

Mojica, J. F., Sallarès, V., and Biescas, B. (2018). High-resolution diapycnal mixing map of the Alboran Sea thermocline from seismic reflection images. *Ocean Sci.* 14, 403–415. doi: 10.5194/os-14-403-2018

Munk, W. H. (1966). Abyssal recipes. *Deep Sea Res.* 13, 707–730. doi: 10.1016/0011-7471(66)90602-4

Munk, W., and Wunsch, C. (1998). Abyssal recipes II: energetics of tidal and wind mixing. *Deep Sea Res. Part I* 45, 1977–2010. doi: 10.1016/S0967-0637(98)00070-3

Nandi, P., Holbrook, W. S., Pearse, S., Páramo, P., and Schmitt, R. W. (2004). Seismic reflection imaging of water mass boundaries in the Norwegian Sea. *Geophys. Res. Lett.* 31:L23311. doi: 10.1029/2004GL021325

Osborn, T. (1980). Estimates of the local rate of vertical diffusion from dissipation measurements. *J. Phys. Oceanogr.* 10, 83–89. doi: 10.1175/1520-0485(1980)010<0083:EOTLRO>2.0.CO;2

Osborn, T. R., and Cox, C. S. (1972). Oceanic fine structure. *Geophys. Fluid Dyn.* 3, 321–345. doi: 10.1080/03091927208236085

Plueddemann, A., and Farrar, J. (2006). Observations and models of the energy flux from the wind to mixed-layer inertial currents. *Deep Sea Res. Part II* 53, 5–30. doi: 10.1016/j.dsr2.2005.10.017

Pollard, R. T. (1970). On the generation by winds of inertial waves in the ocean. *Deep Sea Res.* 17, 795–812. doi: 10.1016/0011-7471(70)90042-2

Polzin, K., Toole, J., Ledwell, J., and Schmitt, R. (1997). Spatial variability of turbulent mixing in the abyssal ocean. *Science* 276, 93–96. doi: 10.1126/science.276.5309.93

Price, J. F., Weller, R. A., and Pinkel, R. (1986). Diurnal cycling: observations and models of the upper ocean response to diurnal heating, cooling, and wind mixing. *J. Geophys. Res.* 91, 8411–8427. doi: 10.1029/JC091iC07p08411

Ruddick, B. (2018). Seismic oceanography's failure to flourish: a possible solution. *J. Geophys. Res.* 123, 4–7. doi: 10.1002/2017JC013736

Ruddick, B., SoNg, H., Dong, C., and Pinheiro, L. (2009). Water column seismic images as maps of temperature gradient. *Oceanography* 22, 192–205. doi: 10.5670/oceanog.2009.19

Ryan, W. B., Carbotte, S. M., Coplan, J. O., O'Hara, S., Melkonian, A., Arko, R., et al. (2009). Global multi-resolution topography synthesis. *Geochem. Geophys. Geosyst.* 10:Q03014. doi: 10.1029/2008GC002332

Sallarès, V., Biescas, B., Buffett, G., Carbonell, R., Dañobeitia, J. J., and Pelegrí, J. L. (2009). Relative contribution of temperature and salinity to ocean acoustic reflectivity. *Geophys. Res. Lett.* 36:6. doi: 10.1029/2009GL040187

Sheen, K., White, N., and Hobbs, R. (2009). Estimating mixing rates from seismic images of oceanic structure. *Geophys. Res. Lett.* 36:L00D04. doi: 10.1029/2009GL040106

Simmons, H. L. (2008). Spectral modification and geographic redistribution of the semi-diurnal internal tide. *Ocean Modelling* 21, 126–138. doi: 10.1016/j.ocemod.2008.01.002

Sloyan, B. M. (2005). Spatial variability of mixing in the Southern Ocean. *Geophys. Res. Lett.* 32:L18603. doi: 10.1029/2005GL023568

Sloyan, B. M., Wanninkhof, R., Kramp, M., Johnson, G. C., Talley, L. D., Tanhua, T., et al. (2019). The global ocean ship-based hydrographic investigations program (GO-SHIP): a platform for integrated multidisciplinary ocean science. *Front. Mar. Sci.* 6:445. doi: 10.3389/fmars.2019.00445

St Laurent, L. C., and Thurnherr, A. M. (2007). Intense mixing of lower thermocline water on the crest of the Mid-Atlantic Ridge. *Nature* 448:680. doi: 10.1038/nature06043

St. Laurent, L. C., Toole, J. M., and Schmitt, R. W. (2001). Buoyancy forcing by turbulence above rough topography in the abyssal Brazil Basin. *J. Phys. Oceanogr.* 31, 3476–3495. doi: 10.1175/1520-0485(2001)031<3476:BFBTAR>2.0.CO;2

Stramma, L., and England, M. (1999). On the water masses and mean circulation of the South Atlantic Ocean. *J. Geophys. Res.* 104, 20863–20883. doi: 10.1029/1999JC900139

Tang, Q., Gulick, S. P., Sun, J., Sun, L., and Jing, Z. (2019). Submesoscale features and turbulent mixing of an oblique anticyclonic eddy in the Gulf of Alaska investigated by marine seismic survey data. *J. Geophys. Res.* 125:e2019JC015393. doi: 10.1029/2019JC015393

Tang, Q., Jing, Z., Lin, J., and Sun, J. (2021). Diapycnal mixing in the subthermocline of the mariana ridge from high-resolution seismic images. *J. Phys. Oceanogr.* 51, 1283–1300. doi: 10.1175/JPO-D-20-0120.1

Tang, Q., Xu, M., Zheng, C., Xu, X., and Xu, J. (2018). A locally generated high-mode nonlinear internal wave detected on the shelf of the northern south china sea from marine seismic observations. *J. Geophys. Res.* 123, 1142–1155. doi: 10.1002/2017JC013347

Valla, D., Piola, A. R., Meinen, C. S., and Campos, E. (2018). Strong mixing and recirculation in the northwestern Argentine Basin. *J. Geophys. Res.* 123, 4624–4648. doi: 10.1029/2018JC013907

Walsh, K. J., Camargo, S. J., Knutson, T. R., Kossin, J., Lee, T.-C., Murakami, H., et al. (2019). Tropical cyclones and climate change. *Trop. Cyclone Res. Rev.* 8, 240–250. doi: 10.1016/j.tcrr.2020.01.004

Waterhouse, A. F., MacKinnon, J. A., Nash, J. D., Alford, M. H., Kunze, E., Simmons, H. L., et al. (2014). Global patterns of diapycnal mixing from measurements of the turbulent dissipation rate. *J. Phys. Oceanogr.* 44, 1854–1872. doi: 10.1175/JPO-D-13-0104.1

Whalen, C. B., MacKinnon, J. A., and Talley, L. D. (2018). Large-scale impacts of the mesoscale environment on mixing from wind-driven internal waves. *Nat. Geosci.* 11, 842–847. doi: 10.1038/s41561-018-0213-6

Whalen, C., Talley, L., and MacKinnon, J. (2012). Spatial and temporal variability of global ocean mixing inferred from Argo profiles. *Geophys. Res. Lett.* 39:L18612. doi: 10.1029/2012GL053196

Yilmaz, Ö (2001). *Seismic Data Analysis: Processing, Inversion, And Interpretation Of Seismic Data*. Tulsa, OK: Society of exploration geophysicists. doi: 10.1190/1.9781560801580

Young, W., and Jelloul, M. B. (1997). Propagation of near-inertial oscillations through a geostrophic flow. *J. Mar. Res.* 55, 735–766. doi: 10.1357/0022240973224283

Zhai, X., Greatbatch, R. J., and Zhao, J. (2005). Enhanced vertical propagation of storm-induced near-inertial energy in an eddying ocean channel model. *Geophys. Res. Lett.* 32:L18602. doi: 10.1029/2005GL023643

Zhang, K., Zuo, W., Chen, Y., Meng, D., and Zhang, L. (2017). Beyond a gaussian denoiser: residual learning of deep cnn for image denoising. *IEEE Trans. Image Process.* 26, 3142–3155. doi: 10.1109/TIP.2017.2662206

Conflict of Interest: The authors declare that the research was conducted in the absence of any commercial or financial relationships that could be construed as a potential conflict of interest.

Publisher's Note: All claims expressed in this article are solely those of the authors and do not necessarily represent those of their affiliated organizations, or those of the publisher, the editors and the reviewers. Any product that may be evaluated in this article, or claim that may be made by its manufacturer, is not guaranteed or endorsed by the publisher.

frontiers | Frontiers in Marine Science

REVIEW
published: 21 June 2022
doi: 10.3389/fmars.2022.736693

The Next Decade of Seismic Oceanography: Possibilities, Challenges and Solutions

Alex Dickinson[1]* *and Kathryn L. Gunn*[2]*

[1] School of Natural and Environmental Sciences, Newcastle University, Newcastle upon Tyne, United Kingdom, [2] Centre for Southern Hemisphere Oceans Research (CSHOR), CSIRO Oceans and Atmosphere, Hobart, TAS, Australia

Seismic reflection profiling of thermohaline structure has the potential to transform our understanding of oceanic mixing and circulation. This profiling, which is known as seismic oceanography, yields acoustic images that extend from the sea surface to the sea bed and which span horizontal distances of hundreds of kilometers. Changes in temperature and salinity are detected in two, and sometimes three, dimensions at spatial resolutions of ~O(10) m. Due to its unique combination of extensive coverage and high spatial resolution, seismic oceanography is ideally placed to characterize the processes that sustain oceanic circulation by transferring energy between basin-scale currents and turbulent flow. To date, more than one hundred research papers have exploited seismic oceanographic data to gain insight into phenomena as varied as eddy formation, internal waves, and turbulent mixing. However, despite its promise, seismic oceanography suffers from three practical disadvantages that have slowed its development into a widely accepted tool. First, acquisition of high-quality data is expensive and logistically challenging. Second, it has proven difficult to obtain independent observational constraints that can be used to benchmark seismic oceanographic results. Third, computational workflows have not been standardized and made widely available. In addition to these practical challenges, the field has struggled to identify pressing scientific questions that it can systematically address. It thus remains a curiosity to many oceanographers. We suggest ways in which the practical challenges can be addressed through development of shared resources, and outline how these resources can be used to tackle important problems in physical oceanography. With this collaborative approach, seismic oceanography can become a key member of the next generation of methods for observing the ocean.

Keywords: seismic oceanography, acoustic imaging, observational oceanography, submesoscale, internal waves, turbulent mixing, benchmarking, standardization

OPEN ACCESS

Edited by:
Fabien Roquet,
University of Gothenburg, Sweden

Reviewed by:
Robert C. Spindel,
University of Washington,
United States
Louis B. Geli,
Institut Français de Recherche pour l'Exploitation de la Mer (IFREMER),
France

***Correspondence:**
Alex Dickinson
nad38@cantab.ac.uk
Kathryn L. Gunn
kgunn.sc@gmail.com

Specialty section:
This article was submitted to Ocean Observation, a section of the journal Frontiers in Marine Science

Received: *05 July 2021*
Accepted: *21 March 2022*
Published: *21 June 2022*

Citation:
Dickinson A and Gunn KL (2022) The Next Decade of Seismic Oceanography: Possibilities, Challenges and Solutions. Front. Mar. Sci. 9:736693. doi: 10.3389/fmars.2022.736693

1 INTRODUCTION

During the twentieth century our knowledge of oceanic circulation was revolutionized by a host of observational tools. Probes descended beneath the waves to measure the temperature, composition and movement of seawater at great depths, whilst swarms of floating sensors drifted with the currents (e.g., Jacobsen, 1948; Swallow, 1955; Gregg and Cox, 1971; Davis et al., 1992). Colorful dyes

and inert chemicals illuminated the structure of internal waves and the mixing of water masses, and satellite-borne instruments mapped the shape and temperature of the sea surface from space (e.g., Woods, 1968; Born et al., 1979; Ledwell et al., 1986). Measurements made by these, and many other, tools showed that oceanic flow is not governed solely by currents that span thousands of kilometers and which vary on time scales of decades. Instead, circulation is maintained by a constant exchange of energy between global currents and turbulent motions, which mix water over distances of millimeters on time scales of seconds (e.g., Wunsch and Ferrari, 2004; Moum, 2021).

Improved understanding of this exchange is vital to modeling of the ocean's ability to store heat and carbon, and thus to efforts to mitigate the effects of climate change (MacKinnon et al., 2017; Whalen et al., 2020; Richards et al., 2021). However, characterizing the disparate, intermittent and continuously evolving processes that drive circulation has proven challenging. The majority of observational systems are limited to providing time series at a single location, to acquiring measurements in a single spatial direction or along a single travel path, or to monitoring only the surface of the ocean (e.g., moored arrays, probes dropped from a ship, and satellite instruments, respectively; van Haren, 2018). Few observations are available from abyssal regions of the ocean that are thought to play a critical role in controlling mixing of water masses and in modulating climate change (e.g., de Lavergne et al., 2016; Desbruyères et al., 2016; Desbruyères et al., 2017; Levin et al., 2019). Key dynamical phenomena, such as submesoscale currents and lee waves, occur on time and length scales that are not well sampled by common observational tools (e.g., McWilliams, 2016; Legg, 2021).

Seismic reflection profiling[1] of thermohaline structure offers a solution to several of the challenges of ocean observation. This profiling, known as seismic oceanography, is carried out by a ship towing a source of acoustic energy and one or more cables of hydrophones a few meters below the sea surface (**Figure 1A**; Sheriff and Geldart, 1995). At periodic intervals the acoustic source is fired, exciting water-column sound waves by release of either compressed air or electrical charge. Reflection of these waves from changes in temperature and salinity at depth is recorded by the hydrophones. Using these reflections, the properties of thermohaline structure can be investigated.

Use of underwater sound for remote sensing of internal oceanic structure is, of course, not new. For decades, ocean-bottom echosounders have monitored thermocline depths, acoustic tomographic systems have detected basin-wide temperature changes, and acoustic Doppler current profilers (ADCPs) have measured current velocities (Rossby, 1969; Munk and Wunsch, 1979; Pinkel, 1979). High-frequency (i.e., $\gtrsim$ 10 kHz) acoustic surveys provide spectacular images of near-surface internal waves and capture the intensity of turbulent mixing (**Figures 2B, C**; e.g., Proni and Apel, 1975; Geyer et al., 2010; Lavery et al., 2013). Seismic oceanography is distinguished, however, from other acoustic imaging methods in two ways (Fer and Holbrook, 2009). First, it uses low-frequency (i.e., $\lesssim$ 100 Hz) sound that does not attenuate rapidly with depth[2]. Second, each imaged point is repeatedly sampled over a time interval of $\lesssim$ 30 minutes by different configurations of acoustic source and hydrophones, increasing the signal-to-noise ratio (**Figure 1B**). These distinctive features lend seismic oceanography a unique combination of three key characteristics:

- **Multi-dimensional observation of the ocean at high spatial resolution.** Seismic oceanography provides a two-dimensional, and often three-dimensional, view of the ocean at horizontal and vertical resolutions on the order of 10 m. Other observational tools may achieve higher spatial resolutions, but usually provide measurements in only one dimension.
- **Penetration to abyssal depths.** Unlike higher-frequency acoustic methods, seismic oceanography captures thermohaline structure down to depths of several kilometers. This capability allows observation of abyssal regions that are otherwise undersampled.
- **Horizontal coverage over hundreds of kilometers.** Seismic data are continuously recorded along $\lesssim$ 1,000-km-long transects. This coverage provides a holistic view of structures such as eddies that are otherwise only intermittently sampled (e.g., by dropped probes).

Due to these characteristics, seismic oceanography has provided uniquely detailed images of features such as fronts, tidal beams, eddies, thermohaline staircases and turbid layers (e.g., Nakamura et al., 2006; Holbrook et al., 2009; Pinheiro et al., 2010; Fer et al., 2010; Vsemirnova et al., 2012; **Figure 2D**). Importantly, seismic records provide not only spectacular images, but have yielded quantitative insight into dynamical phenomena including thermohaline interleaving, propagation of internal waves, and turbulent mixing (e.g., Papenberg et al., 2010; Tang et al., 2014; Falder et al., 2016; **Figure 3**). Reviews of topics as wide-ranging as stratified turbulence, circumpolar currents and submesoscale flow have cited results from seismic oceanography (e.g., Riley and Lindborg, 2008; Thompson et al., 2018; McWilliams, 2019). In total, more than one hundred peer-reviewed research papers have now presented seismic oceanographic data (**Appendix A; Table A**; see **Supplementary Material** for all appendices and tables).

Despite these successes, seismic oceanography has struggled to establish itself as a standard observational tool. This slow development has two causes. First, the field has been hindered by practical challenges associated with acquiring data and with analyzing records in a consistent and reliable way. Second, and more fundamentally, many physical oceanographers regard the field as a curiosity, with no clear vision or scientific application. To progress further, the seismic oceanographic community needs to identify key scientific questions that it can systematically address.

Here, we discuss the practical challenges that face seismic oceanography and suggest ways in which they can be overcome

[1] In seismic acquisition, the term *profile* describes a two-dimensional map plotted against range and depth. Here, we instead use the oceanographic term *section*. Our use of the term *profile* is limited to description of a one-dimensional series of measurements recorded as a function of depth (Krahmann et al. 2008).

[2] A small number of seismic oceanographic surveys have used sound with frequencies as high as ~ 500 Hz (see *Section 2.1.1*; Ker et al., 2015). However, the great majority have used low-frequency sound.

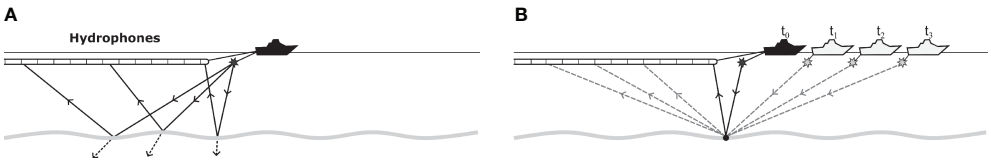

FIGURE 1 | Principles of seismic oceanography. **(A)** Cartoon showing single release of energy by acoustic source. Black star = acoustic source; undulating gray line = change in oceanic temperature and/or salinity; solid black lines with arrows = travel paths for three example sets of incident and reflected sound waves; dashed black lines with arrows = transmitted sound waves. In reality, sound waves travel out from acoustic source in all directions and are recorded at every hydrophone along cable. **(B)** Cartoon illustrating repeated sampling of same spatial point by multiple firings of acoustic source. Black dot = repeatedly sampled point; black star = acoustic source at time t_0; solid black lines with arrows = travel path for sound waves excited at time t_0 and reflected from black dot; gray stars = acoustic source at later times t_1, t_2, t_3; dashed gray lines with arrows = travel paths for sound waves excited at times t_1, t_2, t_3 and reflected from black dot. Note that cable of hydrophones is not illustrated for times t_1, t_2, t_3. For more complete introductions to acquisition of seismic oceanographic data, see Fer and Holbrook (2009), Ruddick et al. (2009) and Holbrook (2009).

(*Section 2*). We then discuss how seismic oceanography can address scientific questions that other tools cannot answer (*Section 3*). Finally, we outline ways in which the seismic oceanographic community can implement these solutions by agreeing on priorities and by working together on collaborative projects (*Section 4*).

2 HOW CAN SEISMIC OCEANOGRAPHY OVERCOME ITS PRACTICAL CHALLENGES?

Seismic oceanography is faced by three practical challenges. Previous works have outlined possible solutions to one or more of these challenges (e.g., Jones et al., 2008; Holbrook, 2009; Jones et al., 2010; Buffett and Carbonell, 2011; Ruddick, 2018). Here, we build on these works to develop a comprehensive strategy for overcoming all three challenges.

2.1 How Can We Acquire Seismic Oceanographic Data?

Perhaps the greatest practical obstacle to further development of seismic oceanography is the logistical difficulty and high cost of acquiring data. Conventional seismic reflection surveys require specialized vessels that are capable of towing powerful acoustic sources and long cables of hydrophones. A small number of research bodies maintain such vessels (e.g., the Alfred Wegener Institute, Germany; the Natural Environmental Research Council, UK; the University-National Oceanographic Laboratory System, USA). Access to ship time is limited and surveys are up to five times more expensive than other ocean-going research cruises (National Research Council, 2015; National Science Foundation, 2016). Chartering of independent seismic exploration companies can cost up to three times as much again (National Science Foundation, 2016). There are two possible solutions to the challenge of high cost and logistical difficulty.

2.1.1 Development of New Seismic Systems

First, data could be acquired using systems that are specially designed for seismic oceanography (e.g., Ruddick, 2018). These systems could be optimized to reduce costs and to target specific oceanographic phenomena. Ideally, they would be deployed alongside other observational instruments and would not require use of specialized vessels. The most obvious way to lower costs and improve deployability is to use weaker acoustic sources and shorter cables of hydrophones. Weaker acoustic sources produce higher-frequency (i.e., $\gtrsim$ 100 Hz) sound waves that provide increased spatial resolution, but the signal-to-noise ratio degrades more quickly with depth (Geli et al., 2009; Hobbs et al., 2009). Although this degradation can be partially compensated for by more frequent firing of the source and by a denser spacing of hydrophones, it seems unlikely that higher-frequency sources will be capable of clearly imaging the water column to abyssal depths (Nakamura et al., 2006). Instead, higher-frequency seismic systems could be optimized for imaging of relatively shallow structures such as seasonal thermoclines (Piété et al., 2013; Ker et al., 2015; Sallares et al., 2016; Mojica et al., 2018). When combined with direct measurements of properties such as temperature and salinity, they could form an excellent tool for investigation of processes that are too coarse to be detected by high-frequency echosounders and yet too fine to be detected by conventional seismic systems.

2.1.2 Use of Existing Datasets

An alternative solution to the difficulty of acquiring new seismic reflection data is to analyze existing records. An overwhelming majority of these records have been acquired by seismic exploration companies, which spend billions of dollars each year on new datasets (McBarnet, 2013). As a consequence, these companies can afford equipment and modes of operation that are far beyond the budgets of research organisations. Commercial seismic records are thus likely to have higher signal-to-noise ratios and to be more accurately spatially positioned than records acquired for scientific research. Dense layouts of overlapping transects are often acquired in a small area over a period of several weeks or months, allowing the temporal evolution of oceanographic phenomena to be tracked (e.g., Dickinson et al., 2020; Gunn et al., 2020b; Zou et al., 2020; Gunn et al., 2021). Many commercial exploration vessels carry several parallel cables of hydrophones, enabling imaging of thermohaline structure in three spatial dimensions (these

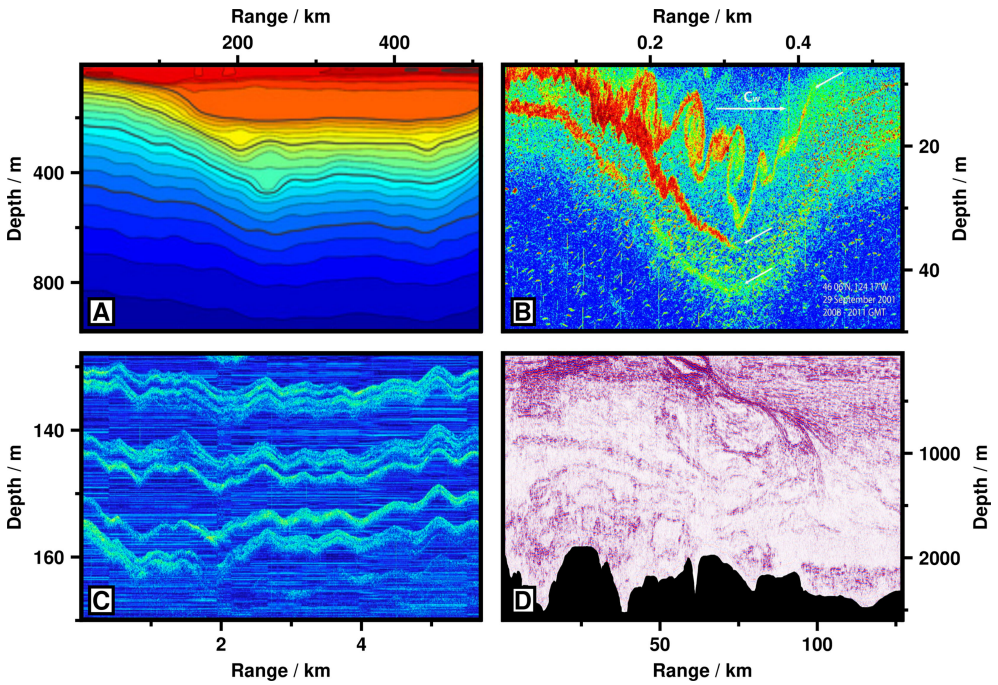

FIGURE 2 | Comparison of seismic oceanography to other observational techniques. **(A)** Temperature section interpolated from measurements made by glider in Gulf of Mexico (after Figure 3D of Meunier et al., 2019). Red = warmer water; blue = cooler water; vertical resolution ≈ 2 m; horizontal resolution ≈ 2,000 m. **(B)** High-frequency (~ 120 kHz) echosounder image of Kelvin-Helmholtz instabilities within internal solitary wave above Oregon continental shelf (after Figure 14 of Moum et al., 2003). Red = high acoustic intensity; blue = low acoustic intensity; vertical resolution ≈ 0.04 m; horizontal resolution ≈ 3 m at depth of 30 m. **(C)** High-frequency (~ 15–25 kHz) echosounder image of thermohaline staircase in Arctic Ocean (after Figure 5 of Stranne et al., 2017). Brighter colors indicate higher acoustic amplitudes; vertical resolution ≈ 0.1 m; horizontal resolution ≈ 15 m at depth of 150 m. **(D)** Seismic oceanographic image of oceanic front at Brazil-Malvinas Confluence (after Figure 3A of Gunn et al., 2020b). Red colors = positive acoustic amplitudes; blue colors = negative acoustic amplitudes; black region = seafloor; vertical and horizontal resolutions ~ O (10) m. Note different ranges and depths of four panels.

surveys are known as three-dimensional; Blacic and Holbrook, 2010; Bakhtiari Rad and Macelloni, 2020; Zou et al., 2021).

Existing surveys are concentrated above continental shelves and slopes, which exploration companies have targeted since they house economically valuable reserves of oil and gas (**Figure 4A**). Recent observational, theoretical and computational work suggests that the mixing that drives oceanic circulation is most intense above these continental margins and above other topographically rough features such as mid-ocean ridges and seamount flanks (e.g., Waterhouse et al., 2014; Ferrari et al., 2016; McDougall and Ferrari, 2017; Drake et al., 2020). Continental margins also host western boundary currents that transport significant quantities of heat, salt and nutrients (e.g., Stommel, 1948; Hu et al., 2015; Buckley and Marshall, 2016). In a warming climate, the intensity and position of these currents is likely to change markedly, yet there are limited direct observations of their magnitude and variability (e.g., Wu et al., 2012; Yang et al., 2016). Existing seismic records span several decades and provide a dataset of unprecedented size and coverage that can be used to investigate in detail these critically important interactions above continental margins.

Thanks to burgeoning open-access initiatives, an increasing number of both academic and commercial datasets are being made publicly available (**Figures 4B, C**; **Appendix B**). Researchers need only cover data-dearchiving and data-shipment costs. Access to other, privately held, commercial datasets might be most easily gained through formation of an international collaboration for all seismic oceanography researchers (Jones et al., 2010; Buffett and Carbonell, 2011). Many seismic exploration companies are currently seeking ways to improve their public image by promoting independent scientific research. Supporting seismic oceanography is particularly attractive since only commercially worthless water-column reflections, and not commercially valuable subsurface reflections, need be supplied.

2.2 How Can We Benchmark Seismic Oceanographic Data?

Estimation of accurate quantitative results from seismic oceanographic datasets requires a reliable understanding of the correspondence between seismic records and hydrographic properties. However, it has remained difficult to gain such an understanding since the strength and form of recorded seismic amplitudes are functions of many variables, which depend both on local thermohaline structure and on the seismic acquisition system. Key questions fall into three areas:

- **Hydrographic sensitivity:** What are the smallest changes in temperature and salinity which seismic reflection surveys can detect? How well do these changes correspond to changes in

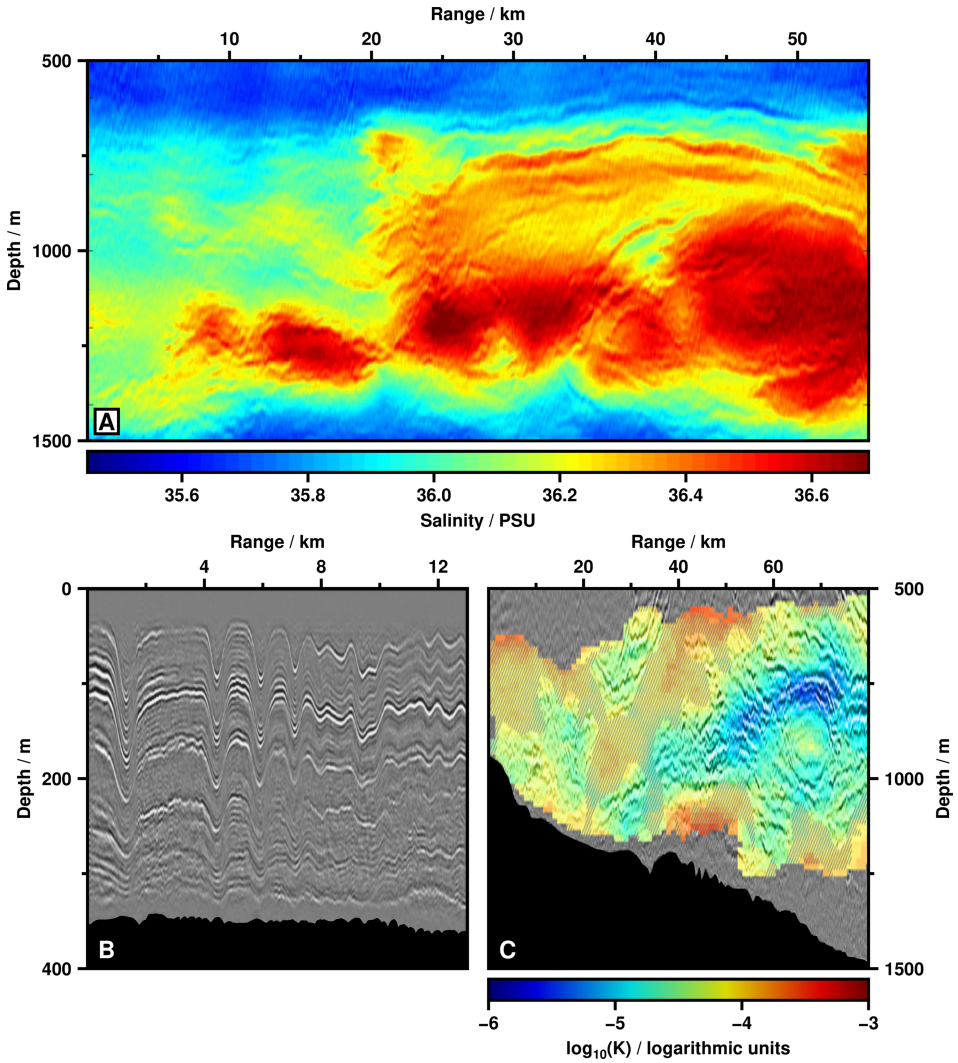

FIGURE 3 | Initial successes of seismic oceanography. **(A)** Values of salinity inverted from seismic oceanographic image of eddy of Mediterranean Water in Gulf of Cadiz (after Figure 6 of Dagnino et al., 2016). Note finely resolved layering along upper side of eddy. **(B)** Internal solitary waves captured in seismic oceanographic image from South China Sea (after Figure 2 of Tang et al., 2016). Grayscale represents response of thermohaline structure to seismic waves; black region = seafloor. Internal-wave velocities can be estimated from seismic records. **(C)** Spatial map of diapycnal diffusivity, K, estimated from seismic oceanographic image above Falkland Plateau (after Figure 15b of Falder et al., 2016). Grayscale = seismic image; colored overlay = estimates of K; hashed pattern = areas where estimates are less certain; black region = seafloor. Note depressed values of K above eddy imaged at range of ~ 60–70 km.

density? On what spatial length scales can these changes be detected?

- **Temporal blurring:** How does motion of thermohaline structure, acoustic source and recording system affect observation of features that are repeatedly sampled during periods of $\lesssim$ 30 minutes?
- **Seismic system:** How do the answers to these questions change with variations in acoustic frequency and in design of the recording system?

Studies have addressed one or more of these questions in isolated circumstances (**Appendix C; Table C**). To analyze seismic data more widely, it would be helpful to systematically investigate these questions across the full range of oceanographic settings. This investigation can be carried out in two ways.

2.2.1 Field Datasets With Hydrographic Calibration

First, seismic records can be compared to coincident, direct measurements of properties such as temperature, salinity and current velocity. These comparisons aid interpretation of imaged phenomena and guide estimation of quantities such as temperature, salinity and diapycnal diffusivity from seismic images (e.g., Papenberg et al., 2010; Holbrook et al., 2013). Coupling seismic records to more familiar oceanographic measurements is also likely to encourage widespread acceptance of seismic oceanography (Ruddick, 2018). Twenty-four existing datasets have such ancillary

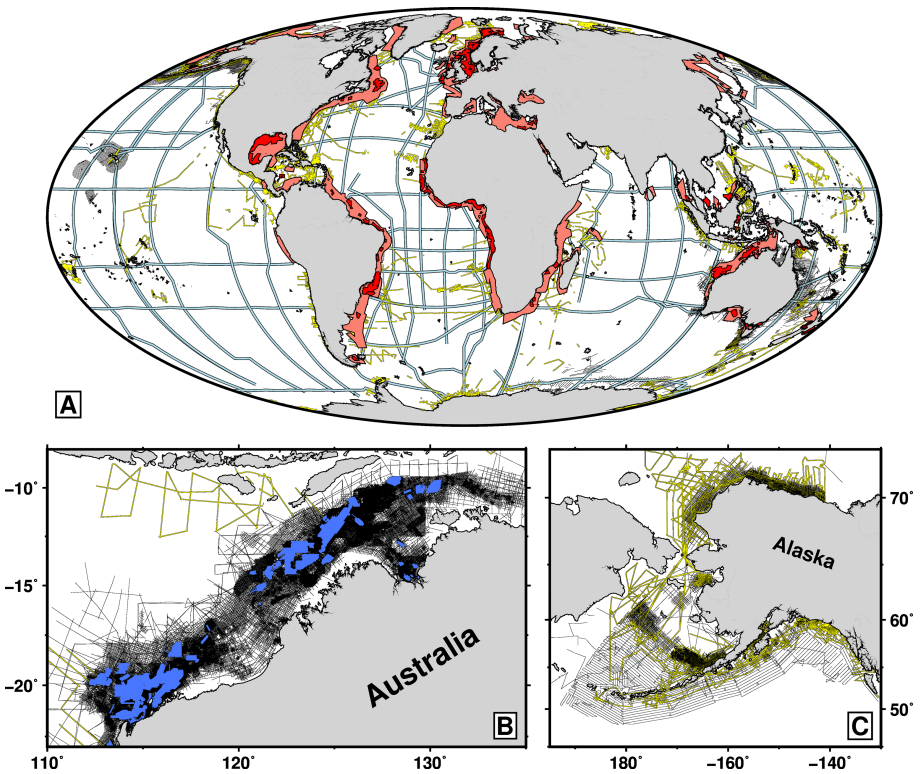

FIGURE 4 | Existing marine seismic reflection data. **(A)** Global distribution. Light red polygons = regions covered by two-dimensional (i.e., single-cable) surveys acquired by seismic exploration companies; dark red polygons = regions covered by three-dimensional (i.e., multi-cable) surveys acquired by seismic exploration companies; thin black lines = publicly available two-dimensional surveys acquired by seismic exploration companies in other regions; yellow lines = publicly available two-dimensional surveys acquired by research institutions; light blue lines = hydrographic transects of World Ocean Circulation Experiment (WOCE; www.ewoce.org). Red polygons were traced from the websites of the five largest exploration companies (CGG, ION, PGS, Schlumberger, TGS) and represent > 6.3 million km of two-dimensional seismic data and > 5.5 million km^2 of three-dimensional seismic data. Publicly available data were downloaded from a range of online repositories (note that plotted transects represent only a small subset of all existing data). **(B)** Zoom of Australia's Northwest Shelf showing only publicly available seismic data. Blue polygons = three-dimensional commercial surveys made available through the National Offshore Petroleum Information Management System (NOPIMS; www.ga.gov.au/nopims). **(C)** Zoom of the Gulf of Alaska and the Bering, Chukchi and Beaufort Seas showing only publicly available seismic data. Note that WOCE transects are not plotted in panels **(B)** or **(C)**. See **Supplementary Material** for further details of data provenance.

data and have been used for seismic oceanographic research (**Appendix C.1**; **Table C.1**). Datasets with hydrographic calibration could in future be acquired by combining specially designed seismic systems of the kind discussed in *Section 2.1.1* with instruments such as expendable bathythermographs (XBTs), ADCPs, and microstructure profilers. However, seismic exploration companies, which carry out the majority of surveys, do not routinely acquire high-quality hydrographic data. More fundamentally, the unique coverage and spatial resolution of seismic reflection data means that coincident hydrographic measurements cannot capture all relevant scales.

2.2.2 Numerical Modeling

Numerical modeling and synthetic datasets offer a way to comprehensively explore scales that hydrographic calibration cannot access. An ideal numerical model would include realistic descriptions of two elements. First, thermohaline structure would be described by a time-variant fluid-dynamical model that resolves time scales of minutes to days and vertical and horizontal length scales of $\sim O(1)$ m (Ménesguen et al., 2018). Second, this simulated structure would be acoustically probed by a modeled seismic acquisition system travelling at finite speed. Models with these two elements could faithfully replicate the characteristics of seismic surveys in a range of oceanographic conditions.

Existing studies have built numerical models of varying sophistication (**Appendix C.2**; **Tables C.2.1, C.2.2**). These models have been used to investigate the effect of fluid flow on wave propagation and on blurring of seismic reflections, to assess correspondence between reflections and isopycnals, to quantify errors in imaging of deep structure due to non-homogeneous near-surface waters, and to simulate the characteristics of new seismic oceanographic acquisition systems (e.g., Vsemirnova et al., 2009; Ji and Lin, 2013; Holbrook et al., 2013; Ji et al., 2013; Biescas et al., 2016). Previous work must now be built upon to form a standardized toolkit for modeling of seismic reflection profiling of thermohaline structure. Using this toolkit, the accuracy of quantitative results derived from seismic images can be assessed.

2.3 How Can We Analyze Seismic Oceanographic Data?

Development of seismic oceanography has to date been advanced by disparate groups of researchers, each of which has developed its own computer codes for signal processing and interpretation. Many of these codes either rely on proprietary software or have not been made publicly available (see **Table D**). Lack of open-source code hampers replication of results and discourages scientists who do not have a background in seismic signal processing.

To realize the full potential of seismic oceanography, the community must now develop standardized open-source codes which can be used with a broad range of seismic datasets. Key to standardization will be rigorous investigation of the effects of different workflows on the accuracy of results (see **Appendix D** for a discussion of workflows for constructing seismic images). Here, we focus on three fields that comprise the majority of existing quantitative work and which are ripe for standardization:

- **Hydrographic Inversion.** Estimation of sound speed, temperature, salinity and density.
- **Propagation of Internal Waves.** Characterization of the size, velocity and decay of internal waves.
- **Spectral Analysis.** Analysis of internal waves and turbulence using wavenumber spectra.

For each of these fields, we summarize previous work, suggest potential future applications, and highlight selected outstanding questions.

2.3.1 Hydrographic Inversion

Propagation of low-frequency acoustic waves within the oceanic water column is governed by changes in sound speed and, to a much smaller extent, in density (Ruddick et al., 2009; Sallares et al., 2009). Sound speed can thus be directly estimated from seismic data and mapped into values of temperature and salinity using an assumed temperature-salinity relationship and the hydrographic equation of state (see **Appendix D.1** and **Table D.1** for a summary of proposed methods). Hydrographic inversion has been used, for example, to investigate stirring at baroclinic fronts, to describe temperature variance in turbulent waters above a continental slope, and to reassess heat transport onto the Antarctic shelf (Biescas et al., 2014; Minakov et al., 2017; Gunn et al., 2018). Inversion results can also act as constraints for other calculations that are made using seismic records (e.g., estimation of diapycnal heat flux, Gunn et al., 2021; see *Sections 3.1* and *3.2*). Key questions for further development of hydrographic inversion include:

- How accurate can inversion results be in the absence of nearby hydrographic data? *See* Bornstein et al. (2013), Padhi et al. (2015) *and* Blacic et al. (2016).
- What are the smallest and greatest spatial scales that can be recovered? *See* Blacic et al. (2016), Minakov et al. (2017) *and* Gunn et al. (2018).
- Can useful inversion results be obtained from records in which water-column reflections are very faint or absent?

2.3.2 Propagation of Internal Waves

Seismic oceanographic images often display prominent internal waves, including tidal beams, lee waves and trains of solitary waves (e.g., Holbrook et al., 2009; Eakin et al., 2011; Tang et al., 2015). The velocities of these waves can be estimated by analyzing changes in reflection amplitude during the interval of $\lesssim$ 30 minutes within which a single point is sampled (**Appendix D.2; Table D.2**). This approach has shed light on stirring at oceanic fronts, on the evolution of solitary waves, and on heat transport by intrathermocline eddies (Sheen et al., 2012; Tang et al., 2014; Gunn et al., 2018). Blacic and Holbrook (2010) and Zou et al. (2020) suggest how these analyses could be extended to mapping internal waves in three dimensions. This mapping could greatly improve our understanding of internal-wave-driven mixing of energy and material, which plays a critical role in global climate (e.g., Helfrich and Melville, 2006; Legg, 2021). Outstanding questions for seismic oceanographic estimation of internal-wave velocities include:

- To what extent is it possible to decouple the velocities of internal waves from the velocities of background currents?
- How does the accuracy of estimated velocities vary with duration of observation?
- How sensitive are estimated internal-wave velocities to errors in the profiles of sound speed that are used to spatially reposition reflections? *See* Klaeschen et al. (2009).

2.3.3 Spectral Analysis

In addition to imaging clearly visible internal waves, seismic oceanographic data capture the signals of the background internal wave field and of turbulent motions. These signals have most commonly been analyzed by computing horizontal-wavenumber spectra from the vertical displacements of tracked seismic reflections (e.g., Holbrook and Fer, 2005; **Appendix D.3; Table D.3**). This approach has been exploited to investigate the nature of the dynamical transition from internal waves to turbulence, to link intensity of turbulent overturning to submesoscale structure, and to estimate diapycnal mixing above regions of rough bathymetry (e.g., Falder et al., 2016; Tang et al., 2020; Tang et al., 2021). Fortin et al. (2016) suggest how spectra can be estimated from regions of a seismic image in which reflections cannot be tracked. To develop a consistent and reliable method for spectrally analyzing seismic oceanographic images, the following outstanding questions must be addressed:

- How closely must reflections track isopycnals for results to be useful? What information can be extracted from the spectra of reflections that do not track isopycnals? *See* Meunier et al. (2019).
- How severely are spectra distorted by temporal blurring? *See* Vsemirnova et al. (2009) *and* Falder et al. (2016).
- How are spectra affected by use of different methods for mapping of recorded seismic amplitudes into spatial images? Which method is most appropriate? *See* Fortin and Holbrook (2009) *and* Holbrook et al. (2013).

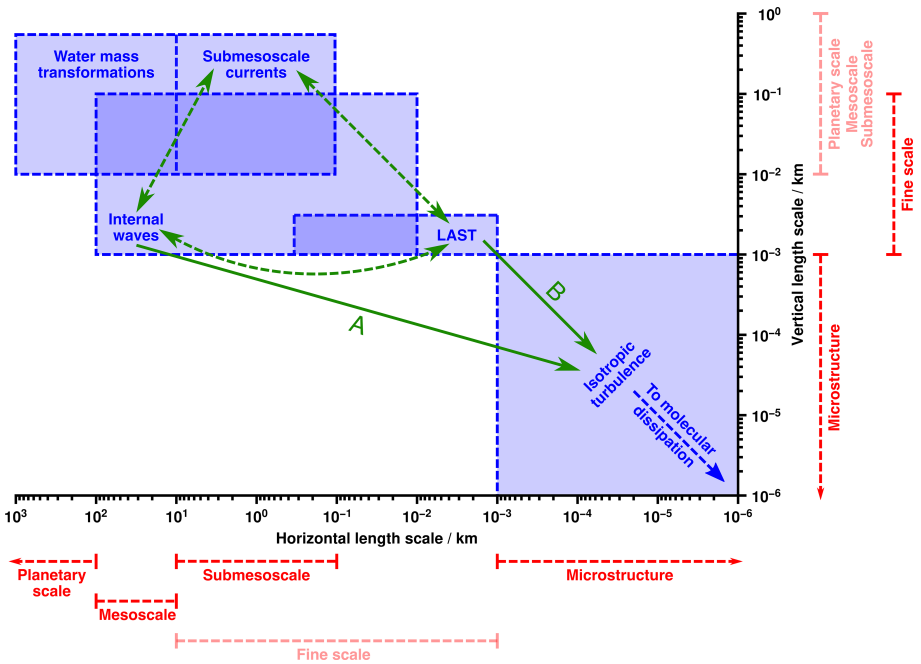

FIGURE 5 | Cartoon showing approximate length scales of processes that can be investigated using seismic oceanography. Red dashed bars show approximate ranges[3] of commonly used descriptive terms. (The term *fine scale* was coined to describe vertically varying structure, and its horizontal extent is not clearly defined. *Planetary scale*, *mesoscale* and *submesoscale* are predominantly used to describe horizontal length scales.) Blue boxes show approximate extents of selected phenomena. LAST = layered anisotropic stratified turbulence[5]. Green arrows show possible parametrizations describing transfer of energy. Solid arrow labeled A = fine-scale parametrizations; solid arrow labeled B = assumption of continuity between LAST and inertial-convective regime of isotropic turbulence[5] ; dashed green arrows = other parametrizations that seismic oceanography could inform. Note that boundaries between phenomena are much more gradational than depicted. Only phenomena referred to in this article are shown. Inspired by Figure 1 of McWilliams (2016) and Figure 1 of Ruddick (2018).

In future, spectra could potentially be computed directly from seismically estimated sections of temperature and salinity, avoiding the need to track reflections (see *Section 3.2*; Xiao et al., 2021).

3 WHAT PROBLEMS CAN SEISMIC OCEANOGRAPHY SOLVE?

To gain widespread acceptance, the seismic oceanographic community must identify ways in which the datasets and tools discussed in *Section 2* can be used to rapidly improve our understanding of oceanic circulation. This circulation encompasses myriad processes that continuously interact on a wide range of time and length scales. No single theory or set of observations can hope to simultaneously capture all of these interactions. Instead, oceanographers conceptualize circulation as a collection of discrete phenomena (e.g., Ferrari and Wunsch, 2009). Transfer of energy between these phenomena is described by parametrizations that are based on a combination of theoretical and empirical evidence (e.g., Garrett, 2006; Polzin et al., 2014; McWilliams, 2017; de Lavergne et al., 2020).

Seismic oceanography straddles a unique combination of scales and is thus ideally placed to revolutionize our understanding of several processes and parametrizations (see **Figure 5**). Here, we outline three areas in which the seismic method can provide key insights within the next decade.

3.1 Turbulent Mixing

It is widely accepted that mechanical mixing[4] by turbulent motions is key to maintaining global overturning circulation (e.g., Munk, 1966; Wunsch and Ferrari, 2004). Observations since the 1990s have shown that turbulent mixing is concentrated above regions of rough bathymetry and at the edges of ocean basins (e.g., Polzin et al., 1997; Mauritzen et al., 2002; Naveira Garabato et al., 2019). These observations have spurred theoretical advances which suggest that mixing in narrow boundary layers forms a critical part of oceanic circulation (Levy et al., 2012; Ferrari et al., 2016; McDougall and Ferrari, 2017; Drake et al., 2020). Further measurements are now needed to refine these theories and to tune climate models (e.g., Mashayek et al., 2015; Mashayek et al., 2017; MacKinnon et al., 2017).

Unfortunately, oceanic turbulence is difficult to sample since it is highly intermittent in both space and time (Ivey et al., 2008; Shroyer et al., 2018; Cael and Mashayek, 2021). Fast-response thermistors

[3]The length scales of depicted descriptive terms and phenomena depend on variables such as latitude, flow velocity, and density structure. For instance, the term *submesoscale* was coined to describe flow on horizontal length scales shorter than the first baroclinic radius of deformation (McWilliams, 1985). For further discussion see Vallis (2017) and Meredith and Naveira Garabato (2022).

and shear probes, which have most commonly been deployed as vertically dropped microstructure profilers, resolve isotropic turbulent[5] fluctuations on length scales as small as ∼*0*(1) mm (**Figure 5**; e.g., Schmitt et al., 1988; Lueck et al., 2002; Lozovatsky et al., 2019). However, microstructure profiles are uncommon and sparsely distributed. For instance, in compiling a global database of turbulence measurements, Waterhouse et al. (2014) found only ∼5,200 profiles of vertical shear. Such small numbers of measurements cannot constrain the global distribution of turbulence.

To overcome this problem, many studies have sought to infer the strength of turbulence using observations of internal waves on vertical length scales of ∼*0*(1-10) m (**Figure 5**; Gregg, 1989; Wijesekera et al., 1993; MacKinnon and Gregg, 2003; Polzin et al., 2014; Ijichi and Hibiya, 2015). These inferences, which are known as fine-scale parametrizations, have underpinned attempts to map the global distribution of mixing using measurements made by conductivity-temperature-depth (CTD) profilers and Argo floats (Whalen et al., 2012; Waterhouse et al., 2014; Whalen et al., 2015; Kunze, 2017). However, few studies have benchmarked the results of fine-scale parametrizations against direct measurements of turbulence (e.g., Liang et al., 2018; Takahashi and Hibiya, 2019; Takahashi and Hibiya, 2021; Fine et al., 2021).

Instruments that record structure on horizontal scales of $\gtrsim O(10)$ m offer an alternative way to both directly measure turbulence and benchmark fine-scale parametrizations (Moum, 2021). On horizontal length scales of $\lesssim$ 300 m, observations reveal a regime of layered anisotropic stratified turbulence (LAST)[5] that can be straightforwardly related to the intensity of isotropic turbulence (**Figure 5**; Brethouwer et al., 2007; Klymak and Moum, 2007b; Maffioli and Davidson, 2016; Kunze, 2019). Internal-wave signals on greater horizontal length scales can be analyzed using modified fine-scale parametrizations to yield indirect estimates of the strength of turbulent mixing (e.g., Klymak and Moum, 2007a; Sheen et al., 2009; Dickinson et al., 2017).

The horizontal signals of internal waves and LAST are captured both by towed instruments and by seismic oceanography (e.g., LaFond, 1963; McKean and Ewart, 1974; Holbrook and Fer, 2005; Holbrook et al., 2013). However, seismic oceanography is distinguished by its ability to record unprecedentedly large volumes of data in short periods of time. For instance, one 175-km-long seismic image acquired over a 20-hour period shows reflective boundaries with a cumulative length of more than 5,000 km (Dickinson et al., 2017). This length is over thirty times greater than the combined length of the datasets on which Garrett and Munk (1972) based the horizontal-wavenumber description of their original semi-empirical internal-wave spectrum. Rapid acquisition also distinguishes seismic oceanography from more recent campaigns that have acquired horizontal measurements over periods of several weeks (e.g., Ferrari and Rudnick, 2000).

Spectral analysis of extensive seismic oceanographic datasets thus has the potential to provide a global catalogue of oceanic horizontal-wavenumber spectra that is unrivalled in size (cf. Polzin and Lvov, 2011). Statistical investigation of this catalogue could address questions that include:

- How accurate is the Garrett-Munk spectrum for internal waves? How do the spectral properties of internal waves vary in different oceanic environments? *See* Levine (2002), Polzin and Lvov (2011) *and* Pinkel (2020).
- What is the nature of the dynamical transition between internal waves and LAST on horizontal length scales of ∼*0*(100) m? *See* Falder et al. (2016), Sallares et al. (2016), Kunze (2019) *and* Howland et al. (2020).
- How accurate are existing fine-scale parametrizations when applied to horizontal-wavenumber spectra[6]? Do different parametrizations work better in different oceanic environments? Is it possible to formulate new parametrizations that better apply to horizontal-wavenumber spectra? *See* MacKinnon and Gregg (2003), Klymak and Moum (2007a), Hibiya et al. (2012), Polzin et al. (2014), Waterman et al. (2014) *and* Ijichi and Hibiya (2015).

Perhaps most importantly, seismic oceanography offers a way to map the intensity of turbulent mixing in unprecedented two-dimensional detail across sections that are hundreds of kilometers in length (e.g., Tang et al., 2021; Wei et al., 2022). Advances in oceanographic instrumentation are providing new tools that can be integrated into future seismic surveys to benchmark estimates of mixing (Frajka-Williams et al., 2022). Shear probes will be mounted on Argo floats, whilst expendable profilers will measure velocity fluctuations to depths of ~ 6,000 m (e.g., Shroyer et al., 2016; Shang et al., 2017; Roemmich et al., 2019). Seismometers will record turbulent flow in narrow boundary layers above the ocean floor (Yang et al., 2021). Once seismic methods for estimating mixing have been accurately calibrated using these tools and using numerical simulations, existing seismic datasets will provide a way to investigate possible changes in oceanic mixing during the previous four decades, when few other measurements were available.

[4]The term *mixing* is inconsistently used in the literature (e.g., Eckart, 1948; Muller and Garrett, 2002; Dimotakis, 2005; Naveira Garabato and Meredith, 2022). Here, we follow common convention and use the term *turbulent mixing* to describe the folding and stirring of fluid by eddying motions. By increasing the variance of temperature, salinity and density on microscales, this folding and stirring creates favorable conditions for the molecular diffusion that ultimately mixes different water masses (Moum, 2021).

[5]On length scales of $\lesssim O(1)$ m, the effects of ocean stratification are insignificant and turbulent motions have the same form in the horizontal and the vertical (Ozmidov, 1965; Dillon, 1982). This isotropic turbulence maintains a downscale transfer of energy that is exactly described by theory (Kolmogorov, 1941; Sreenivasan, 1995). On greater length scales, the effects of stratification lead to anisotropic turbulence with a much greater horizontal than vertical extent. We follow Falder et al. (2016) in using the term *layered anisotropic stratified turbulence* (LAST) to refer to this turbulence. For further discussion see Lindborg (2006), Riley and Lindborg (2008), Riley and Lindborg (2012), Caulfield (2020) and Caulfield (2021).

[6]The accuracy of horizontal fine-scale parametrizations can be assessed by comparison to simultaneous observations of LAST in the same seismic image.

3.2 Submesoscale Currents

The submesoscale range plays host not only to internal waves, but to a menagerie of other phenomena that evolve on time scales of hours to days (**Figure 5**; Thomas et al., 2008; Callies et al., 2020). These non-internal-wave phenomena, which we collectively refer to as submesoscale currents[7] following McWilliams (2019), are thought to be vital in sustaining ecosystems and in modulating exchange of energy between mesoscale motions and microscale turbulent flows (e.g., Levy et al., 2018; Naveira Garabato et al., 2022). Unfortunately, they are difficult to discern in observational time series and in measurements made by vertically dropped instruments (McWilliams, 2016). As a result, most *in situ* observations have been obtained using platforms that sample the ocean horizontally, such as towed thermistors or ADCPs (e.g., Samelson and Paulson, 1988; Klymak and Moum, 2007a; Rocha et al., 2016; Qiu et al., 2017).

A more complete description of submesoscale currents requires rapid two- or three-dimensional sampling (McWilliams, 2019). Although gliders provide quasi-two-dimensional observations, they travel at slow horizontal speeds of ∼0.3 m $s^{-1}$and probably only resolve features at horizontal scales greater than ∼30 km (e.g., **Figure 2A**; Rudnick and Cole, 2011; Rudnick, 2016). A few field campaigns have sought three-dimensional descriptions by tracking the spread of inert tracers, by carrying out surveys with two closely spaced ships, and by combining moored, towed and dropped instruments with airborne sensors and with autonomous floats, drifters and gliders (e.g., Allen and Naveira Garabato, 2012; Shcherbina et al., 2013; Shcherbina et al., 2015; Pascual et al., 2017; Marmorino et al., 2018). However, these campaigns have small geographical extents and are limited to the upper ∼ 500 m of the ocean. Satellites and airborne instrumentation have revolutionized our understanding of submesoscale activity at the sea surface (e.g., Gower et al., 1980; Munk et al., 2000; Jolliff et al., 2019; Klein et al., 2019; Martínez-Moreno et al., 2021). However, it is not well known how closely these surface motions correspond to flow at depth (e.g., Wang et al., 2010; Callies and Ferrari, 2013).

In addition to being difficult to observe, submesoscale currents are difficult to theoretically describe (e.g., McWilliams, 2010; McWilliams, 2017). As a result, developments in our understanding have been largely driven by numerical simulations (McWilliams, 2019). At present, most simulations are validated by comparison to satellite or radar observations of sea-surface height and temperature (e.g., Delandmeter et al., 2017; Schubert et al., 2019; Bashmachnikov et al., 2020; Chrysagi et al., 2021). Few studies have compared simulations to subsurface observations (e.g., Rocha et al., 2016; Liu et al., 2017; Viglione et al., 2018). Improving our ability to observe submesoscale currents and to benchmark simulations now requires an efficient way to rapidly sample thermohaline structure between the sea surface and the seafloor.

[7] Our use of the term *submesocale currents* includes submesoscale coherent vortices, which are subsurface eddies with distinct hydrographic properties (McWilliams, 1985). Once formed, they can exist for several years.

Seismic oceanography offers an unrivalled means of achieving this sampling. Unlike gliders, seismic vessels move at fast speeds of ∼ 2.5–3 m s^{-1}, allowing surveys to capture submesoscale structures that evolve on time scales of hours to days. This ability can be exploited in three ways. First, seismic images can reveal the geometries and distributions of subsurface submesoscale structures in unprecedented detail. For instance, Song et al. (2011) present a seismic image which shows how submesoscale coherent vortices generate thermohaline intrusions with forms that are unanticipated by theory. By combining seismic images with inverted sections of temperature, salinity and density, Gunn et al. (2020b) show how submesoscale lenses and filaments interact with a deep-seated oceanic front. Seismic oceanography's ability to visualise submesoscale features can address questions such as:

- How abundant are submesoscale coherent vortices? How quickly do they evolve? *See* Gunn et al. (2018), Gula et al. (2019), Steinberg et al. (2019), Archer et al. (2020), McCoy et al. (2020) *and* Tang et al. (2020).
- How widespread are submesoscale fronts? To what depth do these fronts extend? How are they influenced by the presence of permanent fronts between water masses? *See* Ramachandran et al. (2014), Pascual et al. (2017), Siegelman et al. (2019), Gunn et al. (2020b) *and* Giddy et al. (2021).
- How does the size and form of imaged submesoscale structures vary with depth and with proximity to rough topography? *See* de Lavergne et al. (2016), Dauhajre et al. (2017), Ruan et al. (2017), Callies (2018) *and* Wenegrat et al. (2018).

Second, seismic oceanography can probe the statistical signatures of submesoscale currents. To date, few observational studies have resolved along-isobar and along-isopycnal hydrographic variations on submesoscale length scales, and the distribution of potential energy in the submesoscale range is poorly known (e.g., Cole and Rudnick, 2012; Callies and Ferrari, 2013; Schönau and Rudnick, 2015; Itoh and Rudnick, 2017). Improved observations will show which processes dominate transfer of energy and how they contribute to lateral stirring of water masses (e.g., Rudnick and Martin, 2002; Johnson et al., 2012; Jaeger and Mahadevan, 2018). These observations can be extracted from seismically derived sections of temperature, salinity and density (Xiao et al., 2021). As with internal waves and LAST, analysis of widespread seismic surveys can provide a catalogue of submesoscale spectra[8] that is unmatched in size. This catalogue can address questions that include:

- What are the dominant spectral slopes for temperature, salinity and spice? Are these slopes well described by theory? *See* Ferrari and Rudnick (2000), Callies and Ferrari (2013), Klymak et al. (2015), Kunze et al. (2015) *and* Erickson et al. (2020).
- At what length scale do internal waves start to dominate the spectral signal? *See* Bühler et al. (2014), Rocha et al. (2016), Qiu et al. (2017), Qiu et al., (2018), Callies (2019) *and* Thomas and Yamada (2019).
- How energetic are submesoscale currents beneath the surface mixed layer? How do currents vary with the seasons? *See* Cole et al. (2010), Callies et al. (2015), Buckingham et al. (2016), du

Plessis et al. (2017), Siegelman et al. (2019), Yu et al. (2019), Dong et al. (2020), Erickson et al. (2020) *and* Siegelman (2020).

Finally, seismic oceanography can help calibrate satellite observations of submesoscale flow. Satellite altimetric records with near-global coverage are available for all years after 1992 (Fu et al., 1994; Callies and Wu, 2019). The resolution of these records is highly variable, and it is unclear how well they capture activity in the subsurface ocean (Wunsch, 1997). Comparison of existing seismic oceanographic datasets to historical satellite records will demonstrate the extent to which sea-surface observations can predict motions at depth (e.g., Dickinson et al., 2020; Gunn et al., 2020b; Gunn et al., 2021; Wei et al., 2022). The next generation of satellite-borne altimeters and current meters is expected to achieve resolutions as low as ∼1 km (e.g., Gommenginger et al., 2019; Klein et al., 2019; Martínez-Moreno et al., 2021). Future seismic surveys could be towed along the groundtracks of these satellites, providing spatially coincident and near-contemporaneous observations of subsurface submesoscale motions. Comparison of both historical and newly acquired seismic data to satellite records could investigate questions such as:

- Can satellite observations predict the depths to which surface oceanic fronts extend? What percentage of sub-mixed-layer submesoscale eddies are observable in satellite records? *See* Gunn et al. (2020b).
- Is there a relationship between spectral power laws computed from satellite data and spectral power laws computed from submesoscale structure at depth? *See* Wang et al. (2010) *and* Callies and Ferrari (2013).
- Is there any correlation between submesoscale sea-surface motions and periods of intense turbulence at depth?

To aid calibration of satellite records, and investigation of submesocale currents more broadly, future seismic surveys could integrate novel observational tools such as swarms of autonomous robots (e.g., Jaffe et al., 2017). Autonomous tools are ideally suited to integration with seismic oceanographic surveys since they do not interfere with operation of the seismic vessel.

3.3 Abyssal Water Mass Transformations

Approximately 50% of the ocean's volume lies at depths of 2,000 m or greater (waters at these depths are referred to as the deep ocean; Roemmich et al., 2019). Much of this volume is filled by Antarctic Bottom Water (AABW) and North Atlantic Deep Water (NADW), whose circulations play a key role in distributing heat and salt and thus in controlling global climate (Johnson, 2008; Jayne et al., 2017). Despite its importance, fewer than 10% of hydrographic measurements come from the deep ocean (de Lavergne et al., 2016). Our ability to model abyssal processes and their impacts on climate is severely constrained by this lack of data (e.g., Wunsch and Heimbach, 2014; Forget et al., 2015; Liang et al., 2015).

To date, most of our knowledge of the deep ocean has come from repeated hydrographic measurements made by ships across a globally distributed range of transects (Talley et al., 2016; Sloyan et al., 2019). Occupation of 34 of these transects over a 35-year period has yielded approximately 150 hydrographic sections that sample the deep ocean at a horizontal resolution of ~ 55 km (Desbruyères et al., 2016). In contrast, our knowledge of hydrography in the upper 2,000 m of the ocean depends on the Argo program, which since 1999 has acquired over two million hydrographic profiles using a global array that currently consists of approximately 4,000 autonomous profiling floats (Roemmich et al., 2009; Wong et al., 2020; Roemmich et al., 2022). The Deep Argo program aims to build on this success by acquiring measurements to depths of 6,000 m (e.g., Johnson and Lyman, 2014; Gasparin et al., 2020). However, it seems unlikely that a global deep Argo array will be operational before 2026 (Zilberman et al., 2019).

Seismic oceanography provides a means of extending our historical record of changes in the hydrography of the deep ocean. Although the majority of seismic reflection datasets lie above continental shelves and slopes, a significant number of surveys extend into deep near-shelf regions that are key in formation of abyssal water masses (**Figure 4**; e.g., Dickson and Brown, 1994; Orsi et al., 1999; Morozov et al., 2021). For instance, between the years 1976 and 2011 more than 360,000 km of seismic reflection transects were acquired between the shoreline of Antarctica and regions with water depths of $\gtrsim$ 5,000 m (Breitzke, 2014; note that not all of these transects are plotted in **Figure 4A**). For comparison, five repeat hydrographic transects within the Southern Ocean were occupied a cumulative total of 32 times during the same time period (Desbruyères et al., 2016). Estimation of temperature, salinity and density from seismic transects offers a way to improve the historical record of hydrographic changes and to address questions such as:

- To what extent does heaving of isopycnals in the deep ocean reflect changes in total heat content? *See* Bindoff and Mcdougall (1994), Hakkinen et al. (2016), Desbruyères et al. (2017) *and* Gunn et al. (2020a).
- How do seismic estimates of temperature change correlate to basin-wide changes estimated using acoustic thermometry? How do seismic estimates correlate to changes estimated from highly localised shipboard measurements? What do these comparisons tell us about our ability to assess temperature changes from existing datasets? *See* Munk (2006), Purkey and Johnson (2010), Purkey and Johnson, (2012), Palmer et al. (2019), Wu et al. (2020) *and* Wunsch (2020).
- How are changes in deep-ocean temperature associated with changes in abyssal turbulence, internal waves, and

[8]Most spectral analyses of seismic oceanographic images have depended on tracking continuous seismic reflections, which usually extend along horizontal distances of $\lesssim$ 10 km (*Section 2.3.3*; **Appendix D.3**). This approach is sufficient to resolve the signals of LAST and of the high-wavenumber portion of the internal wave field. However, it does not resolve the full signal of submesoscale currents. Instead of tracking reflections, submesoscale signals could be analyzed by computing horizontal-wavenumber spectra directly from seismically estimated hydrographic sections. Aside from spectra, further statistical properties could be calculated following Klymak et al. (2015).

submesoscale currents? *See* Sheen et al. (2014), Su et al. (2018), Naveira Garabato et al. (2019) *and* Whalen et al. (2020).

To answer these questions, and to investigate turbulent mixing and submesoscale currents, use of seismic oceanography must be guided by a clear and practicable plan for its future development.

4 FUTURE DIRECTIONS

We believe that solutions to the challenges which face seismic oceanography will be best realized through collaboration amongst all researchers in the field. Key to this collaboration will be three parts:

- **Identification of priorities for the next decade of seismic oceanography.** Efficient progress will be made if researchers come together to agree upon a small number of key scientific questions that can be addressed using seismic oceanography. Detailed plans for tackling these questions can be formed. Discussion should include all researchers with an interest in the field.
- **Development of an online repository of publicly available seismic reflection datasets.** Deposited datasets should include all ancillary hydrographic data where this exists. If original seismic records cannot be shared, standardized details of acquisition, processing and data provenance should be published. Data-sharing can build on practices developed as part of observational initiatives such as the Microstructure Database, the Global Ocean Observing System, and Argo (e.g., MacKinnon et al., 2017; Tanhua et al., 2019; Roemmich et al., 2019; see microstructure.ucsd.edu and www.goosocean.org).
- **Development of an online repository of open-source computer codes**. Existing codes should be uploaded and benchmarked against hydrographically calibrated field datasets and numerical simulations. Codes that are shown to be reliable can be developed into standardized tools which will facilitate comparison of datasets. Wherever possible, codes should be automated to minimize subjective judgements. Sharing of code can build on examples such as the repository developed by the turbulent mixing community (github.com/OceanMixingCommunity).

To encourage collaboration, we have set up a Wikipedia page and code repository (en.wikipedia.org/wiki/Seismic_Oceanography and github.com/SeismicOceanographyCommunity). Anyone is welcome to contribute. Session PS06 at the 2022 American Geophysical Union Ocean Sciences meeting discussed priorities for the field, and sparked conversations that can now be taken further (see www.aslo.org/osm2022/scientificsessions/#ps).

As an example of a scientific priority, we suggest that large volumes of existing seismic data should be analyzed using automated methods for estimating the intensity of turbulent mixing (*Section 3.1*). This analysis would require development of three open-source tools:

- ***Tool 1:*** A standardized method for estimating temperature, salinity and density from seismic records in the absence of coincident hydrographic measurements.
- ***Tool 2:*** A standardized method for computing horizontal-wavenumber spectra from seismic images and for estimating diapycnal diffusivity from identified internal-wave and LAST spectral regimes.
- ***Tool 3:*** A standardized method for accurate numerical modeling of seismic reflection profiling of time-variant thermohaline structure.

Tools 1 and ***2*** would include rigorous assessment of uncertainties in estimated quantities. Together, these two components would form a toolkit for rapid, comparable estimation of diapycnal diffusivity and of the form of the internal wave field at disparate locations. Seismic-derived estimates of temperature, salinity and density would free this analysis from dependence upon independent hydrographic data. Accuracy would be tested using the numerical modeling package developed as ***Tool 3***. The unprecedented number of observations of turbulent mixing could be combined with machine-learning techniques to inform improved climate models (Zanna and Bolton, 2021).

Other researchers will no doubt disagree with our suggested priority and have suggestions of their own. We hope that this article will provoke discussion about the best way to proceed, and will lead to development of shared resources and projects. Similar collaborative development is fuelling formation of a new generation of observational tools, including satellite-borne wide-swath altimeters, moored temperature microstructure recorders, autonomous floating seismometers, saildrones and ultra-wideband underwater communication (Fu and Ferrari, 2008; Moum and Nash, 2009; Hello et al., 2011; Cross et al., 2015; Ghaffarivardavagh et al., 2020). It is time for seismic oceanography to join their ranks.

DATA AVAILABILITY STATEMENT

The Supplementary Material - including all appendices, all tables, and sources of data for Figure 4 - can be found online at www.frontiersin.org/articles/10.3389/fmars.2022.736693/full#supplementary-material. Additional supporting information, including editable versions of all figures and tables, is available at doi.org/10.6084/m9.figshare.c.5984767. A repository for future sharing of code and data has been set up at github.com/SeismicOceanographyCommunity.

AUTHOR CONTRIBUTIONS

AD conceived the article, reviewed the literature and drafted the text with advice from KLG. Both authors contributed equally to development of the figures. KLG set up the Wikipedia page and GitHub repository with feedback from AD. Both authors contributed to the article and approved the submitted version.

FUNDING

AD is funded by the North East Local Enterprise Partnership (www.northeastlep.co.uk) and by the Unconventional Hydrocarbons in the UK Energy System programme (www.ukuh.org).

ACKNOWLEDGMENTS

We thank Mark Hoggard, Bryn Pickering and Rosemary Rodney-McDalglish for their valuable comments on a preliminary draft. We also thank David Al-Attar, Rob Hall, Andone Lavery, Jerome Neufeld, Barry Ruddick and Katy Sheen for thought-provoking conversations. We are grateful to Nicky White and to Colm Caulfield for supervising PhD projects that began our interest in seismic oceanography. Particular thanks to Nicky for teaching us the importance of unplanned production downtime (UPD). Figures were plotted using the Generic Mapping Tools (www.generic-mapping-tools.org) and Inkscape (inkscape.org).

SUPPLEMENTARY MATERIAL

The Supplementary Material for this article can be found online at: https://www.frontiersin.org/articles/10.3389/fmars.2022.736693/full#supplementary-material

REFERENCES

Allen, J., and Naveira Garabato, A. (2013). RRS Discovery Cruise 381, 28 Aug - 03 Oct 2012. Ocean Surface Mixing, Ocean Submesoscale Interaction Study (OSMOSIS). *National Oceanography Centre Cruise Report*. A. Forryan, 18. Available at: eprints.soton.ac.uk/346110

Archer, M., Schaeffer, A., Keating, S., Roughan, M., Holmes, R., and Siegelman, L. (2020). Observations of Submesoscale Variability and Frontal Subduction Within the Mesoscale Eddy Field of the Tasman Sea. *J. Phys. Oceanog.* 50, 1509–1529. doi: 10.1175/JPO-D-19-0131.1

Bakhtiari Rad, P., and Macelloni, L. (2020). Improving 3D Water Column Seismic Imaging Using the Common Reflection Surface Method. *J. Appl. Geophys.* 179, 104072. doi: 10.1016/j.jappgeo.2020.104072

Bashmachnikov, I. L., Kozlov, I. E., Petrenko, L. A., Glok, N. I., and Wekerle, C. (2020). Eddies in the North Greenland Sea and Fram Strait From Satellite Altimetry, SAR and High-Resolution Model Data. *J. Geophys. Res.: Ocean.* 125, e2019JC015832. doi: 10.1029/2019JC015832

Biescas, B., Ruddick, B., Kormann, J., Sallarès, V., Nedimović, M. R., and Carniel, S. (2016). Synthetic Modeling for an Acoustic Exploration System for Physical Oceanography. *J. Atmos. Ocean. Technol.* 33, 191–200. doi: 10.1175/JTECH-D-15-0137.1

Biescas, B., Ruddick, B. R., Nedimovic, M. R., Sallarès, V., Bornstein, G., and Mojica, J. F (2014).Recovery of Temperature, Salinity, and Potential Density From Ocean Reflectivity. *J. Geophys. Res.: Ocean.* 119, 3171–3184. doi: 10.1002/2013JC009662

Bindoff, N. L., and Mcdougall, T. J. (1994). Diagnosing Climate Change and Ocean Ventilation Using Hydrographic Data. *J. Phys. Oceanog.* 24, 1137–1152. doi: 10.1175/1520-0485(1994)024<1137:DCCAOV>2.0.CO;2

Blacic, T., and Holbrook, W. (2010). First Images and Orientation of Fine Structure From a 3-D Seismic Oceanography Data Set. *Ocean. Sci.* 6, 431–439. doi: 10.5194/os-6-431-2010

Blacic, T. M., Jun, H., Rosado, H., and Shin, C. (2016). Smooth 2-D Ocean Sound Speed From Laplace and Laplace-Fourier Domain Inversion of Seismic Oceanography Data. *Geophys. Res. Lett.* 43, 1211–1218. doi: 10.1002/2015GL067421

Born, G., Dunne, J., and Lame, D. (1979). Seasat Mission Overview. *Science* 204, 1405–1406. doi: 10.1126/science.204.4400.1405

Bornstein, G., Biescas, B., Sallarès, V., and Mojica, J. (2013). Direct Temperature and Salinity Acoustic Full Waveform Inversion. *Geophys. Res. Lett.* 40, 4344–4348. doi: 10.1002/grl.50844

Breitzke, M. (2014). Overview of Seismic Research Activities in the Southern Ocean — Quantifying the Environmental Impact. *Antarctic. Sci.* 26, 80–92. doi: 10.1017/S095410201300031X

Brethouwer, G., Billant, P., Lindborg, E., and Chomaz, J.-M. (2007). Scaling Analysis and Simulation of Strongly Stratified Turbulent Flows. *J. Fluid. Mechanic.* 585, 343–368. doi: 10.1017/S0022112007006854

Buckingham, C. E., Naveira Garabato, A. C., Thompson, A. F., Brannigan, L., Lazar, A., Marshall, D. P., et al. (2016). Seasonality of Submesoscale Flows in the Ocean Surface Boundary Layer. *Geophys. Res. Lett.* 43, 2118–2126. doi: 10.1002/2016GL068009

Buckley, M. W., and Marshall, J. (2016). Observations, Inferences, and Mechanisms of the Atlantic Meridional Overturning Circulation: A Review. *Rev. Geophys.* 54, 5–63. doi: 10.1002/2015RG000493

Buffett, G., and Carbonell, R. (2011). Seismic Oceanography as a Tool to Monitor Climate Change. *EGU. Newslett.* 35, 5–8. Available at: cdn.egu.eu/static/e2696616/newsletter/eggs/eggs_35.pdf

Bühler, O., Callies, J., and Ferrari, R. (2014). Wave–vortex Decomposition of One-Dimensional Ship-Track Data. *J. Fluid. Mechanic.* 756, 1007–1026. doi: 10.1017/jfm.2014.488

Cael, B. B., and Mashayek, A. (2021). Log-Skew-Normality of Ocean Turbulence. *Phys. Rev. Lett.* 126, 224502. doi: 10.1103/PhysRevLett.126.224502

Callies, J. (2018). Restratification of Abyssal Mixing Layers by Submesoscale Baroclinic Eddies. *J. Phys. Oceanog.* 48, 1995–2010. doi: 10.1175/JPO-D-18-0082.1

Callies, J. (2019). Submesoscale Dynamics Inferred From Oleander Data. *Oceanography* 32, 138–139. doi: 10.5670/oceanog.2019.320

Callies, J., Barkan, R., and Naveira Garabato, A. (2020). Time Scales of Submesoscale Flow Inferred From a Mooring Array. *J. Phys. Oceanog.* 50, 1065–1086. doi: 10.1175/JPO-D-19-0254.1

Callies, J., and Ferrari, R. (2013). Interpreting Energy and Tracer Spectra of Upper-Ocean Turbulence in the Submesoscale Range (1–200 Km). *J. Phys. Oceanog.* 43, 2456–2474. doi: 10.1175/JPO-D-13-063.1

Callies, J., Ferrari, R., Klymak, J. M., and Gula, J. (2015). Seasonality in Submesoscale Turbulence. *Nat. Commun.* 6, 6862. doi: 10.1038/ncomms7862

Callies, J., and Wu, W. (2019). Some Expectations for Submesoscale Sea Surface Height Variance Spectra. *J. Phys. Oceanog.* 49, 2271–2289. doi: 10.1175/JPO-D-18-0272.1

Caulfield, C.-c. P. (2020). Open Questions in Turbulent Stratified Mixing: Do We Even Know What We do Not Know? *Phys. Rev. Fluid.* 5, 110518. doi: 10.1103/PhysRevFluids.5.110518

Caulfield, C. (2021). Layering, Instabilities, and Mixing in Turbulent Stratified Flows. *Annu. Rev. Fluid. Mechanic.* 53, 113–145. doi: 10.1146/annurev-fluid-042320-100458

Chrysagi, E., Umlauf, L., Holtermann, P., Klingbeil, K., and Burchard, H. (2021). High-Resolution Simulations of Submesoscale Processes in the Baltic Sea: The Role of Storm Events. *J. Geophys. Res.: Ocean.* 126, e2020JC016411. doi: 10.1029/2020JC016411

Cole, S. T., and Rudnick, D. L. (2012). The Spatial Distribution and Annual Cycle of Upper Ocean Thermohaline Structure. *J. Geophys. Res.: Ocean.* 117, C02027. doi: 10.1029/2011JC007033

Cole, S. T., Rudnick, D. L., and Colosi, J. A. (2010). Seasonal Evolution of Upper-Ocean Horizontal Structure and the Remnant Mixed Layer. *J. Geophys. Res.: Ocean.* 115, C04012. doi: 10.1029/2009JC005654

Cross, J. N., Mordy, C. W., Tabisola, H. M., Meinig, C., Cokelet, E. D., and Stabeno, P. J. (2015). "Innovative Technology Development for Arctic Exploration," in *OCEANS 2015 - MTS/IEEE Washington* (New York City: Institute of Electrical and Electronics Engineers), 1–8. doi: 10.23919/OCEANS.2015.7404632

Dagnino, D., Sallarès, V., Biescas, B., and Ranero, C. R. (2016). Fine-Scale Thermohaline Ocean Structure Retrieved With 2-D Prestack Full-Waveform

Inversion of Multichannel Seismic Data: Application to the Gulf of Cadiz (SW Iberia). *J. Geophys. Res.: Ocean.* 121, 5452–5469. doi: 10.1002/2016JC011844

Dauhajre, D. P., McWilliams, J. C., and Uchiyama, Y. (2017). Submesoscale Coherent Structures on the Continental Shelf. *J. Phys. Oceanog.* 47, 2949–2976. doi: 10.1175/JPO-D-16-0270.1

Davis, R. E., Regier, L. A., Dufour, J., and Webb, D. C. (1992). The Autonomous Lagrangian Circulation Explorer (ALACE). *J. Atmos. Ocean. Technol.* 9, 264–285. doi: 10.1175/1520-0426(1992)009<0264:TALCE>2.0.CO;2

Delandmeter, P., Lambrechts, J., Marmorino, G. O., Legat, V., Wolanski, E., Remacle, J.-F., et al. (2017). Submesoscale Tidal Eddies in the Wake of Coral Islands and Reefs: Satellite Data and Numerical Modelling. *Ocean. Dynamic.* 67, 897–913. doi: 10.1007/s10236-017-1066-z

de Lavergne, C., Madec, G., Capet, X., Maze, G., and Roquet, F. (2016). Getting to the Bottom of the Ocean. *Nat. Geosci.* 9, 857–858. doi: 10.1038/ngeo2850

de Lavergne, C., Vic, C., Madec, G., Roquet, F., Waterhouse, A. F., Whalen, C. B., et al. (2020). A Parameterization of Local and Remote Tidal Mixing. *J. Adv. Model. Earth Syst.* 12, e2020MS002065. doi: 10.1029/2020MS002065

Desbruyères, D., McDonagh, E. L., King, B. A., and Thierry, V. (2017). Global and Full-Depth Ocean Temperature Trends During the Early Twenty-First Century From ARGO and Repeat Hydrography. *J. Climate* 30, 1985–1997. doi: 10.1175/JCLI-D-16-0396.1

Desbruyères, D. G., Purkey, S. G., McDonagh, E. L., Johnson, G. C., and King, B. A. (2016). Deep and Abyssal Ocean Warming From 35 Years of Repeat Hydrography. *Geophys. Res. Lett.* 43, 10,356–10,365. doi: 10.1002/2016GL070413

Dickinson, A., White, N. J., and Caulfield, C.-c. P. (2017). Spatial Variation of Diapycnal Diffusivity Estimated From Seismic Imaging of Internal Wave Field, Gulf of Mexico. *J. Geophys. Res.: Ocean.* 122, 9827–9854. doi: 10.1002/2017JC013352

Dickinson, A., White, N. J., and Caulfield, C. P. (2020). Time-Lapse Acoustic Imaging of Mesoscale and Fine-Scale Variability Within the Faroe-Shetland Channel. *J. Geophys. Res.: Ocean.* 125, e2019JC015861. doi: 10.1029/2019JC015861

Dickson, R. R., and Brown, J. (1994). The Production of North Atlantic Deep Water: Sources, Rates, and Pathways. *J. Geophys. Res.: Ocean.* 99, 12319–12341. doi: 10.1029/94JC00530

Dillon, T. (1982). Vertical Overturns: A Comparison of Thorpe and Ozmidov Length Scales. *J. Geophys. Res.: Ocean.* 87, 9601–9613. doi: 10.1029/JC087iC12p09601

Dimotakis, P. E. (2005). Turbulent Mixing. *Annu. Rev. Fluid. Mechanic.* 37, 329–356. doi: 10.1146/annurev.fluid.36.050802.122015

Dong, J., Fox-Kemper, B., Zhang, H., and Dong, C. (2020). The Seasonality of Submesoscale Energy Production, Content, and Cascade. *Geophys. Res. Lett.* 47, e2020GL087388. doi: 10.1029/2020GL087388

Drake, H. F., Ferrari, R., and Callies, J. (2020). Abyssal Circulation Driven by Near-Boundary Mixing: Water Mass Transformations and Interior Stratification. *J. Phys. Oceanog.* 50, 2203–2226. doi: 10.1175/JPO-D-19-0313.1

du Plessis, M., Swart, S., Ansorge, I. J., and Mahadevan, A. (2017). Submesoscale Processes Promote Seasonal Restratification in the Subantarctic Ocean. *J. Geophys. Res.: Ocean.* 122, 2960–2975. doi: 10.1002/2016JC012494

Eakin, D., Holbrook, W. S., and Fer, I. (2011). Seismic Reflection Imaging of Large-Amplitude Lee Waves in the Caribbean Sea. *Geophys. Res. Lett.* 38, L21601. doi: 10.1029/2011GL049157

Eckart, C. (1948). An Analysis of the Stirring and Mixing Processes in Compressible Fluids. *J. Mar. Res.* 7, 265–275. Available at: images.peabody.yale.edu/publications/jmr/jmr07-03-11.pdf

Erickson, Z. K., Thompson, A. F., Callies, J., Yu, X., Naveira Garabato, A., and Klein, P. (2020). The Vertical Structure of Open-Ocean Submesoscale Variability During a Full Seasonal Cycle. *J. Phys. Oceanog.* 50, 145–160. doi: 10.1175/JPO-D-19-0030.1

Falder, M., White, N. J., and Caulfield, C. P. (2016). Seismic Imaging of Rapid Onset of Stratified Turbulence in the South Atlantic Ocean. *J. Phys. Oceanog.* 46, 1023–1044. doi: 10.1175/JPO-D-15-0140.1

Fer, I., and Holbrook, S. W. (2009). "Seismic Reflection Methods for Study of the Water Column," in *Encyclopedia of Ocean Sciences* (*3rd* edn.). Eds. J. K. Cochran, H. J. Bokuniewicz and P. L. Yager (Oxford: Academic Press), 11–20. doi: 10.1016/B978-0-12-813081-0.00799-0

Fer, I., Nandi, P., Holbrook, W. S., Schmitt, R. W., and Páramo, P. (2010). Seismic Imaging of a Thermohaline Staircase in the Western Tropical North Atlantic. *Ocean. Sci.* 6, 621–631. doi: 10.5194/os-6-621-2010

Ferrari, R., Mashayek, A., McDougall, T. J., Nikurashin, M., and Campin, J.-M. (2016). Turning Ocean Mixing Upside Down. *J. Phys. Oceanog.* 46, 2239–2261. doi: 10.1175/JPO-D-15-0244.1

Ferrari, R., and Rudnick, D. L. (2000). Thermohaline Variability in the Upper Ocean. *J. Geophys. Res.: Ocean.* 105, 16857–16883. doi: 10.1029/2000JC900057

Ferrari, R., and Wunsch, C. (2009). Ocean Circulation Kinetic Energy: Reservoirs, Sources, and Sinks. *Annu. Rev. Fluid. Mechanic.* 41, 253–282. doi: 10.1146/annurev.fluid.40.111406.102139

Fine, E. C., Alford, M. H., MacKinnon, J. A., and Mickett, J. B. (2021). Microstructure Mixing Observations and Finescale Parameterizations in the Beaufort Sea. *J. Phys. Oceanog.* 51, 19–35. doi: 10.1175/JPO-D-19-0233.1

Forget, G., Ferreira, D., and Liang, X. (2015). On the Observability of Turbulent Transport Rates by Argo: Supporting Evidence From an Inversion Experiment. *Ocean. Sci.* 11, 839–853. doi: 10.5194/os-11-839-2015

Fortin, W. F. J., and Holbrook, W. S. (2009). Sound Speed Requirements for Optimal Imaging of Seismic Oceanography Data. *Geophys. Res. Lett.* 36, L00D01. doi: 10.1029/2009GL038991

Fortin, W. F. J., Holbrook, W. S., and Schmitt, R. W. (2016). Mapping Turbulent Diffusivity Associated With Oceanic Internal Lee Waves Offshore Costa Rica. *Ocean. Sci.* 12, 601–612. doi: 10.5194/osd-12-1433-2015

Frajka-Williams, E., Brearley, J. A., Nash, J. D., and Whalen, C. B. (2022). "Chapter 14 - New Technological Frontiers in Ocean Mixing," in *Ocean Mixing*. Eds. M. Meredith and A. Naveira Garabato (Amsterdam: Elsevier), 345–361. doi: 10.1016/B978-0-12-821512-8.00021-9

Fu, L.-L., Christensen, E. J., Yamarone, C. A.Jr., Lefebvre, M., Ménard, Y., Dorrer, M., et al. (1994). TOPEX/POSEIDON Mission Overview. *J. Geophys. Res.: Ocean.* 99, 24369–24381. doi: 10.1029/94JC01761

Fu, L.-L., and Ferrari, R. (2008). Observing Oceanic Submesoscale Processes From Space. *Eos. Trans. Am. Geophys. Union.* 89, 488–488. doi: 10.1029/2008EO480003

Garrett, C. (2006). Turbulent Dispersion in the Ocean. *Prog. Oceanog.* 70, 113–125. doi: 10.1016/j.pocean.2005.07.005

Garrett, C., and Munk, W. (1972). Space-Time Scales of Internal Waves. *Geophys. Fluid. Dynamic.* 2, 225–264. doi: 10.1080/03091927208236082

Gasparin, F., Hamon, M., Rémy, E., and Traon, P.-Y. L. (2020). How Deep Argo Will Improve the Deep Ocean in an Ocean Reanalysis. *J. Climate* 33, 77–94. doi: 10.1175/JCLI-D-19-0208.1

Geli, L., Cosquer, E., Hobbs, R., Klaeschen, D., Papenberg, C., Thomas, Y., et al. (2009). High Resolution Seismic Imaging of the Ocean Structure Using a Small Volume Airgun Source Array in the Gulf of Cadiz. *Geophys. Res. Lett.* 36, L00D09. doi: 10.1029/2009GL040820

Geyer, W. R., Lavery, A. C., Scully, M. E., and Trowbridge, J. H. (2010). Mixing by Shear Instability at High Reynolds Number. *Geophys. Res. Lett.* 37, L22607. doi: 10.1029/2010GL045272

Ghaffarivardavagh, R., Afzal, S. S., Rodriguez, O., and Adib, F. (2020). "Ultra-Wideband Underwater Backscatter via Piezoelectric Metamaterials," in *Proceedings of the Annual Conference of the ACM Special Interest Group on Data Communication on the Applications, Technologies, Architectures, and Protocols for Computer Communication*, vol. 20. (New York, NY, USA: Association for Computing Machinery), 722–734. doi: 10.1145/3387514.3405898

Giddy, I., Swart, S., du Plessis, M., Thompson, A. F., and Nicholson, S.-A. (2021). Stirring of Sea-Ice Meltwater Enhances Submesoscale Fronts in the Southern Ocean. *J. Geophys. Res.: Ocean.* 126, e2020JC016814. doi: 10.1029/2020JC016814

Gommenginger, C., Chapron, B., Hogg, A., Buckingham, C., Fox-Kemper, B., Eriksson, L., et al. (2019). SEASTAR: A Mission to Study Ocean Submesoscale Dynamics and Small-Scale Atmosphere-Ocean Processes in Coastal, Shelf and Polar Seas. *Front. Mar. Sci.* 6. doi: 10.3389/fmars.2019.00457

Gower, J. F. R., Denman, K. L., and Holyer, R. J. (1980). Phytoplankton Patchiness Indicates the Fluctuation Spectrum of Mesoscale Oceanic Structure. *Nature* 288, 157–159. doi: 10.1038/288157a0

Gregg, M. C. (1989). Scaling Turbulent Dissipation in the Thermocline. *J. Geophys. Res.: Ocean.* 94, 9686–9698. doi: 10.1029/JC094iC07p09686

Gregg, M., and Cox, C. (1971). Measurements of the Oceanic Microstructure of Temperature and Electrical Conductivity. *In. Deep. Sea. Res. Oceanog. Abstract.* 18, 925–934. doi: 10.1016/0011-7471(71)90067-2

Gula, J., Blacic, T. M., and Todd, R. E. (2019). Submesoscale Coherent Vortices in the Gulf Stream. *Geophys. Res. Lett.* 46, 2704–2714. doi: 10.1029/2019GL081919

Gunn, K. L., Beal, L. M., Elipot, S., McMonigal, K., and Houk, A. (2020a). Mixing of Subtropical, Central, and Intermediate Waters Driven by Shifting and Pulsing of the Agulhas Current. *J. Phys. Oceanog.* 50, 3545–3560. doi: 10.1175/JPO-D-20-0093.1

Gunn, K. L., Dickinson, A., White, N. J., and Caulfield, C.-c. P. (2021). Vertical Mixing and Heat Fluxes Conditioned by a Seismically Imaged Oceanic Front. *Front. Mar. Sci.* 8. doi: 10.3389/fmars.2021.697179

Gunn, K. L., White, N., and C-c, P. (2020b). Time-Lapse Seismic Imaging of Oceanic Fronts and Transient Lenses Within South Atlantic Ocean. *J. Geophys. Res.: Ocean.* 125, e2020JC016293. doi: 10.1029/2020JC016293

Gunn, K. L., White, N. J., Larter, R. D., and Caulfield, C.-c. P. (2018). Calibrated Seismic Imaging of Eddy-Dominated Warm-Water Transport Across the Bellingshausen Sea, Southern Ocean. *J. Geophys. Res.: Ocean.* 123, 3072–3099. doi: 10.1029/2018JC013833

Hakkinen, S., Rhines, P. B., and Worthen, D. L. (2016). Warming of the Global Ocean: Spatial Structure and Water-Mass Trends. *J. Climate* 29, 4949–4963. doi: 10.1175/JCLI-D-15-0607.1

Helfrich, K. R., and Melville, W. K. (2006). Long Nonlinear Internal Waves. *Annu. Rev. Fluid. Mech.* 38, 395–425. doi: 10.1146/annurev.fluid.38.050304.092129

Hello, Y., Ogé, A., Sukhovich, A., and Nolet, G. (2011). Modern Mermaids: New Floats Image the Deep Earth. *Eos. Trans. Am. Geophys. Union.* 92, 337–338. doi: 10.1029/2011EO400001

Hibiya, T., Furuichi, N., and Robertson, R. (2012). Assessment of Fine-Scale Parameterizations of Turbulent Dissipation Rates Near Mixing Hotspots in the Deep Ocean. *Geophys. Res. Lett.* 39, L24601. doi: 10.1029/2012GL054068

Hobbs, R. W., Klaeschen, D., Sallarès, V., Vsemirnova, E., and Papenberg, C. (2009). Effect of Seismic Source Bandwidth on Reflection Sections to Image Water Structure. *Geophys. Res. Lett.* 36, L00D09. doi: 10.1029/2009GL040215

Holbrook, W. S. (2009). "Seismic Oceanography: Imaging Oceanic Finestructure With Reflection Seismology," in *Oceanography in 2025: Proceedings of a Workshop*. Ed. D. Glickson (Washington, DC: National Academies Press), 157–162. doi: 10.17226/12627

Holbrook, W. S., and Fer, I. (2005). Ocean Internal Wave Spectra Inferred From Seismic Reflection Transects. *Geophys. Res. Lett.* 32, L15604. doi: 10.1029/2005GL023733

Holbrook, W. S., Fer, I., and Schmitt, R. W. (2009). Images of Internal Tides Near the Norwegian Continental Slope. *Geophys. Res. Lett.* 36, L00D10. doi: 10.1029/2009GL038909

Holbrook, W. S., Fer, I., Schmitt, R. W., Lizarralde, D., Klymak, J. M., Helfrich, L. C., et al. (2013). Estimating Oceanic Turbulence Dissipation From Seismic Images. *J. Atmos. Ocean. Technol.* 30, 1767–1788. doi: 10.1175/JTECH-D-12-00140.1

Howland, C. J., Taylor, J. R., and Caulfield, C. P. (2020). Mixing in Forced Stratified Turbulence and its Dependence on Large-Scale Forcing. *J. Fluid. Mechanic.* 898, A7. doi: 10.1017/jfm.2020.383

Hu, D., Wu, L., Cai, W., Gupta, A. S., Ganachaud, A., Qiu, B., et al. (2015). Pacific Western Boundary Currents and Their Roles in Climate. *Nature* 522, 299–308. doi: 10.1038/nature14504

Ijichi, T., and Hibiya, T. (2015). Frequency-Based Correction of Finescale Parameterization of Turbulent Dissipation in the Deep Ocean. *J. Atmos. Ocean. Technol.* 32, 1526–1535. doi: 10.1175/JTECH-D-15-0031.1

Itoh, S., and Rudnick, D. L. (2017). Fine-Scale Variability of Isopycnal Salinity in the California Current System. *J. Geophys. Res.: Ocean.* 122, 7066–7081. doi: 10.1002/2017JC013080

Ivey, G. N., Winters, K. B., and Koseff, J. R. (2008). Density Stratification, Turbulence, But How Much Mixing? *Annu. Rev. Fluid. Mechanic.* 40, 169–184. doi: 10.1146/annurev.fluid.39.050905.110314

Jacobsen, A. (1948). An Instrument for Recording Continuously the Salinity, Temperature, and Depth of Sea Water. *Trans. Am. Insti. Electric. Engi.* 67, 714–722. doi: 10.1109/T-AIEE.1948.5059738

Jaeger, G. S., and Mahadevan, A. (2018). Submesoscale-Selective Compensation of Fronts in a Salinity-Stratified Ocean. *Sci. Adv.* 4, e1701504. doi: 10.1126/sciadv.1701504

Jaffe, J. S., Franks, P. J. S., Roberts, P. L. D., Mirza, D., Schurgers, C., Kastner, R., et al. (2017). A Swarm of Autonomous Miniature Underwater Robot Drifters for Exploring Submesoscale Ocean Dynamics. *Nat. Commun.* 8, 14189. doi: 10.1038/ncomms14189

Jayne, S. R., Roemmich, D., Zilberman, N., Riser, S. C., Johnson, K. S., Johnson, G. C., et al. (2017). The Argo Program: Present and Future. *Oceanography* 30, 18–28. doi: 10.5670/oceanog.2017.213

Ji, L., and Lin, M. (2013). Numerical Analysis of the Effect of Mesoscale Eddies on Seismic Imaging. *Pure. Appl. Geophys.* 170, 259–270. doi: 10.1007/s00024-012-0497-1

Ji, L., Lin, M., and Hao, T. (2013). The Effect of Inhomogeneous Water on Seismic Imaging in Deepwater Areas of the South China Sea. *Chin. Sci. Bull.* 58, 4443–4449. doi: 10.1007/s11434-013-5975-z

Johnson, G. C. (2008). Quantifying Antarctic Bottom Water and North Atlantic Deep Water Volumes. *J. Geophys. Res.: Ocean.* 113, C05027. doi: 10.1029/2007JC004477

Johnson, G. C., and Lyman, J. M. (2014). Where's the Heat? *Nat. Climate Change* 4, 956–957. doi: 10.1038/nclimate2409

Johnson, G. C., Schmidtko, S., and Lyman, J. M. (2012). Relative Contributions of Temperature and Salinity to Seasonal Mixed Layer Density Changes and Horizontal Density Gradients. *J. Geophys. Res.: Ocean.* 117, C04015. doi: 10.1029/2011JC007651

Jolliff, J. K., Lewis, M. D., Ladner, S., and Crout, R. L. (2019). Observing the Ocean Submesoscale With Enhanced-Color GOES-ABI Visible Band Data. *Sensors* 19. doi: 10.3390/s19183900

Jones, S., Hardy, R., Hobbs, R., and Hardy, D. (2008). The New Synergy Between Seismic Reflection Imaging and Oceanography. *First. Break.* 26, 51–57. doi: 10.3997/1365-2397.2008010

Jones, S. M., Sutton, C., Hardy, R. J. J., and Hardy, D. (2010). Seismic Imaging of Variable Water Layer Sound Speed in Rockall Trough, NE Atlantic and Implications for Seismic Surveying in Deep Water. *Geo. Soc. London. Petroleum. Geo. Conf. Ser.* 7, 549–558. doi: 10.1144/0070549

Ker, S., Le Gonidec, Y., Marie, L., Thomas, Y., and Gibert, D. (2015). Multiscale Seismic Reflectivity of Shallow Thermoclines. *J. Geophys. Res.: Ocean.* 120, 1872–1886. doi: 10.1002/2014JC010478

Klaeschen, D., Hobbs, R. W., Krahmann, G., Papenberg, C., and Vsemirnova, E. (2009). Estimating Movement of Reflectors in the Water Column Using Seismic Oceanography. *Geophys. Res. Lett.* 36, L00D03. doi: 10.1029/2009GL038973

Klein, P., Lapeyre, G., Siegelman, L., Qiu, B., Fu, L.-L., Torres, H., et al. (2019). Ocean-Scale Interactions From Space. *Earth Space. Sci.* 6, 795–817. doi: 10.1029/2018EA000492

Klymak, J. M., Crawford, W., Alford, M. H., MacKinnon, J. A., and Pinkel, R. (2015). Along-Isopycnal Variability of Spice in the North Pacific. *J. Geophys. Res.: Ocean.* 120, 2287–2307. doi: 10.1002/2013JC009421

Klymak, J. M., and Moum, J. N. (2007a). Oceanic Isopycnal Slope Spectra. Part I: Internal Waves. *J. Phys. Oceanog.* 37, 1215–1231. doi: 10.1175/JPO3073.1

Klymak, J. M., and Moum, J. N. (2007b). Oceanic Isopycnal Slope Spectra. Part II: Turbulence. *J. Phys. Oceanog.* 37, 1232–1245. doi: 10.1175/JPO3074.1

Kolmogorov, A. N. (1941). The Local Structure of Turbulence in Incompressible Viscous Fluid for Very Large Reynolds Numbers. *Dokl. Akad. Nauk. SSR.* 30, 301–305.

Krahmann, G., Brandt, P., Klaeschen, D., and Reston, T. (2008). Mid-Depth Internal Wave Energy Off the Iberian Peninsula Estimated From Seismic Reflection Data. *J. Geophys. Res.: Ocean.* 113, C12016. doi: 10.1029/2007JC004678

Kunze, E. (2017). Internal-Wave-Driven Mixing: Global Geography and Budgets. *J. Phys. Oceanog.* 47, 1325–1345. doi: 10.1175/JPO-D-16-0141.1

Kunze, E. (2019). A Unified Model Spectrum for Anisotropic Stratified and Isotropic Turbulence in the Ocean and Atmosphere. *J. Phys. Oceanog.* 49, 385–407. doi: 10.1175/JPO-D-18-0092.1

Kunze, E., Klymak, J. M., Lien, R.-C., Ferrari, R., Lee, C. M., Sundermeyer, M. A., et al. (2015). Submesoscale Water-Mass Spectra in the Sargasso Sea. *J. Phys. Oceanog.* 45, 1325–1338. doi: 10.1175/JPO-D-14-0108.1

LaFond, E. C. (1963). Detailed Temperature Structures of the Sea Off Baja California. *Limnol. Oceanog.* 8, 417–425. doi: 10.4319/lo.1963.8.4.0417

Lavery, A. C., Geyer, W. R., and Scully, M. E. (2013). Broadband Acoustic Quantification of Stratified Turbulence. *J. Acoust. Soc. Am.* 134, 40–54. doi: 10.1121/1.4807780

Ledwell, J. R., Watson, A. J., and Broecker, W. S. (1986). A Deliberate Tracer Experiment in Santa Monica Basin. *Nature* 323, 322–324. doi: 10.1038/323322a0

Legg, S. (2021). Mixing by Oceanic Lee Waves. *Annu. Rev. Fluid. Mechanic.* 53, 173–201. doi: 10.1146/annurev-fluid-051220-043904

Levin, L. A., Bett, B. J., Gates, A. R., Heimbach, P., Howe, B. M., Janssen, F., et al. (2019). Global Observing Needs in the Deep Ocean. *Front. Mar. Sci.* 6. doi: 10.3389/fmars.2019.00241

Levine, M. D. (2002). A Modification of the Garrett–Munk Internal Wave Spectrum. *J. Phys. Oceanog.* 32, 3166–3181. doi: 10.1175/1520-0485(2002)032<3166:AMOTGM>2.0.CO;2

Lévy, M., Ferrari, R., Franks, P. J. S., Martin, A. P., and Rivière, P. (2012). Bringing Physics to Life at the Submesoscale. *Geophys. Res. Lett.* 39, L14602. doi: 10.1029/2012GL052756

Lévy, M., Franks, P. J. S., and Smith, K. S. (2018). The Role of Submesoscale Currents in Structuring Marine Ecosystems. *Nat. Commun.* 9,4758. doi: 10.1038/s41467-018-07059-3

Liang, C.-R., Shang, X.-D., Qi, Y.-F., Chen, G.-Y., and Yu, L.-H. (2018). Assessment of Fine-Scale Parameterizations at Low Latitudes of the North Pacific. *Sci. Rep.* 8, 10281. doi: 10.1038/s41598-018-28554-z

Liang, X., Wunsch, C., Heimbach, P., and Forget, G. (2015). Vertical Redistribution of Oceanic Heat Content. *J. Climate* 28, 3821–3833. doi: 10.1175/JCLI-D-14-00550.1

Lindborg, E. (2006). The Energy Cascade in a Strongly Stratified Fluid. *J. Fluid. Mechanic.* 550, 207–242. doi: 10.1017/S0022112005008128

Liu, Z., Lian, Q., Zhang, F., Wang, L., Li, M., Bai, X., et al. (2017). Weak Thermocline Mixing in the North Pacific Low-Latitude Western Boundary Current System. *Geophys. Res. Lett.* 44, 10–530. doi: 10.1002/2017GL075210

Lozovatsky, I., Shearman, K., Pirro, A., and Fernando, H. J. S. (2019). Probability Distribution of Turbulent Kinetic Energy Dissipation Rate in Stratified Turbulence: Microstructure Measurements in the Southern California Bight. *J. Geophys. Res.: Ocean.* 124, 4591–4604. doi: 10.1029/2019JC015087

Lueck, R. G., Wolk, F., and Yamazaki, H. (2002). Oceanic Velocity Microstructure Measurements in the 20th Century. *J. Oceanog.* 58, 153–174. doi: 10.1023/A:1015837020019

MacKinnon, J. A., and Gregg, M. C. (2003). Mixing on the Late-Summer New England Shelf — Solibores, Shear, and Stratification. *J. Phys. Oceanog.* 33, 1476–1492. doi: 10.1175/1520-0485(2003)033<1476:MOTLNE>2.0.CO;2

MacKinnon, J. A., Zhao, Z., Whalen, C. B., Waterhouse, A. F., Trossman, D. S., Sun, O. M., et al. (2017). Climate Process Team on Internal Wave-Driven Ocean Mixing. *Bull. Am. Meteorolog. Soc.* 98, 2429–2454. doi: 10.1175/BAMS-D-16-0030.1

Maffioli, A., and Davidson, P. A. (2016). Dynamics of Stratified Turbulence Decaying From a High Buoyancy Reynolds Number. *J. Fluid. Mechanic.* 786, 210–233. doi: 10.1017/jfm.2015.667

Marmorino, G. O., Smith, G. B., North, R. P., and Baschek, B. (2018). Application of Airborne Infrared Remote Sensing to the Study of Ocean Submesoscale Eddies. *Front. Mech. Eng.* 4. doi: 10.3389/fmech.2018.00010

Martínez-Moreno, J., Hogg, A. M., England, M. H., Constantinou, N. C., Kiss, A. E., and Morrison, A. K. (2021). Global Changes in Oceanic Mesoscale Currents Over the Satellite Altimetry Record. *Nat. Climate Change* 11, 397–403. doi: 10.1038/s41558-021-01006-9

Mashayek, A., Ferrari, R., Nikurashin, M., and Peltier, W. R. (2015). Influence of Enhanced Abyssal Diapycnal Mixing on Stratification and the Ocean Overturning Circulation. *J. Phys. Oceanog.* 45, 2580–2597. doi: 10.1175/JPO-D-15-0039.1

Mashayek, A., Salehipour, H., Bouffard, D., Caulfield, C. P., Ferrari, R., Nikurashin, M., et al. (2017). Efficiency of Turbulent Mixing in the Abyssal Ocean Circulation. *Geophys. Res. Lett* 44, 6296–06. doi: 10.1002/2016GL072452

Mauritzen, C., Polzin, K. L., McCartney, M. S., Millard, R. C., and West-Mack, D. E. (2002). Evidence in Hydrography and Density Fine Structure for Enhanced Vertical Mixing Over the Mid-Atlantic Ridge in the Western Atlantic. *J. Geophys. Res.* 107, 3147. doi: 10.1029/2001JC001114

McBarnet, A. (2013). "How the Seismic Map is Changing," in *Offshore Engineer*, vol. 38 (New York City: AtComedia), 30–36. Available at: www.oedigital.com/subsea/item/2403-how-the-seismic-map-is-changing.

McCoy, D., Bianchi, D., and Stewart, A. L. (2020). Global Observations of Submesoscale Coherent Vortices in the Ocean. *Prog. Oceanog.* 189, 102452. doi: 10.1016/j.pocean.2020.102452

McDougall, T. J., and Ferrari, R. (2017). Abyssal Upwelling and Downwelling Driven by Near-Boundary Mixing. *J. Phys. Oceanog.* 47, 261–283. doi: 10.1175/JPO-D-16-0082.1

McKean, R. S., and Ewart, T. E. (1974). Temperature Spectra in the Deep Ocean Off Hawaii. *J. Phys. Oceanog.* 4, 191–199. doi: 10.1175/1520-0485(1974)004<0191:TSITDO>2.0.CO;2

McWilliams, J. C. (1985). Submesoscale, Coherent Vortices in the Ocean. *Rev. Geophys.* 23, 165–182. doi: 10.1029/RG023i002p00165

McWilliams, J. C. (2010). "A Perspective on Submesoscale Geophysical Turbulence," in *IUTAM Symposium on Turbulence in the Atmosphere and Oceans*. Ed. D. Dritschel (Dordrecht: Springer Netherlands), 131–141. doi: 10.1007/978-94-007-0360-5_11

McWilliams, J. C. (2016). Submesoscale Currents in the Ocean. *Proc. R. Soc A* 472, 20160117. doi: 10.1098/rspa.2016.0117

McWilliams, J. C. (2017). Submesoscale Surface Fronts and Filaments: Secondary Circulation, Buoyancy Flux, and Frontogenesis. *J. Fluid. Mechanic.* 823, 391–432. doi: 10.1017/jfm.2017.294

McWilliams, J. C. (2019). A Survey of Submesoscale Currents. *Geosci. Lett.* 6, 3. doi: 10.1186/s40562-019-0133-3

Ménesguen, C., Gentil, S. L., Marchesiello, P., and Ducousso, N. (2018). Destabilization of an Oceanic Meddy-Like Vortex: Energy Transfers and Significance of Numerical Settings. *J. Phys. Oceanog.* 48, 1151–1168. doi: 10.1175/jpo-d-17-0126.1

Meredith, M., and Naveira Garabato, A. (Eds.) (2022). *Ocean Mixing* (Amsterdam: Elsevier). doi: 10.1016/C2019-0-03674-6

Meunier, T., Sanz, E. P., Tenreiro, M., Ochoa, J., Angulo, A. R., and Buckingham, C. (2019). Observations of Layering Under a Warm-Core Ring in the Gulf of Mexico. *J. Phys. Oceanog.* 49, 3145–3162. doi: 10.1175/JPO-D-18-0138.1

Minakov, A., Keers, H., Kolyukhin, D., and Tengesdal, H. C. (2017). Acoustic Waveform Inversion for Ocean Turbulence. *J. Phys. Oceanog.* 47, 1473–1491. doi: 10.1175/JPO-D-16-0236.1

Mojica, J. F., Sallarès, V., and Biescas, B. (2018). High-Resolution Diapycnal Mixing Map of the Alboran Sea Thermocline From Seismic Reflection Images. *Ocean. Sci.* 14, 403–415. doi: 10.5194/os-14-403-2018

Morozov, E. G., Tarakanov, R. Y., and Frey, D. I. (2021). "Deep Water Masses of the South and North Atlantic," in *Bottom Gravity Currents and Overflows in Deep Channels of the Atlantic Ocean* (Cham: Springer International Publishing), 1–42. doi: 10.1007/978-3-030-83074-8_1

Moum, J. N. (2021). Variations in Ocean Mixing From Seconds to Years. *Annu. Rev. Mar. Sci.* 13, 201–226. doi: 10.1146/annurev-marine-031920-122846

Moum, J. N., and Nash, J. D. (2009). Mixing Measurements on an Equatorial Ocean Mooring. *J. Atmos. Oceanic Tech* 26, 317–336. doi: 10.1175/2008JTECHO617.1

Moum, J., Farmer, D., Smyth, W., Armi, L., and Vagle, S. (2003). Structure and Generation of Turbulence at Interfaces Strained by Internal Solitary Waves Propagating Shoreward Over the Continental Shelf. *J. Phys. Oceanog.* 33, 2093–2112. doi: 10.1175/1520-0485(2003)033<2093:SAGOTA>2.0.CO;2

Müller, P., and Garrett, C. (2002). From Stirring to Mixing in a Stratified Ocean. *Oceanography* 15, 12–19. doi: 10.5670/oceanog.2002.10

Munk, W. H. (1966). Abyssal Recipes. *Deep. Sea. Res. Oceanog. Abstract.* 13, 707–730. doi: 10.1016/0011-7471(66)90602-4

Munk, W. (2006). "Ocean Acoustic Tomography," in *Physical Oceanography*. Eds. M. Jochum and R. Murtugudde (New York, NY: Springer New York), 119–138. doi: 10.1007/0-387-33152-2_8

Munk, W., Armi, L., Fischer, K., and Zachariasen, F. (2000). Spirals on the Sea. *Proc. R. Soc. London. Ser. A: Math. Phys. Eng. Sci.* 456, 1217–1280. doi: 10.1098/rspa.2000.0560

Munk, W., and Wunsch, C. (1979). Ocean Acoustic Tomography: A Scheme for Large Scale Monitoring. *Deep. Sea. Res. Part A. Oceanog. Res. Paper.* 26, 123–161. doi: 10.1016/0198-0149(79)90073-6

Nakamura, Y., Noguchi, T., Tsuji, T., Itoh, S., Niino, H., and Matsuoka, T. (2006). Simultaneous Seismic Reflection and Physical Oceanographic Observations of Oceanic Fine Structure in the Kuroshio Extension Front. *Geophys. Res. Lett.* 33, L23605. doi: 10.1029/2006GL027437

National Research Council (2015). *Sea Change: 2015-2025 Decadal Survey of Ocean Sciences* (Washington, DC: The National Academies Press). doi: 10.17226/21655

National Science Foundation (2016). *NSF Workshop on Portable Seismic Systems and Commercial Seismic Acquisition* (Alexandria, Virginia: Marine Seismic Research Oversight Committee, University-National Oceanographic Laboratory System). Available at: www.nsf.gov/geo/oce/pubs/Seismic_Workshop%20Report_final_2016.pdf

Naveira Garabato, A. C., Frajka-Williams, E. E., Spingys, C. P., Legg, S., Polzin, K. L., Forryan, A., et al. (2019). Rapid Mixing and Exchange of Deep-Ocean

Waters in an Abyssal Boundary Current. *Proc. Natl. Acad. Sci.* 116, 13233–13238. doi: 10.1073/pnas.1904087116

Naveira Garabato, A., and Meredith, M. (2022). "Chapter 1 - Ocean Mixing: Oceanography at a Watershed," in *Ocean Mixing*. Eds. M. Meredith and A. Naveira Garabato (Amsterdam: Elsevier), 1–4. doi: 10.1016/B978-0-12-821512-8.00008-6

Naveira Garabato, A. C., Yu, X., Callies, J., Barkan, R., Polzin, K. L., Frajka-Williams, E. E., et al. (2022). Kinetic Energy Transfers Between Mesoscale and Submesoscale Motions in the Open Ocean's Upper Layers. *J. Phys. Oceanog.* 52, 75–97. doi: 10.1175/JPO-D-21-0099.1

Orsi, A., Johnson, G., and Bullister, J. (1999). Circulation, Mixing, and Production of Antarctic Bottom Water. *Prog. Oceanog.* 43, 55–109. doi: 10.1016/S0079-6611(99)00004-X

Ozmidov, R. V. (1965). On the Turbulent Exchange in a Stably Stratified Ocean. *Izv. Acad. Sci. USSR. Atmos. Ocean. Phys.* 1, 853–860.

Padhi, A., Mallick, S., Fortin, W., Holbrook, W. S., and Blacic, T. M. (2015). 2-D Ocean Temperature and Salinity Images From Pre-Stack Seismic Waveform Inversion Methods: An Example From the South China Sea. *Geophys. J. Int.* 202, 800–810. doi: 10.1093/gji/ggv188

Palmer, M. D., Durack, P. J., Chidichimo, M. P., Church, J. A., Cravatte, S., Hill, K., et al. (2019). Adequacy of the Ocean Observation System for Quantifying Regional Heat and Freshwater Storage and Change. *Front. Mar. Sci.* 6. doi: 10.3389/fmars.2019.00416

Papenberg, C., Klaeschen, D., Krahmann, G., and Hobbs, R. (2010). Ocean Temperature and Salinity Inverted From Combined Hydrographic and Seismic Data. *Geophys. Res. Lett.* 37, L04601. doi: 10.1029/2009GL042115

Pascual, A., Ruiz, S., Olita, A., Troupin, C., Claret, M., Casas, B., et al. (2017). A Multiplatform Experiment to Unravel Meso- and Submesoscale Processes in an Intense Front (AlborEx). *Front. Mar. Sci.* 4. doi: 10.3389/fmars.2017.00039

Piété, H., Marié, L., Marsset, B., Thomas, Y., and Gutscher, M.-A. (2013). Seismic Reflection Imaging of Shallow Oceanographic Structures. *J. Geophys. Res.: Ocean.* 118, 2329–2344. doi: 10.1002/jgrc.20156

Pinheiro, L. M., Song, H., Ruddick, B., Dubert, J., Ambar, I., Mustafa, K., et al. (2010). Detailed 2-D Imaging of the Mediterranean Outflow and Meddies Off W Iberia From Multichannel Seismic Data. *J. Mar. Syst.* 79, 89–100. doi: 10.1016/j.jmarsys.2009.07.004

Pinkel, R. (1979). Observations of Strongly Nonlinear Internal Motion in the Open Sea Using a Range-Gated Doppler Sonar. *J. Phys. Oceanog.* 9, 675–686. doi: 10.1175/1520-0485(1979)009<0675:OOSNIM>2.0.CO;2

Pinkel, R. (2020). The Poisson Link Between Internal Wave and Dissipation Scales in the Thermocline. Part II: Internal Waves, Overturns, and the Energy Cascade. *J. Phys. Oceanog.* 50, 3425–3438. doi: 10.1175/JPO-D-19-0287.1

Polzin, K. L., and Lvov, Y. V. (2011). Toward Regional Characterizations of the Oceanic Internal Wavefield. *Rev. Geophys.* 49, RG4003. doi: 10.1029/2010RG000329

Polzin, K. L., Naveira Garabato, A. C., Huussen, T. N., Sloyan, B. M., and Waterman, S. (2014). Finescale Parameterizations of Turbulent Dissipation. *J. Geophys. Res.: Ocean.* 119, 1383–1419. doi: 10.1002/2013JC008979

Polzin, K. L., Toole, J. M., Ledwell, J. R., and Schmitt, R. W. (1997). Spatial Variability of Turbulent Mixing in the Abyssal Ocean. *Science* 276, 93–96. doi: 10.1126/science.276.5309.93

Proni, J. R., and Apel, J. R. (1975). On the Use of High-Frequency Acoustics for the Study of Internal Waves and Microstructure. *J. Geophys. Res.* 80, 1147–1151. doi: 10.1029/JC080i009p01147

Purkey, S. G., and Johnson, G. C. (2010). Warming of Global Abyssal and Deep Southern Ocean Waters Between the 1990s and 2000s: Contributions to Global Heat and Sea Level Rise Budgets. *J. Climate* 23, 6336–6351. doi: 10.1175/2010JCLI3682.1

Purkey, S. G., and Johnson, G. C. (2012). Global Contraction of Antarctic Bottom Water Between the 1980s and 2000s. *J. Climate* 25, 5830–5844. doi: 10.1175/JCLI-D-11-00612.1

Qiu, B., Chen, S., Klein, P., Wang, J., Torres, H., Fu, L.-L., et al. (2018). Seasonality in Transition Scale From Balanced to Unbalanced Motions in the World Ocean. *J. Phys. Oceanog.* 48, 591–605. doi: 10.1175/JPO-D-17-0169.1

Qiu, B., Nakano, T., Chen, S., and Klein, P. (2017). Submesoscale Transition From Geostrophic Flows to Internal Waves in the Northwestern Pacific Upper Ocean. *Nat. Commun.* 8, 14055. doi: 10.1038/ncomms14055

Ramachandran, S., Tandon, A., and Mahadevan, A. (2014). Enhancement in Vertical Fluxes at a Front by Mesoscale-Submesoscale Coupling. *J. Geophys. Res.: Ocean.* 119, 8495–8511. doi: 10.1002/2014JC010211

Richards, K. J., Whitt, D. B., Brett, G., Bryan, F. O., Feloy, K., and Long, M. C. (2021). The Impact of Climate Change on Ocean Submesoscale Activity. *J. Geophys. Res.: Ocean.* 126, e2020JC016750. doi: 10.1029/2020JC016750

Riley, J. J., and Lindborg, E. (2008). Stratified Turbulence: A Possible Interpretation of Some Geophysical Turbulence Measurements. *J. Atmos. Sci.* 65, 2416–2424. doi: 10.1175/2007JAS2455.1

Riley, J. J., and Lindborg, E. (2012). "Recent Progress in Stratified Turbulence," in: *Ten Chapters in Turbulence*. Eds. P. Davidson, Y. Kaneda and K. Sreenivasan. (Cambridge: Cambridge University Press), 269–317. doi: 10.1017/CBO9781139032810.008

Rocha, C. B., Chereskin, T. K., Gille, S. T., and Menemenlis, D. (2016). Mesoscale to Submesoscale Wavenumber Spectra in Drake Passage. *J. Phys. Oceanog.* 46, 601–620. doi: 10.1175/JPO-D-15-0087.1

Roemmich, D., Alford, M. H., Claustre, H., Johnson, K., King, B., Moum, J., et al. (2019). On the Future of Argo: A Global, Full-Depth, Multi-Disciplinary Array. *Front. Mar. Sci.* 6. doi: 10.3389/fmars.2019.00439

Roemmich, D., Johnson, G. C., Riser, S., Davis, R., Gilson, J., Owens, W. B., et al. (2009). The Argo Program: Observing the Global Ocean With Profiling Floats. *Oceanography* 22, 34–43. doi: 10.5670/oceanog.2009.36

Roemmich, D., Wilson, W. S., Gould, W. J., Owens, W. B., Le Traon, P.-Y., Freeland, H. J., et al. (2022). "Chapter 4 - The Argo Program," in *Partnerships in Marine Science*. Eds. G. Auad and F. K. Wiese (Amsterdam: Elsevier), 53–69. doi: 10.1016/B978-0-323-90427-8.00004-6

Rossby, T. (1969). On Monitoring Depth Variations of the Main Thermocline Acoustically. *J. Geophys. Res.* 74, 5542–5546. doi: 10.1029/JC074i023p05542

Ruan, X., Thompson, A. F., Flexas, M. M., and Sprintall, J. (2017). Contribution of Topographically Generated Submesoscale Turbulence to Southern Ocean Overturning. *Nat. Geosci.* 10, 840–845. doi: 10.1038/ngeo3053

Ruddick, B. (2018). Seismic Oceanography's Failure to Flourish: A Possible Solution. *J. Geophys. Res.: Ocean.* 123, 4–7. doi: 10.1002/2017JC013736

Ruddick, B., Song, H., Dong, C., and Pinheiro, L. (2009). Water Column Seismic Images as Maps of Temperature Gradient. *Oceanography* 22, 192–205. doi: 10.5670/oceanog.2009.19

Rudnick, D. L. (2016). Ocean Research Enabled by Underwater Gliders. *Annu. Rev. Mar. Sci.* 8, 519–541. doi: 10.1146/annurev-marine-122414-033913

Rudnick, D. L., and Cole, S. T. (2011). On Sampling the Ocean Using Underwater Gliders. *J. Geophys. Res.: Ocean.* 116. doi: 10.1029/2010JC006849

Rudnick, D. L., and Martin, J. P. (2002). On the Horizontal Density Ratio in the Upper Ocean. *Dynamic. Atmos. Ocean.* 36, 3–21. doi: 10.1016/S0377-0265(02)00022-2

Sallarès, V., Biescas, B., Buffett, G., Carbonell, R., Dañobeitia, J. J., and Pelegrí, J. L. (2009). Relative Contribution of Temperature and Salinity to Ocean Acoustic Reflectivity. *Geophys. Res. Lett.* 36, L00D06. doi: 10.1029/2009GL040187

Sallarès, V., Mojica, J. F., Biescas, B., Klaeschen, D., and Gràcia, E. (2016). Characterization of the Submesoscale Energy Cascade in the Alboran Sea Thermocline From Spectral Analysis of High-Resolution MCS Data. *Geophys. Res. Lett.* 43, 6461–6468. doi: 10.1002/2016GL069782

Samelson, R. M., and Paulson, C. A. (1988). Towed Thermistor Chain Observations of Fronts in the Subtropical North Pacific. *J. Geophys. Res.: Ocean.* 93, 2237–2246. doi: 10.1029/JC093iC03p02237

Schmitt, R. W., Toole, J. M., Koehler, R. L., Mellinger, E. C., and Doherty, K. W. (1988). The Development of a Fine- and Microstructure Profiler. *J. Atmos. Ocean. Technol.* 5, 484–500. doi: 10.1175/1520-0426(1988)005<0484:TDOAFA>2.0.CO;2

Schönau, M. C., and Rudnick, D. L. (2015). Glider Observations of the North Equatorial Current in the Western Tropical Pacific. *J. Geophys. Res.: Ocean.* 120, 3586–3605. doi: 10.1002/2014JC010595

Schubert, R., Schwarzkopf, F. U., Baschek, B., and Biastoch, A. (2019). Submesoscale Impacts on Mesoscale Agulhas Dynamics. *J. Adv. Model. Earth Syst.* 11, 2745–2767. doi: 10.1029/2019MS001724

Shang, X., Qi, Y., Chen, G., Liang, C., Lueck, R. G., Prairie, B., et al. (2017). An Expendable Microstructure Profiler for Deep Ocean Measurements. *J. Atmos. Ocean. Technol.* 34, 153–165. doi: 10.1175/JTECH-D-16-0083.1

Shcherbina, A. Y., D'Asaro, E. A., Lee, C. M., Klymak, J. M., Molemaker, M. J., and McWilliams, J. C. (2013). Statistics of Vertical Vorticity, Divergence, and Strain

in a Developed Submesoscale Turbulence Field. *Geophys. Res. Lett.* 40, 4706–4711. doi: 10.1002/grl.50919

Shcherbina, A. Y., Sundermeyer, M. A., Kunze, E., D'Asaro, E., Badin, G., Birch, D., et al. (2015). The LatMix Summer Campaign: Submesoscale Stirring in the Upper Ocean. *Bull. Am. Meteorolog. Soc.* 96, 1257–1279. doi: 10.1175/BAMS-D-14-00015.1

Sheen, K., Garabato, A. N., Brearley, J., Meredith, M., Polzin, K., Smeed, D., et al. (2014). Eddy-Induced Variability in Southern Ocean Abyssal Mixing on Climatic Timescales. *Nat. Geosci.* 7, 577. doi: 10.1038/ngeo2200

Sheen, K., White, N., Caulfield, C., and Hobbs, R. (2012). Seismic Imaging of a Large Horizontal Vortex at Abyssal Depths Beneath the Sub-Antarctic Front. *Nat. Geosci.* 5, 542–546. doi: 10.1038/ngeo1502

Sheen, K. L., White, N. J., and Hobbs, R. W. (2009). Estimating Mixing Rates From Seismic Images of Oceanic Structure. *Geophys. Res. Lett.* 36, L00D04. doi: 10.1029/2009GL040106

Sheriff, R. E., and Geldart, L. P. (1995). *Exploration Seismology* (Cambridge: Cambridge University Press). doi: 10.1017/CBO9781139168359

Shroyer, E. L., Nash, J. D., Waterhouse, A. F., and Moum, J. N. (2018). "Measuring Ocean Turbulence," in *Observing the Oceans in Real Time*. Eds. R. Venkatesan, A. Tandon, E. D'Asaro and M. Atmanand (Cham: Springer International Publishing), 99–122. doi: 10.1007/978-3-319-66493-4_6

Shroyer, E. L., Rudnick, D. L., Farrar, J. T., Lim, B., Venayagamoorthy, S. K., Laurent, L. C. S., et al. (2016). Modification of Upper-Ocean Temperature Structure by Subsurface Mixing in the Presence of Strong Salinity Stratification. *Oceanography* 29, 62–71. doi: 10.5670/oceanog.2016.39

Siegelman, L. (2020). Energetic Submesoscale Dynamics in the Ocean Interior. *J. Phys. Oceanog.* 50, 727–749. doi: 10.1175/JPO-D-19-0253.1

Siegelman, L., O'Toole, M., Flexas, M., Rivière, P., and Klein, P. (2019). Submesoscale Ocean Fronts Act as Biological Hotspot for Southern Elephant Seal. *Sci. Rep.* 9, 5588. doi: 10.1038/s41598-019-42117-w

Sloyan, B. M., Wanninkhof, R., Kramp, M., Johnson, G. C., Talley, L. D., Tanhua, T., et al. (2019). The Global Ocean Ship-Based Hydrographic Investigations Program (GO-SHIP): A Platform for Integrated Multidisciplinary Ocean Science. *Front. Mar. Sci.* 6. doi: 10.3389/fmars.2019.00445

Song, H., Chen, J., Pinheiro, L., Ruddick, B., Guan, Y., and Bai, Y. (2018). "Seismic Oceanography," in *Comprehensive Remote Sensing*. Ed. S. Liang (Oxford: Elsevier), 197–230. doi: 10.1016/B978-0-12-409548-9.10398-7

Song, H., Pinheiro, L. M., Ruddick, B., and Teixeira, F. C. (2011). Meddy, Spiral Arms, and Mixing Mechanisms Viewed by Seismic Imaging in the Tagus Abyssal Plain (SW Iberia). *J. Mar. Res.* 69, 827–842. doi: 10.1357/002224011799849309

Sreenivasan, K. R. (1995). On the Universality of the Kolmogorov Constant. *Phys. Fluid.* 7, 2778–2784. doi: 10.1063/1.868656

Steinberg, J. M., Pelland, N. A., and Eriksen, C. C. (2019). Observed Evolution of a California Undercurrent Eddy. *J. Phys. Oceanog.* 49, 649–674. doi: 10.1175/JPO-D-18-0033.1

Stommel, H. (1948). The Westward Intensification of Wind-Driven Ocean Currents. *Eos. Trans. Am. Geophys. Union.* 29, 202–206. doi: 10.1029/TR029i002p00202

Stranne, C., Mayer, L., Weber, T. C., Ruddick, B. R., Jakobsson, M., Jerram, K., et al. (2017). Acoustic Mapping of Thermohaline Staircases in the Arctic Ocean. *Sci. Rep.* 7, 15192. doi: 10.1038/s41598-017-15486-3

Su, Z., Wang, J., Klein, P., Thompson, A. F., and Menemenlis, D. (2018). Ocean Submesoscales as a Key Component of the Global Heat Budget. *Nat. Commun.* 9, 775. doi: 10.1038/s41467-018-02983-w

Swallow, J. C. (1955). A Neutral-Buoyancy Float for Measuring Deep Currents. *Deep. Sea. Res.* 3, 74–81. doi: 10.1016/0146-6313(55)90037-X

Takahashi, A., and Hibiya, T. (2019). Assessment of Finescale Parameterizations of Deep Ocean Mixing in the Presence of Geostrophic Current Shear: Results of Microstructure Measurements in the Antarctic Circumpolar Current Region. *J. Geophys. Res.: Ocean.* 124, 135–153. doi: 10.1029/2018JC014030

Takahashi, A., and Hibiya, T. (2021). Influence of the Distortion of Vertical Wavenumber Spectra on Estimates of Turbulent Dissipation Using the Finescale Parameterization: Observations in the Antarctic Circumpolar Current. *J. Geophys. Res.: Ocean.* 126, e2020JC016613. doi: 10.1029/2020JC016613

Talley, L., Feely, R., Sloyan, B., Wanninkhof, R., Baringer, M., Bullister, J., et al. (2016). Changes in Ocean Heat, Carbon Content, and Ventilation: A Review of the First Decade of GO-SHIP Global Repeat Hydrography. *Annu. Rev. Mar. Sci.* 8, 185–215. doi: 10.1146/annurev-marine-052915-100829

Tang, Q., Gulick, S. P., Sun, J., Sun, L., and Jing, Z. (2020). Submesoscale Features and Turbulent Mixing of an Oblique Anticyclonic Eddy in the Gulf of Alaska Investigated by Marine Seismic Survey Data. *J. Geophys. Res.: Ocean.* 125, e2019JC015393. doi: 10.1029/2019JC015393

Tang, Q., Hobbs, R., Wang, D., Sun, L., Zheng, C., Li, J., et al. (2015). Marine Seismic Observation of Internal Solitary Wave Packets in the Northeast South China Sea. *J. Geophys. Res.: Ocean.* 120, 8487–8503. doi: 10.1002/2015JC011362

Tang, Q., Hobbs, R., Zheng, C., Biescas, B., and Caiado, C. (2016). Markov Chain Monte Carlo Inversion of Temperature and Salinity Structure of an Internal Solitary Wave Packet From Marine Seismic Data. *J. Geophys. Res.: Ocean.* 121, 3692–3709. doi: 10.1002/2016JC011810

Tang, Q., Jing, Z., Lin, J., and Sun, J. (2021). Diapycnal Mixing in the Sub-Thermocline of the Mariana Ridge From High-Resolution Seismic Images. *J. Phys. Oceanog.* 51, 1283–1300. doi: 10.1175/JPO-D-20-0120.1

Tang, Q., Wang, C., Wang, D., and Pawlowicz, R. (2014). Seismic, Satellite, and Site Observations of Internal Solitary Waves in the NE South China Sea. *Sci. Rep.* 4, 5374. doi: 10.1038/srep05374

Tanhua, T., McCurdy, A., Fischer, A., Appeltans, W., Bax, N., Currie, K., et al. (2019). What We Have Learned From the Framework for Ocean Observing: Evolution of the Global Ocean Observing System. *Front. Mar. Sci.* 6. doi: 10.3389/fmars.2019.00471

Thomas, L. N., Tandon, A., and Mahadevan, A. (2008). "Submesoscale Processes and Dynamics," in *Ocean Modeling in an Eddying Regime*, Eds. M. W. Hecht and H. Hasumi (Washington, DC: American Geophysical Union), 17–38. doi: 10.1029/177GM04

Thomas, J., and Yamada, R. (2019). Geophysical Turbulence Dominated by Inertia–Gravity Waves. *J. Fluid. Mechanic.* 875, 71–100. doi: 10.1017/jfm.2019.465

Thompson, A. F., Stewart, A. L., Spence, P., and Heywood, K. J. (2018). The Antarctic Slope Current in a Changing Climate. *Rev. Geophys.* 56, 741–770. doi: 10.1029/2018RG000624

Vallis, G. K. (2017). *Atmospheric and Oceanic Fluid Dynamics: Fundamentals and Large-Scale Circulation* (*2nd edn.*) (Cambridge: Cambridge University Press). doi: 10.1017/9781107588417

van Haren, H. (2018). Grand Challenges in Physical Oceanography. *Front. Mar. Sci.* 5. doi: 10.3389/fmars.2018.00404

Viglione, G. A., Thompson, A. F., Flexas, M. M., Sprintall, J., and Swart, S. (2018). Abrupt Transitions in Submesoscale Structure in Southern Drake Passage: Glider Observations and Model Results. *J. Phys. Oceanog.* 48, 2011–2027. doi: 10.1175/JPO-D-17-0192.1

Vsemirnova, E. A., Hobbs, R. W., and Hosegood, P. (2012). Mapping Turbidity Layers Using Seismic Oceanography Methods. *Ocean. Sci.* 8, 11–18. doi: 10.5194/os-8-11-2012

Vsemirnova, E., Hobbs, R., Serra, N., Klaeschen, D., and Quentel, E. (2009). Estimating Internal Wave Spectra Using Constrained Models of the Dynamic Ocean. *Geophys. Res. Lett.* 36, L00D07. doi: 10.1029/2009GL039598

Wang, D.-P., Flagg, C. N., Donohue, K., and Rossby, H. T. (2010). Wavenumber Spectrum in the Gulf Stream From Shipboard ADCP Observations and Comparison With Altimetry Measurements. *J. Phys. Oceanog.* 40, 840–844. doi: 10.1175/2009JPO4330.1

Waterhouse, A. F., MacKinnon, J. A., Nash, J. D., Alford, M. H., Kunze, E., Simmons, H. L., et al. (2014). Global Patterns of Diapycnal Mixing From Measurements of the Turbulent Dissipation Rate. *J. Phys. Oceanog.* 44, 1854–1872. doi: 10.1175/JPO-D-13-0104.1

Waterman, S., Polzin, K. L., Naveira Garabato, A. C., Sheen, K. L., and Forryan, A. (2014). Suppression of Internal Wave Breaking in the Antarctic Circumpolar Current Near Topography. *J. Phys. Oceanog.* 44, 1466–1492. doi: 10.1175/JPO-D-12-0154.1

Wei, J., Gunn, K. L., and Reece, R. (2022). Mid-Ocean Ridge and Storm Enhanced Mixing in the Central South Atlantic Thermocline. *Front. Mar. Sci.* 8. doi: 10.3389/fmars.2021.771973

Wenegrat, J. O., Callies, J., and Thomas, L. N. (2018). Submesoscale Baroclinic Instability in the Bottom Boundary Layer. *J. Phys. Oceanog.* 48, 2571–2592. doi: 10.1175/JPO-D-17-0264.1

Whalen, C. B., de Lavergne, C., Naveira Garabato, A. C., Klymak, J. M., MacKinnon, J. A., and Sheen, K. L. (2020). Internal Wave-Driven Mixing:

Governing Processes and Consequences for Climate. *Nat. Rev. Earth Environ.* 1, 606–621. doi: 10.1038/s43017-020-0097-z

Whalen, C. B., MacKinnon, J. A., Talley, L. D., and Waterhouse, A. F. (2015). Estimating the Mean Diapycnal Mixing Using a Finescale Strain Parameterization. *J. Phys. Oceanog.* 45, 1174–1188. doi: 10.1175/JPO-D-14-0167.1

Whalen, C. B., Talley, L. D., and MacKinnon, J. A. (2012). Spatial and Temporal Variability of Global Ocean Mixing Inferred From Argo Profiles. *Geophys. Res. Lett.* 39, L18612. doi: 10.1029/2012GL053196

Wijesekera, H., Padman, L., Dillon, T., Levine, M., Paulson, C., and Pinkel, R. (1993). The Application of Internal-Wave Dissipation Models to a Region of Strong Mixing. *J. Phys. Oceanog.* 23, 269–286. doi: 10.1175/1520-0485(1993)023<0269:TAOIWD>2.0.CO;2

Wong, A. P. S., Wijffels, S. E., Riser, S. C., Pouliquen, S., Hosoda, S., Roemmich, D., et al. (2020). Argo Data 1999–2019: Two Million Temperature-Salinity Profiles and Subsurface Velocity Observations From a Global Array of Profiling Floats. *Front. Mar. Sci.* 7. doi: 10.3389/fmars.2020.00700

Woods, J. D. (1968). Wave-Induced Shear Instability in the Summer Thermocline. *J. Fluid. Mechanic.* 32, 791–800. doi: 10.1017/S0022112068001035

Wu, L., Cai, W., Zhang, L., Nakamura, H., Timmermann, A., Joyce, T., et al. (2012). Enhanced Warming Over the Global Subtropical Western Boundary Currents. *Nat. Climate Change* 2, 161–166. doi: 10.1038/nclimate1353

Wunsch, C. (1997). The Vertical Partition of Oceanic Horizontal Kinetic Energy. *J. Phys. Oceanog.* 27, 1770–1794. doi: 10.1175/1520-0485(1997)027<1770:TVPOOH>2.0.CO;2

Wunsch, C. (2020). Advance in Global Ocean Acoustics. *Science* 369, 1433–1434. doi: 10.1126/science.abe0960

Wunsch, C., and Ferrari, R. (2004). Vertical Mixing, Energy, and the General Circulation of the Oceans. *Annu. Rev. Fluid. Mechanic.* 36, 281–314. doi: 10.1146/annurev.fluid.36.050802.122121

Wunsch, C., and Heimbach, P. (2014). Bidecadal Thermal Changes in the Abyssal Ocean. *J. Phys. Oceanog.* 44, 2013–2030. doi: 10.1175/JPO-D-13-096.1

Wu, W., Zhan, Z., Peng, S., Ni, S., and Callies, J. (2020). Seismic Ocean Thermometry. *Science* 369, 1510–1515. doi: 10.1126/science.abb9519

Xiao, W., Sheen, K. L., Tang, Q., Shutler, J., Hobbs, R., and Ehmen, T. (2021). Temperature and Salinity Inverted for a Mediterranean Eddy Captured With Seismic Data, Using a Spatially Iterative Markov Chain Monte Carlo Approach. *Front. Mar. Sci.* 8. doi: 10.3389/fmars.2021.734125

Yang, C.-F., Chi, W.-C., and van Haren, H. (2021). Deep-Sea Turbulence Evolution Observed by Multiple Closely Spaced Instruments. *Sci. Rep.* 11, 3919. doi: 10.1038/s41598-021-83419-2

Yang, H., Lohmann, G., Wei, W., Dima, M., Ionita, M., and Liu, J. (2016). Intensification and Poleward Shift of Subtropical Western Boundary Currents in a Warming Climate. *J. Geophys. Res.: Ocean.* 121, 4928–4945. doi: 10.1002/2015JC011513

Yu, X., Naveira Garabato, A. C., Martin, A. P., Buckingham, C. E., Brannigan, L., and Su, Z. (2019). An Annual Cycle of Submesoscale Vertical Flow and Restratification in the Upper Ocean. *J. Phys. Oceanog.* 49, 1439–1461. doi: 10.1175/JPO-D-18-0253.1

Zanna, L., and Bolton, T. (2021). "Deep Learning of Unresolved Turbulent Ocean Processes in Climate Models," in *Deep Learning for the Earth Sciences*. Eds. G. Camps-Valls, D. Tuia, X. X. Zhu and M. Reichstein (Hoboken: John Wiley Sons, Ltd), 298–306. doi: 10.1002/9781119646181.ch20

Zilberman, N., King, B., Purkey, S., Thierry, V., and Roemmich, D. (2019) *Report on the 2nd Deep Argo Implementation Workshop. Hobart, May 13–15th 2019.* Available at: www.argo.ucsd.edu/wp-content/uploads/sites/361/2020/04/DAIW2report.pdf.

Zou, Z., Bakhtiari Rad, P., Macelloni, L., and Zhang, L. (2020). Three-Dimensional Acoustic Imaging of the Temporal Evolution of Internal Wave Fields in the Gulf of Mexico. *Earth Space. Sci. Open Arch.*. doi: 10.1002/essoar.10505004.1

Zou, Z., Bakhtiari Rad, P., Macelloni, L., and Zhang, L. (2021). Temporal and Spatial Variations in Three-Dimensional Seismic Oceanography. *Ocean. Sci.* 17, 1053–1066. doi: 10.5194/os-17-1053-2021

Conflict of Interest: The authors declare that the research was conducted in the absence of any commercial or financial relationships that could be construed as a potential conflict of interest.

Advantages of publishing in Frontiers

OPEN ACCESS
Articles are free to read for greatest visibility and readership

FAST PUBLICATION
Around 90 days from submission to decision

HIGH QUALITY PEER-REVIEW
Rigorous, collaborative, and constructive peer-review

TRANSPARENT PEER-REVIEW
Editors and reviewers acknowledged by name on published articles

Frontiers
Avenue du Tribunal-Fédéral 34
1005 Lausanne | Switzerland

Visit us: www.frontiersin.org
Contact us: frontiersin.org/about/contact

REPRODUCIBILITY OF RESEARCH
Support open data and methods to enhance research reproducibility

DIGITAL PUBLISHING
Articles designed for optimal readership across devices

FOLLOW US
@frontiersin

IMPACT METRICS
Advanced article metrics track visibility across digital media

EXTENSIVE PROMOTION
Marketing and promotion of impactful research

LOOP RESEARCH NETWORK
Our network increases your article's readership